frontiers | Research Topics

Rock landslide risk assessment, stability analysis and monitoring for the development of early warning systems and reinforcement measures

Edited by
Mowen Xie, Yan Du, Yujing Jiang and Bo Li

Published in
Frontiers in Earth Science
Frontiers in Environmental Science

FRONTIERS EBOOK COPYRIGHT STATEMENT

The copyright in the text of individual articles in this ebook is the property of their respective authors or their respective institutions or funders. The copyright in graphics and images within each article may be subject to copyright of other parties. In both cases this is subject to a license granted to Frontiers.

The compilation of articles constituting this ebook is the property of Frontiers.

Each article within this ebook, and the ebook itself, are published under the most recent version of the Creative Commons CC-BY licence. The version current at the date of publication of this ebook is CC-BY 4.0. If the CC-BY licence is updated, the licence granted by Frontiers is automatically updated to the new version.

When exercising any right under the CC-BY licence, Frontiers must be attributed as the original publisher of the article or ebook, as applicable.

Authors have the responsibility of ensuring that any graphics or other materials which are the property of others may be included in the CC-BY licence, but this should be checked before relying on the CC-BY licence to reproduce those materials. Any copyright notices relating to those materials must be complied with.

Copyright and source acknowledgement notices may not be removed and must be displayed in any copy, derivative work or partial copy which includes the elements in question.

All copyright, and all rights therein, are protected by national and international copyright laws. The above represents a summary only. For further information please read Frontiers' Conditions for Website Use and Copyright Statement, and the applicable CC-BY licence.

ISSN 1664-8714
ISBN 978-2-8325-1194-7
DOI 10.3389/978-2-8325-1194-7

About Frontiers

Frontiers is more than just an open access publisher of scholarly articles: it is a pioneering approach to the world of academia, radically improving the way scholarly research is managed. The grand vision of Frontiers is a world where all people have an equal opportunity to seek, share and generate knowledge. Frontiers provides immediate and permanent online open access to all its publications, but this alone is not enough to realize our grand goals.

Frontiers journal series

The Frontiers journal series is a multi-tier and interdisciplinary set of open-access, online journals, promising a paradigm shift from the current review, selection and dissemination processes in academic publishing. All Frontiers journals are driven by researchers for researchers; therefore, they constitute a service to the scholarly community. At the same time, the *Frontiers journal series* operates on a revolutionary invention, the tiered publishing system, initially addressing specific communities of scholars, and gradually climbing up to broader public understanding, thus serving the interests of the lay society, too.

Dedication to quality

Each Frontiers article is a landmark of the highest quality, thanks to genuinely collaborative interactions between authors and review editors, who include some of the world's best academicians. Research must be certified by peers before entering a stream of knowledge that may eventually reach the public - and shape society; therefore, Frontiers only applies the most rigorous and unbiased reviews. Frontiers revolutionizes research publishing by freely delivering the most outstanding research, evaluated with no bias from both the academic and social point of view. By applying the most advanced information technologies, Frontiers is catapulting scholarly publishing into a new generation.

What are Frontiers Research Topics?

Frontiers Research Topics are very popular trademarks of the *Frontiers journals series*: they are collections of at least ten articles, all centered on a particular subject. With their unique mix of varied contributions from Original Research to Review Articles, Frontiers Research Topics unify the most influential researchers, the latest key findings and historical advances in a hot research area.

Find out more on how to host your own Frontiers Research Topic or contribute to one as an author by contacting the Frontiers editorial office: frontiersin.org/about/contact

Rock landslide risk assessment, stability analysis and monitoring for the development of early warning systems and reinforcement measures

Topic editors

Mowen Xie — University of Science and Technology Beijing, China
Yan Du — University of Science and Technology Beijing, China
Yujing Jiang — Nagasaki University, Japan
Bo Li — Tongji University, China

Citation

Xie, M., Du, Y., Jiang, Y., Li, B., eds. (2023). *Rock landslide risk assessment, stability analysis and monitoring for the development of early warning systems and reinforcement measures*. Lausanne: Frontiers Media SA.
doi: 10.3389/978-2-8325-1194-7

Table of contents

frontiers | Frontiers in Earth Science

TYPE Editorial
PUBLISHED 16 December 2022
DOI 10.3389/feart.2022.1118991

Check for updates

OPEN ACCESS

EDITED AND REVIEWED BY
Gordon Woo,
Risk Management Solutions,
United Kingdom

*CORRESPONDENCE
Yan Du,
mutulei@163.com

SPECIALTY SECTION
This article was submitted to Geohazards and Georisks, a section of the journal Frontiers in Earth Science

RECEIVED 08 December 2022
ACCEPTED 09 December 2022
PUBLISHED 16 December 2022

CITATION
Xie M, Du Y, Jiang Y, Li B, Chicas SD and Ding J (2022), Editorial: Rock landslide risk assessment, stability analysis and monitoring for the development of early warning systems and reinforcement measures.
Front. Earth Sci. 10:1118991.
doi: 10.3389/feart.2022.1118991

COPYRIGHT
© 2022 Xie, Du, Jiang, Li, Chicas and Ding. This is an open-access article distributed under the terms of the Creative Commons Attribution License (CC BY). The use, distribution or reproduction in other forums is permitted, provided the original author(s) and the copyright owner(s) are credited and that the original publication in this journal is cited, in accordance with accepted academic practice. No use, distribution or reproduction is permitted which does not comply with these terms.

Editorial: Rock landslide risk assessment, stability analysis and monitoring for the development of early warning systems and reinforcement measures

Mowen Xie[1], Yan Du[1]*, Yujing Jiang[2], Bo Li[3], Santos Daniel Chicas[4] and Junhui Ding[1]

[1]School of Civil and Resource Engineering, University of Science and Technology Beijing, Beijing, China, [2]State Key Laboratory of Mining Disaster Prevention and Control, Shandong University of Science and Technology, Qingdao, China, [3]School of Civil Engineering, Tongji University, Shanghai, China, [4]Integrative Research Institute on Transformations of Human-Environment Systems, Humboldt-Universität zu Berlin, Berlin, Germany

KEYWORDS

rock landslide, unstable rock mass, early identification, warning technology, stability analysis, reinforcement measures

Editorial on the Research Topic
Rock landslide risk asssessment, stability analysis and monitoring for the development of early warning systems and reinforcement measures

Introduction

Rock landslide is one of the common geological disasters in the world, characterized by complex causes, wide distribution, strong concealment and suddenness, which result in great harm to human life and property (Corominas et al., 2005; Perkins, 2012; Ferrari et al., 2016). Yet, the early identification and warning technology of rock landslides have been difficult to effectively achieve. For instance, in China over 15,734 rock landslides occurred from 2011–2020, which caused approximately 4,394 casualties (Sreelakshmi et al., 2022). Therefore, it has important theoretical significance and application value to carry out a risk assessment and stability analysis for rock landslides, realize its early warning and implement effective control measures.

Based on research on the causal mechanism and early warning of rock landslides or collapse, it was concluded that the quantitative identification and fuzzy evaluation of rock bridges are the main controlling factors of these disasters (Du et al., 2021a). This innovative concepts in conjunction with technology have been applied in the identification of dangerous rocks, achieving remarkable results (Du et al., 2021b;

Chen et al., 2021; Huo et al., 2021; Du and Xie, 2022). However, there are still many deficiencies in the quantitative identification of rock landslides, real-time stability evaluation, and monitoring indicators that can be applied in the field. Recently, new monitoring technologies, theoretical models of instability and multi-source monitoring indicators provide new opportunities for early identification, monitoring and early warning of rock landslides (Colombero et al., 2018; Francesco et al., 2018; Jan et al., 2018; Jia et al., 2019; Bolla and Paronuzzi, 2020; Du et al., 2020; Gebremedhin et al., 2020). This Research Topic aims to present the latest risk assessment methods for identifying dangerous rocks, dynamic stability assessment techniques, early monitoring and warning systems, and reinforcement measures.

Identification of unstable rock masses

Unstable rock is a rock in a state of instability, which is one of the common types of the hidden danger points of geological hazards in hilly areas (Skrzypczak et al., 2021). Exfoliation of rock deteriorates cliffs through the formation and subsequent opening of fractures, which in turn can lead to potentially hazardous rockfalls. Although, a number of mechanisms are known to trigger rockfalls, many rockfalls occur during periods when likely triggers such as precipitation, seismic activity and freezing conditions are absent (Collins and Stock, 2016). The quantitative identification of unstable rock mass is the premise of rock mass monitoring and early warning. Due to many difficulties in rock bridge damage identification and rock mass dynamic stability evaluation, it is still impossible to objectively and accurately identify high-risk dangerous rock mass from the mechanical point of view at this stage.

In this Research Topic, we systematically carried out research on the rapid identification technology, method and discrimination system of unstable rock mass. By monitoring the dynamic characteristic parameters of the structure (such as natural vibration frequency), Jia et al. carried out research on the quantitative identification test of unstable rock mass. Firstly, through theoretical derivation and experimental verification, they established the quantitative relationship between rock mass, foundation reaction coefficient, rock burial depth and horizontal natural vibration frequency. The combination of the research results and the limit equilibrium model can realize the stability evaluation of the unstable rock based on the natural vibration frequency, and the safety factor can be monitored. Secondly, they present a dynamic characteristic model of rock tilting and identify the quantitative and qualitative relationship between dynamic characteristic parameters and the bonded area of the structural plane, which can be used to evaluate the damage degree of the structural surface of the overturned dangerous rock.

Although, there are many technical means for rapid identification of unstable rock mass, there are still some deficiencies in the quantitative identification of unstable rock mass from the aspect of mechanical indicators. Through triaxial compression tests on rock specimens with different bedding angles under different confining pressures, Zhang et al. studied the fracture characteristics and strength criteria of layered sandstone. Luo et al. comprehensively analyzed the influence of filling degree and shape fluctuation degree on the normal deformation characteristics of filling rock joints. Based on the multi boundary blasting theory, Shi et al. determined the theoretical value of the critical damage width of rock wall demolition blasting. On the basis of predecessors, Luo et al. conducted shear strength tests on weak intercalated rock joints with different filling degrees and water content under multi-stage normal stress. These studies provide theoretical reference for rapid quantitative identification of dangerous rock mass.

Dynamic stability assessment

Generally speaking, the dynamic stability evaluation technology of rock mass is the basis for effective implementation of monitoring and early warning. The whole process of rock mass from stability to collapse is also accompanied by real-time degradation of strength. The occurrence and development of damage and fracture of the main structural plane is the key to the study of collapse disaster mechanism and early warning prevention (Chen et al., 2015; Du et al., 2019a). Therefore, the identification and dynamic monitoring of rock bridge damage is one of the key problems to be solved in the early warning of rock collapse disaster.

Freeze-thaw cycles can heavily damage the internal structures of rocks. To explore damage evolution in granite in a freeze-thaw environment, Li et al. took a granite specimen of Linzhi area, Tibet as the research object, and analyzed the ro ck freezing and thawing damage by combining computed tomography scanning and three-dimensional visualization. Ai et al. introduced the strain-softening model and the vibration deterioration model to express the attenuation law of rock strength parameters, making the slope stability evaluation results more accurate and reliable. Song et al. put forward a mesh free particle approach named smoothed particle hydrodynamics method and improved the damage and failure process of rock slope to better describe the mechanism of brittle failure of rock slope.

At present, mature stability analysis methods for rock landslides have been developed and applied in engineering practice. Zhao et al. put forward and verified the effectiveness of limit equilibrium method in slope stability analysis of Tanjianshan Gold Mine. Based on GIS, Yu et al. established a three-dimensional limit equilibrium model for slope stability analysis, which provides a theoretical basis for the establishment of three-dimensional symmetric slope limit equilibrium method. Xu et al. proposes a method to

determine the stability stage of creeping landslides as per their displacement characteristics. Based on this, a stability stage criterion method for landslide is formed.

Early monitoring and warning systems

Rock mass is an extremely complex structure. Its failure is not only controlled by two major internal control factors, but also affected by a variety of external disaster causing factors. Therefore, only by collecting more information on disaster causing factors through a variety of new monitoring technologies can the early warning and prevention of collapse disasters be effectively realized (Du et al., 2019b). Compared with so many information and data requirements, the existing monitoring technologies that can be used in practical projects are still relatively simple. The results in many technical problems in obtaining key information of internal disasters in rock mass, such as internal fractures of rock mass, rock bridge penetration rate, *etc.* Based on the critical deceleration theory, Tang et al. proposed that the CSD index can be used as a monitoring and early warning for the stability of field geotechnical engineering. Jin et al. applied the *in situ* stress measurement technology for the long-term monitoring of induced stress in slope engineering, and proposed a dual temperature compensation circuit and experimental calibration technology to improve the measurement accuracy. Jiang et al. proposed a new prediction model combining variable selection, sparrow search algorithm, and deep extreme learning machine. Minglei et al. summarized the typical deformation and failure modes of the tunnel, providing technical support for identifying landslide types through tunnel deformation characteristics in practical engineering applications.

Rock mass collapse is usually the dynamic failure caused by the continuous reduction of the bonding degree between rock mass and its slope. In this changing process, high-precision stress and strain monitoring and corresponding environmental parameter monitoring have certain effect in identifying collapse (Zhao et al., 2022). Based on this concept, Na et al. investigated mechanical creep characteristics and fracture evolution processes in rock masses with different fracture angles, lengths, and rock bridge dip angles. Zhang et al. investigated the creep behaviour of deep soft rocks and siltstone-like materials subjected to different unloading confining pressures coupled with a high stress field and seepage. All these provide a theoretical basis for the study of creep fracture law of rock mass and warning system of rock collapse.

Reinforcement measures

For many years, emergency response and post-event construction of structural measures were the main components of natural hazard management. In the past decades, an integrated risk management approach (IRM) emphasizing risk rather than hazards has been developed (Blaikie et al., 2004). IRM involves three main components (Christine et al., 2017): 1) Preparedness for a natural hazard event. 2) Response to an event. 3) Recovery after an event includes event analysis and permanent reconstruction. In this Research Topic, Jiaxing et al. proposed a set of building reinforcement and community elasticity enhancement methods that can resist slope deformation. In addition, a three-level disaster emergency setting system has been established in the urban area around the open-pit mine, and a disaster prevention and disaster resistance enhancement strategy has been established in the communities around the slope, so as to promote sustainable urban development.

In terms of rock landslide prevention and management, Du et al. introduced the characteristics, application, research methods and practical cases of anchor bolts, and looked forward to their application prospects in slope engineering. Chen et al. studied the reinforcement effect of bolts with negative Poisson's ratio on rocks and believed that this would be one of the development directions of bolt materials in the future. Yang et al. use phosphogypsum to prepare cementitious materials for backfilling the goaf, which provides a practical reference for the treatment of landslides. Guangming et al. explored the law of stratum collapse and surface settlement caused by the boulder in the process of tunnel excavation, which provided a theoretical basis for the protection of rock collapse.

Author contributions

MX: Conceptualization, and Writing—Review and Editing; YD: Conceptualization, Data Curation, Writing—Original Draft, Writing—Review and Editing and Funding acquisition; YJ: Writing—Review and Editing; BL: Writing—Review and Editing; SDC: Writing—Review and Editing; JD: Data Curation, Writing—Original Draft and Writing —Review and Editing.

Acknowledgments

The authors gratefully acknowledge the financial support from the National Key Research and Development Project of China (2018YFE0101100), National Natural Science Foundation of China (41702371), Project Supported by State Key Laboratory of Earth Surface Processes and Resource Ecology (2022-KF-01), and State Key Laboratory for GeoMechanics and Deep Underground Engineering, China University of Mining and Technology, Beijing (SKLGDUEK2130).

Conflict of interest

The authors declare that the research was conducted in the absence of any commercial or financial relationships that could be construed as a potential conflict of interest.

Publisher's note

All claims expressed in this article are solely those of the authors and do not necessarily represent those of their affiliated organizations, or those of the publisher, the editors and the reviewers. Any product that may be evaluated in this article, or claim that may be made by its manufacturer, is not guaranteed or endorsed by the publisher.

References

Blaikie, P., Cannon, T., Davis, I., and Wisner, B. (2004). *At Risk: Natural hazards, people's vulnerability and disasters*. 2nd ed. England,UK: Routledge. doi:10.4324/9780203714775

Bolla, A., and Paronuzzi, P. (2020). Numerical investigation of the pre-collapse behavior and internal damage of an unstable rock slope. *Rock Mech. Rock Eng.* 53 (5), 2279–2300. doi:10.1007/s00603-019-02031-z

Chen, C., Xie, M. W., Jiang, Y. J., Jia, B., and Du, Y. (2021). A new method for quantitative identification of potential landslide. *Soils Found.* 61 (5), 1475–1479. doi:10.1016/j.sandf.2021.07.004

Chen, W., Xu, Z. M., and Liu, W. L. (2015). Mechanical model and failure mechanism of unstable cantilevered rock blocks due to differential weathering. *Rock Soil Mech.* 36 (1), 195–204. doi:10.16285/j.rsm.2015.01.027

Christine, M., Peter, B., Massimiliano, S., Stoffel, M., Sudmeier-Rieux, K., and Dorren, L. (2017). Ecosystem-based disaster risk reduction in mountains. *Earth-Sci. Rev.* 177, 497–513. doi:10.1016/j.earscirev.2017.12.011

Collins, B. D., and Stock, G. M. (2016). Rockfall triggering by cyclic thermal stressing of exfoliation fractures. *Nat. Geosci.* 9 (5), 395–400. doi:10.1038/NGEO2686

Colombero, C., Comina, C., Vinciguerra, S., and Benson, P. M. (2018). Microseismicity of an unstable rock mass: From field monitoring to laboratory testing. *J. Geophys. Res.-Solid Earth* 123 (2), 1673–1693. doi:10.1002/2017JB014612

Corominas, J., Copons, R., Moya, J., Vilaplana, J. M., Altimir, J., and Amigo, J. (2005). Quantitative assessment of the residual risk in a rockfall protected area. *Landslides* 2, 343–357. doi:10.1007/s10346-005-0022-z

Du, Y., Huo, L., Xie, M., Jiang, Y., Jia, B., and Cong, X. (2021b). Monitoring and early warning experiment of rock collapse. *J. Theor. App Mech.* 53 (04), 1212–1221. doi:10.6052/0459-1879-20-441

Du, Y., Lu, Y., Xie, M., and Jia, J. (2020). A new attempt for early warning of unstable rocks based on vibration parameters. *Bull. Eng. Geol. Environ.* 79 (8), 4363–4368. doi:10.1007/s10064-020-01839-2

Du, Y., Wu, Z. X., and Xie, M. W. (2019b). Early-warning method of rock collapse and its experimental verification. *J. China Coal Soc.* 44 (10), 3069–3075. doi:10.13225/j.cnki.jccs.2018.1467

Du, Y., and Xie, M. W. (2022). Indirect method for the quantitative identification of unstable rock. *Nat. Hazards* 112 (1), 1005–1012. doi:10.1007/s11069-021-05197-4

Du, Y., Xie, M. W., and Jiang, Y. J. (2021a). A review of research on the mechanism and early warning of rock collapse disasters. *Metal. Mines* 2021 (01), 106–119. doi:10.19614/j.cnki.jsks.202101008

Du, Y., Xie, M. W., Jiang, Y. J., Liu, W., Liu, R., Liu, Q., et al. (2019a). Research progress on dynamic monitoring index for early warning of rock collapse. *Chin. J. Eng.* 41 (4), 427–435. doi:10.13374/j.issn2095-9389.2019.04.002

Ferrari, F., Giacomini, A., and Thoeni, K. (2016). Qualitative rockfall hazard assessment: A comprehensive review of current practices. *Rock Mech. Rock Eng.* 49, 2865–2922. doi:10.1007/s00603-016-0918-z

Francesco, P., Ali, T., Roman, M., Naumov, D., Miao, X. Y., Kolditz, O., et al. (2018). Experimental characterization and numerical modelling of fracture processes in granite. *Int. J. Solids Struct.* 163, 102–116. doi:10.1016/j.ijsolstr.2018.12.019

Gebremedhin, B., Mulubrhan, K., and Nawal, A. (2020). Landslide susceptibility mapping and rock slope stability assessment using frequency ratio and kinematic analysis in the mountains of Mgulat area, Northern Ethiopia. *Bull. Eng. Geol. Environ.* 80, 285–301. doi:10.1007/s10064-020-01905-9

Huo, L. C., Du, Y., and Xie, M. W. (2021). Unstable rock mass identification method based on time and frequency domain dynamic parameters. *Chin. J. Rock Mech. Eng.* 40 (S2), 3156–3162. doi:10.13722/j.cnki.jrme.2021.0337

Jan, B., Valentin, G., Jeffrey, R. M., and Donat, F. (2018). Ambient vibration characterization and monitoring of a rock slope close to collapse. *Geophys. J. Int.* 212, 297–310. doi:10.1093/gji/ggx424

Jia, B., Wu, Z., and Du, Y. (2019). Real-time stability assessment of unstable rocks based on fundamental natural frequency. *Int. J. Rock Mech. Min. Sci.* 124, 104134. doi:10.1016/j.ijrmms.2019.104134

Perkins, S. (2012). Death toll from landslides vastly underestimated. *Nat. News* 8, 1–1. doi:10.1038/nature.2012.11140

Skrzypczak, I., Kokoszka, W., Zientek, D., Tang, Y., and Kogut, J. (2021). Landslide hazard assessment map as an element supporting spatial planning: The flysch carpathians region study. *Remote Sens.* 13 (2), 317. doi:10.3390/rs13020317

Sreelakshmi, S., Vinod Chandra, S. S., and Shaji, E. (2022). Landslide identification using machine learning techniques: Review, motivation, and future prospects. *Earth Sci. Inf.* 15, 2063–2090. doi:10.1007/s12145-022-00889-2

Zhao, M. H., Liu, J. Y., and Zhao, H. (2022). Stability analysis of rock slopes based on MSDP criterion. *Chin. J. Rock Mech. Eng.* 41 (01), 10–18. doi:10.13722/j.cnki.jrme.2021.0362

frontiers | Frontiers in Earth Science

ORIGINAL RESEARCH
published: 04 April 2022
doi: 10.3389/feart.2022.879332

Fracture Characteristics and Anisotropic Strength Criterion of Bedded Sandstone

Liang Zhang[1,2], Fujun Niu[1], Minghao Liu[1]*, Xin Ju[1,2], Zhiwei Wang[3], Jinchang Wang[3] and Tianchun Dong[3]*

[1]State Key Laboratory of Frozen Soil Engineering, Northwest Institute of Eco-Environment and Resources, Chinese Academy of Sciences, Lanzhou, China, [2]University of Chinese Academy of Sciences, Beijing, China, [3]China Railway Qinghai-Tibet Group Co., Ltd., China National Railway Group Co., Ltd., Xining, China

Bedded sandstone is classified as sedimentary rock, which is a typical bedded rock with obvious layered structure characteristics. Bedded rocks formed different bedding orientations in the long and complicated geological tectonic evolution and thus have anisotropic mechanical characteristics. Therefore, the strength anisotropy of bedded sandstone depends on the bedding dip angles. In this study, the fracture characteristics and strength criterion of bedded sandstone were studied by triaxial compression tests on rock specimens with different bedding dip angles under different confining pressure. The test results show that the failure mode and strength of the bedded sandstone are related to the bedding dip angles, showing obvious anisotropy. The experimental data are broadly in line with the Jaeger's surface of weakness (JPW) model. However, considering the difference in the strength of sandstone specimens with horizontal bedding dip ($\beta = 0^{\circ}$) and vertical bedding dip ($\beta = 90^{\circ}$), an improved JPW model is proposed to distinguish the strength criteria for the aforementioned differences. On the basis of considering the nonlinear relationship between confining pressure and rock strength, the JPW model is improved accordingly to make it suitable for predicting the strength behavior of bedded rocks.

Keywords: bedded rock, fracture characteristics, anisotropic, JPW, strength criterion

OPEN ACCESS

Edited by:
Bo Li,
Tongji University, China

Reviewed by:
Fei Song,
Universitat Politecnica de Catalunya, Spain
Siyuan Zhao,
Sichuan University, China

***Correspondence:**
Fujun Niu
niufujun@lzb.ac.cn
Minghao Liu
liuminghao@lzb.ac.cn

Specialty section:
This article was submitted to Geohazards and Georisks, a section of the journal Frontiers in Earth Science

Received: *19 February 2022*
Accepted: *07 March 2022*
Published: *04 April 2022*

Citation:
Zhang L, Niu F, Liu M, Ju X, Wang Z, Wang J and Dong T (2022) Fracture Characteristics and Anisotropic Strength Criterion of Bedded Sandstone. Front. Earth Sci. 10:879332. doi: 10.3389/feart.2022.879332

1 INTRODUCTION

There is a long tradition of research on the structure of rocks. In the Earth's lithosphere, the main components are magmatic rocks, metamorphic rocks, and sedimentary rocks. The sedimentary rocks with a special bedded structure are distributed in two-thirds of the natural land (Blenkinsop, 2000). Rocks show anisotropy on micro- and macroscales. The combination of rock components and mineral aggregates has a great influence on the anisotropy of rock mechanics. Therefore, when considering the mechanical properties of rock, it is necessary to take into account its structural type. In practical engineering application, a set of comprehensive physical and mechanical parameters for a certain range of rock is usually proposed for designing calculation, but the relationship between anisotropy of rock and the condition of multiple engineering forces is rarely considered (Cheng et al., 2015). The anisotropic characteristics of the rock have a great impact on civil engineering, mining, oil exploration, nuclear waste storage, and other projects (Li et al., 2018; Winn et al., 2019; Hu et al., 2021; Zhang et al., 2021). As shown in **Figure 1A**, for tunnel engineering, the angle between the direction of tunnel axis and the bedding orientations has a great influence on the failure mode of the

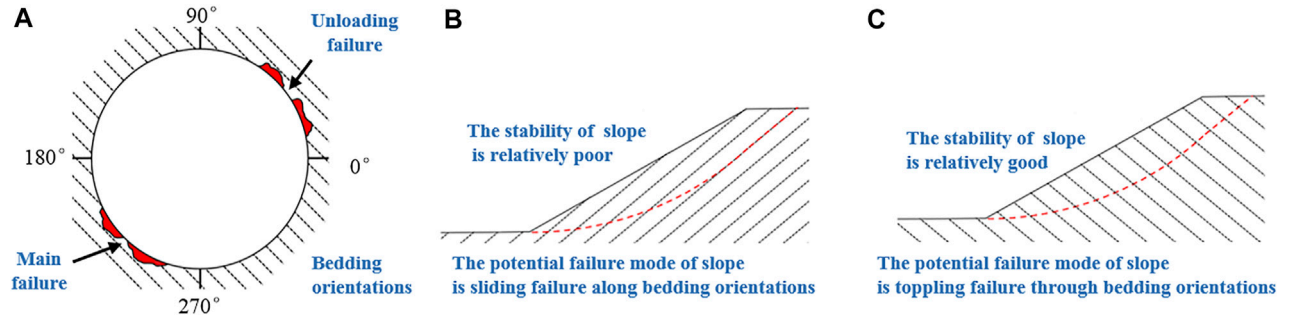

FIGURE 1 | Influence of the anisotropy of rock mass on the tunnel failure mode and the stability of slope. **(A)** Failure mode of the surrounding rock after tunnel excavation; **(B)** Stability analysis of bedded rock slope with small difference between slope angle and bedding orientation **(C)** Stability analysis of bedded rock slope with large difference between slope angle and bedding orientation.

surrounding rock and the bearing mode of the supporting structure after tunnel excavation. As shown in **Figures 1B,C**, in order to evaluate the stability of bedded rock slopes with two different bedding orientations, the physical and mechanical parameters used for strength and deformation analysis should be analyzed according to the bedding orientations of rock.

The structural characteristics of bedded rock are due to the symmetrical arrangement of its crystal structures, and its mechanical behavior can be described by five independent elastic constants (Dieter, 1987). The rock bedding formation makes the sedimentary rock possess the initial anisotropy of the microlevel surface, which can be simplified to a transversely isotropic material, owing to its symmetry arrangement (Hobbs et al., 1976). The bedding direction determines its physical and mechanical anisotropy (Ramamurthy, 1993; Amadei, 1996; Nasseri et al., 2003; Hakala et al., 2007; Gonzaga et al., 2008).

The strength criterion of anisotropic rock is derived based on its mechanical behavior. The existing anisotropic rock strength criteria include mainly the mathematical continuity strength, empirical continuity strength, and discontinuous strength criteria (Duveau et al., 1998; Cho et al., 2012; Alejano et al., 2021). The mathematical continuum strength criterion is based on the classical continuum mechanics theory, assuming that the strength criterion is a continuously changing function. The empirical continuous medium yield criterion assumes that the strength parameters in the criterion change according to some empirical laws. The anisotropic parameter in the expression is considered to be an empirical function of the loading direction angle (McLamore and Gray, 1967; Jaeger, 1971; Ramamurthy et al., 1988; Amadei 1996). The anisotropic rock failure modes are divided based on the discontinuous yield criterion. Different failure modes correspond to different loading angles and are expressed by different piecewise functions (Jaeger, 1960; Hoek, 1983; Duveau et al., 1998; Tien and Kuo, 2001). While mathematical continuity strength criteria are preferred for numerical modeling purposes, rock mechanics practitioners tend to prefer the so-called discontinuous approaches (namely the Jaeger's plane of weakness model). In these discontinuous models, strength is associated to a type mechanism (sliding through bedding, shearing, or tensile failure through intact rock); moreover, the required parameters are not many, and they have a clear physical meaning, so they can be more easily extended to practical applications such as well-stability or underground excavation design.

In this study, the anisotropic fracture characteristics and strength criterion of bedded rock are studied by the triaxial loading test of bedded sandstone. The directional dependency of strength of bedded rock is described by the JPW criterion. In addition, based on the existing strength criterion, the different possibilities of the JPW (Jaeger's weak surface) strength method are analyzed and extended. Considering the difference of strength between rocks with horizontal bedding and vertical bedding, the Mohr–Coulomb failure criterion, different from intact rocks, is preliminarily analyzed, and an improved JPW strength criterion for determining the strength parameters of intact rocks according to the bedding dip angle (β) is proposed. In addition, the strength and confining pressure of rock are usually regarded as a simple linear relationship, which is very different from the actual situation. The compressive strength prediction based on the nonlinear strength criterion still needs to be further developed.

2 JAEGER'S PLANE OF WEAKNESS THEORY FOR BEDDED ROCKS

To our best knowledge, rock mechanics practitioners tend to the so-called discontinuous approaches (namely the Jaeger's plane of weakness model) (Cho et al., 2012; Ambrose, 2014; Setiawan and Zimmerman, 2018). In these discontinuous models, strength is associated to a type mechanism (sliding through bedding, shearing, or tensile failure through intact rock); moreover, the required parameters are not many, and they have a clear physical meaning, so they can be more easily extended to practical applications such as well-stability or underground excavation design.

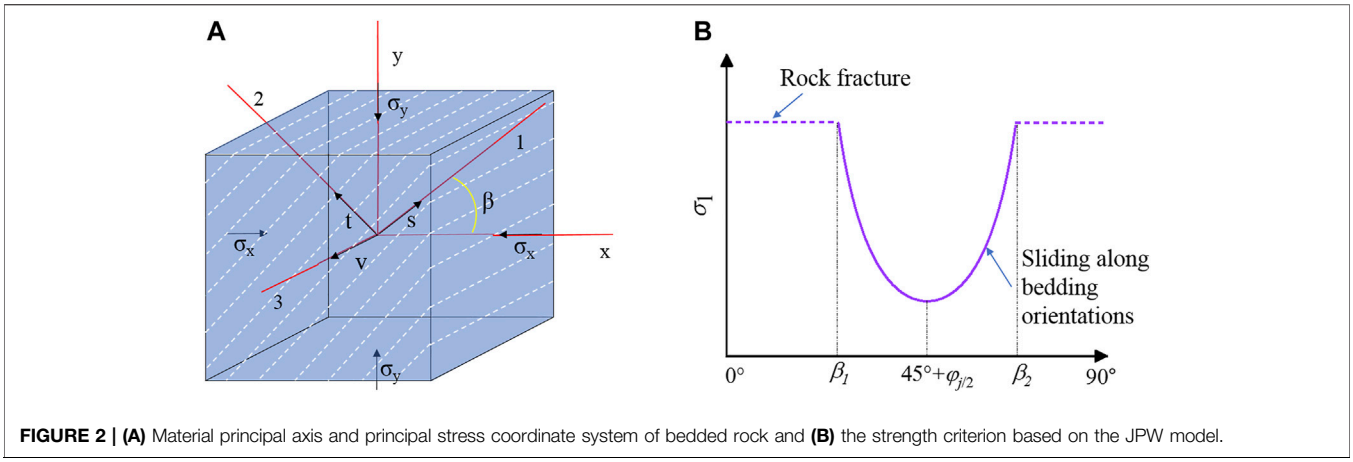

FIGURE 2 | (A) Material principal axis and principal stress coordinate system of bedded rock and **(B)** the strength criterion based on the JPW model.

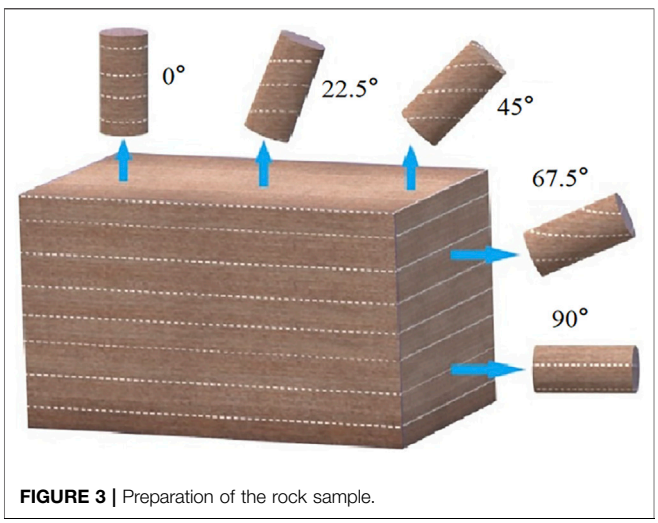

FIGURE 3 | Preparation of the rock sample.

As shown in **Figure 2A**, there are layered structural planes inside the rock, and it is assumed that the angle between the inside of the layer and the largest principal plane is β. From the Mohr's stress circle theory, the normal stress and shear stress acting on the structural plane are

$$\left.\begin{aligned}\sigma &= \frac{\sigma_1+\sigma_3}{2}+\frac{\sigma_1-\sigma_3}{2}\cos 2\beta\\ \tau &= \frac{\sigma_1-\sigma_3}{2}\sin 2\beta\end{aligned}\right\}. \tag{1}$$

The shear strength inside the layer is assumed to obey the Coulomb–Navier failure criterion as follows:

$$\tau_f = \sigma tg\varphi_j + c_j. \tag{2}$$

Substituting **Eq. 2** into **Eq. 1**, the conditions for shear failure along bedding orientations can be obtained as follows (Zimmerman et al., 2018):

$$\sigma_1 = \sigma_3 + \frac{2\left(c_j+\sigma_3 tg\varphi_j\right)}{\left(1-tg\varphi_j ctg\beta\right)\sin 2\beta}, \tag{3}$$

where c_j and φ_j are the cohesion force and friction angle of the bedding planes, respectively. It can be seen from **Eq. 3** that the rock strength changes with the bedding dip angle. When $\beta \to \varphi_j$ or $\beta \to 90^{\circ}$, rock will not be sheared along the bedding orientations.

3 LABORATORY TESTS

3.1 Specimen Preparation

The schematic flowchart of preparation of rock specimens with different bedding dip angles is shown in **Figure 3**. The rock specimens used in the test were taken from the tawny bedded sandstone of Shannan, Qinghai Province, China. The porosity of bedded sandstone is 12.8%, and the dry density is 2.19 g cm^{-3}. According to the International Society of Rock Mechanics standards, the sample was processed into a cylindrical shape with 50 mm diameter and 100 mm height. The length error of all samples was less than 2 mm, and the unevenness of both ends after polishing was within ±0.05 mm. The end face was perpendicular to the axis, the maximum deviation was no more than 0.25°, and the angles between the specimen and the axial direction of the specimen were 0°, 22.5°, 45°, 67.5°, and 90°, respectively, as shown in **Figure 3**. In order to minimize the influence of the unevenness of the sample on the test results, all samples were taken from different directions on the same rock.

3.2 Testing Methods

Equipment used was the GCTS RTR-1000 rock triaxial test system, as shown in **Figure 4**. The equipment was controlled by a dynamic and static closed-loop digital electro-hydraulic servo system, which can perform strain or stress control as well as conduct behavior tests after rock failure. The maximum axial load of test equipment is 1,000 kN, and the loading frame

FIGURE 4 | Test devices.

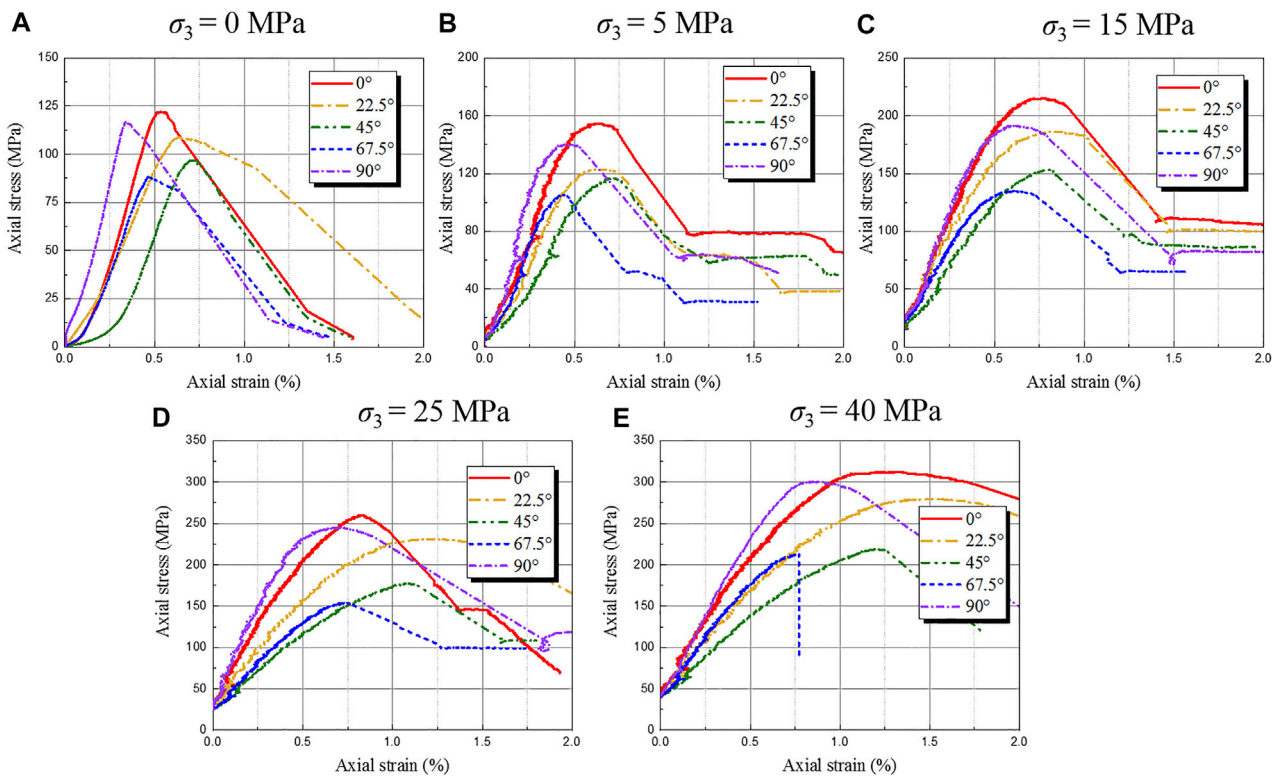

FIGURE 5 | Experimental data of compressive strength of bedded rock. **(A)** σ_3 = 0 MPa; **(B)** σ_3 = 5 MPa; **(C)** σ_3 = 15 MPa; **(D)** σ_3 = 25 MPa; **(E)** σ_3 = 40 MPa.

stiffness is 1,750 kN/mm. The integrated confining pressure can reach 140 MPa, the pressure resolution is 0.01 MPa, and the liquid volume resolution is 0.01 CC. The rock sample size was up to 75 mm (3 inches). The equipment has an axial and radial linear variable differential transformer measurement, deformation range of ±2.5 mm, and deformation resolution of 0.001 mm.

The test confining pressure was set to 0, 5, 15, 25, and 40 MPa. The confining pressure was kept constant during each of the four levels of the test, and then the axial force was applied through the displacement control method. The loading rate was 0.01 mm/min, until the specimen was broken. The system automatically recorded the axial and circumferential deformations of the specimen during the test. In order to reduce the influence of the nonuniformity of specimens on the test results, the larger discrete type was removed. The test results were considered valid only when three or more similar results were obtained.

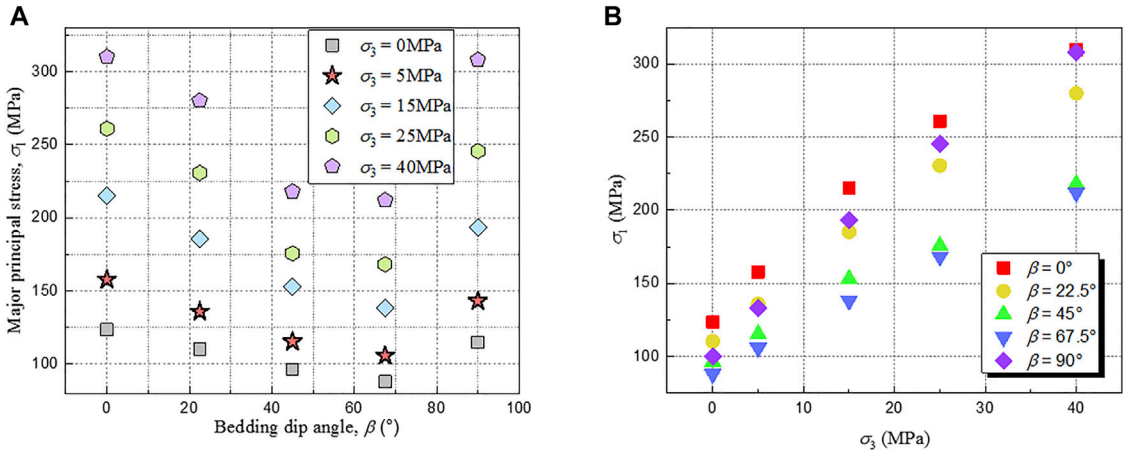

FIGURE 6 | Experimental data of compressive strength of bedded rock. **(A)** Strength of specimens with different bedding dip angles under the same confining pressure; **(B)** strength of specimens with the same bedding dip angle under different confining pressure.

4 TEST RESULTS ANALYSIS

4.1 The Whole Process Characteristics of Bedded Sandstone Under Triaxial Loading

Figure 5 shows the typical stress–strain curves of bedded rocks with different layer dip angles of $\beta = 0^{\circ}$, $\beta = 22.5^{\circ}$, $\beta = 45^{\circ}$, $\beta = 67.5^{\circ}$, and $\beta = 90^{\circ}$, respectively, under different confining pressure of 0 MPa, 5 MPa, 15 MPa, 25 MPa, and 40 MPa. The bedding dip angle of bedded sandstone has a significant impact on its stress–strain relationship. The strength of the bedded sandstone initially decreases with an increase in the bedding dip angle, and reaches a minimum when the bedding dip angle is 67.5°. Subsequently, the strength of bedded sandstone increases with a further increase in the bedding dip angle, reaching a maximum when the bedding dip angle is 90°.

The trend of stress–strain curves of bedded sandstone is consistent with each other. The bedded sandstone experienced, as a whole, four stages of development: the pore and fissure compaction stage; the elastic deformation to the microfracture stable development stage; the stable fracture development stage; and the post-destruction stage. In the rock elastic deformation stage, the elastic modulus of bedded sandstone initially decreased with the increase in the bedding dip angle, and the elastic modulus reached the minimum when the bedding dip angle was 45°. Then, it continuously increased with the increase of the bedding dip angle, and the elastic modulus reached the maximum when the bedding dip angle was 90°. At the beginning of the test, the nonlinear deformation of the curve is due to the gradual compaction of the feeble plane of the bedding and the internal micro-cracks under load. The compression volume deformation of the specimen is also related to the bedding dip angle.

As shown in **Figure 6**, the confining pressure has an effect on the peak strength of the rock. The triaxial compressive strength σ_1 of the rock increases with the increase of the confining pressure σ_3, and the increase rate of σ_1 corresponding to the rock with different bedding dip angles exhibits significant differences. In addition, the confining pressure also affects the residual strength of the rock. Under uniaxial loading (σ_3 = 0 MPa), brittle failure occurs after the rock reaches the maximum strength, and the residual strength is very low; with the increase of the confining pressure, the brittleness of the rock weakens, the plasticity increases, and the residual strength after the peak becomes more obvious.

By comparing the test results of the compressive strength of the bedded sandstone with different confining pressure, it can be found that under the condition of confining pressure σ_3 = 0 MPa, the difference value between the compressive strength of the bedded sandstone with bedding dip angles of $\beta = 67.5^{\circ}$

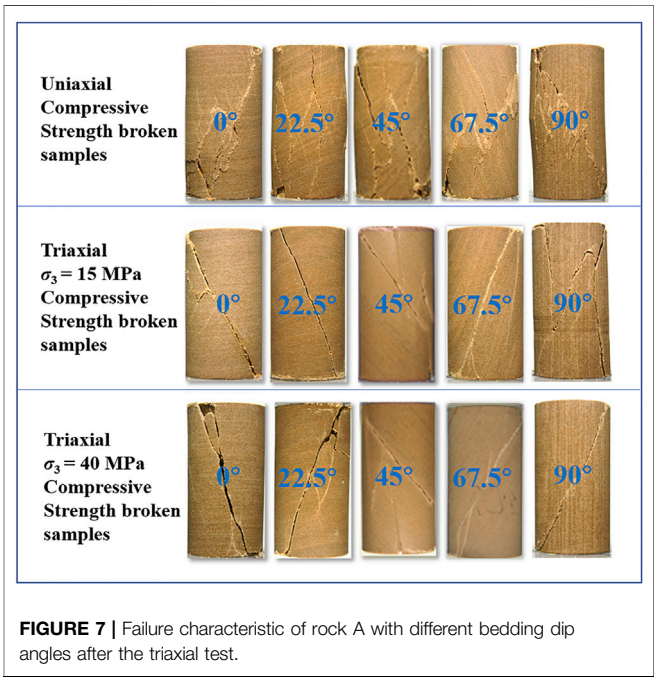

FIGURE 7 | Failure characteristic of rock A with different bedding dip angles after the triaxial test.

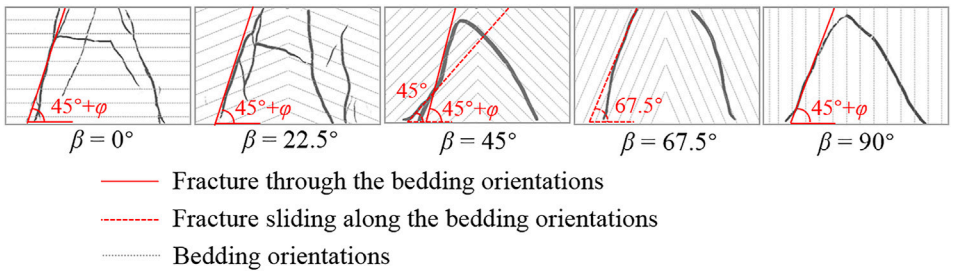

FIGURE 8 | Failure characteristic of rock B with different bedding dip angles after the triaxial test.

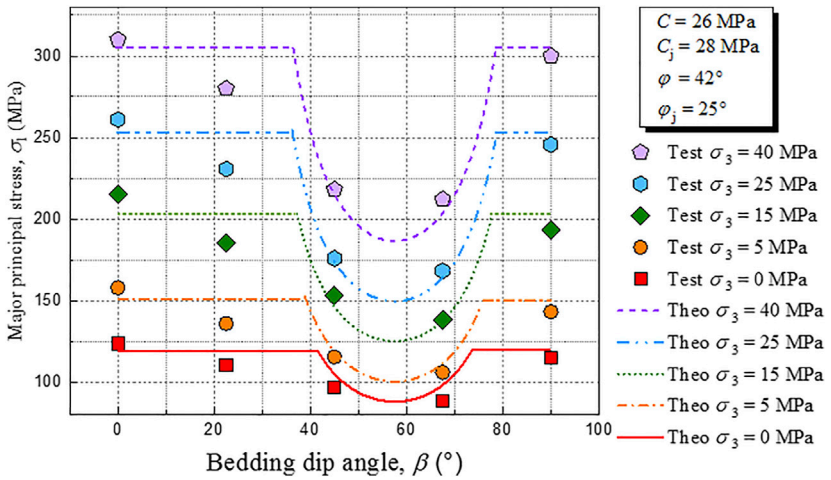

FIGURE 9 | Predicted strength curves of the JPW model and experimental values.

and $\beta = 90^{\circ}$ is 35.56 MPa. Under the conditions of confining pressure $\sigma_3 = 5$ MPa, $\sigma_3 = 15$ MPa, $\sigma_3 = 25$ MPa, and $\sigma_3 = 40$ MPa, respectively, the difference values between the compressive strength of the bedded sandstone with bedding dip angles of $\beta = 45^{\circ}$ and $\beta = 90^{\circ}$ are 51.98, 76.98, 92.74, and 98 Mpa, and compared with $\sigma_3 = 0$MPa, the difference values of compressive strength increased by 46.2%, 116.5%, 160.8%, and 175.6%, respectively. The strength anisotropy of bedded rock is more significant with the increase of confining pressure.

4.2 Compression Failure Mode of Bedded Sandstone

Bedded sandstone is a transversely isotropic rock, and specimens with different bedding dip angles exhibit different deformation and failure behaviors. The failure modes of bedded sandstone with different bedding dip angles under different confining pressure can be judged by the distribution of rock cracks after the triaxial compression test. It can be seen from **Figure 7**, with the change of rock bedding dip, the failure mode of bedded sandstone changes accordingly. The failure mode of the bedded sandstone can be divided into three categories as follows: mode I is shear failure, and the rock matrix is cut by the fracture surface. The fracture surface intersects the bedding planes of the rock. Mode II is failed along bedding orientations (weakness planes), and this is a typical failure type of bedded rock. During the loading process, the cracks are formed in a bedding plane locally along the bedding orientations, and then the specimen suffered shear failure along the bedding orientations. Mode III is splitting tension failure. During the loading process, the cracks are formed in multiple bedding planes locally along the bedding orientations, and then the specimen was split along the bedding plane.

Under the condition of low confining pressure, the failure mode of bedded sandstone changes from mode I shear failure through the bedding orientations to mode II shear failure along the bedding orientations and finally to mode III splitting tensile failure as the bedding dip angle β increases from 0° to 90°. With the increase of confining pressure, the number of cracks in the rock sample decreases obviously, and the macro-cracks are mainly distributed near the maximum shear stress action surface.

The fractures were scanned when the rock sample is damaged, and the stratification diagram was drawn (see **Figure 8**). When the bedding dip angle is close to the angle of the maximum shear stress acting plane, the failure mode is the sliding failure in the bedding; on the contrary, the fracture mode is through the

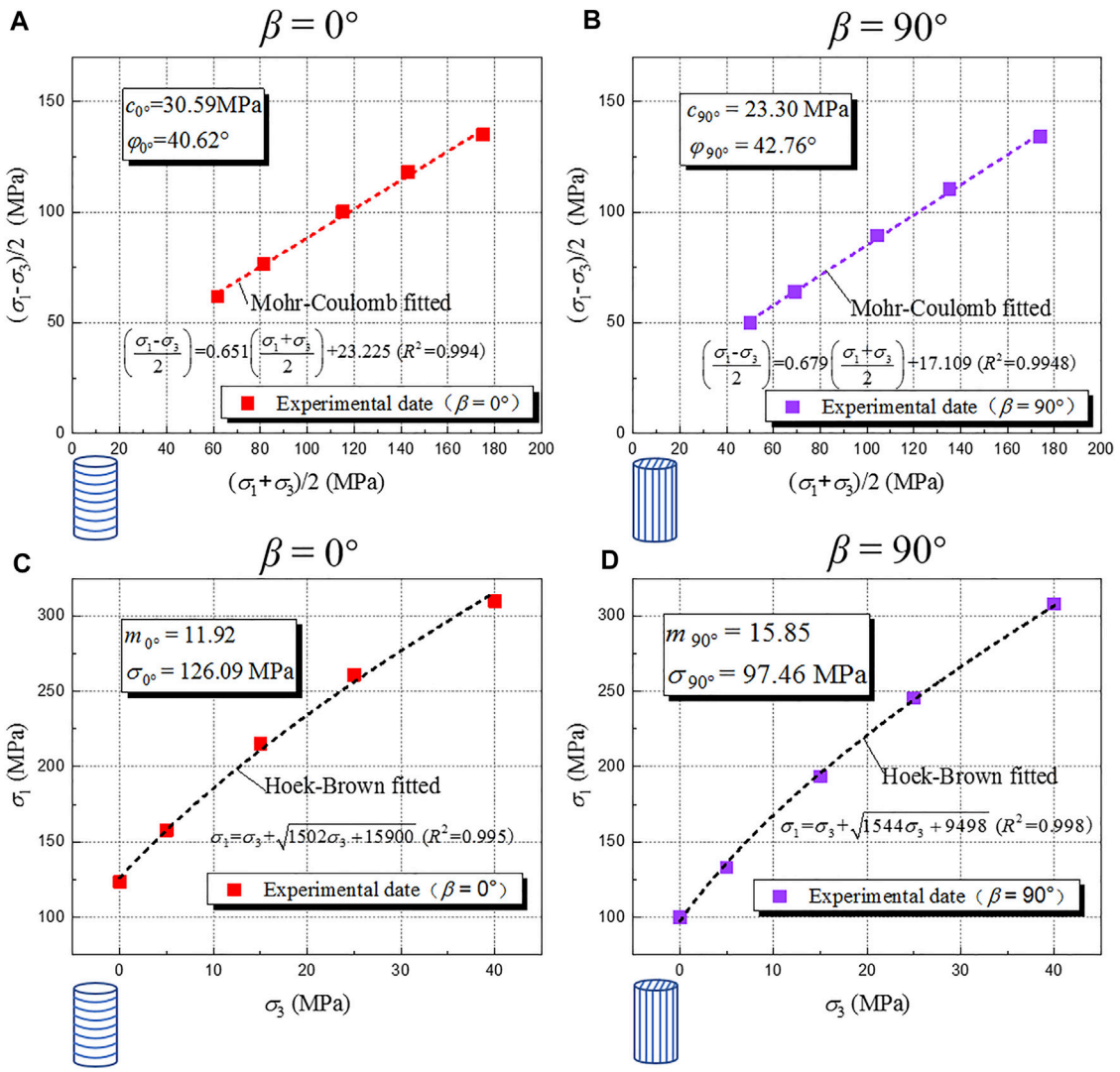

FIGURE 10 | Determination of strength parameters of layered sandstone. **(A)** Mohr–Coulomb strength of bedded sandstone with horizontal bedding dip, **(B)** Mohr–Coulomb strength of bedded sandstone with vertical bedding dip, **(C)** Hoek–Brown strength of bedded sandstone with horizontal bedding dip, and **(D)** Hoek–Brown strength of bedded sandstone with vertical bedding dip.

bedding plan. The failure mode is closely related to bedding dip angle and confining pressure, and the difference of failure mode also affects the anisotropic characteristics of the aforementioned bedded sandstone.

4.3 Optimization of the JPW Strength Anisotropy Model

In the first instance, the original Jaeger's plane of weakness (JPW) model was used to fit the triaxial experimental data of the bedded sandstone, and then two revised JPW models were proposed as further refinements to the original JPW model and used to fit the experimental data. The JPW model is an empirical strength theory based on the Mohr–Coulomb criterion, which assumes two different fracture mechanisms for bedded rocks. The first is related to the intact rock fracture mechanism, which depends on the cohesion (c_0) and the internal friction angle (φ_0) of the intact rock. The second is related to the bedding plane fracture mechanism, which depends on the cohesion (c_b) and the internal friction angle (φ_b).

Figure 9 shows the results of fitting according to the JPW model, combined with **Figure 7**, illustrating that the fracture model of the specimens with $\beta = 45^{\circ}$ and $\beta = 67.5^{\circ}$ slipping along the bedding planes, while the specimens with $\beta = 0^{\circ}$ and $\beta = 90^{\circ}$ penetrate fracture through the bedding planes. For the specimen with $\beta = 22.5^{\circ}$, the JPW model does not explain these data well. In future studies, other models will be considered to explore the suitability of the strength criterion under this bedding dip.

The JPW model predicts that bedded rocks exhibit the same peak strength under horizontal bedding dip and vertical bedding dip, which is independent of the bedding dip angle. However, **Figure 9** shows a significant difference in peak strength between

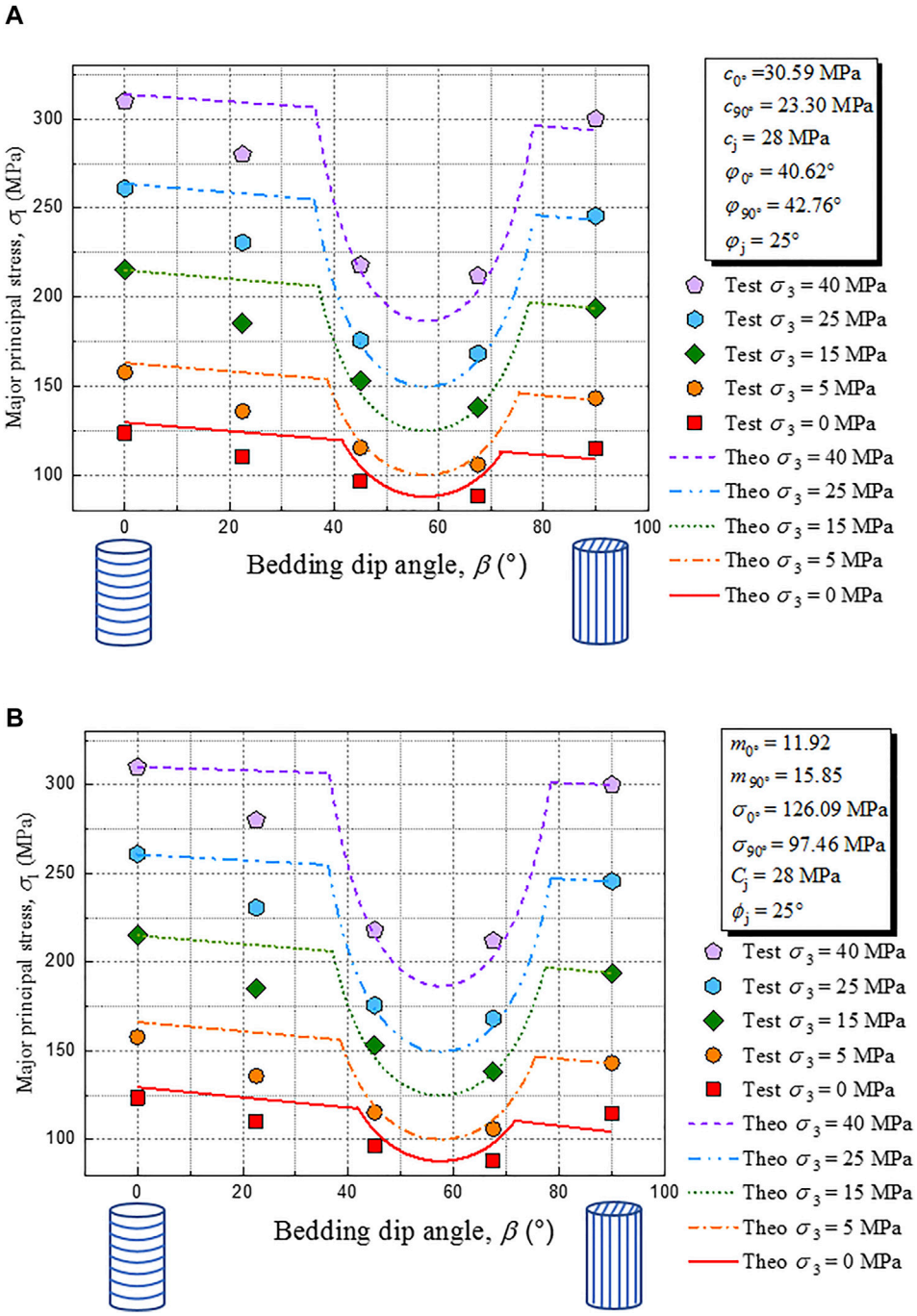

FIGURE 11 | (A) Predicted strength curves of the JPW-MC model and experimental values and **(B)** predicted strength curves of the JPW-HB model and experimental values.

specimens with $\beta = 0^{\circ}$ and those with $\beta = 90^{\circ}$, which has also been confirmed in other authors' studies (Donath, 1961; Amadei, 1983; Ramamurthy et al., 1988; Duveau and Shao, 1998; Bagheripour et al., 2011; Li et al., 2021). Therefore, the JPW model has a limitation that it cannot accurately represent the mechanical properties that intact rock strength may change continuously with bedding orientation.

In order to overcome the aforementioned shortcoming of the JPW strength criterion for bedded rock, an improved theoretical prediction method of strength anisotropy, called the JPW-MC model, is proposed. The model determines strength parameters of intact rock according to the bedding orientation. In addition, the facture model evolution is also considered the strength of intact rock from fracture through the bedding planes ($\beta = 0^{\circ}$) to splitting

tensile failure ($\beta = 90^{\circ}$). This model combines two different failure criteria: for shear failure mode on bedding planes, using the JPW model representation of **Eq. 3**; for the failure mode on the intact rock, a strength criterion related to the bedding dip is proposed, as shown in **Eq. 4**.

$$\sigma_1(\beta) = \sigma_1^{0^{\circ}} + \frac{\sigma_1^{90^{\circ}} - \sigma_1^{0^{\circ}}}{90}\beta. \tag{4}$$

When determining the parameters corresponding to the intact rock in the JPW-MC criterion, the first step is to determine the strength parameters of the specimens with $\beta = 0^{\circ}$ and $\beta = 90^{\circ}$ based on the linear strength criterion. As shown in **Figures 10A,B**, by fitting the relationship between $\tau_m = (\sigma_1-\sigma_3)/2$ and $\sigma_m = (\sigma_1+\sigma_3)/2$, the cohesion ($c_b$) and the internal friction angle (φ_b) were determined. Then, the peak strength corresponding to any bedding dip angle β can be calculated according to **Eq. 4**. **Figure 11A** shows the results of curve fitting of the JPW-MC criterion. Compared with the JPW criterion, the prediction accuracy of the failure criterion for intact rock is significantly improved.

Considering that the rock's strength envelope is usually nonlinear when the confining pressure changes greatly, an improved theoretical prediction method of strength anisotropy is introduced, called the JPW-HB model. The model is based on the Hoek–Brown nonlinear strength criterion, as shown in **Eq. 5**.

$$\frac{\sigma_1}{\sigma_c} = \frac{\sigma_3}{\sigma_c} + \left(1 + m\frac{\sigma_3}{\sigma_c}\right)^{0.5}. \tag{5}$$

When determining the parameters corresponding to the intact rock in the JPW-HB criterion, the first is to determine the strength parameters of the specimens with $\beta = 0^{\circ}$ and $\beta = 90^{\circ}$ based on the linear strength criterion, as shown in **Figures 10C,D**, through fitting the relationship between σ_1 and σ_3 and determining the strength parameters m and σ_{ci}. Then, the peak strength corresponding to any bedding dip angle β can be calculated from **Eq. 4**. **Figure 11B** shows the results of curve fitting of the JPW-HB criterion.

There is a significant difference in the strength of the bedded rock between $\beta = 0^{\circ}$ and $\beta = 90^{\circ}$. In terms of numerical prediction, compared with the JPW model, the JPW-MC and JPW-HB models, especially the last one, can significantly improve the prediction accuracy of the strength anisotropic behavior of bedded rocks. Since the highest confining pressure of the test conducted in this study is 40 MPa, the advantages of the JPW-HB model are not prominent compared with those of the JPW-MC model. However, when the confining pressure changes greatly in engineering, the strength envelope of the rock is usually a nonlinear curve; at this time, the prediction accuracy of the JPW-HB model based on the nonlinear strength criterion will be more in line with the actual situation.

5 CONCLUSION

Different fracture characteristics were observed in triaxial tests on bedded sandstone specimens. The specimens of β in the range of 45°–67.5° failed along bedding orientations (weakness planes), while the specimens with $\beta = 0^{\circ}$ and 90° failed through bedding orientations. However, under the condition, it is also observed that the fracture characteristic of the specimens with $\beta = 90^{\circ}$ exhibits splitting tensile failure and lower strength than specimens with $\beta = 0^{\circ}$.

The mechanical anisotropy of bedded rock can be directly expressed by the failure mode, which is closely related to not only the bedding dip angle but also the confining pressure. The stress-induced anisotropy of bedded rock caused by confining pressure makes its anisotropic strength more significant with the increase in confining pressure.

The JPW model is proved to be suitable for predicting the anisotropic strength of bedded rock by comparison with experimental data. However, the JPW model has a limitation that it cannot accurately represent the mechanical feature that intact rock strength may change continuously with bedding orientation. The JPW-MC and JPW-HB models proposed in this study improved this shortcoming of the JPW model.

Considering that the rock's strength envelope is usually nonlinear when the confining pressure changes greatly, the JPW-HB criterion is established on the basis of the Hoek–Brown nonlinear strength criterion. Its prediction accuracy will be more in line with the actual situation in engineering when the confining pressure changes greatly.

DATA AVAILABILITY STATEMENT

The original contributions presented in the study are included in the article/Supplementary Material, further inquiries can be directed to the corresponding authors.

AUTHOR CONTRIBUTIONS

LZ and FN were responsible for the work concept or design; LZ and XJ were responsible for data collection; LZ and ML were responsible for drafting the manuscript; FN and ZW were responsible for making important revisions to the manuscript; JW and TD were responsible for approving the final version of the manuscript for publication.

FUNDING

This research was supported by the Second Tibetan Plateau Scientific Expedition and Research (STEP) Program (Grant No. 2019QZKK0905), the National Key R&D Program of China (Grant No. 2018YFC1505001), the West Light Foundation of Chinese Academy of Sciences (granted to ML), the Program of the State Key Laboratory of Frozen Soil Engineering (Grant No. SKLFSE-ZT-202110), and the Science Technology Research and Development Plan of Qinghai-Tibet Railway Group Corporation (QZ2021-G02).

REFERENCES

Alejano, L. R., González-Fernández, M. A., Estévez-Ventosa, X., Song, F., Delgado-Martín, J., Muñoz-Ibáñez, A., et al. (2021). Anisotropic Deformability and Strength of Slate from NW-Spain. *Int. J. Rock Mech. Mining Sci.* 148, 104923. doi:10.1016/j.ijrmms.2021.104923

Amadei, B. (1996). Importance of Anisotropy when Estimating and Measuring *In Situ* Stresses in Rock. *Int. J. Rock Mech. Mining Sci. Geomechanics Abstr.* 33 (3), 293–325. doi:10.1016/0148-9062(95)00062-3

Amadei, B. (1983). *Rock Anisotropy and the Theory of Stress Measurements*. New York, Tokio: Springer-Verlag. doi:10.1007/978-3-642-82040-3

Ambrose, J. (2014). *Failure of Anisotropic Shales under Triaxial Stress Conditions*. London: Imperial College. Ph.D. Thesis.

Bagheripour, M. H., Rahgozar, R., Pashnesaz, H., and Malekinejad, M. (2011). A Complement to Hoek-Brown Failure Criterion for Strength Prediction in Anisotropic Rock. *Geomechanics Eng.* 3, 61–81. doi:10.12989/gae.2011.3.1.061

Blenkinsop, T. (2000). *Deformation Microstructures and Mechanisms in Minerals and Rocks*. Amsterdam, Netherlands: Kluwer Academic Publishers.

Cheng, W., Jin, Y., and Chen, M. (2015). Reactivation Mechanism of Natural Fractures by Hydraulic Fracturing in Naturally Fractured Shale Reservoirs. *J. Nat. Gas Sci. Eng.* 23, 431–439. doi:10.1016/j.jngse.2015.01.031

Cho, J.-W., Kim, H., Jeon, S., and Min, K.-B. (2012). Deformation and Strength Anisotropy of Asan Gneiss, Boryeong Shale, and Yeoncheon Schist. *Int. J. Rock Mech. Mining Sci.* 50, 158–169. doi:10.1016/j.ijrmms.2011.12.004

Dieter, G. E. (1987). *Mechanical Metallurgy*. New York: McGraw-Hill, 751–752.

Donath, F. A. (1961). Experimental Study of Shear Failure in Anisotropic Rocks. *Geol. Soc. America Bull.* 72, 985–989. doi:10.1130/0016-7606(1961)72[985:esosfi]2.0.co;2

Duveau, G., and Shao, J. F. (1998). A Modified Single Plane of Weakness Theory for the Failure of Highly Stratified Rocks. *Int. J. Rock Mech. Mining Sci.* 35 (6), 807–813. doi:10.1016/s0148-9062(98)00013-8

Duveau, G., Shao, J. F., and Henry, J. P. (1998). Assessment of Some Failure Criteria for Strongly Anisotropic Geomaterials. *Mech. Cohes.-Frict. Mater.* 3, 1–26. doi:10.1002/(sici)1099-1484(199801)3:1<1::aid-cfm38>3.0.co;2-7

Gonzaga, G. G., Leite, M. H., and Corthesy, R. (2008). Determination of Anisotropic Deformability Parameters from a Single Standard Rock Specimen. *Int. J. Rock Mech. Min. Sci.* 45, 14201438. doi:10.1016/j.ijrmms.2008.01.014

Hakala, M., Kuula, H., and Hudson, J. A. (2007). Estimating the Transversely Isotropic Elastic Intact Rock Properties for *In Situ* Stress Measurement Data Reduction: A Case Study of the Olkiluoto Mica Gneiss. *Finland. Int. J. Rock Mech. Min. Sci.* 44, 1446. doi:10.1016/j.ijrmms.2006.04.003

Hobbs, B. E., Means, W. D., and Williams, P. F. (1976). *An Outline of Structural Geology*. New York: Wiley, 571–572.

Hoek, E. (1983). Strength of Jointed Rock Masses. *Géotechnique* 33 (3), 187–223. doi:10.1680/geot.1983.33.3.187

Hu, Z., Shen, J., Wang, Y., Guo, T., Liu, Z., and Gao, X. (2021). Cracking Characteristics and Mechanism of Entrance Section in Asymmetrically-Load Tunnel with Bedded Rock Mass: A Case Study of a Highway Tunnel in Southwest China. *Eng. Fail. Anal.* 122, 105221. doi:10.1016/j.engfailanal.2021.105221

Jaeger, J. C. (1971). Friction of Rocks and Stability of Rock Slopes. *Géotechnique* 21 (2), 97–134. doi:10.1680/geot.1971.21.2.97

Jaeger, J. C. (1960). Shear Failure of Anisotropic Rocks. *Geol. Mag.* 97, 65–72.

Li, A., Xu, N., Dai, F., Gu, G., Hu, Z., and Liu, Y. (2018). Stability Analysis and Failure Mechanism of the Steeply Inclined Bedded Rock Masses Surrounding a Large Underground Opening. *Tunnelling Underground Space Technology* 77, 45–58. doi:10.1016/j.tust.2018.03.023

Li, B., Cui, X., Zou, L., and Cvetkovic, V. (2021). On the Relationship Between Normal Stiffness and Permeability of Rock Fractures. *Geophys. Res. Letters* 48, e2021GL095593. doi:10.1029/2021GL095593

McLamore, R., and Gray, K. E. (1967). The Mechanical Behavior of Anisotropic Sedimentary Rocks. *Trans. Am. Soe. Mech. Eng. Ser. B.* 89, 62–73. doi:10.1115/1.3610013

Nasseri, M. H. B., Rao, K. S., and Ramamurthy, T. (2003). Anisotropic Strength and Deformational Behavior of Himalayan Schists. *Int. J. Rock Mech. Mining Sci.* 40, 3–23. doi:10.1016/s1365-1609(02)00103-x

Ramamurthy, T., Rao, G. V., and Singh, J. (1988). "A Strength Criterion for Anisotropic Rocks," in Proceedings of the Fifth Australia-Newzeland Conference on Geomechanics, Sydney, August 22–26, 1988, 253–257.

Ramamurthy, T. (1993). *Strength and Modulus Responses of Anisotropic Rocks*. Oxford: Pergamon Press, 313–329.

Setiawan, N. B., and Zimmerman, R. W. (2018). Wellbore Breakout Prediction in Transversely Isotropic Rocks Using True-Triaxial Failure Criteria. *Int. J. Rock Mech. Mining Sci.* 112, 313–322. doi:10.1016/j.ijrmms.2018.10.033

Tien, Y. M., and Kuo, M. C. (2001). A Failure Criterion for Transversely Isotropic Rocks. *Int. J. Rock Mech. Mining Sci.* 38, 399–412. doi:10.1016/s1365-1609(01)00007-7

Winn, K., Wong, L. N. Y., and Alejano, L. R. (2019). Multi-approach Stability Analyses of Large Caverns Excavated in Low-Angled Bedded Sedimentary Rock Masses in Singapore. *Eng. Geology*. 259, 105164. ISSN 0013-7952. doi:10.1016/j.enggeo.2019.105164

Zhang, X., Liu, W., Jiang, D., Qiao, W., Liu, E., Zhang, N., et al. (2021). Investigation on the Influences of Interlayer Contents on Stability and Usability of Energy Storage Caverns in Bedded Rock Salt. *Energy* 231, 120968. doi:10.1016/j.energy.2021.120968

Zimmerman, R. W., Ambrose, J., and Setiawan, N. B. (2018). "Failure of Anisotropic Rocks Such as Shales, and Implications for Borehole Stability," in *ISRM International Symposium-10th Asian Rock Mechanics Symposium* (Singapore: International Society for Rock Mechanics and Rock Engineering).

Conflict of Interest: Authors ZW, JW and TD were employed by the company China Railway Qinghai-Tibet Group Co., Ltd.

The remaining authors declare that the research was conducted in the absence of any commercial or financial relationships that could be construed as a potential conflict of interest.

Publisher's Note: All claims expressed in this article are solely those of the authors and do not necessarily represent those of their affiliated organizations, or those of the publisher, the editors, and the reviewers. Any product that may be evaluated in this article, or claim that may be made by its manufacturer, is not guaranteed or endorsed by the publisher.

Copyright © 2022 Zhang, Niu, Liu, Ju, Wang, Wang and Dong. This is an open-access article distributed under the terms of the Creative Commons Attribution License (CC BY). The use, distribution or reproduction in other forums is permitted, provided the original author(s) and the copyright owner(s) are credited and that the original publication in this journal is cited, in accordance with accepted academic practice. No use, distribution or reproduction is permitted which does not comply with these terms.

frontiers | Frontiers in Earth Science

ORIGINAL RESEARCH
published: 04 May 2022
doi: 10.3389/feart.2022.912356

Damage Evolution of Frozen-Thawed Granite Based on High-Resolution Computed Tomographic Scanning

Bo Li[1,2], *Guanghua Zhang*[1], *Gang Wang*[1,3]* *and Jiaxing Qiao*[1]

[1]Key Laboratory of Rock Mechanics and Geohazards of Zhejiang Province, Shaoxing University, Shaoxing, China, [2]Department of Geotechnical Engineering, Tongji University, Shanghai, China, [3]School of Civil Engineering, Wuhan University, Wuhan, China

Freeze-thaw damage of rocks is one of significant natural causes for geo-hazards such as collapse and rockfall in alpine areas. To explore damage evolution in granite in a freeze-thaw environment, specimens of granite in Nyingchi Prefecture, Tibet, China were collected as research objects. Saturated and dry rock specimens were subjected to cyclic freeze-thaw tests of 0, 36, 72, and 144 cycles and freeze-thaw damage of the rock was analyzed by combining computed tomography (CT) scanning and three-dimensional (3D) visualization. Results show that the peak stress of granite decreases to different extents with the increasing number of freeze-thaw cycles; compared with dry rock specimens, saturated granite deteriorates more significantly and shows obviously different stress–strain curves under loading. The moisture condition exerts significant influences on the degree of freeze-thaw damage to granite: after 144 freeze-thaw cycles, the mass loss rates of dry and saturated rock specimens are 0.06% and 0.44% and their loss rates of uniaxial compressive strength (UCS) reach 4.08% and 26.2%, respectively. Under freeze-thaw cycles, the frost heave of pore water causes initiation and development of micro-defects and new micro-cracks mainly develop along relatively weak areas such as inherent defects (pores and fractures) and boundaries between different mineral crystals, resulting in intergranular and transgranular cracking. For dry rock specimens, the non-uniform contraction and expansion of minerals therein are main causes for deterioration inside the rock. The freeze-thaw damage of rocks is calculated using the improved elastic modulus loss method. The damage development trend conforms to the strength deterioration trend and the pore development in the rock, reflecting the evolution of freeze-thaw damage to granite.

Keywords: rock mechanics, freeze-thaw action, computed tomographic scanning, pore development, uniaxial compressive strength, damage index

OPEN ACCESS

Edited by:
Yan Du,
University of Science and Technology Beijing, China

Reviewed by:
Lin Ni,
The University of Newcastle, Australia
Richeng Liu,
China University of Mining and Technology, China

***Correspondence:**
Gang Wang
gangw277842@whut.edu.cn

Specialty section:
This article was submitted to Geohazards and Georisks, a section of the journal Frontiers in Earth Science

Received: *05 April 2022*
Accepted: *20 April 2022*
Published: *04 May 2022*

Citation:
Li B, Zhang G, Wang G and Qiao J (2022) Damage Evolution of Frozen-Thawed Granite Based on High-Resolution Computed Tomographic Scanning. Front. Earth Sci. 10:912356. doi: 10.3389/feart.2022.912356

Abbreviations: CT, computed tomography; D, freeze-thaw damage index; UCS, uniaxial compressive strength; SEM, scanning electron microscopy.

INTRODUCTION

With the implementation of the Belt and Road Initiative, more engineering works are under construction in the alpine area of the Tibet Plateau, including a Sichuan–Tibet railway and China–Nepal railway. In these regions, rocks can be severely damaged under the effect of large day/night and seasonal temperature difference, affecting normal engineering operations (Qi et al., 2017; Peng et al., 2020). Therefore, studying the freeze-thaw damage of rocks and the mechanism of such damage is of important theoretical and practical significance for engineering construction and maintenance therein.

To ascertain the damage mechanism to rocks under freeze-thaw actions, scholars have investigated the physico-mechanical properties of rocks subject to freeze-thaw cycling. Nicholson et al. (2000) conducted cyclic freeze-thaw tests on several types of rocks to compare influences of lithology on damage and fracture of rocks. Based on cyclic freeze-thaw tests on rock specimens at different moisture contents, Kodama et al. (2013) studied influences of saturation on the strength loss and failure mode of rocks. Park et al. (2015) performed cyclic freeze-thaw tests on basalt and tuff and considered that frost heave of water inside rocks is the main cause for rock weathering, manifest mainly as increased porosity, crack initiation, and particle falling induced by volume expansion after the water-ice phase change. Jiang et al. (2017) assessed the influences of saturation and the number of freeze-thaw cycles on the uniaxial compressive strength of sandstone and identified the number of freeze-thaw cycles as an important factor affecting the strength loss. Bayram (2012) evaluated the impact strength, elastic modulus, and water absorption of frozen-thawed limestone and established a statistical model for the rate of loss of the UCS. Luo et al. (2014) and Khanlari et al. (2015) conducted cyclic freeze-thaw tests on sandstone and limestone and found the decrease of P-wave velocity in rocks. By studying the freeze-thaw properties of several types of rocks at −45 to 15°C, Aoki et al. (1990) found that the P-wave velocity of rocks decreases significantly, and the tensile strength is decreased by as much as 15% after freeze-thaw cycling. Zou et al. (2017) stated that the initiation of new cracks is caused by temperature change and mainly occurs in the cooling stage of the freeze-thaw cycles, which is macroscopically shown as strength reduction in rocks induced by freeze-thaw damage. In summary, numerous scholars have discussed influences of freeze-thaw action on the physico-mechanical parameters (strength, porosity, and wave velocity) of rocks under conditions of different freeze-thaw environments, lithology, fracture characteristics and saturations, and analyzed the damage mechanism and evolution model of rocks (Yamabe and Neaupane, 2001; Park et al., 2004; Zhang et al., 2008; Tan et al., 2011; Yavuz, 2011; Martinez-Martinez et al., 2013; Ghobadi and Babazadeh, 2015; Momeni et al., 2016). However, changes in macroscopic physical and mechanical properties of rocks are caused by the superposition and evolution of mesoscopic mechanical properties and it is difficult to expound the failure mechanism of rocks from the macroscopic perspective solely.

In recent years, many scholars have found that microscopic and mesoscopic quantitative and qualitative analysis of rocks can reveal the deterioration characteristics and failure mechanisms of rocks. For example, some scholars explored micro and mesoscopic damage evolution in rocks using techniques such as scanning electron microscopy (SEM) and computed tomography (CT). By using SEM, Liu et al. (2005) and Fang et al. (2014) observed that freeze-thaw damage of rocks starts from locations of pre-existing defects, and damage of cement between particles and extrusion and dislocation of local particles facilitate initiation and development of microcracks. Tian et al. (2021) used SEM to study red sandstone subjected to freeze-thaw cycles and found that micropores and microcracks increase significantly in frozen-thawed red sandstone. Based on SEM, Qin et al. (2017) investigated pore structures in coal after different numbers of freeze-thaw cycles and calculated the sizes of defects therein. With the development of new techniques, research on damage is no longer limited to analysis of surface cracks or bonding characteristics of particles. Researchers have used CT visualization technology to study the fracture propagation on the entire cross section of rocks from the mesoscopic perspective. Yang et al. (2002) used CT to conduct cyclic freeze-thaw tests on soft rocks and discussed the constitutive relationship pertaining to damage propagation in rocks. In addition, they adopted the CT number as a variable to define freeze-thaw damage of rocks. Song et al. (2019) studied two-dimensional (2D) CT scanning images of rocks by virtue of programming software and described the development of new pores and the evolution mechanism of freeze-thaw damage. Based on CT, Bubeck et al. (2017) performed quantitative and visual processing on data including the size, volume, and spatial orientation of pores, which compensated for the limitation of traditional 2D image analysis. By means of the non-destructive testing approach of CT scanning, Maji et al. (2019) conducted 3D visualization analysis on sandstone and chalk under freeze-thaw cycles and explored the deterioration of mesoscopic structures under the cyclic freeze-thaw effect. They proposed three probability functions for describing freeze-thaw damage to rocks.

Meso-scale observation results indicate that freeze-thaw cycles can heavily damage the internal structures of rocks, which is the primary cause for changes in the macroscopic mechanical properties of rocks. However, the resolution of images acquired in freeze-thaw cycles is generally above 20 μm, taking CT techniques, with their favorable visualization effect, as an example (Promentilla and Sugiyama, 2010; Kock et al., 2015; Deprez et al., 2020; Fan et al., 2021; Yang et al., 2021). They cannot readily reveal the characteristics of rocks in the initiation, development, and coalescence of micro-cracks. Considering this, the spatial resolution of the CT scanner used in this study is significantly improved to explore internal freeze-thaw damage of rocks and the limit crack width that the CT scanner can measure is 0.2 μm. The CT scanning results are analyzed and linked to uniaxial compression testing results to establish a damage index that can effectively quantify the strength deterioration of rocks subject to freeze-thaw actions.

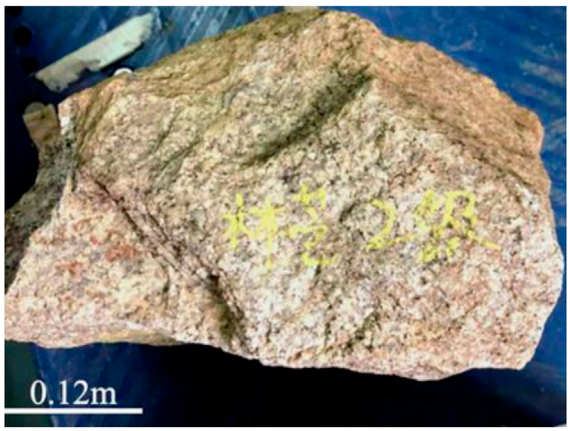

FIGURE 1 | Medium weathered granite collected in the Tibet Plateau.

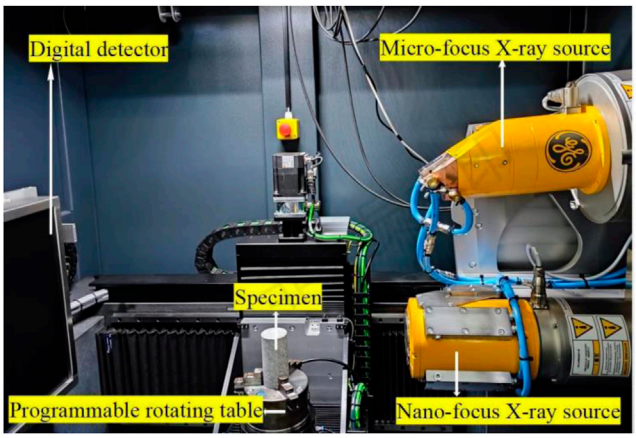

FIGURE 3 | Configuration of the CT scanning system.

FIGURE 2 | Granite specimens.

MATERIALS AND METHODS

Specimen Preparation

Moderately weathered fine- and medium-grained granite (**Figure 1**) collected at Binghu (Cuomujiri Lake) Hydropower Station in Nyingchi Prefecture, south-eastern Tibet, China was used in the cyclic freeze-thaw tests. Selection of the specimens met requirements for the same location, same batch, and similar mechanical properties. Minerals were detected using a polarizing microscope, revealing compositions of the granite (**Table 1**).

The specimens in the cyclic freeze-thaw tests were prepared as follows: 1) a core drilling machine was used to drill rock cores at a low speed; 2) the top and bottom of each specimen were slowly cut and ground using a manual grinding tool to avoid damage at the edges; 3) cylindrical granite specimens with a diameter of 10 mm and height of 25 mm (**Figure 2**) were obtained. Cylindrical specimens were selected to avoid production of artefacts in the CT scanning process and specimens were machined to maximize the spatial resolution possible during CT scanning. During the imaging process, the artifacts on CT images refer to abnormal images unrelated to the scanned tissue structure.

Test Methods

A Phoenix v|tome|x m micro-focus CT scanning system was used in the test, which comprised two ray tubes (micron- and nanometer-sized ones), a rotating stage, and an X-ray detector. The resolution of the detector reached 4048 × 4048 pixels that can detect a feature as small as 0.8 μm. During CT scanning, high-energy electrons bombard a metal target to produce conical X-ray beams, which were focused on the rock specimen placed on the stage. Then, the detection panel automatically acquired the omnidirectional ray images of the specimen, thus realizing 3D measurement and non-destructive analysis of internal structures of rocks, such as spatial distribution of cracks, porosity distribution, and density changes of rocks. For the nondestructive probing technology, the CT scanning will not affect the subsequent freeze-thaw test. **Figure 3** shows the CT scanning system.

In the test process, specimens were wrapped in thin foam to avoid artefacts caused by shaking in the scanning process. The specimens were scanned for 45 min in each time and the

TABLE 1 | Constituents of the tested granite.

Quartz (%)	Mica (%)	Plagioclase (%)	Chlorite (%)	Heavy mineral (%)
34	10	54	1.8	0.2

TABLE 2 | CT scan parameters.

Target Metal Target	Voltage (Kv)	Current (*u*A)	Exposuretime (ms)	The Number of Scan Images
Masurium	120	190	500	1,200

acquisition parameters during scanning are listed in **Table 2**. Among the CT scanning parameters provided, the current and voltage separately determine the number and penetration intensity of X-rays.

A high and low alternating temperature and humidity test chamber (**Figure 4**) was used in the cyclic freeze-thaw tests (internal dimensions: 500 mm × 600 mm × 750 mm). The test chamber could operate across the temperature range of -40–150°C with a tolerance of ± 0.5 °C. The test chamber has the programming control function, through which the temperature and humidity can be switched automatically.

The rock specimens were tested under two moisture conditions: dry and saturated. The dry specimens were obtained by drying the rock at 60°C for 48 h in a thermostat, while the saturated specimens were prepared by placing the rock in a water container which was then immersed for 72 h under a vacuum pressure. The freeze-thaw temperature range was set as (−20 °C, 20°C) and freezing and thawing both took 6 h, in a complete cycle. 144 freeze-thaw cycles were designed and the humidity in the freeze-thaw chamber was maintained at around 100% throughout.

After 0, 36, 72, and 144 freeze-thaw cycles, CT scanning and uniaxial compression tests were conducted on saturated and dry specimens. It is worth noting that to reveal the development of fractures in rocks under freeze-thaw cycles, the same rock specimen was selected for CT scanning after different numbers of freeze-thaw cycles.

FIGURE 4 | High-low temperature alternating test chamber.

MICRO-FOCUS COMPUTED TOMOGRAPHIC SCANNING

Computed Tomography Images

Figures 5, **6** present comparisons of CT cross-sectional images of dry and saturated specimens after different numbers of freeze-thaw cycles. The lower and upper parts of the figures illustrate the grey-scale map and porosity diagram of granite on the same cross section. The numbers at the lower right corner of the porosity diagram represent the proportion of pore area within the total cross sectional area.

As shown in **Figure 5**, there are a few cracks on the cross section of dry granite specimens before freeze-thaw cycles, and many micro-defects measuring 5–10 μm are distributed within the rock cores. Over all freeze-thaw cycles, the defects on the cross-section change little and no obvious crack initiation and pore expansion are observed. Only slight debris falling on side edges is observed after 72 freeze-thaw cycles. Such falling is shown as the increased dark and black area around the circumference in the porosity diagrams. After 0, 36, 72, and 144 freeze-thaw cycles, the proportions of pores on cross sections demonstrated are 1.49%, 1.51%, 1.52%, and 1.55%, respectively, showing slow growth.

Figure 6 demonstrates that there are a few cracks on the cross section of saturated granite specimens before freeze-thaw cycles and the proportions of pores are 1.65%, 1.68%, 1.85% and 2.48% after 0, 36, 72, and 144 freeze-thaw cycles, respectively. This indicates that the debris spalling from the sides of saturated granite specimens is more obvious in the freeze-thaw process compared with dry specimens and significant fracture development is observed on the circular cross-section after 144 cycles.

To explore the development of defects in dry granite, the area marked by the red rectangular box on the cross-sectional image of the dry granite specimen (**Figure 5**) was studied, and the amplified image is shown in **Figure 7**. **Figures 7A–D** show the grey-scale images of the same selected area after 0, 36, 72, and 144 freeze-thaw cycles, respectively. Microcracks at k1, k2, k3, and k4 are selected for analysis, wherein the widths of cracks are 13.4, 13.4, 13.8, and 15.8 μm, respectively. That is, the crack width only increases by 2.4 μm after 144 cycles, proving that dry granite shows favorable freeze-thaw resistance.

The area indicated by the red rectangular box in the saturated granite specimen (**Figure 6**) was selected to investigate the development of defects in saturated granite, as shown in **Figure 8**. **Figures 8A–D** indicate grey-scale images of the same selected area after 0, 36, 72, and 144 freeze-thaw cycles, respectively. Microcracks at m and n on the cross section are

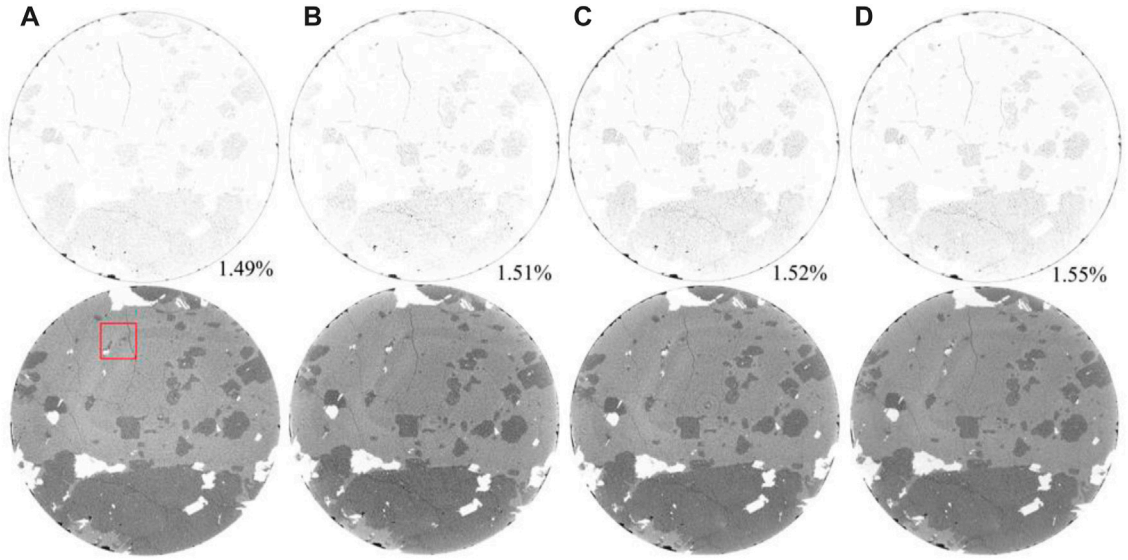

FIGURE 5 | 2D cross-sectional CT images of a dry granite sample (a~d) scanned after different freeze-thaw cycles: **(A)** 0 cycle, **(B)** 36 cycles, **(C)** 72 cycles, and **(D)** 144 cycles. The lower half shows the original grayscale CT images and the upper half shows the extracted pores and micro-cracks in each figure. The number indicates the fractional number of defect pixels over the total pixel number.

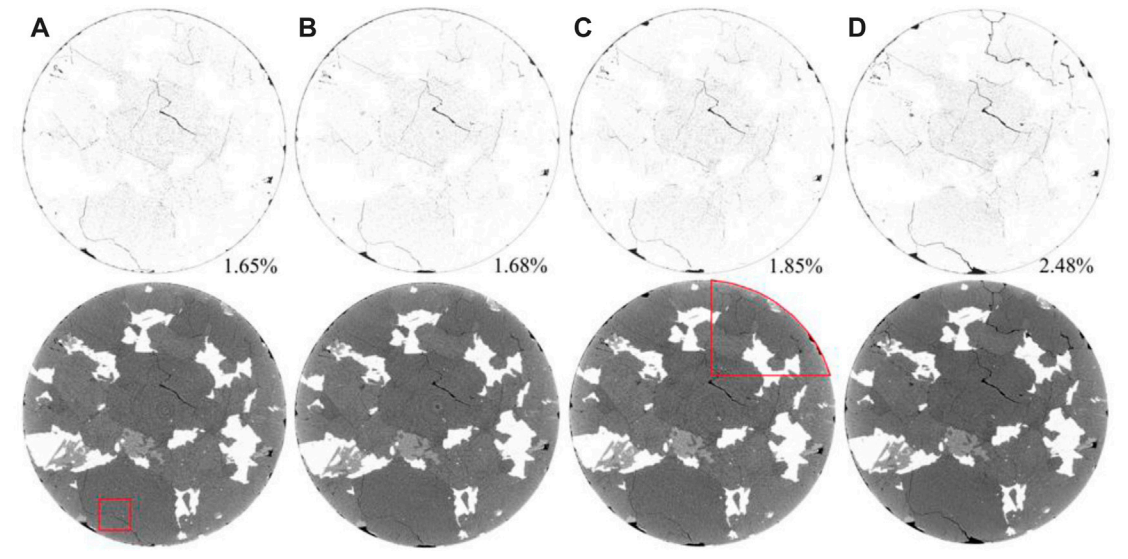

FIGURE 6 | 2D cross-sectional CT images of a saturated granite sample (a~d) scanned after different freeze-thaw cycles: **(A)** 0 cycle, **(B)** 36 cycles, **(C)** 72 cycles, and **(D)** 144 cycles.

selected for analysis, where crack widths at m1, m2, m3, and m4 are 12.6, 12.6, 12.8, and 17.2 μm; while those at n1, n2, n3, and n4 are 17.6, 17.6, 18.0, and 24.8 μm, respectively. The result indicates that the cracks develop slowly in saturated granite in the first 72 freeze-thaw cycles and crack development mainly takes place between 72 and 144 freeze-thaw cycles.

Furthermore, the red fan-shaped area marked in **Figure 6** (showing a saturated granite specimen) was selected for analysis. Differences in pores on the cross sections of saturated granite after 72 and 144 freeze-thaw cycles are illustrated in **Figure 9**. Cross-sections in **Figures 9A,B** represent grey-scale images of the selected cross section after 72 and 144 freeze-thaw cycles, respectively. Areas L and P marked by red boxes show representative debris falling at side edges of saturated granite. Large defects appear in area L in **Figure 9A** after 144 freeze-thaw cycles, that is, falling of local debris particles. Compared with **Figure 9B**, water accumulates and expands after being frozen and

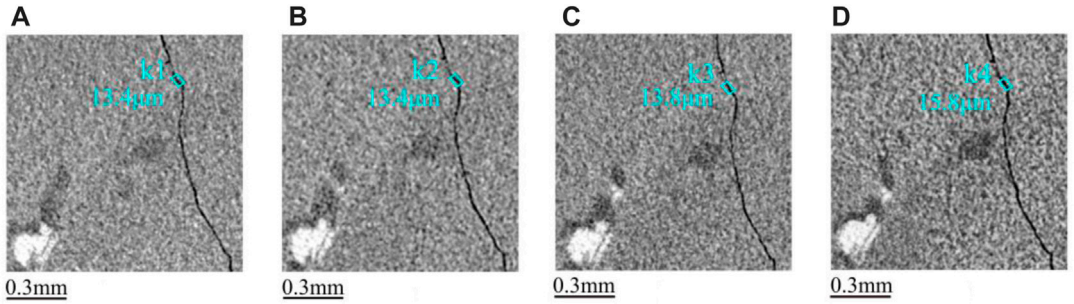

FIGURE 7 | Evolution trend of defect in the rectangle areas of dry granite sample scanned after different freeze-thaw cycles. **(A)** 0 cycle, **(B)** 36 cycles, **(C)**72 cycles, and **(D)** 144 cycles.

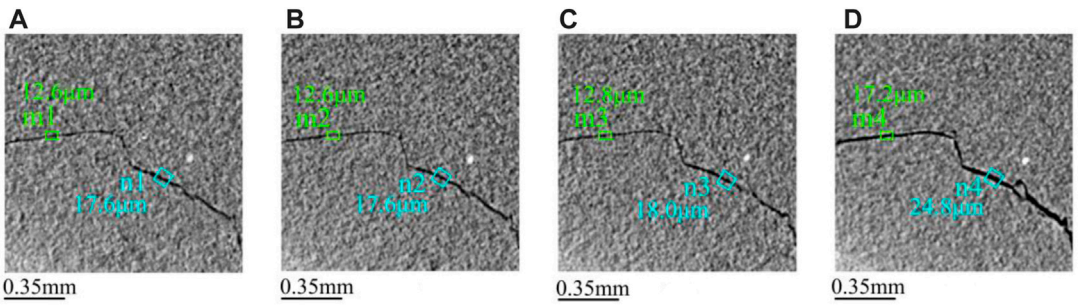

FIGURE 8 | Evolution trend of defect in rectangle areas of saturated granite sample scanned after different freeze-thaw cycles. **(A)** 0 cycle, **(B)** 36 cycles, **(C)**72 cycles, and **(D)** 144 cycles.

microcracks initiate in area L after the occurrence of defects. The microcracks develop rapidly along the inherent defects (microcracks at y1) beneath the area because the frost-heave stress generated by the water-ice phase-change in a new cycle exceeds the ultimate tensile strength of the rock. The microcracks propagate to area Q and develop intergranular cracks at the boundary between mica and plagioclase in the area. Here, y1 and y2 represent the width of microcracks and are 9.8 and 17.4 μm respectively, indicative of apparent crack development. Then, cracks further develop along the direction of inherent defects (cracks) marked in area V, which are shown as local transgranular cracks in mica in areas T and U and obvious intergranular fractures in areas R and S. The transgranular cracks occur over small areas because their occurrence calls for more energy, that is, a greater frost-heave force. Dimensions x1 and x2 denote the widths of inherent cracks after 72 and 144 freeze-thaw cycles and are 22.0 and 31.8 μm, respectively; z1 and z2 represent widths of new cracks, which are 17.0 and 12.2 μm, respectively. Under these conditions, cracks in areas L, Q, V, T, R, U, and S (**Figure 9A**) have been coalesced, where the granite is at a higher risk of damage and spalling. A comparison of CT images and data indicates that damage of saturated granite generally develops from defects at edges to the interior of the rock core. The interior of the rock core is not obviously damaged after a small number of freeze-thaw cycles, which is highly consistent with the development of defects shown in **Figure 9**.

In summary, debris falling on external surface occurs to both the saturated and dry rock specimens after 72 freeze-thaw cycles; whereas, new microcracks only initiate at defects on external surfaces of saturated rock specimens in the process from 72 to 144 cycles and they develop along directions of two weak areas, that is, inherent cracks and defects inside specimens and boundaries between different mineral compositions. These microcracks develop to wide coalesced cracks after repeated freeze-thaw cycles. Defects on the cross section displayed in the dry rock specimen do not change to any significant extent after 144 cycles because of the absence of frost-heave force generated by the water-ice phase change as the driving force for development of defects. Apparently, occurrence of new cracks is the essential cause of the accelerated development of defects in these saturated rock specimens.

3D Reconstruction of Rocks

CT scan slices were imported in VG Studio and Avizo for image processing and the reconstruction method based on superposition was used to attain the 3D reconstructed model of the granite. To reveal the nature and extent of the damage caused by freeze-thaw cycling, internal defects such as pores and cracks were taken as research objects. The 3D visualization software was used to analyze grey values of the CT images

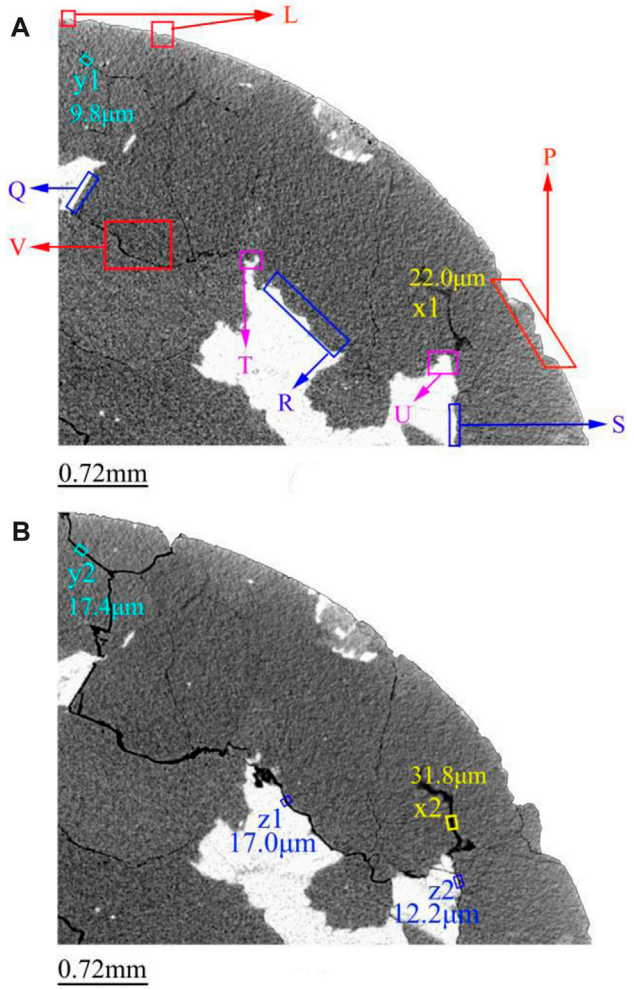

FIGURE 9 | Defect evolution in fan-shaped area of a saturated granite sample scanned after different freeze-thaw cycles: **(A)** 72 cycles, **(B)** 144 cycles.

and calculate the porosity. **Figure 10** shows the change trends of porosity of saturated and dry specimens, as well as fitted curves and goodness of fit R^2 of corresponding data. *P* in the fitting formula represents the porosity of the rock. It can be seen that as the number of freeze-thaw cycles increases, the porosity of saturated and dry specimens increases in a quasi-linear manner and the saturated specimen is more sensitive to the freeze-thaw cycles with a change rate of porosity being 7.2 times that of dry granite.

Figure 11 shows renderings of cracks and relatively large pores in saturated granite after different numbers of freeze-thaw cycles. Pores with a volume of less than 0.001 mm^3 are ignored to improve the visualization effect in 3D reconstruction. **Figures 11A–D** display results after 0, 36, 72, and 144 freeze-thaw cycles, respectively. It can be seen from the figure that the volume of inherent defects in the saturated specimen is between 0.001 and 0.594 mm^3 before freeze-thaw actions. After 36 freeze-thaw cycles, the isolated crack with the largest volume (0.600 mm^3) appears in the red area at the bottom of the specimen in **Figure 11B** and the crack only expands slightly compared with the initial state. After 72 cycles, the volume of the defect in the red area at the bottom of the granite in **Figure 11C** changes to 0.630 mm^3, remaining the largest defect. After 144 cycles, the spatial form of 3D defects in the saturated specimen begins to change significantly. The volume of the crack (green area) at the bottom of the rock in **Figure 11D** increases to 1.0 mm^3, while the crack of the largest volume (1.450 mm^3) appears at the top of the rock. The rate of crack development at the ends of the saturated specimen is apparently larger than that of the interior because granite is an intrusive magmatic rock in plutonitic masses, in which mineral crystals are highly compact. However, cracks inside the granite are not highly coalesced after 144 freeze-thaw cycles but remain as isolated segments. The volume of defects is larger at the two ends while smaller in the middle. Because defects change insignificantly in the dry granite after 144 freeze-thaw cycles, they are not analyzed in detail herein.

STRENGTH DETERIORATION OF GRANITE SUBJECT TO FREEZE-THAW ACTIONS

Stress–Strain Curves

An MTS 815 testing system was used to conduct uniaxial compression tests on frozen-thawed granite specimens to reveal their mechanical properties. **Figure 12** shows the compression test results on cylindrical granite specimens, which were obtained by with a static resistance strain gauge. To ensure the accuracy of strain measurement, the test followed recommendations of the International Society for Rock

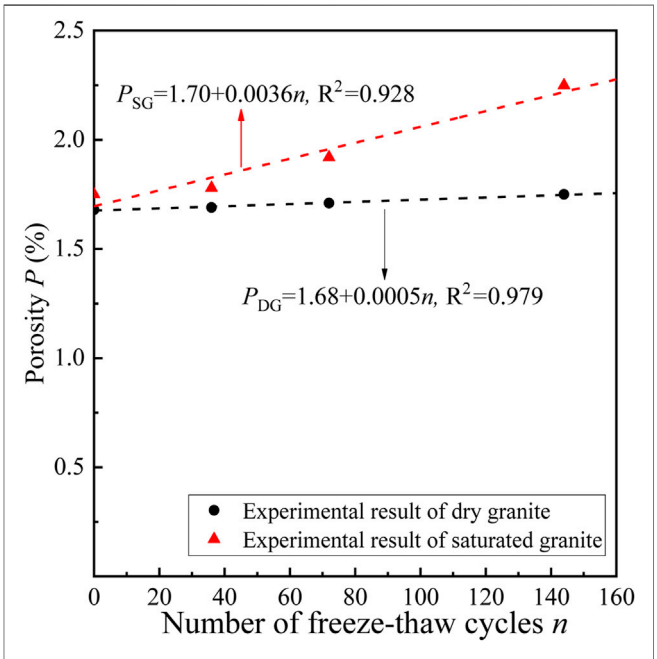

FIGURE 10 | Porosity evolutions of granite samples after different freeze-thaw cycles.

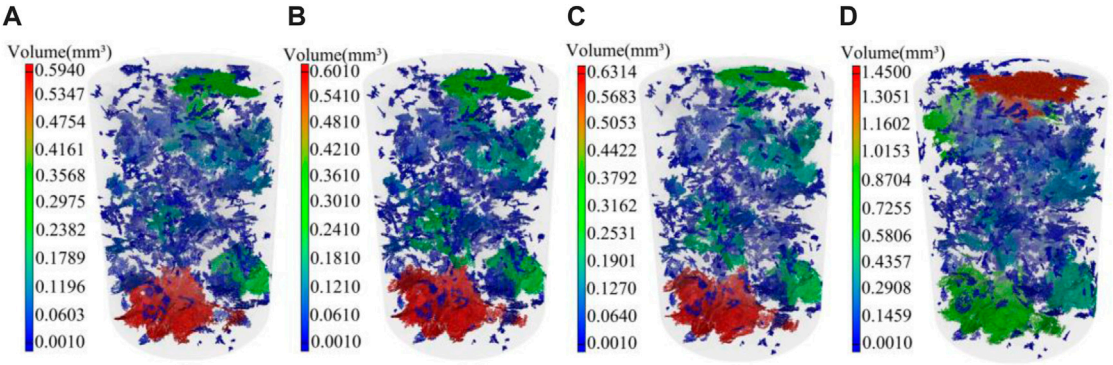

FIGURE 11 | Evolutions of defect volume in 3D reconstructed models of a saturated granite sample (a~d) after different freeze-thaw cycles: **(A)** 0 cycle, **(B)** 36 cycles, **(C)** 72 cycles, and **(D)** 144 cycles.

FIGURE 12 | Uniaxial compression test of a granite specimen on a MTS 815 system.

Mechanics (Fairhurst and Hudson, 2000). The displacement-controlled mode was selected to apply load to the rock specimens at a cross-head displacement rate of 0.001 mm/s. At room temperature, uniaxial compression tests were conducted on saturated and dry granite specimens after different numbers of freeze-thaw cycles.

Figures 13A,B illustrate the stress–strain curves of dry and saturated specimens after different freeze-thaw cycles. The strength of dry granite specimens decreases to the least extent after freeze-thaw cycles, and the stress–strain curves tend to stretch rightward and descend with the increasing number *n* of freeze-thaw cycles, resulting in a longer compaction stage and slight loss of elastic modulus of the granite. In the process of 0–72 freeze-thaw cycles, stress–strain curves of saturated granite show a small difference; while the elastic modulus and UCS of saturated granite decrease significantly with increasing axial strain after 144 freeze-thaw cycles. Observation of test curves after 144 freeze-thaw cycles in **Figure 13B** shows that, after reaching the peak strength, the curves descend slowly at first and then rapidly. This is because defects on two ends of saturated granite develop at a rate faster than those in the core of the rock specimens, so that local compressive failure occurs at the ends of the specimen in the uniaxial compression test.

Strength Deterioration

To quantify the strength deterioration trend of granite in the freeze-thaw process, **Figure 14** displays UCS of the granite after different freeze-thaw cycles. In the figure, R^2 represents the fitting degree (subscripts SG and DG to the dependent variables represent saturated and dry granite, respectively).

It can be seen from **Figure 14** that the strength of both saturated and dry granite decreases linearly and the absolute values of slopes of their fitted curves are 0.11 and 0.03, respectively; after 144 freeze-thaw cycles, strength losses of dry and saturated granite reach 4.08% and 26.2%, respectively, which indicates that the strength deterioration rate of the saturated granite is significantly higher than that of the dry granite. Because strength deterioration of dry granite is mainly attributed to differences in the coefficients of thermal expansion and cold contraction of mineral compositions, incompatible deformation occurs in the cyclic cold contraction and reheating that impairs rock structures. This is supported by falling of debris from the external surface and occurrence of microcracks inside. In comparison, the complex water-ice phase change also occurs in the saturated granite, exerting extra damages to the rock.

EVOLUTION OF FREEZE-THAW DAMAGE TO TEH ROCK

Mass Loss Characteristics

Surface spalling of rocks during freeze-thaw cycles resembles rockfall of frozen rocks in cold-region engineering. To comprehensively explore the evolution of rock appearance in freeze-thaw cycles, saturated granite with greater debris

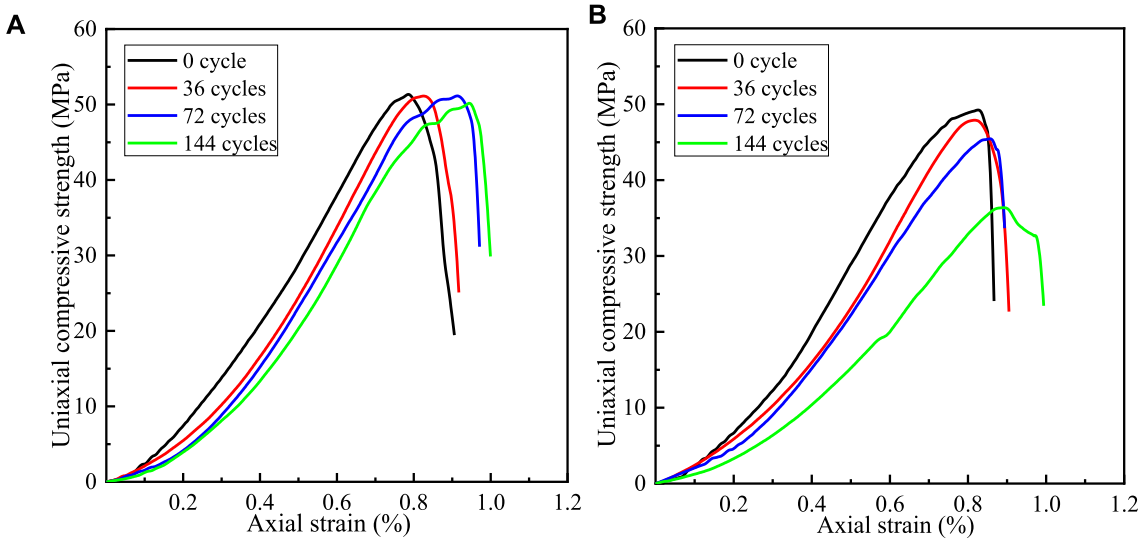

FIGURE 13 | Representative stress-strain curves of **(A)** dry granite and **(B)** saturated granite samples subject to different freeze-thaw cycles.

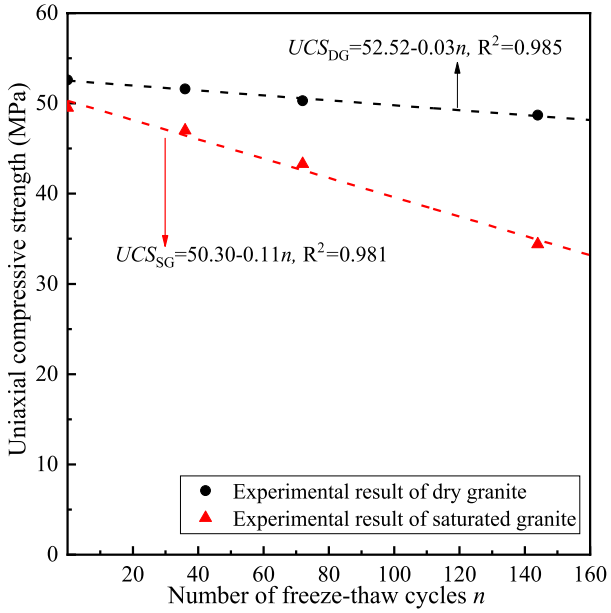

FIGURE 14 | Evolutions of the uniaxial compressive strength of dry and saturated samples subject to cyclic freeze-thaw actions.

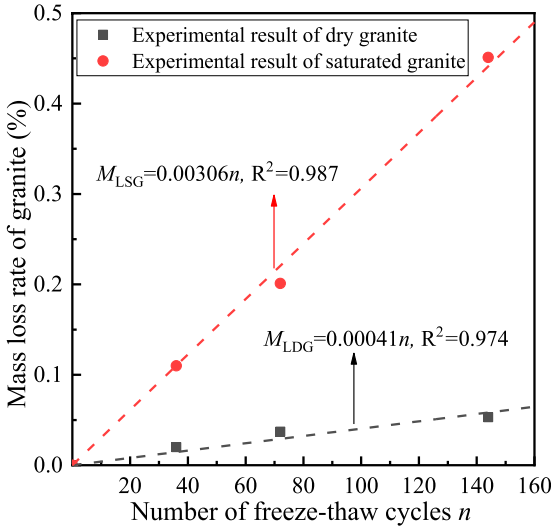

FIGURE 15 | Evolutions of the mass loss rates of granite samples during freeze-thaw cycles.

falling was taken as an example. It shows that visible (yet tiny) fragments of debris begin to appear on the external surface after 72 freeze-thaw cycles. After 144 cycles, obvious small-scale defects are seen on ends of multiple cylindrical granite specimens. Changes in the appearance of granite match the CT visualization results.

The mass loss rate of rocks subject to freeze-thaw actions is defined as the proportion of lost mass of a dry specimen at the end of freeze-thaw cycles in the total mass of the dry specimen before freeze-thaw cycles, and saturated rock specimens need to be dried before calculating their mass loss rate. **Figure 15** shows the mass loss rates of saturated and dry granite after n freeze-thaw cycles. The fitted curves and R^2 of corresponding data are also provided. In the fitting formula, M_{LSG} and M_{LDG} represent the mass loss rates of saturated and dry granite, respectively. Tests results are statistical means of data from multiple test specimens.

With the increase in the number n of freeze-thaw cycles, the fitted curves for mass loss rates of dry and saturated granite are both shown as the first-order function model, whose slope reflects the difficulty with which the rock sheds mass under freeze-thaw

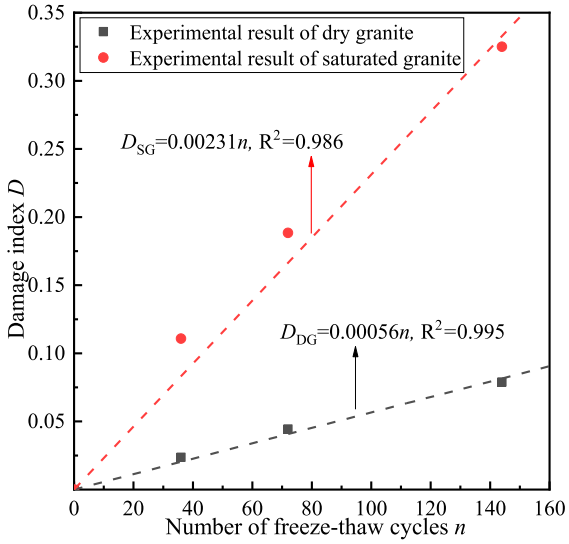

FIGURE 16 | Relations between the damage index D and the number of freeze-thaw cycles n of granite.

cycling: the greater the slope, the easier the mass is lost from the rock in the freeze-thaw process. It is worth noting that changes in the appearance and mass loss rate of the rock only mirror the resistance of the surface and local areas of the rock to freeze-thaw damage but fail to comprehensively describe freeze-thaw damage to the rock.

Quantitative Description of the Freeze-Thaw Damage

To quantify the damage evolution in granite after different numbers of freeze-thaw cycles, it is considered that responses of the macroscopic mechanical properties of the rock can reflect deterioration within the rock from the perspective of the macroscopic damage mechanics. The damage variable is expressed as follows based on the degree of loss of elastic modulus:

$$D = 1 - z*\frac{E_n}{E_0} \tag{1}$$

where D represents the damage index of granite due to freeze-thaw cycles, and E_n represents the elastic modulus of the rock after n freeze-thaw cycles and E_o denotes the initial elastic modulus of the rock before freeze-thaw cycling.

Considering the random distribution of defects inside the rock, the pore content and degree of fracture coalescence both significantly influence the failure process, hence, changes in the effective load-bearing area of the rock in the freeze-thaw process are considered and used as an improvement coefficient Z, as shown below:

$$z = \frac{V_e}{V} = \frac{V_e}{V_e + V_p - V_{po}} \tag{2}$$

where V_e and V represent the effective load-bearing volume and apparent load-bearing volume of the rock (mm^3), respectively, and V_{po} is the initial pore volume in the rock (mm^3). Here, V is composed of two parts: one is the matrix volume V_e, that is, the effective load-bearing volume; another is the volume of pores and cracks V_p (mm^3), which is also termed the initial damage considering various defects in the rock itself. To eliminate influences of this initial damage, the initial pore volume V_{P0} in the rock is subtracted from V. Combining **Eqs 1**, **2**, the damage variable is given by

$$D = 1 - \frac{E_n}{E_0} \times \frac{V_e}{V_e + V_p - V_{po}} \tag{3}$$

According to mechanical tests on the rock and analysis results of the 3D visualization software, the freeze-thaw damage index D of the rock could be calculated using **Eq. 3**. To date, many scholars have proposed the mathematical model for the relationship between the freeze-thaw damage index and the number of freeze-thaw cycles (Altindag et al., 2004; Oezbek, 2014; Liu et al., 2015). Based on properties and test data of the studied rock, the first-order function model of $D(n) = kn$ could be used to describe the damage evolution. In this model, parameter k represents the sensitivity of the rock to the freeze-thaw action, and the larger the value is, the faster the damage accumulates. According to the equation, the damage-evolution models (**Eqs 4**, **5** were obtained for the saturated and dry granite:

$$D_{SG} = 0.00231n \tag{4}$$

$$D_{DG} = 0.00056n \tag{5}$$

where D_{SG} and D_{DG} represent the freeze-thaw damage index of saturated granite and dry granite, respectively.

Figure 16 illustrates comparison of the predicted curve and measured value of the damage index of granite: the predicted

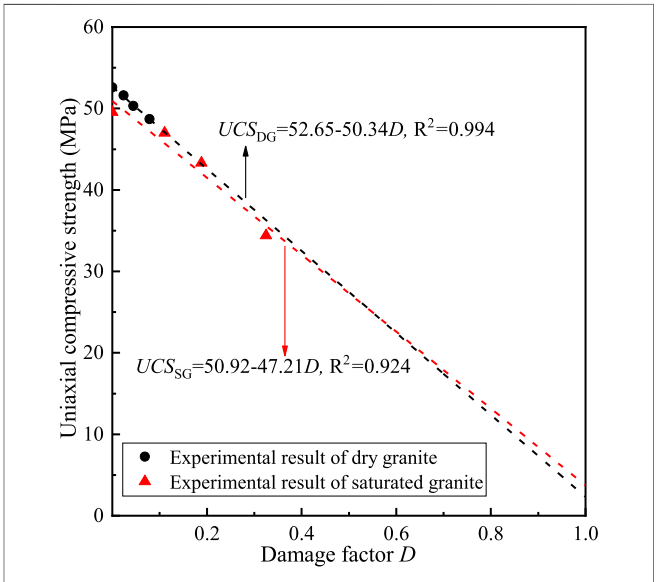

FIGURE 17 | Relations between the uniaxial compressive strength UCS and the damage index D of granite.

values are a good fit to the measured data. The slope of the fitted curve reflects the rate of change in the damage. The growth rate of damage of saturated granite is about four times that of dry granite.

To test the reasonability of calculation of the freeze-thaw damage index D, the relationship between the freeze-thaw damage index D and UCS was drawn, as shown in **Figure 17**, in which the fitted curve agrees well with the measured strength. This finding can verify the feasibility of the improved elastic modulus loss method. The UCS linearly decreases as the damage index D changes. When $D = 0$, there is no loss of UCS; when $D = 1$, the UCSs of the saturated and dry granite both approximate 0 on the fitted curve, that is, the rock has completely lost its bearing capacity.

CONCLUSION

To explore damage evolution in granite under cyclic freeze-thaw actions, characteristics of microcracks and evolution of macroscopic mechanical parameters in the freeze-thaw process were quantitatively analyzed. In the process, cyclic freeze-thaw tests, high-resolution CT scanning, and uniaxial compression tests were carried out. The main concluding remarks are

1) The number of freeze-thaw cycles and the moisture condition significantly influence the mechanical properties of granite. As the number of freeze-thaw cycles increases, the peak stress of granite decreases to different extents. Compared with dry rock specimens, saturated granite shows more significant deterioration. After 144 freeze-thaw cycles, the strength losses of dry and saturated granite are 4.08% and 26.2%, respectively.
2) High-resolution CT scanning allowed visualization of the freeze-thaw processes underway in the rock, which intuitively shows the evolution of damage and deterioration of granite. Under freeze-thaw cycles, the frost heave of pore water in saturated granite causes new micro-defects to initiate and develop and new cracks mainly develop from surface defects to the interior of the rock cores, accompanied by non-uniform deformation of different mineral compositions. This facilitates pores and cracks in the rock to constantly propagate and coalesce. For dry rock specimens, the non-uniform contraction and expansion of minerals therein are main causes for internal deterioration of the rock, and its rate of structural deterioration is much lower than that of saturated granite specimens.
3) The elastic modulus loss method introduced with the correction coefficient of effective load-bearing volume deliver a high accuracy when calculating freeze-thaw damage to granite. The damage index D increases linearly with the increase in the number of freeze-thaw cycles and it matches the strength deterioration trend and pore development of the granite, thus reflecting the evolution of freeze-thaw damage in granite.

DATA AVAILABILITY STATEMENT

The original contributions presented in the study are included in the article/Supplementary Material, further inquiries can be directed to the corresponding author.

AUTHOR CONTRIBUTIONS

BL: Formal analysis, Investigation, Visualization, Funding acquisition. GZ: Conceptualization, Methodology, Writing-original draft, Supervision. GW: Writing- review andediting, Funding acquisition. JQ: Writing—review and editing.

FUNDING

Natural Science Foundation of Zhejiang Province (Grant No.LR19E090001), Natural Science Foundation of China (Grant Nos. 42077252, 41831290), Hubei Key Laboratory of Roadway Bridge and Structure Engineering (Wuhan University of Technology) (Grant No.DQJJ202104)

REFERENCES

Altindag, R., Alyildiz, I. S., and Onargan, T. (2004). Mechanical Property Degradation of Ignimbrite Subjected to Recurrent Freeze-Thaw Cycles. *Int. J. Rock Mech. Min. Sci.* 41 (6), 1023–1028. doi:10.1016/j.ijrmms.2004.03.005

Aoki, K., Hibiya, K., and Yoshida, T. (1990). Storage of Refrigerated Liquefied Gases in Rock Caverns: Characteristics of Rock under Very Low Temperatures. *Tunn. Undergr. Space Technol.* 5 (4), 319–325. doi:10.1016/0886-7798(90)90126-5

Bayram, F. (2012). Predicting Mechanical Strength Loss of Natural Stones after Freeze-Thaw in Cold Regions. *Cold Regions Sci. Technol.* 83-84, 98–102. doi:10.1016/j.coldregions.2012.07.003

Bubeck, A., Walker, R. J., Healy, D., Dobbs, M., and Holwell, D. A. (2017). Pore Geometry as a Control on Rock Strength. *Earth Planet. Sci. Lett.* 457, 38–48. doi:10.1016/j.epsl.2016.09.050

De Kock, T., Boone, M. A., De Schryver, T., Van Stappen, J., Derluyn, H., Masschaele, B., et al. (2015). A Pore-Scale Study of Fracture Dynamics in Rock Using X-Ray Micro-CT under Ambient Freeze-Thaw Cycling. *Environ. Sci. Technol.* 49 (5), 2867–2874. doi:10.1021/es505738d

Deprez, M., De Kock, T., De Schutter, G., and Cnudde, V. (2020). A Review on Freeze-Thaw Action and Weathering of Rocks. *Earth-Science Rev.* 203, 103143. doi:10.1016/j.earscirev.2020.103143

Fairhurst, C. E., and Hudson, J. A. (2000). Draft ISRM Suggested Method for the Complete Stress-Strain Curve for Intact Rock in Uniaxial Compression. *Chin. J. Rock Mech. Eng.* 19 (06), 802–808. doi:10.3321/j.issn:1000-6915.2000.06.025

Fan, W., Yang, P., and Yang, Z. (2021). Freeze-Thaw Impact on Macropore Structure of Clay by 3D X-Ray Computed Tomography. *Eng. Geol.* 280, 105921. doi:10.1016/j.enggeo.2020.105921

Fang, Y., Qiao, L., Chen, X., Yan, S.-j., Zhai, G.-l., and Liang, Y.-w. (2014). Experimental Study of Freezing-Thawing Cycles on Sandstone in Yungang Grottos. *Rock Soil Mech.* 35 (09), 2433–2442. doi:10.16285/j.rsm.2014.09.003

Ghobadi, M. H., and Babazadeh, R. (2015). Experimental Studies on the Effects of Cyclic Freezing-Thawing, Salt Crystallization, and Thermal Shock on the Physical and Mechanical Characteristics of Selected Sandstones. *Rock Mech. Rock Eng.* 48 (3), 1001–1016. doi:10.1007/s00603-014-0609-6

Jiang, Z.-h., Yao, Z.-m., and Chen, J.-h. (2017). The Effect of Freezing-Thaw Cycle and Water Content on Uniaxial Compressive Strength of Sandstone. *Min. Res. Dev.* 37 (1), 85–88. doi:10.13827/j.cnki.kyyk.2017.01.020

Khanlari, G., Sahamieh, R. Z., and Abdilor, Y. (2015). The Effect of Freeze-Thaw Cycles on Physical and Mechanical Properties of Upper Red Formation Sandstones, Central Part of Iran. *Arab. J. Geosci.* 8 (08), 5991–6001. doi:10.1007/s12517-014-1653-y

Kodama, J., Goto, T., Fujii, Y., and Hagan, P. (2013). The Effects of Water Content, Temperature and Loading Rate on Strength and Failure Process of Frozen Rocks. *Int. J. Rock Mech. Min. Sci.* 62, 1–13. doi:10.1016/j.ijrmms.2013.03.006

Liu, C.-y., He, M.-c., Wang, S.-r., and Hu, J.-c. (2005). Experimental Investigation Freeze Thawing Damage Characteristics of Granite at Low Temperature. *J. Hunan Univ. Sci. Technol. Nat. Sci. Ed.* 20 (01), 37–40. doi:10.3969/j.issn.1672-9102.2005.01.010

Liu, Q. S., Huang, S. B., and Kang, Y. S. (2015). Fatigue Damage Model and Evaluation Index for Rock Mass under Freezing-Thawing Cycles. *Chin. J. Rock Mech. Eng.* 34 (6), 1116–1127. doi:10.13722/j.cnki.jrme.2014.1189

Luo, X., Jiang, N., Zuo, C., Dai, Z., and Yan, S. (2014). Damage Characteristics of Altered and Unaltered Diabases Subjected to Extremely Cold Freeze-Thaw Cycles. *Rock Mech. Rock Eng.* 47 (04), 1997–2004. doi:10.1007/s00603-013-0516-2

Maji, V., and Murton, J. B. (2020). Micro-computed Tomography Imaging and Probabilistic Modelling of Rock Fracture by Freeze-Thaw. *Earth Surf. Process. Landforms* 45 (3), 666–680. doi:10.1002/esp.4764

Martínez-Martínez, J., Benavente, D., Gomez-Heras, M., Marco-Castaño, L., and García-del-Cura, M. Á. (2013). Non-linear Decay of Building Stones during Freeze-Thaw Weathering Processes. *Constr. Build. Mater.* 38, 443–454. doi:10.1016/j.conbuildmat.2012.07.059

Momeni, A., Abdilor, Y., Khanlari, G. R., Heidari, M., and Sepahi, A. A. (2016). The Effect of Freeze-Thaw Cycles on Physical and Mechanical Properties of Granitoid Hard Rocks. *Bull. Eng. Geol. Environ.* 75 (4), 1649–1656. doi:10.1007/s10064-015-0787-9

Nicholson, D. T., and Nicholson, F. H. (2000). Physical Deterioration of Sedimentary Rocks Subjected to Experimental Freeze-Thaw Weathering. *Earth Surf. Process. Landforms* 25 (12), 1295–1307. doi:10.1002/1096-9837(200011)25:12<1295::AID-ESP138>3.0.CO;2-E

Özbek, A. (2014). Investigation of the Effects of Wetting-Drying and Freezing-Thawing Cycles on Some Physical and Mechanical Properties of Selected Ignimbrites. *Bull. Eng. Geol. Environ.* 73 (2), 595–609. doi:10.1007/s10064-013-0519-y

Park, C., Synn, J. H., Shin, H. S., Cheon, D. S., Lim, H. D., and Jeon, S. W. (2004). Experimental Study on the Thermal Characteristics of Rock at Low Temperatures. *Int. J. Rock Mech. Min. Sci.* 41 (s1), 81–86. doi:10.1016/j.ijrmms.2003.12.08410.1016/j.ijrmms.2004.03.023

Park, J., Hyun, C.-U., and Park, H.-D. (2015). Changes in Microstructure and Physical Properties of Rocks Caused by Artificial Freeze-Thaw Action. *Bull. Eng. Geol. Environ.* 74 (2), 555–565. doi:10.1007/s10064-014-0630-8

Peng, J.-b., Cui, P., and Zhuang, J.-q. (2020). Challenges to Engineering Geology of Sichuan-Tibet Railway. *Chin. J. Rock Mech. Eng.* 39 (12), 2377–2389. doi:10.13722/j.cnki.jrme.2020.0446

Promentilla, M. A. B., and Sugiyama, T. (2010). X-Ray Microtomography of Mortars Exposed to Freezing-Thawing Action. *Act* 8 (2), 97–111. doi:10.3151/jact.8.97

Qi, L.-r., Wang, J.-d., Zhang, D.-f., Zhang, Y.-s., Li, Z.-x., Sun, J.-x., et al. (2017). A Study of Granite Damage in the Macro and Microscopic Scales under Freezing-Thawing Cycles. *Hydrogeol. Eng. Geol.* 48 (05), 65–73. doi:10.16030/j.cnki.issn.1000-3665.202103073

Qin, L., Zhai, C., Liu, S., Xu, J., Yu, G., and Sun, Y. (2017). Changes in the Petrophysical Properties of Coal Subjected to Liquid Nitrogen Freeze-Thaw - A Nuclear Magnetic Resonance Investigation. *Fuel* 194, 102–114. doi:10.1016/j.fuel.2017.01.005

Song, Y.-j., Yang, H.-m., Zhang, L.-t., and Ren, J.-x. (2019). CT Real-Time Monitoring on Uniaxial Damage of Frozen Red Sandstone. *Rock Soil Mech.* 40 (S1), 152–160. doi:10.16285/j.rsm.2018.2371

Tan, X., Chen, W., Yang, J., and Cao, J. (2011). Laboratory Investigations on the Mechanical Properties Degradation of Granite under Freeze-Thaw Cycles. *Cold Regions Sci. Technol.* 68 (3), 130–138. doi:10.1016/j.coldregions.2011.05.007

Tian, Z., Zhang, J.-y., Wang, G.-b., and Tang, M.-h. (2021). Experimental Study on Microstructure Damage of Freeze-Thaw Red Sandstone. *Min. Res. Dev.* 41 (10), 61–66. doi:10.13827/j.cnki.kyyk.2021.10.011

Yamabe, T., and Neaupane, K. M. (2001). Determination of Some Thermo-Mechanical Properties of Sirahama Sandstone under Subzero Temperature Condition. *Int. J. Rock Mech. Min. Sci.* 38 (7), 1029–1034. doi:10.1016/s1365-1609(01)00067-3

Yang, G.-s., Pu, Y.-b., and Ma, W. (2002). Discussion on the Damage Propagation for the Rock under the Frost and Thaw Condition of Frigid Zone. *J. Exp. Mech.* 17 (2), 220–226. doi:10.3969/j.issn.1001-4888.2002.02.015

Yang, H.-r., Liu, P., Sun, B., Yi, Z.-y., Wang, J.-j., and Yue, Y.-q. (2021). Study on Damage Mechanisms of the Microstructure of Sandy Conglomerate at Maijishan Grottoes under Freeze-Thaw Cycles. *Chin. J. Rock Mech. Eng.* 40 (03), 545–555. doi:10.13722/j.cnki.jrme.2020.0767

Yavuz, H. (2011). Effect of Freeze-Thaw and Thermal Shock Weathering on the Physical and Mechanical Properties of an Andesite Stone. *Bull. Eng. Geol. Environ.* 70 (2), 187–192. doi:10.1007/s10064-010-0302-2

Zhang, J.-z., Miu, L.-c., and Yang, Z.-f. (2008). Research on Rock Degradation and Deterioration Mechanisms and Mechanical Characteristics under Cyclic Freezing-Thawing. *Chin. J. Rock Mech. Eng.* 27 (8), 1688–1694. doi:10.3321/j.issn:1000-6915.2008.08.020

Zou, X.-q., Pei, X.-j., and Mu, J.-q. (2017). Preliminary Study on the Deformation Characteristics of Cracked Sandstone under the Freeze-Thaw Cycles. *Sci. Technol. Eng.* 17 (8), 235–238. doi:10.3969/j.issn.1671-1815.2017.08.040

Conflict of Interest: The authors declare that the research was conducted in the absence of any commercial or financial relationships that could be construed as a potential conflict of interest.

Publisher's Note: All claims expressed in this article are solely those of the authors and do not necessarily represent those of their affiliated organizations, or those of the publisher, the editors and the reviewers. Any product that may be evaluated in this article, or claim that may be made by its manufacturer, is not guaranteed or endorsed by the publisher.

Copyright © 2022 Li, Zhang, Wang and Qiao. This is an open-access article distributed under the terms of the Creative Commons Attribution License (CC BY). The use, distribution or reproduction in other forums is permitted, provided the original author(s) and the copyright owner(s) are credited and that the original publication in this journal is cited, in accordance with accepted academic practice. No use, distribution or reproduction is permitted which does not comply with these terms.

frontiers | Frontiers in Earth Science

ORIGINAL RESEARCH
published: 11 May 2022
doi: 10.3389/feart.2022.899755

Numerical Experiment Research on Failure Characteristics of Anchored Rock With Negative Poisson's Ratio Bolt

Feng Chen[1]*, *Xue-Bin Wang*[2], *Yan-Hong Du*[1] and *Chun-An Tang*[3]

[1]School of Mechanics and Engineering, Liaoning Technical University, Fuxin, China, [2]Institute of Computational Mechanics, Liaoning Technical University, Fuxin, China, [3]Institute of Rock Instability and Seismicity Research, Dalian University of Technology, Dalian, China

With the continuous increase in the mining depth and engineering burying depth, the nonlinear physical and mechanical phenomena exhibited by rock are more complicated. The load value often exceeds the yield strength of the traditional Poisson's ratio support materials, resulting in failure of the support body. Therefore, the bolt still needs further in-depth research into new materials. In this study, the numerical model with a negative Poisson's ratio bolt had been established, the properties of negative Poisson's ratio materials and the working principle of RFPA software were introduced, and RFPA software was used to study the reinforcement effect of negative Poisson's ratio bolt on the rock. The numerical experiment results show that compared with the positive Poisson's ratio bolt, the negative Poisson's ratio bolt can significantly increase the bearing capacity of anchored rock; enhance the friction between the bolt, body, and the surrounding rock; and limit the rock movement. The anchored rock with a negative Poisson's ratio bolt can absorb more energy. A negative Poisson's ratio material is one of the future development directions of the bolt material.

Keywords: rock engineering, negative Poisson's ratio, bolt, RFPA, bearing capacity

OPEN ACCESS

Edited by:
Yan Du,
University of Science and Technology Beijing, China

Reviewed by:
Dong Zhuo,
Henan Polytechnic University, China
Ning Liu,
Guizhou University, China

***Correspondence:**
Feng Chen
cflucky@sina.cn

Specialty section:
This article was submitted to Geohazards and Georisks, a section of the journal Frontiers in Earth Science

Received: *19 March 2022*
Accepted: *11 April 2022*
Published: *11 May 2022*

Citation:
Chen F, Wang X-B, Du Y-H and Tang C-A (2022) Numerical Experiment Research on Failure Characteristics of Anchored Rock With Negative Poisson's Ratio Bolt. Front. Earth Sci. 10:899755. doi: 10.3389/feart.2022.899755

1 INTRODUCTION

A bolt is a kind of support body that transmits the tensile load to the stable rock layer to improve the stability and strength of the rock medium, and has a lower cost in terms of material and manpower, so it has been widely used in mining, transportation, water conservancy, and urban underground space engineering (He et al., 2005; Hyett et al., 2015; Vandermaat et al., 2016; Kim et al., 2017). With the development of rock anchoring, problems in the direction of "large, deep, and difficult" sudden engineering disasters and major malignant accidents caused by nonlinear large deformation damage have occurred frequently in recent years (He et al., 2005). The reason for these problems is that the traditional supporting materials including traditional bolts, anchor cables, U-shaped steel brackets, and other traditional supporting materials frequently fail (Jalalifar, 2006; Kang et al., 2013). One of the root causes is that the materials of these supporting bodies belong to the traditional Poisson's ratio materials, that is, plastic hardening materials, which instantly reach the yield strength and lose the bearing capacity under a large load, leading to the failure of the support (Wan et al., 2004; Alderson and Alderson, 2007; He et al., 2014; Yu et al., 2016).

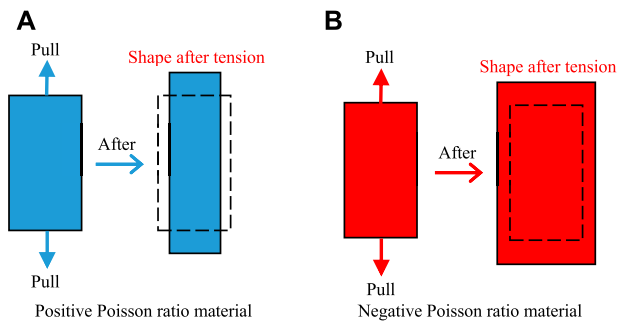

FIGURE 1 | Deformation of axial tension material. **(A)**Positive Poisson ratio material. **(B)** Negative Poisson ratio material.

Poisson's ratio ν is called the transverse deformation coefficient, which refers to the value of the ratio changed in the sign of the transverse strain to the axial normal strain when the material is subjected to uniaxial tension or compression. It is the elastic constant reflecting the material transverse deformation and is expressed by the formula as $\nu = -\frac{\varepsilon'}{\varepsilon}$ (ε' is the transverse normal strain and ε is the axial normal strain). Common materials shrink in the vertical cross-sectional direction when they are stretched (see **Figure 1A**) but expand in the direction perpendicular to the section when they are compressed by an external force. It is generally considered that almost all materials have a positive Poisson's ratio (Horrigan et al., 2009).

According to the thermodynamic theory, Poisson's ratio of isotropic material ranges from −1 to 1, so there are negative Poisson's ratio materials in theory (Horrigan et al., 2009; Gaspar, 2010). Lakes was the first to obtain a new type of material of a concave unit structure with a Poisson's ratio −0.7 in a series of treatments of ordinary polyurethane foam in 1987 (Shi et al., 2012). This also means that when the material is subjected to axial tension, it will cause lateral expansion deformation (see **Figure 1B**). This kind of auxetic behavior greatly improves the material mechanical properties such as shear modulus, fracture toughness, energy absorption, and indentation resistance. In addition, negative Poisson's ratio materials have a good stress dispersion effect, a very high shear modulus, and a very low bulk modulus (Evans, 2010; Liu and Hu, 2010; Critchley et al., 2013; Saxena et al., 2016). Because negative Poisson's ratio materials have a higher value of the strength than positive Poisson's ratio materials, they can be used as structural materials and functional materials at the same time. Therefore, they have broad application space in the fields of biomedicine and national defense technology (Lakes, 1987; Martz et al., 1996; Li et al., 2019).

Because the physical and mechanical parameters of different experimental samples have a certain degree of discreteness, it is impossible to change only one physical and mechanical parameter of the experimental sample while keeping other physical and mechanical parameters the same in indoor and outdoor comparative experiments (Tang et al., 2018; Chen et al., 2019). However, the numerical experiment method can quickly adjust the parameters.

Based on the special mechanical properties of negative Poisson's ratio material, as well as the advantages of the numerical experiment method, we used RFPA^{2D}-Basic software to study the failure characteristics of an anchored rock with a negative Poisson's ratio bolt. The similarities and differences in stress, displacement, and acoustic emission (AE) of anchored rocks with the positive Poisson's ratio bolt and the negative Poisson's ratio bolt had been compared and analyzed.

2 NEGATIVE POISSON'S RATIO MATERIAL PROPERTIES

Since Lakes (1987) first pointed out that a material with a cellular structure can produce a negative Poisson's ratio during deformation, a large number of negative Poisson's ratio materials and structures have been discovered, synthesized, and prepared, ranging from a molecular microscopic scale to macrostructure scale (Grima et al., 2005; Alderson et al., 1998; Ravirala et al., 2006; Alderson et al., 2002; Lakes, 1993). **Figure 2** shows negative Poisson's ratio materials at different scale levels. The structure of negative Poisson's ratio materials is also diverse, including negative Poisson's ratio foam structure, microscopic negative Poisson's ratio structure, and negative Poisson's ratio

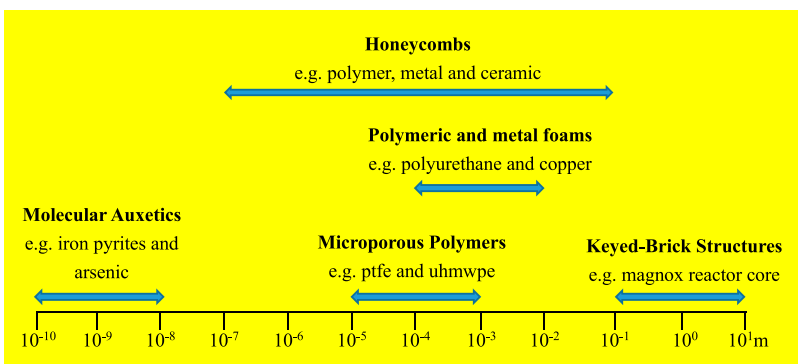

FIGURE 2 | Different scale materials with negative Poisson's ratio.

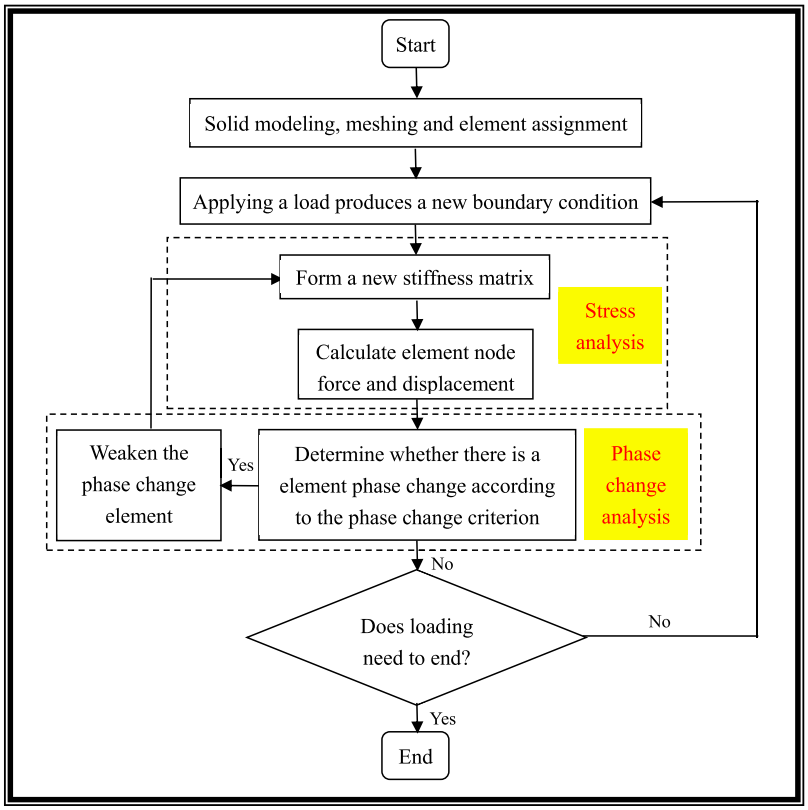

FIGURE 3 | RFPA software workflow picture.

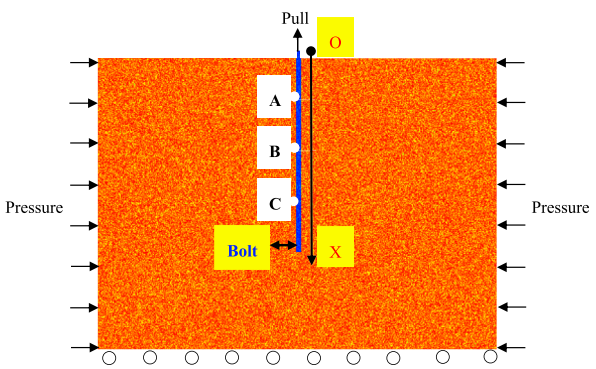

FIGURE 4 | Numerical model.

composite structure (Wojciechowski, 1989; Grima et al., 2006; Gercek, 2007; Miller et al., 2009).

Negative Poisson's ratio material can improve the service performance of the structure by designing the mechanical properties of the structure (Alderson et al., 2002; Grima et al., 2006). The elastic properties of the material can be expressed by four elastic constants in elastic theory, namely, Young's modulus E, shear modulus G, bulk modulus K, and Poisson's ratio ν. These four constants are not independent of each other for the isotropic material, and they are related to each other by the following equation: $G= E/(2(1+\nu))$ and $K= E/(3(1-2\nu))$。. Many materials require G to be larger than K. If we change ν by changing the microstructure of the material under the condition that the E of the material remains unchanged, we can change the values of K and G. For example, when ν is reduced to −1, a shear modulus that is much higher than a bulk modulus can be obtained. In other words, the material is not prone to shear deformation but prone to volume changes.

TABLE 1 | Physical and mechanical parameters of the rock and the bolt with a positive Poisson's ratio.

Parameter	Rock	Bolt
Inhomogeneous index	2	50
Strength (MPa)	150	345
Young's modulus (MPa)	20,000	210,000
Poisson's ratio	0.2	−0.3
Density (kg/m^3)	2,250	7,800
Friction angle (°)	55	30

3 INTRODUCTION TO RFPA SOFTWARE

Tang et al. (1998) proposed a new numerical simulation software named RFPA (Realistic Failure Process Analysis).

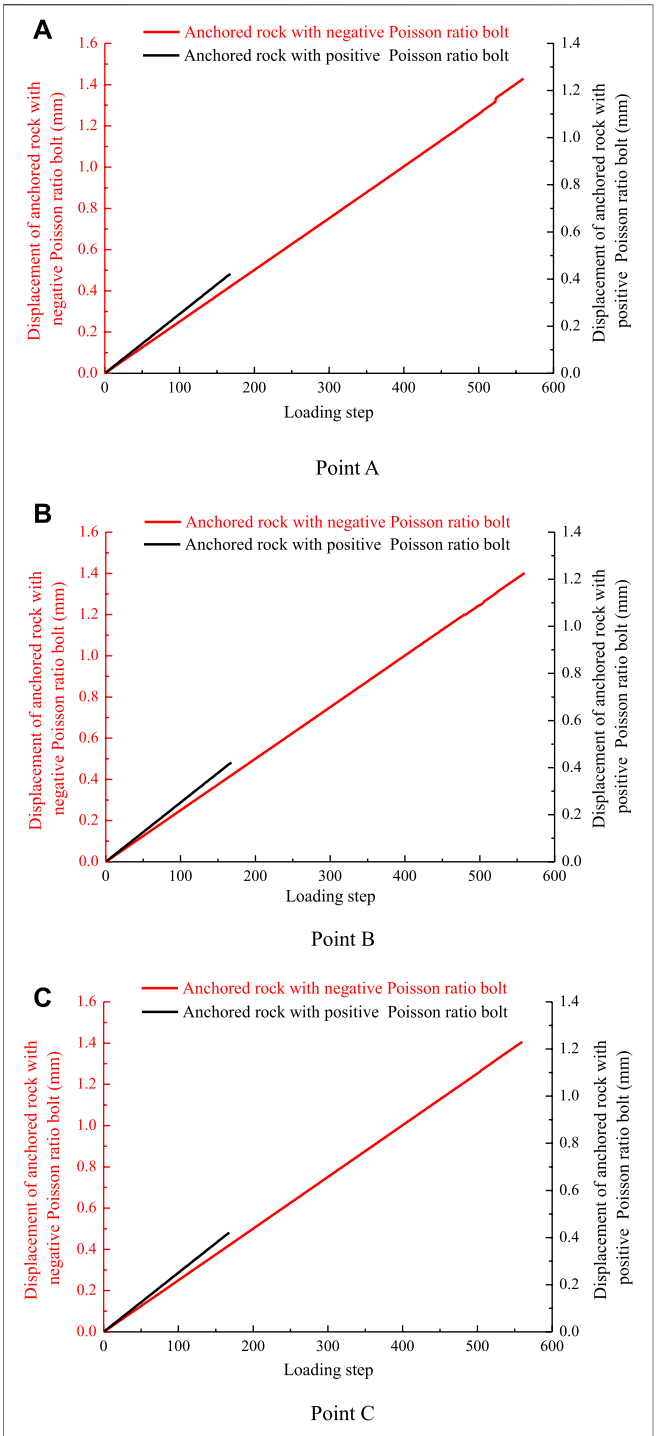

FIGURE 5 | Displacement comparison curves of points A, B, and C of two kinds of anchored rock. **(A)** Point A. **(B)** Point B. **(C)** Point C.

RFPA software is a numerical experiment tool that can simulate the progressive failure process of the material. The calculation method of this software is based on finite element theory and statistical damage theory. This method has considered the nonuniformity of material properties and the randomness of defect distribution and combined the statistical

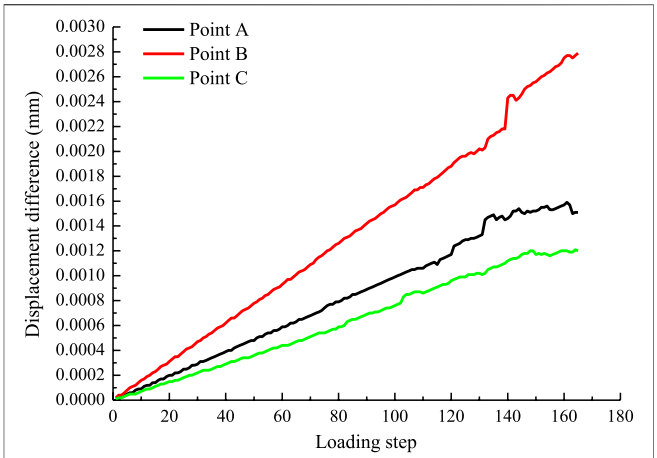

FIGURE 6 | Displacement difference curve of points A, B, and C of two kinds of anchored rock.

distribution assumptions of this material property into the numerical calculation method (finite element method). The elements which satisfy the given strength criterion are destroyed, so that the numerical simulation of the failure process of heterogeneous materials can be realized (Li and Tang, 2015; Huang et al., 2017; Li et al., 2018; Tang et al., 2020).

The entire workflow can be seen in **Figure 3**. For each given displacement increment, RFPA software first performs stress calculation and then checks whether there are phase change primitives in the model according to the phase change criterion. If there is no phase change element, this software will continue loading to add a displacement component and proceed to the next step of stress calculation (Tang, 1997; Tang and Kaiser, 1998; Tang, 2003). If there is a phase change element, the stiffness will be weakened according to the stress state of the element, and then the stress calculation of the current step is performed again until no new phase change element appears. The

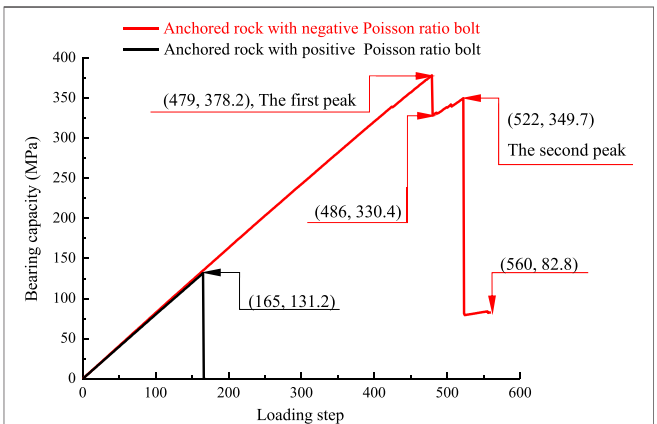

FIGURE 7 | Stress curve of two different anchored rocks.

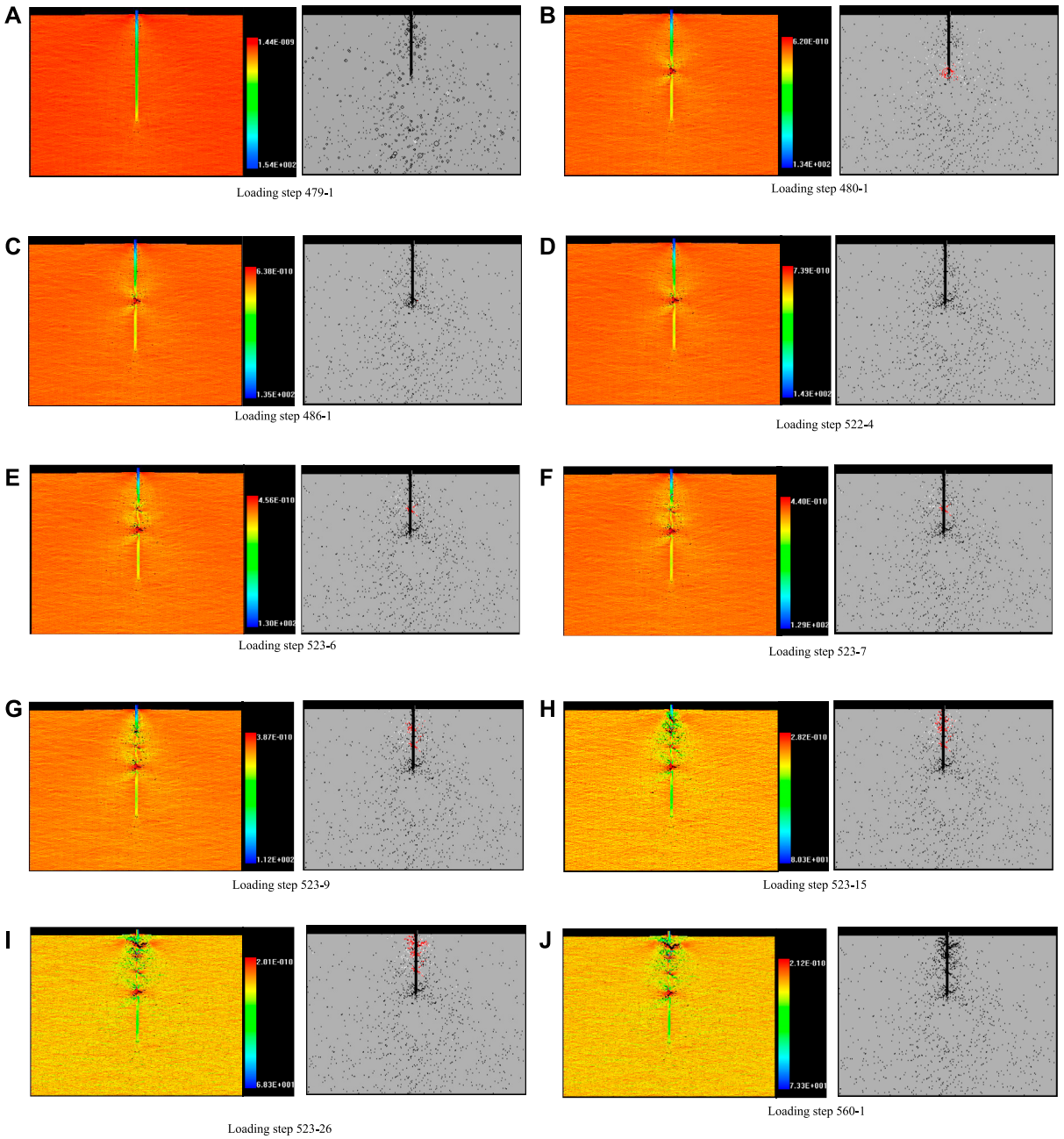

FIGURE 8 | Failure process of anchored rock with the negative Poisson's ratio bolt (the left column is the minimum principal stress nephogram, and the right column is the acoustic emission diagram). **(A)** Loading step 479-1. **(B)** Loading step 480-1. **(C)** Loading step 486-1. **(D)** Loading step 522-4. **(E)** Loading step 523-6. **(F)** Loading step 523-7. **(G)** Loading step 523-9. **(H)** Loading step 523-15. **(I)** Loading step 523-26. **(J)** Loading step 560-1.

aforementioned process is repeated until the applied load, deformation, or macro fracture of the whole medium is reached (Zhang et al., 2007; Du et al., 2019; Du et al., 2021).

4 NUMERICAL MODEL

In order to study the negative Poisson's ratio effect of the bolt, a numerical model has been established (see **Figure 4**). The one-dimensional coordinate system is established along the axial direction of the bolt for the convenience of marking, and the origin O of the coordinate is located on the upper side of the bolt. The overall size of the model is 2000 × 1,500 mm, and the number of divided units is 400 × 300. The bottom side of this numerical model is fixed. Displacement compression load is applied to the left and right sides of the model, and the displacement increment is 0.002 mm. The tensile load is applied to the upper-end face of the bolt, and the

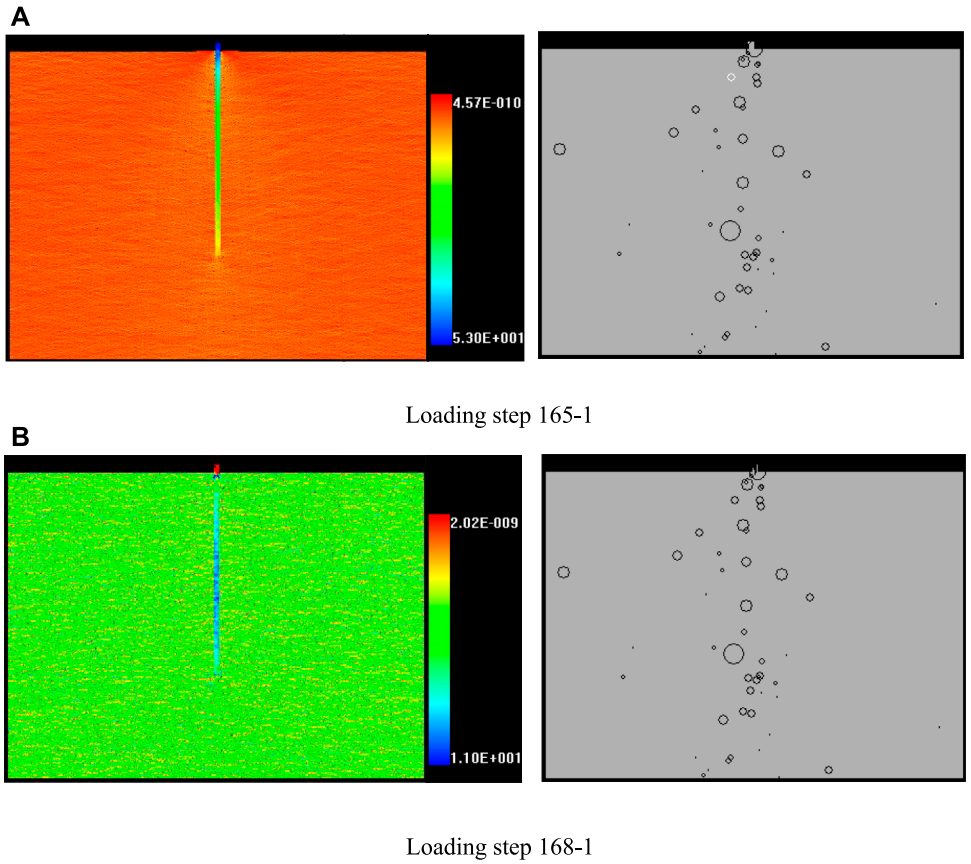

FIGURE 9 | Failure process of anchored rock with the positive Poisson's ratio bolt (the left column is the minimum principal stress nephogram, and the right column is the acoustic emission diagram). **(A)** Loading step 165-1. **(B)** Loading step 168-1.

displacement increment is also 0.002 mm. The bolt size is 1,000 × 20 mm, which is located in the transverse middle of this model. Three points A, B, and C are marked along the left boundary of the bolt to analyze the lateral displacement of the rock. The coordinates of the aforementioned three points along the axial direction of the bolt are 250 mm, 500, and 750 mm, respectively. The physical and mechanical parameters of rock mass and bolt are shown in **Table 1**. At the same time, the numerical model of the bolt with a positive Poisson's ratio is established. The Poisson's ratio of the bolt with a positive Poisson's ratio is 0.3, and the other physical and mechanical parameters are the same as that of the bolt with a negative Poisson's ratio. The constitutive relation of the rock bolt is simplified as an elastic-plastic model, and the rock is endowed with an ideal elastic-plastic constitutive relation. The anchoring effects of two kinds of bolts are compared and analyzed.

5 NUMERICAL EXPERIMENT RESULTS

5.1 Displacement Change Analysis

As shown in **Figure 5**, the displacements of points A, B, and C of anchored rock with the negative Poisson's ratio bolt all increase linearly under the action of external force, the slopes of displacement curves are the same. The displacement values of the three points are 1.4293, 1.4018, and 1.4063 mm, respectively, after the negative Poisson's ratio bolt is broken. Under the action of external force, the displacements of points A, B, and C of the anchored rock with the positive Poisson's ratio bolt also show a linear increase and the changing trend of displacement curves is the same. The displacement values of the three points are 0.4219, 0.4221, and 0.4211 mm, respectively, after the positive Poisson's ratio bolt is broken. Because the anchored rock with the positive Poisson's ratio bolt ends the numerical experiment in loading step 168, the horizontal coordinates of the displacement and stress comparison curves of two anchored rocks are taken to loading step 168. The displacements of points A, B, and C of anchored rock with the positive Poisson's ratio bolt are greater than those of anchored rock with the negative Poisson's ratio bolt at any loading moment. This is because the positive Poisson's ratio material undergoes lateral contraction deformation, the surrounding rock can further deform toward the bolt body, while the negative Poisson's ratio material undergoes lateral expansion deformation, which limits the deformation of the surrounding rock to the bolt body and reduces the displacement of surrounding rock. The aforementioned numerical experiment results are in line with the actual situation,

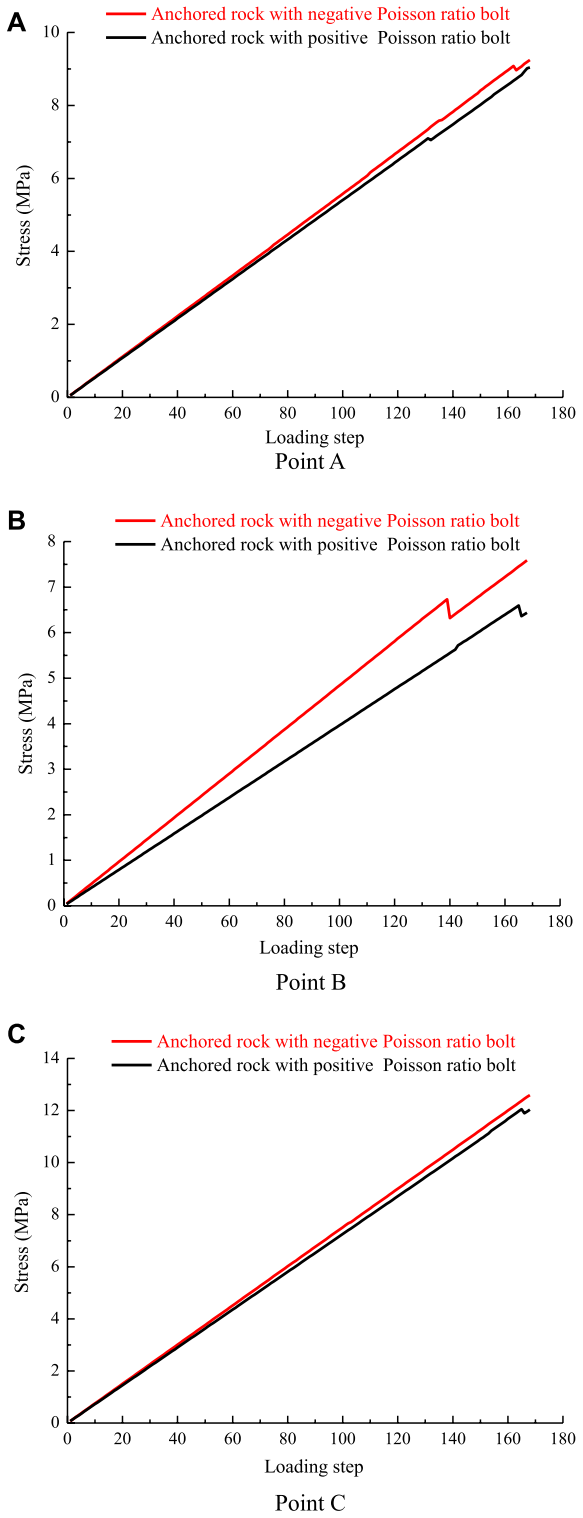

FIGURE 10 | Stress comparison curves of points A, B, and C of two kinds of anchored rock before loading step 168. **(A)** Point A. **(B)** Point B. **(C)** Point C.

indicating that it is feasible and reliable to use numerical experimental methods to study this problem. In addition, the displacement differences of points A, B, and C generally increase

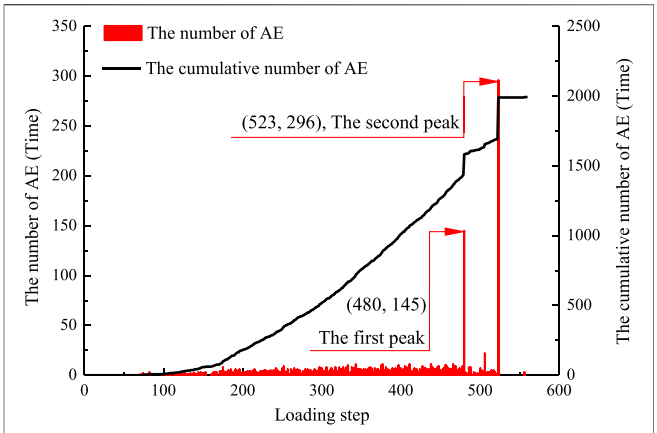

FIGURE 11 | AE curve of anchored rock with the negative Poisson's ratio bolt.

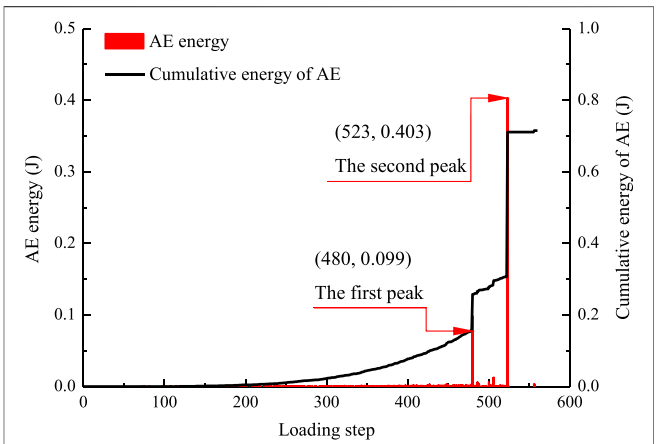

FIGURE 12 | AE energy curve of anchored rock with the negative Poisson's ratio bolt.

linearly, the maximum displacement differences of the aforementioned three points are 0.0015, 0.0028, and 0.0012 mm (see **Figure 6**).

5.2 Stress Analysis

It can be seen from **Figure 7** that the bearing capacity of anchored rock with the negative Poisson's ratio bolt reaches the maximum value of 378.2 MPa in loading step 479, this bolt is not damaged at this time (see **Figure 8A**). When loading continues, the bearing capacity begins to drop, and then the bolt first breaks in the middle of the bolt body at loading step 480 (see **Figure 8B**).

The bearing capacity drops to 330.4 MPa in the 486th step. Then the bearing capacity increases slightly and reaches the second peak of 349.7 MPa. The other parts of the bolt body are not damaged at this stage (see **Figures 8C~D**). At the next loading step when the stress reaches the second peak, i.e., loading step 523, the failure occurs successively at 5/8, 6/8, and 7/8 positions of the bolt body (see **Figures 8E~I**).

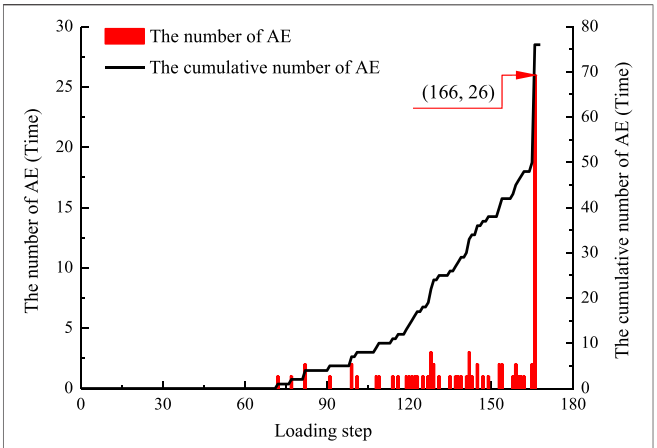

FIGURE 13 | AE curve of anchored rock with the positive Poisson's ratio bolt.

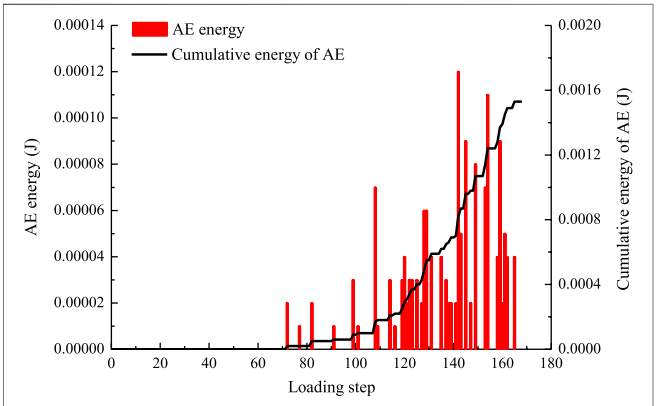

FIGURE 14 | AE energy curve of anchored rock with the positive Poisson's ratio bolt.

Through the aforementioned analysis, it can be seen that the failure of the bolt body occurs in the next loading step after the stress reaches the peak value, which is also the stage of stress decrease. On the other hand, there is only one failure in the anchored rock mass with the positive Poisson's ratio bolt (see **Figure 9**).

When the loading is over, the bearing capacity of the rock strengthened by the positive Poisson's ratio bolt is reduced to 0, while the rock strengthened by the negative Poisson's ratio bolt still has a certain bearing capacity, which is 82.8 MPa. The maximum bearing capacity of the rock reinforced with positive and negative Poisson's ratio bolts is 131.2 and 378.2 MPa, respectively. It can be seen that the addition of a negative Poisson's ratio bolt in the rock can improve the stress state of the rock mass, enhance the bearing capacity of the anchored rock mass, and make up for the defects of the traditional bolt.

As shown in **Figure 10**, the stress of points A, B, and C of the anchored rock with the negative Poisson's ratio bolt is greater than that of the corresponding points of anchored rock with the positive Poisson's ratio bolt. This is because the expansion deformation of the bolt body increases the friction between the bolt body and the surrounding rock, and the increased friction in turn also limits the displacement of the surrounding rock.

5.3 Acoustic Emission Characteristic Analysis

When it is loaded to loading step 480, both AE quantity and AE energy of the anchored rock mass with the negative Poisson's ratio bolt appear to rise suddenly, reaching the first peak value, and their values are 145 times and 0.099 J, respectively (see **Figure 11** and **Figure 12**). When it is loaded to loading step 523, the number and energy of AE increase again, reaching the second peak value, which is 296 time and 0.403 J, respectively. The difference is that the second peak value of stress is lower than the first peak value, while the second peak value of AE quantity and AE energy are both higher than the first peak. This also shows that the AE quantity and AE energy mainly occur in the stress drop stage. The number of AE quantity reaches the peak value for the anchored rock with the positive Poisson's ratio bolt when loaded to loading step 166 (see **Figure 13**). The peak of AE quantity is also after the stress peak, but the AE energy does not show obvious regularity (see **Figure 14**).

It can be seen from **Table 2** that the maximum and cumulative values of AE energy of the anchored rock mass with the positive Poisson's ratio bolt are 0.00012 and 0.00153 J, respectively. The maximum and cumulative value of AE energy of anchored rock with the negative Poisson's ratio are much larger than that of anchored rock with the negative Poisson's ratio, and the values are 0.40329 and 0.71482 J, respectively. The aforementioned phenomena show that more energy would be absorbed after the negative Poisson's ratio bolt is driven into the rock. That is to say, after adding a negative Poisson's ratio bolt to rock, the negative Poisson's ratio bolt can better protect the integrity of the surrounding rock and prevent the occurrence of geological disasters under the condition of the same geological conditions and load.

TABLE 2 | Number and energy of AE in two different anchored rocks after loading.

	Maximum number of AE/time	Total AE/time	Maximum AE energy/J	Total AE energy/J
Anchored rock with the negative Poisson's ratio bolt	296	1994	0.40329	0.71482
Anchored rock with the positive Poisson's ratio bolt	26	76	0.00012	0.00153

Mogi (1985) summarized three basic types of AE by analyzing the AE characteristics of different types of materials, namely, main shock type, foreshock–main shock–aftershock type, and swarm shock type. According to this AE classification basis, it can be known that the AE quantity and AE energy for the anchored rock with the negative Poisson's ratio bolt belong to the main shock type, while the AE quantity and AE energy of the anchored rock with the positive Poisson's ratio bolt belong to the main shock type and the swarm shock type, respectively.

6 CONCLUSION

(1) Under the action of external force, the expansion deformation of the negative Poisson's ratio bolt prevents the surrounding rock from moving toward the bolt, causing the displacement of the surrounding rock around the bolt with the negative Poisson's ratio to be smaller than that around the bolt with the positive Poisson's ratio. The numerical experiment results are in good agreement with the actual situation, which also proves the reliability of the numerical experiment.

(2) The negative Poisson's ratio bolt has been damaged sequentially from one half of the bolt body to the bolt head under the stress of surrounding rock, the failure mode of rock mass near the bolt failure is a tensile failure, and the bolt failure occurs in the stage of stress reduction. When the bolt Poisson's ratio changes from positive to negative, the bearing capacity of anchored mass rock is greatly increased, and the maximum bearing capacity is increased by 2.9 times. The anchored rock with the negative Poisson's ratio bolt still has a certain residual bearing capacity value after loading, which increases the strength of the reinforced body. The surrounding rock stress of the negative Poisson's ratio bolt is higher than the surrounding rock stress of the positive Poisson's ratio bolt, which means that the friction between the bolt and the surrounding rock has been increased, the movement of the surrounding rock has been restricted, and the integrity of surrounding rock has been protected.

(3) The peak values of AE quantity and AE energy of anchored rock with the negative Poisson's ratio bolt occur in the next loading step of the peak bearing capacity. The maximum loadable energy and cumulative energy of anchored rock with the negative Poisson's ratio bolt are far greater than that of anchored rock with the positive Poisson's ratio bolt, indicating that the reinforcement body with a negative Poisson's ratio bolt can absorb more energy and increase the strength and stiffness of anchored rock. In addition, the AE quantity and AE energy of the anchored rock with the negative Poisson's ratio bolt belong to the main shock type, and the AE quantity and AE energy of the anchored rock with the positive Poisson's ratio bolt belong to the main shock type and the swarm shock type, respectively.

DATA AVAILABILITY STATEMENT

The raw data supporting the conclusion of this article will be made available by the authors, without undue reservation.

AUTHOR CONTRIBUTIONS

FC: data curation and manuscript writing; X-BW: supervision; Y-HD: conceptualization; and C-AT: software.

FUNDING

This study was supported by the Chinese National Natural Science Foundation (No. 52074142).

REFERENCES

Alderson, A., and Alderson, K. L. (2007). Auxetic Materials. *Proc. Institution Mech. Eng. Part G J. Aerosp. Eng.* 221, 565–575. doi:10.1243/09544100jaero185

Alderson, K. L., Alderson, A., Webber, R. S., and Evans, E. (1998). Evidence for Uniaxial Drawing in the Fibrillated Microstructure of Auxetic Microporous Polymers[J]. *J. Mater. Sci.* 17 (16), 1415–1419. doi:10.1023/a:1026409404057

Alderson, K. L., Alderson, A., Smart, G., Simkins, V. R., and Davies, P. J. (2002). Auxetic Polypropylene fibres:Part 1 - Manufacture and Characterisation. *Plastics, Rubber Compos.* 31 (8), 344–349. doi:10.1179/146580102225006495

Chen, F., Tang, C. A., Sun, X. M., Ma, T. H., and Du, Y. H. (2019). Supporting Characteristics Analysis of Constant Resistance Bolts under Coupled Static-Dynamic Loading[J]. *J. Mt. Sci.* 16 (05), 217–226. doi:10.1007/s11629-018-5044-9

Critchley, R., Corni, I., Wharton, J. A., Walsh, F. C., Wood, R. J. K., and Stokes, K. R. (2013). A Review of the Manufacture, Mechanical Properties and Potential Applications of Auxetic Foams. *Phys. Status Solidi B* 250 (10), 1963–1982. doi:10.1002/pssb.201248550

Du, Y., Xie, M. W., Jiang, Y. J., Liu, W. N., Liu, R. C., and Liu, Q. Q. (2019). Research Progress on Dynamic Monitoring Index for Early Warning of Rock Collapse [J]. *Chin. J. Eng.* 41 (04), 427–435. doi:10.13374/j.issn2095-9389.2019.04.002

Du, Y., Xie, M. W., Jiang, Y. J., Chen, C., Jia, B. N., and Huo, L. C. (2021). Review on the Formation Mechanism and Early Warning of Rock Collapse[J]. *Metal. Mine* 535 (01), 106–119. doi:10.19614/j.cnki.jsks.202101008

Evans, K. E. (2010). Auxetic Materials: Functional Materials and Structures from Lateral Thinking. *J. Adv. Mater.* 12 (9), 617–628.

Gaspar, N. (2010). A Granular Material with a Negative Poisson's Ratio. *Mech. Mater.* 42, 673–677. doi:10.1016/j.mechmat.2010.05.001

Gercek, H. (2007). Poisson's Ratio Values for Rocks. *Int. J. Rock Mech. Min. Sci.* 44, 1–13. doi:10.1016/j.ijrmms.2006.04.011

Grima, J. N., Gatt, R., Alderson, A., and Evans, K. E. (2006). An Alternative Explanation for the Negative Poisson's Ratios in α-cristobalite. *Mater. Sci. Eng. A* 423, 219–224. doi:10.1016/j.msea.2005.08.230

Grima, J. N., Gatt, R., Alderson, A., and Evans, K. E. (2005). On the Potential of Connected Stars as Auxetic Systems. *Mol. Simul.* 31 (13), 925–935. doi:10.1080/08927020500401139

He, M. C., Xie, H. P., Peng, S. P., and Jiang, Y.-D. (2005). Study on Rock Mechanics in Deep Mining Engineering[J]. *Chin. J. Rock Mech. Eng.* 24 (16), 2803–2813.

He, M., Gong, W., Wang, J., Qi, P., Tao, Z., Du, S., et al. (2014). Development of a Novel Energy-Absorbing Bolt with Extraordinarily Large Elongation and

Constant Resistance. *Int. J. Rock Mech. Min. Sci.* 67 (1), 29–42. doi:10.1016/j.ijrmms.2014.01.007

Horrigan, E. J., Smith, C. W., Scarpa, F. L., Gaspar, N., Javadi, A. A., Berger, M. A., et al. (2009). Simulated Optimisation of Disordered Structures with Negative Poisson's Ratios. *Mech. Mater.* 41 (8), 919–927. doi:10.1016/j.mechmat.2009.04.008

Huang, X., Tang, S. B., Tang, C. A., Xie, L. M., and Tao, Z. Y. (2017). Numerical Simulation of Cracking Behavior in Artificially Designed Rock Models Subjected to Heating from a Central Borehole. *Int. J. Rock Mech. Min. Sci.* 98, 191–202. doi:10.1016/j.ijrmms.2017.07.016

Hyett, A. J., Moosavi, M., and Bawden, W. F. (2015). Load Distribution along Fully Grouted Bolts with Emphasis on Cable Bolt Reinforcement[J]. *Int. J. Numer. Anal. Methods Geomechanics* 20 (7), 517–544.

Jalalifar, H. (2006). *A New Approach in Determining the Load Transfer Mechanism in Fully Grouted bolts[D]*. Australia: University of Wollongong.

Kang, H., Wu, Y., Gao, F., Lin, J., and Jiang, P. (2013). Fracture Characteristics in Rock Bolts in Underground Coal Mine Roadways. *Int. J. Rock Mech. Min. Sci.* 62 (5), 105–112. doi:10.1016/j.ijrmms.2013.04.006

Kim, Y., Hossain, M. S., and Lee, J. (2017). Dynamic Installation of a Torpedo Anchor in Two-Layered Clays[J]. *Can. Geotechnical J.* (2), 446–454. doi:10.1139/cgj-2016-0607

Lakes, R. (1987). Foam Structures with a Negative Poisson's Ratio. *Science* 235 (4792), 1038–1040. doi:10.1126/science.235.4792.1038

Lakes, R. (1993). Materials with Structural Hierarchy. *Nature* 361 (6412), 511–515. doi:10.1038/361511a0

Li, G., and Tang, C.-A. (2015). A Statistical Meso-Damage Mechanical Method for Modeling Trans-scale Progressive Failure Process of Rock. *Int. J. Rock Mech. Min. Sci.* 74, 133–150. doi:10.1016/j.ijrmms.2014.12.006

Li, J. W., Qiao, J. G., Fu, X., and Liu, X. (2019). Research Progress on Material/Structure and Mechanical Properties of Energy-Absorbing Bolt Used in Ground Anchorage[J]. *Mater. Rep.* 33 (5), 1567–1574. doi:10.11896/cldb.18100030

Li, Z., Li, L., Li, M., Zhang, L., Zhang, Z., Huang, B., et al. (2018). A Numerical Investigation on the Effects of Rock Brittleness on the Hydraulic Fractures in the Shale Reservoir. *J. Nat. Gas Sci. Eng.* 50, 22–32. doi:10.1016/j.jngse.2017.09.013

Liu, Y. P., and Hu, H. (2010). A Review on Auxetic Structures and Polymeric Materials[J]. *Sci. Res. Essays* 5 (10), 1052–1063. doi:10.1073/pnas.1003503107

Martz, E. O., Lee, T., Lakes, R. S., Goel, V. K., and Park, J. B. (1996). Re-entrant Transformation Methods in Closed Cell Foams [J]. *Cell. Polym.* 15 (4), 229–249.

Miller, W., Hook, P. B., Smith, C. W., Wang, X., and Evans, K. E. (2009). The Manufacture and Characterisation of a Novel, Low Modulus, Negative Poisson's Ratio Composite. *Compos. Sci. Technol.* 69 (5), 651–655. doi:10.1016/j.compscitech.2008.12.016

Mogi, K. (1985). *Earthquake prediction[M]*. Tokyo: Academic Press, 20–123.

Ravirala, N., Alderson, K. L., Davies, P. J., Simkins, V. R., and Alderson, A. (2006). Negative Poisson's Ratio Polyester Fibers. *Text. Res. J.* 76 (7), 540–546. doi:10.1177/0040517506065255

Saxena, K. K., Das, R., and Calius, E. P. (2016). Three Decades of Auxetics Research – Materials with Negative Poisson's Ratio: A Review. *Adv. Eng. Mat.* 18, 1847–1870. doi:10.1002/adem.201600053

Shi, Z.-c., Fan, R.-h., Zhang, Z.-d., Qian, L., Gao, M., Zhang, M., et al. (2012). Random Composites of Nickel Networks Supported by Porous Alumina toward Double Negative Materials. *Adv. Mat.* 24 (17), 2349–2352. doi:10.1002/adma.201200157

Tang, C. A., Chen, F., Sun, X. M., Ma, T. H., and Du, Y. H. (2018). Numerical Analysis for Support Mechanism of Constant-Resistance Bolts[J]. *Chin. J. Geotechnical Eng.* 40 (12), 2281–2288.

Tang, C. A., Yang, W. T., Fu, Y. F., and Xu, X. H. (1998). A New Approach to Numerical Method of Modelling Geological Processes and Rock Engineering Problems-Continuum to Discontinuum and Linearity to Nonlinearity. *Eng. Geol.* 49 (3-4), 207–214. doi:10.1016/s0013-7952(97)00051-3

Tang, C. A. (2003). *Numerical Experiments of Rock Failure process[M]*. Beijing: Science Press. (in Chinese).

Tang, C. A., Webb, A. A. G., Moore, W. B., Wang, Y. Y., Ma, T. H., and Chen, T. T. (2020). Breaking Earth's Shell into a Global Plate Network. *Nat. Commun.* 11 (3621), 3621–3626. doi:10.1038/s41467-020-17480-2

Tang, C. A., and Kaiser, P. K. (1998). Numerical Simulation of Cumulative Damage and Seismic Energy Release during Brittle Rock Failure-Part I: Fundamentals. *Int. J. Rock Mech. Min. Sci.* 35 (2), 113–121. doi:10.1016/s0148-9062(97)00009-0

Tang, C. (1997). Numerical Simulation of Progressive Rock Failure and Associated Seismicity. *Int. J. Rock Mech. Min. Sci.* 34 (2), 249–261. doi:10.1016/s0148-9062(96)00039-3

Vandermaat, D., Saydam, S., Hagan, P. C., and Crosky, A. G. (2016). Examination of Rockbolt Stress Corrosion Cracking Utilising Full-Size Rockbolts in a Controlled Mine Environment. *Int. J. Rock Mech. Min. Sci.* 81, 86–95. doi:10.1016/j.ijrmms.2015.11.007

Wan, H., Ohtaki, H., Kotosaka, S., and Hu, G. (2004). A Study of Negative Poisson's Ratios in Auxetic Honeycombs Based on a Large Deflection Model. *Eur. J. Mech. - A/Solids* 23 (1), 95–106. doi:10.1016/j.euromechsol.2003.10.006

Wojciechowski, K. W. (1989). Two-dimensional Isotropic System with a Negative Poisson's Ratio[J]. *Phys. Lett. A* 137 (1), 60–64. doi:10.1016/0375-9601(89)90971-7

Yu, C., Ji, S., and Li, Q. (2016). Effects of Porosity on Seismic Velocities, Elastic Moduli and Poisson's Ratios of Solid Materials and Rocks. *J. Rock Mech. Geotechnical Eng.* 8 (1), 35–49. doi:10.1016/j.jrmge.2015.07.004

Zhang, J. X., Tang, C. A., Zhou, X. Y., Hui, X. J., Liang, Z. Z., Wang, S. H., et al. (2007). Numerical Simulation of Failure Process of Reinforced Concrete Specimen under Uniaxial Tension[J]. *Chin. J. Comput. Mech.* 24 (4), 454–458. (in Chinese). doi:10.4028/www.scientific.net/KEM.353-358.949

Conflict of Interest: The authors declare that the research was conducted in the absence of any commercial or financial relationships that could be construed as a potential conflict of interest.

Publisher's Note: All claims expressed in this article are solely those of the authors and do not necessarily represent those of their affiliated organizations, or those of the publisher, the editors, and the reviewers. Any product that may be evaluated in this article, or claim that may be made by its manufacturer, is not guaranteed or endorsed by the publisher.

Copyright © 2022 Chen, Wang, Du and Tang. This is an open-access article distributed under the terms of the Creative Commons Attribution License (CC BY). The use, distribution or reproduction in other forums is permitted, provided the original author(s) and the copyright owner(s) are credited and that the original publication in this journal is cited, in accordance with accepted academic practice. No use, distribution or reproduction is permitted which does not comply with these terms.

frontiers | Frontiers in Earth Science

ORIGINAL RESEARCH
published: 17 June 2022
doi: 10.3389/feart.2022.879387

Stability Control of Slopes in Open-Pit Mines and Resilience Methods for Disaster Prevention in Urban Areas: A Case Study of Fushun West Open Pit Mine

Zhou Jiaxing[1], *Li Fei*[1]*, *Wang Jin-an*[1,2], *Gao Anqi*[3] *and He Chengyuan*[4,5]

[1]School of Civil and Resource Engineering, University of Science and Technology Beijing, Beijing, China, [2]State Key Lab of Education Ministry for High Efficient Mining and Safety of Metal Mine, University of Science and Technology Beijing, Beijing, China, [3]Shanxi Academy of Building Research Co., Ltd., Taiyuan, China, [4]China Railway Bridge Research Institute, Ltd., Wuhan, China, [5]State Key Laboratory for Health and Safety of Bridge Structure, Wuhan, China

OPEN ACCESS

Edited by:
Bo Li,
Tongji University, China

Reviewed by:
Haiping Yuan,
Hefei University of Technology, China
Lei Wang,
ANHUI.HUAINAN, China
Kang Zhao,
Jiangxi University of Science and Technology, China

***Correspondence:**
Li Fei
lifei3522883@163.com

Specialty section:
This article was submitted to Geoscience and Society, a section of the journal Frontiers in Earth Science

Received: 19 February 2022
Accepted: 11 May 2022
Published: 17 June 2022

Citation:
Jiaxing Z, Fei L, Jin-an W, Anqi G and Chengyuan H (2022) Stability Control of Slopes in Open-Pit Mines and Resilience Methods for Disaster Prevention in Urban Areas: A Case Study of Fushun West Open Pit Mine. Front. Earth Sci. 10:879387. doi: 10.3389/feart.2022.879387

During the century-long mining process of the Fushun west open pit, slope slippage and deformation caused varying degrees of horizontal deformation, uneven settlement, and ground cracks on the surface of the urban areas, which caused a certain degree of damage to buildings and infrastructure and affected the livings of residents in the surrounding communities. In this study, a set of building reinforcement and community resilience enhancement methods that can resist slope deformation was proposed to improve the ability of urban areas to cope with slope geological hazards and emergency response. The main research contents included: Firstly, this paper systematically analyzed the deformation mechanism of the dip sloping and the inverse dip sloping section of the open pit mine, which was based on the field measured data and simulation calculation results. In other words, the horizontal deformation of the stratum in the dip sloping section was dominant, while the stratum in the inverse dip sloping section was prone to ground cracks and uneven settlement. In view of this, three surface deformation characteristic subdivisions of the surrounding urban area were proposed. In addition, a study on the damage characteristics of buildings with different types of foundations and structures under the influence of side slope deformation were carried out, and the anti-deformation reinforcement measures for load-bearing members mainly based on steel fiber concrete, carbon fiber materials and profile steel were proposed. Finally, a three-level disaster emergency setting system for urban areas around open pit mine was established, and the disaster prevention and resilience enhancement strategy for build and unbuilt the communities around the side slopes was constructed. The study aims to provide technical support to the overall resilience and response of the urban communities adjacent to open-pit mine slopes against consequent geological hazards and emergencies, thereby promoting sustainable urban development.

Keywords: open pit slope, solpe deformation, deformation-resistant reinforcement, disaster resilience, building damage

INTRODUCTION

The Fushun western open pit has a 100-years mining history and has now formed a deep and large pit with an east-west length, north-south width, and depth of 6.6 km, 2 km and 400 m, respectively, disturbing over an area of 15 km^2. Since the mining of the western open pit and the development and construction of the city were in the same period of history, the city of Fushun has formed a complex urban spatial layout with "a mine in the city and a city on the mine." The engineering geology and hydrogeological conditions of the western open-pit mine area are exceptionally intricate, and there are various environmental and geological hazards such as water pollution, landslides, and ground cracks, which have caused different degrees of damage and impact on the urban buildings and infrastructure around the western open-pit mine, thus causing serious impacts on the safety of urban residential areas.

In recent years, a number of studies have been carried out on the building resistance against slope deformation and geological hazards in urban areas (Du et al., 2020). In terms of landslide prevention and emergency response, Du et al. (2021) analyzed the mechanism of slope rock collapse disaster genesis, developed high-precision remote sensing vibration monitoring and early warning technology, and established monitoring and early warning protocols with bedrock separation damage precursors as the core. Chen et al. (2015) established a real-time, effective, and intelligent geological disaster prevention and control management system, which realized disaster information management, real-time monitoring, forecasting and warning of geological disasters, and emergency evacuation of the public. Ou et al. (2021) based 14 geo-environmental factors such as slope, elevation, fault, rainfall, and lithology, and used the binary logistic regression model (LRM) to evaluate the landslide hazard, in order to provide technical support for disaster mitigation and prevention in Jiangxi province. Xu et al. (2020) established a geological disaster prevention strategy that combines disaster risk management with disaster mitigation, sustainable livelihoods, and poverty alleviation, thereby improving the community's resilience to landslide hazards. Tsai et al. (2021) investigates water saturation changes over time using time-lapse Electrical Resistivity Tomography (ERT) images, providing a powerful method for monitoring landslide events. Shao (2019) analyzed the characteristics of geological hazards in mines caused by high-intensity mining, established a database of hazards, and proposed measures to enhance landslide hazard prevention and control. La et al. (2021) based on the "disaster scenario—rescue task—rescue object—demand prediction—object deployment," the NSGA-II algorithm for the rescue object deployment model was established using a data of 18 representative slope disaster rescue operations in the past, so as provide effective guidelines for the rescue work. Moreover, the deep displacement-based monitoring method is of great significance to the investigation of early warning indicators and deformation monitoring of natural landslides, to reduce/avoiding the consequences caused by landslides (Chen et al., 2021). Aiming at the mechanism of rainfall-induced landslides and the mechanism of rainfall impact on slopes, a set of Spatio-temporal monitoring and early warning system of landslides based on multi-scale Spatio-temporal analysis and remote sensing technology was established to provide a basis for the prevention of disasters (He et al., 2022). Regarding the deformation resistance of buildings, an improved high-performance polymer cement mortar (PCM) and glass fiber reinforced plastic (GFRP) composites were used by (Qiao et al., 2022) to strengthen and repair masonry structures. Mostafa et al. (2021) proposed glass fiber reinforced concrete beams containing transverse reinforcement, which effectively enhanced the buckling resistance of beams under service and ultimate loads. Gulec et al. (2021) used prefabricated cages to strengthen T-section concrete beams, which show better flexural and ductile properties than conventional reinforcement methods. Rf et al. (2020) investigated a reinforcement solution for concrete floor slabs having a higher top reinforcement near the column, which significantly increased the impact resistance and reduced the flexural deflection. Resan et al. (2020) proposed a composite beam structure with embedded steel plates in shear span based on the results of the four-point load limit damage test, which effectively improved the stiffness and strength of the structure.

However, the available literature only covers two basic aspects of disaster prevention and control or emergency response and does not provide systematic guidelines to enhance the disaster prevention and resilience of buildings and residents in areas affected by geological hazards. To aims to effectively improve the disaster resilience and sustainable urban development of the residential communities in the impact area, this study systematically analyzed the damage characteristics of buildings and surfaces in urban areas, and proposed a deformation-resistant reinforcement scheme for buildings and an optimized strategy for communities disaster prevention and mitigation in the Fushun west open-pit mine impact zone.

SURFACE DEFORMATION ZONING IN URBAN AREAS AROUND THE SLOPES OF OPEN PIT MINES

Surface Monitoring and Characterization of Urban Areas

Figure 1 shows the trend of surface displacement variables in the Fushun west open-pit mine and the surrounding urban area from 2016 to 2020. Relevant data derived from the Interferometric Synthetic Aperture Radar on Board technology (InSAR) monitoring the regional surface. The areas with large surface deformation in the city are the Qian-tai mountain area in the south bank (within the former landslide body), the central and western part of the north bank (former petroleum plant No. 1), the eastern part of the north bank and the western drainage field. In the area of the discharge site on the west bank, the vertical displacement of the surface has increased significantly due to the continuous accumulation and settlement of the discharge. The surface deformation in this area is independent of the pit slope deformation and engineering disturbance, and its no impact on the surface deformation in the urban area.

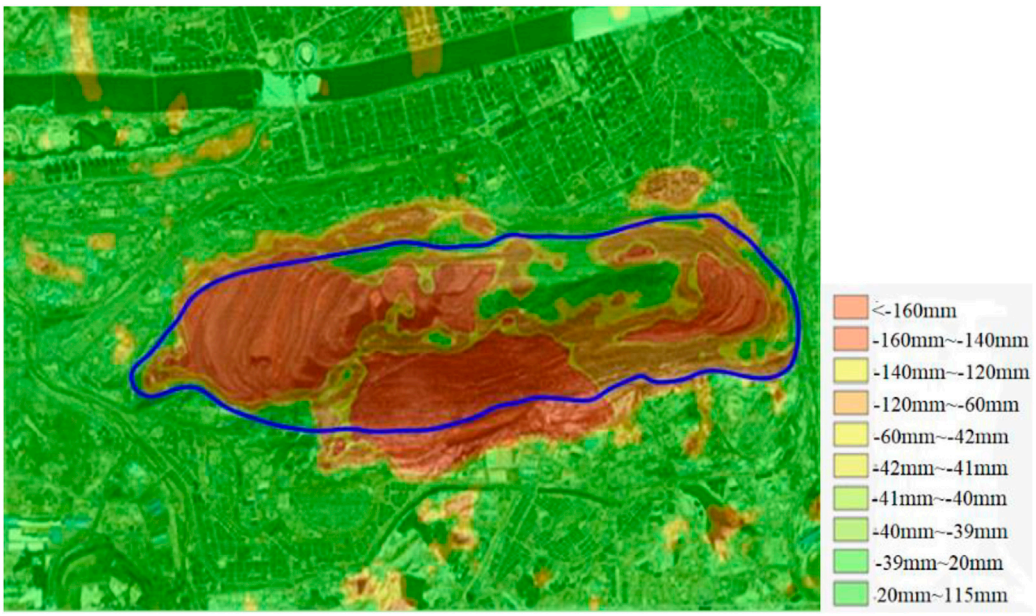

FIGURE 1 | Cumulative surface displacement map of west open pit and affected area from 2016 to 2020.

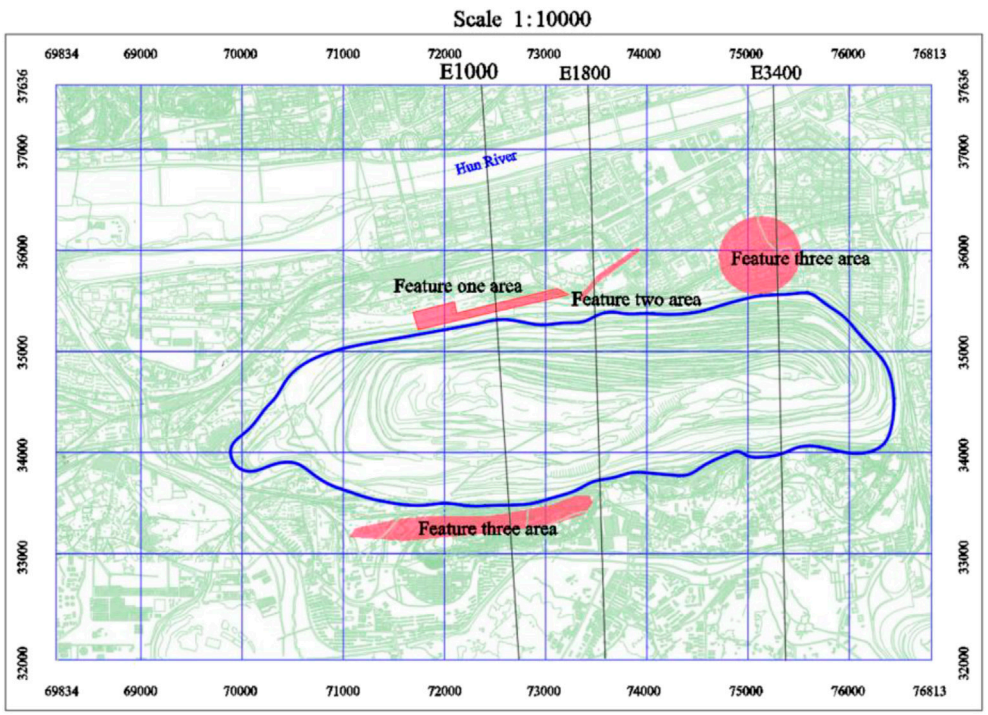

FIGURE 2 | Deformation zone map of the west open-pit influence area.

The central part of the northern bank is dominated by vertical deformation of the ground surface under the influence of ground fracture and slope creep deformation. Surface deformation in the area of ground cracks in the east-central part of the northern bank is subjugated by uneven settlement and horizontal deformation. The area of Qian-tai mountain on the south bank falls within the original landslide zone. In recent years, with the implementation of backfill and other slope management projects, the vertical deformation of the stratum has been reduced; consequently, the horizontal deformation of the ground surface is dominant. The

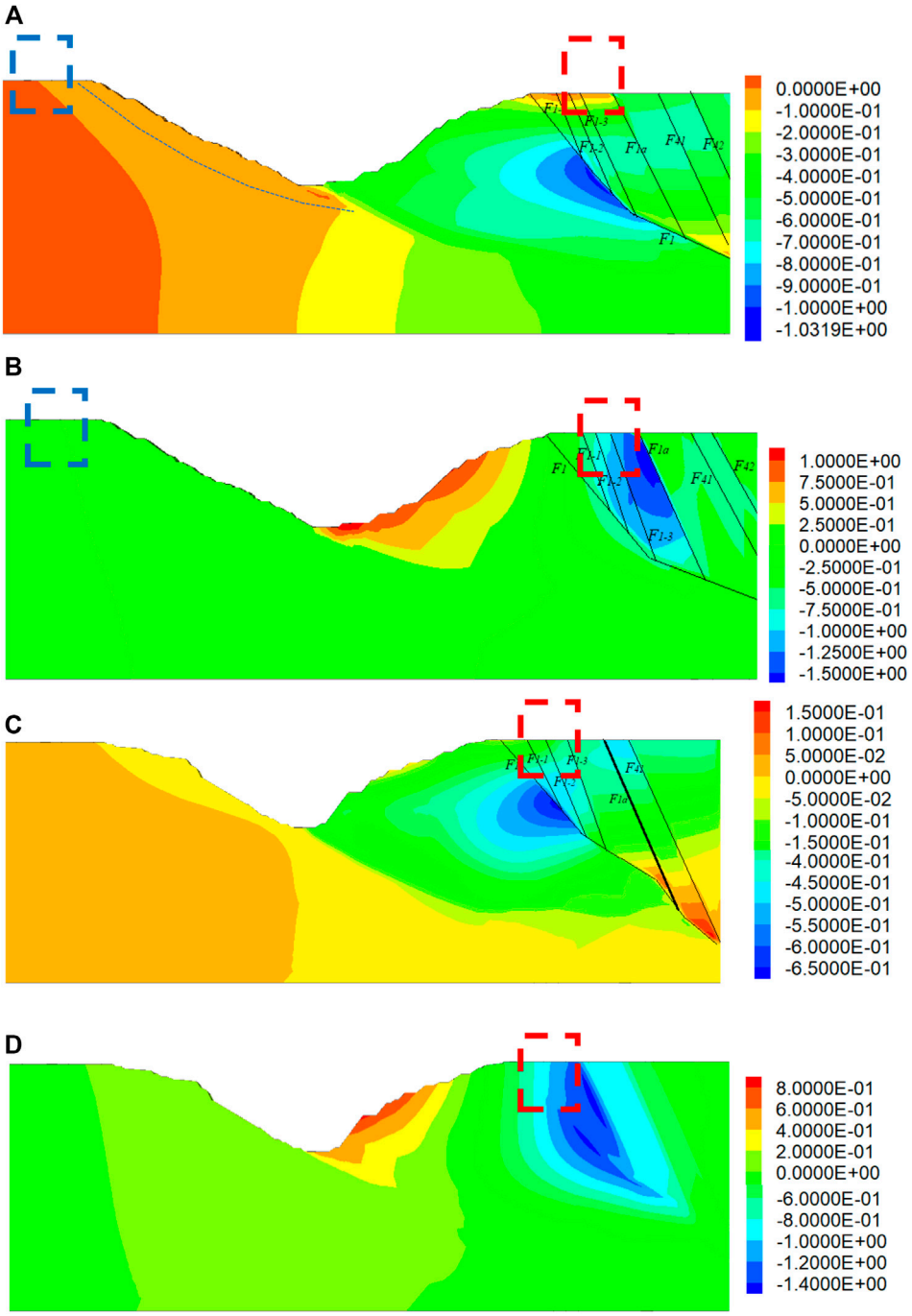

FIGURE 3 | (Continued).

eastern area of the north bank is adjacent to the F_1 fault, the overall stability of the strata is reduced, and the horizontal deformation of the ground surface has increased. In this study, the four areas with large surface displacements monitored on-site were divided into three deformation characteristic zones as shown in **Figure 2** (Gao et al., 2021) based on the actual field survey and relevant literature.

Calculation and Analysis of Slopes Deformation Trends

To analyze the deformation characteristics of the strata affected by previous excavation disturbance in each part of the urban area and to reveal the induced mechanism of surface deformation in each area, FLAC3D numerical simulation software was used. A two-dimensional model was prepared for computation, in which

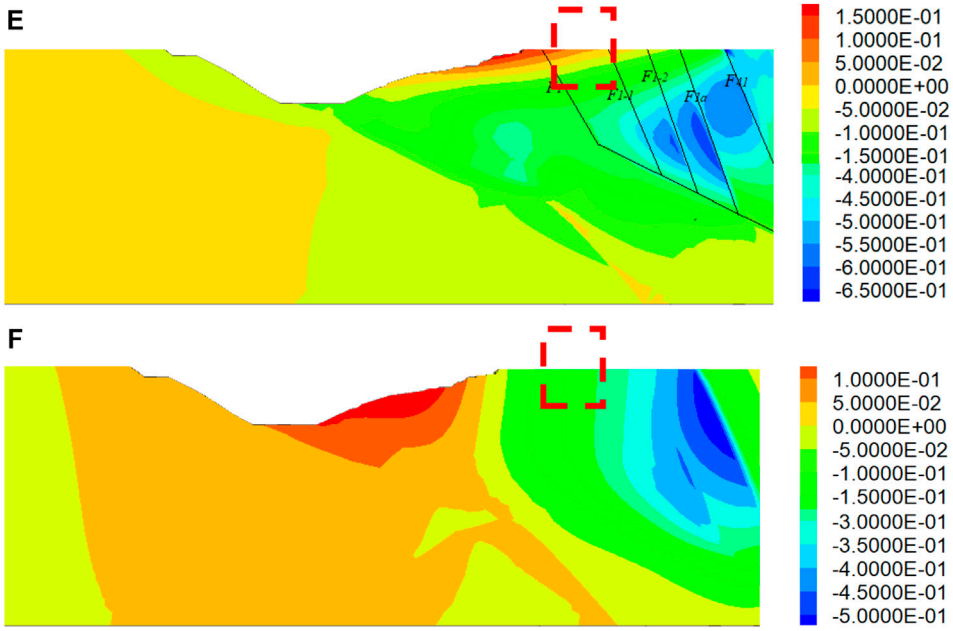

FIGURE 3 | (Continued). Distribution of stratigraphic displacements in each feature zone: **(A)** stratigraphic horizontal displacement of the E1000 profile in feature-1; **(B)** vertical displacement of strata of the E1000 profile in feature-1; **(C)** stratigraphic horizontal displacement of the E1800 profile in feature-2; **(D)** vertical displacement of strata of the E1800 profile in feature-2. **(E)** stratigraphic horizontal displacement of the E3400 profile in feature-3; **(F)** vertical displacement of strata of the E3400 profile in feature-3.

the width of the fault was defined in accordance with the actual width, and the mechanical parameters of the fault units was discount. The material parameters and excavation timing of the computation model were in line with (Gao, 2020). The slope excavations from 1950 to the hitherto were analyzed for the E1000, E1800 E3400 profiles involved in deformation feature-1, feature-2, and feature-3, respectively. The displacement field distribution of each profile is shown in **Figure 3**.

Figure 3A,B shows the distribution of slope and surface deformation in the E1000 section of the west open-pit slope, wherein the stratigraphic range of feature-1 is highlighted by the red box, and the stratigraphic range of the Qian-tai mountain area is highlighted by the blue box. The horizontal deformation of the stratum mainly occurred at the F_1 fault structure in the north bank area due to the effect of the slope excavation disturbance since 1950. It was observed that the amount of horizontal ground displacement within the feature-1 area was large, and the value of the variation of displacement in the area was about 400 mm. The area having maximum vertical deformation in the strata was the neighboring area of $F_{1\text{-}1}$, $F_{1\text{-}2}$, and $F_{1\text{-}3}$ faults, and the accumulated surface deformation was about 1500 mm. The area of maximum deformation was located within the feature-1 area. The amount of variation of horizontal displacement of the surface in the area of the Qian-tai mountain was large; meanwhile, the variation of vertical displacement was relatively small.

Figure 3C,D shows the distribution of slope and surface deformation in the E1800 profile, wherein the surface area of feature-2 is indicated in the red box. The horizontal deformation of the north bank stratum mainly occurred in the same level section between the F_1 fault and the bottom of the pit. The accumulated maximum deformation was about 650 mm, and the maximum horizontal deformation of the ground surface was relatively small. The maximum vertical deformation area of the stratum was involved $F_{1\text{-}1}$, $F_{1\text{-}2}$, and $F_{1\text{-}3}$ faults, and the accumulated deformation of the surface was about 1400 mm, which was less than the feature-1 zone. The surface deformation of the south bank was small, and the stability of the stratum was relatively high.

Figure 3E,F shows the distribution of slope and surface deformation in the E3400 profile of the west open-pit mine, wherein the red box shows the surface area of feature-3. The stratigraphic stability of the north bank was observed to be relatively stable, and the surface deformation was small. The horizontal displacement of the stratum in the north bank is large in the feature-3 area, with a peak of around 200 mm. Meanwhile, the differential settlement deformation was relatively small in this area.

Slope Deformation-Induced Mechanisms

(1) Feature-1 Area: both horizontal and vertical displacements were relatively large

Feature-1 area is the area near the former petroleum plant on the north bank, and the regional stratigraphy is formed by sandstone wedge bodies bounded by the F_1 fault and the F_{1A} fault, as shown in **Figure 4A**. Due to the low strength and hardness of the rock formation, the wedge (red filled area) was affected by the coupled effect of the lateral pressure of the hard granite stress field on the east side and the unloading force on the surface near the side slope body on the west side. This resulted in

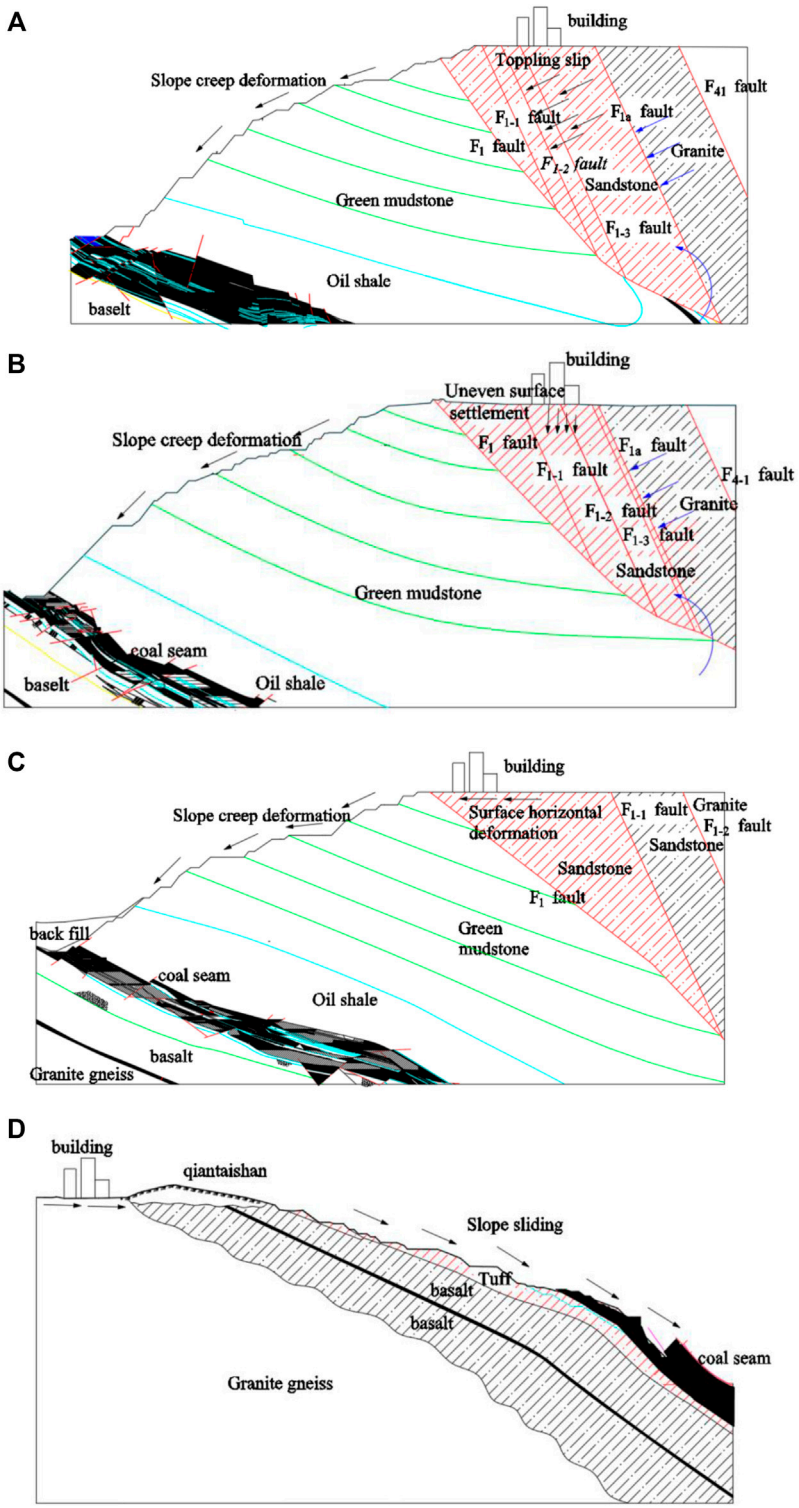

FIGURE 4 | Sliding deformation mechanism of slopes in each feature zone: **(A)** feature-1 Zone Wedge Rotating Slip; **(B)** feature-2 Zone Wedge Dumping Slip; **(C)** feature-3 zone Wedge Flush Slip; **(D)** feature-3 area south gang slope body downward sliding.

an overall rotational slip at the intersection of the two faults, which caused a large horizontal and vertical ground surface displacement. Owing to this, the surface deformation in the central part of the northern bank was mainly influenced by two geological feature-s, i.e., 1) the adjacent slope body, which undergoes creep deformation and results in an increased

horizontal deformation of the ground surface; 2) the large faults across the region, which induce misalignment of ground fracture zone and cause uneven ground settlement. Moreover, this area is adjacent to the slope having a landslide history in 2016 due to the heavy rainfall; thus, the foundation and bottom wall of the building (structure) in this area are prone to failure, i.e., cracking and shedding.

(2) Feature-2 area: vertical displacement was relatively large

Feature-2 area is the junction region of roads, i.e., Xi'san Street, Jie'fang Road, and Xi'qi Road in the east-central part of the north bank, which is the majorly affected area by the ground fracture misalignment induced by the activation of the F_{1a} fault. As shown in **Figure 4B**, a layer of fault fracture zone exists between the east side of the wedge and the granite area, which decreases the lateral pressure from the east side. The distance of the west side of the wedge from the slope increases, leading to a decrease in the unloading force by the slope. The wedge geologic body undergoes dumping slip and induces fault activation in the upper part of the wedge. Therefore, the area is dominated by vertical deformation, buildings and roads are prone to failure, i.e., cracking and tumbling.

(3) Feature-3 area: horizontal displacement was relatively large

The south of Nan'yang Road is located at the eastern surface of the north bank wedge, and there is no large fracture structure inside the wedge geological body in this area. Its overall stiffness is relatively high, and its east side is subjected to weaker thrusts from the geological body composed of granite. As shown in **Figure 4C**, the F_1 fault is close to the slope surface, the overall stability of this stratum is low. The wedge-shaped geological body is prone to translating and triggering a large horizontal deformation of the ground surface. Also, the horizontal deformation of the ground surface is induced by the influence of creep deformation of the slope. The foundations of the buildings are susceptible to shear damage, due to which the superstructure can be separated from the foundation by cracking.

The Qian-tai mountain area has a landslide history. As shown in **Figure 4D**, the surface deformation is relatively large due to the influence of adverse geological conditions, i.e., two sets of large fracture zones and down-sloping slopes. In recent years, with the implementation of slope management projects such as backfilling, the vertical deformation of the stratum has been reduced. The surface deformation in the area is mainly horizontal, and the exterior walls of the buildings are prone to cracking.

ANALYSIS OF DETERIORATION CHARACTERISTICS AND DEFORMATION RESISTANCE OF BUILDINGS AROUND SLOPES

In order to analyze of deformation damage characteristics and mechanisms of buildings in urban areas, the surface deformation monitoring data of three typical subdistricts were used as a reference. The horizontal and vertical deformations of the surface in the feature-1 area were relatively large; the maximum horizontal deformation and vertical settlement deformation were set to 14.4 mm/m and 13 mm/m, respectively. Feature-2 area was subjugated by vertical deformation of the ground surface; the horizontal deformation and vertical settlement were set to 4 mm/m and 10 mm/m, respectively. Feature-3 area was dominated by horizontal deformation of the ground surface, and its horizontal deformation and vertical settlement were set to 14.4 mm/m and 3 mm/m, respectively. In addition, the impact of mining-induced earthquakes on buildings in urban areas was also considered.

Analysis of Building Deterioration Characteristics

The calculation model of ABAQUS software and the form of the applied load are shown in **Figure 5**, and the length of the element was about 280 mm. The six-story masonry and frame building structures were considered for the analysis. To eliminate the calculation boundary effect and accurately reflect the coupling effect between the foundation and the building, the length, width, and depth of the lower stratum were taken as 37.9, 25.9, and 40 m, respectively. The horizontal and vertical deformation along the longitudinal direction of the building increased from zero to the maximum value in the subjected feature area. The mine seismic load was realized by applying the dynamic acceleration in the horizontal direction in the lower soil layer, as shown in **Figure 5D**. The time curve was selected from 1995 to 2003 after converting the maximum mine seismic level to the relevant data (Du, 2007).

The density, elastic modulus, and Poisson's ratio of the fourth soil layer were about 1860 kg/m^3, 400 MPa, and 0.2, respectively. The material of the structure and the foundation of the building were reinforced concrete, and the material properties of each component were shown in **Table 1**. The concrete damage plasticity model was used for the analysis, and the parameters of the model were considered in accordance with (Chengyuan, 2020) and they are not stated here.

Figure 6 shows the damage distribution of a masonry building affected by ground deformation action in each subjected region. Analysis showed that the masonry building in the feature-1 area was the most damaged, and the foundation part was almost completely damaged, and the damage to the bottom wall was also observed to be severe. Moreover, there were a few damaged areas existing at the top and bottom of the load-bearing columns in low level, while the damage to the non-bottom wall was relatively small, with only partial tilt-through cracks. This could also explain the dense and irregular distribution of reticulated cracks in the walls of the lower floors, the severe cracking and breakage of the bottom slabs of the balconies, and the severe penetration joints in the corners of the window and door openings of the buildings in this area. The damage to the foundation and walls of the building was relatively severe in the feature-2 area, as shown in **Figure 7**. Since the feature-3 area

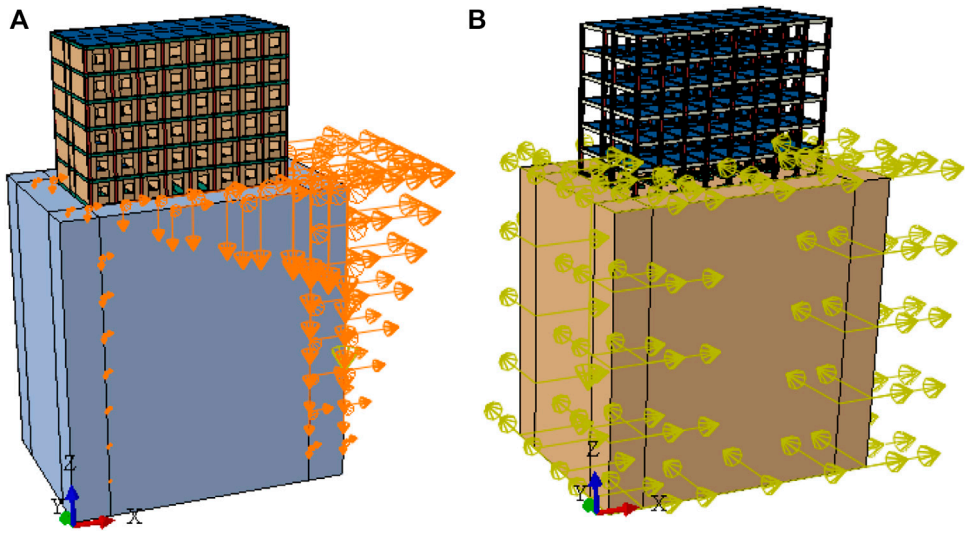

FIGURE 5 | Calculation model and load distribution: **(A)** ground deformation load applied to buildings; **(B)** buildings subjected to mine seismic loads.

TABLE 1 | Material properties of building components.

Components	Modulus of Elasticity/GPa	Poisson's Ratio	Density/kg·m^{-3}
Beams, foundations	30.340	0.2	2400
Column	31.530	0.2	2400
Floor	31.255	0.2	2400
Wall	30.340	0.2	2400

was under the influence of horizontal displacement of the ground surface, the foundation components were mainly damaged, and the upper wall had a low degree of damage. This can better explain the problem of cracking and detachment of superstructure and foundation of building in this area (**Figure 8**).

Figure 9 shows the damage distribution of frame structured buildings affected by ground deformation in each subjected area. Analysis showed that the framed buildings have better resistance to deformation than masonry buildings. By the superposition of horizontal and vertical displacement of the ground surface, the foundation part produced a small damage in a frame structure building. In addition, under the effect of uneven ground settlement, the structural columns of the ground floor and foundation components produced partial and large damage, respectively.

Figure 10 shows the damage distribution of the building under the coupled influence of mine quake and maximum ground deformation. The analysis showed that the damage to the walls of the masonry buildings was relatively serious, and the damage to main load-bearing elements, such as beams, slabs, and columns, was minor. The foundation was affected by the ground deformation and produced penetration damage. Masonry buildings with combined pile-raft foundations showed better resistance to deformation than buildings with raft foundations. The former significantly reduced the wall breakage on the ground floor of the building and showed a higher degree of damage in the upper walls.

Analysis of Reinforcement Scheme for Building Elements Under the Action of Slope Deformation

(1) Performance study of wall reinforcement material—steel fiber concrete

The results of both field research and numerical simulation of buildings in urban areas showed that buildings in each deformation feature area are damaged to a different extent. Repairing damaged parts of buildings in each region and enhancing resistance to deformation are prerequisites for improving the resilience of buildings against disasters. Therefore, to propose steel fiber reinforcement solutions for each characteristic deformation zone, the performance of various types of steel fiber concrete materials was simulated and calculated.

For this purpose, a 150 mm × 150 mm×150 mm standard specimen composed of C30 concrete and steel fiber of Q235 steel was used as an object for loading and force analysis. The range of steel fiber doping was 0.8%–1.5%, the range of steel fiber diameter was 0.6–0.9 mm, and the range of steel fiber length was 40–90 mm. The specifications of each group test are shown in **Table 1**. The length of steel fiber and concrete elements was 4.5 and 10 mm, respectively. The load applied to the specimen was divided into a uniform displacement of 10 mm and an inhomogeneous displacement standardized by the amount of

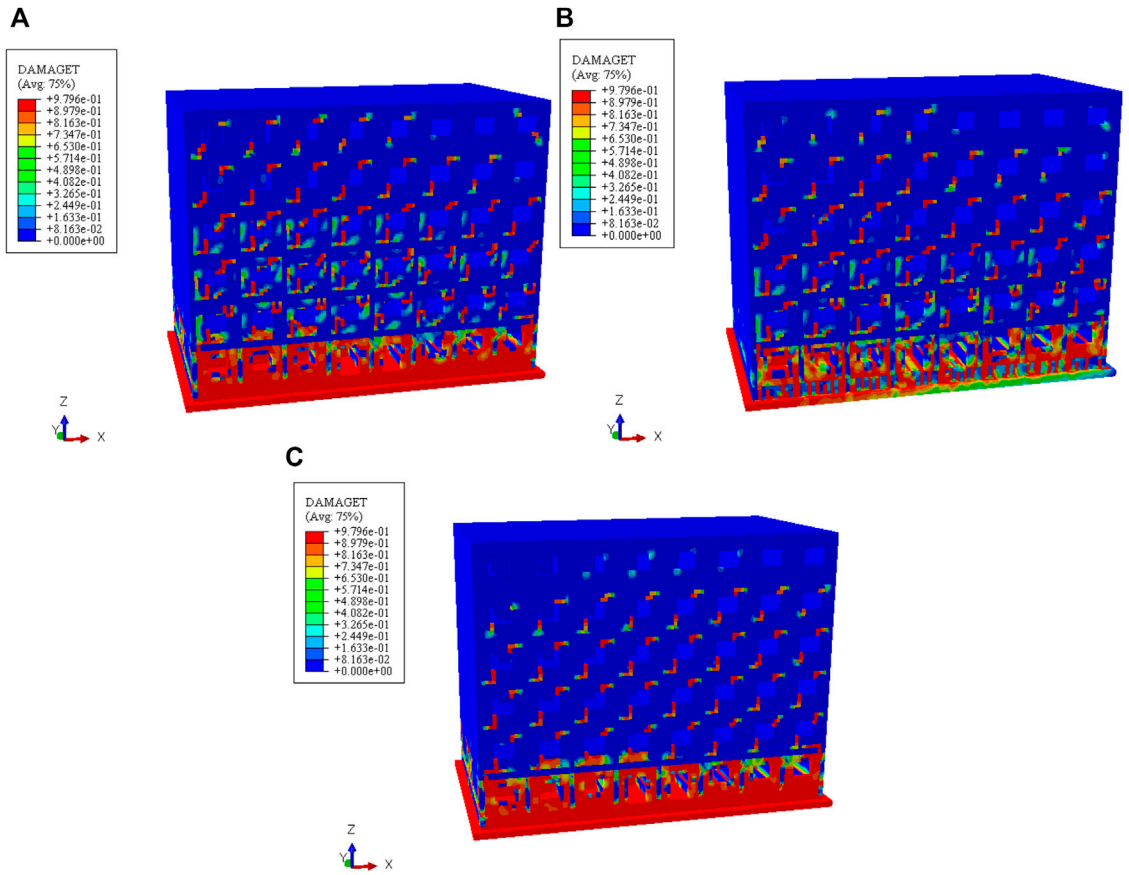

FIGURE 6 | Deformation damage distribution of masonry buildings in each deformation zone: **(A)** building damage under the effect of surface deformation in feature-1 area; **(B)** buildings damage under the effect of surface deformation in feature-2 area; **(C)** buildings damage under the effect of surface deformation in feature-3 area.

ground deformation in the three deformation feature areas, as per **Eqs 1–3**.

$$z_1 = -0.0274 \times (x - 75) \quad (1)$$

$$z_2 = -0.0141 \times (x - 75) \quad (2)$$

$$z_3 = -0.0174 \times (x - 75) \quad (3)$$

Figure 11 shows a simulated specimen block of steel fiber concrete with internal fibers depicted by randomly generated line segments, thus coinciding with the actual preparation test process. The deformation resistance of concrete specimens of each mixing scheme (Groups 1–6 in **Table 2**) was analyzed under different loads, and the calculated results are shown in **Figure 12**.

The analysis showed that concrete with 0.8% steel fiber has a 10% higher resistance to deformation under uniform tensile load than standard concrete. However, a small increase in the deformation resistance of concrete specimens was observed with the increase in the amount of steel fiber admixture beyond 0.8%. It was observed that under relatively large non-homogeneous loads representative of the effect of maximum deformation of the ground surface in the feature-1 area (**Figure 12B**), the steel fiber concrete showed an almost 100% increase in the deformation resistance as compared to standard concrete. In addition, an increase in the length of the steel fiber was also observed to strengthen the deformation resistance of the concrete. Under relatively small non-homogeneous loads representative of the effect of surface displacement deformation in the feature-2 area, there was a small increase of up to 10% in the deformation resistance by steel fiber concrete compared to the standard concrete. Therefore, steel fiber concrete is more suitable for strengthening the more vulnerable parts of the buildings in the feature-1 area that show cracking and other tensile damages; less vulnerable parts of the buildings, both plain concrete and steel fiber concrete, are of similar suitability.

(2) Analysis of deformation resistance of Concrete columns and Beams

① Analysis of deformation-resistant reinforcement of concrete columns

Improving the deformation resistance of structural columns can effectively reduce the overall damage and cracking of the

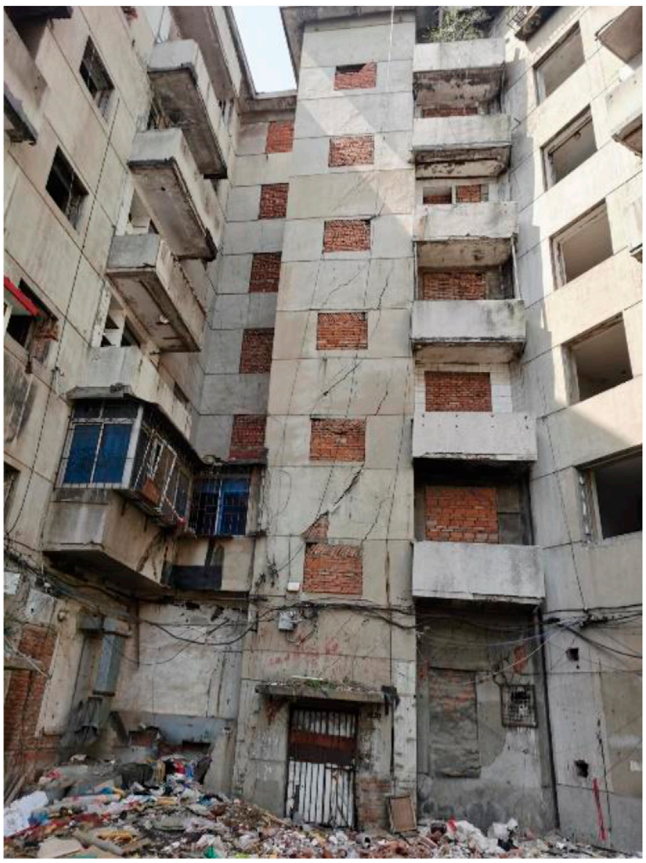

FIGURE 7 | Cracking of building wall and damage of balcony in feature-2 area.

buildings since they are the main load-bearing components of the buildings. For the deformation characteristics and forms of urban ground, the reinforcement methods of carbon-fiber-reinforced polymer (CFRP)-reinforced concrete columns and carbon-fiber-board-covered concrete columns are proposed.

Analysis showed that the CFRP-reinforced concrete columns had better-sustained resistance to deformation than ordinary concrete columns, and the concrete columns had better resistance to deformation even after partial damage, and CFRP-reinforced concrete columns had high peak stresses. As shown in **Figure 13B**, CFRP concrete reinforced columns and CFRP wrapped concrete columns had better resistance to deformation in each area of ground deformation, which is especially suitable for reinforcement of building elements with a large degree of deformation. The specific indexes and data of the deformation resistance of the three types of concrete columns under the influence of side slope deformation are shown in **Table 3**.

Figure 14 shows the damage distribution of CFRP-wrapped concrete reinforced columns, CFRP reinforced concrete columns, and plain concrete columns subjected to uneven loading. For the simulation, the site condition of the building in the urban area was used as a reference; the cross-sectional width and height of the concrete square column were 380 and 2800 mm, respectively, and the type of concrete was C30. The CFRP-wrapped concrete reinforced columns were reinforced using 25 mm thick CFRP plates wrapped around the concrete columns, and the CFRP reinforced concrete columns were reinforced using 16 mm CFRP columns arranged at 50 mm intervals.

The analysis of the damage distribution state of the three types of concrete columns under the uneven ultimate load showed that the damage of the CFRP-reinforced concrete columns and the CFRP-wrapped concrete columns was minor compared to the ordinary concrete columns. The upper part of the ordinary concrete column was almost completely broken. It is feasible to strengthen the concrete columns of existing buildings with CRFP slabs, and build CFRP columns reinforced load-bearing concrete columns.

② Analysis of deformation resistance of concrete beams

The beams are the central part of the building structure to bear the force deformation and are easy to break; using a CRFP plate for its reinforcement can effectively improve the overall deformation resistance performance. A concrete beam with a span of 5,900 mm and a cross-sectional height and width of 380 and 370 mm, respectively, was used to compute and analyze the deformation resistance with and without CFRP slab reinforcement. The simulation results are shown in **Figure 15**.

The degree of damage in the middle and lower regions was significantly reduced as the CFRP wrapped concrete beam was used, and no concrete dislodgement was observed, and the CFRP-wrapped concrete beam had partial load-carrying capacity. However, the small concrete peeling area on the upper surface of both ends of the beam can be repaired by steel fiber concrete filling. The degree of damage to ordinary concrete beams was relative of severe nature, and concrete dislodging was observed in the middle, corner, and lower parts. Consequently, the overall resistance to deformation of the ordinary concrete was significantly low.

FIGURE 8 | Separation of building a wall from the foundation in feature-3 area.

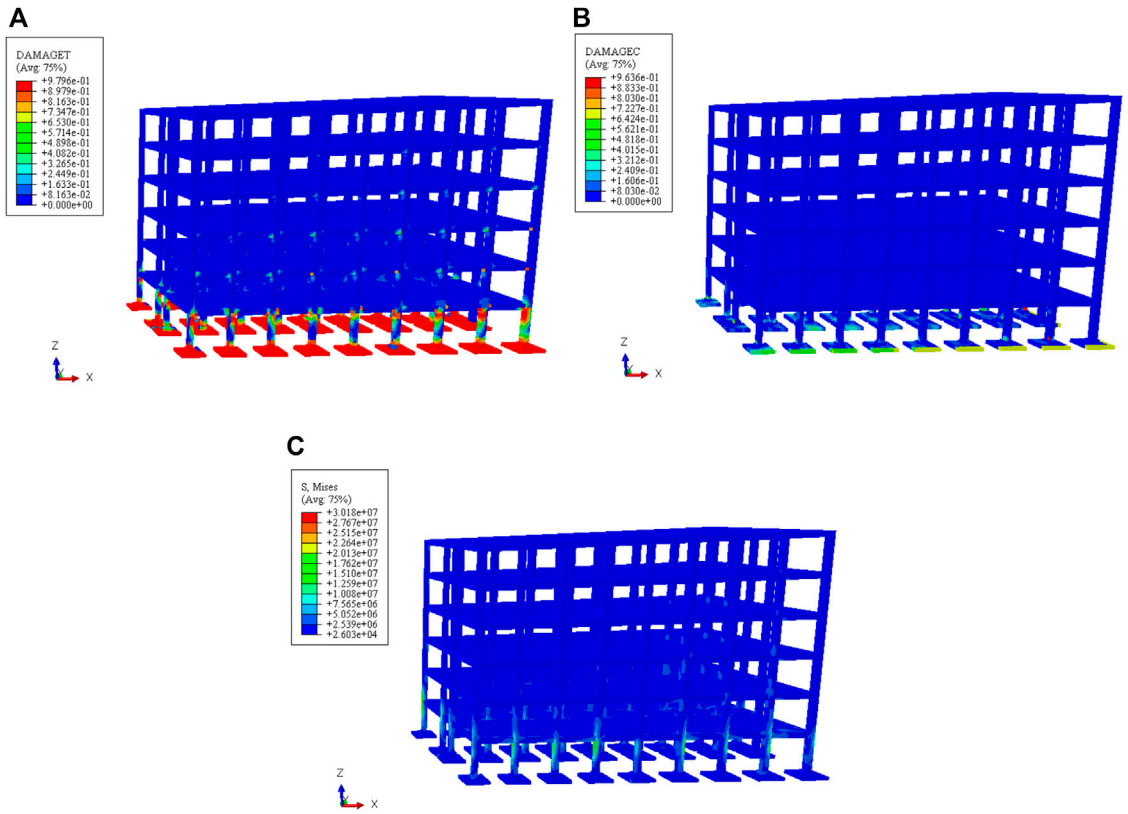

FIGURE 9 | Distribution of deformation and damage of frame structures in each deformation area: **(A)** buildings damage under the effect of surface deformation in feature-1 area; **(B)** buildings damage under the effect of surface deformation in feature-2 area; **(C)** buildings damage under the effect of surface deformation in feature-3 area.

(3) Study on flexural performance of reinforced Concrete slabs wrapped with profile steel

The floor slab of the building was more severely damaged due to the uneven settlement caused by the ground deformations. It was hypothesized that by wrapping the concrete slab with C and E-shaped steel plates, the deformation resistance of the concrete slab could be improved. The compressive bending deformation of an ordinary and shaped steel plates strengthened of the concrete slab was considered for analysis, and the length width and thickness of the concrete slab were taken as 100 mm, 45 mm, and 8 mm, respectively. Moreover, the applied displacement deformation was taken as 10% of the thickness, and the types of concrete and steel were set to C30 and Q235R, respectively.

The plastic deformation under the load was selected as the evaluation index of the deformation resistance of the concrete slab. As shown in **Figure 16**, the plastic deformation of the C-shaped steel-wrapped concrete slab was only one-third of that of ordinary concrete. Thus, the bottom and top floor slabs of buildings in urban areas with serious damage could be strengthened by steel sections to improve stability.

Toughness Enhancement Scheme of Buildings Against Slope Deformation

(1) Building foundation and wall reinforcement

Some buildings in feature-1, feature-2, and feature-3 areas were affected by side slope deformation and ground cracks and showed serious wall cracking, external bulging, and shear damage to the foundation. Based on the analysis results in this study, it was recommended that pertinent parts of buildings be reinforced with steel fiber concrete to mitigate and repair the aforementioned damages.

(2) Building wall column and Balcony reinforcement

The wall column and balcony reinforcement areas were severely damaged in the northern (feature-1 and feature-2 areas) and the south bank, and there existed many vulnerable buildings in these areas construction of which was more than 30 years old. The buildings in these regions were subjected to uneven ground settlement deformation forces, resulting in wall cracking, wall misalignment, damage to wall-column joints, and balcony breakage. This damage could be reinforced with CRFP wrapped concrete columns, balcony slabs, etc.

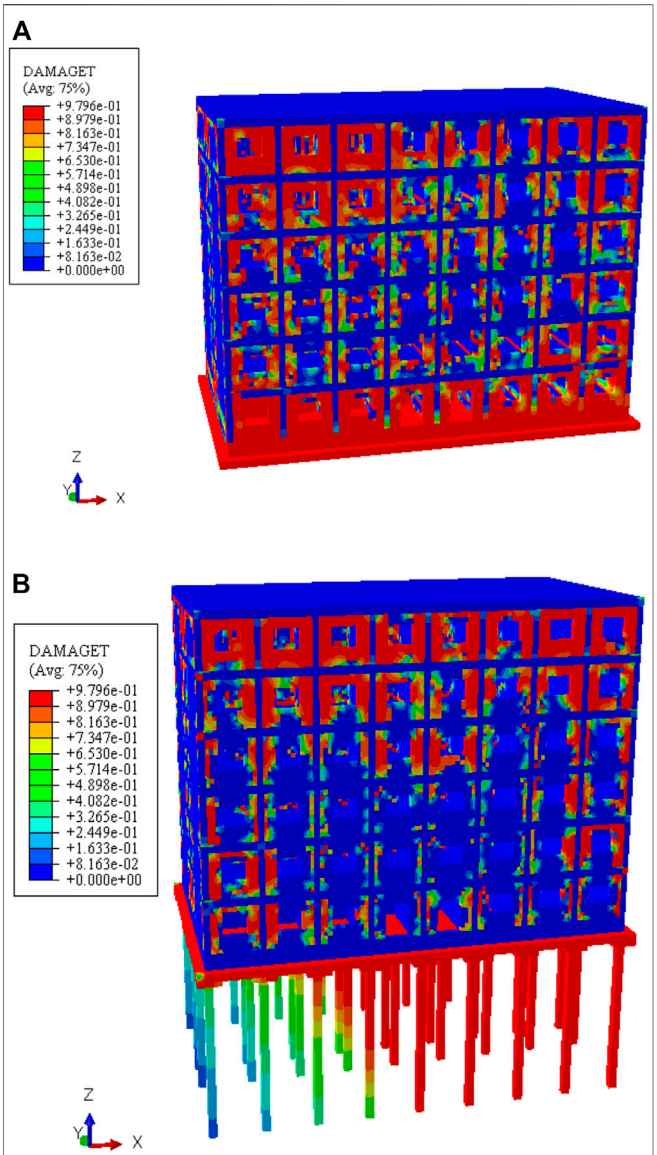

FIGURE 10 | Distribution of deformation and damage of masonry buildings with different foundation forms: **(A)** masonry buildings with raft foundations; **(B)** masonry buildings with combined pile-raft foundations.

(3) Beam and floor slab reinforcement

In the area close to the slope of the mine, the ground surface was prone to be affected by the slope deformation thus could have a large horizontal ground surface deformation. Multi-story masonry structure buildings in these areas experienced beam damage, floor deflection and other pertinent phenomena. As per the findings of this study, to mitigate and repair the beam-and floor-related damages, external CFRP wrapping of beam and reinforcement of slab with steel section could be employed, respectively. Moreover, the steel fiber concrete filler could be used to strengthen the concrete shedding areas in these parts of buildings. Similarly, buildings with different deterioration characteristics could be reinforced with different measures, as shown in **Table 4**.

DISASTER PREVENTION AND EMERGENCY RESILIENCE ENHANCEMENT IN URBAN AREAS AROUND SLOPES

A comprehensive and multifaceted approach to disaster resilience enhancement based on the criteria of disaster resilience grading zones in urban areas was established to improve the ability of geological disaster prevention and emergency response in the urban areas around the Fushun West Open-pit mine. This approach was aimed to protect the lives and properties of residents of this region and provide a scientific basis for the rational planning and construction of the to-be-built communities.

Urban Disaster Prevention and Emergency Zoning

Figure 17 shows the zoning of the emergency geohazard protection level in the urban area around the west open pit of Fushun City; the zoning was based on the field monitoring of displacement, the population density of the cluster, the stratigraphic stability conditions, and the landslide history of the slopes. The protection levels were set as levels one, two, and three, wherein the required care increased from high to low. The residential areas in the south of Nan'yang Road, on the northeast bank, on the south bank of Qian-tai mountain, in the mine area were the key areas with high population density marked as to require level 1 protection (shown by the red region in **Figure 17**). The northern area of Nan'yang Road in the northern bank, the Dong'li and the Wu'lao community area in the southern bank, were classified to require level 2 protection (shown by the orange region in **Figure 17**). The low population concentration areas, including the industrial park on the north bank, the industrial park on the southwest bank, and the industrial park on the south bank, were jointly designated as level 3 protection regions (shown by the green region in **Figure 17**).

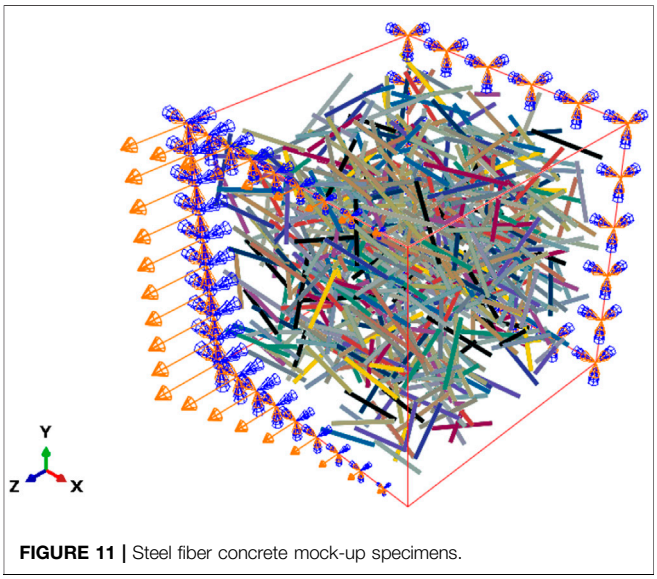

FIGURE 11 | Steel fiber concrete mock-up specimens.

TABLE 2 | Fiber mixing scheme for each group of test blocks.

Number	Fiber Dose (%)	Fiber Diameter (mm)	Fiber Length Range	Number of Fibers
Group one	0.8	0.8	60–90 mm	716
Group two	1.0	0.6	50–70 mm	1989
Group three	1.0	0.9	55–95 mm	707
Group four	0.8	0.9	85–95 mm	472
Group five	1.2	0.7	50~-90 mm	1503
Group six	1.2	0.6	45–75 mm	2387
Group seven	1.5	0.7	80–100 mm	1461
Group eight	1.5	0.8	40–80 mm	1679

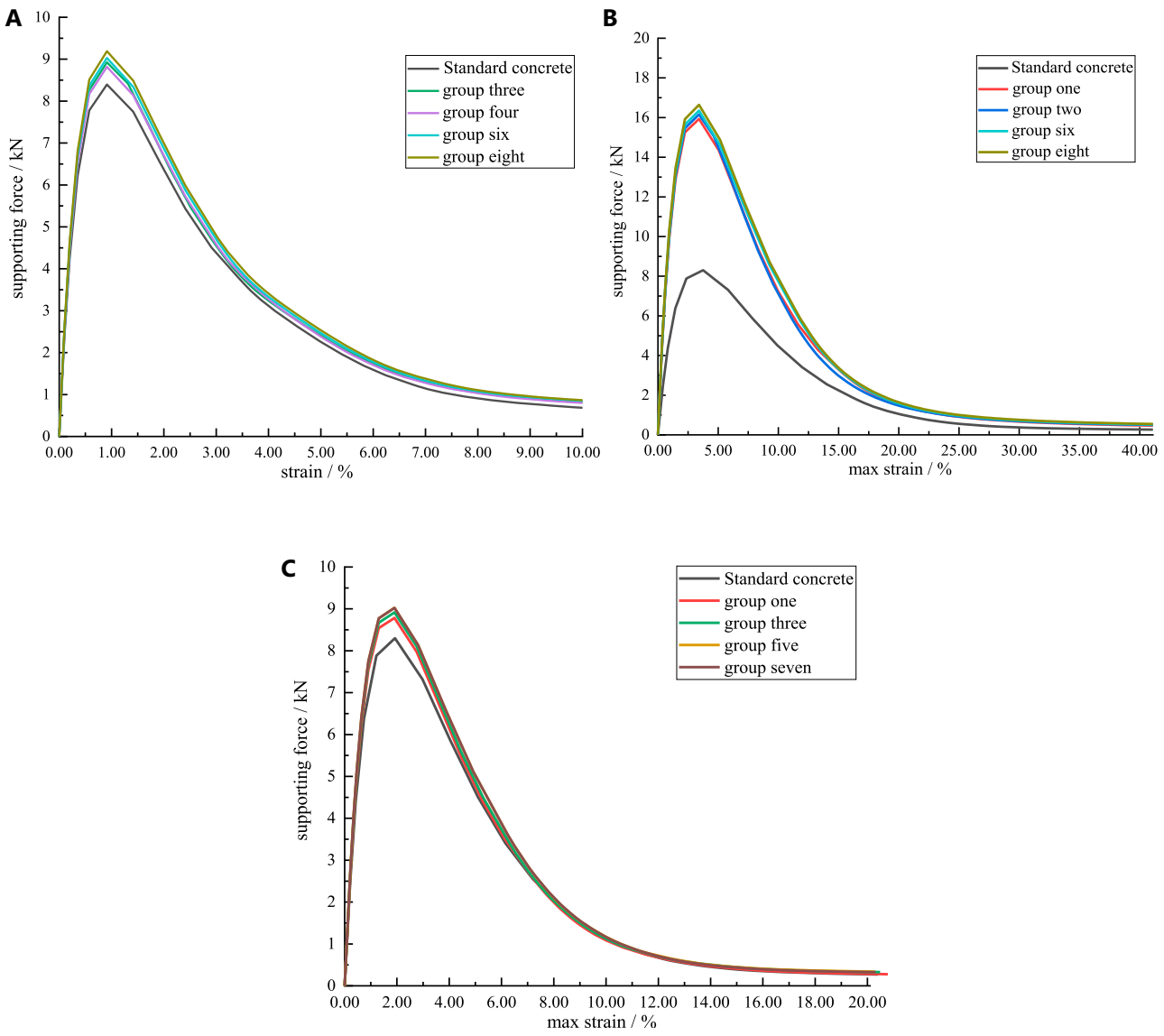

FIGURE 12 | Comparison of deformation resistance curves of steel fiber concrete specimens and standard specimens: **(A)** support force and strain curve of test block under uniform tension; **(B)** support force versus strain curves of test blocks under equivalent non-uniform tension in the feature-1 area; **(C)** support force versus strain curves of test blocks under equivalent non-uniform tension in feature-2 area.

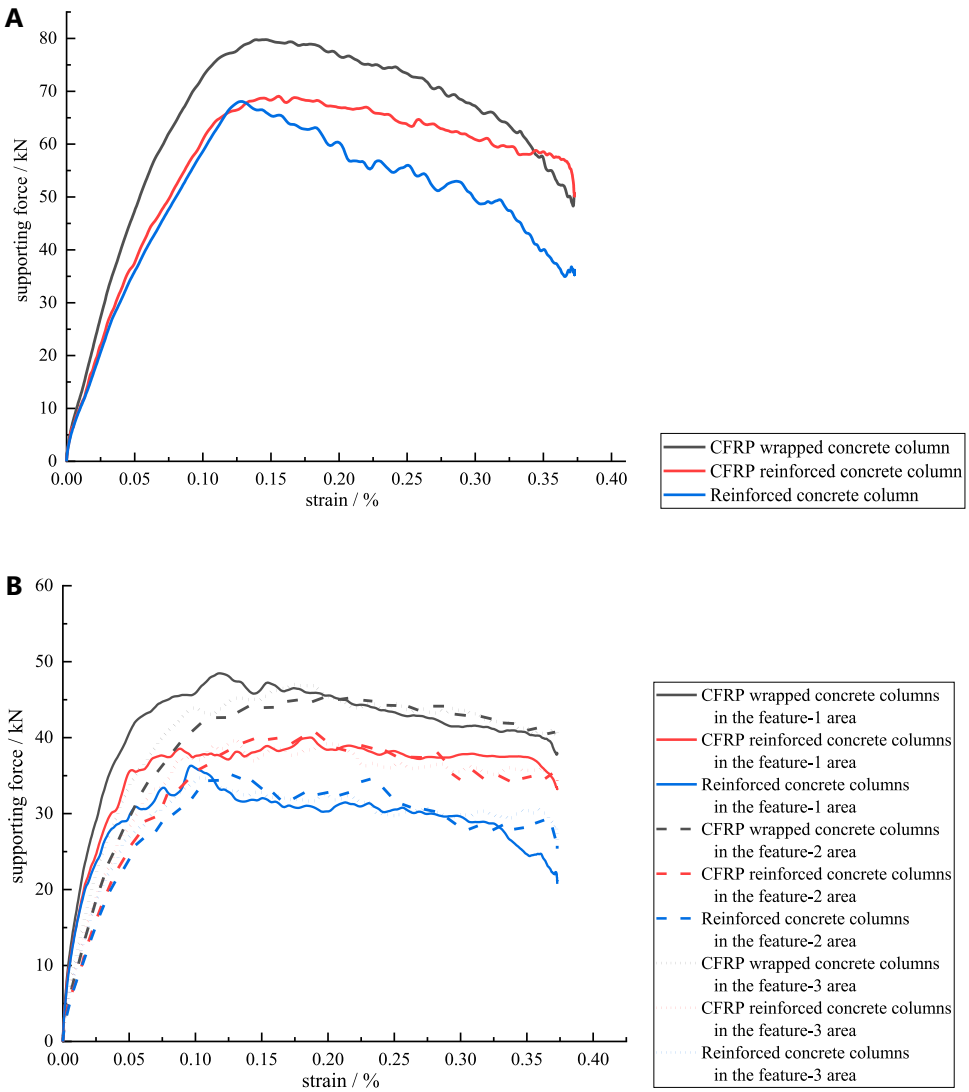

FIGURE 13 | Analysis of deformation resistance of CFRP concrete reinforced columns: **(A)** support force and strain curves of concrete columns under uniform load; **(B)** support force and strain curves of concrete columns under loads in each characteristic zone.

TABLE 3 | Deformation resistance of each type of column.

Column types	Resistance to Uniform Deformation		Resistance to Uneven Deformation	
	Ultimate Bearing Capacity (kN)	Post-peak Load-Bearing Capacity (kN)	Ultimate Bearing Capacity (kN)	Post-peak Load-Bearing Capacity (kN)
reinforced concrete columns	79776.9	63336.1	48472.6	42031.7
			45302.8	42163.6
			46997.0	42436.3
CFRP concrete reinforced columns	69088.3	59984.3	40012.0	36618.8
			40682.5	35872.5
			39661.1	36061.9
CFRP wrapped concrete columns	68071.8	48039.0	36306.1	27851.8
			35221.6	29730.9
			34743.1	30340.4

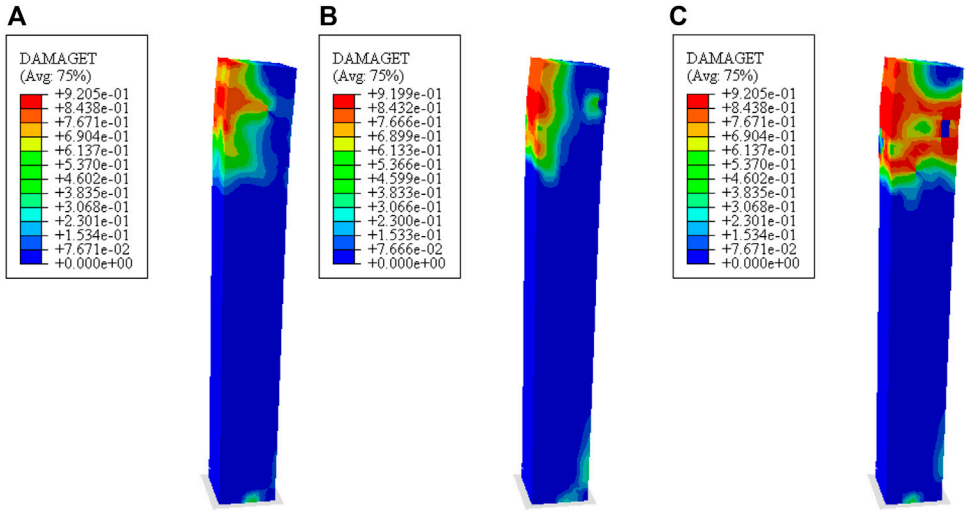

FIGURE 14 | Breakage of various types of concrete columns under equivalent ultimate load in feature-1 zone: **(A)** CFRP-wrapped concrete reinforced columns; **(B)** CFRP reinforced concrete columns; **(C)** ordinary reinforced concrete columns.

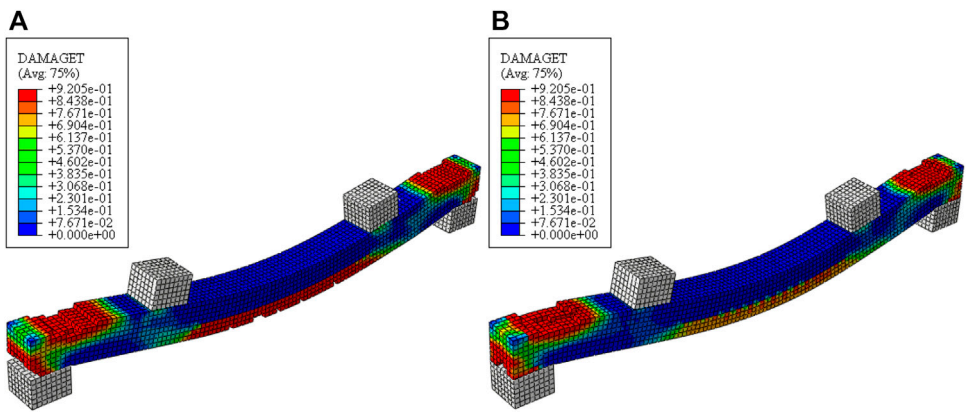

FIGURE 15 | Concrete beams under load damage: **(A)** ordinary reinforced concrete beams; **(B)** CFRP wrapped concrete reinforced beams.

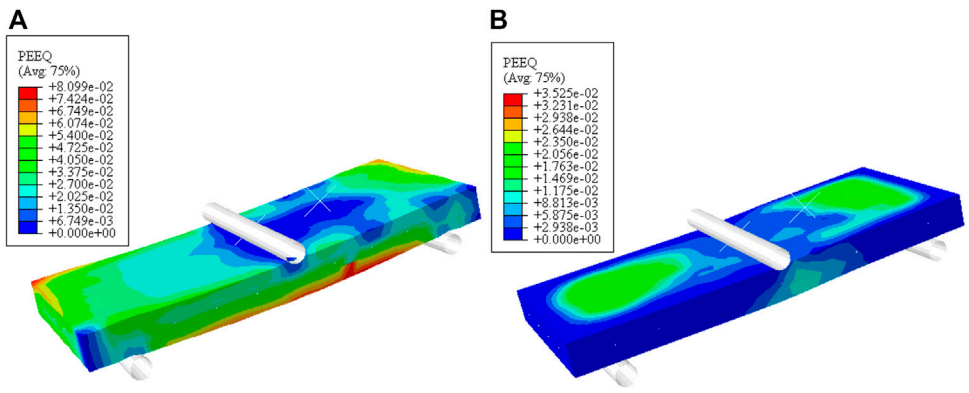

FIGURE 16 | Plastic deformation of concrete slabs under load: **(A)** plastic deformation of the reinforced concrete slab; **(B)** plastic deformation of C-shaped steel wrapped concrete slab.

TABLE 4 | Causes of damage to building elements and reinforcement measures in each region.

Type of Damage	Causes of Damage	Reinforcement Measures	Scope of Application (Type of Building and Number of Floors)
Wall cracking	Uneven settlement of foundation; unreasonable building construction, poor integrity of old and new walls	Steel fiber concrete repair and reinforcement	Masonry and frame buildings with more than five floors
Wall misalignment	Horizontal deformation of the ground surface		
Beam cracking	Ground deformation, insufficient stiffness	CFRP concrete reinforcement	Masonry and frame buildings with more than five floors
Column tilt and cracking	Uneven ground settlement, insufficient stiffness	Overmolded steel reinforcement	Masonry buildings of five floors and below
Base plate cracking		CFRP concrete reinforcement	Masonry and frame buildings with more than five floors
Balcony breakage	Ground deformation, construction causes	Balcony bracing method reinforcement, CFRP concrete reinforcement	Masonry buildings of five floors and below
Basic detachment	Uneven foundation settlement, insufficient foundation stiffness or excessive foundation stiffness	High toughness and high strength concrete reinforcement	Masonry structure

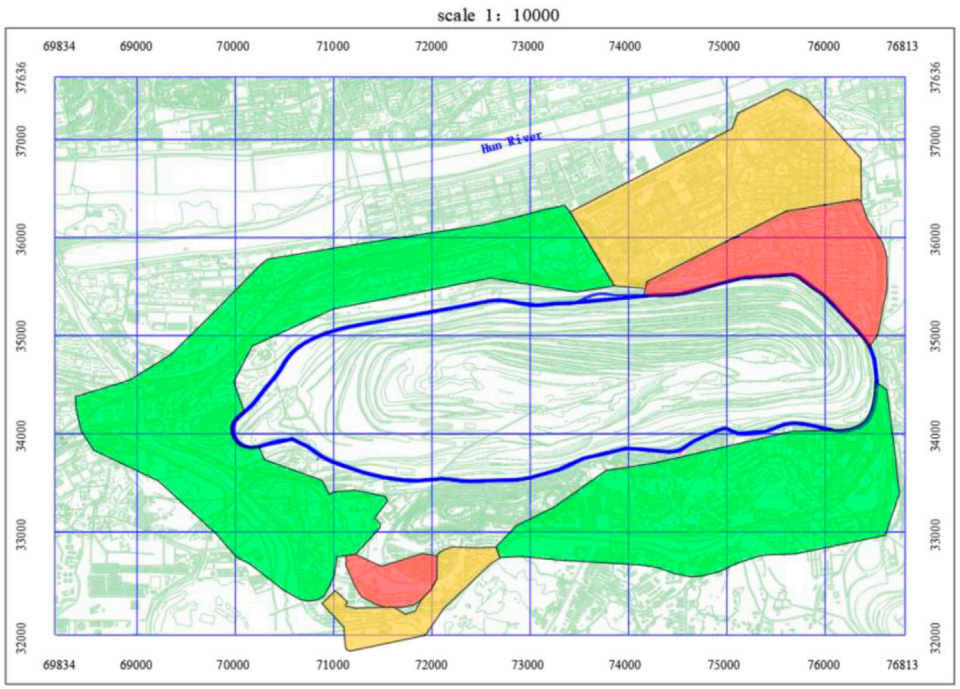

FIGURE 17 | Emergency fortification zoning of slope disasters in the affected area.

Disaster Preparedness Resilience Enhancement Methods for Established Communities

The resilience enhancement approach for established communities needs to consider community resilience enhancement strategies in terms of redundancy, efficiency, and adaptability. The strategies are established based on three major aspects, i.e., engineering, organization, and system.

From the perspective of engineering, concrete or mortar filling, and reinforcement are recommended to be employed on the exterior walls, columns, and balconies of existing buildings (structures) in the community. The foundations of buildings in areas with large surface displacement variables are recommended to be repaired and reinforced. Permanent or temporary shelters are recommended to be established according to the population density and age structure of people in the community, and necessary emergency signs should be set up.

In terms of organization, a set of organizational structure systems is recommended to be established by making the community neighborhood committee a governing body. The contacts of the community with the municipal emergency management bureau, fire rescue teams, and other

departments are recommended to be strengthened to achieve timely and effective information sharing and rescuing. The community should be scientifically zoned to establish multiple responsibility areas with dedicated staff responsible for managing day-to-day disaster prevention and mitigation matters, especially in special circumstances, i.e., the rainy season. The necessary emergency devices should be used, and emergency access should be set up to improve the efficiency of community disaster prevention and emergency response. Moreover, disaster prevention and mitigation education and drills should be conducted for the communities.

From the perspective of system construction, the establishment and implementation of disaster detection prevention and reporting systems are recommended.

Disaster Resilience Enhancement Methods for Unbuilt Communities

For unbuilt and to-be-built communities, technical feasibility and economic applicability are the principles according to national norms and geological characteristics of the urban areas. The three proposed resilience enhancement methods and strategies are as follows.

(1) New communities should be sited as far away from the west open pit as possible, avoiding adverse geological area such as faults and fractures.
(2) The deformation of the ground surface of the characteristic area and geological emergency defense level must be considered. The foundation type and building structure with a better bearing capacity of regional surface deformation should be chosen. Reasonable design of building elements such as settlement joints, expansion joints and flexible bearings can absorb part of the building deformation, thus improving the deformation resistance of community buildings.
(3) A reasonable disaster-proof space and a sound management system should be designed and built. This implies that we should improve infrastructure construction, increase medical services, plan community-specific disaster prevention land, and increase the area of public open space. In the primary prevention area, the new community should develop a complete emergency and disaster prevention plan for geological hazards and engage professional staff to monitor and warn about the hidden hazards throughout the year. In the secondary prevention area, new communities should formulate emergency and disaster prevention plans for geological hazards and strengthen the inspection of potential disaster sites during the rainy seasons and freezing and thawing periods.

CONCLUSION

(1) The slope deformation of the west open pit and the surrounding urban areas from 2016 to 2020 is slow, and there are roughly three areas of relatively large surface deformation within the pit. There are roughly three areas with relatively large surface deformation in the pit, namely, the western drainage field, the south bank of slope area (former landslide body area), and the eastern area of the north bank.
(2) The surface of the surrounding urban area is mainly affected by slope creep deformation, ground fracture. According to the different magnitudes of horizontal and vertical deformations of the ground surface, the northern bank, the eastern part of the northern bank, the central part in the northern bank, and the area of Qian-tai mountain in the south can be divided into three deformation featured partitions. The deformation in the area of petroleum plant No.1 is a coupled horizontal and vertical ground surface deformations, the vertical ground surface deformation is dominant in the area affected by the fracture in the middle of the north bank, and the horizontal deformation is dominant in the Qian-tai mountain area.
(3) Frame structure has better resistance to side slope deformation than masonry structure, and the buildings of both types of structural forms have a pronounced damage under the coupled action of the horizontal and vertical side slope deformations. The foundation part of the building of the masonry structure is affected by the horizontal deformation to a higher degree, and the upper wall is affected by the uneven settlement, while the foundation of the frame structure is affected by vertical deformation of the slope.
(4) Steel fiber concrete reinforced walls, CFRP concrete reinforced beams and columns, and section steel reinforced floor slabs are proposed methods to enhance the deformation resistance and resilience of buildings in urban areas. All these methods can effectively improve the ability of buildings in urban areas to resist side slope deformation.
(5) A three-level urban geological disaster prevention and emergency treatment zone map is established based on the side slope deformation, population density and the degree of building damage in each feature area of the urban region, and the resilience enhancement methods for the built and to-be-built communities are also established.

DATA AVAILABILITY STATEMENT

The original contributions presented in the study are included in the article/supplementary material, further inquiries can be directed to the corresponding author.

AUTHOR CONTRIBUTIONS

The first author,ZJ, is responsible for the general writing of the full text and completing the main work; the second author,LF, and the third author, WJ, are responsible for gatekeeping; the fourth author, GA, and the fifth author,HC, are responsible for consulting on a small number of issues.

FUNDING

We acknowledge the funding support from the National Key Research and Development Project of China (Grant No. 2017YFC1503104).

REFERENCES

Chen, H., Li, G., Fang, R., and Zheng, M. (2021). Early Warning Indicators of Landslides Based on Deep Displacements: Applications on Jinping Landslide and Wendong Landslide, China[J]. *Front. Earth Sci.* 9. doi:10.3389/feart.2021.747379

Chen, Z., Fang, C., and Deng, R. (2015). "Research and Application of Jinggangshan Geological Disaster Prevention System Based on Wireless Sensor Network System[J]," in 2015 23rd International Conference on Geoinformatics (Wuhan, China: IEEE), 1–5.

Chengyuan, H. E. (2020). *Research on Damage Analysis and Deformation Control of Buildings in the Influence Area of Fushun West Open-Pit Mine [D]*. Beijing: University of Science and Technology. (In Chinese).

Du, D. (2007). *Research on Mining-Induced Seismicity in Fushun Laohutai Coal Mine and its Effect on Building [D]*. Liaoning: Liaoning Technical University. (In Chinese).

Du, Y., Xie, M., Jiang, Y., Huo, L., Chen, C., Jia, B., et al. (2021). Review on the Formation Mechanism and Early Warning of Rock Collapse[J]. *Metal. Mine* 535 (01), 106–119. (In Chinese). doi:10.19614/j.cnki.jsks.202101008

Du, Y., Xie, M., and Jia, J. (2020). Stepped Settlement: A Possible Mechanism for Translational Landslides. *CATENA* 187, 104365. doi:10.1016/j.catena.2019.104365

Gao, A. (2020). *Study on Damaged Location Characteristics and Anti-deformation Methods of Buildings in Affected Area of Fushun Western Open-Pit Mine[D]*. Beijing: University of Science and Technology. (In Chinese).

Gao, A., Wang, J., Li, F., and Xie, J. (2021). Locational Characteristics of Damage on Buildings Around the West Open-Pit Mine[J]. *Meitan Xuebao/Journal China Coal Soc.* 46 (4), 1320–1330. (In Chinese).

Gulec, A., Kose, M. M., and Gogus, M. T. (2021). Experimental Investigation of Flexural Performance of T-Section Prefabricated Cage Reinforced Beams with Self-Compacting Concrete. *Structures* 33 (5), 2190–2197. doi:10.1016/j.istruc.2021.05.074

He, F., Tan, S., and Liu, H. (2022). Mechanism of Rainfall Induced Landslides in Yunnan Province Using Multi-Scale Spatiotemporal Analysis and Remote Sensing Interpretation. *Microprocess. Microsystems* 90, 104502. doi:10.1016/j.micpro.2022.104502

La, R., Lv, T., Bai, P., and Zhang, Z. (2021). Research on Collaborative and Optimal Deployment and Decision Making Among Major Geological Disaster Rescue Subjects[J]. *Geotechnical Geol. Eng.* 1, 1–13.

Mostafa, K., Rahmat, M., Carlos, C., Mohammad Reza, E., and Luc, C. (2021). Numerical Study on the Flexural Behaviour of Normal- and High-Strength Concrete Beams Reinforced with GFRP Bar, Using Different Amounts of Transverse Reinforcement[J]. *Structures* 34, 3113–3124.

Ou, P., Wu, W., Qin, Y., Zhou, X., Huangfu, W., Zhang, Y., et al. (2021). Assessment of Landslide Hazard in Jiangxi Using Geo-Information Technology. *Front. Earth Sci.* 9, 648342. doi:10.3389/feart.2021.648342

Qiao, J., Liu, B., Li, Y., Li, S., and Zhang, W. (2022). Experimental Study on Shear Performance of Improved High-Performance Polymer Cement Mortar-Glass Fiber Reinforced Plastic Reinforced Masonry Wall. *Adv. Struct. Eng.* 25 (2), 247–258. doi:10.1177/13694332211046347

Resan, S. F., Zemam, S. K., and Abed, M. S. (2020). Developing Tension Field Action of Embedded Steel Plates-Stiffened Rebars Composite Reinforcement within Concrete Deep Beams[J]. *Adv. Struct. Eng.* 23 (7), 1710141054. doi:10.1177/1369433220919065

Rf, A., Rui, M. A., Apr, B., and Cj, A. (2020). Influence of the Top Reinforcement Detailing in the Behaviour of Flat Slabs[J]. *Structures* 23, 718–730.

Shao, L. (2019). Geological Disaster Prevention and Control and Resource Protection in Mineral Resource Exploitation Region[J]. *Int. J. low carbon Technol.* 14, 142–146. doi:10.1093/ijlct/ctz003

Tsai, W. N., Chen, C. C., Chiang, C. W., Chen, P. Y., Kuo, C. Y., Wang, K. L., et al. (2021). Electrical Resistivity Tomography (ERT) Monitoring for Landslides: Case Study in the Lantai Area, Yilan Taiping Mountain, Northeast Taiwan[J]. *Front. Earth Sci.* 9, 1. doi:10.3389/feart.2021.737271

Xu, Y., Qiu, X., Yang, X., Lu, X., and Chen, G. (2020). Disaster Risk Management Models for Rural Relocation Communities of Mountainous Southwestern China under the Stress of Geological Disasters. *Int. J. Disaster Risk Reduct.* 50, 101697. doi:10.1016/j.ijdrr.2020.101697

Conflict of Interest: Author GA was employed by the company Shanxi Academy of Building Research Co., Ltd. Author HC was employed by the company China Railway Bridge Research Institute, Ltd.

The remaining authors declare that the research was conducted in the absence of any commercial or financial relationships that could be construed as a potential conflict of interest.

Publisher's Note: All claims expressed in this article are solely those of the authors and do not necessarily represent those of their affiliated organizations, or those of the publisher, the editors and the reviewers. Any product that may be evaluated in this article, or claim that may be made by its manufacturer, is not guaranteed or endorsed by the publisher.

Copyright © 2022 Jiaxing, Fei, Jin-an, Anqi and Chengyuan. This is an open-access article distributed under the terms of the Creative Commons Attribution License (CC BY). The use, distribution or reproduction in other forums is permitted, provided the original author(s) and the copyright owner(s) are credited and that the original publication in this journal is cited, in accordance with accepted academic practice. No use, distribution or reproduction is permitted which does not comply with these terms.

frontiers | Frontiers in Environmental Science

MINI REVIEW
published: 05 July 2022
doi: 10.3389/fenvs.2022.928064

Progress and Perspectives of Geotechnical Anchor Bolts on Slope Engineering in China

Yan Du[1], *Heng Li*[1]*, *Santos D. Chicas*[2] *and Leichen Huo*[1]

[1]School of Civil and Resource Engineering, University of Science and Technology Beijing, Beijing, China, [2]Integrative Research Institute on Transformations of Human-Environment Systems (IRI THESys), Humboldt-Universitat Zu Berlin, Berlin, Germany

Geotechnical anchoring technology is an important tool for disaster prevention and mitigation in slope engineering. Anchor bolts which are commonly used in slope engineering can be divided into prestressed anchors and non-prestressed anchors. Due to the superiority of anchor support technology, research on various aspects of anchor bolts, such as mechanical mechanism, anchorage effect, and the development of new-type anchor bolts, has been a significant research topic for scholars. This mini-review sums up the diverse past and current literature on anchor support technology of slope engineering in China. It focuses on the characteristics, applications, research methods, and practical cases of anchor bolts and briefly describes the history of slope anchor bolt development in China in the past 3 decades. Nowadays, the demand for engineering construction processes is increasing, and engineering geological conditions are becoming more complex, which promotes the development of anchor support technology. At the international level, achieving carbon neutrality is both an international trend and a general objective. Against the background of global commitment to carbon neutrality, the potential future perspectives for the developments of anchor support technology have been prospected in light of actual engineering needs.

Keywords: slope engineering, anchor bolt, energy-absorbing anchor, nonmetal bolt, carbon neutrality, ecological slope protection

OPEN ACCESS

Edited by:
Yifei Sun,
Hohai University, China

Reviewed by:
Shao-Heng He,
Zhejiang University, China
Richeng Liu,
China University of Mining and Technology, China

***Correspondence:**
Heng Li
liheng_0_1@163.com

Specialty section:
This article was submitted to Environmental Informatics and Remote Sensing, a section of the journal Frontiers in Environmental Science

Received: *25 April 2022*
Accepted: *19 May 2022*
Published: *05 July 2022*

Citation:
Du Y, Li H, Chicas SD and Huo L (2022) Progress and Perspectives of Geotechnical Anchor Bolts on Slope Engineering in China. Front. Environ. Sci. 10:928064. doi: 10.3389/fenvs.2022.928064

1 INTRODUCTION

Landslide is one of the most common geological disasters in the world, which causes great harm to the life and property of people. Geotechnical anchoring technology is an important tool for disaster prevention and mitigation. As a significant branch of geotechnical engineering, geotechnical anchoring techniques are widely applied to engineering construction due to their economy and efficiency (Ding et al., 2022). Anchor bolts play a crucial role in geotechnical anchoring (Shan et al., 2021), which could restrain the displacement of rock and soil mass (Nie et al., 2014b) so as to prevent disasters, such as landslides (Xu et al., 2014) and rock avalanches (Fan et al., 2017).

Anchor bolts have been exploited for over 100 years to reinforce rock and soil mass, which dated back to 1913, where they were generally utilized in the American mining industry until the 1940s (Grasselli, 2005). Due to the superiority of anchor support technology, China has been using anchor bolts in coal systems since the 1950s (Kang, 2016). With the development of China's hydraulic engineering, power engineering, and urban construction, the application of anchor support technology in China entered a boom period in the 1980s (Cheng, 2001).

The reinforcement effects of anchor bolts are apparent as they can transfer the tension caused by rock deformation to the stable rock layer. The dangerous rock mass is combined with the stable rock mass through bolts (Li et al., 2016; Li Y. et al., 2017). Compared with the original rock, the uniaxial compressive strength and elastic modulus of the bolted rock improve to some extent (Yang et al., 2020). The bolting area can limit the extension and propagation of tensile cracks and slow down the failure process (Zong et al., 2014).

In this mini-review, we sum up the diverse past and current literature about anchor support technology of slope engineering in China. The characteristics, applications, and practical cases of various types of anchor bolts are the focus of our attention. Some research methods and the development history of anchor support technology are briefly described, and finally, the potential future perspectives for developments in the field are highlighted.

2 CLASSIFICATION OF ANCHOR BOLTS IN SLOPE ENGINEERING

In slope engineering, anchors bolts are divided into two categories: the prestressed anchors and the non-prestressed anchors; the former can also be called prestressed anchor cables if the reinforcement body consists of steel strands and wires, while the latter are often called full grouted bolts (Cheng et al., 2015). The prestressed anchor implements the pre-stress in advance is a sort of active supporting technology, while the non-prestressed anchor is activated by the deformation of the surrounding rock; this is a sort of passive supporting technology (Guo et al., 2019).

2.1 The Prestressed Anchors

Prestressed anchors have excellent characteristics of lightweight and high strength, which could decrease the amount of material for reinforcing structures so that the weight of the supporting structure would be controlled (Deng et al., 2021). In order to ensure the optimal position and length of the prestressed anchors, previous scholars have carried out remarkable studies. Hryciw (1991) proposed a theoretical research to confirm the optimum orientation of anchors by surface load. Yang et al. (2015) obtained a better reinforcement arrangement of prestressed anchors which relied on slope stress and displacement fields. An et al. (2020) presented a new three-dimensional optimization equation for the anchorage direction angle. Although the prestressed anchors can efficiently reinforce slopes, they still have many limitations. Elices et al. (2012) found that the common prestressed anchors with damage fail to warn against brittle failures. In addition to brittle failures caused by loads greatly exceeding the strength, stress corrosion cracking in complex geotechnical environments is another major cause of the deterioration (Karalis et al., 2012; Mak et al., 2019). Wang Y. et al. (2019) showed that the anchor head is relatively fragile through the collection and analysis of field samples. Sun et al. (2021)demonstrated that shear failure occurs with the extension and evolution of cracks by means of laboratory simulation tests. As a main defect of the prestressed anchors, it is necessary to study the mechanism of prestressing loss (Gao et al., 2021). Zhang et al. (2009) showed that the prestressing loss is divided into three parts according to the construction process: tensioning, locking, and time-dependent and specified the calculation formulas. Chen et al. (2013) further divided the prestressing loss into two parts based on a soft rock slope measurement analysis: instantaneous loss and time loss. Liu et al. (2021) revealed that the accelerated creep of the rock mass will contribute to tension failure or debonding failure of the bolt. Prestressed anchors are suitable for most projects, and they are most suitable for the excavation of high-steep slopes (Yang et al., 2020).

2.2 The Non-Prestressed Anchors

Passive, fully grouted bolts can provide extra tensile and shear strength to the joints it intersects at the anchorage part when installed in a jointed rock mass, and it is a crucial support technology for the joint rock slope (Siad, 2001). The rock–bolt interface of fully grouted bolts is formed by bonding the grout materials (cement, resin, etc.), which generates the load-bearing capacity by its shear strength (Nie et al., 2014a). This shear strength is related to the frictional rather than bonding strength of the rock–bolt interface (Hyett et al., 1992). Furthermore, the relatively high axial load may motivate the formation of slippage at the rock bolt–grout interface, which results in the loss of supporting capability (Kaiser et al., 1992). Freeman (1978) explored the behavior of fully grouted bolts relatively early. The following scholars used laboratory tests, analytical methods, and numerical models in studying the mechanical property of fully grouted bolts (Hyett et al., 1996; Li and Stillborg, 1999; Blanco Martín et al., 2013; Liu and Li, 2020; Singh and Spearing, 2021). The increase in bolt length and cross-sectional area can boost the bearing capacity of the fully grouted bolts through the data of tests (Benmokrane et al., 1995; Kılıc et al., 2002). The strength of the rod material is one of the main factors in the bearing capacity of the fully grouted bolts (Li and Liu, 2019), and the bolting angle, properties of grouting materials, and rock mass quality also have an impact (Feng et al., 2017; Li and Liu, 2019). It is understood that ultima failure is caused by debonding of the rock–bolt interface if the bolt tensile strength is relatively strong (Li and Stillborg, 1999). Ho et al. (2019) confirmed that under high confining pressures, the damage is mainly due to shear failure, while under low confining pressures, the grout is destroyed by cracking from expansion. Luga and Periku (2021) also obtained similar results through multiple *in situ* fully grouted bolt pull-out tests.

It is indispensable to rationalize the anchoring scheme and maximize the supporting effect of anchor bolts. This is possible through the research of the optimal installation position and failure mechanism, mentioned above, which have their own unique contributions. Revealing the failure mechanism facilitates the innovation of new-type anchor bolts. **Table 1** summarizes the features, advantages, disadvantages, applications, examples, and practical cases of some geotechnical anchors.

Table 1 summarizes the features, advantages, disadvantages, examples, and practical cases of some geotechnical anchors (Siad, 2001; Wu et al., 2005; Qin et al., 2007; Wang et al., 2008; Dong et al., 2010; Nie et al., 2014a; Chen et al., 2014; Cheng et al., 2015; Xu and Yin, 2016; Zhu et al., 2017; Wu S. G. et al., 2018; Wu X.

TABLE 1 | Summary of the features, advantages, disadvantages, examples, and practical cases of some geotechnical anchors (Siad, 2001; Wu et al., 2005; Qin et al., 2007; Wang et al., 2008; Dong et al., 2010; Nie et al., 2014a; Cheng et al., 2015; Xu and Yin, 2016; Zhu et al., 2017; Wu S. G. et al., 2018; Wu X. et al., 2018; Tao et al., 2018; Mak et al., 2019; Tang et al., 2019; Gao et al., 2021).

Type	Examples	Advantages	Disadvantages	Practical Cases
The Prestressed Anchors	Large anchor cables The tension–compression dispersive anchor cable Sand consolidated anchorage prestressed bolt Self-reinforced anchor bolt The frame supporting structure with prestressed anchors	1. Active supporting technology 2. High load-bearing capacity 3. Almost the unique option of the excavation high-steep slope 4. Strong ability to control ground deformation 5. Rapid and simple installation 6. Relatively inexpensive	1. Presence of prestress loss 2. Susceptible to corrosion	The Lianziya rock mass Tang et al. (2019) A rock slope in Chongqing Wu et al. (2018a) Fengtian hydropower station Qin et al. (2007) An expressway cutting slope located in Zhengzhou city of China Wu et al. (2005) Lanzhou Xiaxiyuan Fund Development Building Dong et al. (2010)
The non-prestressed Anchors	Hollow grouted bolt Self-drilling anchor GFRP anchor Yielding anchor CRLD bolt	1. Most commonly used anchor bolts 2. Relatively excellent corrosion resistance 3. Can be used for permanent reinforcement engineering 4. Crucial support technology for joint rock slope 1. Provides both high load capacity and a certain amount of yield energy absorption	1. Passive supporting technology 2. Relatively weak ability to control ground deformation 3. Relatively expensive 4. Necessary to wait for the setting time if using cement 1. Relatively expensive 2. Susceptible to corrosion 3. Not widely used	K60 + 535-K60 + 585 of road S246 in Xin'an county, Luoyang City, Henan ProvinceWang et al. (2008) One Western modem artificially accumulated slag platform Chen et al. (2014) A field project in Hong Kong (Xu and Yin, 2016) The left bank of Jinping Hydropower Station Zhu et al. (2017) Tonglushan ancient copper mine relics Tao et al. (2018)

et al., 2018; Tao et al., 2018; Mak et al., 2019; Tang et al., 2019; Gao et al., 2021).

3 ANCHOR BOLT DEVELOPMENT IN THE PAST THREE DECADES

Before 2000s, anchor support technology was mostly exploited for the reinforcement and prevention of high-steep rock slopes of hydropower stations, open-pit mines, and highways (Zhang, 1995; Han et al., 1996; Li and Zhao, 1997). With the vigorous construction of the Three Gorges Project, the complex geological conditions in the Three Gorges area have given rise to numerous research needs and significant research on slope reinforcement, including excavation and reinforcement design, planar finite element calculations, stability analysis, field tests, and the establishment of the constitutive model for the high-steep rock slopes of the Three Gorges locks (Zhu and Zhang, 1996; Xu and Yang, 1997; Zhang and Zhu, 1997; Gao and Yang, 1998; Xu, 2000; Zhu and Cheng, 2000). Between 2000 and 2012, the research hotspots were the development of new anchor bolts and the study of the mechanical effects of anchorage. The development of load-dispersed anchors (cables), repeated grouting techniques, hollow-grouted anchors, and under-reamed anchors has occurred rapidly (Cheng, 2005). For the study of mechanical properties and the support effect of anchorage, numerical simulation and mechanical tests are mainly used (Zhang and Chen, 2003; Lin et al., 2005; Li et al., 2012). Inheriting previous developments, more complex problems were discovered during the project since 2012. When excavating slopes in areas of high *in situ* stress or extremely soft rock, ordinary anchors (cables) can no longer meet the needs of deformation in these areas, and the development of yield-absorbing anchors has become a significant research topic (Zhu et al., 2017).

In **Table 2**, we summarize the anchor bolts adopted by Chinese engineers in dealing with different slopes and the performances of practical engineering.

4 RESEARCH METHODS OF ANCHOR BOLTS

In terms of a performance study of anchor bolts, mechanical test, numerical simulation, and non-destructive test are three common research methods. Conventional mechanical tests generally include tensile test (Chang et al., 2017), pull-out test (Teymen and Kılıç, 2018; Xu et al., 2018), shear test (Li et al., 2019), shaking table test (Su et al., 2021), the drop hammer test, and the Split Hopkinson Pressure Bar test (Wu et al., 2019; Wang et al., 2022). Those tests include comparatively accurate mechanical properties such as tensile strength, elongation, and shear strength. However, the conventional mechanical tests are mostly laboratory tests, which are difficult to be applied in practical engineering situations and relatively expensive (Li et al., 2019).

The emergence of numerical simulation technology was welcomed by scholars due to its high precision, economy, and repeatability. By setting different working conditions, numerical simulation technology can calculate the parameters of anchor bolts in various working conditions (Chen and Li, 2022). Numerical analysis methods can be divided into continuous analysis methods and discontinuous analysis methods.

TABLE 2 | Summary of the anchor bolts used as support for different kinds of slopes and their performance (Wang et al., 2008; Tang et al., 2012; Zhou et al., 2013; Nie et al., 2014a; Tao et al., 2015; Zhu et al., 2017; Bai et al., 2018; Xiang et al., 2022).

Anchor bolt	Slope type		Environment			Performances			
	Soil slope	Rock slope	Corrosion	Freezing–thawing cycle	High in-situ stress slope	Charge	Deformation	Environmentally friendly	Combined with monitor
Prestressed anchor bolt/cable	△	○	□	□	△	L	L	L	N
Compression dispersion anchor	—	○	□	×	△	H	L	L	N
Frame support anchor	○	△	□	○	—	H	L	L	N
Hollow grouted bolt	○	○	○	□	—	L	L	L	N
Fully grouted bolt	○	○	○	□	△	L	L	L	Y
GFRP anchor	○	○	○	—	—	L	L	H	Y
Yielding anchor	△	○	□	○	○	H	H	L	N
CRLD bolt	△	○	□	○	○	H	H	L	Y

○ *suitable,* △ *useful,* — *to be investigated,* × *unsuitable.*
H, high; L, low; Y, yes; N, no.

Apparently, the finite element method (FEM) is the most preferred numerical method because of its applicability for solving mechanical problems (Soparat and Nanakorn, 2008). Advances in computer arithmetic have driven advances in discontinuous analysis methods (Yokota et al., 2019b). The discrete element method (DEM) can model jointed rock masses by using UDEC (Gao and Kang, 2016). The discontinuous deformation analysis (DDA) can efficiently simulate the crack formation and evolution (Yokota et al., 2019a).

It is difficult to obtain the installation defects and progressive damage to the installed anchor bolts. The installation defects and progressive damage are significant factors. Unlike the first two research methods, a non-destructive test (NDT) can carry out a quality inspection and assessment of the installed anchor bolts. For instance, in the aspect of bonding quality inspection of fully grouted bolts, vibration methods and wave propagation methods are two commonly used methods (Zima and Rucka, 2017; Bačić et al., 2020). Liu L. et al. (2022) proposed a new stress wave reflection NDT method using a two-sensor acquisition. Liu L. L. et al. (2022) presented an effective means of detecting internal defects based on an ultrasonic waveguide and an improved empirical mode decomposition method. Nevertheless, it is difficult to obtain the mechanical parameters of the installed anchors, such as the actual bearing capacity, which needs to be addressed.

5 DISCUSSION AND FUTURE PERSPECTIVES

5.1 Energy-Absorbing Anchor Bolts

The ideal anchor provides both high load capacity and a certain amount of yield energy absorption (Chunlin Li, 2010). The earliest concept of energy-absorbing anchors was introduced in South Africa in the late 20th century and was applied in South African coal mines (Li et al., 2014). The currently available energy-absorbing anchors mainly achieve the purpose of absorbing energy through the yielding structure (Wu X. et al., 2018), such as the Garford bolt (Varden, 2009), Roofex (Charette and Plouffe, 2007), the CRLD bolt (He et al., 2014), etc. However, there are relatively few innovative studies on rod material. The team of He successfully developed a new type of anchor steel rebar with a negative Poisson's ratio effect (Gu et al., 2022). The new-type NPR anchor steel can balance the contradiction between high strength and high ductility of metal materials and realize the large deformation and energy-absorbing characteristics of anchor bolts from the material nature (Tao et al., 2022). According to the recent results of the drop hammer test and Split Hopkinson Pressure Bar Test, the elongation and energy-absorbing capacity of the constant resistance energy-absorbing material are superior to those of the common materials (Wang et al., 2022). The successful development of NPR anchor steel proves that the effect of ideal anchor bolts can also be achieved through the innovation of rod materials and that the combination of a reasonable yield-absorbing structure can maximize its yield-absorbing effect.

5.2 Nonmetal Anchor Bolts

Metal anchors are often corroded by water seeping through cracks in the rock or by solutions containing chloride and sulfate ions (Gamboa and Atrens, 2003; Villalba and Atrens, 2009; Karalis et al., 2012; Kang et al., 2013). Investigations of anchor bolt failures have shown that the life of anchor bolts is principally controlled by corrosion, which influences the exposed free length (Jiang et al., 2014), while nonmetallic anchors based on fiber-reinforced polymer bars can overcome this drawback (Xu and Yin, 2016). In recent years, there have been many studies on the performance of glass fiber–reinforced polymer (GFRP) materials (Dutta and Hui, 2000; Yeung et al., 2007; Yu et al., 2007; Keller et al., 2008; Li C. et al., 2017). It is believed that GFRP materials and high-pressure grouting technology are sufficient to substitute steel reinforcement (Yeung et al., 2007). After glass fiber–reinforced polymer (GFRP), carbon fiber–reinforced polymer (CFRP), and aramid fiber composite–reinforced polymer (AFRP) are known,

basalt fiber composite–reinforced polymer (BFRP) has arisen the interest of scholars (Lu and Xian, 2018; Wang X. et al., 2019; Bai et al., 2020). Compared to carbon fiber, basalt fiber is cheaper and simpler to manufacture (Larrinaga et al., 2014); compared to glass fiber, the mechanical performance is similar or even better (Fiore et al., 2015). Basalt fiber has excellent modulus, high strength and temperature resistance, non-toxic, natural, stable, easy to process, eco-friendly, and relatively cheap (Lopresto et al., 2011; Wei et al., 2011; Borhan, 2012). Compared with ordinary steel anchor bolts in laboratory shear test, the peak shear strength of the BFRP anchor rod is relatively low, while the residual shear strength and the ductility are relatively high, and the anchoring effect of the jointed rock body anchored by BFRP anchors is affected by the anchoring angle, and the shear strength is relatively higher when the anchoring angle is less than 60° (Zhang et al., 2022). The BFRP rebar was mostly exploited in reinforced concrete structures, and nowadays, it is increasingly applied in slope reinforcement engineering due to its excellent performance and progress of the process (Wu et al., 2021). Combined with the practical engineering needs, it is of extraordinary significance to design and manufacture new anchor bolts with mature properties, which is a research hot spot (Alraie et al., 2021).

5.3 Ecological Slope Protection

Research on ecological slope protection technology has been a significant research topic, which can ensure the required strength and is more eco-friendly. Ecological slope protection and carbon reduction can be achieved by reducing the use of steel and integrating ecology and anchoring technologies. FRP material has great potential to replace steel and is environmentally friendly. FRP anchors have high tensile strength and strong corrosion resistance but insufficient shear strength (Guo et al., 2018). How to improve the shear strength of FRP anchors is a critical issue. The plant root system not only retains soil and water but also has been proven to be effective in strengthening slopes (Lin et al., 2010; Ma'ruf, 2012; Cao et al., 2018). Integrating anchoring technology with the ecological environment is another direction to achieving low-carbon anchoring. This could attain the balance between ecological performance and mechanical performance (Su et al., 2021). Su et al. (2018) proposed new style of ecological slope protection using "Anchor + Hinged Block", which realized a better reinforcement and seismic performance. In addition, as a new-type material that has both biocompatibility and engineering function, it has not been studied; for instance, the feasibility of vegetation growing recycled concrete for grouting (Wang F. et al., 2019). In the context of global efforts to achieve carbon neutrality, these low-carbon and eco-friendly slope anchoring technologies will certainly become a vital part of slope support technology in the future.

6 CONCLUSION

In China, the anchor support technology for slope engineering is pretty mature. A reasonable anchoring scheme according to the actual slope conditions needs to be selected in order to maximize the support capacity of anchors and ensure engineering quality and safety.

1) In this mini-review, we introduce geotechnical anchors for slope engineering and their research methods, briefly describe the history of anchor development, and summarize the anchor bolts used to support different kinds of the slopes and their performances. This serves as a reference for engineers to quickly select applicable anchor bolts according to the actual engineering conditions. Meanwhile, we highlight the potential future perspectives for developments in the field.
2) In terms of improving the anchor support capacity, there are more improvements to the anchor structure but less development and use of new materials. FRP material has great potential to replace steel and is environmentally friendly; however, shear strength is insufficient. Finally, it is difficult to obtain the mechanical property parameters of the installed anchors by the existing research methods.
3) Nowadays, engineering geological conditions are becoming more complex and the ecological environment is more fragile, such as Sichuan—Tibet railway. The improvement of anchoring technology should be based on the actual engineering situation. In the context of global efforts to achieve carbon neutrality, scholars should strengthen the research on the integration of ecological slope protection and anchor support technology, which will contribute to the goal of carbon neutrality.

AUTHOR CONTRIBUTIONS

YD, HL, and LH were responsible for the work concept or design; HL were responsible for literature collection; YD and HL were responsible for drafting the manuscript; YD, HL, and SDC were responsible for making important revisions to the manuscript; YD and HL were responsible for approving the final version of the manuscript for publication.

FUNDING

The National Key Research and Development Program of China (2018YFE0101100), the National Natural Science Foundation of China (41702371), USTB-NTUT Joint Research Program (TW2019011), and State Key Laboratory for GeoMechanics and Deep Underground Engineering, China University of Mining and Technology, Beijing (SKLGDUEK2130).

ACKNOWLEDGEMENTS

This work was supported by the National Key Research and Development Project of China (2018YFE0101100), the National Natural Science Foundation of China (41702371), USTB-NTUT Joint Research Program (TW2019011), and State Key Laboratory for GeoMechanics and Deep Underground Engineering, China University of Mining and Technology, Beijing (SKLGDUEK2130).

REFERENCES

Alraie, A., Sahoo, D. R., and Matsagar, V. (2021). Development of Optimal Anchor for Basalt Fiber-Reinforced Polymer Rods. *J. Compos. Constr.* 25 (3), 04021011. doi:10.1061/(ASCE)CC.1943-5614.0001119

An, C. L., Liang, Y., Wang, L. Q., Deng, S., Sun, Z. H., Fan, B. Q., et al. (2020). Three-dimensional Optimization Design for the Direction Angle of Anchor Cable Reinforcement in Wedge Rock Slope. *Rock Soil Mech.* 41 (8), 2765–2772. doi:10.16285/j.rsm.2019.1710

Bačić, M., Kovačević, M. S., and Jurić Kaćunić, D. (2020). Non-Destructive Evaluation of Rock Bolt Grouting Quality by Analysis of its Natural Frequencies. *Materials* 13 (2), 282. doi:10.3390/ma13020282

Bai, X. Y., Jing, D. S., Wang, H. G., Yan, N., Wang, Y. H., and Zhang, M. Y. (2020). Research Status of Basalt Fiber-Reinforced Polymer Anchor in Slope Support Engineering. *Sci. Technol. Eng.* 20 (31), 12702–12710. doi:10.3969/j.issn.1671-1815.2020.31.004

Bai, X. Y., Zhang, M. Y., Kuang, Z., Wang, Y. H., Yan, N., and Zhu, L. (2018). Application of Fiber Grating Sensing Technology in Pull-Out Test on Glass Fiber Reinforced Polymer Anti-floating Anchor. *Rock Soil Mech.* 39 (10), 3891–3899. doi:10.16285/j.rsm.2017.2395

Benmokrane, B., Chennouf, A., and Mitri, H. S. (1995). Laboratory Evaluation of Cement-Based Grouts and Grouted Rock Anchors. *Int. J. Rock Mech. Min. Sci. Geomechanics Abstr.* 32 (7), 633–642. doi:10.1016/0148-9062(95)00021-8

Blanco Martín, L., Tijani, M., Hadj-Hassen, F., and Noiret, A. (2013). Assessment of the Bolt-Grout Interface Behaviour of Fully Grouted Rockbolts from Laboratory Experiments under Axial Loads. *Int. J. Rock Mech. Min. Sci.* 63, 50–61. doi:10.1016/j.ijrmms.2013.06.007

Borhan, T. M. (2012). Properties of Glass Concrete Reinforced with Short Basalt Fibre. *Mater. Des.* 42, 265–271. doi:10.1016/j.matdes.2012.05.062

Cao, W., Omran, B. A., Lei, Y., Zhao, X., Yang, X., Chen, Q., et al. (2018). Studying Early Stage Slope Protection Effects of Vegetation Communities for Xinnan Highway in China. *Ecol. Eng.* 110, 87–98. doi:10.1016/j.ecoleng.2017.08.033

Chang, X., Wang, G., Liang, Z., Yang, J., and Tang, C. (2017). Study on Grout Cracking and Interface Debonding of Rockbolt Grouted System. *Constr. Build. Mater.* 135, 665–673. doi:10.1016/j.conbuildmat.2017.01.031

Charette, F., and Plouffe, M. (2007). "Roofex® –Results of Laboratory Testing of a New Concept of Yieldable Tendon," in *Deep Mining 2007: Fourth International Seminar on Deep and High Stress Mining*. Editor Y. Potvin (Perth: Australian Centre for Geomechanics).

Chen, J., and Li, D. (2022). Numerical Simulation of Fully Encapsulated Rock Bolts with a Tri-linear Constitutive Relation. *Tunn. Undergr. Space Technol.* 120, 104265. doi:10.1016/j.tust.2021.104265

Chen, T. L., Zhou, J., Wang, A. M., and Li, H. (2014). "Application of Self-Drilling Anchor on Coal Gangue Slope Treatment," in *Advances in Civil and Industrial Engineering IV* (Haikou, China: Trans Tech Publications). doi:10.4028/www.scientific.net/amm.580-583.935

Chen, Y. J., Yin, J., and Hu, Y. F. (2013). Research on Prestress Quantitative Loss Law of Soft Rock Slope Anchor Cable. *Chin. J. Rock Mech. Eng.* 32 (8), 1685–1691. doi:10.3969/j.issn.1000-6915.2013.08.022

Cheng, L. K. (2001). Present Status and Development of Ground Anchorages. *Chin. Civ. Eng. J.* 03, 7–12+34. doi:10.3321/j.issn:1000-131X.2001.03.002

Cheng, L. K. (2005). Research and New Progress in Ground Anchorage. *Chin. J. Rock Mech. Eng.* 21, 5–13. doi:10.3321/j.issn:1000-6915.2005.21.001

Cheng, L. K., Zhang, P. W., and Wang, F. (2015). Several Mechanical Concepts for Anchored Structures in Rock and Soil. *Chin. J. Rock Mech. Eng.* 34 (04), 668–682. doi:10.13722/j.cnki.jrme.2015.04.003

Chunlin Li, C. (2010). A New Energy-Absorbing Bolt for Rock Support in High Stress Rock Masses. *Int. J. Rock Mech. Min. Sci.* 47 (3), 396–404. doi:10.1016/j.ijrmms.2010.01.005

Deng, D. P., Li, L., and Zhao, L. H. (2021). Stability Analysis of Slopes Reinforced with Anchor Cables and Optimal Design of Anchor Cable Parameters. *Eur. J. Environ. Civ. Eng.* 25 (13), 2425–2440. doi:10.1080/19648189.2019.1631216

Ding, W., Wang, Z., Huang, X., Chen, L., and Zheng, Y. (2022). Influence of Corrosion on Anchoring Bond Behavior of Jointed Rock Mass. *KSCE J. Civ. Eng.* 26 (4), 1914–1928. doi:10.1007/s12205-022-0324-x

Dong, J., Zhu, Y., Zhou, Y., and Ma, W. (2010). Dynamic Calculation Model and Seismic Response for Frame Supporting Structure with Prestressed Anchors. *Sci. China Technol. Sci.* 53 (7), 1957–1966. doi:10.1007/s11431-010-3241-z

Dutta, P. K., and Hui, D. (2000). Creep Rupture of a GFRP Composite at Elevated Temperatures. *Comput. Struct.* 76 (1), 153–161. doi:10.1016/S0045-7949(99)00176-5

Elices, M., Valiente, A., Caballero, L., Iordachescu, M., Fullea, J., Sánchez-Montero, J., et al. (2012). Failure Analysis of Prestressed Anchor Bars. *Eng. Fail. Anal.* 24, 57–66. doi:10.1016/j.engfailanal.2012.03.007

Fan, X., Xu, Q., Scaringi, G., Dai, L., Li, W., Dong, X., et al. (2017). Failure Mechanism and Kinematics of the Deadly June 24th 2017 Xinmo Landslide, Maoxian, Sichuan, China. *Landslides* 14 (6), 2129–2146. doi:10.1007/s10346-017-0907-7

Feng, X., Zhang, N., Li, G., and Guo, G. (2017). Pullout Test on Fully Grouted Bolt Sheathed by Different Length of Segmented Steel Tubes. *Shock Vib.* 2017, 1–16. doi:10.1155/2017/4304190

Fiore, V., Scalici, T., Di Bella, G., and Valenza, A. (2015). A Review on Basalt Fibre and its Composites. *Compos. Part B Eng.* 74, 74–94. doi:10.1016/j.compositesb.2014.12.034

Freeman, T. J. (1978). The Behaviour of Fully-Bonded Rock Bolts in the Kielder Experimental Tunnel. *Tunn. Tunn. Int.* 10 (5), 37–40.

Gamboa, E., and Atrens, A. (2003). Environmental Influence on the Stress Corrosion Cracking of Rock Bolts. *Eng. Fail. Anal.* 10 (5), 521–558. doi:10.1016/S1350-6307(03)00036-0

Gao, F. Q., and Kang, H. P. (2016). Effects of Pre-existing Discontinuities on the Residual Strength of Rock Mass - Insight from a Discrete Element Method Simulation. *J. Struct. Geol.* 85, 40–50. doi:10.1016/j.jsg.2016.02.010

Gao, F., and Yang, Q. G. (1998). Field Test of Rock Anchoring Technique for TGP. *Yangtze River* 1, 17–18+21+47. doi:10.16232/j.cnki.1001-4179.1998.01.006

Gao, X., Tian, W., Li, J., Qi, H., and Zhang, Z. (2021). Research on Prediction Model of Prestress Loss of Anchor Cable in Soil-Rock Dual-Structure Slope. *Adv. Mater. Sci. Eng.* 2021, 1–10. doi:10.1155/2021/4986245

Grasselli, G. (2005). 3D Behaviour of Bolted Rock Joints: Experimental and Numerical Study. *Int. J. Rock Mech. Min. Sci.* 42 (1), 13–24. doi:10.1016/j.ijrmms.2004.06.003

Gu, J. B., Wang, J. Y., and Lu, W. (2022). An Experimental Assessment of Ultra High Performance Concrete Beam Reinforced with Negative Poisson's Ratio (NPR) Steel Rebar. *Constr. Build. Mater.* 327, 127042. doi:10.1016/j.conbuildmat.2022.127042

Guo, X., Riad, A., Chennareddy, R., and Reda Taha, M. M. (2018). Seismic Resistance of GFRP Bolted Joints with Carbon Nanotubes. *J. Eng. Mech.* 144 (11), 04018106. doi:10.1061/(ASCE)EM.1943-7889.0001528

Guo, X. X., Wang, B., Ma, Z. W., and Wang, Z. Y. (2019). Testing Mechanical Properties of Rock Bolt under Different Supports Using Fiber Bragg Grating Technology. *Sensors* 19 (19), 4098. doi:10.3390/s19194098

Han, H. Z., Wen, J. Q., and Wang, X. N. (1996). Collapse Mechanism and Protective Measures of Expansive Rock Slope along Nankun Line. *Chin. J. Rock Mech. Eng.* 2, 88–93.

He, M., Gong, W., Wang, J., Qi, P., Tao, Z., Du, S., et al. (2014). Development of a Novel Energy-Absorbing Bolt with Extraordinarily Large Elongation and Constant Resistance. *Int. J. Rock Mech. Min. Sci.* 67, 29–42. doi:10.1016/j.ijrmms.2014.01.007

Ho, D. A., Bost, M., and Rajot, J. P. (2019). Numerical Study of the Bolt-Grout Interface for Fully Grouted Rockbolt under Different Confining Conditions. *Int. J. Rock Mech. Min. Sci.* 119, 168–179. doi:10.1016/j.ijrmms.2019.04.017

Hryciw, R. D. (1991). Anchor Design for Slope Stabilization by Surface Loading. *J. Geotechnical Eng.* 117117 (8), 12608–21274. doi:10.1061/(ASCE)0733-941010.1061/(asce)0733-9410(1991)117:8(1260)

Hyett, A. J., Bawden, W. F., and Reichert, R. D. (1992). The Effect of Rock Mass Confinement on the Bond Strength of Fully Grouted Cable Bolts. *Int. J. Rock Mech. Min. Sci. Geomechanics Abstr.* 29 (5), 503–524. doi:10.1016/0148-9062(92)92634-O

Hyett, A. J., Moosavi, M., and Bawden, W. F. (1996). Load Distribution along Fully Grouted Bolts, with Emphasis on Cable Bolt Reinforcement. *Int. J. Numer. Anal. Methods Geomech.* 20 (7), 517–544. doi:10.1002/(sici)1096-9853(199607)20:7<517::aid-nag833>3.0.co;2-l

Jiang, S. H., Li, D. Q., Zhang, L. M., and Zhou, C. B. (2014). Time-dependent System Reliability of Anchored Rock Slopes Considering Rock Bolt Corrosion Effect. *Eng. Geol.* 175, 1–8. doi:10.1016/j.enggeo.2014.03.011

Kaiser, P. K., Yazici, S., and Nosé, J. (1992). Effect of Stress Change on the Bond Strength of Fully Grouted Cables. *Int. J. Rock Mech. Min. Sci. Geomechanics Abstr.* 29 (3), 293–306. doi:10.1016/0148-9062(92)93662-4

Kang, H. P. (2016). Sixty Years Development and Prospects of Rock Bolting Technology for Underground Coal Mine Roadway in China. *J. China Univ. Min. Technol.* 45 (06), 1071–1081. doi:10.13247/j.cnki.jcumt.000583

Kang, H., Wu, Y., Gao, F., Lin, J., and Jiang, P. (2013). Fracture Characteristics in Rock Bolts in Underground Coal Mine Roadways. *Int. J. Rock Mech. Min. Sci.* 62, 105–112. doi:10.1016/j.ijrmms.2013.04.006

Karalis, D. G., Melanitis, N. E., and Pantelis, D. I. (2012). Failure Analysis of a Rock Anchor Made of Stainless Steel in Marine Environment. *Eng. Fail. Anal.* 19, 123–130. doi:10.1016/j.engfailanal.2011.09.011

Keller, T., Haas, C., and Vallée, T. (2008). Structural Concept, Design, and Experimental Verification of a Glass Fiber-Reinforced Polymer Sandwich Roof Structure. *J. Compos. Constr.* 12 (3), 454–468. doi:10.1061/(ASCE)1090-026810.1061/(asce)1090-0268(2008)12:4(454)

Kılıc, A., Yasar, E., and Celik, A. G. (2002). Effect of Grout Properties on the Pull-Out Load Capacity of Fully Grouted Rock Bolt. *Tunn. Undergr. Space Technol.* 17 (4), 355–362. doi:10.1016/S0886-7798(02)00038-X

Larrinaga, P., Chastre, C., Biscaia, H. C., and San-José, J. T. (2014). Experimental and Numerical Modeling of Basalt Textile Reinforced Mortar Behavior under Uniaxial Tensile Stress. *Mater. Des.* 55, 66–74. doi:10.1016/j.matdes.2013.09.050

Li, C. C., Stjern, G., and Myrvang, A. (2014). A Review on the Performance of Conventional and Energy-Absorbing Rockbolts. *J. Rock Mech. Geotechnical Eng.* 6 (4), 315–327. doi:10.1016/j.jrmge.2013.12.008

Li, C., Gao, D., Wang, Y., and Tang, J. (2017a). Effect of High Temperature on the Bond Performance between Basalt Fibre Reinforced Polymer (BFRP) Bars and Concrete. *Constr. Build. Mater.* 141, 44–51. doi:10.1016/j.conbuildmat.2017.02.125

Li, C., and Stillborg, B. (1999). Analytical Models for Rock Bolts. *Int. J. Rock Mech. Min. Sci.* 36 (8), 1013–1029. doi:10.1016/S1365-1609(99)00064-7

Li, L., Hagan, P. C., Saydam, S., Hebblewhite, B., and Zhang, C. (2019). A Laboratory Study of Shear Behaviour of Rockbolts under Dynamic Loading Based on the Drop Test Using a Double Shear System. *Rock Mech. Rock Eng.* 52 (9), 3413–3429. doi:10.1007/s00603-019-01776-x

Li, X., He, S., and Wu, Y. (2012). Limit Analysis of the Stability of Slopes Reinforced with Anchors. *Int. J. Numer. Anal. Meth. Geomech.* 36 (17), 1898–1908. doi:10.1002/nag.1093

Li, Y., Li, C., Zhang, L., Zhu, W., Li, S., and Liu, J. (2017b). An Experimental Investigation on Mechanical Property and Anchorage Effect of Bolted Jointed Rock Mass. *Geosci. J.* 21 (2), 253–265. doi:10.1007/s12303-016-0043-8

Li, Y., and Liu, C. (2019). Experimental Study on the Shear Behavior of Fully Grouted Bolts. *Constr. Build. Mater.* 223, 1123–1134. doi:10.1016/j.conbuildmat.2019.06.207

Li, Y. T., and Zhao, H. L. (1997). Reinforcement Design of High Rock Slope at Xiaolangdi Project Inlet. *Yellow River* 2, 52–56.

Li, Y., Zhou, H., Zhang, L., Zhu, W., Li, S., and Liu, J. (2016). Experimental and Numerical Investigations on Mechanical Property and Reinforcement Effect of Bolted Jointed Rock Mass. *Constr. Build. Mater.* 126, 843–856. doi:10.1016/j.conbuildmat.2016.09.100

Lin, D. G., Huang, B. S., and Lin, S. H. (2010). 3-D Numerical Investigations into the Shear Strength of the Soil-Root System of Makino Bamboo and its Effect on Slope Stability. *Ecol. Eng.* 36 (8), 992–1006. doi:10.1016/j.ecoleng.2010.04.005

Lin, H., Cao, P., and Zhen, Z. Y. (2005). Simulating Effects of Wholly Grouted Anchor Rods with FLAC3D. *Rock Soil Mech.* 26 (S2), 167–170. doi:10.16285/j.rsm.2005.s2.057

Liu, C., and Li, Y. (2020). Predicting the Shear Resistance Contribution of Passive Fully Grouted Bolts to Jointed Rock. *Int. J. Geomech.* 20 (2), 04019174. doi:10.1061/(ASCE)GM.1943-5622.0001581

Liu, L., Li, S., Jiang, X., and Tao, F. (2022a). A New Two-Sensor Non-destructive Testing Method of Grouted Rock Bolts. *Constr. Build. Mater.* 317, 125919. doi:10.1016/j.conbuildmat.2021.125919

Liu, L. L., Zhu, J., Zhang, S. H., and Sun, H. P. (2022b). Non-destructive Detection of Anchor Defects Using Ultrasonic Guided Wave and ICEEMDAN Method. *Earth Sci. (Wuhan. China)* 1, 17. doi:10.3799/dqkx.2022.102

Liu, Y., Zheng, P., and Wang, P. (2021). Multi-factors Influence of Anchorage Force on Surrounding Rock under Coupling Effect of Creep Rock Mass and Bolt/cable. *Geomatics, Nat. Hazards Risk* 12 (1), 328–346. doi:10.1080/19475705.2021.1872717

Lopresto, V., Leone, C., and De Iorio, I. (2011). Mechanical Characterisation of Basalt Fibre Reinforced Plastic. *Compos. Part B Eng.* 42 (4), 717–723. doi:10.1016/j.compositesb.2011.01.030

Lu, Z., and Xian, G. (2018). Resistance of Basalt Fibers to Elevated Temperatures and Water or Alkaline Solution Immersion. *Polym. Compos.* 39 (7), 2385–2393. doi:10.1002/pc.24220

Luga, E., and Periku, E. (2021). A Pioneer *In-Situ* Investigation on the Bearing Capacity and Failure Causes of Real Scale Fully Grouted Rockbolts. *Constr. Build. Mater.* 310, 124826. doi:10.1016/j.conbuildmat.2021.124826

Mak, M. W. T., Desnerck, P., and Lees, J. M. (2019). Corrosion-induced Cracking and Bond Strength in Reinforced Concrete. *Constr. Build. Mater.* 208, 228–241. doi:10.1016/j.conbuildmat.2019.02.151

Ma'ruf, M. F. (2012). Shear Strength of apus Bamboo Root Reinforced Soil. *Ecol. Eng.* 41, 84–86. doi:10.1016/j.ecoleng.2012.01.003

Nie, W., Zhao, Z. Y., Ning, Y. J., and Guo, W. (2014a). Numerical Studies on Rockbolts Mechanism Using 2D Discontinuous Deformation Analysis. *Tunn. Undergr. Space Technol.* 41, 223–233. doi:10.1016/j.tust.2014.01.001

Nie, W., Zhao, Z. Y., Ning, Y. J., and Sun, J. P. (2014b). Development of Rock Bolt Elements in Two-Dimensional Discontinuous Deformation Analysis. *Rock Mech. Rock Eng.* 47 (6), 2157–2170. doi:10.1007/s00603-013-0525-1

Qin, W. M., Ge, X. R., and Wang, H. (2007). Experimental Study on Sand Consolidated Anchorage Prestressed Bolt and its Applications. *J. Rock Mech. Eng.* 26 (4), 769–774. doi:10.1109/CISE.2010.5676771

Shan, R., Zhang, S., Xiao, S., and Liang, J. (2021). Research on Anchor Cable and C-Shaped Tube Support Method in Deep Layers Roadway, Experimental Study, and Numerical Simulation. *Shock Vib.* 2021, 1–13. doi:10.1155/2021/7537979

Siad, L. (2001). Stability Analysis of Jointed Rock Slopes Reinforced by Passive, Fully Grouted Bolts. *Comput. Geotechnics* 28 (5), 325–347. doi:10.1016/S0266-352X(01)00004-0

Singh, P., and Spearing, A. J. S. (2021). An Improved Analytical Model for the Elastic and Plastic Strain-Hardening Shear Behaviour of Fully Grouted Rockbolts. *Rock Mech. Rock Eng.* 54 (8), 3909–3925. doi:10.1007/s00603-021-02439-6

Soparat, P., and Nanakorn, P. (2008). Analysis of Anchor Bolt Pullout in Concrete by the Element-free Galerkin Method. *Eng. Struct.* 30 (12), 3574–3586. doi:10.1016/j.engstruct.2008.06.004

Su, H., Hang, Y., Song, Y., Mao, K., Wu, D., and Qiu, X. (2018). Seismic Response of Anchor + Hinged Block Ecological Slope by Shaking Table Tests. *Adv. Mater. Sci. Eng.* 2018, 1–13. doi:10.1155/2018/7684831

Su, H., Wu, D., Lu, Y., Peng, X., Wang, X., Chen, W., et al. (2021). Experimental and Numerical Study on Stability Performance of New Ecological Slope Protection Using Bolt-Hinge Anchored Block. *Ecol. Eng.* 172, 106409. doi:10.1016/j.ecoleng.2021.106409

Sun, G., Hu, J., Wang, H., and Li, P. (2021). Experimental Study on the Deformation and Failure Characteristics of Anchor under Graded Loading and Corrosion. *Adv. Mater. Sci. Eng.* 2021, 1–11. doi:10.1155/2021/8701180

Tang, H., Wasowski, J., and Juang, C. H. (2019). Geohazards in the Three Gorges Reservoir Area, China - Lessons Learned from Decades of Research. *Eng. Geol.* 261, 105267. doi:10.1016/j.enggeo.2019.105267

Tang, X. X., Luo, X. Y., Sun, Q., and Kuang, Y. C. (2012). "Test Research on Mechanical Property of GFRP Bolt under Freeze-Thaw Cycle Conditions," in 2012 International Conference on Materials Science and Nanotechnology, November 16, 2012 - November 18, 2012 (Kem: Trans Tech Publications Ltd), 689–694. doi:10.4028/www.scientific.net/kem.531-532.689

Tao, Z. G., Li, H. P., Sun, G. L., Yin, L. J., and Zhang, X. L. (2015). Development of Monitoring and Early Warning System for Landslides Based on Constant Resistance and Large Deformation Anchor Cable and its Application. *Rock Soil Mech.* 36 (10), 3032–3040. doi:10.16285/j.rsm.2015.10.038

Tao, Z. G., Ren, S. L., He, M. C., and Xia, M. (2022). Study on Static Tensile and Bolting Shear Mechanical Properties of Micro-NPR Bolt Steel in Underground Engineering. *J. China Coal Soc.* 1, 14. doi:10.13225/j.cnki.jccs.XR21.1703

Tao, Z., Zhu, C., Zheng, X., and He, M. (2018). Slope Stability Evaluation and Monitoring of Tonglushan Ancient Copper Mine Relics. *Adv. Mech. Eng.* 10 (8), 168781401879170. doi:10.1177/1687814018791707

Teymen, A., and Kılıç, A. (2018). Effect of Grout Strength on the Stress Distribution (Tensile) of Fully-Grouted Rockbolts. *Tunn. Undergr. Space Technol.* 77, 280–287. doi:10.1016/j.tust.2018.04.022

Varden, R. P. (2009). "Implementation of the Garford Dynamic Bolt at Kanowna Belle Mine," in *Controlling Seismic Hazard and Sustainable Development of Deep Mines: 7TH International Symposium On Rockburst and Seismicity in Mines (RASIM7)* (Dalian, China: Rinton Press).

Villalba, E., and Atrens, A. (2009). Hydrogen Embrittlement and Rock Bolt Stress Corrosion Cracking. *Eng. Fail. Anal.* 16 (1), 164–175. doi:10.1016/j.engfailanal.2008.01.004

Wang, F., Sun, C., Ding, X., Kang, T., and Nie, X. (2019a). Experimental Study on the Vegetation Growing Recycled Concrete and Synergistic Effect with Plant Roots. *Materials* 12 (11), 1855. doi:10.3390/ma12111855

Wang, Q., Xu, S., He, M., Jiang, B., Wei, H., and Wang, Y. (2022). Dynamic Mechanical Characteristics and Application of Constant Resistance Energy-Absorbing Supporting Material. *Int. J. Min. Sci. Technol.* 32 (3), 447–458. doi:10.1016/j.ijmst.2022.03.005

Wang, S. W., Jiang, T., Liu, H. D., and Gao, D. Y. (2008). Study on Testing in Reinforced Slope with Hollow Grouted Bolt. *Chin. J. Rock Mech. Eng.* 27 (Suppl. 2), 3963–3967. doi:10.3321/j.issn:1000-6915.2008.z2.096

Wang, X., Zhao, X., and Wu, Z. (2019b). Fatigue Degradation and Life Prediction of Basalt Fiber-Reinforced Polymer Composites after Saltwater Corrosion. *Mater. Des.* 163, 107529. doi:10.1016/j.matdes.2018.12.001

Wang, Y., Sun, X., and Ren, A. (2019c). Investigations of Rock Anchor Corrosion and its Influence Factors by Exhumations in Four Typical Field Sites. *Eng. Fail. Anal.* 101, 357–382. doi:10.1016/j.engfailanal.2019.03.022

Wei, B., Cao, H., and Song, S. (2011). Degradation of Basalt Fibre and Glass Fibre/epoxy Resin Composites in Seawater. *Corros. Sci.* 53 (1), 426–431. doi:10.1016/j.corsci.2010.09.053

Wu, H., Wu, Z., Lei, H., and Lai, T. (2021). Application of BRFP New-type Anchor Cable Material in High Slopes against Earthquakes. *Adv. Civ. Eng.* 2021, 1–19. doi:10.1155/2021/6689718

Wu, Q., Li, X., Weng, L., Li, Q., Zhu, Y., and Luo, R. (2019). Experimental Investigation of the Dynamic Response of Prestressed Rockbolt by Using an SHPB-Based Rockbolt Test System. *Tunn. Undergr. Space Technol.* 93, 103088. doi:10.1016/j.tust.2019.103088

Wu, S. C., Zhang, Y. P., and Gao, Y. T. (2005). Analysis of Cutting Slope Reinforcement in Swelling Rock and Soil. *J. Univ. Sci. Technol. Beijing* 27 (2), 137–141+155. doi:10.13374/j.issn1001-053x.2005.02.035

Wu, S. G., Fu, H. M., and Zhang, Y. Y. (2018a). Study on Anchorage Mechanism and Application of Tension-Compression Dispersive Anchor Cable. *Rock Soil Mech.* 39 (6), 2155–2163. doi:10.16285/j.rsm.2016.1904

Wu, X., Jiang, Y., Guan, Z., and Wang, G. (2018b). Estimating the Support Effect of Energy-Absorbing Rock Bolts Based on the Mechanical Work Transfer Ability. *Int. J. Rock Mech. Min. Sci.* 103, 168–178. doi:10.1016/j.ijrmms.2018.01.041

Xiang, T., Li, Y. X., Gao, X. Y., and Shi, D. M. (2022). Multi-field Coupling Analysis of Frame-Anchor Supporting Slope Displacement in Seasonal Frozen Zone. *J. China Coal Soc.* 1, 11. doi:10.13225/j.cnki.jccs.2020.1681

Xu, C., Li, Z., Wang, S., Wang, S., Fu, L., and Tang, C. (2018). Pullout Performances of Grouted Rockbolt Systems with Bond Defects. *Rock Mech. Rock Eng.* 51 (3), 861–871. doi:10.1007/s00603-017-1373-1

Xu, C., Xu, X., Yao, X., and Dai, F. (2014). Three (Nearly) Complete Inventories of Landslides Triggered by the May 12, 2008 Wenchuan Mw 7.9 Earthquake of China and Their Spatial Distribution Statistical Analysis. *Landslides* 11 (3), 441–461. doi:10.1007/s10346-013-0404-6

Xu, D. S., and Yin, J. H. (2016). Analysis of Excavation Induced Stress Distributions of GFRP Anchors in a Soil Slope Using Distributed Fiber Optic Sensors. *Eng. Geol.* 213, 55–63. doi:10.1016/j.enggeo.2016.08.011

Xu, L. X., and Yang, Q. G. (1997). Study on High Excavated Rock Slope at TGP Shiplocks. *Yangtze River* 10, 29–31+55. doi:10.16232/j.cnki.1001-4179.1997.10.011

Xu, N. F. (2000). Excavation and Reinforcement Design for High Slope of TGP Permanent Shiplock. *Chin. J. Rock Mech. Eng.* 19 (S1), 1071–1076. doi:10.3321/j.issn:1000-6915.2000.z1.055

Yang, G., Zhong, Z., Zhang, Y., and Fu, X. (2015). Optimal Design of Anchor Cables for Slope Reinforcement Based on Stress and Displacement Fields. *J. Rock Mech. Geotechnical Eng.* 7 (4), 411–420. doi:10.1016/j.jrmge.2015.04.004

Yang, W. D., Luo, G. Y., Bo, C. J., Wang, L., Lü, X. X., Wang, Y. N., et al. (2020). Mechanical Properties and Reinforcement Effect of Jointed Rock Mass with Pre-stressed Bolt. *J. Cent. South Univ.* 27 (12), 3513–3530. doi:10.1007/s11771-020-4469-9

Yeung, A. T., Cheng, Y. M., Tham, L. G., Au, A. S., So, S. T., and Choi, Y. K. (2007). Field Evaluation of a Glass-Fiber Soil Reinforcement System. *J. Perform. Constr. Facil.* 21 (1), 26–34. doi:10.1061/(asce)0887-3828(2007)21:1(26)

Yokota, Y., Zhao, Z., Nie, W., Date, K., Iwano, K., and Okada, Y. (2019a). Experimental and Numerical Study on the Interface Behaviour between the Rock Bolt and Bond Material. *Rock Mech. Rock Eng.* 52 (3), 869–879. doi:10.1007/s00603-018-1629-4

Yokota, Y., Zhao, Z., Shang, J., Nie, W., Date, K., Iwano, K., et al. (2019b). Effect of Bolt Configuration on the Interface Behaviour between a Rock Bolt and Bond Material: A Comprehensive DDA Investigation. *Comput. Geotechnics* 105, 116–128. doi:10.1016/j.compgeo.2018.09.017

Yu, B., Till, V., and Thomas, K. (2007). Modeling of Thermo-Physical Properties for FRP Composites under Elevated and High Temperature. *Compos. Sci. Technol.* 67 (15), 3098–3109. doi:10.1016/j.compscitech.2007.04.019

Zhang, B. R. (1995). Study on Strengthening Technique for Toppling Rock Slope. *Chin. Civ. Eng. J.* 5, 70–75.

Zhang, J. L., Xu, W. Y., Xu, F., and Cai, D. W. (2009). Study on Prestress Loss Law of Anchor Cables in Deep Unloading Deformed Ripped Blocks. *Chin. J. Rock Mech. Eng.* 28 (Suppl. 2), 3965–3970. doi:10.3321/j.issn:1000-6915.2009.z2.098

Zhang, S. B., Wang, C. S., Wang, G., Wu, X. Z., Zheng, X., He, P., et al. (2022). Experimental Study on the Shear Behaviors of Bolted Rock Joints Reinforced with BFRP Bars. *Chin. J. Rock Mech. Eng.* 41 (04), 712–724. doi:10.13722/j.cnki.jrme.2021.0894

Zhang, S. P., and Chen, C. (2003). Study on Pull-Out Tests of Pressure Type Anchor in Rock. *J. Chongqing Jianzhu Univ.* 3, 22–25+90. doi:10.3969/j.issn.1674-4764.2003.03.005

Zhang, Y. J., and Zhu, W. S. (1997). Plane Finite Element Calculation of Anchorage Scheme for High Slope of Shiplock of TGP. *Chin. J. Geotech. Eng.* 1, 72–76.

Zhou, D. P., Liu, S. X., and Liu, H. (2013). Some Problems to Be Considered in Design for Compression Dispersion-type Anchor Cables. *Chin. J. Rock Mech. Eng.* 32 (08), 1513–1519. doi:10.3969/j.issn.1000-6915.2013.08.001

Zhu, A. L., Zhang, Y., Dai, M. L., and Xu, J. Q. (2017). Reinforcement Mechanism of Slopes with Yielding Anchor Cables Based on Numerical Simulation of FLAC3D. *Chin. J. Geotech. Eng.* 39 (4), 713–719. doi:10.11779/CJGE201704017

Zhu, W. S., and Cheng, F. (2000). Constitutive Model of Energy Dissipation and its Application to Stability Analysis of Ship-Lock Slope in Three Gorges Project. *Chin. J. Rock Mech. Eng.* 19 (3), 261–264. doi:10.3321/j.issn:1000-6915.2000.03.001

Zhu, W. S., and Zhang, Y. J. (1996). Primary Research on Stability Analysis and Reinforcement Schemes for Jointed Rock Mass of High Slope of Three Gorges Flight Lock. *Chin. J. Rock Mech. Eng.* 4, 2–8.

Zima, B., and Rucka, M. (2017). Non-destructive Inspection of Ground Anchors Using Guided Wave Propagation. *Int. J. Rock Mech. Min. Sci.* 94, 90–102. doi:10.1016/j.ijrmms.2017.03.005

Zong, Y., Han, L., Qu, T., and Yang, S. (2014). Mechanical Properties and Failure Characteristics of Fractured Sandstone with Grouting and Anchorage. *Int. J. Min. Sci. Technol.* 24 (2), 165–170. doi:10.1016/j.ijmst.2014.01.004

Conflict of Interest: The authors declare that the research was conducted in the absence of any commercial or financial relationships that could be construed as a potential conflict of interest.

Publisher's Note: All claims expressed in this article are solely those of the authors and do not necessarily represent those of their affiliated organizations, or those of the publisher, the editors, and the reviewers. Any product that may be evaluated in this article, or claim that may be made by its manufacturer, is not guaranteed or endorsed by the publisher.

Copyright © 2022 Du, Li, Chicas and Huo. This is an open-access article distributed under the terms of the Creative Commons Attribution License (CC BY). The use, distribution or reproduction in other forums is permitted, provided the original author(s) and the copyright owner(s) are credited and that the original publication in this journal is cited, in accordance with accepted academic practice. No use, distribution or reproduction is permitted which does not comply with these terms.

frontiers | Frontiers in Earth Science

REVIEW
published: 06 July 2022
doi: 10.3389/feart.2022.906884

Deformation and Failure Mode Analysis of the Tunnel Structure Based on the Tunnel-Related Landslides Cases

Sun Minglei[1,2,3], *Liang Hongwei*[1], *Zhu Yongquan*[1]*, *Gao Xinqiang*[1,2,3], *Liu Huan*[1] and *Zhu Zhengguo*[1,2]

[1]State Key Laboratory of Mechanical Behavior and System Safety of Traffic Engineering Structures, Shijiazhuang Tiedao University, Shijiazhuang, China, [2]Key Laboratory of Roads and Railway Engineering Safety Control (Shijiazhuang Tiedao University), Ministry of Education, Shijiazhuang, China, [3]Hebei Province Technical Innovation Center of Safe and Effective Mining of Metal Mines, Shijiazhuang, China

When the tunnel passes through the slope area, once the slope stability changes or landslide disasters occur, large additional stress, deformation, or cracking are easily caused in the tunnel, which results in high risk to the tunnel operation. The deformation and failure mode of the tunnel induced by different types of tunnel-related landslides are different. However, there is no systematic classification of tunnel structure deformation and the failure mode in the tunnel-related landslides systems. By investigating the typical cases of tunnel diseases caused by landslide in China, this study analyzes the relationship between the tunnel-related landslide types and tunnel disease characteristics. It also summarizes five typical tunnel deformation failure modes and corresponding deformation characteristics and determines the relationship between tunnel-related landslide types and deformation failure modes. This study can provide a technical support for the identification of landslide types through the tunnel deformation characteristics in practical engineering applications. Finally, it provides a reference for tunnel location selection, the design of tunnel structure, and the treatment of landslide in landslide areas.

Keywords: tunnel, landslide, deformation and failure mode, deformation characteristics, cases

OPEN ACCESS

Edited by:
Yan Du,
University of Science and Technology Beijing, China

Reviewed by:
Ben-Guo He,
Northeastern University, China
Yajun Jiang,
Southwest Jiaotong University, China

***Correspondence:**
Zhu Yongquan
7935526@163.com

Specialty section:
This article was submitted to Geohazards and Georisks, a section of the journal Frontiers in Earth Science

Received: *29 March 2022*
Accepted: *13 June 2022*
Published: *06 July 2022*

Citation:
Minglei S, Hongwei L, Yongquan Z, Xinqiang G, Huan L and Zhengguo Z (2022) Deformation and Failure Mode Analysis of the Tunnel Structure Based on the Tunnel-Related Landslides Cases. Front. Earth Sci. 10:906884. doi: 10.3389/feart.2022.906884

1 INTRODUCTION

Landslide or rock collapse are the main types of geological disasters in slope areas, which often obstructs traffic, destroys the village, or causes casualties. Many researchers have studied the causes, development patterns, and control measures of landslides and rock collapse (Ma and Wu, 2011; Yang et al., 2016; Du et al., 2021). Based on the study on the causal mechanism and early warning of rock collapse disasters, Du et al. (2021) deduced that the quantitative identification and fuzzy evaluation of rock bridges is the key to the early warning and prevention of rock collapse disasters in the future. Based on the latest study and survey results, Du et al. (2020) studied the cause of translational landslides, built a corresponding model, and validated the reliability of the genetic mechanism using case studies. They deduced that increasing the total stress caused by a higher water level is one of the main reasons for translational landslides. A large number of engineering practices proved that the landslide occurs or the ancient landslide is revived due to natural and human factors (Wang et al.,

2020). When the relative position relationship between the tunnel and the landslide is unfavorable, the landslides often cause additional stress and deformation of the tunnel structure in the slope section. In some cases, serious diseases occurred on the structure, such as cracking and falling blocks, which endanger the operation safety. This type of landslides which can bring risk to the tunnel is referred to as tunnel-related landslides. All of them are collectively referred to as the tunnel-related landslides system.

In fact, it is necessary to perform an in-depth study in tunnel diseases in the landslide region. For instance, Ma (2003) and Ma and Wu (2016) developed six geological structure modes of tunnel deformation in a typical slope disease section. They also summarized the characteristics of tunnel deformation under the action of landslide, raise corresponding technical measures for the prevention and control by performing inductive analysis on documents of tunnel deformation, and cracking in the slope disease section using field test methods. In addition, they performed large-scale model test and numerical simulation based on the investigation and study on living examples of tunnel deformation in the slope disease section from 1980s. Zhou et al. (2002) summarized five geological structure models and four characteristics of tunnel deformation in slope disease section, based on the analysis of the characteristics of tunnel deformation and cracking, as well as the relationship between deformation and cracking. Tao, (2003) and Tao and Zhou (2003) demonstrated that the relative position relationship between the tunnel and the sliding surface is the main factor determining the characteristics of tunnel deformation. A total of four geomechanical models were then developed to analyze the interrelation between landslide and tunnel deformation. Moreover, the stress mode of tunnel under different relative position relations was analyzed. Ashtiani et al. (2010) demonstrated that the interaction between the tunnel and side slope is related to the position of the tunnel in the side slope. Based on the Jimei Tunnel in China, which orthogonally traverses a large bedrock landslide, Zhu et al. (2021) inverted the physical parameters of the landslide using a uniform design and a radial basis function neural network model. Consequently, they developed a model for the interaction between the tunnel and landslide. Furthermore, the relationship between the stability of the slope and deformation of tunnel structures was studied. Zhang et al. (2017) focused on the analytical derivation and numerical simulation analysis in order to predict the interaction influences between a landslide and a new tunnel in mountain areas. Zhang et al. (2021) proposed a simplified analytical method to evaluate the deformation of existing tunnels induced by landslides. Wu (2012) and Wu et al. (2012) divided the tunnel–landslide system into parallel, orthogonal, and oblique relations, according to the angle between the main axis of landslide and the tunnel axis. It was then classified into the tunnel inside the landslide body and the tunnel intersected with the sliding surface, based on the relative location between the tunnel and the landslide surface.

Using a field test, model test, and numerical simulation, these studies analyzed the relationship between the slope diseases and characteristics of tunnel deformation and cracking. They also developed the corresponding geological structure models and main characteristics of tunnel deformation. Finally, they demonstrated that the relative position of tunnel and landslide were the main factors determining the deformation and failure characteristics of the tunnel. However, they failed to clearly determine the deformation and failure classifications of tunnel, under the action of landslide. Moreover, they did not determine the corresponding relationship between the landslide types and tunnel deformation modes from the tunnel perspective. In fact, it is expected to determine the direct relationship between the landslide types and characteristics of tunnel deformation and failure using the case investigation of the interaction between landslide and the tunnel. Consequently, the landslide type can be analyzed, or the landslide tunnel interaction mode can be defined according to the characteristics of tunnel deformation or failure. Therefore, a basis for landslide type identification, landslide prediction, and prediction of the tunnel structure changing trend can be provided in specific projects. Moreover, targeted treatment and reinforcement of potential landslide and the tunnel can be implemented, so as to avoid further deterioration of landslide and reduce tunnel diseases. Therefore, studying the relation between tunnel-related landslides type (i.e., type of interaction between tunnels and landslides) and characteristics of tunnel diseases has a theoretical guiding significance and engineering application value.

Consequently, based on a large number of studies, almost 40 typical cases of tunnel diseases caused by landslide are considered, and types of tunnel-related landslides are sorted out. Furthermore, the corresponding landslide characteristics and tunnel diseases are assessed and analyzed. Finally, typical deformation and failure modes of tunnel are summarized.

2 TUNNEL-RELATED LANDSLIDES CLASSIFICATION AND STATISTICS

2.1 Tunnel-Related Landslides Classification

The tunnel-related landslides can be classified according to the time of occurrence. According to the construction stage (landslides occurred during tunnel construction) or the tunnels operation stage, they can be divided into landslides in the project period and landslides in the operation period.

However, the specific classification is based on the spatial location relationship between the landslide and tunnel. The different spatial relationships lead to different impacts on the tunnel such as stress, deformation, and failure characteristics. The relative positions between the tunnel and sliding surface determine the deformation form, stress characteristics, and failure law of the tunnel. In other words, they directly determine the deformation and failure mode of the tunnel. Based on the existing studies, the tunnel-related landslides are divided into three types: parallel, orthogonal, and oblique, according to the plane position (Wu et al., 2012). The parallel system refers to an angle of 0°–20° between the main sliding

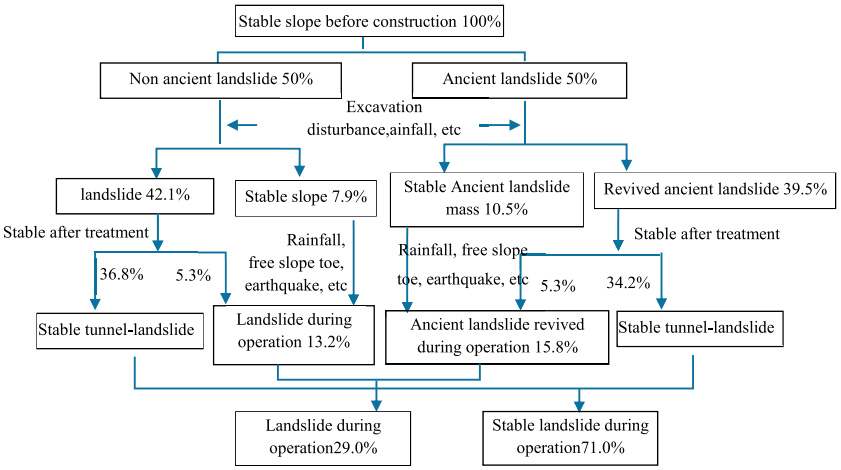

FIGURE 1 | Statistics of tunnel-related landslides cases during the operation period.

direction of the landslide and the axial direction of the tunnel, which are parallel or approximately parallel. According to the crossing position, they are divided into two types: with tunnel located below the sliding surface and passing through the sliding surface. The parallel system is mostly seen in the landslide on the front slope of the tunnel top at the entrance. The orthogonal system refers to an angle of 70°–90° between the main sliding direction of the landslide and the axial direction of the tunnel, that are vertical or approximately vertical. They are divided into three types: with tunnel located below the sliding surface, passing through the sliding surface, and above the sliding surface. The oblique system refers to an angle of 20°–70° between the main sliding direction of the landslide and the axial direction of the tunnel.

2.2 Tunnel-Related Landslides Statistics

2.2.1 According to the Time of Occurrence

Figure 1 presents the statistics of tunnel-related landslides cases during the operation period. In the statistical cases, 50% of the slopes are not ancient landslides and originally stable, while 50% of them are ancient landslides and stable. In addition, 81.6% of landslides occur during the engineering period. Most of them are stable after treatment. However, the landslides occur again during the operation period in 10.6% of them. Moreover, 18.4% of landslides occur during the operation period. However, the slope is stable during the construction period (10.5% of which are revived ancient landslides). The main inducing factors of landslide during the engineering period are the tunnel construction disturbance, rainfall, free face at the foot of the slope, and earthquake. The main factors of landslide during the operation period are the rainfall, free face at the foot of the slope, earthquake, and continuous influence of disturbance during the construction period.

About 29.0% of the tunnel-related landslides cases occur during the operation period. They often lead to additional deformation or damage to the tunnel structure, which brings a great threat to the safe operation of the tunnels. Furthermore, it is very difficult to make early warning, identification, and treatment of landslides.

2.2.2 According to the Relative Position

Figure 2 shows the tunnel-related landslides types according to the relative position and the proportion of different types of case investigation.

The statistical results show that the proportions of the parallel system, orthogonal forms, and oblique forms are 18.4%, 60.5%, and 21.1%, respectively. In addition, the disease tunnels are caused when the tunnel passes through the sliding surface in the 63.1% of all the cases. The landslides in the cases of the Yangpoli, Yuantaizi, Beier, Yaotou No.2, Chaijiapo, Chibanggou, Tuoping, Hongtupo, Pingzhong No. 2, and Sunjiaya tunnels, accounting for 26.3% of the total number of cases, are potential landslides in the creep stage. However, they also lead to tunnel diseases.

3 INVESTIGATION ON LANDSLIDE TYPES AND TUNNEL DISEASE CHARACTERISTICS

Based on the investigation and induction of typical engineering applications, the causes, characteristics, and typical engineering cases of tunnel failure are analyzed and summarized according to the different relative position relationships of tunnel landslide systems (cf. **Table. 1**).

3.1 Parallel System

3.1.1 With Tunnel Located Below the Sliding Surface

In the Guojiashan Tunnel (Wu et al., 2012) of Wudu–Guanzigou Expressway, the overlying strata of the tunnel are loose accumulation, phyllite, and metamorphic slate. The sliding surface of the landslide is located at the contact surface between the accumulation and bedrock, while the sliding body has a thickness less than 60 m. The tunnel diseases are mainly the

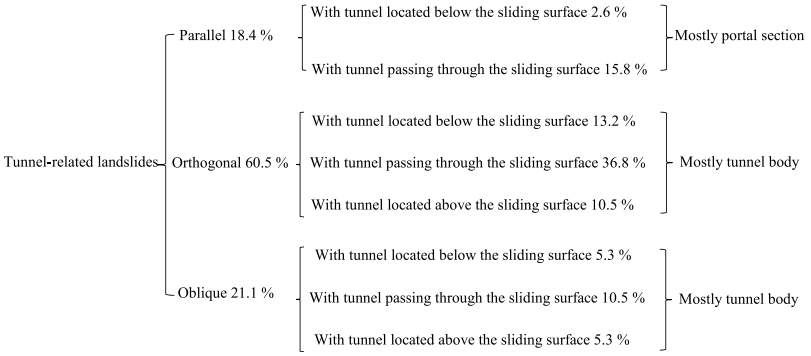

FIGURE 2 | Statistics of the tunnel-related landslides types.

TABLE 1 | Types of tunnel-related landslides and tunnel failure characteristics.

Type		Tunnel failure characteristics	Cause of damage	Typical project
Parallel	With a tunnel located below the sliding surface	Circumferential cracking of vault	Longitudinal traction and extrusion	Guojiashan Tunnel (one tunnel in total)
	With a tunnel passing through the sliding surface	Circumferential cracking of vault and transverse shear	Longitudinal extrusion and shear	Yangpoli Tunnel, Yuantaizi Tunnel, a tunnel of Xiangli Expressway, Yuyuan Tunnel, Beichenting Tunnel, etc (six tunnels in total)
Orthogonal	With a tunnel located below the sliding surface	Longitudinal cracking under small bias	Transverse traction and extrusion	Baoziliang Tunnel, Gongqingtuan Jialingjiang Tunnel, Beier Tunnel, Yaotou No.2 Tunnel, etc (five tunnels in total)
	With a tunnel passing through the sliding surface	Longitudinal cracking and longitudinal shearing under large bias	Transverse extrusion and shear	Chaijiapo Tunnel, Liangxin Tunnel, Nanping Tunnel, Maotouma No.1 Tunnel, etc (14 tunnels in total)
	With a tunnel located above the sliding surface	Longitudinal crack and transverse shear of sliding extrusion	Transverse ship	Lingchang Tunnel, Dongronghe No.1 Tunnel, Sunjiagou Tunnel, and Goumowan Tunnel (four tunnels in total)
Oblique	With a tunnel located below the sliding surface	Orthogonal and parallel	Skew lateral traction and extrusion	Luoping Tunnel and Wenling Tunnel (two tunnels in total)
	With a tunnel passing through the sliding surface	Orthogonal and parallel	Oblique transverse extrusion and shear	Hongtupo Tunnel, Nanping No.2 Tunnel, K12+813 Tunnel, and Qingshashan Tunnel (four tunnels in total)
	With a tunnel located above the sliding surface	Orthogonal and parallel	Skew transverse ship	Fenjieiang Tunnel and Sunjiaya Tunnel (two tunnels in total)

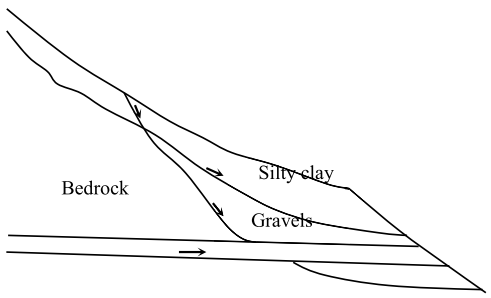

FIGURE 3 | Location relationship between the right entrance of Yuantaizi tunnel and the landslide.

crushing cracking of the arch crown, while the abutment dislocation occurs in serious cases. In particular, the crack width of the portal section is large and elongated. The closer it is to the entrance, the greater the deformation.

3.1.2 With Tunnel Passing Through the Sliding Surface

The typical cases include the Yangpoli Tunnel of Wudu–Guanzigou Expressway, Yuantaizi Tunnel of Wudu–Guanzigou Expressway, tunnel-landslide of Xianggelila–Lijiang Expressway, Yuyuan Tunnel and Beichenting Tunnel of Jingdezhen–Yingtan Expressway, and Lishiguan Tunnel of Shiyan–Manchuan Expressway. The slope stratum at the exit of the right line of the Yuantaizi Tunnel (Wang et al., 2012; Pai et al., 2018; Zhao, 2019) is mainly composed of gravelly soil. The shallow surface layer is silty clay having a thickness of almost 6 m. The tunnel excavation disturbance leads to the creep deformation of the slope. In addition, the sliding direction is coherent with the line direction, and the sliding surface passes through the tunnel 41 m away from the tunnel exit. The location relationship between the right entrance of the tunnel and the landslide is shown in **Figure 3**.

It can be seen that near the sliding surface, due to the sliding shear action of the landslide thrust, the tunnel arch is tensioned, with circumferential shear cracks and longitudinal tension cracks,

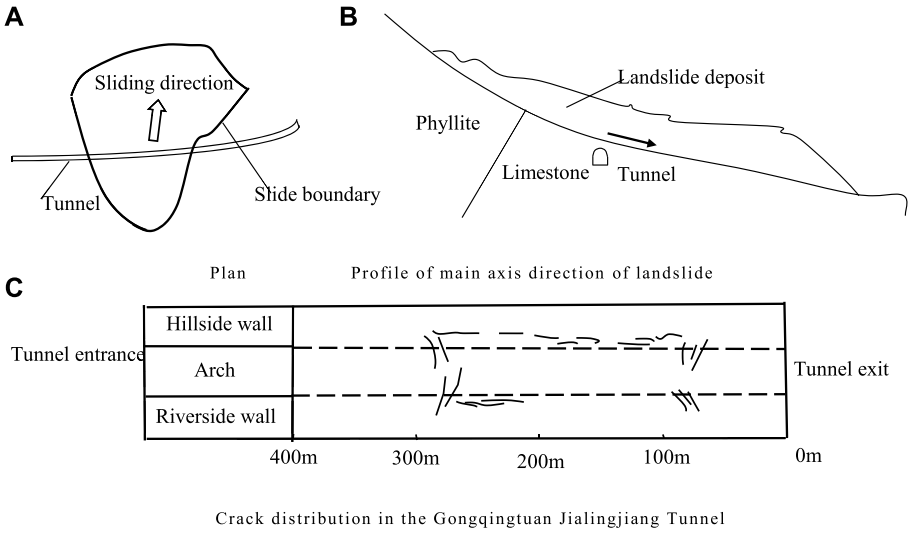

FIGURE 4 | Gongqingtuan Jialingjiang tunnel and the Nanshan landslide system.

serious vault subsidence, arch concrete cracking, and falling blocks.

3.2 Orthogonal System

3.2.1 With Tunnel Located Below the Sliding Surface

The typical cases include the Baoziliang Tunnel of Baoji–Zhongwei Railway, Beier Tunnel and Yaotou No.2 Tunnel of Mengzi–Xinjie Highway, New Mingyuexia Tunnel of Baoji–Chengdu Railway, and the Jialingjiang Tunnel of Gongqingtuan line. The maximum buried depth of the Gongqingtuan Jialingjiang Tunnel (Lu 2012) is almost 60 m. It passes through the middle of Nanshan ancient landslide, whose terrain is steep at the top and gentle at the bottom. The slope has a length of 300 m and a width of 250 m, while the average thickness of the accumulation layer is 25 m. The sliding body is silty clay mixed with block stone and gravel, and the sliding surface (belt) is the contact surface between the accumulation layer and limestone. The landslide is originally stable but resurrected under the joint action of local continuous rainfall and human factors. The positional relationship between the tunnel and Nanshan landslide is illustrated in **Figures 4A,B**.

Longitudinal and diagonal cracks appear in the tunnel. However, circumferential cracks do not exist. The cracks start at 80 m near the entrance and end at 200 m away from the exit, while the starting position coincides with the landslide boundary. At the landslide boundary, diagonal cracks (almost 45° from the longitudinal axis of the tunnel) appear in the arch foot and sidewall of the tunnel, and water seepage occurs. Longitudinal cracks appear at the foot of the arch and the sidewall of the tunnel under the sliding mass. The crack width is 5–20 mm, while the maximum length of a single crack exceeds 10 m. The cracks distribution is shown in **Figure 4C**.

3.2.2 With Tunnel Located Passing Through the Sliding Surface

The typical cases include the Nanping Tunnel of Datong–Zhungeer Railway, Maotouma 1# Tunnel of Chengdu–Kunming Railway, Bozicun No.1 Tunnel of Nanning–Kunming Railway, Chahe Tunnel of Kunming–Dongchuan Railway, Chuanzhusi Tunnel of G213 Line of National Highway, Liupo No.1 Tunnel of a Highway, Dayuan No.1 Tunnel of Lechuan–Guangzhou Expressway, Chaijiapo Tunnel of Xiangyang–Chongqing Railway, Liangxin Extra Long Tunnel of Huxian–Mianxian Expressway, Chibanggou Tunne of Shenmu–Yan'an Railway, Gutian Tunnel of Ganzhou–Longyan Railway, Dayangtan Tunnel of Naxi–Xuyong Railway, railway tunnel ancient landslide, and Qigangou Tunnel of Xiangyang–Chongqing Railway. The crossing stratum of the Nanping Tunnel (Kong 2017; Luo et al., 2018; Wang 2018) is mainly quaternary Q3 loess, artificial fill, Upper Permian sandstone, and sandstone. During the tunnel operation, cracks in the sidewalls and partial water seepage are observed with a rapid development.

The position relationship of landslide in the Nanping Tunnel is illustrated in **Figure 5**. The angle between the main direction of landslide and longitudinal direction of the tunnel is 87°, while the sliding surface intersects at the sidewall of the tunnel. The sliding body is mainly composed of loess, artificial filling, completely weathered sandstone, and mudstone, having a thickness of 17–43 m. The slide zone is mainly interbedded between strongly weathered sandstone and mudstone having a thickness of 0.5–1.0 m. The water content of rock and soil in the slide zone is high, and the rock mass is clearly wrinkled.

It can be seen that the tunnel is seriously damaged by landslide such as lining cracking, water leakage, swelling, and uplift of ditch. In addition, staggered abutment of construction joint occurs in the tunnel. The cracks are mainly in the longitudinal

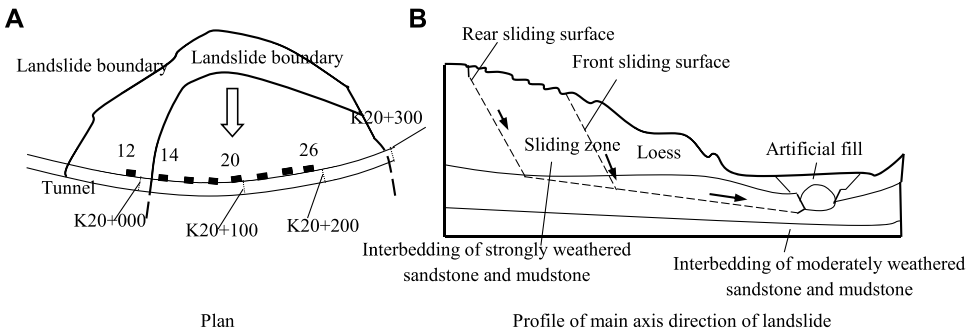

FIGURE 5 | Location relationship between the Nanping tunnel and landslide.

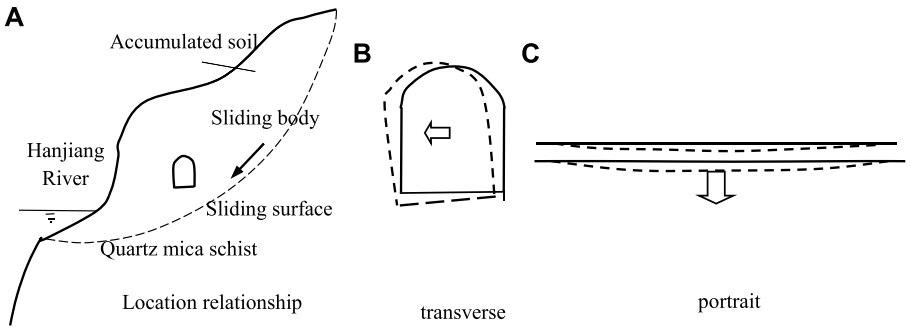

FIGURE 6 | Location relationship and deformation characteristics.

direction, distributed in the left and right sidewalls of the tunnel. More precisely, there are five longitudinal through cracks between No. 14–18 Avoidance Tunnel on the side of the hill, with an extension of 75 m and a width of 3–5 mm. The circumferential cracks are relatively few and mainly located near the construction cracks, while few diagonal cracks exist. Several staggered construction joints exist at the sidewall of the tunnel, and the maximum staggered platform is 5 cm.

3.2.3 With Tunnel Located Above the Sliding Surface

The typical cases include the Linchang Tunnel of Chengdu–Kunming Railway, Dongronghe No. 1 Tunnel of Chengdu–Kunming Railway, Sunjiagou Tunne of Linxian–Lishi Expressway in Shanxi Province, and Goummowan Tunnel of Hunan–Chongqing Railway. During the Goumowan Tunnel (Zhao, 2019) construction, the slope body slides due to continuous rainfall. The landslide is mainly the sliding of accumulated soil along the underlying quartz mica schist, with a sliding surface having a depth of 80 m on the main shaft section. The location relationship between the tunnel and landslide is presented in **Figure 6A**.

The tunnel deformation is mainly based on the overall river side displacement and longitudinal bending, in which the overall movement to the Hanjiang River is 0.079–0.299 m. Staggered platforms exist in local locations. In addition, transverse annular cracks appear in the sidewalls. Few longitudinal cracks and distortions occur in the expansion joints. **Figures 6B,C** show the tunnel deformation characteristics.

3.3 Oblique System

3.3.1 With Tunnel Located Below the Sliding Surface

The typical cases include the Luoping Tunnel of an expressway and Wenling Tunnel of Daying–Shenchi Expressway. The relative position relationship between the Wenling Tunnel (Deng 2014; Li 2017) and landslide at the entrance is illustrated in **Figure 7**. During the tunnel construction, the excavation at the bottom of the slope results in the free face, which is not timely supported. In addition, the infiltration of rainwater softens the soil–rock interface. Eventually, the tunnel construction and rainwater induce the sliding of the overburden with a thickness of 6–10 m. In addition, the tunnel direction is diagonally intersected with the sliding direction. The sliding mass causes crushing and cracking of the cover arch at the tunnel exit.

3.3.2 With Tunnel Passing Through the Sliding Surface

The typical cases include the Hongtupo Tunnel (Deng and Zhang, 2005) of Xianglin Expressway, Pingzhong No.2 Tunnel on Nanning–Kunming Railway, K12+813 Tunnel of an expressway in southwest mountainous area, and Qingshashan Tunnel of Pingan–A'Dai Expressway. The location relationship between the Hongtupo Tunnel and landslide is illustrated in

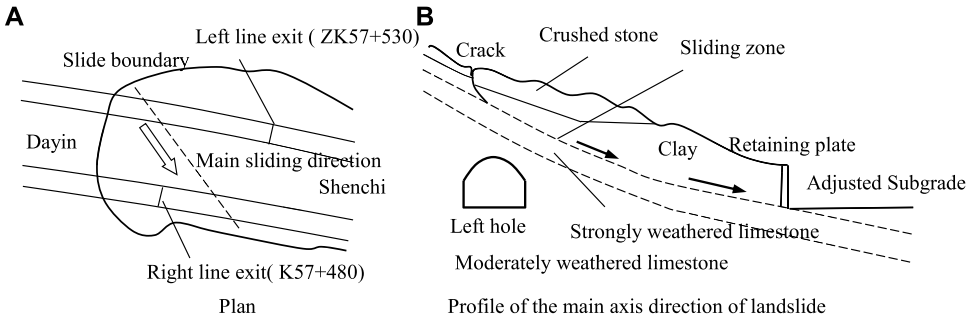

FIGURE 7 | Location relationship between the entrance of the Wenling tunnel and landslide.

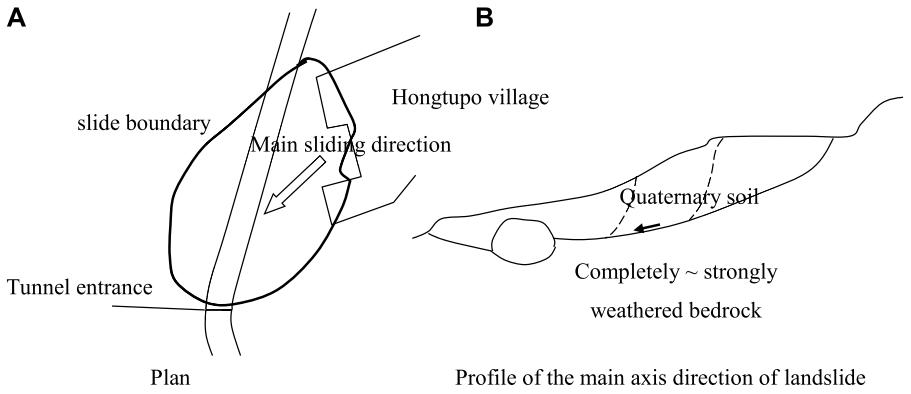

FIGURE 8 | Location relationship between the entrance of the Hongtupo tunnel and landslide.

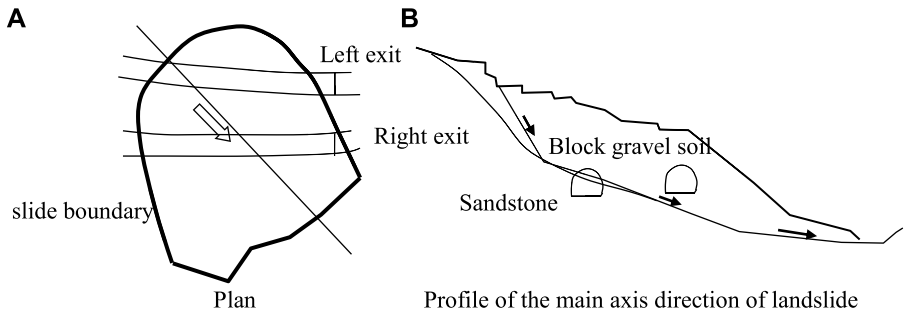

FIGURE 9 | Location relationship between the Fenjieliang tunnel and ancient landslide.

Figure 8. It can be seen that the landslide is in the stage of creep deformation. The sliding body has a thickness of 10–17 m. The main sliding direction obliquely intersects with the axis of the tunnel (angle of 40°), and the sliding surface intersects with the tunnel at the sidewall. The tunnel leads to severe bias pressure, structural deformation, and cracking. The deformation is mainly the settlement of the arch crown and the clear shear displacement of the arch ring above the camber line, in which the tunnel structure above the camber line displaces about 2 cm to the river side.

3.3.3 With Tunnel Located Above the Sliding Surface

The typical cases include Fenjieliang Tunnel of Chongqing–Yichang Expressway and Sunjiaya Tunnel of Fengjie–Wuxi Expressway in Chongqing. The entrance of Fenjieliang Tunnel is located in an ancient landslide with an average thickness of 18 m. The entrance of the left-line tunnel goes through the slip zone, while the body of the right-line tunnel is all within the accumulation of ancient landslide. The relationship between the Fenjieliang Tunnel and the ancient landslide is illustrated in **Figure 9**.

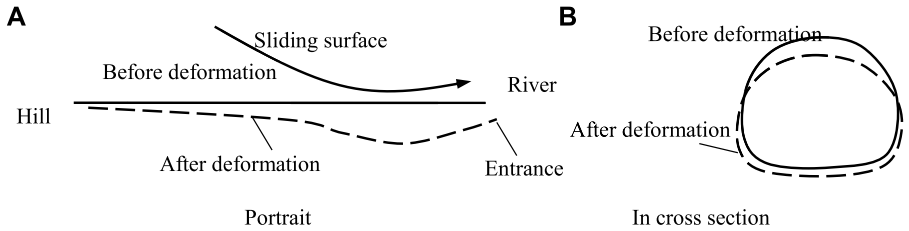

FIGURE 10 | Deformation diagram of the "longitudinal pull" mode.

The ancient landslide is revived by tunnel construction and heavy rainfall. Affected by the landslide, the right-line tunnel is mainly displaced as a whole. In addition, tension cracks appear at the sidewall and arch foot against the mountain. These cracks appear outside the expansion joints in a staggered manner. Longitudinal cracks having a width of almost 1–5 mm exist near the right side of the arch of the left-line tunnel. The extension length is almost 10 m, and the overall movement is not clearly observed.

4 TUNNEL-RELATED LANDSLIDES DEFORMATION MODE

When the tunnel-related landslide is an oblique system, the stress and deformation characteristics can be considered as the combination of parallel and orthogonal systems. Therefore, this study only analyzes the deformation mode of the tunnel-related landslide in parallel and orthogonal forms.

4.1 "Longitudinal Pull" Mode

For the parallel form of tunnel-related landslides, when the tunnel is located below the slide surface, the sliding mass causes an action of "oblique pull" on the surrounding rock and tunnel, that are below the sliding surface. This pull action can be divided into longitudinal and vertical actions, which results in longitudinal (along the axial direction of the tunnel) deformation and subsidence of the tunnel arch, as well as circumferential cracking of the arch crown in serious cases. The displacement of the tunnel is mainly manifested as "longitudinal deformation and sinking in the transverse section." The effect of "Longitudinal pull" is gradually decreased when the distance increases between the sliding surface and the tunnel. The deformation form is illustrated in **Figure 10**.

4.2 "Longitudinal Shear" Mode

For the parallel form of tunnel-related landslides, when the tunnel goes through the sliding surface and only the entrance of the tunnel is located in the landslide body, the tunnel can be approximated by a cantilever beam structure, and it is directly subjected to the action of "longitudinal extrusion and shear forces." That is, besides the pressure of surrounding rock on the transverse section, the tunnel structure is also directly subjected to the action of the landslide's longitudinal thrust, which can be divided into longitudinal and vertical load components of the tunnel. Sinking, tensile deformation and bending deformation longitudinally exist along the tunnel. Moreover, the tunnel structure near the slide surface may have circular cracks in the vault or shear cracks along the sliding direction, which can lead the tunnel to shear and misalign in serious cases. The displacement of the tunnel is mainly manifested as "longitudinal displacement and staggered sinking." The deformation scheme is presented in **Figure 11**.

4.3 "Transverse Pull" Mode

For the orthogonal form of tunnel-related landslides, when the tunnel is located below the slide surface, the sliding of the slip mass produces a "horizontal pull" on the tunnel. This pull can be divided into horizontal and vertical action. This action can be divided into lateral and vertical actions. The tunnel bears small bias load. Therefore, the arch deflects towards the river side, and longitudinal cracks appear in some serious cases. The tunnel displacement mainly occurs in the transverse section, and a "small deflection displacement" exists in the cross section (cf. **Figure 12**). Simultaneously, this pulls effect of the slip mass on the tunnel is gradually weakened with the increase of the vertical distance between the tunnel and sliding surface.

4.4 "Transverse Shear" Mode

For the orthogonal form of tunnel-related landslides, when the tunnel goes through the slide surface with its lower part located in the sliding bed and upper part in the sliding mass, the tunnel lining in the sliding mass is subjected to the landslide thrust. The tunnel will then be put in shear and bear large bias load. The tunnel structure will be "sheared off" if it cannot stop the sliding mass, which forms longitudinal cracks and longitudinal shear under large bias load as well as large deflection (tilt) displacement of the cross section around the bottom of the wall. The tunnel displacement is mainly manifested in the transverse section, with a "large deflection displacement" in the cross section (cf. **Figure 13**).

4.5 "Transverse Ship" Mode

For the orthogonal form of tunnel-related landslides, when the tunnel is located above the sliding surface, the tunnel inside the sliding body slides with it, and a longitudinal bending occurs under the landslide thrust. The tunnel structure near the boundary of the sliding body will be in a shear state, and it will be transversely sheared in serious cases. After shearing, the tunnel displacement is dominated by the overall outward

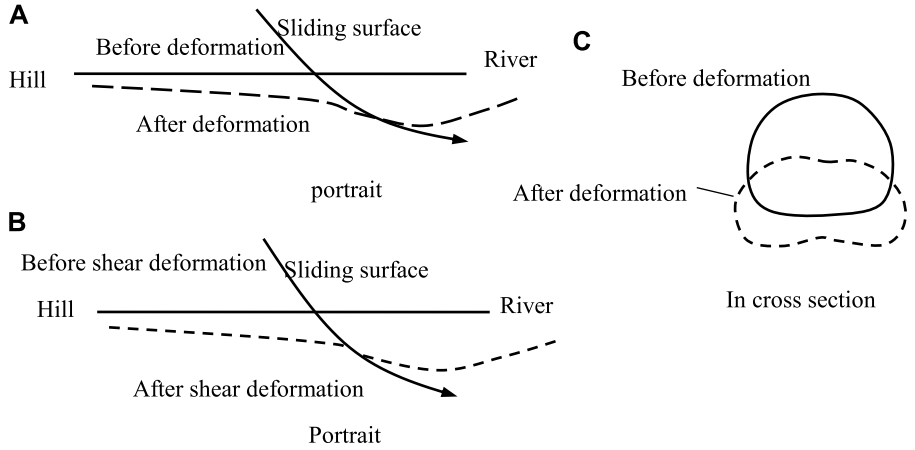

FIGURE 11 | Deformation diagram of the "longitudinal shear" mode.

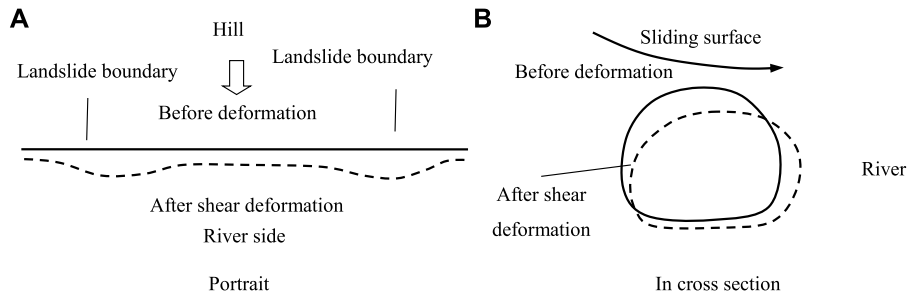

FIGURE 12 | Deformation diagram of the "transverse pull" mode.

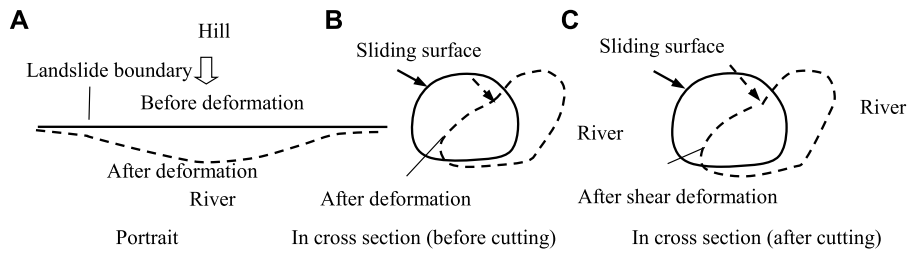

FIGURE 13 | Deformation diagram of the "transverse shear" mode.

displacement, which is commonly known as "lateral translation motion." The tunnel displacement is mainly within the traverse section. In addition, a "misalignment translation" exists in the cross section. The deformation is illustrated in **Figure 14**.

5 DISCUSSION

The geological environment is weak in Sichuan–Tibet Plateau, China, and the mountain disasters are extremely serious. Landslides, collapses and rockfalls frequently occur due to rock freezing and thawing damage (Li et al., 2022; Zhang et al., 2022). After the development of the Sichuan–Tibet Railway project, many key technical problems should be urgently solved. Firstly, a decent choice of the tunnel location in landslide area is crucial. In addition, the quick identification of the landslide type and its relative position with the tunnel is essential.

1) Even if the tunnel is located below the sliding surface, the landslide may cause its deformation or destruction. In these investigated cases, the maximum vertical distance between the

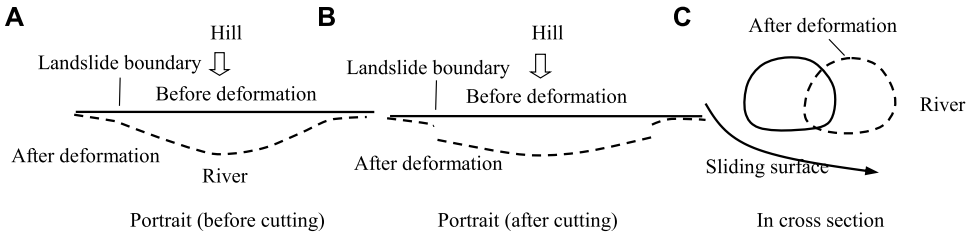

FIGURE 14 | Deformation diagram of the "transverse ship" mode.

TABLE 2 | Division of monitoring areas and monitoring items.

Type of tunnel-related landslides		Division of monitoring areas	Main monitoring items
Parallel	With a tunnel located below the sliding surface	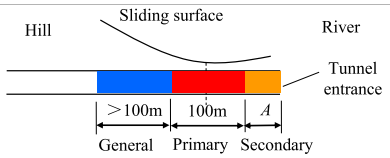	Longitudinal distance, vertical displacement, and longitudinal stress
	With a tunnel Passing through the sliding surface	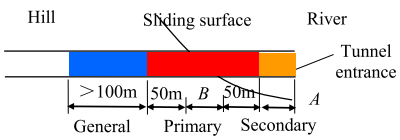	Longitudinal distance, vertical displacement, and longitudinal stress
Orthogonal	With a tunnel located below the sliding surface	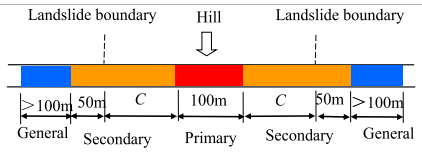	Horizontal and vertical displacement in the transverse section and circumferential stress
	With a tunnel Passing through the sliding surface	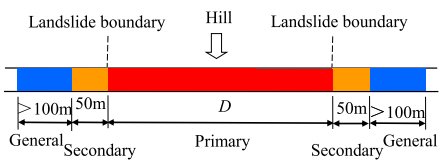	Horizontal and vertical displacement in the transverse section and circumferential stress
	With a tunnel located above the sliding surface	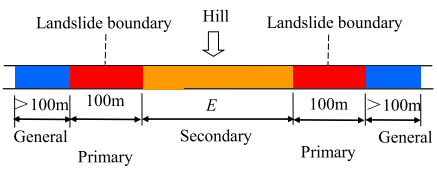	Horizontal and vertical displacement in the transverse section and circumferential and longitudinal stress

sliding surface and the tunnel is 20 m, while 90% of them occur within 10 m. Therefore, the safe vertical distance between the sliding surface and the tunnel is greater than 20 m. Therefore, when the tunnel passes through the slope section, the stability analysis of the slope body, especially the ancient landslide body, should be performed based on geological survey, and the ancient slide surface or potential

TABLE 3 | Recommended distance between monitoring sections.

Monitoring areas	Displacement of tunnel structure	Stress of tunnel structure
Primary	10	20
Secondary	15	30
General	25	50

landslide surface should be found. Afterward, when determining the location of the tunnel, the best plan for the tunnel is to pass through the landslide more than 20 m below the sliding surface.

2) During the construction of the tunnel which passes through the landslide area, many displacement monitoring sections should be arranged along its axial direction. If the automatic data acquisition system is equipped, automatic monitoring of three-dimensional structure displacement can be performed in the whole process of tunnel construction and operation. The plane position relationship between the tunnel and the main slip direction can be determined by analyzing the angle between the horizontal displacement direction and the tunnel axial direction. A further analysis can be performed on the distribution rules of displacement of each monitoring point along the tunnel longitudinal direction and in the cross section. The vertical position relationship between the tunnel and the sliding surface can be determined according to the deformation diagram of different modes presented in **Section 4**. In addition, the development trend of landslide can be predicted by analyzing the displacement-time relationship curve of each monitoring point.
3) The safety of the tunnel structure should be guaranteed with minimal monitoring. Therefore, according to the analysis presented in **Sections 3**, **4**, the monitoring items of tunnels with different tunnel landslide types are determined. At the same time, the tunnel is divided into several monitoring areas according to the importance, and different monitoring section spacing is set for different areas. **Table 2** shows the division of monitoring areas and main monitoring items. **Table 3** presents the recommended distance between monitoring sections.

6 CONCLUSION

In this study, the characteristics of tunnel deformation and diseases with different relative positions of sliding zone are analyzed by investigating and summarizing typical cases of tunnel-related landslides. The following conclusions are drawn.

1) Based on the investigations and statistics of typical cases, it can be concluded that most of the landslides occurred during the engineering period. They are mainly triggered by the disturbance of tunnel construction, rainfall, dangling bottom of slope and earthquake. Only 29% of tunnel-related landslides occurred during the operation period, which resulted in the greater deformation or damage to the tunnel structure, in which it is extremely difficult to retreat. The main factors of landslides are the rainfall, dangling bottom of slope, earthquake, and continuous influence of construction disturbance. In addition, although the ancient landslides are usually identified and analyzed for stability during the tunnel location selection, the proportion of revival ancient landslides is 50%.
2) The relative position relationship between the tunnel and landslide determines the deformation form and failure characteristics of the tunnel, which can be used for the classification of tunnel-related landslides. Based on the plane relationship between the tunnel and sliding surface, the tunnel-related landslides are divided into three types: parallel, orthogonal and oblique. According to the crossing position, the landslides are divided into three types: with tunnel located below the sliding surface, passing through the sliding surface and above the sliding surface. According to the statistical results, most of the disease cases are caused by the orthogonal form, which accounts for 60.5% of the total cases, followed by the oblique form. In addition, compared with tunnels under or above the sliding surface, they are more susceptible to diseases when passing through the sliding surface. These cases account for 63.1% of the total. Moreover, the tunnels under the sliding surface have fewer diseases.
3) According to the investigation and analysis of the tunnel-related landslides disease characteristics, corresponding tunnel deformation modes are summarized and developed based on the classification of the tunnel-related landslide. They are divided into five basic modes: longitudinal pull, longitudinal shear, transverse pull, transverse shear, and transverse ship. These deformation modes can explain the deformation characteristics of the tunnels with different relative positions. They can also provide a theoretical basis for studying slope diseases, tunnel destruction and diseases.
4) Based on the comprehensive analysis of interaction mechanism between the landslide and tunnel on deformation modes, five corresponding tunnel deformation characteristics are summarized: longitudinal deformation and sinking, longitudinal deformation and staggered sinking, small deflection displacement of section, large deflection of section, and cross section misalignment translation. Finally, the results of this study can provide a comparative basis for tunnel authorities to determine the location of the tunnel and identify landslide hazard types by tunnel deformation characteristics.

AUTHOR CONTRIBUTIONS

SM and ZY were responsible for the whole study; LHo and LHu were responsible for data collection; SM and ZY were responsible for drafting the manuscript; GX and ZZ were responsible for making important revisions to the manuscript; SM and GX were responsible for approving the final version of the manuscript for publication.

FUNDING

This work was supported by the National Natural Science Foundation of China under Grant No. 52178391, and the State Key Laboratory of Mechanical Behavior and System Safety of Traffic Engineering Structures under Grant No. ZZ 2021-09.

REFERENCES

Ashtiani, M., Palassi, M., and Ahmadi, A. (2010). *Effect of Excavation of Tunnels in the Convex Slopes Using Distinct Element Method*. International Society for Rock Mechanics.

Deng, X. (2014). Analysis and Comprehensive Treatment of Landslide for Wenling Tunnel. *Highway* 59 (05), 119–122.

Deng, X., and Zhang, X. (2005). Cause of Deformation and Reinforced Methods of Hongtupo Tunnel on Xiang-lin(Xianyun-Lincang) Highway in Yunnan Province. *Chin. J. Geol. hazards Prev.* 16 (02), 74–79. doi:10.16031/j.cnki.issn.1003-8035.2005.02.016

Du, Y., Xie, M., and Jia, J. (2020). Stepped Settlement: A Possible Mechanism for Translational Landslides. *Catena* 187, 104365. doi:10.1016/j.catena.2019.104365

Du, Y., Xie, M., Jiang, Y., Chen, C., Jia, B., and Huo, L. (2021). Review on the Formation Mechanism and Early Warning of Rock Collapse [J]. *Metal. Mine* 535 (01), 106–119. doi:10.19614/j.cnki.jsks.202101008

Kong, X. (2017). *Mechanism Analysis and Treatment of Tunnel Diseases Caused by landslide[D]*. Shijiazhuang: Sijiazhuang Tiedao University.

Li, B., Zhang, G., Wang, G., and Qiao, J. (2022). Damage Evolution of Frozen-Thawed Granite Based on High-Resolution Computed Tomographic Scanning. *Front. Earth Sci.* 10, 912356. doi:10.3389/feart.2022.912356

Li, X. (2017). Research on Stability Analysis and Treatment of Portal Landslide for Expressway Tunnel. *Highway* 62 (12), 292–295.

Lu, Y. (2012). *The Analysis about Effect of Landslide Stability on Tunnel deformation[D]*. Xi'an: Chang'an University.

Luo, X., Lan, X., Shu, Z., L, X., et al. (2018). Deformation Characteristics and Treatment Techniques of Nanping Tunnel–Landslide System in Datong-Zhungeer Railway. *Railw. Eng.* 58 (10), 55–59. doi:10.3969/j.issn.1003-1995.2018.10.14

Ma, H. (2003). Discussion on Problems of Slope Disaster and Tunnel Deformation [J]. *Chin. J. Rock Mech. Eng.* 22 (Suppl. 2), 2719–2724. doi:10.3321/j.issn:1000-6915.2003.z2.039

Ma, H., and Wu, H. (2011). Practices on High Slope Disease Control of Highways in Mountainous Area[J]. *Chin. J. Railw. Eng. Soc.* 7, 34–41. doi:10.3969/j.issn.1006-2106.2011.07.007

Ma, H., and Wu, H. (2016). Progress and Expectation of Research on Tunnel-Landslide System. *Chin. J. Undergr. Space Eng.* 12, 522–530.

Pai, L., Lai, T., and Wu, H. (2018). Land Traff. Tunnel-Landslide Parallel System Model Establishment and Experimental Validation[J]. *Railw. Eng.* 58 (12), 64–68. doi:10.3969/j.issn.1003-1995.2018.12.16

Tao, Z. (2003). *Study on Tunnel Deformation Mechanism at Landslide Site and Disaster Predicting and controlling[D]*. Xi'an: Southwest Jiaotong University.

Tao, Z., and Zhou, D. (2003). Model Test on Deformation Mechanism of Tunnel at Landslide Site[J]. *J. Eng. Geol.* 11, 323–327.

Wang, H. (2018). *Numerical Simulation of the Interaction Mechanism between Nanping Tunnel and landslide[D]*. Chongqing: Southwest University of Science and Technology.

Wang, Y., Ding, W., and Tang, X. (2012). Study of Deformation and Failure Mechanism and Reinforcement Effect of Yangpoli Tunnel Longitudinally Traversing Landslide[J]. *Rock Soil Mech.* 33 (07), 2142–2148. doi:10.16285/j.rsm.2012.07.016

Wang, Z. F., Shi, F. G., Li, D. D., and Li, H. (2020). Tunneling-induced Deep-Seated Landslides: a Case Study in Gulin County, Sichuan, China[J]. *Arabian J. Geosciences* 13, 1039. doi:10.1007/s12517-020-06048-5

Wu, H. (2012). *Research on Deformation Mechanism and Control Technology of Tunnel–Landslide system[D]* 31. Beijing: China Academy of Railway Sciences.

Wu, H., Wu, D., Ma, H., and Zhang, H. (2012). Research on Type of Tunnel-Landslide System and Tunnel Deformation Mode[J]. *Chin. J. Rock Mech. Eng.* (S2), 3632–3642.

Yang, G., Zhong, Z., Zhang, Y., and Fu, X. (2016). Analysis of Mechanism and Mechanical Characteristics of Landslide Disaster [J]. *Chin. J. Rock Mech. Eng.* 35 (S2), 4009–4017. doi:10.13722/j.cnki.jrme.2016.0804

Zhang, L., Niu, F., Liu, M., Ju, X., Wang, Z., Wang, J., et al. (2022). Fracture Characteristics and Anisotropic Strength Criterion of Bedded Sandstone. *Front. Earth Sci.* 10, 879332. doi:10.3389/feart.2022.879332

Zhang, Z. G., Zhao, Q. H., Xu, C., and Xu, X. Y. (2017). Interaction Analyses between Tunnel and Landslide in Mountain Area. *J. Mt. Sci.* 14, 1124–1139. doi:10.1007/s11629-016-3999-y

Zhang, Z., Zhang, M., Zhao, Q., Fang, L., Ma, S., and Lv, X. (2021). A Simplified Analytical Solution for Deformation Behavior of Existing Tunnels Subjected to Influences of Landslides[J]. *Bull. Eng. Geol. Environ.* 80, 4651–4672. doi:10.1007/s10064-021-02230-5

Zhao, J. (2019). *Research on Stress Model and Deformation Mechanism of Tunnel-Landslide system[D]*. Lanzhou: Lanzhou Jiaotong University.

Zhou, P., Mao, J., Zhang, L., and Ma, H. (2002). Relationship between Tunnel Deformation with Slope Disasters and its Prediction Model J]. *J. China Railw. Soc.* 24 (1), 81–86. doi:10.3321/j.issn:1001-8360.2002.01.018

Zhu, C., Yang, F., Zheng, J., Lin, G., and Tian, Z. (2021). Interaction and Treatment for Tunnels Orthogonally Traversing Large Bedrock Landslides [J]. *KSCE J. Civ. Eng.* 25, 2758–2769. doi:10.1007/s12205-021-2231-y

Conflict of Interest: The authors declare that the research was conducted in the absence of any commercial or financial relationships that could be construed as a potential conflict of interest.

Publisher's Note: All claims expressed in this article are solely those of the authors and do not necessarily represent those of their affiliated organizations, or those of the publisher, the editors, and the reviewers. Any product that may be evaluated in this article, or claim that may be made by its manufacturer, is not guaranteed or endorsed by the publisher.

Copyright © 2022 Minglei, Hongwei, Yongquan, Xinqiang, Huan and Zhengguo. This is an open-access article distributed under the terms of the Creative Commons Attribution License (CC BY). The use, distribution or reproduction in other forums is permitted, provided the original author(s) and the copyright owner(s) are credited and that the original publication in this journal is cited, in accordance with accepted academic practice. No use, distribution or reproduction is permitted which does not comply with these terms.

frontiers | Frontiers in Earth Science

ORIGINAL RESEARCH
published: 07 July 2022
doi: 10.3389/feart.2022.884558

Study on Critical Damage Width of Parallel Double-Free Surface Blasting

Jianjun Shi[1], *Xiaopeng Miao*[1], *Haili Meng*[2], *Huaming An*[3]* *and Wei Zhang*[1]

[1]School of Civil and Resource Engineering, University of Science and Technology Beijing, Beijing, China, [2]Institute of Railway Construction, China Railway Research Institute Group Co., LTD., Beijing, China, [3]Faculty of Public Security and Emergency Management, Kunming University of Science and Technology, Kunming, China

Reserved rock wall is usually used in blasting operation when one side has an important protection object. Rock wall demolition blasting was essentially a parallel double-free surface blasting; blasting is the ideal effect of casting a side fully broken rock mass, throwing, on the other side (protection) of rock mass at the injury status of "broken and do not come loose"; the minimum thickness of the rock wall last could hole to protect the width of side of the free surface, called the critical damage width. First, based on the theory of multi-boundary blasting, the relationship among the throwing effect, boundary condition, and charge quantity of parallel double-free surface blasting is expounded in this article. The model of equivalent sub-charge package was established to deduce the relationship of bilateral resistance lines, and the theoretical value of critical damage width was 2.05 W (minimum resistance line). Second, according to the rock wall demolition and blasting of the Yangtou station renovation project in the second line of Yuhuai, the critical damage width of 2.5 W was measured through a single row and hole-by-hole detonation field test. The results of study on critical damage width of parallel double-free surface blasting can provide theoretical guidance for similar projects.

Keywords: rock blasting, critical damage, free surface, blasting excavation, rock wall collapse

OPEN ACCESS

Edited by:
Bo Li,
Tongji University, China

Reviewed by:
Liansheng Liu,
Jiangxi University of Science and Technology, China
Shiwei Lu,
Yangtze University, China

***Correspondence:**
Huaming An
huaming.an@kust.edu.cn

Specialty section:
This article was submitted to Geohazards and Georisks, a section of the journal Frontiers in Earth Science

Received: *26 February 2022*
Accepted: *02 June 2022*
Published: *07 July 2022*

Citation:
Shi J, Miao X, Meng H, An H and Zhang W (2022) Study on Critical Damage Width of Parallel Double-Free Surface Blasting. Front. Earth Sci. 10:884558. doi: 10.3389/feart.2022.884558

1 INTRODUCTION

Under the condition that one side has an important protection object, the blasting construction method of reserved rock wall is often adopted (Yang et al., 2010), that is, a rock wall of certain thickness is reserved on the side close to the protection object (**Figure 1**). The rock block blasting in the whole blasting area is divided into internal main rock block blasting and external rock wall demolition blasting. During blasting, the internal main stone is first exploded, and then the external rock wall is removed. The rock mass inside the rock wall is constructed by a conventional deep hole step control blasting method. When the inner rock mass of the rock wall is blasted, the rock wall, as a natural barrier, can prevent the lateral escape of the explosion pile, and at the same time, the rock wall can maintain a relative stability, avoiding the damage, stripping and rolling of slope rock block. In this way, the shielding effect of the reserved rock wall can reduce the difficulty of the main rock block blasting construction and the harm to the surrounding environment (Meng, 2015; Miao, 2020).

Meng et al. (2012) used rock wall control blasting technology in the expansion project of Chongqing–Fuzhou Railway adjacent to the existing line, pointing out that the internal main blast area of the deep hole blasting the direction of the air front parallel to the direction of the existing line. This technology can effectively control the impact of flying rocks, rolling rocks, and blasting vibration on the existing line, and then put the safety control point of the whole project on the

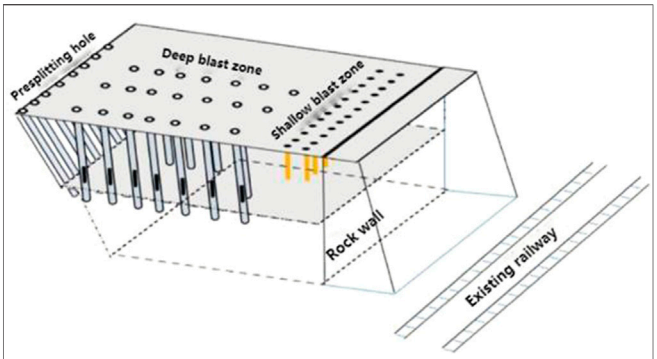

FIGURE 1 | Schematic diagram of rock wall blasting.

demolition of the reserved rock wall. The construction method of the rock wall becomes the key to ensure the safety of the adjacent protection objects (Meng, 2015).

In the process of reserved rock wall removal, Tang et al. (2019) used diamond rope saw to cut the reserved rock wall, and this method is similar to the mechanical removal by rock drill, which can effectively ensure the safety of existing railway lines or surrounding buildings. However, both of them have the disadvantages of high economic cost and slow construction progress, which are not suitable for large area promotion and use. In order to achieve convenient construction and economic and reasonable purposes, the use of blasting demolition of rock walls has become possible.

Reserved rock wall blasting is a kind of step blasting, but it also has its particularity. The main characteristics are as follows: 1) it is greatly affected by groove blasting in the early stage. Due to the large amount of clamps used in trench blasting, it is necessary to increase the single consumption of explosive and the ratio of drilling hole properly, but it cannot cause damage to the rock wall. 2) There are often important facilities around the explosion area that are needed to be protected. The collapse of blasting heap and the rolling stones generated by high steep slope during blasting and rock excavation are easy to damage the environment. The flying stones and vibration of blasting must also be strictly controlled. 3) The blasting area is long and the geological conditions vary greatly, so the blasting parameters must be constantly adjusted, and the blasting medium must be fully broken or disintegrated. 4) Rock wall with the main blasting area synchronization drop, rock wall blasting adopts precision deep hole loose blasting control or shallow hole blasting; the blasting area is covered with the protective and facade multivariate stereoscopic protection system of the comprehensive protection, and the gun head machine and high-power drivers to construction are arranged, to ensure that the protected objects are safe during the rock wall blasting (Guo and xue, 2015).

The blasting resistance line of rock wall demolition deviates from the protected object, which can effectively control blasting vibration and the harm of the flying rock (Tang et al., 2019). Rock wall demolition blasting strictly belongs to parallel double-free face multi-boundary blasting. The throwing effect at this time depends on two factors: boundary conditions and charge amount (Wang et al., 2008).To tie in with the construction, the side of the ideal casting blasting effect is a fully broken rock mass, casting, protect the rock on one side of the object to the "broken and not loose" (damage and do not break), the critical instability state, and

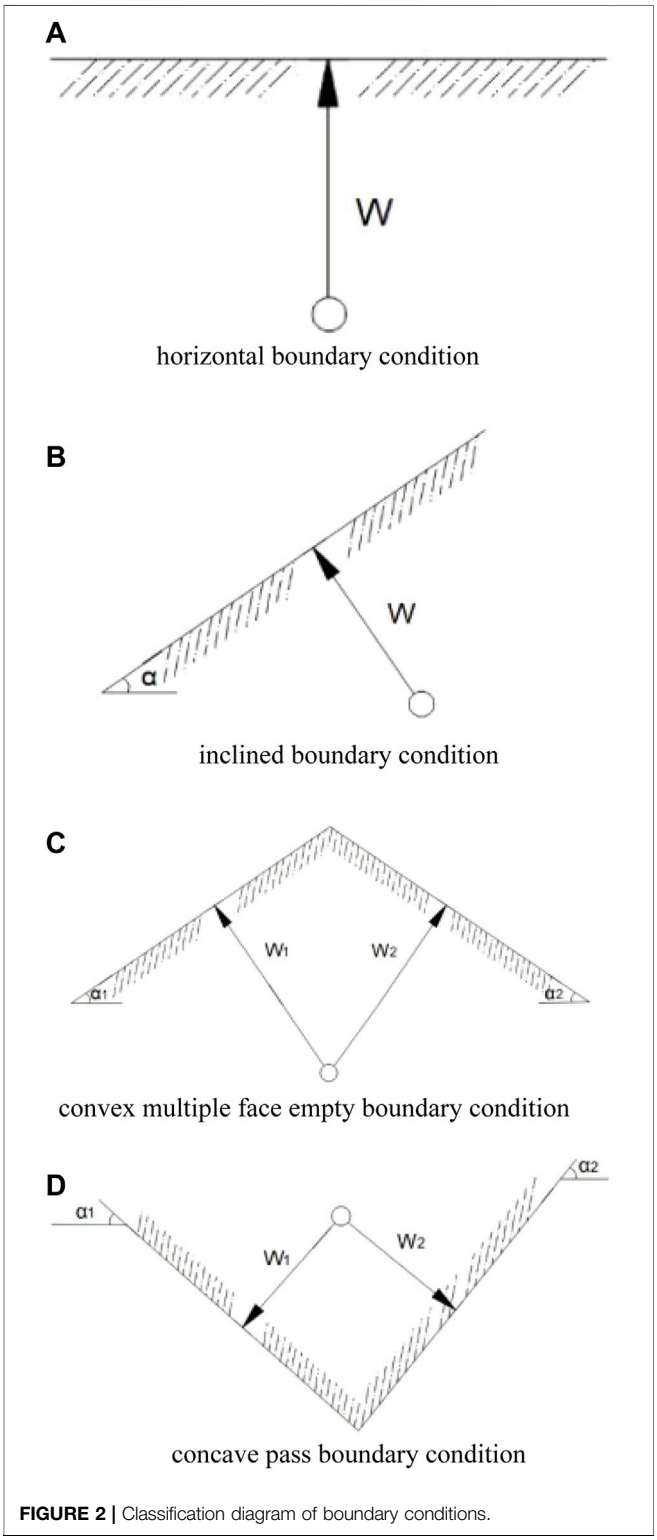

FIGURE 2 | Classification diagram of boundary conditions.

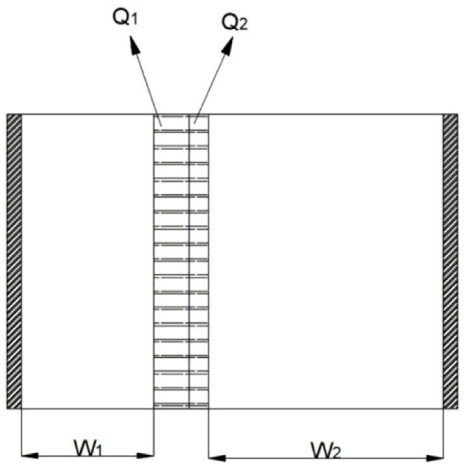

FIGURE 3 | Model diagram of equivalent sub-charge package.

it does not allow individual slungshot, both to ensure the safety of protection objects, and can easily remove the broken part of the stone. Due to the particularity of parallel double-free face blasting, the initiation of row-by-row and hole-by-hole must be adopted (Wang, 1992). If strengthening loose blasting is used to charge, the blasting effect only depends on the width from the last row of holes to the inner side of the rock wall, which is called the critical damage width.

Meng (2015) believed that when the stress wave reached the inner side of the rock wall, its strength should not be greater than the compressive strength of the rock mass, and the critical damage width should not be less than 1.5 times the minimum resistance line. Meng et al. (2012) found that the critical damage width was greater than two times the minimum resistance line in the cutting expansion project adjacent to the existing line of Yuan–Fuzhou Railway and Yang Lin (Yang et al., 2010) in the An Tuoshan remediation project.

Most of the previous determinations of critical damage widths come from engineering experience and lack a certain theoretical basis. Based on the multi-boundary blasting theory, an equivalent surcharge-package model was established to derive the relationship between parallel double-free surface resistance lines to determine the theoretical value of the critical damage width for rock wall demolition blasting. In addition, the minimum resistance line of 2.5 times of the critical damage width was determined based on the blasting of the rock wall of the Yangtou–Yuexing station renovation project of the Yuhuai 2 line, where the blasting effect of "broken but not scattered" unexploded rock was achieved after three blasts.

2 CALCULATION FORMULA OF MULTI-BOUNDARY BLASTING CHARGE

The multi-boundary condition refers to the boundary condition of micro-terrain, which belongs to the shape geometry condition compared with the horizontal boundary condition. Terrain changes not only affect the blasting effect but also affect the calculating blasting role within the scope of damage index and effective utilization of explosive energy (Huang, 2006).

According to the blasting efficiency and geological characteristics, the micro-terrain boundary conditions can be divided into horizontal boundary conditions, tilt boundary conditions, boundary conditions of convex multi surface free terrain and topographic boundary conditions of the concave pass, as shown in **Figure 2**. 1) The characteristic quantity of the tilt boundary condition is that the slope angle α ranges from 0 to 90°, and the general flat terrain is a special case of the slope boundary condition α = 0. 2) For boundary conditions of convex multi surface free terrain, general characteristics are on either side of the ridge slopes α1 and α2, (rock wall demolition blasting is the convex face more empty terrain, α1 and α2 approximate to 90°), through the study of hill facing more empty blasting, with energy distribution coefficient control medicine package location arrangement, usable slow lateral ground slope angle of the characteristics of representative face more empty terrain, and the multi-faced empty terrain can be converted into inclined boundary condition. 3) For topographic boundary conditions of the concave pass, the reciprocal of convex boundary condition can be approximated. In this way, the slope angle in the boundary conditions of multi-boundary blasting can be used as the basis of model calculation by the ground slope angle α, a characteristic quantity of slope boundary conditions.

a) Horizontal boundary condition,
b) inclined boundary condition,
c) convex multiple face empty boundary conditions, and
d) concave pass boundary condition.

In multi-boundary blasting, the blasting effect is measured by a throwing rate (E), which refers to the volume of rock thrown out as a percentage of the overall volume of rock being blasted, expressed in **Eq. 1**:

$$E = \frac{V_{throw}}{V_{blast}} \times 100\%. \tag{1}$$

When the throw rate E = 27%, the throw rate is defined as the standard state. Hongqu Wang and Wenxue Gao (Gao and Liu, 2007) derived the calculation formula of multi-boundary blasting charge based on the principle of conservation of mechanical energy and functional balance, as shown in **Eq. 2**:

$$Q = KW^3 F_{\phi}(E, a). \tag{2}$$

In the equation, K is the charge amount per cubic meter when forming a standard throwing funnel; W is the minimum resistance line length; and $F_{\phi}(E,\alpha)$ is the theoretical explosive package property index. Wang and Gao derived the theoretical explosive package property index as:

$$F_{\phi(E,\alpha)} = \frac{10^{0.0129E}}{\left(\sqrt{0.05\alpha}+1\right)\left[1.11 - \frac{86.133}{E}\lg f(\alpha)\right]}. \tag{3}$$

In the aforementioned equation, E is the throw rate; α is the natural ground slope; and $f(\alpha)$ is the throw factor, which is

FIGURE 4 | Blasting excavation site.

consistent with the meaning of the terrain coefficient; $f_\phi(\alpha,E)$ is the terrain factor, which means the terrain is favorable, the effective utilization rate of explosive energy increases or the projectile volume increases, and the charge should be reduced, also known as the charge attenuation coefficient (Gao et al., 2010).

$$f(\alpha) = \begin{cases} 1 - \dfrac{\alpha^2}{7000} \ or \ \cos\alpha, & \alpha < 30°, \\ \dfrac{26}{\alpha}, & \alpha \geq 30°. \end{cases} \tag{4}$$

When explosive conversion coefficient e and plugging coefficient d are added, the theoretical calculation formula of multi-boundary blasting charge is as follows (Liu, 1999):

$$\begin{aligned} Q &= edKW^3 F_\phi(E,\alpha) \\ &= edKW^3 \frac{10^{0.0129E}}{\left(\sqrt{0.05\alpha}+1\right)\left[1.11 - \frac{86.33}{E}\lg f(\alpha)\right]}. \end{aligned} \tag{5}$$

The aforementioned formula describes the inner relationship among the throwing effect, boundary condition, and charge amount. Q is the charge quantity, and the throwing effect is reflected by the throwing rate E, α can be used to describe the inclined boundary conditions of blasting rock and soil mass (horizontal boundary conditions, convex and concave boundary conditions can all be used as models for subsequent calculation).

3 ESTABLISHMENT OF AN EQUIVALENT SUBPACKAGE MODEL AND DISTRIBUTION FORMULA OF SUBPACKAGE

The explosive amount of a multi-directional charge is decomposed into sub-charge directed by each surface, according to the proportion of the space resistance line of each surface, so that its blasting action and blasting parameters are equivalent to one-way charge, which is called equivalent sub-charge.

According to the equivalent sub-charge blasting energy distribution model and multi-direction group charge blasting energy distribution model, the following model is established for rock wall demolition blasting (double resistance line and double face blasting).Suppose a small cylindrical cartridge of equal diameter is set on the axis of a homogeneous, unequal radius, and infinite length thick-walled circle, and its volume is negligible compared with that of the thick-walled circle. Take a unit length from it, as shown in **Figure 3**. There is no problem of energy dissipation in the axis direction of the intercepted cylindrical charge of unit length, and the explosive energy can only spread evenly along the radial direction (resistance line direction) of the thick-walled circle, so that it is broken and generates speed. At this point, the momentum obtained by monomers on both sides (the throwing funnel of single concentrated charge blasting, the joint action area of adjacent charge blasting of single row unidirectional group charge blasting, and the action area of single unidirectional prolonged charge blasting, except for the end being thrown out of the body, are collectively called monomers) is equal to the impulse of explosive gas acting on the hole air cavity, as shown in **Eq. 6**.

$$m_1 v_1 = \int_0^t Pa\theta dt = m_2 v_2, \tag{6}$$

$$m = \frac{1}{2}\theta W^2 \rho. \tag{7}$$

In the equation, v_1 and v_2 are the velocity of monomers on both sides, m_1 and m_2 are the mass of monomers on both sides, a is the radius of the gun hole, P is the pressure of the explosion gas, θ is the angle of the gun aperture toward the center of the circle, t is the action time, W is the minimum resistance line, and ρ is the density of rock mass. By combining **Eq. 6** with **Eq. 7**, it can be obtained that the square of resistance line of monomer velocity on both sides is inversely proportional, as shown in **Eq. 8**.

$$v_1 W_1^2 = v_2 W_2^2. \tag{8}$$

Under the condition of double air surface (bilateral resistance line), the conventional strip charge was decomposed into two equivalent sub-charge packets, with the equivalent charge quantity of Q_1 and Q_2, respectively.

The monomer velocity formula is as follows (Gao et al., 2010):

$$v = K_v \left(\frac{Q}{VW^3}\right)^{\frac{2}{3}}. \tag{9}$$

In the equation, K_v is the velocity coefficient and V is the volume of monomer. Combining **Eq. 8** with **Eq. 9**,

$$\frac{W_1}{W_2} = \left(\frac{Q_2}{Q_1}\right)^{\frac{2}{3}}. \tag{10}$$

According to **Eq. 10**, $\frac{Q_1}{Q_2}$ tends to decrease with the increase of $\frac{W_1}{W_2}$, in line with the principle of minimum resistance line. As the explosive energy propagates along the cylinder, the particle is

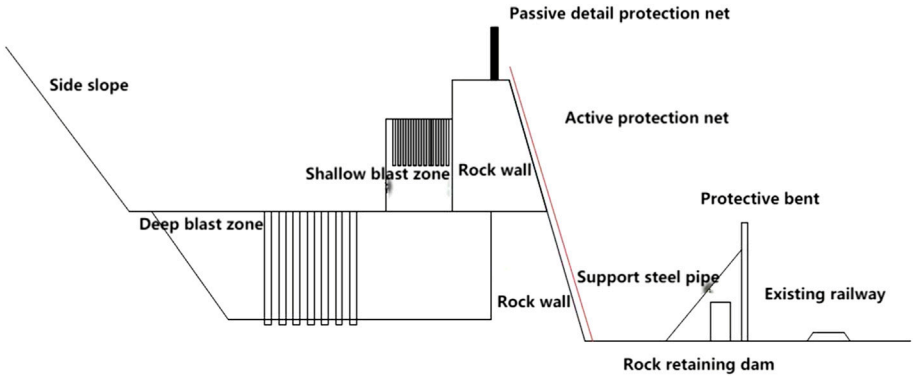

FIGURE 5 | Schematic diagram of main blasting scheme for reserved rock wall.

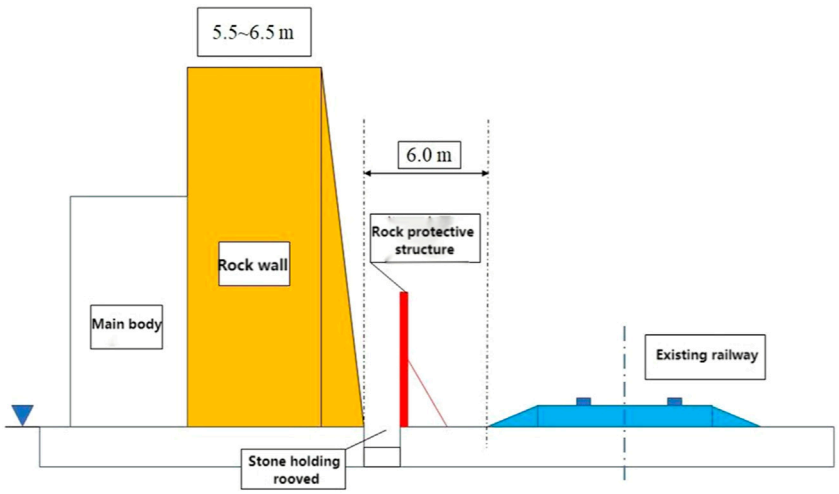

FIGURE 6 | Excavation profile diagram.

displaced. Since there is no barrier of outer medium on each surface, the medium on the surface produces outward radial motion, which promotes the fracture of rock mass near the surface. At the same time, the reflected stretching wave is generated in each plane, and the layer-by-layer propagates to the center of the charge package from the plane, so that the medium also moves in the direction of the plane, causing damage. The motion of explosion wave and reflected wave overlapped and interfered with each other, resulting in the increase of the motion velocity of the medium along the resistance line direction, and the symmetry of motion was destroyed due to the difference of resistance line. Because the explosion energy obtained along the air surface of the minimum resistance line is the most, and the resistance is the least, the wave travel route is the shortest, the reflected wave appears the earliest, the intensity is the largest, the expansion effect of the explosion product is the largest, and along the direction of the medium movement speed is the largest, the medium throws the largest degree.

4 THEORETICAL DERIVATION OF CRITICAL DAMAGE WIDTH

In the theoretical calculation formula of multi-boundary blasting charge, let

$$a = ed\frac{10^{0.0129E}}{\left(\sqrt{0.05\alpha}+1\right)\left[1.11-\frac{86.133}{E}\lg f(a)\right]}. \tag{11}$$

Then the formula for calculating the amount of charge on multiple surfaces can be simplified as (Liu and Gao, 2006):

$$Q = aKW^3. \tag{12}$$

The rock wall demolition blasting belongs to convex double-sided aerial terrain, and α_1 and α_2 are approximately 90°. After determining the energy distribution of both sides of the sub-charge through the equivalent sub-charge package model, **Eqs 10**, **12** are jointly solved as follows:

FIGURE 7 | Main rock blasting of reserved rock wall.

$$\frac{W_1}{W_2} = \frac{\sqrt[3]{\frac{Q_1}{a_1 K}}}{\sqrt[3]{\frac{Q_2}{a_2 K}}} = \sqrt[3]{\frac{Q_1 a_2}{Q_2 a_1}} = \left(\frac{Q_1}{Q_2}\right)^{\frac{1}{3}}\left(\frac{a_2}{a_1}\right)^{\frac{1}{3}} = \sqrt{\frac{W_2}{W_1}}\left(\frac{a_2}{a_1}\right)^{\frac{1}{3}}, \quad (13)$$

$$\frac{W_1}{W_2} = \left(\frac{a_2}{a_1}\right)^{\frac{2}{5}}. \quad (14)$$

It can be seen from the analysis that the inner relationship among the throwing effect, boundary conditions, and charge amount of throwing blasting can be quantitatively described by **Eq. 12** for the calculation of charge amount of multi-boundary blasting. **Eq. 14** can be used to further quantitatively determine the relationship between the resistance lines on both sides of double-free surface blasting. It can be seen from **Eq. 14** that the ratio of double resistance lines is related to explosive conversion coefficient, plugging coefficient, and theoretical charge property index (drop rate and boundary ground slope angle).

The ideal throwing effect of rock wall demolition blasting is that one side is thrown, one side is loose, and the throwing rate of the throwing side is in accordance with the standard throwing rate of blasting under inclined boundary conditions, that is, E_1 = 27%, $\alpha_1 = 90^{\circ}$; On the loose side, $E_1 = 0$, $\alpha_1 = 90^{\circ}$, and the throw rate is zero. According to the theoretical explosive package property index table (Wang, 1994; Di Xinning Yuan, 2001), $f_{\phi 1}(E,\alpha)$ and $f_{\phi 2}(E,\alpha)$, so

$$\frac{a_1}{a_2} = 25.4. \quad (15)$$

The ratio of bilateral resistance lines is

$$\frac{W_2}{W_1} = \left(\frac{a_1}{a_2}\right)^{\frac{2}{5}} = 2.05. \quad (16)$$

In the equation, W_1 is the minimum burden length; W_2 is the critical instability width in the critical instability state; and a_1 and a_2 are theoretical explosive package property indexes.

According to the analysis results of **Eq. 16**, the theoretical value of the critical width of dynamic self-stability in rock wall demolition blasting is 2.05 W.

5 ENGINEERING TEST

5.1 Project Summary

During the construction of Yuhuai second line Yangtou crossing station transformation project, roadbed filling, and road cutting excavation should be carried out on the left side of the existing roadbed, including 27,923 cubic meters of subgrade earthwork filling, 41,437 cubic meters of earthwork excavation, and 168,636 cubic meters of stonework excavation. Due to the large amount of stone excavation, considering the construction period and cost, blasting excavation has become an inevitable choice. Yangtou of the line station roadbed construction is adjacent to existing lines, to be blasting excavation areas with both Yuhuai line left only 10–100 m apart, blasting vibration and flying rock may impact on existing lines, especially the

FIGURE 8 | Rock wall site for demolition blasting test.

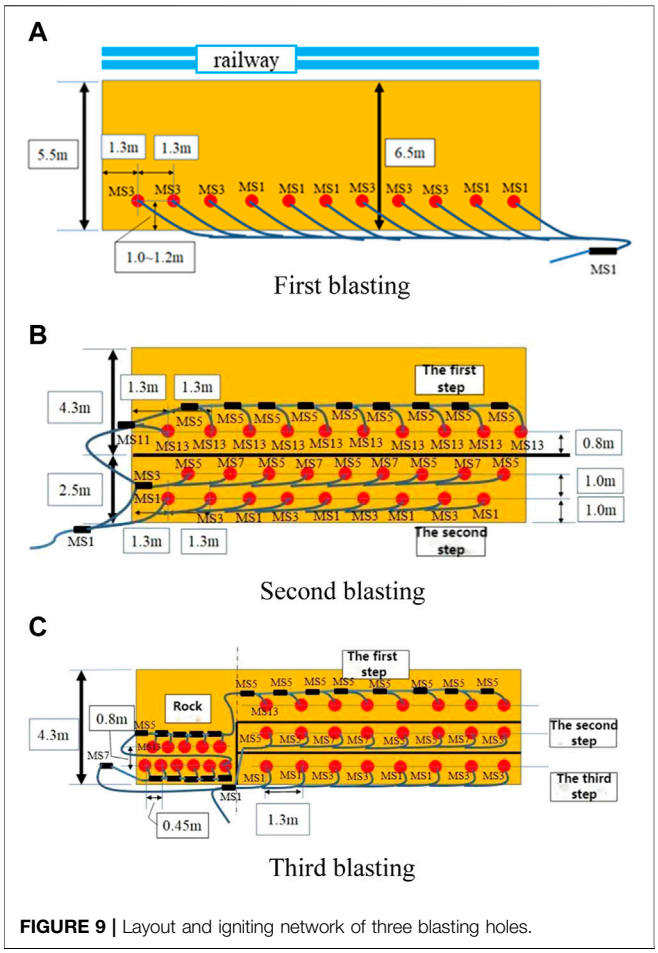

FIGURE 9 | Layout and igniting network of three blasting holes.

adjacent existing lines of high slope cutting stone controlled blasting excavation, the risk of falling rocks flying rock damage both driving equipment construction interference and security risk is very big. The area to be excavated is shown in **Figure 4**.

5.2 The Construction Plan

1) The overall construction scheme

From the perspective of safety, efficiency, and low cost, according to the geological terrain and surrounding environmental conditions of the project, and combined with the practical experience of previous similar projects, determined the overall design principles of the project as follows:

1) The reserved rock wall precise micro-vibration control blasting technology is adopted as a whole. Deep hole blasting is used for excavation at a distance from the existing railway (Wang et al., 2010; Gao et al., 2016). The step height is 10 m. Based on the existing terrain and initiation sequence, the free surface direction of the main explosion area is set parallel to the existing railway direction, and the free surface direction of rock wall demolition blasting is set to be away from the existing cable. Schematic diagram of the main blasting scheme of the reserved rock wall is shown in **Figure 5**, and schematic diagram of excavation section is shown in **Figure 6**.
2) Diction dike demolition use shallow hole blasting and mechanical crushing combination of weak down, step-by-step away from existing side by shallow hole blasting way by row by hole blasting, resistance line 0.8 ~ 1.2 m, when residual unexploded rock wall rock to achieve dynamic around critical width, unexploded rock mass reach the state of the "broken and not loose" on the part of the rock mass with the method of mechanical removal, **Figure 7** shows the main stone blasting of the reserved dike.

5.3 Rock Wall Demolition Blasting Test Scheme

In order to conduct a reasonable and accurate blasting test study on rock wall demolition, open terrain rock wall was selected. Before blasting, the width, length, and height of the rock wall were

TABLE 1 | Blasting parameters for triple blasting tests.

Blasting order	01	02		03	
Hole pitch/m	1.3	1.3		1.3	
Row pitch/m	—	1.0		0.8	
Hole depth/m	2.5	2.5		2.5	
Stemming length/m	1.7	1.9		1.9	
Minimum burden/m	1.2	1.0		0.8	
Total charge/kg	14.7	22.8		26.3	
Maximum section charge/kg	7.35	Upper bench	3	Upper bench	3.5
		Lower bench	0.6	Lower bench	0.6
Charging mode	Continuous decoupled charge	Upper bench	Interval decoupled charge	Upper bench	Interval decoupled charge
		Lower bench	Continuous decoupled charge	Lower bench	Continuous decoupled charge
Hole layout principle	-—	Quincunx hole layout in multiple rows	Quincunx hole layout in multiple rows		
Initiation mode	Millisecond initiation	Upper bench	Hole-by-hole initiation	Upper bench	Hole-by-hole initiation
		Lower bench	Millisecond initiation	Lower bench	Millisecond initiation

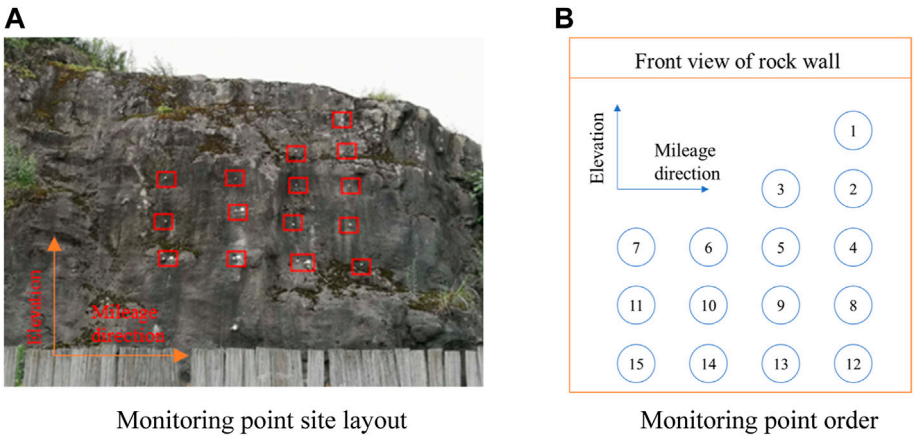

FIGURE 10 | Site layout and detail arrangement of 15 monitoring points.

FIGURE 11 | Field measurement using a total station instrument.

5.5, 27.3, and 4.6 m, respectively, and the specific parameters are shown in **Figure 8**.

In order to accurately determine the value of the critical width of dynamic self-stability of the rock wall, the selection and cause analysis of the detonation mode of the three blasting of rock wall are as follows:

1) The first blasting adopts millisecond initiation. On the one hand, this method can play a good role in blasting synergy and provide a good critical surface for the subsequent two blasts. On the other hand, when MS1 and MS3 detonators are arranged at intervals, the phenomenon of mutual dryness of stress waves is more obvious, and the stress on the rocks will be greatly reduced in the mutual dryness area, and then large rocks will appear, so as to control flying and rolling rocks.
2) The second and third rock wall blastings are divided into upper and lower steps. The upper step adopts hole-by-hole initiation, and the lower step adopts millisecond initiation. For one thing, the hole-by-hole initiation method can greatly reduce the blasting vibration and control the influence of flying stones on the existing line. For another, the considerable millisecond reduces the stress wave of adjacent blast holes, reduces the blasting synergy to the greatest extent, and makes the upper step loose.

The damage and crack cracking state of the remaining unexploded rock mass were determined by the RSM-SY5 (T) nonmetallic acoustic detector and camera at each blasting. It is confirmed that the unexploded rock mass has reached the state of "broken but not scattered" after three blasts. Schematic diagram of the layout of blasting holes and blasting network for three blasts is shown in **Figure 9**, in which the first step is the upper bench, and the second and third steps are the lower bench. Blasting parameters are shown in **Table 1**. Among them, MS1, MS3, MS5, MS7, and MS13 in **Figure 9** represent delay 0, 50, 110, 200, and 650 milliseconds, respectively.

5.4 Monitoring and Analysis of Spatial Displacement of Particle and Global Movement of Dike in the Whole Movement of Interpoint Moving Rock

5.4.1 1) Analysis of Particle Spatial Displacement Monitoring Results

Fifteen network displacement monitoring points are arranged on the side of the reserved rock wall close to the existing railway (in **Figure 10**). The 15 monitoring points are located in the west of the rock wall as a whole, and the horizontal and vertical distance between each measuring point is about 1 m. Leica TSP1200 total station and its supporting facilities (in **Figure 11**) were used to collect the coordinate data of 15 particles before and after blasting. These coordinate data were statistically analyzed, and the displacement differences of 15 particles on the rock wall before and after blasting were plotted as shown in **Figure 12**. The total displacement differences represent the cumulative displacement differences of three blasting. In the figure, x direction is the side of the vertical rock wall pointing to the

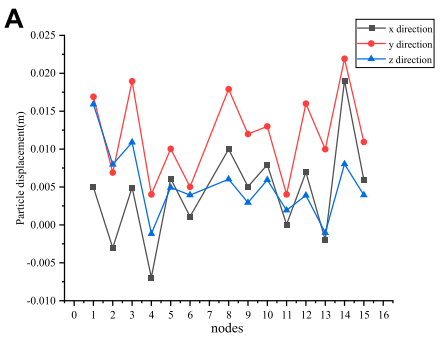

Particle displacement difference for first blasting

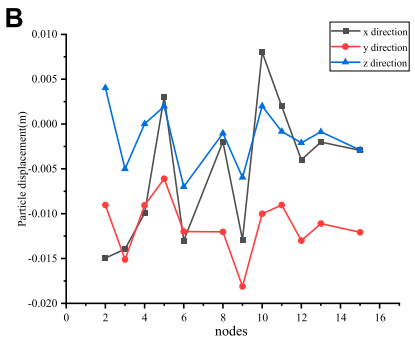

Particle displacement difference for second blasting

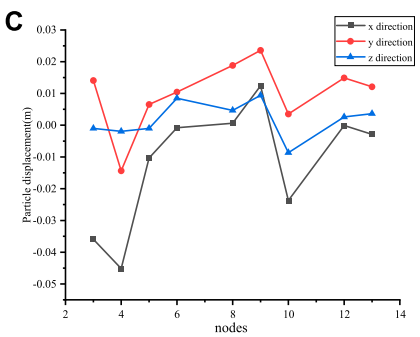

Particle displacement difference for third blasting

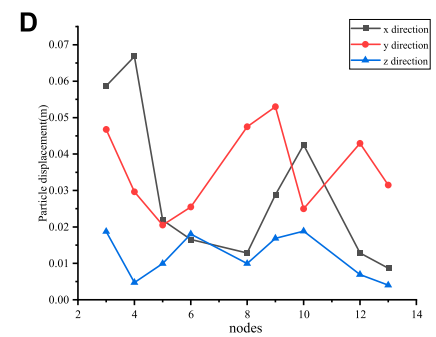

Total particle displacement difference for three blastings

FIGURE 12 | Particle displacement difference of rock wall after three blastings. By analyzing the coordinate data of 15 particles on the back of the rock wall, the following conclusions can be drawn.

railway side, Y direction is parallel to the side of the rock wall pointing to the right face, and Z direction is vertically upward.

1) Under the action of explosion shock wave and explosion stress wave, the rock mass enters the dynamic damage stage, and the cracks in the rock mass are activated and spread, which is the fundamental cause of the displacement of particles on the side of the rock wall.
2) Locally, the interpore displacement of each particle is disorganized, the law is not obvious, and the difference is relatively large, which reflects the anisotropy of cracks and joints in the rock mass and the anisotropy of damage in the rock mass.
3) The phenomenon of iron flakes falling off in the blasting process at some particles indicates that the blasting vibration speed at this particle is high and the rock mass produces stripping damage.
4) Test results show that the particle displacement in y direction is larger than that in x direction, and the particle displacement in the z direction is the smallest, this is because an explosive source is too short, which is only 3.756–8.63 m, cylindrical charge after blasting, detonation wave travels along the y direction in wall rock at first side (free surface) of the particle, after refraction, reflection, and transmission in the free surface, the detonation wave propagation velocity in the y direction is the fastest, In addition, the subsequent detonation wave is superimposed with the refracted and reflected detonation wave, resulting in the maximum particle displacement in the y direction. In addition, only y direction is a two-way surface, *x* and *z* directions are one-way surface, from the principle of the surface, also particle displacement in Y direction is the largest. Similarly, it can explain the minimum particle displacement in the z direction. When the detonation wave propagates along the z direction, it reaches the roadbed rock mass and then spreads to the railway line foundation. The energy generated by the detonation wave dissipates in the foundation, and the superposition effect on the particles on the side of the rock wall is weakened, so the displacement in the z direction is the minimum.
5) It can be seen from **Figure 12** that the displacement variation trend in the three directions is consistent on the whole, that is, the particle displacement in the *x*, *y*, and *z* directions increases or decreases synchronously. When the particle displacement is large, it can be considered that the damage degree of rock mass is high. It can be seen from **Figure 12**, 1) that, except for some measuring points, the remaining measuring points are all positive, indicating that after the first blasting, the rock wall moves in the positive direction of the coordinate system on the whole, that is, the rock wall moves to the right face, railway side, and upper face on the whole. It can be seen from **Figure 12**, 2) that most of the measuring points are negative, indicating that after the second blasting, the rock wall moves in the negative direction of the coordinate system as a whole,

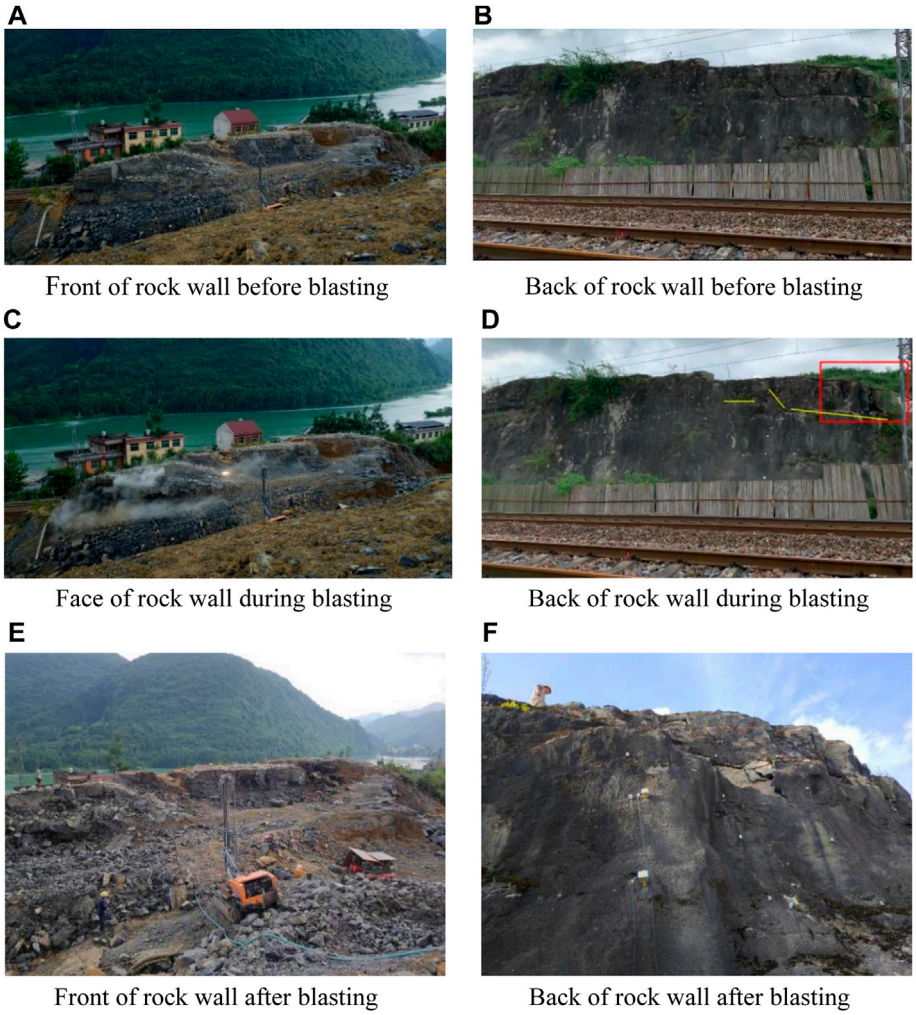

FIGURE 13 | Site map of the third rock wall blasting.

that is, the rock wall moves to the left of the rock mass, away from the railway line, and vertically downward (in the direction of foundation), which is exactly opposite to the particle displacement movement after the first blasting. As can be seen from **Figure 12**, 3), the displacement value in the x direction is negative, and the displacement values in the *y* and *z* directions are positive, indicating that after the third blasting, the rock wall as a whole moves to the left rock mass, railway side, and upper open face.

6) According to the particle displacement data after the three blastings, the particle displacement of the third time is the largest, the second time is the second largest, and the first time is the smallest. This is because with the increase of blasting times, the distance between blasting sources becomes smaller and smaller, and the cumulative blasting damage increases, which is reflected in the increase of particle displacement on the side of the rock wall. The third mass displacement was the largest, up to 50 mm, and there were iron pieces falling off at multiple masses, which had the most serious damage. 2) Analysis of monitoring results of reserved dike

will be captured by high-speed camera installed in can clear rock wall near the existing side safety area, using high-speed cameras to the reserved rock wall in the process of blasting; blasting rock wall under the action of movement record three times, if the reserved rock wall can appear crack damage phenomenon, such as timely embedding crack observation device, and cracks in the camera system can record the crack initiation process. The third rock wall blasting site is shown in **Figure 13**.

It can be seen from the video of the direction of the blasting face of the rock wall: the first blasting effect is good. Due to the use of micro-difference initiation, almost all the rocks are thrown to the blasting face, and the rock breaking area extends 0.7 m inward from the hole of the gun. From the photos taken at the top, there are some flying stones thrown at the top of the rock wall, but no flying stones thrown at the side of the railway line, only some soil was scattered on the top of the rock wall against the railway line. There are no visible

FIGURE 14 | Distance between free face and back of rock wall after each blasting.

cracks or cracks on the surface of the rock mass in the reserved layer, and the integrity of the rock wall is good. The second blast, as can be seen from the video of the direction of the rock wall blasting proximity surface, the entire blast can be clearly visible into the lower bench micro-differential detonation and the upper bench hole-by-hole detonation. All the rocks of the lower bench were thrown out to the hollow surface, and the rocks were larger; the rocks of the upper bench were not all thrown out, and the rock breaking area was from the shell hole to the hollow surface, which did not extend to the interior of the rock wall, which belonged to loose blasting. From the video on the back of the rock wall, at the upper rock, large cracks have penetrated to airport surface, the part has been out of the rock wall rock blasting, abnormal fluctuation significantly, up to a few centimeters, crackle, top rock wall, partly on the metope with crushed stone fell off, but the rock wall integrity is good, does not produce larger gravel and transverse crack at the top of the distance of 2.5 m, roughly equal to the length of the hole. In the third blasting, it can be seen from the video of the blasting face direction of the rock wall that the rock is not thrown out. The rock breaking area is the rock from the hole to the face of the rock wall, which does not extend to the inside of the rock wall. It is also a loose blasting. From the rock wall on the back of the video to see, at the upper rock (top of the rock distance 2.5 m) is broken, there were dropped chunk, and clear to the rail lateral movement to the rock, rock fall, almost the whole rock can be clear internal joint and fissure, slip on the top of the rock wall surface and have small gravel, and have more than one iron loss, The damage is extremely serious. From the point of view of the whole rock wall, the cracks are mainly concentrated at 2.5 m away from the top (the hole depth is 2.5 m), indicating that within the hole depth, the rock is almost broken and the damage degree is large, and the rock cannot bear another blasting impact. But the rock below the hole, no large rock slide, and damage degree is relatively low.

5.5 The Determination of the Critical Width of Dynamic Self-Stability of Wall

Before blasting, precise measurement was carried out on the whole dike, and the width of the whole reserved dike was 5.5 m. After blasting and removing the stones, the width of the reserved dike was measured, as shown in **Figure 14**. As can be seen from the figure, the remaining width after the first blasting test is 3.6 m, the remaining width after the second blasting test is 2.8 m, and the width of the rock wall after the last blasting test is 2.0 m. Through field test again and again by hole blasting test successive approximation are single railway rock wall on the side, after three times of blasting, from the high-speed camera shooting process and failure of rock mass damage degree, the rock mass has been reached "broken and do not come loose blasting effect," must not again take place to any degree of blasting, at this point since dynamic instability critical width is about 2 m, 2.5 times of resistance line (minimum resistance line is 0.8 m). Therefore, through three on-site blasting tests, it can be concluded that the critical damage width of rock wall demolition blasting is about 2.5 W under the charge of 0.23 kg/m^3 and the method of hole-by-hole initiation (MS5 is adopted for the time of slight difference).

6 CONCLUSION AND DISADVANTAGES

In this article, the critical damage width of parallel double-free surface blasting is studied and analyzed by combining theoretical analysis and the field test. The conclusions are as follows:

1) Multi-boundary blasting charge calculation formula $Q = aKW^3$, which can quantitatively describe the inner relationship among the throwing effect, boundary conditions, and charge of the throwing blasting; The equivalent sub-charge package model was established, and the relationship between the resistance lines of the double-free surfaces was deduced as $\frac{W_1}{W_2} = (\frac{a_2}{a_1})^{\frac{2}{3}}$, and the theoretical value of the critical width of dynamic self-stability was determined as 2.05 W.
2) Through three on-site blasting tests, we obtained the critical damage width of wall demolition blasting to be about 2.5W under the charge of 0.23 kg/m^3, and the method of hole-by-hole initiation is adopted (MS5 is adopted for the time of slight difference).

3) The values of the critical width of instability obtained from theoretical analysis and field experiments are not the same, and generally range from 2w–3w. On the one hand, different rock types and geological conditions give different experimental results, which make them deviate from the theoretical values. On the other hand, the explosive package property indices a_1, a_2 are obtained based on empirical values, which makes the theoretical values not uniquely determined. In addition, whether the field topography and rock type, the minimum resistance line, and the choice of blast vibration particles have any effect on the results in the field tests need to be further investigated.

DATA AVAILABILITY STATEMENT

The original contributions presented in the study are included in the article/Supplementary Material; further inquiries can be directed to the corresponding author.

AUTHOR CONTRIBUTIONS

All authors listed have made a substantial, direct, and intellectual contribution to the work and approved it for publication.

REFERENCES

Di Xinningand Yuan, Ye. (2001). Discussion about Directional Throwing Blasting in Multiaspect Facing Empty [J]. *Copp. Eng.* 4, 14. doi:10.3969/j.issn.1009-3842.2001.04.004

Gao, G., Wang, Z., Song, Z., Shugang, N. A., and Jiang, Y. (2016). Practice of Blasting Technology in High Slope Rock Wall Excavation under Complex Conditions [J]. *Water Conservancy Sci. Technol.* (24), 231.

Gao, W., and Liu, Y. (2007). Blasting Theory of High and Steep Road Cutting Rock Slope With Multilateral Boundary and its Application [J].. *Chinese. J. Rock Mech. Eng.* S1, 3397. doi:10.3321/j.issn:1000-6915.2007.z1.122

Gao, W., Xu, S., Liu, M., Wan, J-W., Deng, L., et al. (2010). *Reseach on Principle of Charge Amount Calculation in Multilateral Boundary Rock and its Practice*. Beijing: Blasting. doi:10.3963/j.issn.1001-487X.2010.03.002

Guo, Y., and xue, li. (2015). Research on Reserved Rock Wall Precision Deep-Hole Controlled Blasting Technology [J]. *Shanxi Archit.* 16 (06), 65

Huang, C. (2006). Technology of Controlled Blasting Excavation in Railway Cutting under Complex Environment [J]. *China Min. ind.* 07, 71–73. doi:10.3969/j.issn.1006-7051.2010.02.008

Liu, D. (1999). *Practical Manual of Engineering blasting[M]*. Beijing: China Metallurgical Industry Press

Liu, Y., and Gao, W. (2006). *Modern Road Blasting engineering[M]*. Beijing: China Communications Press

Meng, H. (2015). Demolition Technology of Rock Wall by Controlled Blasting with Large Aperture, Wide Hole Spacing and Shallow Hole [J]. *Railw. Constr.* 07, 86. doi:10.3969/j.issn.1003-1995.2015.07.24

Meng, H., Guo, Y., and Shi, J. (2012). *The Technology of Cutting Expansion and Controlled Blasting of Yuzhou-Fuzhou Railway Close to the Existing Line*. Guangzhou, China,F: The 10th National Engineering Blasting Academic Conference

Miao, X. (2020). *Damage Effect and Damage Mechanism of Rock Mass in Rock-Wall Controlled Blasting [D]*. Beijing, China: University of Science and Technology Beijing.

Tang, H., Yi, S., and Lin, D. (2019). Research on Safety Technology of Railway Cutting Blasting Excavation in Complex Environment [J]. *Eng. Blasting* 25 (01), 24. doi:10.3969/j.issn.1006-7051.2019.01.005

Wang, H. (1992). Dimensional Analysis of Calculation Formula of Multi-Boundary Charge [J], *J. Beijing Univ. Technol.*, 01, 45

Wang, H. (1994). *Multi-boundary Stone Blasting Engineering [M]*. Beijing: People's Communications Press.

Wang, S., Jin, J., and Li, M. (2008). Rock Blasting Technology in Complex Environment of Xindu Mountain Field Level Project [J]. *Eng. blasting* 02, 42. doi:10.3969/j.issn.1006-7051.2008.02.010

Wang, Z., Song, Z., Na, S., and Jiang, Y. (2010). Application of Blasting Technology in High Slope Rock Wall Excavation Under Complex Conditions [J]. *Engineering Blasting* 2, 31–34. doi:10.3969/j.issn.1006-7051.2010.02.008

Yang, L., Shi, Y., and Liang, X. (2010). Deep Hole Controlled Blasting Excavation Technology of Reserved Rock Wall [J]. *Eng. blasting* 16 (04), 30. doi:10.3969/j.issn.1006-7051.2010.04.008

Conflict of Interest: HM was employed by China Railway Research Institute Group Co., Ltd.

The remaining authors declare that the research was conducted in the absence of any commercial or financial relationships that could be construed as a potential conflict of interest.

Publisher's Note: All claims expressed in this article are solely those of the authors and do not necessarily represent those of their affiliated organizations, or those of the publisher, the editors, and the reviewers. Any product that may be evaluated in this article, or claim that may be made by its manufacturer, is not guaranteed or endorsed by the publisher.

Copyright © 2022 Shi, Miao, Meng, An and Zhang. This is an open-access article distributed under the terms of the Creative Commons Attribution License (CC BY). The use, distribution or reproduction in other forums is permitted, provided the original author(s) and the copyright owner(s) are credited and that the original publication in this journal is cited, in accordance with accepted academic practice. No use, distribution or reproduction is permitted which does not comply with these terms.

frontiers | Frontiers in Earth Science

TYPE Original Research
PUBLISHED 22 July 2022
DOI 10.3389/feart.2022.942025

Check for updates

OPEN ACCESS

EDITED BY
Yan Du,
University of Science and Technology Beijing, China

REVIEWED BY
Lei Xue,
(CAS), China
Wang Liwei,
Yanshan University, China

*CORRESPONDENCE
Guo Yu,
yuguob@scut.edu.cn

SPECIALTY SECTION
This article was submitted to Geohazards and Georisks, a section of the journal Frontiers in Earth Science

RECEIVED 12 May 2022
ACCEPTED 29 June 2022
PUBLISHED 22 July 2022

CITATION
Jia Y, Jiang T, Yin Y, Yu G and Wang L (2022), Experimental research on damage identification of topping dangerous rock structural surface based on dynamic characteristic parameters. *Front. Earth Sci.* 10:942025. doi: 10.3389/feart.2022.942025

COPYRIGHT
© 2022 Jia, Jiang, Yin, Yu and Wang. This is an open-access article distributed under the terms of the Creative Commons Attribution License (CC BY). The use, distribution or reproduction in other forums is permitted, provided the original author(s) and the copyright owner(s) are credited and that the original publication in this journal is cited, in accordance with accepted academic practice. No use, distribution or reproduction is permitted which does not comply with these terms.

Experimental research on damage identification of topping dangerous rock structural surface based on dynamic characteristic parameters

Yanchang Jia[1], Tong Jiang[1], Yanli Yin[1], Guo Yu[2]* and Lijin Wang[1]

[1]North China University of Water Resources and Electric Power, Zhengzhou, China, [2]South China University of Technology, Guangzhou, China

Rock block tilting is one of the most common types of dangerous rock block failures with no clear indicator of displacement prior to failure. Existing stability evaluation methods remain limited in their ability to constrain the non-penetrating section area, which is closely related to rock stability, and stability evaluations are therefore associated with large uncertainties. The dynamic characteristic parameters of toppling dangerous rock are closely related to structural plane strength. Under vibration loading, rainfall, and/or excavation unloading conditions, the structural plane becomes damaged and the dynamic characteristic parameters change. In this study, we present a dynamic characteristic model of rock tilting and identify the quantitative and qualitative relationship between dynamic characteristic parameters and the bonded area of the structural plane. The model accuracy is verified by experiments. The experimental results show that the damping ratio decreases linearly with structural plane damage, whereas the maximum vibration speed and particle trajectory increases nonlinearly and the natural vibration frequency decreases nonlinearly. The dynamic characteristic model and experimental results can be used to evaluate the degree of structural surface damage of toppling dangerous rock.

KEYWORDS

toppling dangerous rock, dynamic characteristic model, dynamic characteristic parameters, frequency, damage identification

Introduction

The collapse of toppling dangerous rock is characterized by a sudden burst and spatial dispersion. Rock block stability is related to many external factors (e.g., rainfall, seismic activity, blasting, excavation unloading) whereas internal factors (e.g., rock strength, mechanical properties and conditions) control the structural plane. A combination of internal and external factors may ultimately lead to cracking of the structural plane and bond area reduction, which reduce the structural plane strength and anti-tipping torque. Rock falls occur when the anti-falling torque is smaller than the tilting moment. Selection

of appropriate bonding condition analysis indicators is therefore a key factor for evaluating the stability of toppling dangerous rock. Previous studies have shown that dynamic characteristic parameters change regularly during gradual separation and structural plane damage processes. Damage evaluation modeling based on dynamic characteristic parameters is therefore of great theoretical significance and can help engineering applications to identify, evaluate and monitor the stability of toppling dangerous rock, and predict rock failure (Jia, 2018).

Structural damage identification and stability evaluation based on dynamic characteristics are widely used in the field (Han and Shi, 2011). Proposed damage identification of a derrick steel structure based on the frequency and equivalent damage coefficient. Damage location has been identified using the second-order frequency change ratio and frequency squared change ratio, and the rate of frequency change has been used to identify the degree of damage. This approach is simple, easy, and efficien. Chen et al. (2010) assessed structural damage according to formation and perturbation changes before and after the damage, and checked the evaluation accuracy based on the natural vibration frequency change. The feasibility of the method was verified by numerical simulation. Zhang and He (2014) expressed a structure's mass matrix and stiffness matrix as a function of unit damage parameters according to the matrix perturbation theory and proposed a method to identify the structural damage based on frequency and mode perturbation.

Structural damage identification techniques have been developed in the field of rock damage identification but currently remain in the basic experimental stage (Liao et al., 2016; Li et al., 2022; Zhang et al., 2022). Studied the vibration characteristics during fan blade fatigue loading, analyzed the vibration frequency variation, and established a dynamic characteristic model. The experimental results showed that the difference between the driving and natural frequency is closely related to the vibration amplitude and frequency fluctuation in the forced vibration. Ma et al. (2012) and Ma et al. (2011) measured the vibration frequencies of concrete blocks with different bonding conditions. The experimental results showed that the natural vibration frequency was closely related to adhesion conditions. Du et al. (2022), Du et al. (2020) and Du et al. (2016) determined the relationship between the natural vibration frequency and cohesive force of rock blocks through stress analysis and reported a stability evaluation based on the natural vibration frequency. Yao (2016) and Ye et al. (2015) studied falling rock qualitatively and established a stability evaluation model based on dynamic characteristic parameters. Jia et al. (2017) established a dynamic characteristic model of crash-damaged and slip-damaged rock blocks. The relationship between the safety factor and natural vibration frequency was identified on the basis of the dynamic characteristic model and limit equilibrium method, and safety evaluation and early warning monitoring plans for rock blocks were established based on the natural vibration frequency (Du and Xie, 2022). Du et al. (2022), Du et al. (2021) and Du et al. (2017) studied the collapse mechanism and early warning index of dangerous rock through experiments. Fukata et al. (2013) assessed the soil burial depth of rock blocks according to the natural vibration frequency in three directions, the size of the rock block, and the soil mechanical properties.

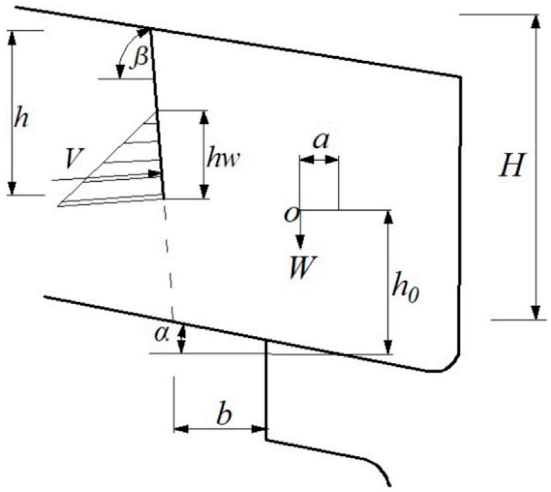

FIGURE 1
Force diagram of toppling dangerous rock.

The damage identification method of rock structures based on dynamic characteristic parameters can rapidly assess rock block stability. (Jia et al., 2021). However, the existing dynamic characteristic model is narrow in focus and does not accurately reflect the variation law of the dynamic characteristic parameters of rock masses in all failure modes. In this paper we present a theoretical study of the dynamic characteristics model and dynamic characteristic parameter behavior of collapsing rock blocks. We perform experiments to verify the model results.

Dynamic characteristic model

Toppling dangerous rock

The back edge of a toppling dangerous rock has a large angle along the main control structure plane, and the bottom has a concave cavity formed by differential weathering. Under internal and external forces, the rock block forms a destructive torque that rotates outwards and forms a vandal-resistant moment that turns inwards When the breaking torque that turns outwards is greater than the outward turning moment, the rock block collapses. The rock block swing is shown in Figure 1.

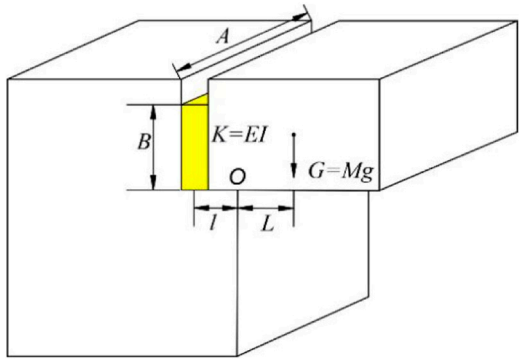

FIGURE 2
Simplified mechanical model of toppling dangerous rock.

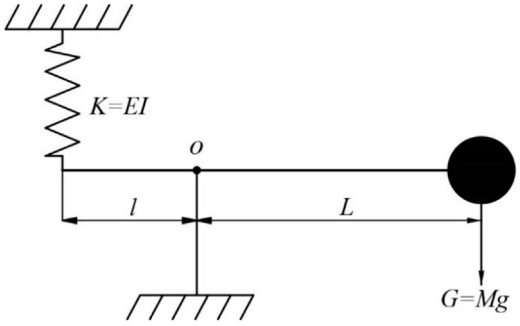

FIGURE 3
Vibration model of toppling dangerous rock.

The stability of a rock block is closely related to the load it bears. In the natural state, the load of the block is caused mostly by gravity, vibrational load, and internal and external cavity water pressure.

1) Gravity

The rock block volume can be obtained through site surveys. In the stability calculation, gravity is generally applied to the center of gravity and the direction of gravity is vertically downward:

$$W = abh\gamma \tag{1}$$

Where W and γ represent rock weight (kN) and bulk density (kN/m^3), respectively.

2) Vibration load

The vibration load acting on a rock block is usually obtained using the pseudo-static calculation method where the vibration load acts on the weight of the rock block:

$$P = \lambda W \tag{2}$$

Where P is the vibration load (kN) and λ is the dimensionless vibration load coefficient. When the horizontal vibration load coefficient is selected, the calculated vibration load is the horizontal vibration load (i.e., the direction horizontal to the free surface) and when the vertical vibration load coefficient is selected, the vibration load can be calculated as a vertical vibration load in the vertically downward direction.

3) Fissure water pressure

In the existing stability analysis of slope rocks, the fissure water pressure is calculated based on the linear distribution of the static water pressure, which is perpendicular to the main control structure plane and acts as a filling height of 1/3 above the tip of the main control structure plane.

$$V = 1/3\gamma_w h_w^2 \tag{3}$$

Where V represents the fissure water produced by the static pressure (kN/m), γ_w is the fissure water bulk density (kN/m^3), and h_w is the water filling height (m).

Dynamic characteristics

The damage to a rock block structure is directly reflected in its dynamic characteristic parameters (e.g., natural vibration frequency, vibration mode, damping ratio, changes in amplitude and particle trajectory), which are easy to obtain and can produce high-precision results without parameter analysis using a complicated mathematical model. These parameters are therefore important for assessing the structural plane damage of a dangerous rock block.

When an object is free to vibrate, it reciprocates periodically over a given time period. Once a rock block is disturbed by natural or artificial external forces, the structural plane becomes damaged and the bond strength of the slope rock body decreases continuously. These features are reflected in the particle trajectory and amplitude. A dangerous rock block is not only the particle track of a stable rock block, but also enhances the waveform amplitude. Damage of the structural plane generally leads to a reduction of the structural plane area or bond strength. The friction between the blocks increases, resulting in a change in the system's damping. The damage degree of the structural plane can be judged to some extent using the damping variation. The study of vibration resistance of dangerous rock blocks is therefore of great significance for understanding slope stability. In addition to the natural vibration frequency, the particle trajectory, amplitude, and damping ratio can be used

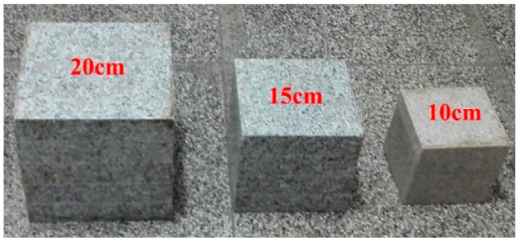

FIGURE 4
Experimental model of rock blocks.

FIGURE 5
Doppler laser vibrometer.

for structural damage identification. Using these methods, laboratory experiments have identified the damage degree of rock block structures.

Modeling procedure

Toppling dangerous rock are typically relatively isolated single rocks with good block integrity and high overall stiffness. Forces are mainly transmitted by a relatively weak structural plane and the physical properties of the main control structural plane significantly influence the dynamic characteristics of the block.

In terms of vibrational characteristics, the rock block pivots on the edge of the concave cavity, forms a rotational force distance outside the inclined slope, and swings up and down when subjected to external forces. The simplified model of the pendulum vibration rock block, without damping, is shown in Figure 2.

Rock block tilting is caused by gravity, vibrational load, and fissure water pressure. When the shear strength of the structural plane is insufficient to resist the gravitational load, vibrational load, and fissure water pressure, the rock body falls. The parent rock can be regarded as an infinite block relative to the rock block. The overall stiffness of the pedestal and rock block is high. The strength of the structural face of the rock block is weak relative to the strength of the rock block and parent rock. When subjected to external forces, the rock block can be regarded as a ball, the structural plane is regarded as a spring, and the parent rock transmits power to the rock block through the structural plane. The block body swings along the pivot because the parent rock is regarded as an infinite block body which does not affect the system swing. Pendulum vibration can be used to model the dynamic characteristics of toppling dangerous rock failure. The theoretical model of pendulum vibration in a rock block is shown in Figure 3.

The parent rock is assumed to be large relative to the rock block, and the latter is represented by a ball. The main controlling structural plane is isotropic and the system damping ratio is less than 1. Deformation in the amplitude range is linear elastic, and the vibration model of the rock block can be simplified into a pendulum dynamic characteristic model, with the constitutive equation given by Eqs. 4, 5 (Jia et al., 2021):

$$\boldsymbol{MgL} + \boldsymbol{EIl} = 0 \tag{4}$$

$$\boldsymbol{I} = \boldsymbol{AB}^3/12 \tag{5}$$

Then the vibration frequency can be derived as Eqn. 6:

$$\boldsymbol{f} = \frac{1}{\boldsymbol{\pi}}\sqrt{\frac{\boldsymbol{EIAB}^3}{48\boldsymbol{ML}}} \tag{6}$$

Where f is the natural frequency of undamped system (Hz); E is the elastic modulus (Pa); M is the mass of toppling dangerous rock (kg); I is moment of inertia of structural section; L is the distance between the centroid of toppling dangerous rock and O (m); l is the distance between O and the centroid of bounding surface (m); A is the bonding surface width of toppling dangerous rock (m); B is the bonding surface length of toppling dangerous rock (m).

In the above theory, the system damping effect is neglected. When the system damping ratio is equal to 1 (critical damping) or is greater than 1 (overdamped), the motion of the system is rapidly attenuated, there is no vibration characteristic, and the vibration frequency of the rock block does not exist. The model therefore does not apply to the critical damping and over-damping rock block system. When the damping ratio of the

TABLE 1 Experimental results.

Side length/cm	Bonding area/cm^2	Theoretical frequency/Hz	Measured frequency/Hz	Frequency error (%)	Particle trajectory/mm	Damping ratio	Maximum vibration speed/mm/s
10	20	1.12	1.08	3.48	0.310	0.178	0.0506
10	40	3.16	3.27	3.32	0.150	0.151	0.0450
10	60	5.81	5.85	0.61	0.070	0.119	0.0350
10	80	8.95	9.57	6.90	0.032	0.089	0.0340
10	100	12.51	12.12	3.12	0.017	0.051	0.0320
15	45	1.37	1.42	3.61	0.170	0.120	0.0380
15	90	3.88	3.79	2.23	0.090	0.085	0.0140
15	135	7.12	7.13	0.12	0.040	0.062	0.0120
15	180	10.96	10.32	5.87	0.019	0.040	0.0118
15	225	15.32	15.96	4.16	0.010	0.011	0.0110
20	80	1.58	1.48	6.48	0.150	0.081	0.0127
20	160	4.48	4.58	2.32	0.050	0.050	0.0047
20	240	8.22	8.65	5.19	0.010	0.036	0.0040
20	320	12.66	12.69	0.24	0.005	0.014	0.0039
20	400	17.69	18.13	2.47	0.003	0.008	0.0037

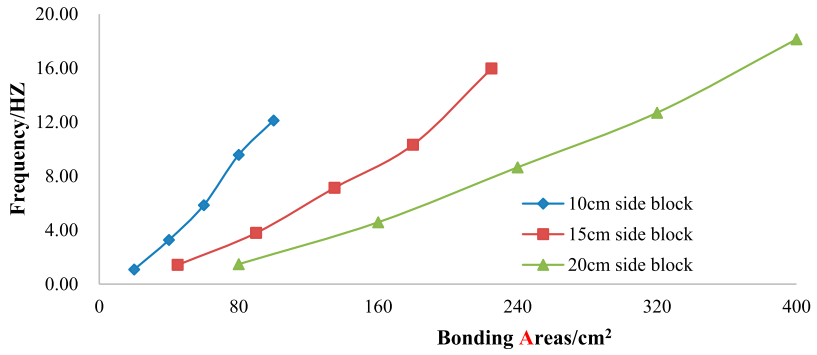

FIGURE 6
Natural vibration frequency of different size blocks with different bonding areas.

rock block is less than 1 (weak damping system), the natural vibration frequency of the damped pendulum vibration of the rock block can be obtained.

$$f_d = \frac{\sqrt{1-\xi^2}}{\pi}\sqrt{\frac{EIS^3}{48MLA^2}} \tag{7}$$

Where f_d is the natural frequency of damped system (Hz); ξ is the damping ratio of the system (unitless); S is the bonding surface area (m^2);

It can be seen from Eqn. 7 that the rock block bonding area is positively correlated with the natural vibration frequency, and the pendulum length and mass are negatively correlated with the natural vibration frequency.

Experimental study

An orthogonal experiment was carried out by selecting two factors: rock block mass and bonding area. The natural vibration frequency of the experimental block was monitored and compared with the theoretically calculated natural vibration frequency. The experimental design was also used to monitor the dynamic characteristics of the experimental model, and the

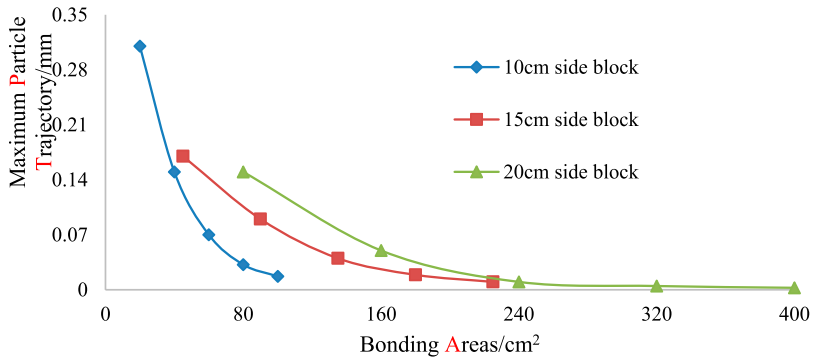

FIGURE 7
Relationship between maximum particle trajectory and bonded area under the same excitation.

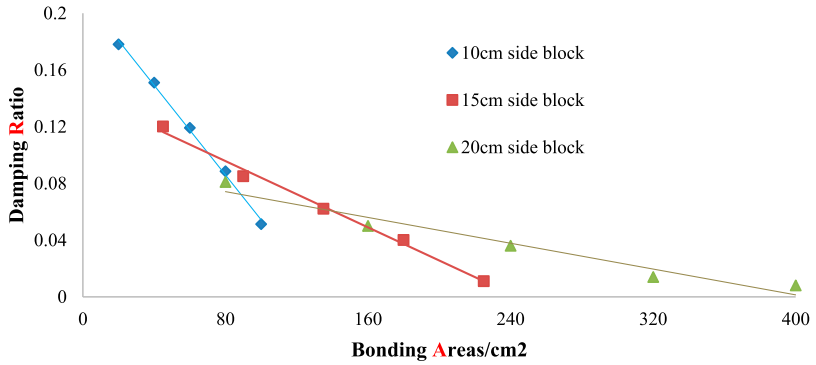

FIGURE 8
Relationship between damping ratio and bonded area.

variation of the dynamic characteristic parameters with the bonding area was further analyzed.

Experimental design

1) Model verification experiment design

In the experiments, a block of marble with side lengths of 10 cm, 15 cm and 20 cm was selected and each block was measured for its dynamic characteristics under different bonding areas. The bonding surface was made of a 2.5-cm-thick Elastic plastic plate that was not corroded by glue. The elastic modulus of the structural plane is 2.0 GPa. The rock mass and bonding surface were bonded with non-corrosive epoxy resin. In the experiment the earth was used as the pedestal to ensure that the pedestal was infinite relative to the experimental rock block and that the pedestal has no effect on the vibration of the block during the experiment (Figure 4).

The marble block, bonding surface, and vertical wall surface were bonded by glue to change the contact area between the foam board and rock block. The natural vibration frequency of the rock block under different bonding areas was measured for nine sets of experiments.

2) Additional dynamic characteristics experiment

The experiment uses Doppler laser vibrometer to monitor the damping ratio, particle trajectory, and the maximum vibration speed of the experimental blocks under different bonding areas. We then studied the relationship between structural damage and the dynamic characteristic parameters.

The Doppler laser vibrometer is a high-precision vibration measuring device based on the principle of optical interference. It

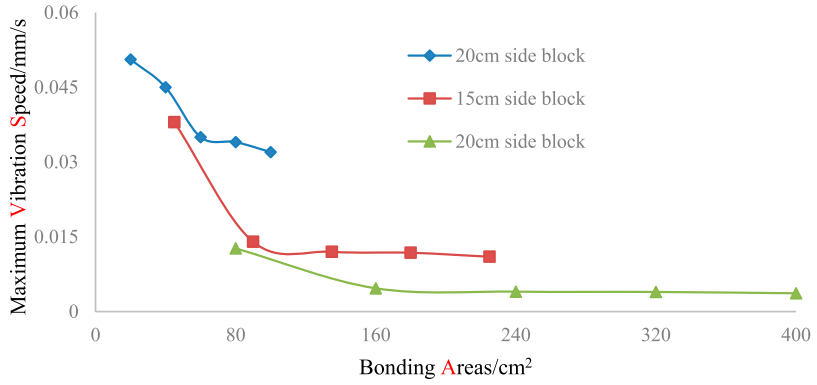

FIGURE 9
Relationship between maximum vibration speed and bonded area.

can accurately measure vibration signals, including displacement and velocity. The maximum frequency can reach 10000 Hz and the measurement resolution can reach 2.5 nm/s and 2 pm. Doppler laser vibrometer is shown in Figure 5.

Experimental results

The experimental results are listed in Table 1. Under different bonding area conditions, the difference between the theoretical and measured natural vibration frequencies is less than 6.90% with an average error of 3.34%, indicating good agreement between the theoretical value and the measured value. The theoretical value is consistent with the measured value, indicating the accuracy of the theoretical model.

Discussion

Relationship between vibration frequency and bonding area

In the experiment, the block was struck for excitation and the vibration time-domain curve of the marble block was recorded using a laser vibrometer. The vibration time-domain curve obtained from the experiments was Fourier transformed and filtered to obtain the experimental blocks of the experimental block frequency-domain diagram. The measured vibration frequency of different sized experimental rock masses under different bonding areas and the theoretical values calculated by the model are plotted in Figure 6.

For the 10-cm blocks with bonded areas of 20, 40, 60, 80, and 100 cm^2, the natural vibration frequencies were1.08, 3.27, 5.85, 9.57, and 12.12 Hz, respectively (Table 1 and Figure 6). For the 15-cm blocks with bonded areas of 45, 90, 135, 180 and 225 cm^2, the natural vibration frequencies were 1.42, 3.79, 7.13, 10.32, and 15.96 Hz, respectively (Table 1 and Figure 6). For the 20-cm blocks with bonded areas of 80,160, 240, 320 and 400 cm^2, the natural vibration frequencies were 1.48, 4.58, 8.65, 12.69, and 18.13 Hz, respectively, (Table 1 and Figure 6).

For the blocks, the natural vibration frequency increased with bonding area when other conditions were held constant, that is, the natural vibration frequency of the rock block gradually decreased with damage of the structural plane. The natural vibration frequency can quantitatively identify the bonding area of the structural surface, and then realize the stability evaluation of the toppling dangerous rock.

Relationship between particle trajectory and bonded area

Analysis of the five groups of experiments show a relationship between the particle trajectory and bonded area, as shown in Table 1. Figure 7 shows that the maximum value of the particle trajectory of the experimental block decreases linearly with increasing bonded area.

In summary, for the 10-cm blocks, the particle trajectory of the experimental block decreases with increasing bonding area under the same excitation conditions. When the bonding area was 20 cm^2, the particle trajectory range does not exceed 0.31 mm, and the bonding area is 40 cm^2. The particle trajectory range of motion does not exceed 0.15 mm. When the bonded area is 60 cm^2, the particle trajectory range does not exceed 0.07 mm. When the bonded area is 80 cm^2, the particle trajectory range does not exceed 0.032 mm. When the bonded area is 100 cm^2, the particle trajectory range does not exceed 0.017 mm. For 15-cm blocks, the particle trajectory of the experimental block decreases with increasing bonding area under

the same excitation conditions. When the bonding area was 45 cm^2, the particle trajectory range does not exceed 0.17 mm, and the bonding area is 90 cm^2. The particle trajectory range of motion does not exceed 0.09 mm. When the bonded area is 135 cm^2, the particle trajectory range does not exceed 0.04 mm. When the bonded area is 180 cm^2, the particle trajectory range does not exceed 0.019 mm. When the bonded area is 225 cm^2, the particle trajectory range does not exceed 0.01 mm. For 20-cm blocks, the particle trajectory of the experimental block decreases with increasing bonding area under the same excitation conditions. When the bonding area was 80 cm^2, the particle trajectory range does not exceed 0.15 mm, and the bonding area is 160 cm^2. The particle trajectory range of motion does not exceed 0.05 mm. When the bonded area is 240 cm^2, the particle trajectory range does not exceed 0.01 mm. When the bonded area is 320 cm^2, the particle trajectory range does not exceed 0.005 mm. When the bonded area is 400 cm^2, the particle trajectory range does not exceed 0.003 mm.

After being disturbed by external force, the structural surface is damaged, and the bond strength of the toppling dangerous rock decreases continuously. The active area of the particle trajectory is significantly expanded, so the particle trajectory can quantitatively identify the damage and stability of the structural plane of the toppling dangerous rock.

Relationship between damping ratio and bonding area

For the same experimental block, the damping ratio decreases as the bonded area between the experimental block and ground increases (Figure 8).

Based on the damping and experimental data of the bonded area, the relationship between the damping ratio and bonded area of the block is shown in table and Figure 7. For the experimental block with a side length of 10 cm under the same excitation, the damping ratio of the experimental block decreases with increasing bonded area. The damping ratio is 0.178, 0.151, 0.119, 0.089 and 0.051 when the bonded area is 20, 40, 60, 80 and 100 cm^2, respectively. For the experimental block with a side length of 15 cm under the same excitation, the damping ratio of the experimental block decreases with increasing bonded area. The damping ratio is 0.12, 0.085, 0.06, 0.04 and 0.011 when the bonded area is 45, 90, 135, 180 and 225 cm^2, respectively. In summary, the damping ratio of the experimental block decreases with increasing bonding area under the same excitation conditions. For the experimental block with a side length of 20 cm under the same excitation, the damping ratio of the experimental block decreases with increasing bonded area. The damping ratio is 0.081, 0.050, 0.036, 0.014 and 0.008 when the bonded area is 80, 160, 240, 320 and 400 cm^2, respectively. In summary, the damping ratio of the experimental block decreases with increasing bonding area under the same excitation conditions.

The damping is mainly determined by the properties of the structural surface. When the structural surface is damaged, the area of the structural surface decreases or the bond strength decreases, the frictional force changes and the damping changes. Therefore, the damage degree of the structural surface can be judged to a certain extent through the damping change. According to the variation law of the structural plane damping, when the structural plane is damaged, the damping of the toppling dangerous rock decreases linearly, and the stability of the dangerous rock becomes worse.

Relationship between bonding areas and maximum vibration speed

The relationship between natural vibration frequency and maximum velocity and bonding area is shown in Table 1. According to the measured value, the maximum vibration speed and the bonded area is plotted in Figure 9.

It can be seen from Figure 9 that the maximum vibration velocity increases nonlinearly as the bonding area decreases under the same excitation conditions. When the bonding rate is greater than 50%, the maximum vibration velocity changes little with the structural surface damage. When the bonding rate is less than 50%, the maximum velocity change can qualitatively identify the damage degree of the structural surface.

Conclusion

1) Based on the theory of rock block dynamics, we established the relationship between the natural vibration frequency of toppling dangerous rock, the bonding area of the rock block and bedrock, the elastic modulus, and rock block quality. The dynamic characteristic model was verified through laboratory experiments.
2) The dynamic characteristic model and experimental results show that the dynamic characteristics of toppling dangerous rock change regularly with structural plane damage. The maximum vibration speed and maximum particle trajectory increases nonlinearly, while natural vibration frequency of the structural plane damage decreases nonlinearly and the damping ratio decreases linearly.
3) The stability evaluation of toppling dangerous rock based on dynamic characteristic parameters can be realized by combining the variation law of the dynamic characteristic parameters with the limit equilibrium model. The research results can be applied to the stability evaluation of hydropower slope or road slope toppling dangerous rock.

Data availability statement

The original contributions presented in the study are included in the article/Supplementary Material, further inquiries can be directed to the corresponding author.

Author contributions

YJ and TJ were responsible for the work concept or design. YJ and GY were responsible for data collection. YY were responsible for drafting the manuscript. LW were responsible for making important revisions to the manuscript. YJ and YY were responsible for approving the final version of the manuscript for publication.

Funding

This research was supported by the National Natural Science Foundation of China (No. U1704243) and Natural Science Foundation granted by Department of Education, Anhui Province (No. KJ 2020A0235).

Conflict of interest

The authors declare that the research was conducted in the absence of any commercial or financial relationships that could be construed as a potential conflict of interest.

Publisher's note

All claims expressed in this article are solely those of the authors and do not necessarily represent those of their affiliated organizations, or those of the publisher, the editors and the reviewers. Any product that may be evaluated in this article, or claim that may be made by its manufacturer, is not guaranteed or endorsed by the publisher.

References

Chen, H., He, W., Wang, B., and Li, J. B. (2010). Study on structure damage detection based on perturbations of frequency and mode shapes. *Chin. J. Eng. Mech.* 27 (12), 244–249.

Du, Y., Li, H., Chicas, S. D., and Huo, L. (2022). Progress and perspectives of geotechnical anchor bolts on slope engineering in China. *Front. Environ. Sci.* 10, 928064. doi:10.3389/fenvs.2022.928064

Du, Y., Xie, M., and Jia, J. L. (2020). Stepped settlement: a possible mechanism for translational landslides. *Catena* 187, 104365. doi:10.1016/j.catena.2019.104365

Du, Y., and Xie, M. W. (2022). Indirect method for the quantitative identification of unstable rock. *Nat. Hazards (Dordr).* 112 (1), 1005–1012. doi:10.1007/s11069-021-05197-4

Du, Y., Xie, M. W., Jiang, Y. J., Chen, C., Jia, B. N., and Huo, L. C. (2021). Review on the formation mechanism and early warning of rock collapse. *Chin. J. Metal Mine* 50 (1), 106–119. doi:10.19614/j.cnki.jsks.202101008

Du, Y., Xie, M. W., Jiang, Y. J., Li, B., and Chicas, S. (2017). Experimental rock stability assessment using the frozen-thawing test. *Rock Mech. Rock Eng.* 50 (4), 1049–1053. doi:10.1007/s00603-016-1138-2

Du, Y., Xie, M. W., Jiang, Y. J., Li, B., Gao, Y., and Liu, Q. Q. (2016). Safety monitoring experiment of unstable rock based on natural vibration frequency. *Chin. J. Rock Soil Mech.* 37 (10), 3035–3040. doi:10.16285/j.rsm.2016.10.039

Fukata, T., Taniguchi, T., and Shibuya, S. (2013). A proposal of estimation method for rockfall risk degree based on vibration measurement of the boulder. *J. Jpn. Soc. Civ. Eng. Ser C Geosph. Eng.* 69 (1), 140–151. doi:10.2208/jscejge.69.140

Han, D. Y., and Shi, P. M. (2011). Damage identification of derrick steel structures based on frequency and equivalent damage coefficient. *Chin. J. Eng. Mech.* 28 (9), 109–114. doi:10.6052/j.issn.1000-4750.2010.01.0037

Jia, Y. C., Jiang, T., and Liu, H. D. (2021). Stability evaluation model of toppling unstable rock based on natural vibration frequency. *J. Appl. Sci. Eng.* 24 (2), 177–184. doi:10.6180/jase.202104_24(2).0007

Jia, Y. C. (2018). *Study on stability model of slope dangerous rock block based on dynamic characteristics*. Beijing: University of Science and Technology of Beijing.

Jia, Y. C., Xie, M. W., Chang, S. X., and Lyu, F. X. (2017). A model for evaluation of stability of sliding-and falling-type dangerous rock blocks based on natural vibration frequency. *Chin. J. Rock Soil Mech.* 38 (7), 2149–2156. doi:10.19614/j.cnki.jsks.202101008

Li, B., Zhang, G., Wang, G., and Qiao, J. (2022). Damage evolution of frozen-thawed granite based on high-resolution computed tomographic scanning. *Front. Earth Sci. (Lausanne)* 760, 912356. doi:10.3389/feart.2022.912356

Liao, G. H., Wu, J. Z., and Zhang, L. A. (2016). Analysis on coupling vibration frequency characteristics of wind turbine blade rotating fatigue loading system. *Chin. J. Vib. Meas. Diagnosis* 36 (6), 1085–1090+1235. doi:10.16450/j.cnki.issn.1004-6801.2016.06.008

Ma, G. C., Sawada, K., Saito, H., Uehan, F., and Yashima, A. (2012). Study on evaluating rock block stability by using a remotely positioned laser Doppler vibrometer. *Geomate* 2 (4), 247–252. doi:10.21660/2012.4.3j

Ma, G. C., Sawada, K., Yashima, A., Uehan, F., Murata, O., and Saito, H. (2011). "Study of scale effect in rock block stability by remote vibration measurements and numerical experiments," in Proceedings of the 40th Symposium on Rock Mechanics, Committee on Rock Mechanics, Anchorage, AK, June 25–29, 2005, 339–344.

Yao, G. Z. (2016). *Vibration characteristics of falling unstable rock under different stability states*. Guizhou: Guizhou University.

Ye, Y. S., Cai, D. G., Yan, H. Y., Yao, G. Z., and Yao, J. P. (2015). Experiment study on vibration characteristics of falling unstable rock under excitation. *China Railw. Sci.* 36 (6), 16–21. doi:10.3969/j.issn.1001-4632.2015.06.03

Zhang, F. H., and He, R. (2014). Natural frequency analysis of wind turbines based on flexible multi-body dynamics. *Proc. CSEE* 34 (11), 1807–1814. doi:10.13334/j.0258-8013.pcsee.2014.11.012

Zhang, L., Niu, F. J., Liu, M. H., Ju, X., Wang, Z. W., Wang, J. C., et al. (2022). Fracture characteristics and anisotropic strength criterion of bedded sandstone. *Front. Earth Sci. (Lausanne).* 451, 879332. doi:10.3389/feart.2022.879332

frontiers | Frontiers in Earth Science

TYPE Original Research
PUBLISHED 25 July 2022
DOI 10.3389/feart.2022.923620

Check for updates

OPEN ACCESS

EDITED BY
Yan Du,
University of Science and Technology Beijing, China

REVIEWED BY
Jingshu Xu,
Beijing University of Technology, China
Fei Guo,
China Three Gorges University, China
Hao Shen,
Coffey International, Australia

*CORRESPONDENCE
Guo Yu,
547848584@qq.com

SPECIALTY SECTION
This article was submitted to Geohazards and Georisks, a section of the journal Frontiers in Earth Science

RECEIVED 19 April 2022
ACCEPTED 29 June 2022
PUBLISHED 25 July 2022

CITATION
Yu G, Bu L, Wang C and Farooq A (2022), Composition analysis and distributed assumption GIS model of normal stress on the slope sliding surface. *Front. Earth Sci.* 10:923620. doi: 10.3389/feart.2022.923620

COPYRIGHT
© 2022 Yu, Bu, Wang and Farooq. This is an open-access article distributed under the terms of the Creative Commons Attribution License (CC BY). The use, distribution or reproduction in other forums is permitted, provided the original author(s) and the copyright owner(s) are credited and that the original publication in this journal is cited, in accordance with accepted academic practice. No use, distribution or reproduction is permitted which does not comply with these terms.

Composition analysis and distributed assumption GIS model of normal stress on the slope sliding surface

Guo Yu[1]*, Lei Bu[2], Chengfeng Wang[1] and Asim Farooq[3]

[1]School of Civil Engineering and Transportation, South China University of Technology, Guangzhou, China, [2]China Coal Technology and Engineering Group Nanjing Design and Research Institute Co., Ltd., Nanjing, China, [3]Center of Excellence in Transportation Engineering, Pak Austria Facshhoule Institute of Applied Sciences and Technology, Haripur, Pakistan

For the limit equilibrium method based on the assumption model of sliding surface normal stress, the more reasonable the assumed sliding surface normal stress model is, the higher the accuracy of the calculation results will be, which is of great significance to improve the theoretical calculation accuracy. Combined with the powerful spatial data analysis ability of Geographic Information Systems (GIS), the expression of the normal stress distribution function of the slip surface is deduced by establishing a GIS-based three-dimensional slope stability analysis model and limit equilibrium equations. By analyzing the composition of the normal stress distribution on the sliding surface, the composition of the normal stress on the sliding surface is obtained, and then the assumed model of the normal stress distribution on the sliding surface is constructed. Finally, the assumed GIS model of the sliding surface normal stress distribution is verified by calculating the proportion. The model overcomes the problem that the stability factor of the slope will cause large errors in the three-dimensional state, and provides a theoretical calculation basis for the establishment of a three-dimensional slope limit equilibrium method based on the assumption of normal stress on the slip surface in GIS.

KEYWORDS

3D slope, limit equilibrium, sliding surface normal stress, GIS, grid units

1 Introduction

Limit equilibrium method is a common analysis method to analyze the stability of slope, and after years of development (Zhou and Cheng, 2013; Du et al., 2019; Du et al., 2020; Du et al., 2021), relevant theories currently have been improved and played an important role in the stability analysis method. Scholars have been exploiting the analysis method of 2D slopes into 3D slopes, for example, Hovland (1979), Hungr (1987), Cheng and Yip (2007), Low Wilson (1997). Extended the two-dimensional models of Hovland, Bishop and Janbu into three-dimensional models, but these methods all need to solve the stability factor by assuming the force between bars or columns, and it is difficult to meet

the strict calculation of static balance conditions. Later, Bell (1968), Zhu and Lee (2002), Zhu et al. (2004), Zhu et al. (2009), Yang (2004), Zheng and Tham (2010) assumed that the normal stress distribution pattern of the sliding surface is a function containing multiple dimensionless parameters, to find the stability factor. The advantage of this method is that it does not need to assume the stress and distribution between bars or columns, and the obtained stability factor is closer to the true value. However, the normal stress distribution mode assumed in this kind of method cannot truly reflect the normal stress of the slip surface, so the accuracy of the results calculated by this kind of method is not high.

At the same time, in the calculation of slope stability, GIS is more widely used because it has powerful spatial data processing abilities, as well as unique advantages in the processing of three-dimensional data, and the complex mathematical calculations and difficult algorithms encountered in the process can also be well solved in GIS (Zhou et al., 2003; Ayalew and Yamagishi, 2005). In the study of GIS combined with the limit equilibrium method, Xie et al. (2003), Xie et al. (2006a, 2006b). Extended the 2D model of Hovland, Bishop and Janbu to a 3D model based on the advantages of GIS 3D data processing and developed a 3D limit equilibrium analysis software 3DSlope. However, the establishment of the three-dimensional limit equilibrium method based on the assumption of the normal stress of the sliding surface in GIS has not been studied by scholars. The key step of this method is to establish an assumed model of the normal stress distribution of the sliding surface based on GIS. The more reasonable the assumed model is, the smaller the impacts on stability factors closer the results to the actual value.

Regarding the assumed mode of the normal stress distribution on the sliding surface, for a two-dimensional slope, the difference in the influence of different normal stress distributions on the sliding surface on the slope stability factor is about 19%. After the rationality verification of the inter stripe force distribution, the difference can be reduced to within 7%, to meet the needs of engineering. However, the influence range of three-dimensional state will be greatly increased. Therefore, establish a three-dimensional limit equilibrium method based on the normal stress of the sliding surface in GIS, it is necessary to construct a reasonable three-dimensional sliding surface normal stress assumption model based on GIS to ensure the accuracy of calculation results.

In this paper, by introducing GIS and using its spatial data analysis capability, a hypothetical model of the normal stress distribution of a three-dimensional slope sliding surface is constructed based on the grid column units. Based on GIS, a three-dimensional slope stability analysis limit equilibrium model is established, and the limit equilibrium equation for solving the stability factor is deduced according to the limit equilibrium conditions. And then under the assumption of no force, the distribution composition of normal stress on sliding surface based on the grid column units is deduced and analyzed and later a hypothetical model of the normal stress distribution of the three-dimensional symmetrical slope sliding surface based on GIS is constructed. The assumed model not only overcomes the problem of large errors in the slope stability factor in the three-dimensional state, but also provides a theoretical basis for the establishment of a three-dimensional symmetrical slope limit equilibrium method in GIS based on the assumption of sliding surface normal stress.

2 GIS-based 3D limit equilibrium model

Generally, slope data is mostly expressed in the form of two-dimensional vector data, such as ground contours, rock formations, groundwater and mechanical parameters. In GIS, these two-dimensional vector data layers can be converted into GIS-based three-dimensional grid column unit structure data layers by using the spatial analysis function. Therefore, all the data related to the slope can come from the GIS data layer. And based on the 3D grid column unit data structure of GIS, the limit equilibrium equation for 3D slope stability analysis can be established.

As shown in Figures 1A,B, a grid column unit $ABCDA_1B_1C_1D_1$ is taken in the three-dimensional slide body. For the entire slide body, the force between columns is the internal force, and the force is 0, so it is not marked in the figure. And the acting forces on the grid column mainly include: the weight of the grid column unit W; the horizontal seismic inertial force kW with k as the earthquake influence coefficient; the external force P on the slope surface; the normal total stress and shear stress on the sliding surface are respectively σ and τ; the pore water pressure u on the sliding surface.

Figure 1C shows the spatial relationship of each calculation parameter in the 3D model. On the sliding surface, according to the Mohr-Coulomb criterion:

$$F_{S3D} = \frac{c' + (\sigma - u)\tan\varphi'}{\tau} \tag{1}$$

where c' and φ' are the effective cohesion force and the effective internal friction angle, respectively, and F_{S3D} is the three-dimensional stability factor of the slide body.

According to the static force balance of the slide body, for the entire slide body, the force balance equations on the X, Y, and Z axes and a moment balance equation for a rotating axis perpendicular to the sliding direction can be established. The combined force between columns in every axis is 0, then the four equations can be expressed as:

$$X = \sum_J \sum_I \left(A\tau\cos\theta_r\cos\beta - A\sigma\sin\theta\cos\alpha - kW\right) = 0 \tag{2}$$

$$Y = \sum_J \sum_I \left(A\tau\cos\theta_r\sin\beta - A\sigma\sin\theta\sin\alpha\right) = 0 \tag{3}$$

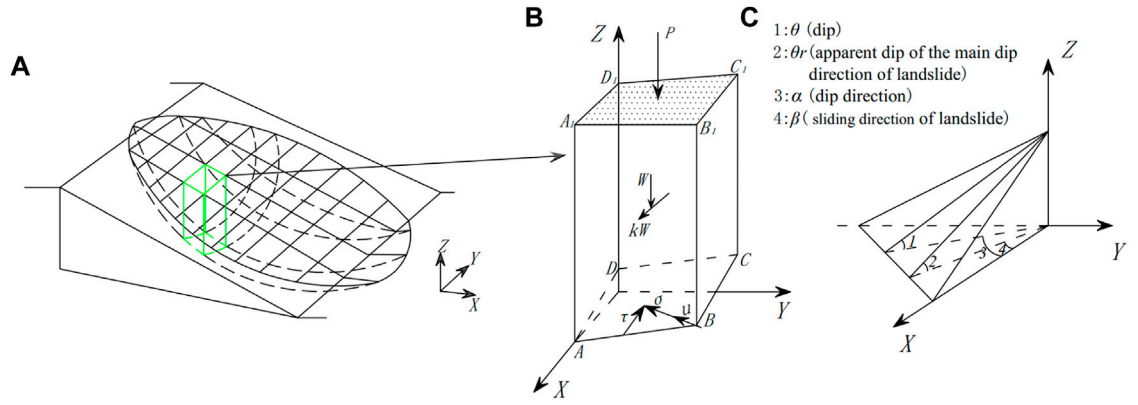

FIGURE 1
Computational modeling and three-dimensional spatial relationship. **(A)** 3D model of slide body, **(B)** typical column force analysis, **(C)** 3D spatial relationship.

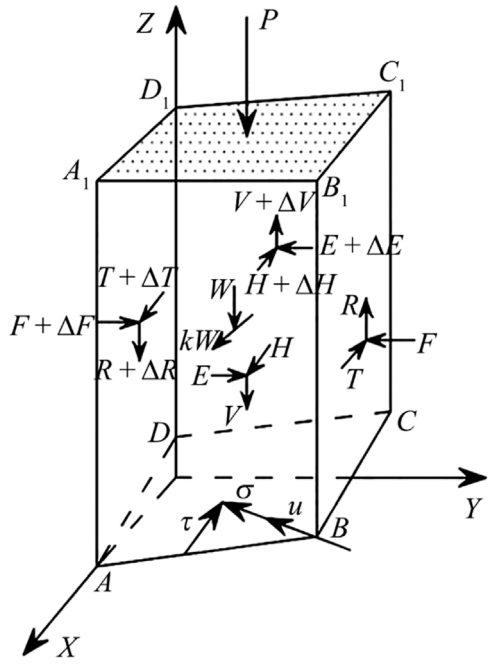

FIGURE 2
Force analysis of a single column.

$$Z = \sum_{J}\sum_{I}(A\tau\sin\theta_r + A\sigma\cos\theta - W - P) = 0 \quad (4)$$

$$M = \sum_{J}\sum_{I}[A\tau - (W + P)\sin\theta_r] = 0 \quad (5)$$

In the formula: J and I are the number of rows and columns of grid units within the slide body range; A is the sliding surface area.

Eqs 1–5 constitute the equilibrium equations for solving the three-dimensional stability factor. Under the assumption of no force, the above 5 equations are simultaneously solved to achieve the normal stress of F_{S3D} and the sliding surface of (J×I) columns, with a total of (J×I+1) unknown numbers, and the number of unknowns is more than the that of equations, hence the equations cannot be solved. If the distribution of the normal stress $^{\sigma}$ on the sliding surface can be known, it can be solved.

3 Composition analysis of normal stress distribution on sliding surface

For a single grid column unit, the forces between the columns cannot cancel each other out. Figure 2 is a schematic diagram of the force of a single column. The forces between the columns are horizontal tangential forces T and T+△T on the left and right sides of the column, vertical tangential forces R and R+△R normal Forces F and F+△F; horizontal tangential forces E and E+△E on the front and rear sides, vertical tangential forces V and V+△V, and normal forces H and H+△H. Under the assumption of no force, according to the static balance conditions of a single column, the force balance equation on the X, Y, and Z axes can be obtained as:

$$X = A\tau\cos\theta_r\cos\beta - A\sigma\sin\theta\cos\alpha - kW + \Delta T - \Delta H = 0 \quad (6)$$

$$Y = A\tau\cos\theta_r\sin\beta - A\sigma\sin\theta\sin\alpha + \Delta F - \Delta E0 \quad (7)$$

$$Z = A\tau\sin\theta_r + A\sigma\cos\theta - W - P + \Delta V - \Delta R = 0 \quad (8)$$

By eliminating $^{\tau}$ from Eqs 6–8, the normal stress distribution function of the sliding surface can be obtained as:

$$\sigma = \frac{(W+P)\cos\theta_r(\sin\beta+\cos\beta) + kW\sin\theta_r}{A\cos\theta\cos\theta_r(\sin\beta+\cos\beta) + A\sin\theta\sin\theta_r(\sin\alpha+\cos\alpha)} + \frac{(\Delta V-\Delta R)\cos\theta_r(\sin\beta+\cos\beta) - (\Delta T-\Delta H+\Delta F-\Delta E)\sin\theta_r}{A\cos\theta\cos\theta_r(\sin\beta+\cos\beta) + A\sin\theta\sin\theta_r(\sin\alpha+\cos\alpha)} \quad (9)$$

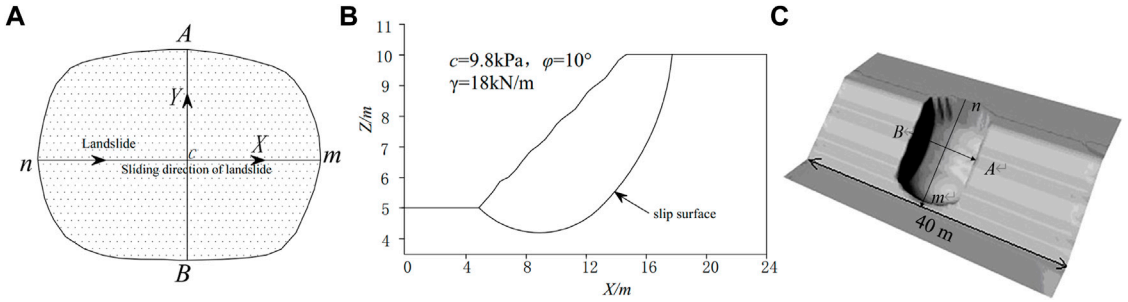

FIGURE 3
Plane and cross-section of slope. **(A)** plane of slope, **(B)** cross-section of slope, **(C)** the DEM model of slope surface.

It can be seen from Eq 9 that the distribution of the normal stress on the sliding surface can be divided into two parts, one of which is contributed by the self-weight W of the slide body and the external force P, and the other is contributed by the force between the columns, which can be denoted as $\sigma 1$ and $\sigma 2$ respectively. So, formula (9) can be simplified as:

$$\sigma = \sigma_1 + \sigma_2 \tag{10}$$

where

$$\sigma_1 = \frac{(W+P)\cos\theta_r(\sin\beta+\cos\beta)+kW\sin\theta_r}{A\cos\theta\cos\theta_r(\sin\beta+\cos\beta)+A\sin\theta\sin\theta_r(\sin\alpha+\cos\alpha)} \tag{11}$$

$$\sigma_2 = \frac{(\Delta V-\Delta R)\cos\theta_r(\sin\beta+\cos\beta)-(\Delta T-\Delta H+\Delta F-\Delta E)\sin\theta_r}{A\cos\theta\cos\theta_r(\sin\beta+\cos\beta)+A\sin\theta\sin\theta_r(\sin\alpha+\cos\alpha)} \tag{12}$$

If the sliding surface is known, all the parameters in Eq. 11 are known, so σ^1 belongs to a known function; however, because the distribution of the force between the columns cannot be accurately obtained, σ^2 belongs to an unknown function. At present, in most limit equilibrium analysis methods, certain conditions are generally assumed to solve the stability factor. For example, the Swedish strip method assumes that there is no interaction force between the blocks, the simplified Bishop method assumes that the force between the strips is only horizontal, the simplified Janbu method ignores the shear force between the bars, and the simplified Spencer method assumes that the inclination of the force between bars is a constant.

In order to study the contribution of $\sigma 1$ and $\sigma 2$ to the normal stress of the sliding surface, the distribution of $\sigma 1$ and $\sigma 2$ is calculated by a calculation example, so that the contribution of each component to the normal stress distribution can be obtained through the actual calculation data. The symmetric slope calculation example is shown in Figure 3 and this calculation example does not consider the influence of earthquake, and the size of the grid unit based on GIS is 0.5 m × 0.5 m.

For this example, the 3D slope stability analysis extension module 3DSlope, which is developed by this research team based on GIS, is used, and two methods, the extended Bishop method and the extended Janbu method based on GIS are applied. The normal stress σ of the sliding surface, as well as the sum of the two component $\sigma 1$ and $\sigma 2$ are calculated. A cross-section is drawn along the sliding direction nm of the slide body and perpendicular to the sliding direction AB of the slide body respectively, and then the results of σ、$\sigma 1$ and $\sigma 2$ are recorded in Figure 4. Due to the limitation of the three-dimensional effect, only the curves on nm and AB are shown here.

It can be concluded from Figure 4: (1) In the composition of the normal stress σ distribution of the sliding surface, the self-weight of the slide body and the external force (σ^1) make a large contribution to the normal stress of the sliding surface, while the force between the columns (σ^2) contributes very little to the normal stress of the sliding surface; (2) The normal stress of sliding surface σ、$\sigma 1$ and $\sigma 2$ are continuous and approximately smooth curves.

It can be concluded from above that: (1) For the sliding direction along the slide body, since the normal stress of the sliding surface accounts for a small proportion and is a continuous and approximately smooth curve, an appropriate function pair can be used for approximation fitting; (2) For the direction perpendicular to the sliding direction of the slide body, the normal stress distribution on the sliding surface is approximated and fitted by a parabola symmetrical along the sliding direction of the slide body.

4 Construction of the approximation distribution function of the normal stress on the sliding surface

If the sliding surface is known, in the distribution function of the normal stress σ of the sliding surface, σ^1 belongs to a known function, σ^2 belongs to an unknown function because the force between the columns is difficult to calculate, hence in order to

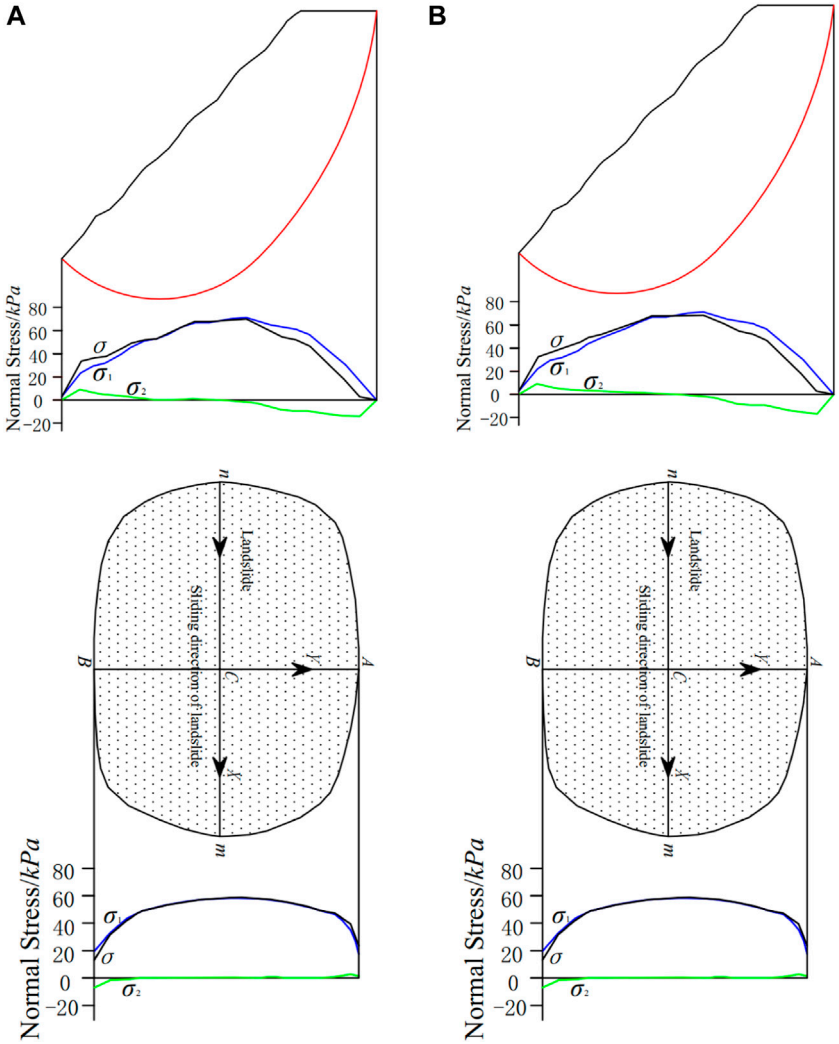

FIGURE 4
Normal stress distributions of slip surface with different calculations. **(A)** the Bishop method based on GIS (Along the sliding direction of the slide body) and (Perpendicular to the direction of the slide body); **(B)** the Janbu method based on GIS (Along the sliding direction of the slide body) and (Perpendicular to the direction of the slide body).

make Eqs 1–5 have solutions, it is necessary to construct the distribution function $^{\sigma(x,\ y)}$ in the normal stress of the sliding surface.

Figure 5 shows the assumed model of the normal stress on the sliding surface. The center of the slide body is *C*, *nm* is the long axis direction, *FR* is the short axis direction, *n* and *m* are the peak and the lowest point of the slide body respectively, and the *X*-axis direction is along the sliding surface with the *Y*-axis direction perpendicular to the sliding direction. Also, *AA* and *BB* represent the two-dimension features of the slide body respectively, and at 1/3 and 2/3 of the *X*-axis, take two points, m_1、m_2, respectively, there are:

$$m_1 = m + \frac{1}{3}(n - m) \tag{13}$$

$$m_2 = m + \frac{2}{3}(n - m) \tag{14}$$

4.1 Normal stress distribution $\sigma(x)$ along the sliding direction of the slide body

For the cross-section *nm* along the sliding direction of the slide body, it is obtained through the research in this paper that since $^{\sigma 2(x)}$ occupies a small proportion in the composition of the

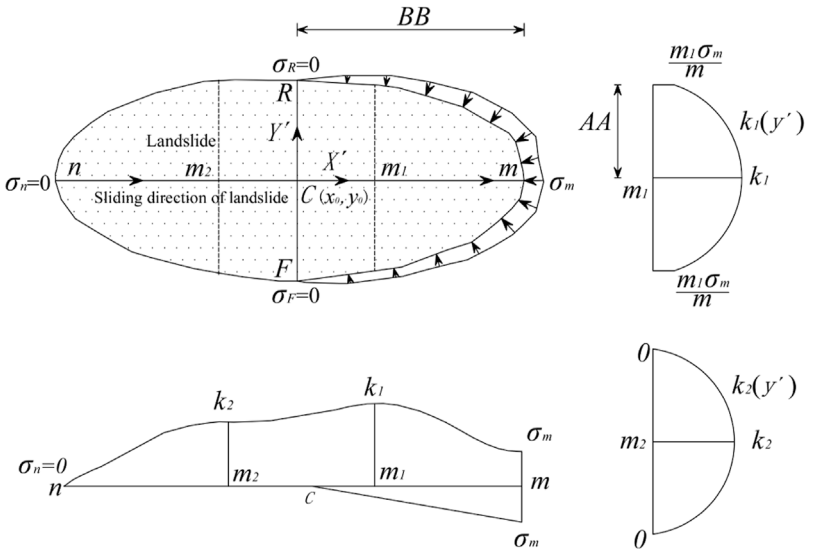

FIGURE 5
Normal stress assumption on the slip surface.

normal stress $^{\sigma(x)}$ of the sliding surface, and it is a continuous and approximately smooth curve, it can be considered that $^{\sigma 2(x)}$ can be expressed by an approximation function. Since the proportion of $^{\sigma 2(x)}$ is small, different approximation functions have little effect on the results, so that the normal stress $^{\sigma(x)}$ of the sliding surface is closer to the distribution in the strict method. Function.

Assuming that the approximation function is $\beta(x)$, so the distribution function of the normal stress of the sliding surface in the sliding direction of the slide body can be expressed as

$$\sigma(x) = \sigma_1(x) + \beta(x) \tag{15}$$

In the formula: $^{\sigma(x)}$ is the distribution function of the normal stress of the sliding surface in the sliding direction of the slide body; $^{\sigma 1(x)}$ is the component of the normal stress of the sliding surface caused by the self-weight of the slide body and the external force in the sliding direction of the slide body, which can be obtained from the formula (11) is determined and belongs to a known function.

For the approximation function $\beta(x)$, that is, based on the research of Zhu et al., over the section on the X-axis of the sliding direction of the slide body, it is assumed that the normal stress distribution of the sliding surface is a third order Lagrangian polynomial:

$$\beta(x) = k_1 g_1(x) + k_2 g_2(x) + g_3(x) \tag{16}$$

where

$$g_1(x) = \frac{(x-m)(x-n)(x-m_2)}{(m_1-m)(m_1-n)(m_1-m_2)} \tag{17}$$

$$g_2(x) = \frac{(x-m)(x-n)(x-m_1)}{(m_2-m)(m_2-n)(m_2-m_1)} \tag{18}$$

$$g_3(x) = \beta_m \frac{(x-n)(x-m_1)(x-m_2)}{(m-n)(m-m_1)(m-m_2)} + \beta_n \frac{(x-n)(x-m_1)(x-m_2)}{(n-m)(n-m_1)(n-m_2)} \tag{19}$$

In the formula: k_1 and k_2 are the dimensionless calculation parameters; x is the coordinate value of the center of the bottom surface in each grid column unit on the X axis; β_m is the corresponding part of the normal stress $^{\sigma 2}$ of the lowest point m of the slide body; β_n is the vertex n of the slide body The corresponding part of the normal stress $^{\sigma 2}$.

Since the normal stress at the boundary of the upper half of the slide body is small (Leshchinsky, 1990), it is assumed that its normal stress is 0, then $\beta_n = 0$. And assuming that the normal stress at the boundary of the lower half of the slide body is linearly distributed, that is, its normal stress is $x\ \sigma(m)/m$, then:

$$\beta_m = \sigma(m) - \sigma_1(m) \tag{20}$$

4.2 Normal stress distribution $\sigma(y)$ perpendicular to the sliding direction of the slide body

For the cross-section perpendicular to the sliding direction of the slide body, the distribution of the normal stress is approximated and fitted by a parabola symmetrical along the sliding direction of the slide body (that is, along the X axis).

Then the normal stress distribution $^{\sigma b(y)}$ of any cross-section in the lower half of the slide body and the normal stress distribution $^{\sigma a(y)}$ of any section in the upper half of the slide body are expressed as

$$\sigma_b(y) = h_1 y^2 + h_2 y + h_3 \tag{21}$$

$$\sigma_a(y) = \lambda_1 y^2 + \lambda_2 y + \lambda_3 \tag{22}$$

Considering the boundary conditions, Eqs 21, 22 can be expressed as

$$h_1 = (AA^2)^{-1}\left(\frac{x\sigma(m)}{m} - \sigma(x)\right),\ h2 = 0,\ h3 = \sigma(x) \tag{23}$$

$$\lambda_1 = -(AA^2)^{-1}\sigma(x),\ \lambda_2 = 0,\ \lambda_3 = \sigma(x) \tag{24}$$

4.3 Distribution $\sigma(x, y)$ of normal stress on sliding surface

After obtaining the normal stress distribution $^{\sigma(x)}$ along the sliding direction of the slide body and the normal stress distribution $^{\sigma}(y)$ perpendicular to the sliding direction of the slide body, for the entire sliding surface, the normal stress distribution $^{\sigma(x,y)}$of the sliding surface of any grid column unit can be expressed as

$$\left.\begin{aligned} \sigma_b(x, y) &= (AA_x^2)^{-1} y^2 \left\{\frac{\sigma(m)}{m} x - (\sigma_1(x) + \beta(x))\right\} + \\ &\quad \sigma_1(x) + \beta(x) \\ \sigma_a(x, y) &= \left\{1 - (AA_x^2)^{-1} y^2\right\}(\sigma_1(x) + \beta(x)) \end{aligned}\right\} \tag{25}$$

In the formula: $^{\sigma b(y)}$ represents the normal stress distribution of the sliding surface in the lower half of the slide body; $^{\sigma a(y)}$ represents the normal stress distribution on the sliding surface of the upper half of the slide body; AA_x is the short axis dimension corresponding to the x axis; y is the corresponding coordinate value on the Y axis.

4.4 Example verification

During the example verification, the approximation function shown in Eq 25 is used for the normal stress of the sliding surface, and the Eqs 1–5 and Eq 25 are combined together. The final four equations, after dividing and eliminating the difference, contain four unknowns (F_{S3D}、 $^{\sigma(m)}$、 k_1 and k_2), and the number of equations is equal to that of unknowns, so the three-dimensional stability factor F_{S3D} can be solved. For the specific calculation process, please refer to the calculation method proposed by this research team (Yu et al., 2019).

4.4.1 Example 1

The case shown in Figure 3 is used in combination with the proposed method to calculate, together with the GIS-based 3D Hovland method (Xie et al., 2003), 3D modification Hovland method (Xie et al., 2006a), 3D Bishop method (Xie et al., 2006b), 3D Janbu method (Xie et al., 2006b), 3D Spencer method (Low and Wilson, 1997), and 3D M-P method (Chen and Zhu, 2010), proposed. and used for comparative calculation, and the results are shown in Table 1.

From the analysis of the results in Table 1, it can be seen that.

(1) According to the classification method proposed by Deng Dongping, the 3D Hovland method, the 3D modification Hovland method, the 3D Bishop method, and the 3D Janbu method satisfy a smaller amount of equilibrium conditions, so the obtained stability factor is conservative. The method is close to the non-strict method; the Spencer method satisfies the balance conditions of the five forces and is a quasi-strict method; the M-P method satisfies the force and moment balance conditions most, and is a strict method, that is, it is the closest to the true value. And the strict method has the largest result, the quasi-strict method is the second, and the non-strict method is the smallest.
(2) Since the approximation function used by the proposed method is close to the real function, the calculation result of the proposed method is closer to the real value, that is, it is close to the strict method. Seen from the calculation result, the proposed method achieves the biggest data, close to that of the M-P method, as well as that of a strict method, which shows the rationality of the approximation function proposed in this paper.
(3) Compared with the strict method (three-dimensional Spencer method), the results of the proposed method differ by 3.2%, compared with the non-strict method (three-dimensional Bishop method) by 7.3%, and are close to the difference obtained by Deng Dongping et al. (The difference between the strict method and the quasi-strict one is 1–3.8%, and the difference is 6–12.8% compared with the non-strict method), which further shows that the calculation results of the proposed method are close to the correctness of the strict method.

4.4.2 Example 2

Figure 6 shows a slope with a weak discontinuity. The mechanical parameters of layers 1 to 4 are as follows: the effective friction angles are 35°, 25°, 30°, and 16° respectively, the effective cohesion forces are 9.8, 58.8, 19.8, and 9.8 kPa, and the unit weights are 19.6, 18.62, 21.07, and 21.07 kN/m^3. The grid unit is 0.5 m × 0.5 m. The calculation process is the same as that of calculation example 1, and the results are shown in Table 2.

Analysis of the results from Table 2:

(1) The results of the 3D Hovland method, the 3D modification Hovland method, the 3D Bishop method, and the 3D Janbu

TABLE 1 Calculation results.

Method	3D Hovland method	3D modification Hovland method	3D Bishop method	3D Janbu method	3D Spencer method	3D M-P method	The proposed method
Safety factor	1.431	1.573	1.616	1.431	1.688	1.736	1.743

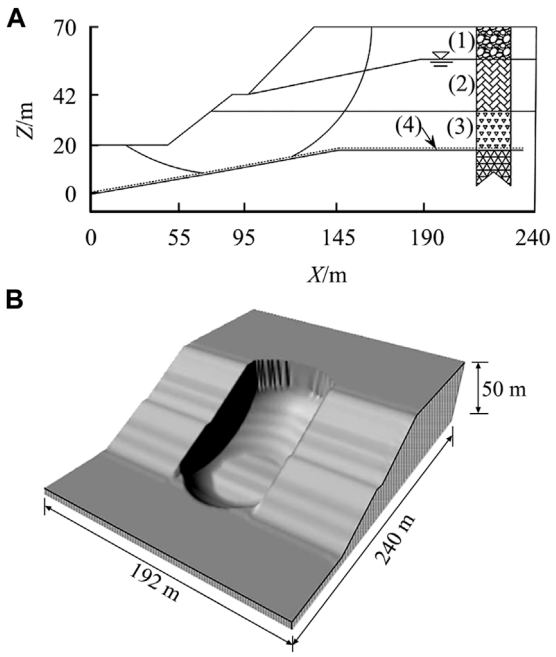

FIGURE 6
Slope example 2. **(A)** Cross section of slope, **(B)**The DEM model on the surface of the slope.

method are smaller, followed by the results of the Spencer method. The M-P method and the proposed method have the largest calculation results, and the results obtained by the strict method are the largest, followed by the quasi-strict method, and the non-strict method is the smallest.

(2) According to the calculation result, the rationality of the approximation function, that is, the calculation result of the proposed method, is close to the real value;

(3) The result of the proposed method is 2.7% different from the quasi-strict method (three-dimensional Spencer method), and 6% different from that of the non-strict method (three-dimensional Bishop method), which is like Deng Dong's (Deng and Liang, 2017). The difference obtained by equality is close, which verifies the correctness of the calculation result of the proposed method to be close to the strict method.

5 Discussion

5.1 Discussion on the advantages of GIS-based limit equilibrium method

GIS can provide a unified platform for complex and multi-source data, and all target-related data can be converted into GIS raster datasets based on columnar raster cells. Based on the GIS platform, combined with its advantages in processing complex spatial data, the limit equilibrium method can be easily extended to 3D (Carter, 1994).

For complex slope engineering problems, the factors affecting the three-dimensional stability evaluation mainly include topography, strata, geotechnical parameters, and groundwater. Due to the multi-source and complexity of these data, it is difficult to express these spatial data in the general slope stability analysis system, and GIS can provide a unified platform to process these complex spatial data.

By adding professional models to GIS, a three-dimensional slope stability analysis model based on grid-column units can be established to analyze the stability of three-dimensional slopes. The model has the advantages of simple data processing and easy programming.

5.2 Discussion on the influence of the normal stress distribution on the sliding surface on the stability factor

If the distribution pattern of the normal stress on the sliding surface has a significant influence on the stability factor, the stability factor obtained by assuming the normal stress distribution on the sliding surface is unreasonable. Therefore, it is necessary to develop a discussion of the sensitivity of the stability factor to the normal stress distribution of the sliding surface.

Lu et al. (2012) studied the influence of the two-dimensional stability factor under different assumptions of normal stress on the sliding surface through calculation examples. The research results show that the error of the two-dimensional stability factor values obtained from different normal stresses on the sliding surface is small, but the distribution curves of the normal stress on the sliding surface are completely inconsistent. It can also be concluded that the influence

TABLE 2 Calculation results.

Method	3D Hovland method	3D modification Hovland method	3D Bishop method	3D Janbu method	3D Spencer method	3D M-P method	The proposed method
Safety factor	1.006	1.096	1.114	1.018	1.151	1.179	1.185

of the normal stress distribution on the sliding surface on the two-dimensional stability factor is not significant.

In the three-dimensional state, the influence of different sliding surface normal stress distributions on the stability factor will be greatly increased, which requires constructing a reasonable sliding surface normal stress distribution. In this paper, by analyzing the composition of the normal stress of the sliding surface, an approximation function $^{\sigma(x,\ y)}$ of the normal stress distribution of the sliding surface of the symmetrical slope is constructed, and the approximation function is closer to the distribution function in the strict method. In this way, from the mathematical aspect, the problem that the normal stress of the sliding surface of the symmetrical slope has a significant influence on the stability factor is solved.

5.3 Discussion on approximation function based on grid column unit

GIS is widely used in geotechnical engineering due to its advantages in data processing and analysis capabilities. For example, GIS can not only establish the stability analysis model of a single slope, but also can establish a large-scale regional slope stability analysis model. Compared with the traditional slope stability analysis software, GIS has inherent advantages (Irigaray et al., 2003).

The advantage of the proposed method is that a reasonable three-dimensional sliding surface normal stress assumption model is constructed based on GIS, which provides a theoretical calculation basis for establishing the limit equilibrium method based on the sliding surface normal stress assumption in GIS; secondly, the approximation function constructed in this paper overcomes the influence of large error on the slope stability factor in the three-dimensional state, and makes the calculation result closer to the real value.

6 Conclusion

(1) Using the spatial data analysis ability of GIS, a GIS model of limit equilibrium for three-dimensional slope stability analysis was established, and the limit equilibrium equation for solving the three-dimensional stability factor was deduced according to the limit equilibrium conditions. Using this model, the limit equilibrium method based on the assumption of normal stress on the sliding surface can be established in GIS, and it has the advantages of simple data processing and easy programming.

(2) Under the assumption of no force, the composition of the normal stress distribution of the sliding surface based on the grid column unit is deduced and analyzed, and it is concluded that in the composition of the normal stress σ distribution of the sliding surface, the self-weight of the slide body and the external force ($^{\sigma 1}$). The contribution of the normal stress of the sliding surface is very large, while the contribution of the force between the columns ($^{\sigma 2}$) to the normal stress of the sliding surface is very small.

(3) For the normal stress distribution σ(x, y) along the sliding direction of the slide body, since the proportion of $^{\sigma 2(x)}$ is rather small in the normal stress $^{\sigma(x)}$ on the sliding surface, and it is a continuous and approximately smooth curve, it can be considered to use a third-order Lagrangian polynomial. Due to the small proportion of $^{\sigma 2(x)}$, the approximation function has little effect on the result, making the normal stress of the sliding surface more approximate to the distribution function in the strict method.

(4) For the entire sliding surface, considering the normal stress distribution $^{\sigma(x)}$ and $^{\sigma(y)}$, the approximation function $^{\sigma(x,\ y)}$ of the normal stress distribution of the sliding surface for any grid-column element of the slope can be obtained. The approximation function not only overcomes the influence of large error on the slope stability factor in the three-dimensional state, but also provides a theoretical calculation basis for establishing a three-dimensional symmetrical slope limit equilibrium method based on the assumption of normal stress on the sliding surface in GIS. The rationality of the approximation function is verified by an example.

(5) Through the verification of the case, the results calculated by the method in this paper are close to the results calculated by the strict method, which verifies that the assumed model of the normal stress of the sliding surface proposed in this paper is closer to the real value.

Data availability statement

The original contributions presented in the study are included in the article/supplementary material, further inquiries can be directed to the corresponding author.

Author contributions

GY was responsible for the ideas of the article. LB and CW was responsible for the implementation of the algorithm. AF was responsible for checking the language.

Acknowledgments

I would like to express my sincere gratitude to LB, CW, and AF for their motivation and for providing me access to their immense knowledge during this research work.

Conflict of interest

Author LB was employed by China Coal Technology and Engineering Group Nanjing Design and Research Institute Co., Ltd.

The remaining authors declare that the research was conducted in the absence of any commercial or financial relationships that could be construed as a potential conflict of interest.

Publisher's note

All claims expressed in this article are solely those of the authors and do not necessarily represent those of their affiliated organizations, or those of the publisher, the editors and the reviewers. Any product that may be evaluated in this article, or claim that may be made by its manufacturer, is not guaranteed or endorsed by the publisher.

References

Ayalew, L., and Yamagishi, H. (2005). The application of GIS-based logistic regression for landslide susceptibility mapping in the Kakuda-Yahiko Mountains, Central Japan. *Geomorphology* 65 (1/2), 15–31. doi:10.1016/j.geomorph.2004.06.010

Bell, J. M. (1968). General slope stability analysis. *J. Soil Mech. Found. Div.* 94 (SM6), 1253–1270. doi:10.1061/JSFEAQ.0001196

Carter, B. (1994). *Geographic information systems for geoscientists: Modelling with GIS.* United States: Pergamon.

Chen, C. F., and Zhu, J. F. (2010). A three-dimensional slope stability analysis procedure based on Morgenstern-Price method. *Chin. J. Rock Mech. Eng.* 29 (7), 1473–1480. doi:10.3969/j.issn.1000-6915.2013.01.016

Cheng, Y. M., and Yip, C. J. (200720071544). Three-dimensional asymmetrical slope stability analysis extension of bishop's, janbu's, and morgenstern–price's techniques. *J. Geotech. Geoenviron. Eng.* 133133 (12), 154412–161555. doi:10.1061/(asce)1090-0241(2007)133:12(1544)

Deng, D. P., and Liang, L. (2017). Three-dimensional limit equilibrium method for slope stability based on assumption of stress on slip surface. *Rock Soil Mech.* 38 (1), 189–196. doi:10.16285/j.rsm.2017.01.024

Du, Y., Lu, Y. D., Xie, M., Jia, J. L., Cong, X. M., and Wu, Y. Q. (20202020). Stability evaluation of creeping landslide considering variation of initial conditions. *Chin. J. Rock Mech. Eng.* 39 (S1), 2828–2836. doi:10.13722/j.cnki.jrme.2019.1079

Du, Y., Xie, M., Jiang, Y., Chen, C., Jia, B., and Huo, L. (2021). Review on the formation mechanism and early warning of rock collapse. *Metal. Mine* 50 (01), 106–119. doi:10.19614/j.cnki.jsks.202101008

Du, Y., Xie, M., Wu, Z. X., Liu, Q. Q., and He, Z. (20192019). Genetic mechanism about translational landslide and its safety evaluation. *Chin. J. Rock Mech. Eng.* 38 (S1), 2871–2880. doi:10.13722/j.cnki.jrme.2018.1251

Hovland, H. J. (1979). Closure to "three-dimensional slope stability analysis method". *J. Geotech. Engrg. Div.* 105 (GT5), 693–695. doi:10.1061/ajgeb6.0000806

Hungr, O. (1987). An extension of Bishop's simplified method of slope stability analysis to three dimensions. *Geotechnique* 37 (1), 113–117. doi:10.1680/geot.1987.37.1.113

Irigaray, C., Fernández, T., and Chacón, J. (2003). Preliminary rock-slope-susceptibility assessment using GIS and the SMR classification. *Nat. Hazards* 30 (3), 309–324. doi:10.1023/B:NHAZ.0000007178.44617.c6

Leshchinsky, D. (19901990851). Slope stability analysis: Generalized approach. *J. Geotech. Engrg.* 116116 (5), 8515–8867. doi:10.1061/(asce)0733-9410(1990)116:5(851)

Low, B. K., and Wilson, H. T. (1997). Probabilistic slope analysis using Janbu's generalized procedure of slices. *Comput. Geotechnics* 21 (2), 121–142. doi:10.1016/S0266-352X(97)00019-0

Lu, K. L., Zhu, D, Y., and Yang, Y. (2012). Selection of constitution and distribution model of normal stresses over slip surface of slope. *Rock Soil Mech.* 33 (12), 3741–3746.

Xie, M., Esaki, T., and Cai, M. (2006b). GIS-based implementation of three-dimensional limit equilibrium approach of slope stability. *J. Geotech. Geoenviron. Eng.* 132 (5), 656–660. doi:10.1061/(asce)1090-0241(2006)132:5(656)

Xie, M., Esaki, T., Cheng, Q., and Wang, C. (2006a). Geographical information system-based computational implementation and application of spatial three-dimensional slope stability analysis. *Comput. Geotechnics* 33 (4), 260–274. doi:10.1016/j.compgeo.2006.07.003

Xie, M., Esaki, T., Zhou, G., and Mitani, Y. (200320031109). Geographic information systems-based three-dimensional critical slope stability analysis and landslide hazard assessment. *J. Geotech. Geoenviron. Eng.* 129129 (12), 110912–111118. doi:10.1061/(asce)1090-0241(2003)129:12(1109)

Yang, M. C. (2004). Explicit solution to safety factor for general slice method. *Rock Soil Mech.* 25 (Suppl. 2), 568–573. doi:10.3969/j.issn.1000-7598.2004.z2.120

Yu, G., Xie, M. W., Zheng, Z. Q., Qin, S. H., and Du, Y. (2019). Research on slope stability calculation method based on GIS. *Rock Soil Mech.* 40 (4), 1397–1404. doi:10.16285/j.rsm.2018.0540

Zheng, H., and Tham, L. G. (2010). Improved Bell's method for the stability analysis of slopes. *Int. J. Numer. Anal. Methods Geomech.* 33 (14), 1673–1689. doi:10.1002/nag.794

Zhou, G., Esaki, T., Mitani, Y., and Mori, J. (2003). Spatial probabilistic modeling of slope failure using an integrated GIS Monte Carlo simulation approach. *Eng. Geol.* 68 (3-4), 373–386. doi:10.1016/S0013-7952(02)00241-7

Zhou, X. P., and Cheng, H. (2013). Analysis of stability of three-dimensional slopes using the rigorous limit equilibrium method. *Eng. Geol.* 160 (27), 21–33. doi:10.1016/j.enggeo.2013.03.027

Zhu, D. Y., and Lee, C. F. (2002). Explicit limit equilibrium solution for slope stability. *Int. J. Numer. Anal. Methods Geomech.* 26 (15), 1573–1590. doi:10.1002/nag.260

Zhu, D. Y., Lee, C. F., Jiang, H. D., and Kang, J. W. (2004). Solution of slope safety factor by modifying normal stresses over slip surface. *Chin. J. Rock Mech. Eng.* 23 (16), 2788–2791. doi:10.3321/j.issn:1000-6915.2004.16.023

Zhu, D. Y., Lu, K. J., Tai, J. J., and Chen, J. X. (2009). Limit equilibrium method based on numerical stress field and its application to engineering. *Chin. J. Rock Mech. Eng.* 28 (10), 1969–1975. doi:10.3321/j.issn:1000-6915.2009.10.002

frontiers | Frontiers in Earth Science

TYPE Original Research
PUBLISHED 26 July 2022
DOI 10.3389/feart.2022.901742

Check for updates

OPEN ACCESS

EDITED BY
Yan Du,
University of Science and Technology Beijing, China

REVIEWED BY
Cheng Liu,
Nanjing Forestry University, China
Xiaoping Zhou,
Chongqing University, China
Hadi Haeri,
Islamic Azad University System, Iran

*CORRESPONDENCE
Meng Lixin,
mlx336699@163.com

SPECIALTY SECTION
This article was submitted to Geohazards and Georisks, a section of the journal Frontiers in Earth Science

RECEIVED 22 March 2022
ACCEPTED 29 June 2022
PUBLISHED 26 July 2022

CITATION
Na Z, Lixin M, Laigui W and Yibin Z (2022), Numerical simulation of creep fracture evolution in fractured rock masses.
Front. Earth Sci. 10:901742.
doi: 10.3389/feart.2022.901742

COPYRIGHT
© 2022 Na, Lixin, Laigui and Yibin. This is an open-access article distributed under the terms of the Creative Commons Attribution License (CC BY). The use, distribution or reproduction in other forums is permitted, provided the original author(s) and the copyright owner(s) are credited and that the original publication in this journal is cited, in accordance with accepted academic practice. No use, distribution or reproduction is permitted which does not comply with these terms.

Numerical simulation of creep fracture evolution in fractured rock masses

Zhao Na, Meng Lixin*, Wang Laigui and Zhang Yibin

College of Mechanics and Engineering, Liaoning Technical University, Fuxin, China

The initiation, expansion, and penetration of microscopic cracks in rock is the macroscopic manifestation of creep. This paper investigates mechanical creep characteristics and fracture evolution processes in rock masses with different fracture angles, lengths, and rock bridge dip angles. Single fractures, dual parallel fractures, and fracture groups are considered. The approach comprises discrete element simulation based on continuum mechanics, utilizing the continuous and discontinuous software, GDEM. Single-fracture rock masses are characterized by a progressive fracture development mode dominated by tensile shear failure. The rate of creep and fracture magnitude both increase according to fracture length. With increasing fracture inclination angle, creep rate and fracture magnitude increase and decrease. The creep rate and degree of rupture are highest for fractures inclined at 30°. The dual-fracture rock mass exhibits both tensile crack failure and compressional shear failure. Creep rates are highest, and rupture effects are most apparent at rock bridge inclination angles of 90°. If the rock bridge is too long or too short, the stable creep stage is prolonged, but the creep acceleration stage intensifies due to interaction between fracture-bounded rock masses. The failure mode, in this case, involves collective failure by tension fractures and compressional shear. Creep rate and fracture magnitude increase with the number of fractures, which accelerates rock mass deformation to a certain extent. However, when the number of fractures reaches a certain threshold, a relatively stable structure may become established, slowing down the creep rate, especially during the creep acceleration stage. This study can provide a theoretical basis and reference for investigating the creep rupture law of rock mass engineering and the prevention and control of fractured rock mass geological disasters.

KEYWORDS

crack, creep rupture, crack growth, GDEM, structural heterogeneity

1 Introduction

The deformation and stress of the rock are affected by the time factor. Under constant load, its deformation gradually increases with time, which is called rock creep. The essence of rock creep rupture is the macroscopic manifestation of microscopic crack initiation, expansion, and penetration, mainly due to the non-uniformity of rock. Rock non-uniformity comprises both material and structural heterogeneity: the former relating to a rock's mineralogical composition and the latter corresponding to the pores, fissures, and discontinuities it contains. As a result, natural rock masses have large numbers of fractures and voids of varying sizes, defining smaller fracture-bounded rock masses with different structural forms.

A fractured rock mass is a complex engineering medium widely encountered in slope, tunnel, and cavern engineering projects. As such, there is a significant body of relevant research literature. Du Yan et al. (Du et al., 2022) summarized the development process of rock bolt support technology for slope engineering in China, and made a detailed discussion on the progress and prospect of rock bolt support for slope engineering in my country. Yang Shengqi et al. (Yang et al., 2012; Yang et al., 2014) explored the mechanical properties of fractured sandstones through uniaxial compression tests, analyzing the effect of fracture dip angle on the strength and deformation behavior of sandstone specimens containing defects. Li et al. (2005) tested crack propagation in marble specimens under uniaxial compression, finding that the critical buckling load, strain at failure, and elastic modulus were each lower in specimens with prefabricated cracks. Ren Jianxi (Ren and Hui, 2005) conducted real-time CT scanning of microscopic failure in single-fracture sandstone samples under triaxial compression. Their results showed that the failure process can be divided into stages of linear development, micro-crack initiation and propagation, rapid damage development, and post-peak accelerated damage. Rates of damage development were higher in rocks with pre-existing fractures than in initially intact rocks. Li et al. (2022) freeze-thaw granite based on high-resolution computed tomography, and the results show that the peak stress of granite decreases to different degrees with the increase of the number of freeze-thaw cycles. Xiao Taoli (Xiao et al., 2015) carried out conventional triaxial compression tests on a rectangular sample of high-strength silica fume mortar prepared with a single fracture of well-defined size and orientation. Crack propagation behavior under triaxial compression was found to relate strongly to the inclination angle of the prefabricated crack. Sun Chaoyang (Sun, 2015) investigated the peak strength under uniaxial load of similar materials containing prefabricated fractures of different angles. That study found a trend in which peak strength first decreased and then increased with the increasing fracture angle. Wu Yu et al. (Wu et al., 2021) conducted uniaxial compression tests on single-crack and double-crack rock masses, finding that single-crack examples underwent tensile shear failure. In the double-crack case, the failure mode was more complex because of interaction between the cracks, resulting in a combination of tensile fracturing and compressional shear failure.

In addition to compression tests, some scholars have conducted extensive creep experiments. Wang Yongyan et al. (Wang et al., 2018a) performed uniaxial and triaxial compression creep tests and confining pressure unloading tests on single-fracture rock specimens. They found that steady-state creep rate varied with fracture angle and proposed an equation to describe the creep. Liang Bing et al. (Liang et al., 2019) conducted uniaxial creep tests on pre-fractured diabase samples and derived a creep model for that lithology from analysis of their test data. Sun Qichao (Sun, 2018) analyzed rock deformation, energy consumption, and acoustic emission characteristics during time-delay failure under conditions of high-stress creep. They studied changes in mechanical properties, such as rock strength, after creep involving rupture features. Hu Bo et al. (Hu et al., et al.) conducted a long-term uniaxial compression creep test on a 45° single-crack red sandstone and found that the sample did not experience an accelerated creep failure stage. They established damage creep in the sample on the basis of the effective stress principle. From splitting tensile strength tests (Brazilian Tests), Wang Hui et al. (Wang et al., 2020) obtained fracture characteristics and failure mechanisms developed under the combined influence of bedding and prefabricated fractures. Zhang et al. (2022) studied the fracture characteristics of layered sandstone. They found that the failure mode and strength of layered sandstone were related to the bedding dip angle, showing obvious anisotropy. Zhao Cheng et al. (Zhao et al., 2016) used the digital image correlation method (DICM) as the basis for a systematic study of crack propagation and microscopic damage evolution in rock-like materials with different preset single cracks under uniaxial compression.

Compared with physical experimentation, numerical simulation has the advantages of low cost, fast processing, and richness of analytic results. In addition, multiple comparative experiments can be carried out on an identical numerical rock sample, thus avoiding errors caused by inevitable differences among physical samples. To validate the accuracy of test results, Zhang Shilin et al. (Zhang et al., 2016) used both uniaxial compression tests and numerical simulation to study the expansion mechanism of red sandstone fractures under different opening conditions. Through uniaxial and biaxial compression numerical experiments, Xu et al. (Xu and Li, 2017) found that rock failure initiated in the area around the fracture. By comparing laboratory creep tests on granite with discrete element numerical simulations of those test, Chen et al. (Chen and Konietzky, 2014) were able to propose some

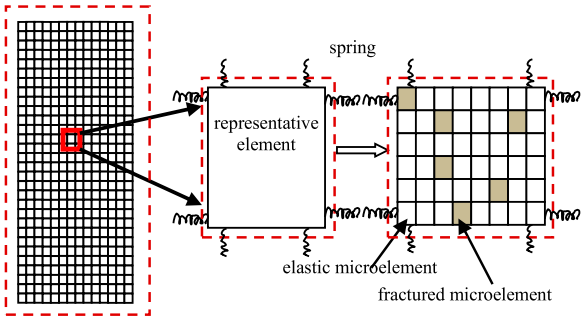

FIGURE 1
Continuous–discontinuous calculation principle.

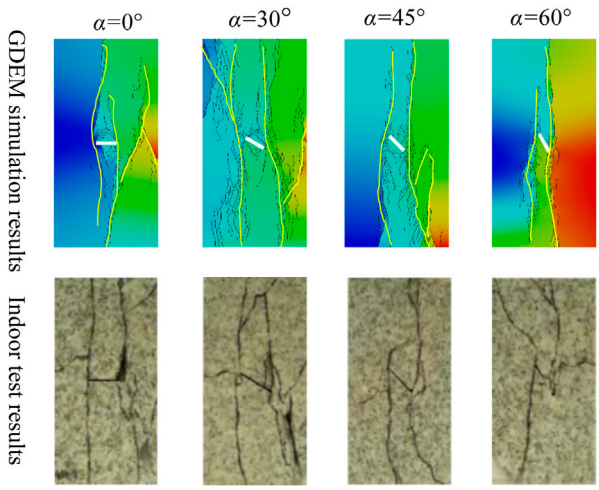

FIGURE 2
Comparison of failure morphology between GDEM simulations and laboratory test specimens.

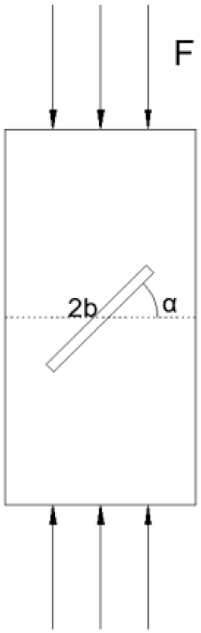

FIGURE 3
Numerical computation model.

TABLE 1 Calculation scheme.

	Crack angle (°)	Crack length (mm)
Scheme 1	0	10
	30	10
	45	10
	60	10
	90	10
Scheme 2	45	10
	45	12
	45	14

generalizations for brittle rocks. NiuJiangrui et al. (Niu et al., 2016) conducted uniaxial compression tests on fractured specimens with different degrees of opening and used the mechanical parameters the obtained in numerical simulations. Zhang Meili (Zhang, 2019) derived crack initiation stress values for rock samples with different fracture orientation, and also carried out uniaxial and multiaxial numerical tests on cross-fractured samples using Rock Failure Process Analysis (RFPA). Hu Guanghui (Hu et al., 2018) conducted uniaxial compression and uniaxial creep tests and employed discrete element modeling software (specifically PFC3D) to simulate time-dependent damage and failure processes for rocks. A combination of laboratory experiments and simulation were used to explore the creep instability mechanism for brittle rocks. Haeri et al. (Sarfarazi et al., 2017a; Sarfarazi et al., 2017b; Haeri et al., 2017; Haeri et al., 2018) conducted extensive research into fractured rock masses using the particle flow simulation method, obtaining fracture toughnesses for different model scenarios and different and external conditions. Wang Hui (Wang et al., 2015) et al. carried out an RFPA numerical simulation study of single-crack rock specimens and found that with increasing crack elongation, the peak strength of the specimen decreased.

In rock engineering, macroscopic fracture instability and failure of fractured rock bodies under prolonged stress relate directly to the distribution of internal micro-cracks and the generation, expansion, and penetration of micro-cracks during deformation. The shape of propagating cracks and the mechanical response to deformation, which vary significantly between different fractured rock masses, will

TABLE 2 Calculated mechanical parameters of the rock mass.

Material density (kg·m3)	Tensile strength (MPa)	Internal friction angle (°)	Elastic modulus (MPa)	Cohesion (MPa)	Dilation angle (°)	Poisson's ratio
2,500	3	40.0	1e4	10	10.0	0.25

TABLE 3 Mechanical parameters of the rock mass contact surface.

Normal stiffness (Pa·m)	Tangential stiffness (Pa·m)	Cohesion (MPa)	Tensile strength (MPa)	Friction angle (°)
5e13	5e13	10	0.4	30.0

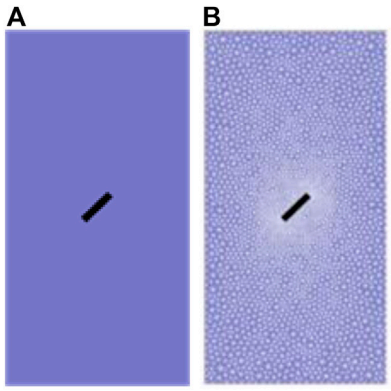

FIGURE 4
Single fracture model and meshing.

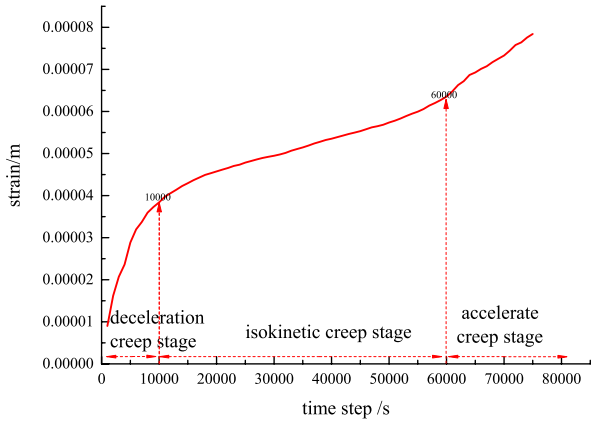

FIGURE 5
Creep deformation curve: single fracture model.

directly affect the engineering stability of the rock. Fractured rock masses can induce sliding deformation and damage to, for example, mine slopes, resulting in frequent engineering accidents and causing loss of life and property. Du Yan et al. (Du et al., 2021; Du and Xie, 2022) reviewed the research on the genesis mechanism and early warning of rock collapse disasters, and proposed a cohesive safety factor (CSF) and a relatively objective analysis method, which can effectively identify unstable rocks. It provides a relatively complete quantitative evaluation index and evaluation standard for rock collapse early warning and prevention. It is significant to study the creep instability characteristics of fractured rock masses for the early warning and prevention of geological disasters in China.

Existing studies have mainly analyzed the expansion and penetration of rock mass cracks under different loading conditions from the perspectives of experiments, theory, and numerical calculation but have not discussed the relationship between the initiation, propagation, and penetration of microscopic cracks and macroscopic creep deformation. The main innovation of the thesis is to analyze the relationship between microscopic crack propagation, penetration, and macroscopic creep deformation under different crack characteristics. At the same time, due to the difficulty in obtaining double-fissure and multi-fissure rock mass specimens, it is not easy to manufacture, and there are relatively few studies. However, the microscopic and macroscopic behavior can be effectively coupled using the continuous–discontinuous simulation software GDEM (discussed further in the next section). The creep process is simulated to explore relationships between different fracture lengths and orientations for rock masses with single fractures, different rock bridge inclination angles and lengths for rock masses with dual fractures, and between creep deformation and rupture for larger groups of fractures. A theoretical basis is provided for the study of creep rupture crack propagation, which is relevant for practical creep control of fractured rock masses.

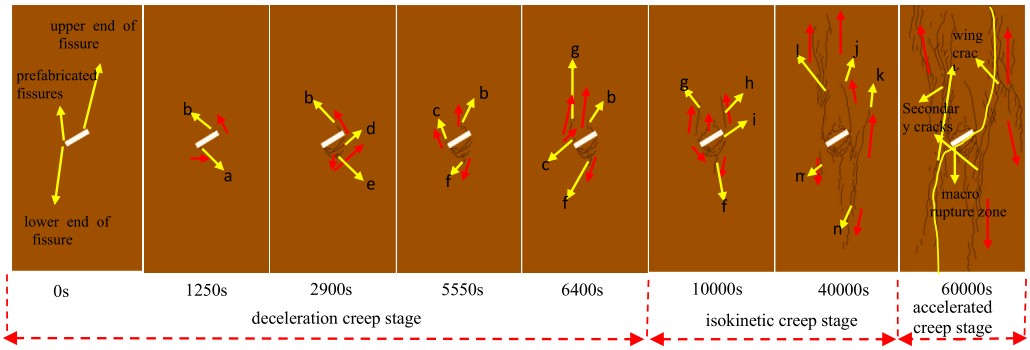

FIGURE 6
Creep rupture crack propagation in a rock mass with a single fracture.

2 Principles of deformation modeling using GDEM software

The continuous–discontinuous deformation simulation used in this study is a discrete element method based on continuum mechanics. The approach couples finite elements and discrete elements: finite element calculations are performed inside the block and discrete element calculations are performed on the block boundary. This allows simulation of material deformation and motion characteristics in both continuous and discontinuous states and can also represent progressive failure processes through that continuum.

The continuous–discontinuous model comprises elastically-coupled characterization elements composed of micro-elements. Each characterization element has a different elastic modulus because of the different fracture conditions of its constituent micro-elements (Figure 1). For a given characterization element, the elastic modulus distribution is calculated from the distribution of fracture degree within it, reflecting the microscopic heterogeneity of the rock. The connections (elastic or fractured) between characterization elements simulate the initiation, propagation, and link-up of microscopic cracks, and thus represents the evolution of macroscopic fractures during progressive rock creep and rupture.

2.1 Numerical example

As an informative example, the continuous–discontinuous software GDEM is used to simulate fracture propagation in a rock with a single pre-existing fracture under constant load. A rock mass model and uniaxial compression numerical experiment can be obtained for the same material parameters and loading stress. Different rock mass fracture patterns result from different initial fracture angles, and these can be compared with the laboratory results of Jiang Mingjing et al. (Jiang et al., 2015), as shown in Figure 2.

Laboratory experiments and GDEM numerical simulations both show that, for different initial fracture angles, α (where α denotes the angle between the crack and the horizontal):

- When α = 0°, the wing crack propagates along the prefabricated crack tip along the axial loading direction, and minor secondary cracks appear over time.
- When α = 30°, the crack initiates and expands along the prefabricated crack, and finally penetrates to form a tensile fracture. The lower end of the right wing crack extends to the right to develop a through-going secondary crack.
- When α = 45°, the crack on the right wing of the main fracture expands and penetrates. The lower right end of the prefabricated crack forms a closed triangular surface with the secondary crack.
- When α = 60°, a shear crack is initiated at the right tip of the prefabricated inclined fracture and propagates along the loading direction until it penetrates.

From this comparison, it is clear that GDEM simulations of crack growth patterns closely resemble laboratory examples, with the advantage that fracture initiation, propagation, and development directions can be more readily followed numerically. Based on this, the continuous–discontinuous deformation software GDEM appears to effective in simulating the evolution processes of rock fracture propagation.

3 Simulation of creep rupture in a rock mass with a single fracture

3.1 Computational model

To better study the details of crack propagation during rock creep, the GDEM software is first used to simulate the deformation of a rock with a single initial fracture under

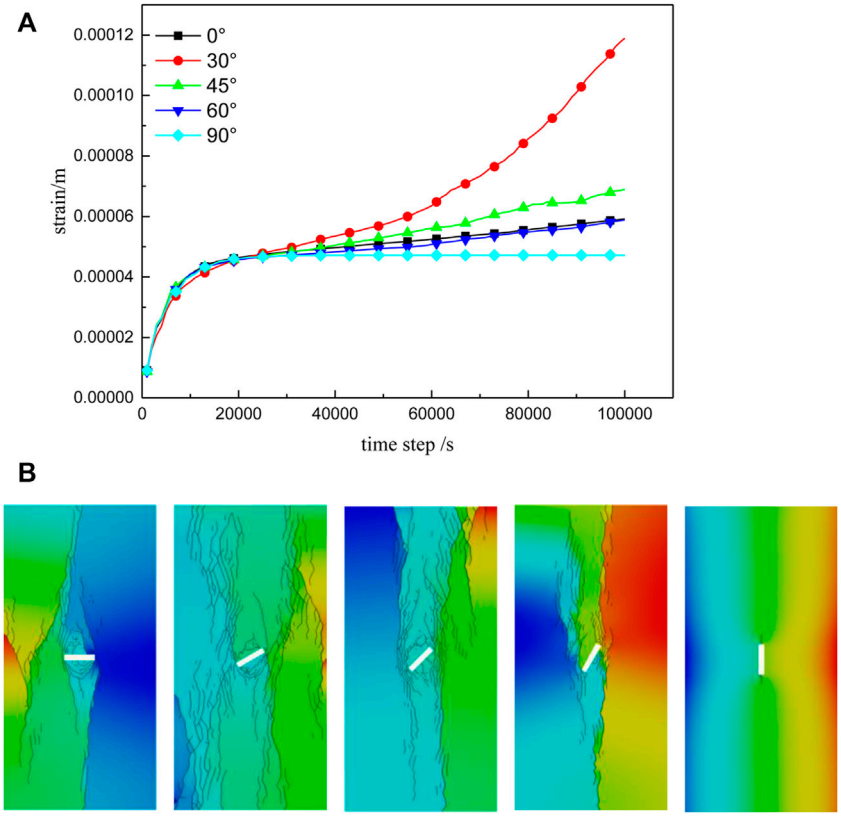

FIGURE 7
Creep curves **(A)** and fracture diagrams **(B)** for single-fracture rock masses with different fracture angles.

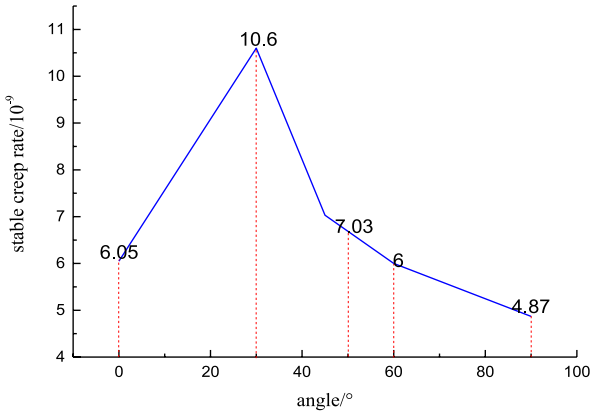

FIGURE 8
Stable creep rate of a fractured rock mass at different angles.

constant load. The analysis is repeated for different fracture lengths and inclination angles to constrain the evolution of creep crack propagation. The calculation model is illustrated in Figure 3, where α is the angle between the crack and the horizontal direction, and b is the half-length of the crack. The size of the model is 50 mm × 100 mm, and different crack angles and lengths are selected for calculation. The experimental scheme is shown in Table 1.

Based on a comparison between data collected in this study and test data for samples of the Jinping marble (Sichuan Province, China), the Mohr–Coulomb model is considered appropriate to represent the process of continuous–discontinuous deformation and rupture. Mechanical parameters are shown in Table 2.

For discrete elements or blocks of a deformable body, the normal stiffness and tangential stiffness are actually the stiffness of the contact surface. For the continuous–discontinuous model, the virtual contact surface of the element contact spring is represented by the deformable element, and the characteristic stiffness of that element is selected 10 times or 100 times to ensure continuity of contact, and to ensure that appropriate values are transferred. A spring connection is used between elements, and the constitutive model of the spring connection is a brittle fracture model (brittleMC). The material parameters are shown in Table 3. Numerical calculations are terminated

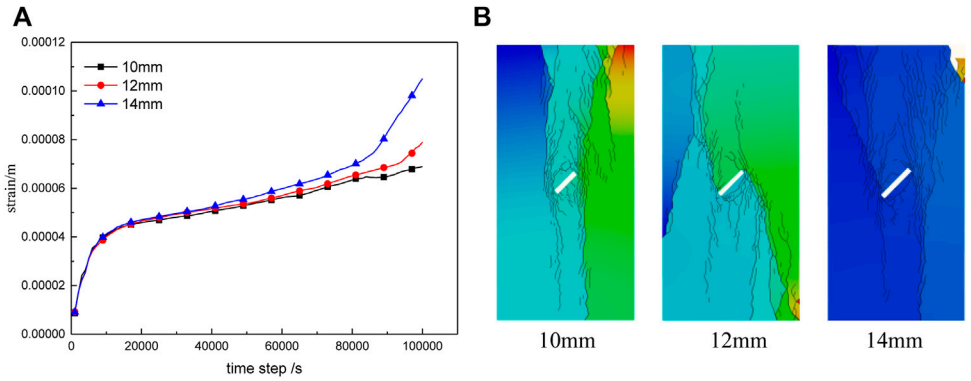

FIGURE 9
Creep curves **(A)** and rupture diagrams **(B)** for different fracture lengths.

when the rock mass develops a throughgoing fracture or if the calculation does not converge.

3.2 Evolution of rock creep rupture crack propagation

A simplified model of a single-fracture rock mass is established using GDEM, as shown in Figure 4A, where the length of the fissure is 10 mm, and the inclination angle is 30°. Elements are defined by a three-node triangular mesh. To resolve crack initiation more clearly, mesh refinement processing is performed near the crack, as shown in Figure 4B. The model has 2,786 nodes and 5,392 elements. The lower boundary of the model is fixed and the upper boundary is loaded with a surface force of 4 MPa.

It can be seen from Figures 5, 6 that, under constant load, a rock mass with single preexisting fracture develops microscopic cracks which gradually extend and expand; the macroscopic manifestation of this is creep deformation. Rock creep can generally be divided into three phases. The first, a deceleration creep stage, initially involves no new secondary cracks in the rock mass (from 0 s to 1,250 s in the simulation) but wing cracks (a and b in Figure 6) are gradually generated at the upper and lower ends of the pre-existing fracture. Midway through this stage (at 2,900 s in the simulation), crack a expands into cracks d and e (Figure 6). Subsequently (at 5,550 s), a secondary crack c initiates at the lower end of the preexisting fracture. In the second phase (from 6,400 s in the simulation), the rock mass enters the constant velocity creep stage with further crack expansion and, extension and initiation of new cracks (g and f in Figure 6). Finally, (at 60,000 s) macroscopic deformation increases as the rock mass enters the accelerated creep stage, as microcracks develop a diverging, branch-like, distribution and coalesce to form a macroscopic fracture surface. At this stage, the rock still has a certain load-bearing capacity. Beyond this, macroscopic deformation accelerates, and the creep rate gradually increases.

3.2.1 Effect of fracture angle on rock creep rupture

In this numerical experiment, a rock model with a single fracture of length 10 mm and width 2 mm is subjected to simulated uniaxial compressive creep. By varying the relative fracture angle (0°, 30°, 45°, 60°, and 90°) while maintaining the same material parameters and loading stress, the creep rupture behavior and equivalent displacement cloud map can be obtained for each angular case. Strain data for specified monitoring points can also be derived for each fracture angle through software post-processing. Figures 7, 8 show the resulting creep curves (strain curves) and stable creep rates for the rock mass with different fracture angles.

It can be seen from Figure 7 that, under constant load, creep-equivalent displacement, and macroscopic behavior when creep rupture occurs differ significantly for the different fracture angle cases. When $\alpha = 0^{\circ}$, the main deformation mode is tensile shear. Vertical wing cracks are generated, and inclined secondary cracks continue to expand and extend, but the structure is relatively stable and the degree of rupture is relatively small. For the case of $\alpha = 30^{\circ}$, wing cracks and coplanar and inclined secondary cracks are generated at the crack tip simultaneously. Cracks continue to develop, and X-type conjugate shear failure occurs through the 'prefabricated' fracture after a certain degree of expansion. For $\alpha = 45^{\circ}$, cracks initiate from the tip of the main fracture and wing cracks continue to expand until penetration rupture occurs. However, at this angle, the rupture volume around the prefabricated fracture is smaller, and the crack rupture effect is slightly weaker than that at $\alpha = 30^{\circ}$. In the case of $\alpha = 60^{\circ}$, the

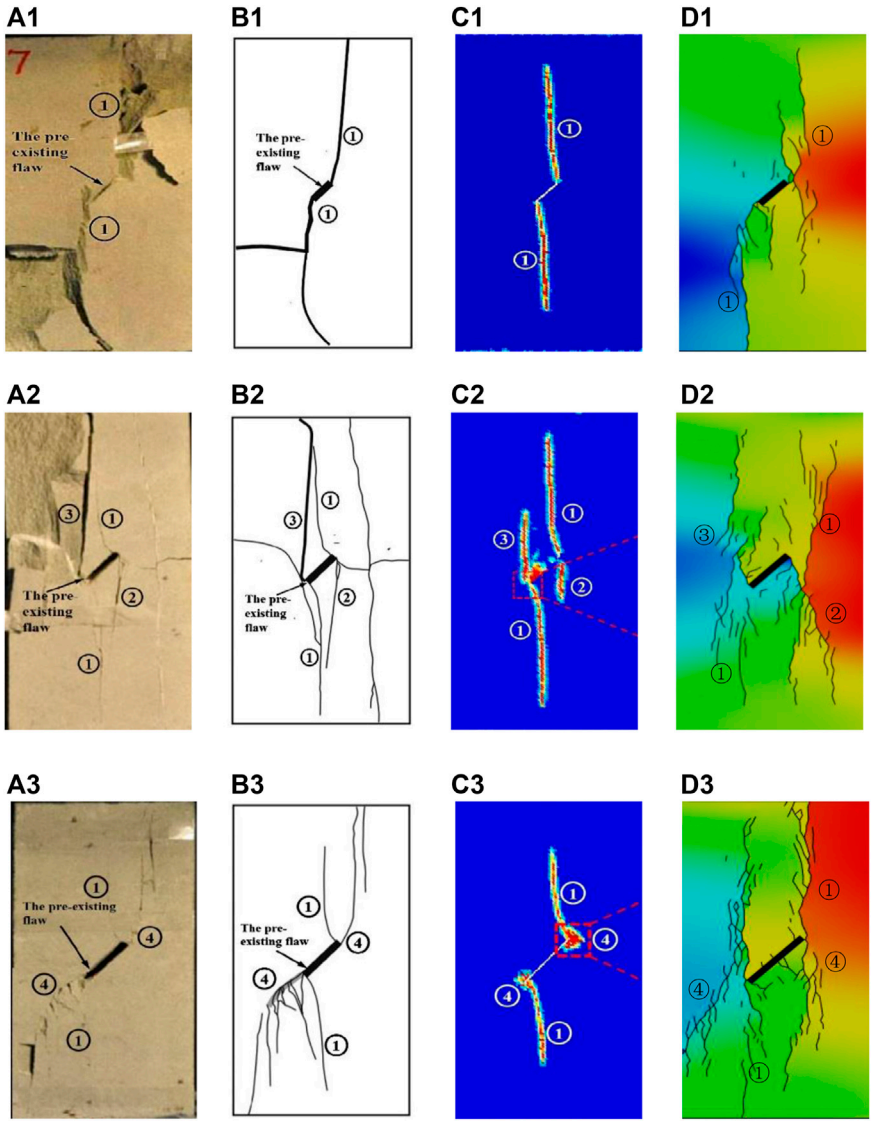

FIGURE 10
Comparison of numerical simulation results.

crack propagation effect appears to be diminished, and vertical penetration develops along the upper end of the main fracture. When $\alpha = 90^{\circ}$, the fractured rock mass forms a relatively stable structure: under load, the greatest principal stress direction is parallel to the longitudinal direction of the fracture, and crack propagation is not obvious.

From Figures 7, 8 it can be seen that, before 1,200 s, the fractured rock mass is characterized by instantaneous elastic deformation for all fracture angles. From 1,200 to 20,000 s, crack initiation occurs with different orientations but the creep curves are similar for each fracture angle; this is the deceleration creep stage. From 20,000 s, deformation enters the constant velocity creep stage. It can be seen from Figure 8 that creep rates for different fracture angles diverge significantly at this time. For $\alpha = 0^{\circ}$ creep rate is 6.05×10^{-9}/s. For $\alpha = 30^{\circ}$ the creep rate is 1.06×10^{-8}/s. For $\alpha = 45^{\circ}$, the creep rate is 7.03×10^{-9}/s. For $\alpha = 60^{\circ}$, creep rate is 6.00×10^{-9}/s. For $\alpha = 90^{\circ}$, the creep rate is 4.87×10^{-9}/s. After about 50,000 s, the case with $\alpha = 30^{\circ}$ begins to show accelerated creep as it enters the third stage (accelerated creep). When loading reaches about 60,000 s, the cases with $\alpha = 45^{\circ}$ and 60° fractures also begin to enter the accelerated creep stage. Overall, the rock mass creep rate first increases and then decreases with increasing initial fracture angle. The rate of creep is highest when the fracture inclination angle is 30°; in this case the rock mass structure is prone to rupture.

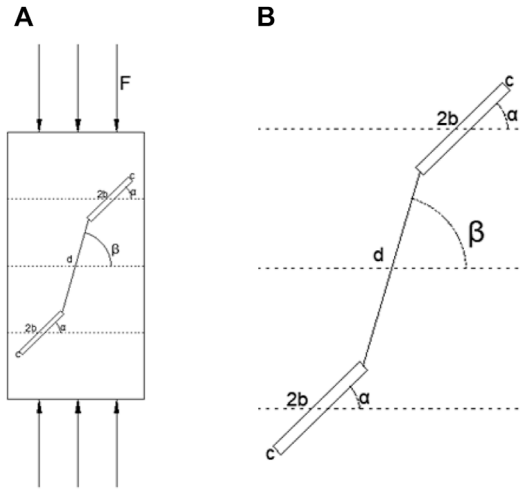

FIGURE 11
Numerical calculation model: **(A)** double-crack axial force diagram; **(B)** partial enlarged view of the rock bridge.

TABLE 4 Calculation scheme: dual parallel fractures.

	Rock bridge angle (°)	Rock bridge length (mm)
Scheme 1	30	10
	45	10
	60	10
	90	10
	135	10
Scheme 2	45	10
	45	16
	45	22

3.2.2 Effect of crack length on creep rupture

A rock mass model with a single 45° fracture of 2 mm width is simulated numerically for uniaxial compressive creep experiments in which different fracture lengths (10 mm, 12 mm, and 14 mm) are tested for constant material parameters and loading stress. Creep rupture curves for single cracks of different lengths are shown in Figure 9.

Figure 9 illustrates that, with increasing fracture length, the void volume of the rock mass enlarges, structural inhomogeneity increases, and crack propagation and rupture become more severe. Creep rate is positively correlated to crack length.

At the onset of creep, creep rates for different crack lengths are similar. When deformation enters the constant velocity stage, the creep rate becomes more obviously affected by crack length: the longer the crack, the higher the creep rate, and earlier the entry into the accelerated creep stage. Both creep rate and fracture degree increase with increasing crack length.

3.2.3 Comparison and validation of simulation results

For the numerical simulation of fractured rock masses, many researchers use peri-dynamics and related methods to determine microscopic parameters and use general particle dynamics and field enrichment finite element methods to explore scale effects (Zhou et al., 2014; Zhou et al., 2015; Bi et al., 2016; Wang et al., 2016; Wang et al., 2018b; Zhou et al., 2018; Zhou et al., 2019; Zhang and Zhou, 2020; Wang and Zhou, 2021; Zhou et al., 2021). To validate the findings this study, simulation results for single-fracture rock scenarios (lengths of 10 mm, 15 mm, and 20 mm) without mesh refinement were selected. Numerical results of Wang et al. (Wang et al., 2016) were used for the comparison, as shown in Figure 10.

It can be seen from Figure 10d1 that, when the fracture length is 10 mm, wing cracks 1) appear at both ends of the prefabricated fracture in the numerical simulation of this study. This agrees well with numerical simulations and experimental results published by

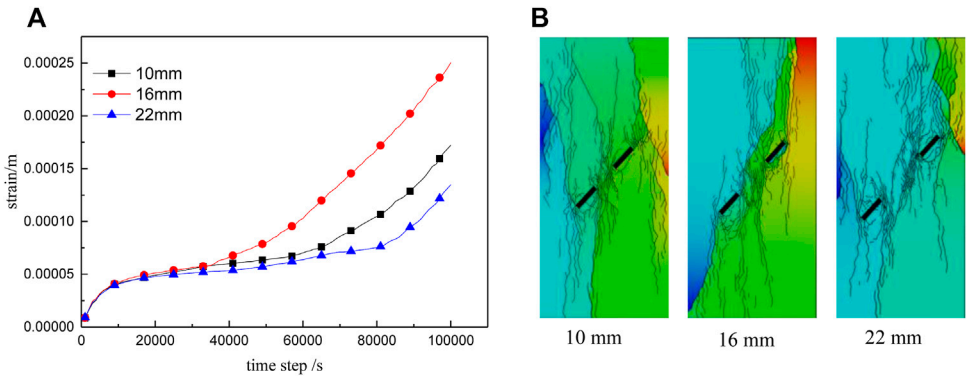

FIGURE 12
Creep curve **(A)** and rupture diagram **(B)** for fractured rock masses with different rock bridge lengths.

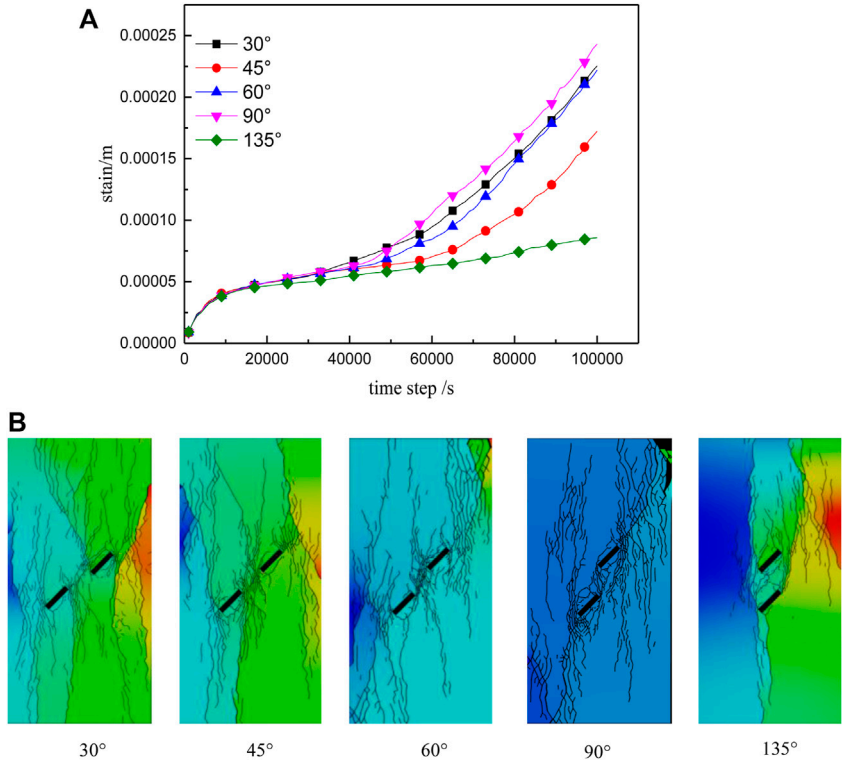

FIGURE 13
Creep curves **(A)** and rupture diagrams **(B)** for fractured rock masses with different rock bridge angles.

other scholars (Figures 10a1–c1). For a fracture length of 15 mm, the wing cracks developed in this study are directly comparable to those seen in numerical simulations and experiments of other researchers. Along the upper and lower ends of the prefabricated fracture, inclined secondary cracks 2) and tensile cracks 3) are secondarily extended, as shown in Figures 10a2–d2. When the crack length is 20 mm, the wing cracks 1) initiate and expand along the upper and lower ends of the prefabricated fracture. A coplanar secondary crack 4) propagates along the prefabricated fracture, as shown in Figures 10a3–d3. In summary, the numerical simulations from this study are in good agreement with the experiments and simulations of previous researchers. The numerical model results appear to be reliable.

4 Simulation of creep rupture in a rock mass with two parallel fractures

4.1 Parametric model for parallel double fractures

To investigate crack propagation during creep of a rock mass with two fractures, GDEM software is used to simulate crack growth under constant load. The fractures are set up to be parallel and offset. The analysis involves varying the length and inclination angle of the intervening rock bridge. The calculation model is shown in Figure 11, where b is the half-length of the fracture, c is the fracture width, α is the inclination angle between the fracture and horizontal, and β is the inclination angle between the rock bridge and horizontal. The size of the model is 50 mm × 100 mm, and different rock bridge lengths and inclination angles are selected for analysis. The calculation scheme is summarized in Table 4.

4.2 Influence of rock bridge length on creep behavior

Numerical simulations of creep in the dual-fracture model are carried out under uniaxial compression. Three different rock bridge length are simulated. Creep rupture curves are derived from the monitoring point data, as shown in Figure 12.

Rock cracks propagate from the main fracture tip and gradually expand under uniaxial compression. The failure mode is dominated by compressional shear failure, accompanied by tensile failure. Fracture modes for different rock bridge lengths are shown in Figure 12. When the rock bridge length, d, is 10 mm, the rock mass expands along the

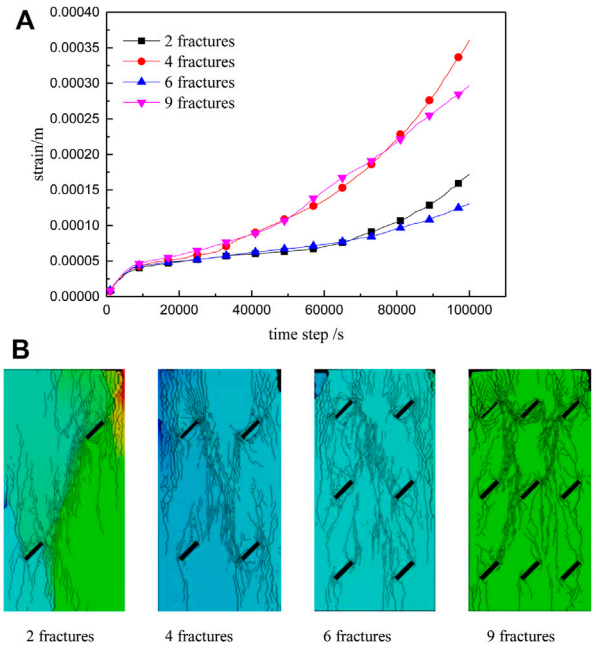

FIGURE 14
Creep curves **(A)** and rupture diagrams **(B)** for rock masses with parallel fracture sets.

fracture tips towards the loading direction, with local shear failure leading to more general fracture instability. When d = 16 mm, the failure mode involves a throughgoing (penetrative) shear fracture accompanied by a high degree of fragmentation. For the case of d = 22 mm, local shear failure occurs on the upper crack, resulting in overall instability and fracture.

As shown by the creep curve (Figure 12A), during the creep deceleration stage, the change curves for different rock bridge lengths are roughly the same. During the constant velocity creep stage, creep rates for rock bridges with d = 10 mm and d = 16 mm are greater than for the d = 22 mm case. The rock mass with the d = 16 mm rock bridge enters the accelerated creep stage earliest, at 33,000 s. The rock mass with the d = 10 mm rock bridge enters the accelerated creep stage somewhat later, at 60,000 s. The onset of accelerated creep is latest for the d = 22 mm case (80,000 s) but, after entering the accelerated creep stage, the creep rate becomes higher than in the other two cases. The length of the rock bridge clearly affects the creep of the rock mass: longer or shorter bridges prolong stable creep deformation, but ultimately lead to higher strain rates during the creep acceleration stage.

4.3 Influence of rock bridge inclination angle on the creep behavior

To assess the impact of rock bridge orientation, uniaxial compressive creep simulations are conducted for five different rock bridge inclination angles (Table 4). The resulting creep rupture curves are shown in Figure 13.

It can be seen from the creep rupture curves for the dual-fracture rock mass (Figure 13A) that when $\beta = 30^{\circ}$, the rock mass crack expands along the tip of the prefabricated fracture and exhibits conformal shear failure. When $\beta = 45^{\circ}$, the rock mass continues to expand along the wing cracks of prefabricated fracture until penetrative rupture occurs, which is shear failure. For the case of $\beta = 60^{\circ}$, cracks extend along the tips and between the fractures until penetrative rupture takes place; this is shear failure. For the simulation with $\beta = 90^{\circ}$, the rock mass expands rapidly around and at the tips of the prefabricated fracture, finally forming a macroscopic fracture, at which stage the upper right corner of the rock mass shows signs of failure and collapse. When $\beta = 135^{\circ}$, fracture propagation occurs along the lower side of the rock mass. In this case, the prefabricated fractures mainly undergo expansion, eventually forming micro-fracture zones, still dominated by shear failure.

From analysis of the creep curves (Figure 13), it is clear that different rock bridge inclinations angles have no obvious effect on the strain rate during the primary creep (deceleration) stage. The rock mass begins to enter the accelerated creep stage earliest (at 42,000 s) for the case with a 90° rock bridge dip angle. The onset of accelerated creep for the $\beta = 30^{\circ}$ and $\beta = 60^{\circ}$ cases occurs slightly later, around 50,000 s. The $\beta = 45^{\circ}$ case shows entry into the accelerated creep stage after 58,000 s. The creep rupture effect is most pronounced when the rock bridge inclination angle is 90°.

5 Simulation of creep rupture in a rock mass with a set of fractures

To progress understanding of creep in fractured rock masses, the simply fractured rock scenario is expanded to rock masses with multiple fractures. This takes the modeling closer toward real-world scenarios. The simulation experiments are initialized with stepped or en echelon sets of disconnected parallel fractures. Cases with two, four, six, and nine fractures are investigated for variations in creep behavior and influencing factors.

It can be seen from the creep rupture diagrams (Figure 14B) that, in moving from two fractures to four fractures, the degree of creep rupture increases. However, when the number of fractures increases to six, the degree of cracking is evidently lower than for four cracks. For nine fractures, the intensity of brittle deformation again becomes severe. From the creep curves (Figure 14A), it is apparent that deformation rate during the first stage of creep is roughly the same for all cases. However, with different fracture numbers, the strain of the rock mass undergoes different step changes into the second stage of creep. For the two-fracture case, the stable creep rate is 1.44×10^{-8}/s. For the four-fracture case, the creep rate reaches the maximum value of 2.24×10^{-8}/s. The rock mass with six fractures develops a creep rate of

1.50×10^{-8}/s. For the nine-fracture case, the rate is 2.23×10^{-8}/s. The models containing nine and four fractures entered the accelerated creep stage first, followed by the two-fracture case. The rock mass with six fractures also entered the third acceleration stage, but with a lower strain rate. Creep rate and degree of strain are highest for the four-fracture case, and slightly lower for the nine-fracture case. The six- and two-fracture cases showed significantly lower strain. With increasing numbers of constituent fracture-bounded rock bodies, the creep rate of the rock mass is accelerated to a certain threshold, beyond which a relatively stable structure may be formed, causing the rock mass to creep. In this way, the rate of change diminishes, especially during the third stage of creep.

6 Conclusion

This research carried out a series of numerical simulation experiments to investigate the creep evolution processes of simple fractured rock masses under loading. A combined discrete element–finite element modeling approach was adopted that used the continuous–discontinuous deformation simulation software GDEM. The following conclusions are drawn:

1) Single-fracture rock masses exhibit a progressive rupture mode dominated by tensile shear failure. The creep rate and degree of rupture increased with increasing fracture length. For $\alpha = 0^{\circ}$ the creep rate is 6.05×10^{-9}/s. For $\alpha = 30^{\circ}$, the creep rate is 1.06×10^{-8}/s. For $\alpha = 45^{\circ}$, the creep rate is 7.03×10^{-9}/s. For $\alpha = 60^{\circ}$, the creep rate is 6.00×10^{-9}/s. For $\alpha = 90^{\circ}$, the creep rate is 4.87×10^{-9}/s. With increasing fracture inclination angle, the deformation rate and intensity increase then decrease around a threshold angle of 30°, where the creep rate and rupture degree are the highest.
2) Dual-fracture rock masses exhibit tensile crack failure and compressional shear failure. When the inclination of the rock bridge between the fractures is 90°, the creep rate is at a maximum, and the rupture effect is most pronounced. A critical rock bridge length promotes early instability. For longer or shorter rock bridges, the phase of stable creep is prolonged, but creep rates during the subsequent acceleration phase are higher. The maximum strain value of the double-fractured rock mass is about twice that of the single-fractured rock mass.
3) In a loaded rock mass containing a group of fractures, an interaction effect leads to a combined failure mode involving tension fractures and compressional shear. For the two-fracture case, the stable creep rate is 1.44×10^{-8}/s. For the four-fracture case, the creep rate reaches the maximum value of 2.24×10^{-8}/s. The rock mass with six fractures develops a creep rate of 1.50×10^{-8}/s. For the nine-fracture case, the rate is 2.23×10^{-8}/s. For specific numbers of fractures, a relatively stable structure may become established, which slows down the creep rate, especially during the creep acceleration stage.

This paper reports a systematic series of numerical simulations with mechanical analysis which explore macro- and mesoscopic creep of fractured rock masses under load. These results are hoped to provide a valuable reference for research into the mechanical behavior and creep control of complex fractured rock masses.

Data availability statement

The raw data supporting the conclusions of this article will be made available by the authors, without undue reservation.

Author contributions

ZN, ML: Numerical simulation experiment design, manuscript writing; WL: Manuscript finalization; ZY: data processing.

Conflict of interest

The authors declare that the research was conducted in the absence of any commercial or financial relationships that could be construed as a potential conflict of interest.

Publisher's note

All claims expressed in this article are solely those of the authors and do not necessarily represent those of their affiliated organizations, or those of the publisher, the editors and the reviewers. Any product that may be evaluated in this article, or claim that may be made by its manufacturer, is not guaranteed or endorsed by the publisher.

References

Bi, J., Zhou, X. P., and Qian, Q. H. (2016). The 3D numerical simulation for the propagation process of multiple pre-existing flaws in rock-like materials subjected to biaxial compressive loads. *Rock Mech. Rock Eng.* 49 (5), 1611–1627. doi:10.1007/s00603-015-0867-y

Chen, W., and Konietzky, H. (2014). Simulation of heterogeneity, creep, damage and lifetime for loaded brittle rocks. *Tectonophysics* 633, 164–175. doi:10.1016/j.tecto.2014.06.033

Du, Y., Li, H., Chicas, S. D., and Huo, L. (2022). Progress and perspectives of geotechnical Anchor bolts on slope engineering in China[J]. *Front. Environ. Sci.*, 806. doi:10.3389/fenvs.2022.928064

Du, Y., and Xie, M. (2022). Indirect method for the quantitative identification of unstable rock. *Nat. Hazards* 112 (1), 1005–1012. doi:10.1007/s11069-021-05197-4

Du, Y., Xie, M., Jiang, Y., Chen, C., Jia, B., and Huo, L. (2021). Review on the formation mechanism and early warning of rock collapse[J]. *Metal. Mine* 50 (01), 106–119. doi:10.19614/j.cnki.jsks.202101008

Haeri, H., Sarfarazi, V., Yazdani, M., Shemirani, A. B., and Hedayat, A. (2018). Experimental and numerical investigation of the center-cracked horseshoe disk method for determining the mode I fracture toughness of rock-like material. *Rock Mech. Rock Eng.* 51 (1), 173–185. doi:10.1007/s00603-017-1310-3

Haeri, H., Sarfarazi, V., and Zhu, Z. (2017). Effect of normal load on the crack propagation from pre-existing joints using Particle Flow Code (PFC). *Comput. Concr.* 19 (1), 99–110. doi:10.12989/cac.2017.19.1.099

Hu, B., Yang, S., Xu, P., and Tian, W. (2019) Time-scale effect of single-fracture sandstone creep model parameters and numerical simulation of particle flow. *Chinese Journal of Geotechnical Engineering* 41 (5), 864–873.

Hu, G., Xu, T., Chen, C., and Yang, X. (2018). Microscopic creep Instability of brittle rock based on discrete element method. *Eng. Mech.* 35 (9), 26–36. doi:10.11779/CJGE201905009

Jiang, M., Zhang, N., Shen, Z., and Chen, H. (2015). Discrete element analysis of crack propagation mechanism under uniaxial compression of fractured rock mass. *Geotech. Mech.* 36 (11), 32933300+3314. doi:10.16285/j.rsm.2015.11.034

Li, B., Zhang, G., Wang, G., and Qiao, J. (2022). Damage evolution of Frozen-Thawed granite based on high-resolution computed tomographic scanning[J]. *Front. Earth Sci.*, 760. doi:10.3389/feart.2022.912356

Li, Y. P., Chen, L. Z., and Wang, Y. H. (2005). Experimental research on pre-cracked marble under compression. *Int. J. Solids Struct.* 42 (9/10), 2505–2516. doi:10.1016/j.ijsolstr.2004.09.033

Liang, B., Zhang, T., Wang, J., Li, G., and Wang, B. (2019). Creep test and model study of fractured diabase. *Exp. Mech.* 34 (2), 351–357.

Niu, J., Huang, K., Yao, C., and Yang, J. (2016). Numerical simulation of rock failure with different fissure openings under uniaxial compression. *People's Yangtze River* 47 (22), 87–91. doi:10.16232/j.cnki.1001-4179.2016.22.019

Ren, J., and Hui, X. (2005). Preliminary CT analysis of meso-mechanism of fractured rock uniaxial compression damage expansion. *Geotech. Mech.* S1, 48–52. doi:10.16285/j.rsm.2005.s1.011

Sarfarazi, V., Haeri, H., and Shemirani, A. B. (2017). Direct and indirect methods for determination of mode I fracture toughness using PFC2D. *Comput. Concr. Int. J.* 20 (1), 39–47. doi:10.12989/cac.2017.20.1.039

Sarfarazi, V., Haeri, H., Shemirani, A. B., and Zhu, Z. (2017). Shear behavior of non-persistent joint under high normal load. *Strength Mater.* 49 (2), 320–334. doi:10.1007/s11223-017-9872-6

Sun, C. (2015). Research on the influence of different fracture angles on rock mass strength. *Coal Technol.* 34 (06), 113–115. doi:10.13301/j.cnki.ct.2015.06.042

Sun, Q. (2018). *Research on mechanical properties and fracture behavior of marble under and after creep*. [D] Quanzhou: Huaqiao University.

Wang, H., Gao, Z., Meng, X., and Ying, Z. (2015). Numerical simulation of single fracture rock failure under uniaxial compression. *Coal Mine Saf.* 46 (1), 29–32. doi:10.13347/j.cnki.mkaq.2015.01.008

Wang, H., Li, Y., Cao, S., Pan, R., Yang, H., Zhang, K., et al. (2020). Brazilian splitting test study on crack propagation and macroscopic failure mode of black shale with prefabricated fractures. *Chin. J. Rock Mech. Eng.* 39 (5), 912–926. doi:10.13722/j.cnki.jrme.2019.0839

Wang, L. F., and Zhou, X. P. (2021). A field-enriched finite element method for simulating the failure process of rocks with different defects. *Comput. Struct.* 250, 106539. doi:10.1016/j.compstruc.2021.106539

Wang, Y., Zhang, J., and Zhang, Y. (2018a). Experimental study on strength properties and creep model of single-fractured rocks. *Sci. Technol. Eng.* 18 (18), 94–100.

Wang, Y., Zhou, X., Wang, Y., and Shou, Y. (2018). A 3-D conjugated bond-pair-based peridynamic formulation for initiation and propagation of cracks in brittle solids. *Int. J. Solids Struct.* 134, 89–115. doi:10.1016/j.ijsolstr.2017.10.022

Wang, Y., Zhou, X., and Xu, X. (2016). Numerical simulation of propagation and coalescence of flaws in rock materials under compressive loads using the extended non-ordinary state-based peridynamics. *Eng. Fract. Mech.* 163, 248–273. doi:10.1016/j.engfracmech.2016.06.013

Wu, Y., Ren, X., Zhang, J., Gao, Y., and Zhang, Z. (2021). Numerical experimental study on uniaxial compression of rock with fractures. *J. China Three Gorges Univ. Nat. Sci. Ed.* 43 (02), 35–41. doi:10.13393/j.cnki.issn.1672-948x.2021.02.007

Xiao, T., Li, X., and Jia, S. (2015). Triaxial compression test study on failure characteristics of prefabricated fractured rock samples with two discontinuous penetrations. *Chinese Journal of Rock Mechanics and Engineering* 34 (12), 2455–2462. doi:10.13722/j.cnki.jrme.2014.1443

Xu, J., and Li, Z. (2017). Damage evolution and crack propagation in rocks with dual elliptic flaws in compression. *Acta Mech. Solida Sin.* 30 (6), 573–582. doi:10.1016/j.camss.2017.11.001

Yang, S. Q., Jing, H. W., and Xu, T. (2014). Mechanical behavior and failure analysis of brittle sandstone specimens containing combined flaws under uniaxial compression. *J. Cent. South Univ.* 21 (5), 2059–2073. doi:10.1007/s11771-014-2155-5

Yang, S., Liu, X., and Li, Y. (2012). Experimental analysis of mechanical properties of sandstone with holes and fissures under uniaxial compression. *Chin. J. Rock Mech. Eng.* 31 (S2), 3539–3547.

Zhang, J. Z., and Zhou, P. (2020). AE event rate characteristics of flawed granite: From damage stress to ultimate failure. *Geophys. J. Int.* 222 (2), 795–814. doi:10.1093/gji/ggaa207

Zhang, L., Niu, F., Liu, M., Ju, X., Wang, Z., Wang, J., et al. (2022). Fracture characteristics and anisotropic strength criterion of bedded sandstone[J]. *Front. Earth Sci.*, 451. doi:10.3389/feart.2022.879332

Zhang, M. (2019). *Numerical simulation of mechanical behavior characteristics of cross-fractured rock mass*. Dalian: Dalian University of Technology.

Zhang, S., Du, Y., Li, T., Zhang, G., and Liu, Q. (2016). Study on the propagation mechanism of three-dimensional transparent fractures in red sandstone with different opening degrees under uniaxial compressive loading. *J. Xi'an Univ. Sci. Technol.* 7 (4), 548–553. doi:10.13800/j.cnki.xakjdxxb.2016.0415

Zhao, C., Liu, F., Tian, J., and Song, T. (2016). Study on single crack propagation and damage evolution law of rock based on uniaxial compression test. *Chin. J. Rock Mech. Eng.* 35 (A02), 3626–3632. doi:10.13722/j.cnki.jrme.2015.1270

Zhou, X., Jia, Z., and Wang, L. (2021). A field-enriched finite element method for brittle fracture in rocks subjected to mixed mode loading. *Eng. Analysis Bound. Elem.* 129, 105–124. doi:10.1016/j.enganabound.2021.04.023

Zhou, X. P., Bi, J., and Qian, Q. H. (2015). Numerical simulation of crack growth and coalescence in rock-like materials containing multiple pre-existing flaws. *Rock Mech. Rock Eng.* 48 (3), 1097–1114. doi:10.1007/s00603-014-0627-4

Zhou, X. P., Cheng, H., and Feng, Y. F. (2014). An experimental study of crack coalescence behaviour in rock-like materials containing multiple flaws under uniaxial compression. *Rock Mech. Rock Eng.* 47 (6), 1961–1986. doi:10.1007/s00603-013-0511-7

Zhou, X. P., Zhang, J. Z., Qian, Q. H., and Niu, Y. (2019). Experimental investigation of progressive cracking processes in granite under uniaxial loading using digital imaging and AE techniques. *J. Struct. Geol.* 126, 129–145. doi:10.1016/j.jsg.2019.06.003

Zhou, X. P., Zhang, J. Z., and Wong, L. N. Y. (2018). Experimental study on the growth, coalescence and wrapping behaviors of 3D cross-embedded flaws under uniaxial compression. *Rock Mech. Rock Eng.* 51 (5), 1379–1400. doi:10.1007/s00603-018-1406-4

frontiers | Frontiers in Earth Science

TYPE Original Research
PUBLISHED 26 July 2022
DOI 10.3389/feart.2022.929825

Check for updates

OPEN ACCESS

EDITED BY
Yan Du,
University of Science and Technology Beijing, China

REVIEWED BY
Xiaodong Fu,
Institute of Rock and Soil Mechanics (CAS), China
Man Hu,
Southwest University, China

*CORRESPONDENCE
Guo Yu,
yuguob@scut.edu.cn

SPECIALTY SECTION
This article was submitted to Geohazards and Georisks, a section of the journal Frontiers in Earth Science

RECEIVED 27 April 2022
ACCEPTED 27 June 2022
PUBLISHED 26 July 2022

CITATION
Jia Y, Song G, Jiang T, Yu G, Liu H and Pan X (2022), Buried depth calculation of the slope of the unstable rock based on natural vibration frequency. *Front. Earth Sci.* 10:929825. doi: 10.3389/feart.2022.929825

COPYRIGHT
© 2022 Jia, Song, Jiang, Yu, Liu and Pan. This is an open-access article distributed under the terms of the Creative Commons Attribution License (CC BY). The use, distribution or reproduction in other forums is permitted, provided the original author(s) and the copyright owner(s) are credited and that the original publication in this journal is cited, in accordance with accepted academic practice. No use, distribution or reproduction is permitted which does not comply with these terms.

Buried depth calculation of the slope of the unstable rock based on natural vibration frequency

Yanchang Jia[1], Guihao Song[1], Tong Jiang[1], Guo Yu[2]*, Handong Liu[1] and Xuwei Pan[1]

[1]North China University of Water Resources and Electric Power, Zhengzhou, China, [2]South China University of Technology, Guangzhou, China

The instability of the slope of the unstable rock poses a great threat to the safety of engineering and people's lives and properties. The buried depth of an unstable rock is a key factor affecting its stability. It is difficult to directly measure the buried depth of the unstable rock. Therefore, it is of vital importance to indirectly and quickly identify the buried depth of the unstable rock. Assuming that the foundation soil is homogeneous and isotropic, the damping ratio is less than 1; it can be found that the deformation is linear elastic deformation within the amplitude range, and the unstable rock vibration model is simplified to a multi-degree-of-freedom vibration model. Through theoretical derivation, the quantitative relationship between the rock mass, foundation reaction force coefficient, rock burial depth, and the natural vibration frequency in the horizontal direction is established. The quantitative relationship was verified to be correct by laboratory tests. From the tests, the relationship is verified and shows that with the increasing buried depth of the unstable rock, its natural vibration frequency increases nonlinearly in the horizontal direction and also acts in a weakening growing trend; the mass of the unstable rock is a monotonically decreasing function of the natural vibration frequency, and it decreases by a one-half square with the increasing mass of the unstable rock. The research results can calculate the buried depth by measuring the vibration frequency of the unstable rock, which provides a new idea and theoretical basis for the stability evaluation of the slope of the unstable rock and the rapid identification and monitoring of the unstable rock.

KEYWORDS

vibration frequency, buried depth calculation, stability evaluation, monitoring, slope of the unstable rock

Introduction

Unstable rocks on high and steep slopes are unstable due to natural or human factors such as rainfall, earthquakes, and vibrations, and the unstable rocks roll at high speed under the action of their gravity, which brings great threats to the safety of engineering and people's lives and properties (Chen, 2014). In recent years, there have been frequent reports that the instability of unstable rocks on high and steep slopes has caused traffic jams and casualties. On 3 August 2014, an earthquake measuring 6.5 on the Richter scale occurred in Ludian, Yunnan Province, and a large number of super-large unstable rocks were accumulated on both sides of the main traffic road leading to the epicenter. After this earthquake, some of the unstable rocks rolled down the road, causing traffic jams (Yin et al., 2016). On 29 May 2012, an unstable rock disaster occurred after the rain on the slope of the Shimian-Luding Highway. The giant unstable rock hit the bus, causing the driver's death. Therefore, it is of great significance to study the stability of unstable rocks. At present, scholars mainly focus on the research of Motion Characteristics Study (Cheng and Su, 2014; Xu et al., 2019), Impact Load Study (He et al., 2008; Wang et al., 2013), Dynamic Response Study (He et al., 2011), Risk Assessment Research (Zhang et al., 2005), and unstable rock protection research (Zhao and Liu, 2005; Yu et al., 2010), and the research results interpret the process of unstable rock movement, movement characteristics, existing risks, and possible hazards, which have important theoretical and guiding significance for the protection and management of unstable rocks. However, the impact energy of unstable rocks is relatively large, so the engineering measures of unstable rock protection and treatment require a lot of human and financial resources, so the passive protection and treatment of unstable rocks are expensive. This study can provide a certain theoretical basis to actively and quickly identify unstable rocks, evaluate their stability and monitor them.

The methods to evaluate unstable rock stability are divided into qualitative stability evaluation methods, quantitative numerical simulation methods, and limit equilibrium methods (Du et al., 2022). Fu et al. (2013) used the block theory to conduct quantitative statistics on the positioned block, the semi-positioned block, and the random block. Dong et al. (2012) according to the three first-level indexes like the hazard resource itself, the slope and the triggering factors, selected 9 second-level indexes corresponding to the first-level ones and 32 basic indexes and established an assessment system of the slope hazard source and degree. Yuan et al. (2011) analyzed and studied the development characteristics of the slope of unstable rocks in the Shuangjiangkou Hydropower Station, classified the stability, and put forward specific preventive measures in consideration of the topography, geology, construction, and other conditions. Yang et al. (2017) used the limit equilibrium method to quantitatively study the stability of the unstable rock of the unstable rock mass in the upper part of the Yufeng rock in the Wenchuan area of Sichuan Province, and the results show that the rainstorm condition mainly attributes to the instability of rolling rock in the unstable rock mass. (Liu et al., 2017) realized the quantitative evaluation of unstable rock stability through force points. (Zhang, 2017) monitored the blasting vibration frequency and the vibration speed of the slope of unstable rocks centroid near the tunnel, and evaluate the stability of the on-site unstable rocks. The results show that due to the differences in rock structure and joints in different directions, the vibration velocity peaks, K values, and α coefficients of the unstable rocks in the *X*, *Y*, and *Z* directions are also significantly different. Zhang et al. (2022) studied the fracture characteristics and anisotropic strength criterion of the structural plane of bedded sandstone through experiments. By using high-resolution computed tomographic scanning, Li et al. (2022) evaluated the damage of freeze-thaw granite. According to the results of (Huang and Liu, 2009), they found that the buried depth of unstable rocks has a particularly significant effect on the recovery coefficient of collision velocity, but there is no quantitative research on the impact of burial depth on the stability of unstable rocks. At present, most scholars assume that the burial depth of unstable rocks is zero, and the calculated safety factor is small. Therefore, it is of great significance to study the burial depth for calculating the stability of rolling stones.

The aforementioned qualitative research methods are difficult to quantitatively evaluate the stability of unstable rocks. The limit equilibrium method and numerical simulation method can realize the quantitative stability evaluation of unstable rocks, but the important factors affecting the stability of unstable rocks, buried depth of unstable rocks, are difficult to obtain directly. With the development of technology, a method for evaluating the stability of unstable rocks based on dynamic characteristic parameters has appeared in recent years. This method judges the stability of unstable rocks through the change of dynamic characteristic parameters. Japanese scholar Fujisawa (2007) studied the dynamic characteristics of the slip-type unstable rock and found that the particle trajectory and amplitude of the stable rock mass are much smaller than those of the unstable rock mass. Ma et al. (2012) further tested and concluded that the vibration frequency is closely related to the bonding state, and the bonding area is positively correlated with the vibration frequency. Ma et al. (2011) found that the vibration frequency of the unstable rock is closely related to the bonding area and quality. Du et al. (2016) further studied the slip-type unstable rock on the single-slip surface and realized their stability evaluation based on the vibration frequency. Yin et al. (2016) and Yao et al. (2015) established a stability evaluation model

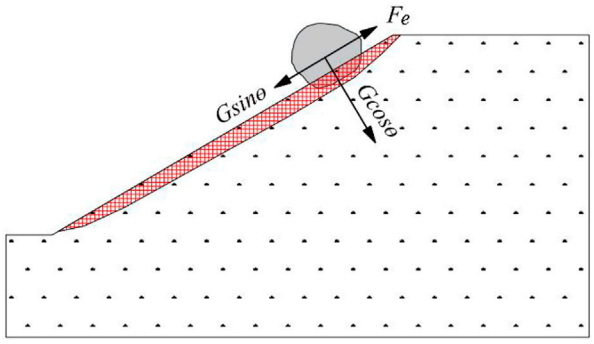

FIGURE 1
Force acting on the slope of the unstable rock.

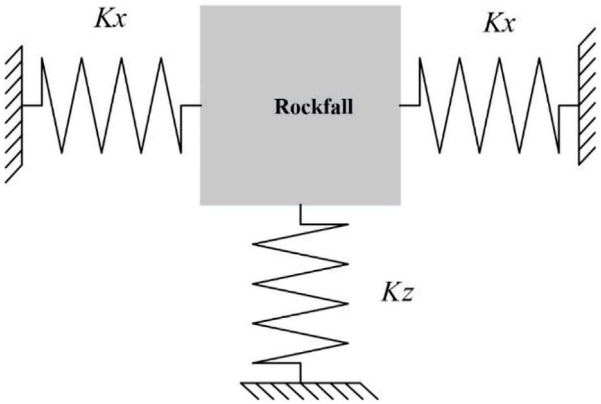

FIGURE 2
Dynamic characteristic model of the slope of the unstable rock.

based on dynamic characteristic parameters for falling unstable rocks. Du et al. (2021) found that natural vibration frequency and other dynamics scientific indicators have obvious application advantages in the rock bridge damage analysis, rapid identification of dangerous rocks, and early warning of collapse. Du et al. (2022), Du et al. (2020), and Du et al. (2017) experimental study finds that the incompatible weakness of the structural plane is a necessary condition for the occurrence of rock burst, and the spatiotemporal difference of the structural plane strength is the main factor that determines the immediate or the time-delayed rock burst. Slow weakening of the structure causes time-delayed rock burst, whereas rapid weakening causes immediate rock burst. Jia et al. (2021), Jia, (2018), and Jia et al. (2017) obtained the fact that the dynamic characteristic parameters of unstable rock like fall type, topping type, and slip type, change with the laws of structural damage through experiments and theoretical analysis, and realized the quantitative stability assessment and monitoring and alarming of unstable rock of fall type, topping type, and slip type based on vibration frequency.

Although the stability evaluation method of unstable rocks based on dynamic characteristic parameters has the advantages of convenience, high efficiency, and accuracy, the current research mostly focuses on the dynamic characteristics of unstable rocks, and there are few reports on how to realize the stability evaluation of unstable rocks based on dynamic characteristic parameters. Taking the slope of unstable rocks as the research object, this study, through theoretical deduction, establishes the quantitative relationship between the unstable rock mass, the coefficient of subgrade reaction, the buried depth of unstable rocks, and the natural vibration frequency in the horizontal direction, and realizes the quick calculation of the buried depth based on the natural vibration frequency so as to verify the correctness of the theoretical model by laboratory experiments. This research study can provide new ideas and a theoretical basis to assess the slope of unstable rocks and quickly identify and monitor unstable rocks.

Slope of unstable rocks

The unstable rock refer to the rock mass that is separated from the parent body, stays on the slope body, and moves downward directly or indirectly under the interference of factors such as rainfall, vibration, geological disasters, freeze-thaw cycles, wind action, animal activities, etc. Unstable rocks tend to have the characteristics of high-speed movement and high-impact energy. In addition to triggering factors, the occurrence of unstable rocks is also related to factors such as the slope conditions where unstable rocks are located, their properties of themselves, and their buried depth. Figure 1 is a schematic diagram of the force acting on the slope of unstable rocks, where G is the gravity, N; θ is the slope angle, °; Gsinθ is the downward component of the unstable rock gravity along the slope, N; Fe is other external forces, including friction, soil pressure, water pressure, etc.

Dynamic characteristic model of the slope of unstable rocks

Under the interference of trigger factors, the unstable rock vibrates. Assuming that isotropic soil is homogeneous in all directions, the damping ratio is less than 1, and the deformation is linear elastic deformation within the amplitude range, the unstable rock vibration model can be simplified to a multi-degree-of-freedom vibration model. See Figure 2.

According to the dynamics theory, when the unstable rock slope is disturbed by an external force, it vibrates along the slope. Assuming that the distance from the origin at a certain moment

is x, the horizontal stiffness of the soil layer is K_x, and according to Newton's second law, the mechanical balance Eqs 1, 2 of the horizontal direction of the unstable rock are obtained (Jia et al., 2017):

$$M\ddot{x} = -K_x x, \tag{1}$$

$$p^2 = K_x/M. \tag{2}$$

Then the undamped free vibration equation of the slope of unstable rocks in Eq. 3.

$$\ddot{x} + p^2 x = 0. \tag{3}$$

The equation is solved as

$$x = e^{xt}. \tag{4}$$

Substitute the solution into Eq. 3 to obtain the equation roots and characteristic equations:

$$s_{12} = \pm ip, \tag{5}$$

$$s^2 + p^2 = 0. \tag{6}$$

The general solution of the equation is further obtained as follows:

$$x = C_1 e^{ipt} + C_2 e^{-ipt}. \tag{7}$$

By applying Euler's formula, the aforementioned formula can be rewritten as

$$x = C\cos pt + D\sin pt. \tag{8}$$

C and D are integration constants whose magnitudes are determined by the initial conditions of the motion. When $t = 0$ is set, substitute $x = x_0, \dot{x} = \dot{x}_0$ into the aforementioned formula to get

$$C = x_0,\ D = \dot{x}_0/p, \tag{9}$$

$$x = x_p \cos pt + \sin pt\dot{x}/p. \tag{10}$$

Through trigonometric transformation, the aforementioned formula can be rewritten as

$$x = A\sin(pt + \alpha), \tag{11}$$

where

$$A = \sqrt{x_0^2 + \left(\frac{\dot{x}_0}{p}\right)^2},\ \alpha = tg^{-1}\frac{px_0}{\dot{x}_0}. \tag{12}$$

The vibration period of the system is

$$T = 2\pi/p = 2\pi\sqrt{M/K_x}. \tag{13}$$

The vibration frequency of the system is

$$f = 1/T = \frac{1}{2\pi}\sqrt{\frac{K_x}{M}}. \tag{14}$$

The stiffness coefficient is a basic physical quantity used to describe the elastic deformation form of the material under the action of external force. The relationship between the stiffness coefficient K_x and the coefficient of subgrade reaction k is formula (15):

$$K_x = khb. \tag{15}$$

Combining Eqs 14, 15, the natural vibration frequency in the horizontal direction of the unstable rock is obtained as Eq. 16:

$$f = \frac{1}{2\pi}\sqrt{\frac{khb}{M}}. \tag{16}$$

Considering the influence of the unstable rock height and the width ratio along the vibration direction on the natural vibration frequency of unstable rocks, and when there is weak damping, the unstable rock block on the slope overcomes the damping force to do work, the amplitude decreases with time, and the mechanical energy of the system is converted into thermal energy and dissipated until the system stops vibrating. Then formula (16) can be transformed into formula (17)

$$f_d = \frac{\sqrt{1-\xi^2}}{2\pi}\sqrt{\frac{\left(\frac{a}{H_s}\right)^2}{\left(\frac{a}{H_s}\right)^2 + 1}}\sqrt{\frac{khb}{M}}, \tag{17}$$

where f_d is the natural vibration frequency of the damped system (Hz); ξ is the damping ratio of the system (unitless); K_x is the stiffness coefficient of the foundation soil, N/m; k is the coefficient of subgrade reaction of the foundation soil, N/m^3; a is the length of the unstable rock along the vibration direction, m; b is the unstable rock length in the vertical vibration direction, m; M is the mass of the unstable rock, kg; h is the buried depth of the unstable rock, m; H is the height of the unstable rock, m; H_s is the height of the unstable rock on the ground, m.

TABLE 1 Performance indexes of the microchip cube.

Parameter	Minimum	Maximum	unit
Range	−5.0	+5.0	g
Sampling ratio	5.0	800	Hz
Resolution	0.50	—	μg

Model test

Test equipment

1) Vibrometer

In the test, the wireless vibrometer of Beijing Beike Andi Technology Development Co., Ltd. - Microchip Cube was used.

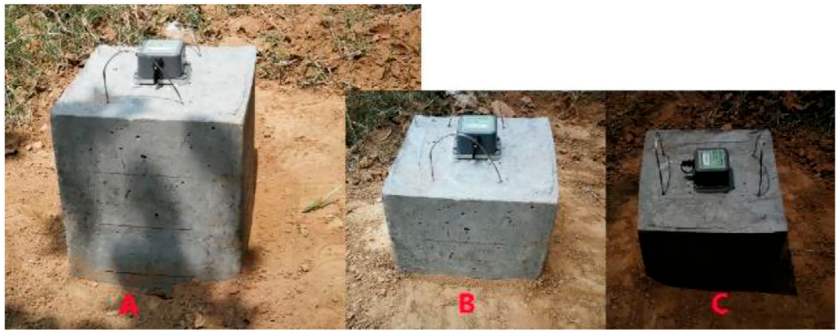

FIGURE 3
Unstable rock test models.

This vibrometer has the characteristics of a high sampling frequency, good signal-to-noise ratio, and wireless transmission, which can be used to measure the three-way vibration acceleration of the object through the fast Fourier transformation to obtain the three-way natural vibration frequency of the object. The specific parameters of the vibration meter are shown in Table 1.

2) Vibration measurement

A vibration sensor is arranged on the top surface of the model, and epoxy resin is used to bond the fixed plate of the vibration sensor to the unstable rock block of the slope. After waiting for 72 h, when the epoxy resin is completely cured and the test model becomes a whole, then install the layout sensor. After excitation by the broadband hammer, the three-way acceleration/velocity of the measured object is triggered, that is, the time-domain diagram of the measured object and then the frequency domain diagram of the measured object is obtained through filter and Fourier transform, calculating the natural vibration frequency of the measured object according to the frequency diagram.

Experimental model

1) Test model

In the test, the unstable rock is simulated by cube concrete, and the size of model A is 0.3*0.3*0.4 m, with a mass of 84.3 kg; the size of model B is 0.3*0.3*0.3 m, with the mass 63.2 kg; the size of model C is 0.3*0.3*0.2 m, with the mass 42.5 kg; the unstable rock model in the test is shown in Figure 3.

2) Foundation soil

The soil on the Monkey Rock landslide mass of the Dadu River National Road slope was taken as the test foundation soil, and the conventional parameters of the soil obtained through the test are shown in Table 2.

TABLE 2 Foundation soil parameters.

Test factor	Average	unit
Natural density (γ)	1.92	g/cm^3
Internal friction angle (φ)	20.0	°
Coefficient of subgrade reaction (k)	6.5*10^4	kN/m^3
Cohesion (C)	7.0	kN/m^2

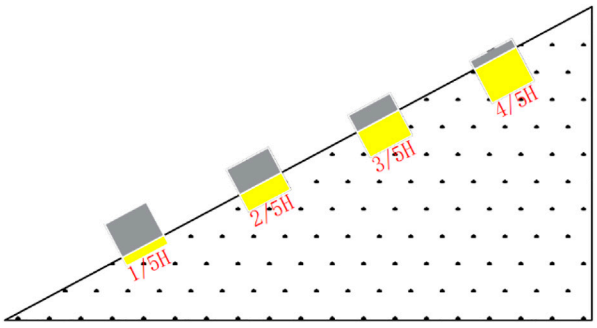

FIGURE 4
Test plan.

Test plan

The unstable rock model is buried in the soil, and the buried depth is controlled at 1/5, 2/5, 3/5, and 4/5 of the unstable rock test model height. Then apply the broadband hammer to hit the unstable rock model so as to obtain its acceleration time-history curve by vibrometer. Filter the

TABLE 3 Horizontal vibration frequencies of unstable rock models.

Model	Buried depth/cm	Measured frequency/HZ	Buried depth calculation/cm	Error (%)
A	8	13.6	7.49	6.37
A	16	23.2	16.72	4.51
A	24	31.8	24.61	2.52
A	32	39.2	31.18	2.56
B	6	16.5	6.34	5.69
B	12	25.3	12.36	3.03
B	18	32.6	17.51	2.73
B	24	39.9	23.51	2.02
C	4	17.7	3.84	3.92
C	8	27.4	8.32	3.97
C	12	35.4	12.82	6.83
C	16	40.9	16.26	1.63

acceleration time-history curve in the horizontal direction of the unstable rock model, and perform Fourier transform on the filtered acceleration time-history curve to obtain the power spectrum of the unstable rock model. The test scheme is shown in Figure 4.

Test results

The horizontal natural vibration frequencies of unstable rock models with different buried depths are counted, and the statistical results are shown in Table 3.

It can be seen from the test results that the maximum error of the inferred unstable rock buried depth is 6.83%, the minimum error is 1.63%, and the average error is 3.82%.

Discussion

The test results are plotted in Figure 5.

Relationship between the unstable rock buried depth and natural vibration frequency

It can be seen from Figure 5 that, in Model A, Model B, and Model C, with the increase of the unstable-rock buried depth, the natural vibration frequency of unstable rock increases nonlinearly, and the natural vibration frequency increases with the growing buried depth.

According to formula (17), the relationship between the buried depth of the unstable rock and the natural vibration frequency is formula (18):

$$h = \frac{4\pi^2 M f_d^2 \left(a/H_s^2 + 1\right)}{kb\left(1 - \xi^2\right)\left(a/H_s\right)^2}. \tag{18}$$

The burial depth h of the unstable rock is a monotonically increasing function of the natural vibration frequency f_d. With the increase of the buried depth of the unstable rock, the natural vibration frequency of the unstable rock increases quadratically. In addition, the average error between the solid buried depth of the unstable rock calculated by the theoretical model 18) and the actual one is 3.82%, indicating that the theoretical model of the natural vibration frequency and the buried depth of the unstable rock is correct.

Relationship between the natural vibration frequency and the unstable rock mass

It can be seen from Figure 5 that when the natural vibration frequencies of Model A, Model B, and Model C are the same, the model with smaller mass has the smallest buried depth, and the model with larger mass has the largest buried depth: Model A buried depth > Model B buried depth > Model C buried depth; under the same buried depth, the natural vibration frequency of the unstable rock with large mass is lower than that of the small mass: Model C natural vibration frequency > Model B natural vibration frequency > Model A natural vibration frequency.

According to Eq. 17, the relationship between the mass of the unstable rock and the natural vibration frequency is Eq. 19:

$$M = \frac{\mathrm{kbh}\left(1 - \xi^2\right)\left(\mathrm{a}/H_s\right)^2}{4\pi^2 \mathrm{f}_\mathrm{d}^2\left(\left(a/H_s\right)^2 + 1\right)}. \tag{19}$$

The experimental results of the relationship between the natural vibration frequency and the mass of the unstable rock

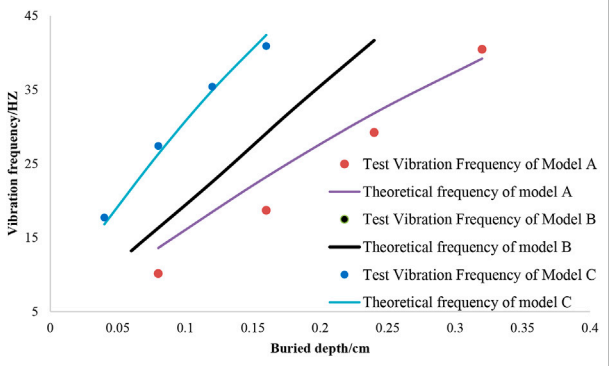

FIGURE 5
Relationship between the natural vibration frequency and the buried depth.

are consistent with the model (19): the mass M of the unstable rock is a monotonically decreasing function of the natural vibration frequency f. As the unstable rock mass increases, its natural vibration frequency decreases to the power of one-half.

Relationship between the natural vibration frequency and the unstable rock safety

The research of this study provides a simple and effective method to measure the buried depth of unstable rock. The deeper the buried depth of the unstable rock is, the higher the safety will be. Therefore, the safety of the unstable rock is positively correlated with the buried depth of the unstable rock, and the vibration frequency is also positively correlated with the buried depth. Therefore, the vibration frequency of unstable rock is positively correlated with its safety. The research results can provide certain new ideas and theoretical basis for the stability evaluation of the slope of the unstable rock and the rapid identification and monitoring of the unstable rock.

Conclusion

1) Based on the dynamic theory, the dynamic characteristic model of the unstable rock is established. Based on this dynamic characteristic model, the buried depth of the unstable rock can be measured by measuring the natural vibration frequency.
2) The test results show that with the increase of the buried depth of the unstable rock, the natural vibration frequency of the unstable rock increases nonlinearly in the horizontal direction, and the increase of the natural vibration frequency tends to weaken with the increase of the buried depth; the mass of the unstable rock is a monotonically decreasing function of the natural vibration frequency. As the mass increases, the natural vibration frequency of the rolling stone decreases to the power of one-half. The test results verify that the dynamic characteristic model of the unstable rock is correct.
3) The combination of the research results and the limit equilibrium model can realize the stability evaluation of the unstable rock based on the natural vibration frequency, and the safety factor can be monitored.

Data availability statement

The original contributions presented in the study are included in the article/supplementary material; further inquiries can be directed to the corresponding author.

Author contributions

YJ and TJ were responsible for the work concept or design; GS and GY were responsible for data collection; XP was responsible for drafting the manuscript; HL was responsible for making important revisions to the manuscript; YJ and XP were responsible for approving the final version of the manuscript for publication.

Funding

This research was supported by the National Natural Science Foundation of China (No. U1704243) and the Natural Science Foundation granted by the Department of Education, Anhui Province (No. KJ 2020A0235).

Conflict of interest

The authors declare that the research was conducted in the absence of any commercial or financial relationships that could be construed as a potential conflict of interest.

Publisher's note

All claims expressed in this article are solely those of the authors and do not necessarily represent those of their affiliated organizations, or those of the publisher, the editors, and the reviewers. Any product that may be evaluated in this article, or claim that may be made by its manufacturer, is not guaranteed or endorsed by the publisher.

References

Chen, G. J. (2014). *Research on motion features and disaster prevention for rockfall disaster of highway slope* (Fuzhou: Fuzhou :Fuzhou University). M.D. Thesis.

Cheng, Q., and Su, S. (2014). Movement characteristics of collapsed stones on slopes induced by Wenchuan earthquake. *Rock Soil Mech.* 35 (3), 772–776. doi:10.16285/j.rsm.2014.03.011

Dong, J. X., Xu, G. L., Li, Z. P., and Zhang, S. (2012). Classification and risk rating assessment of hazard sources in surrounding slope of busigou hydropower project. *J. Eng. Geol.* 20 (5), 760–767. doi:10.3969/j.issn.1004-9665.2012.05.015

Du, Y., Li, H., Chicas, S. D., and Huo, L. (2022). Progress and perspectives of geotechnical anchor bolts on slope engineering in China. *Front. Environ. Sci.* 10, 928064. doi:10.3389/fenvs.2022.928064

Du, Y., Xie, M.-w., Jiang, Y.-j., Li, B., and Chicas, S. (2017). Experimental rock stability assessment using the frozen-thawing test. *Rock Mech. Rock Eng.* 50 (4), 1049–1053. doi:10.1007/s00603-016-1138-2

Du, Y., and Xie, M. (2022). Indirect method for the quantitative identification of unstable rock. *Nat. Hazards* 112 (1), 1005–1012. doi:10.1007/s11069-021-05197-4

Du, Y., Xie, M., and Jia, J. (2020). Stepped settlement: A possible mechanism for translational landslides. *Catena* 187, 104365. doi:10.1016/j.catena.2019.104365

Du, Y., Xie, M. W., Jiang, Y. J., Chen, C., and Huo, L. C. (2021). Review on the formation mechanism and early warning of rock collapse. *Metal. Mine* 50 (01), 106–119. doi:10.19614/j.cnki.jsks.202101008

Du, Y., Xie, M. W., Jiang, Y. J., Li, B., Gao, Y., and Liu, Q. Q. (2016). Safety monitoring experiment of unstable rock based on natural vibration frequency. *Rock Soil Mech.* 37 (10), 3035–3040. doi:10.16285/j.rsm.2016.10.039

Fu, X. D., Sheng, Q., and Zhang, Y. H. (2013). Stepwise excavation process of underground caverns of hydropower station using DDA. *Rock Soil Mech.* 34 (2), 568–574. doi:10.16285/j.rsm.2013.02.035

Fujisawa, K. (2007). Rock slope vibration measurement manual for extracting unstable rock block. *Public Works Res. Inst. Mater.* 40 (51), 42.

He, S. M., Li, X. P., and Wu, Y. (2008). Research on yield property of soil under rock-fall impact. *Chin. J. Rock Mech. Eng.* 27 (Suppl. 1), 2973–2977.

He, S. M., Shen, J., Luo, Y., and Wu, Y. (2011). Study on the characteristics of normal impact of post-earthquake rock-fall on slope. *Eng. Mech.* 28 (6), 118–124.

Huang, R. Q., and Liu, W. H. (2009). *In-situ* test study of characteristics of rolling rock blocks based on orthogonal design. *Chin. J. Rock Mech. Eng.* 28 (5), 882–891. doi:10.3321/j.issn:1000-6915.2009.05.003

Jia, Y. C., Jiang, T., and Liu, H. D. (2021). Stability evaluation model of toppling unstable rock based on natural vibration frequency. *J. Appl. Sci. Eng.* 24 (2), 177–184. doi:10.6180/jase.202104_24(2).0007

Jia, Y. C. (2018). *Study on stability model of slope dangerous rock mass based on dynamic characteristics* (Beijing: University of Science and Technology Beijing). Ph.D. Thesis.

Jia, Y. C., Xie, M. W., Chang, S. X., and Fu-Xia, L. (2017). A model for evaluation of stability of sliding-and falling-type dangerous rock blocks based on natural vibration frequency. *Rock Soil Mech.* 38 (7), 2149–2156. doi:10.16285/j.rsm.2017.07.039

Li, B., Zhang, G., Wang, G., and Qiao, J. (2022). Damage evolution of frozen-thawed granite based on high-resolution computed tomographic scanning. *Front. Earth Sci.* 10, 760. doi:10.3389/feart.2022.912356

Liu, Z. J., Wang, X. N., and Mo, L. (2017). Classification of occurrence form of spheric weathered granite and stability analysis. *J. Geol. Hazards Environ. Preserv.* 29 (04), 40–44. doi:10.11113/jt.v72.4015

Ma, G. C., Sawada, K., Saito, H., Uehan, F., and Yashima, A. (2012). Study on evaluating rock block stability by using a remotely positioned laser Doppler vibrometer. *Geomate J.* 2 (4), 247–252. doi:10.21660/2012.4.3j

Ma, G. C., Sawada, K., Yashima, A., Uehan, F., Murata, O., and Saito, H. (2011). "Study of scale effect in rock block stability by remote vibration measurements and numerical experiments," in *Proceedings of the 40th symposium on rock Mechanics* (Committee on Rock Mechanics), 339–344.

Wang, D. P., He, S. M., Ouyang, C. J., Zhang, X. X., Xiang, B., and Wang, X. F. (2013). Study of dynamic response of shed reinforced concrete slab to impact load of rock-fall. *Rock Soil Mech.* 34 (3), 881–886. doi:10.16285/j.rsm.2013.03.006

Xu, J. J., Tang, X. H., Liu, Q. S., and Feng, Y. F. (2019). Investigation on trajectory of rolling rock affected by rock fragmentation based on energy tracking method. *Rock Soil Mech.* 40 (S1), 541–548. doi:10.16285/j.rsm.2018.2334

Yang, Z. X., Pei, X. J., and Yuan, J. K. (2017). Stability analysis of dangerous rock mass at high and steep slope. *Subgr. Eng.* (01), 25–29. doi:10.13379/j.issn.1003-8825.2017.01.06

Yao, G. Z. (2015). *Vibration characteristics of falling unstable rock under different stability states*. Guizhou: Guizhou University. M.D. Thesis.

Yao, G. Z., Yu, B., and Chen, J. (2015). Study on simulation test method for vibration characteristics of unstable rock. *Railw. Eng.* (12), 88–92. doi:10.3969/j.issn.1003-1995.2015.12.24

Yin, Z. Q., Xu, Y. Q., Chen, H. Q., Sa, L., and Jiang, X. (2016). The development and distribution characteristics of geohazards induced by August 3, 2014 Ludian earthquake and comparison with Jinggu and Yingjiang earthquakes. *Acta Geol. Sin.* 90 (6), 1086–1097. doi:10.1007/s12583-014-0471-1

Yu, H. C., Yu, H. M., Liu, H. D., and Lu, X. S. (2010). The calculation method for protective structure against rockfall based on orthogonal test and kinematics. *J. China coal Soc.* 35 (01), 55–60. doi:10.13225/j.cnki.jccs.2010.01.029

Yuan, G. Q., Tan, R. Q., Zhang, M. S., and Chen, D. X. (2011). Study of slope stability of the Shuangjiangkou hydropower station. *Acta Geol. Sichuan* 31 (04), 435–437+445. doi:10.3969/j.issn.1006-0995.2011.04.014

Zhang, K. S. (2017). Analysis of influence of blasting vibration at tunnel portal section on stability of slope rock. *J. Highw. Transp. Res. Dev.* (07), 323–325.

Zhang, L., Niu, F., Liu, M., Ju, X., Wang, Z., Wang, J., et al. (2022). Fracture characteristics and anisotropic strength criterion of bedded sandstone. *Front. Earth Sci.* 10, 451. doi:10.3389/feart.2022.879332

Zhang, L. Q., Yang, Z. F., and Zhang, Y. J. (2005). Risk analysis of encountering rockfalls on highway and method study. *Chin. J. Rock Mech. Eng.* 24 (21), 5543–5548. doi:10.2116/analsci.20.717

Zhao, X., and Liu, H. D. (2005). Research on protective structures for high slopes rockfall around a hydropower station. *Chin. J. Rock Mech. Eng.* 24 (20), 3742–3748. doi:10.1007/s11769-005-0030-x

frontiers | Frontiers in Earth Science

TYPE Original Research
PUBLISHED 05 August 2022
DOI 10.3389/feart.2022.934498

Check for updates

OPEN ACCESS

EDITED BY
Yan Du,
University of Science and Technology Beijing, China

REVIEWED BY
Linwei Li,
Guizhou University, China
Jia Yanchang,
North China University of water resources and hydropower, China

*CORRESPONDENCE
Xing Zhu,
zhuxing330@163.com

SPECIALTY SECTION
This article was submitted to Geohazards and Georisks, a section of the journal Frontiers in Earth Science

RECEIVED 02 May 2022
ACCEPTED 29 June 2022
PUBLISHED 05 August 2022

CITATION
Tang Y, Zhu X, He C, Hu J and Fan J (2022), Critical slowing down theory provides early warning signals for sandstone failure.
Front. Earth Sci. 10:934498.
doi: 10.3389/feart.2022.934498

COPYRIGHT
© 2022 Tang, Zhu, He, Hu and Fan. This is an open-access article distributed under the terms of the Creative Commons Attribution License (CC BY). The use, distribution or reproduction in other forums is permitted, provided the original author(s) and the copyright owner(s) are credited and that the original publication in this journal is cited, in accordance with accepted academic practice. No use, distribution or reproduction is permitted which does not comply with these terms.

Critical slowing down theory provides early warning signals for sandstone failure

Yao Tang[1,2], Xing Zhu[1,3]*, Chunlei He[1,2], Jiewei Hu[1,2] and Jie Fan[1,2]

[1]State Key Laboratory of Geohazard Prevention and Geological Environmental Protection, Chengdu University of Technology, Chengdu, China, [2]School of Environment and Civil Engineering, Chengdu University of Technology, Chengdu, China, [3]College of Computer Science and Technology (Oxford Brookes Institute), Chengdu University of Technology, Chengdu, China

The critical point of rock mass transition from stable to unstable states is significant for the prevention and control of rock engineering hazards. This study explored the precursor characteristics of instability in sandstone containing prefabricated fractures and intact sandstone based on the critical slowing down (CSD) theory. The results demonstrated that as the input energy drove the dissipation energy dynamic system toward the critical point of two states, the CSD phenomenon appeared, which was manifested by the sudden increase in CSD time series metrics (skewness, kurtosis, and coefficient of variation) and autoregressive model metrics (variance and autocorrelation coefficient). The CSD characteristics of different dissipation energy dynamical systems were different, resulting in different times of CSD phenomena for distinct systems. In addition, the angle of the sandstone fracture affected the characteristics of the dissipation energy dynamical system and hence the appearance time of the precursor information. The precursor time of the sandstone containing 45° parallel fractures appeared earliest among all rock samples, and the ratio of the appearance time of the precursor point to the failure time of all rock samples reached more than 80%, which had good timeliness. The stress at the precursor point reached more than 80% of the peak stress, which corresponded to the plastic stage in the loading process, indicating that the CSD indicators constitute an effective monitoring index, which can provide an important reference for the stability monitoring and early warning of the field rock project.

KEYWORDS

energy release, parallel prefabricated fractured sandstone, rock failure precursor, critical slowing down indicators, early warning signals

Introduction

In general, the destruction of rock bridges causes the rock to change from a stable to an unstable state, which may bring catastrophic consequences and pose a huge threat to the safety of people's lives (Du et al., 2021). Therefore, the crucial point of phase change during rock destruction can be exploited for monitoring and early warning in geotechnical engineering.

For complex dynamical systems in nature, the transition of a system from one state to another is a common phenomenon, which can be produced by external large-scale shocks or by minor perturbations (van de Leemput et al., 2014). The critical slowing down (CSD) theory is a concept in statistical physics that demonstrates that CSD phenomena occur near critical points when systems undergo phase transitions, which is manifested by the slowing down of the recovery of the dynamical system to its original state after a forced perturbation, which is typically observed in terms of variance and autocorrelation coefficients (Wu et al., 2021). The CSD theory has been shown to be a good predictor of the precursor information for the collapse of dynamical systems through several studies. For example, CSD occurs before the collapse of community dynamical systems (Dakos and Bascompte, 2014); before epilepsy, depression, and heart attack (Wichers et al., 2016; Maturana et al., 2020; Nannes et al., 2020); before financial and cryptocurrency crises (Diks et al., 2019; Tu et al., 2020); and before a flood disaster (Syed Musa et al., 2021). The main challenge for the analysis of early warning signals in time series data is to accurately "detrend" them to maintain the statistical properties of the fluctuations (Gama Dessavre et al., 2019). CSD precursor indicators can generally be classified into two categories: 1) time series-based indicators, which usually use different metrics to quantify changes in the statistical characteristics of the time series, and 2) model-based indicators, which fit data to a model to quantify the characteristics of the changes in the time series. The ultimate goal of both types of indicators is to capture the characteristics of the changes in the time series to find the change in the state of the dynamical system (Dakos et al., 2012).

A few scholars have conducted precursor studies on rock damage based on the CSD theory and have found that the acoustic emission count variance and autocorrelation coefficient increase when a rock sample enters the damage critical state, with more fluctuations and spurious signals in the autocorrelation coefficient than in the variance (Wei et al., 2018). High-water-content rock samples have earlier and more visible antecedent data (Li et al., 2021). The earlier onset of electric potential precursors compared to acoustic emission counts (Zhang et al., 2019). The acoustic emission energy precursor information appears later and closer to the damage point compared with acoustic emission counting, RA, and the critical points appear from long to short under several loading methods: compression test, Brazil test, and direct tension test (Zhang et al., 2021).

In summary, although all of the above studies yielded good results when approaching the critical point, skewness changes because of the slower recovery of the system near the critical point, and when the system state is close to the critical point, strong perturbations can drive the system across the boundary between the two states, a phenomenon known as flickering, which tends to increase kurtosis. Reduced robustness and flashing increase the coefficient of variance (Dakos and Bascompte, 2014; Nazarimehr et al., 2020). Current research on CSD of acoustic emission parameters during rock collapse uses variance and autocorrelation as precursors. In addition, owing to the high fluctuation of autocorrelation coefficients and the presence of spurious signals, the main CSD indicator is only one variance, which poses a challenge to the accuracy of early warning, and there is no explanation for the formation mechanism of the CSD phenomenon of rock damage during loading, as well as the effect of fractures on the appearance of the critical point. Therefore, in this study, tests were conducted on intact sandstone and sandstone containing parallel prefabricated fractures under uniaxial conditions. The purpose of this study is to examine the potential of multi-CSD indicators of acoustic emission parameters as early warning indicators during sandstone damage. In addition, the effect of the fracture dip on the critical slowing phenomena and the mechanism of emergence of the CSD phenomena during sandstone damage will be studied.

Test program

According to the findings of research that studied 70 large landslides in China, rocky landslide ratios made up 53% of the total and earthy landslide ratios made up 47%. Among those lithologies, sandstone and mudstone are the types of rock that are most prone to rocky landslides (Wen et al., 2004). In addition, joints in rock masses are characterized collectively as opposed to individually. The composition contains an element of random chance in it (Yang et al., 2017). As a result, during this pilot test, the sandstone with this particular combination of parallel fractures was investigated. A standard specimen of 100 mm in height and 50 mm in diameter was created, and prefabricated fractures were cut using a hydrodynamic cutting system. The upper and lower fractures of the prefabricated fractures each measured 1.5 mm in width and 20 mm in length, and the vertical distance between the two parallel fractures measured 20 mm. The two ends of the rock sample are finely polished using machinery. In this study, the breadth, length, and perpendicular distance of the cracks were taken as constant values. The rock samples were numbered as shown in Figure 1, and the intact rock samples were numbered w1 to w3. Rock samples having 30° parallel cracks were assigned numbers such as 30-1 to 30-3, 45° parallel cracks were assigned numbers such as 45-1 to 45-3, 60° parallel cracks were assigned numbers such as as 60-1 to 60-3, and 75° parallel cracks were assigned numbers such as 75-1 to 75-3. Each group contained three rock samples, for a total of 15 rocks.

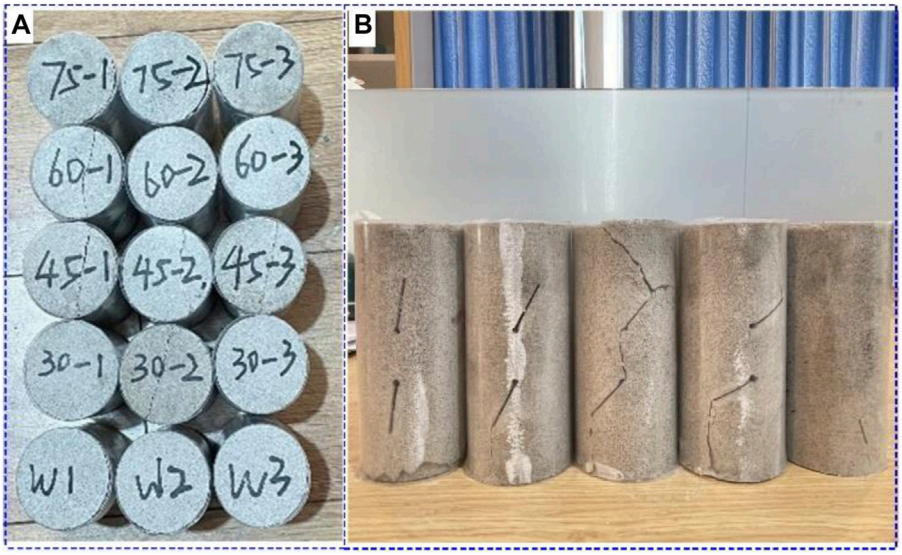

FIGURE 1
Test rock samples. **(A)** specimen number and **(B)** rock fracture pattern.

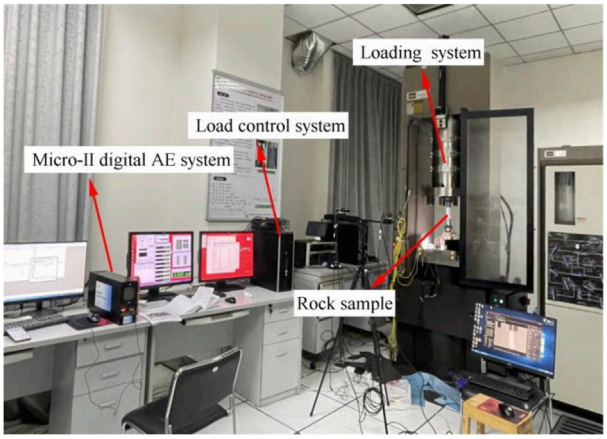

FIGURE 2
Test equipment.

As shown in Figure 2, the testing apparatus consists of a loading system and an acoustic emission acquisition system. The loading system adopts an MTS815.03 rigid press manufactured by MTS USA with the following main technical specifications: frame stiffness of 10.5×10^9 N/m, maximum axial pressure of 4,600 kN, and compatibility with rock sample sizes of 50 mm × 100 mm and 100 mm × 200 mm. During this test, the loading rate of all rock samples was set to 0.2 mm/min.

Acoustic emission uses a Micro-II Digital AE System produced by American Physical Acoustics. The acoustic emission signal acquisition threshold is set to 45 dB, the sampling interval is set to 1 μs, the number of probes is 2, and petroleum jelly is applied to the contact surface of the rock sample and the acoustic emission probe. Before the test, the performance of all equipment was evaluated to ensure that the test was conducted without errors.

Theory and indicators of critical slowing down

In natural dynamic systems, when a system is subjected to external perturbations and shocks that result in a change in the phase state (the system changes from an old phase state to a new phase state), the recovery rate becomes slower after the perturbation when the system state is close to the critical point. Near the critical point, the action of small or large perturbations may drive the system to breach the boundary between two distinct states, a phenomenon known as flicker. Both slow recovery and flicker are characteristics of CSD phenomena (Scheffer et al., 2009). In general, the CSD indicator is used to describe the CSD phenomenon that occurs in a system, where the CSD indicators increase abruptly as the system approaches a critical point. CSD indicators are generally classified into two categories: metric-based indicators and model-based indicators, both of which reflect the changes in the characteristics of the system time series (Dakos et al., 2012), with the difference that the CSD indicators in the autoregressive model have the effect of window length and lag step whereas the metric indicators have the effect of window length only.

Metric-based critical slowing down indicators

System dynamics suggest that the slowing down of flicker and recovery near a critical point can lead to divergence in the variability of system fluctuations. As a result, the coefficient of variation might serve as an indicator of CSD throughout system phase transition (Chen et al., 2014). The variation coefficient can be expressed as Eq. 1.

$$CV = \frac{\sqrt{\frac{1}{n}\sum_{i=1}^{n}(x_i - \bar{x})^2}}{\bar{x}} \tag{1}$$

where CV denotes the coefficient of variation, x_i denotes the i^{th} data point, $\bar{x}$ denotes the mean, and n represents the total number of data.

As a system approaches a critical point due to an increase in the magnitude of the perturbation, the distribution of the values in the time series becomes uneven and leads to an increase in skewness. Of note, skewness may increase or decrease depending on whether the new state to be formed is in a direction greater or less than the current state (Guttal and Jayaprakash, 2008; Rozek et al., 2017). Skewness is a normalized third-order moment distributed around the mean, as shown in Eq. 2.

$$SK = \frac{\frac{1}{n}\sum_{i=1}^{n}(x_i - \bar{x})^3}{\sqrt{\frac{1}{n}\sum_{i=1}^{n}(x_i - \bar{x})^2}} \tag{2}$$

where SK denotes the skewness.

Small perturbations or strong perturbations may also cause the state of the system to reach extremes closer to the transition or to cross a critical point, and this effect may lead to an increase in the kurtosis of the time series (Biggs et al., 2009; Mehrabbeik et al., 2021). Kurtosis is a normalized fourth-order moment distributed around the mean, as shown in Eq. 3.

$$KU = \frac{\frac{1}{n}\sum_{i=1}^{n}(x_i - \bar{x})^4}{\left(\sqrt{\frac{1}{n}\sum_{i=1}^{n}(x_i - \bar{x})^2}\right)^2} \tag{3}$$

where KU denotes the kurtosis.

Based on autoregressive model critical slowing down indicators

As a system approaches the critical point, recovery slows down because of perturbations, which would imply that there is a long-term correlation between the present perturbations and the past, leading to an increase in the autocorrelation coefficient. Near the critical point, the variance increases because the system takes longer to recover from stochastic shock (Tan and Cheong, 2014). In the autoregression model, the CSD phenomenon can be observed through the variance and autocorrelation coefficient (Ma G et al., 2018; Zhang et al., 2021).

Variance is a characteristic quantity that describes the degree to which the sample data deviate from the mean in the sample and can be expressed as Eq. 4.

$$S^2 = \frac{1}{n}\sum_{i=1}^{n}(x_i - \bar{x})^2 \tag{4}$$

where S^2 denotes the variance.

The autocorrelation coefficient is a statistic that describes the correlation between distinct moments of the same variable, and its expression with a lag length of j can be found in Eq. 5.

$$R(j) = \sum_{i=1}^{n-j}\left(\frac{(x_i - \bar{x})}{s}\frac{(x_{i+j} - \bar{x})}{s}\right) \tag{5}$$

where S denotes the standard deviation, Suppose the state variable has a forced disturbance with a period of Δt and is approximately exponential during the perturbation process with a recovery rate of λ. In the autoregressive model, it can be expressed as Eq. 6.

$$\mathrm{y}_{n+1} = e^{\lambda\triangle t}y_n + s\varepsilon_n \tag{6}$$

where y_n is the deviation of the system variables to the equilibrium state and ε_n is a random quantity that conforms to the normal distribution. If λ does not depend on y_n, then the process can be simplified as Eq. 7.

$$\mathrm{y}_{n+1} = Ry_n + s\varepsilon_n \tag{7}$$

where R is the autocorrelation coefficient, $R = e^{\lambda\triangle t}$, and variance can be analyzed by the autoregressive model expressed as Eq. 8.

$$\mathbf{Var}(\mathrm{y}_{n+1}) = E(\mathrm{y}_n^2) + (E(y_n))^2 = \frac{S^2}{1 - R^2} \tag{8}$$

where E is the mathematical expectation (Li et al., 2021).

Mechanical characteristics

During the deformation and failure of the rock, assuming that there is no heat exchange with the outside world during this physical process, the energy generated by the work done by the external force can be expressed according to the conservation of energy and the laws of thermodynamics (Peng et al., 2020) as Eq. 9.

$$U = U^d + U^e \tag{9}$$

where U is the total energy input, U^d is the dissipation energy consumed by rock damage rupture, and U^e is the elastic energy stored inside the rock. Under uniaxial compression, the work done by the loading system on the rock sample can be expressed as in Eq. 10.

$$U = \int \sigma d\varepsilon = \sum_{i=1}^{n}\frac{1}{2}(\varepsilon_{i+1} - \varepsilon_i)(\sigma_{i+1} + \sigma_i) \tag{10}$$

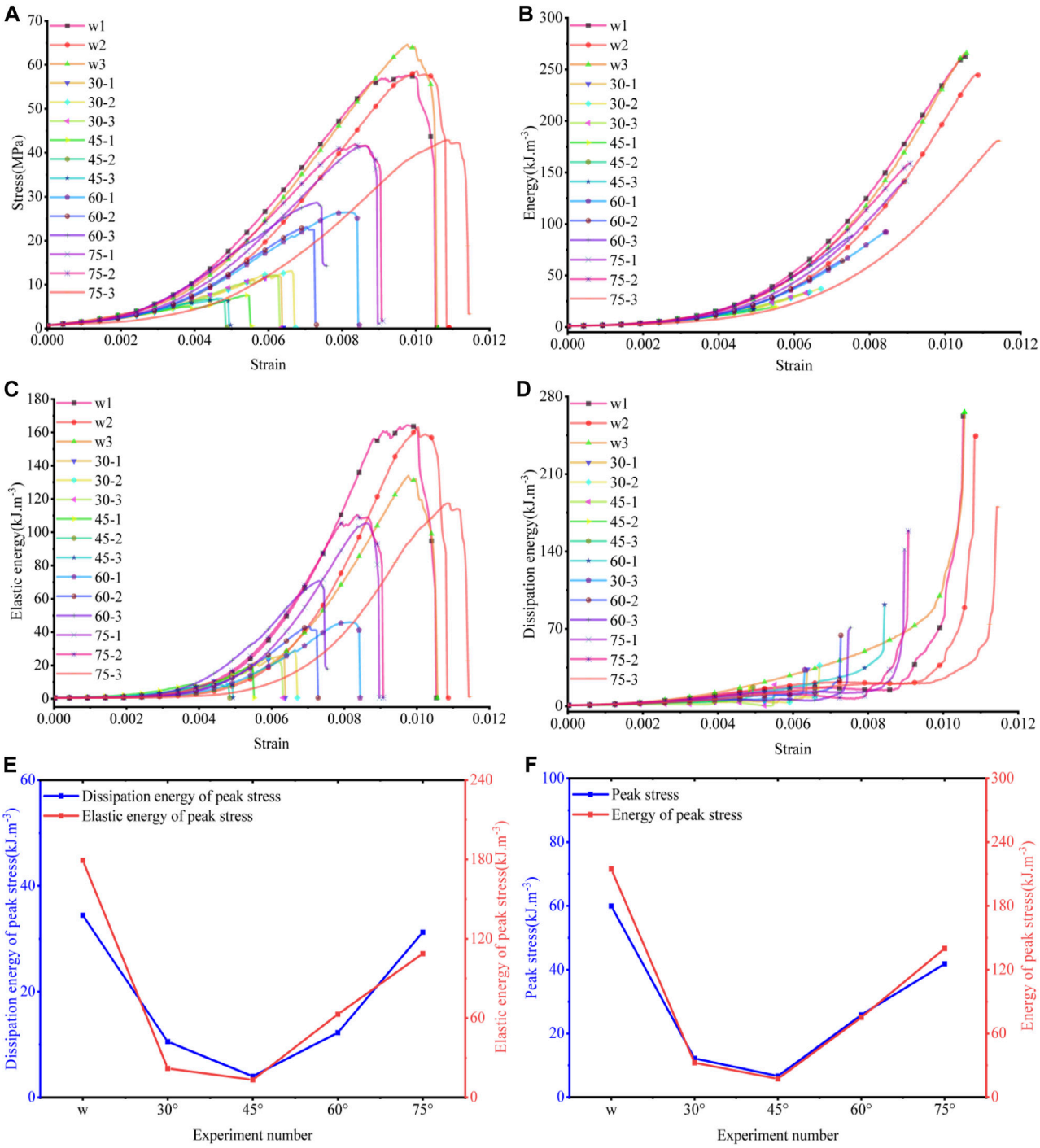

FIGURE 3
Mechanical characteristics. **(A)** stress–strain characteristics, **(B)** total energy characteristics, **(C)** elastic energy characteristics, **(D)** dissipation energy characteristics, and **(E,F)** average mechanical and energy values for each group of rock samples.

where ε is the axial strain and σ is the axial stress. From Hooke's law, the elastic energy of the rock under uniaxial compression is expressed as Eq. 11.

$$U^e = \frac{\sigma_c^2}{2E_u} \approx \frac{\sigma_c^2}{2E_0} \tag{11}$$

where E_0 is the initial elastic modulus.

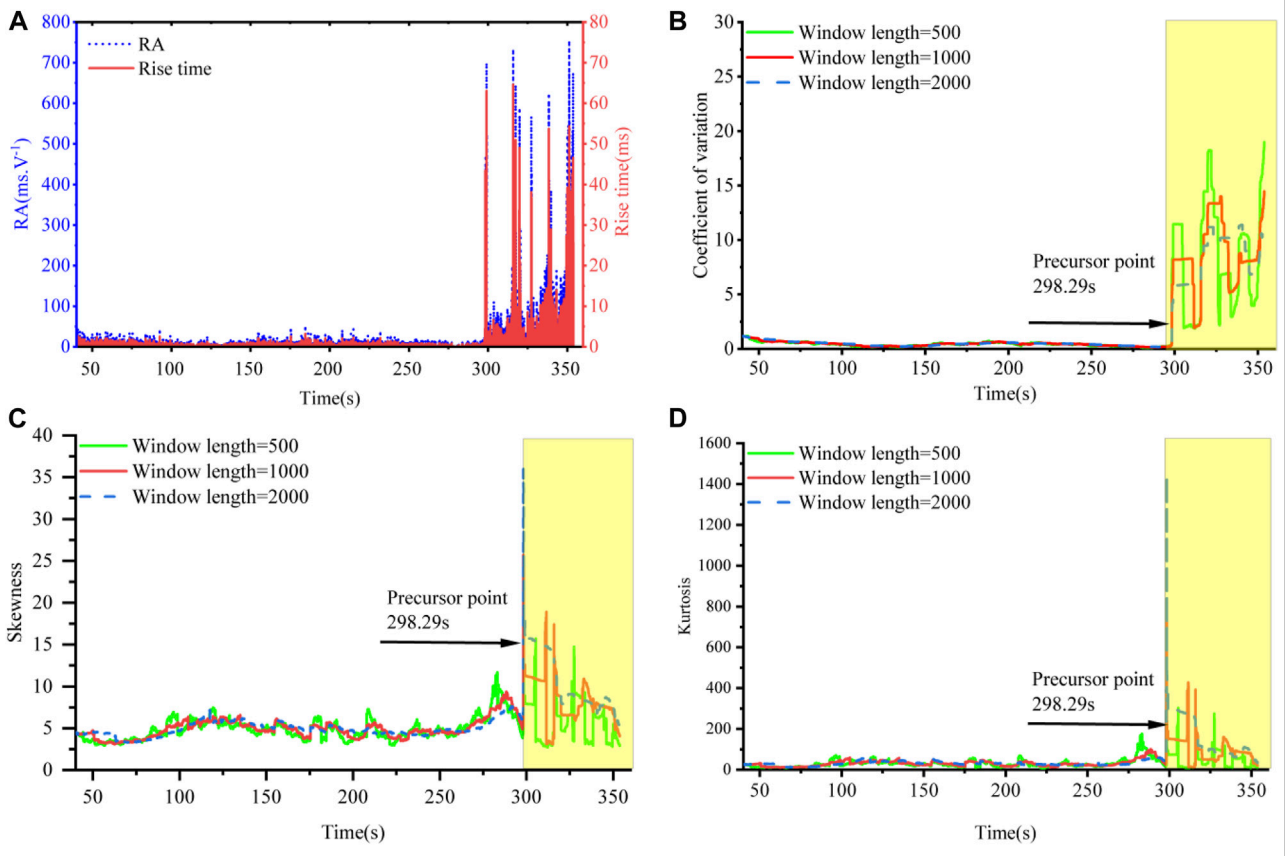

FIGURE 4
Acoustic emission parameters and the effect of window length on the metrics of the critical slowing down (CSD) phenomenon in w1. **(A)** rise time and RA of acoustic emission, **(B)** effect of window length on the coefficient of variation, **(C)** effect of window length on skewness, and **(D)** effect of window length on kurtosis.

After calculating the statistics for the data in Figures 3A–D, as shown in Figures 3E, F, during the loading process, the peak stress, total energy, dissipation energy, and elastic energy of intact rock samples are the largest and 45° is the smallest, 45° parallel fracture is the turning point of the mechanics and energy of rock samples, and the energy and mechanical properties show a decreasing trend from intact rock samples to rock samples containing 45° parallel fracture and an increasing trend from 45° to 75°, consistent with the findings of several scholars (Yang and Jing, 2011; Zhou et al., 2019; Lin et al., 2021), and the reason for the above phenomenon is that 45° dip joints are the most fracture-prone angle (Su et al., 2015). Moreover, the study shows that the elastic modulus reaches the minimum value when the dip angle of bedding is 45° (Zhang et al., 2022).

Effect of window length on the critical slowing down indicators

Acoustic emission rise time (Figure 4A) is time interval experienced when the potential signal triggering threshold voltage reaches the maximum amplitude value (Ali et al., 2019), RA (Figure 4A) is the acoustic emission rise time divided by the amplitude of the acoustic emission signal (Ohno and Ohtsu, 2010), and the aforementioned parameters are closely associated with rock damage rupture. In this article, using the acoustic emission rise time of the w1 rock sample as an illustration, the influence of window length on the CSD index of the time series is explored. As shown in Figure 4B, the coefficient of variation fluctuates more after the precursor point when the window length is 500, the second after the precursor point when the window length is 1,000, and the smallest when the window length is 2,000. However, the precursor point is consistent, and the fluctuation of the coefficient of variation before the precursor point is nearly identical, so the window length will produce only the impression of the coefficient of variation after the precursor point. The effect of window length on the coefficient of variation can be disregarded during the precursor investigation. In Figures 4C, D, the longer the window length is, the smaller are the fluctuations of skewness and kurtosis, which tend to be smooth, and the

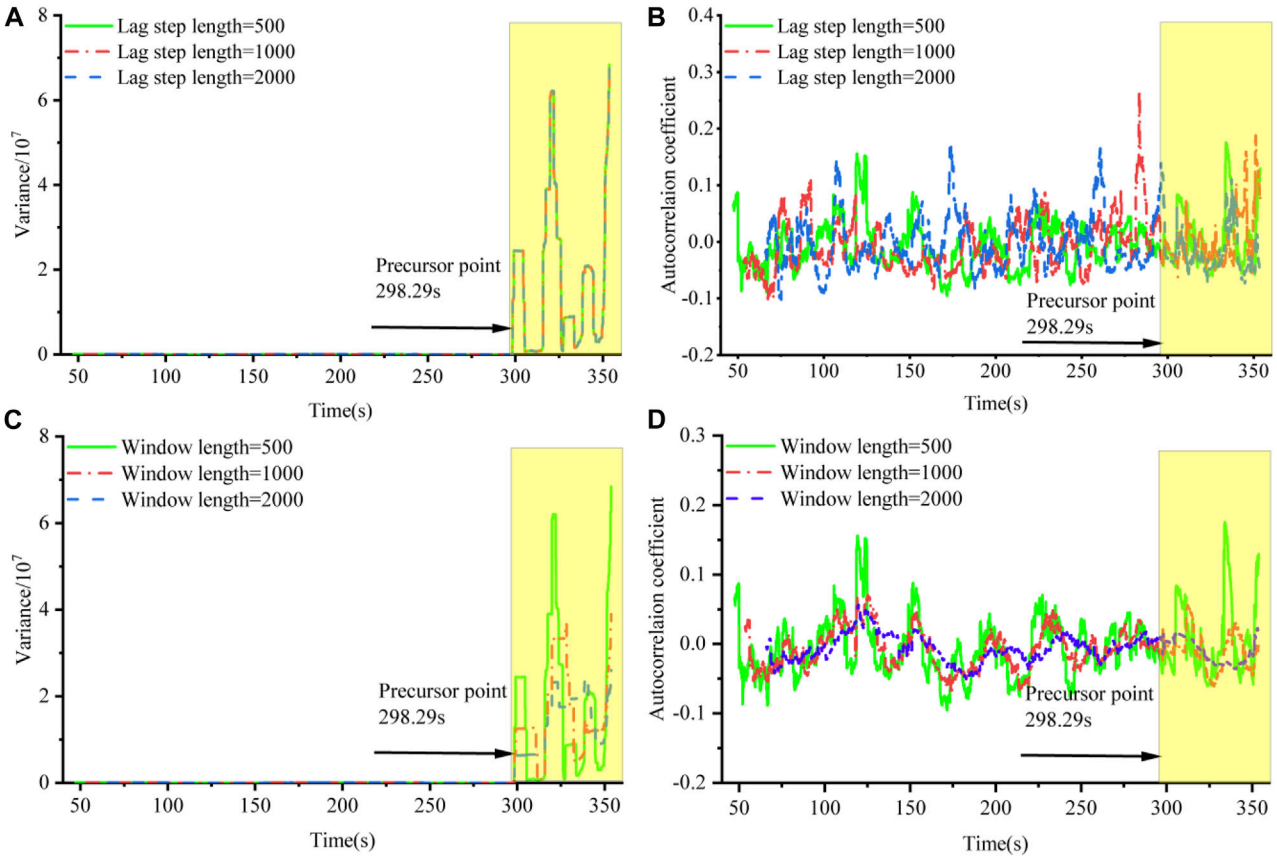

FIGURE 5
Effect of lag step and window length on the CSD indicators of the autoregression model. **(A)** effect of lag step length on variance for a fixed window length, **(B)** effect of lag step length on the autocorrelation coefficient for a fixed window length, **(C)** effect of window length on variance for a fixed lag step length, and **(D)** effect of window length on the autocorrelation coefficient for a fixed lag step length.

volatility of kurtosis is smaller than that of skewness. At the precursors, the size of the window length has no effect on the time of precursor appearance, but the larger the window length is, the greater are the values of skewness and kurtosis. In summary, the window size influences the volatility of the CSD index of the time series and has a negligible effect on the appearance of the precursor point. The coefficient of variation and kurtosis are superior observables compared with skewness.

Effect of window length and lag step length on the critical slowing down indicators of the autoregressive model

This subsection focuses on the effects of the lag step length and window length on the CSD indicators of the autoregressive model. First, we explore the impact of a window length of 500 and lag steps of 500, 1,000, and 2,000 on acoustic emission variance and autocorrelation. Second, we discuss the effects of a lag step of 500 and window lengths of 500, 1,000, and 2,000 on the variance of the rise time of the acoustic emission and the autocorrelation coefficient. Figure 5A demonstrates that the variance almost overlaps with different lag steps, indicating that the lag step has almost no effect on the variance. As shown in Figure 5B, the autocorrelation coefficient shows a chaotic behavior, since time series with different lag steps have different correlations with the original time series (Zhang et al., 2019). Figure 5C reveals that under the condition of a constant lag step, the larger the window length is, the greater is the tendency of the variance indicator to be stable, and the same phenomenon is observed for the autocorrelation coefficient (Figure 5D). The autocorrelation indicator is less resilient to short time or low-resolution time series. Therefore, it varies more and creates more spurious signals compared with variance, but the autocorrelation coefficient indicator is more robust to signals containing noise (Mehrabbeik et al., 2021). Although autocorrelation has the disadvantage of being affected by the lag step, the rise in the variance of the autocorrelation coefficient at the critical point is

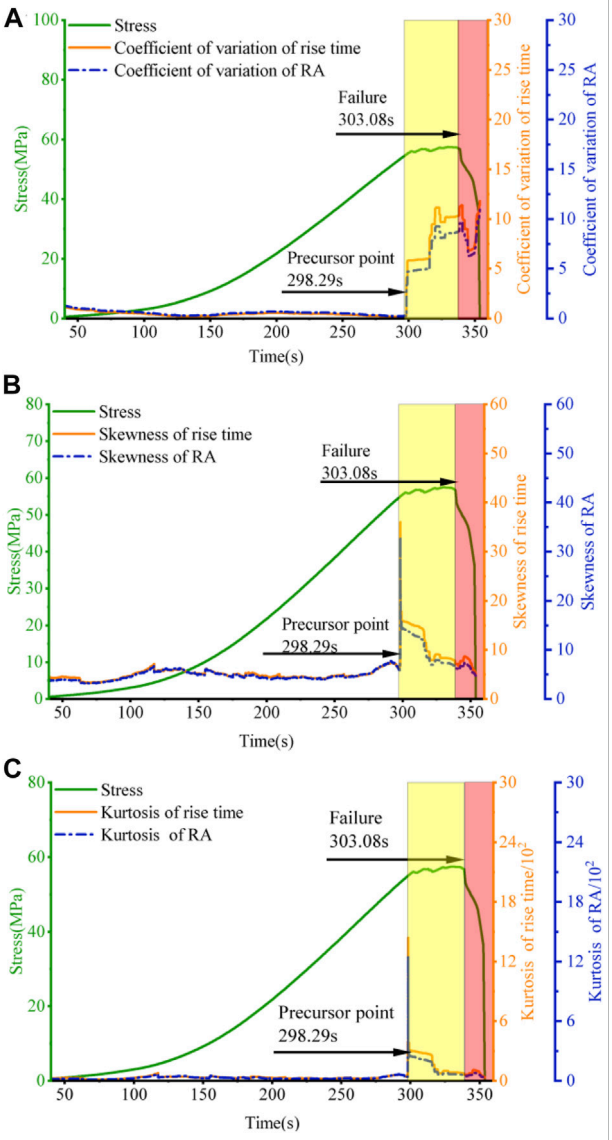

FIGURE 6
The CSD indicator of acoustic emission of rock sample w1. **(A)** variation coefficient characteristics of RA and rise time, **(B)** skewness characteristics of RA and rise time, and **(C)** kurtosis characteristics of RA and rise time.

observed in all cases. Hence, the effect of window size and lag step on the critical slowing characteristics can be ignored.

Critical slowing down phenomenon of sandstone acoustic emission parameters

The characteristics of the CSD metric indicators for the rising time and RA parameters of the w1 rock sample are depicted in Figure 6. During the loading process, the CSD

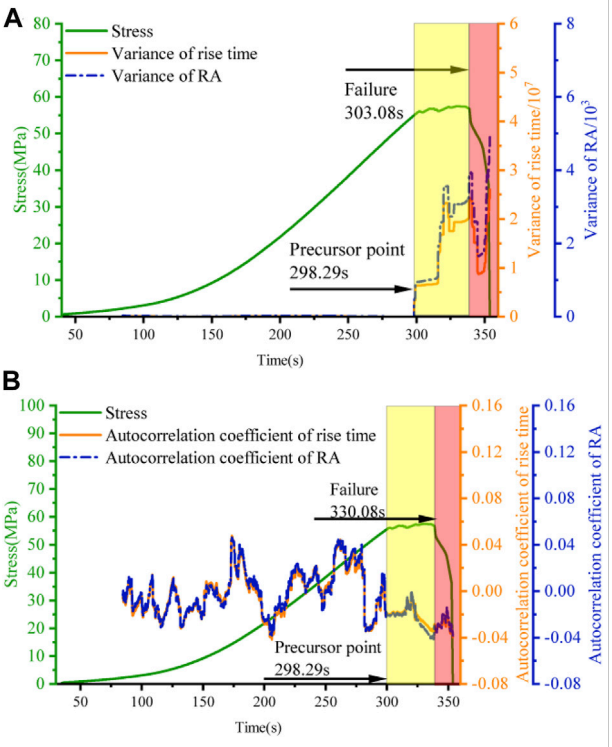

FIGURE 7
Characteristics of the CSD indicators of the autoregression model of the w-1 rock sample. **(A)** variance characteristics of RA and rise time and **(B)** autocorrelation coefficient characteristics of RA and rise time.

metric indicators for the same time series of rising time and RA values almost overlap in the curve before the precursor point, indicating a high degree of similarity in fluctuation. In addition, the coefficient of variation, skewness, and kurtosis of the rise time and RA value at 298.29 s have a significant increase in turning point, which is easily identifiable, making it possible to use the metric indicators as the CSD indicators for the acoustic emission parameters in the sandstone damage process.

As shown in Figures 7A, B, the CSD autoregression model indicators for the acoustic emission rising time and RA parameters exhibit remarkably comparable fluctuations, with the variance almost overlapping before the precursor point. After the precursor point, the variance of the acoustic emission rise time fluctuates much more. Throughout the whole loading process, the autocorrelation coefficients show multiple increases and drops, indicating that there were more false precursor signals and that the increasing trend at the precursor point was not as evident as the variance. Because the variance is readily identifiable as a critical point indicator, it can be employed as the primary reference indicator of the critical point in the autoregressive model for short time periods and time series with low time resolution.

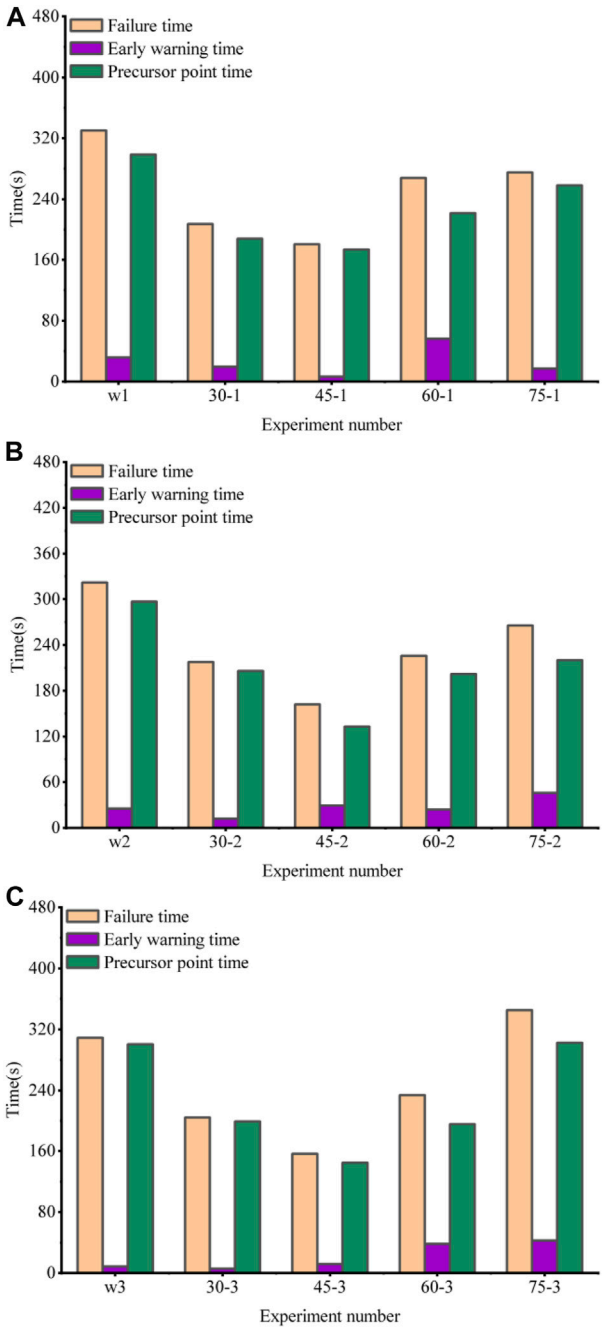

FIGURE 8
Statistics of time characteristics (failure time, early warning time, and precursor point time). **(A)** w1~75-1, **(B)** w2~75-2, and **(C)** w3~75-3.

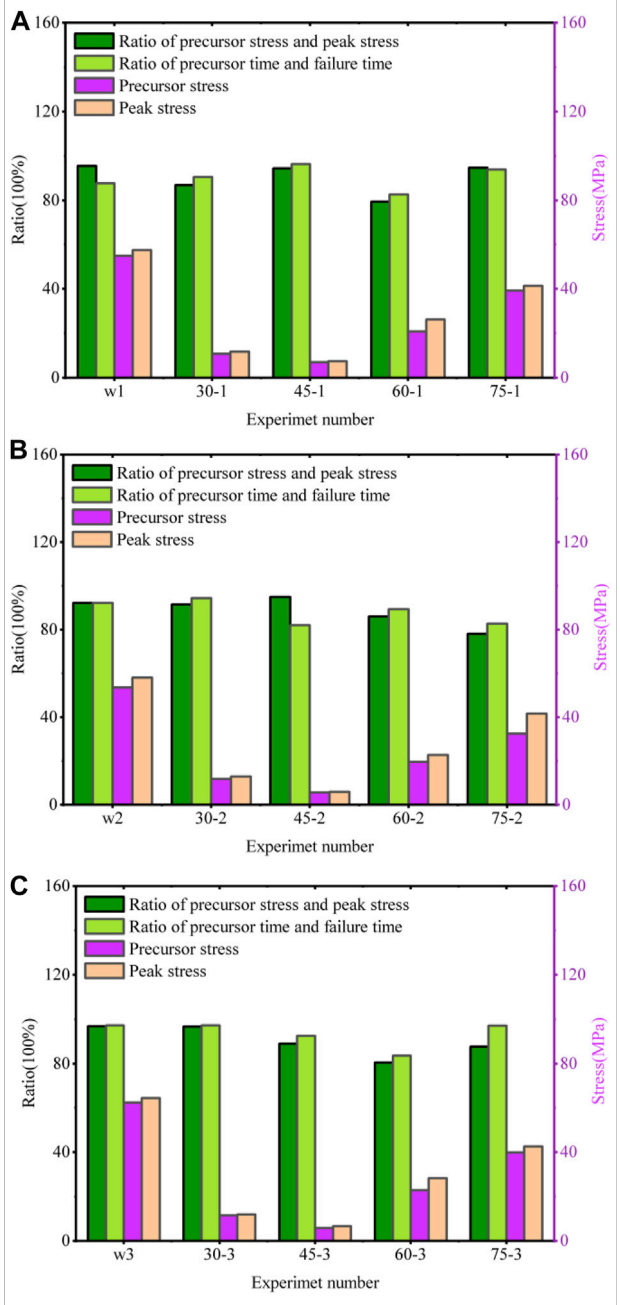

FIGURE 9
A statistical analysis of the time ratio, the stress ratio, and the features of stress. **(A)** w1~75-1, **(B)** w2~75-2, and **(C)** w3~75-3.

Statistics of precursors and mechanical characteristics

The window length and lag step can be selected according to the fluctuation of the data, with greater values being selected for the more fluctuating data and smaller values being selected for the less fluctuating data. The analysis of the window length and lag step in the above section reveals that the calculation results fluctuate less when the window length and lag step are 2,000. Therefore, in this study, both the lag step and the window length are set to 2,000. In practical applications, the window length and the lag step should be selected according to the fluctuation of the

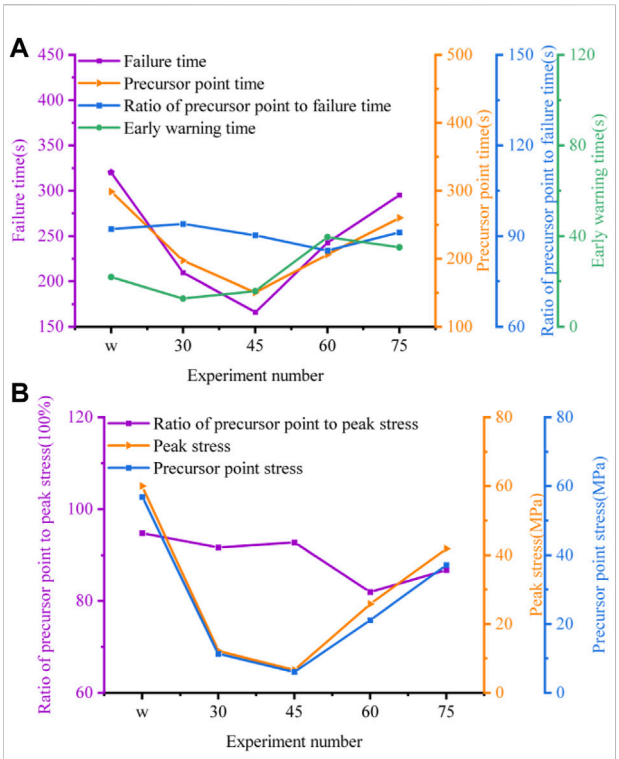

FIGURE 10
Statistics of the mean characteristics of precursors and mechanics. **(A)** temporal characteristics of each group of rock samples and **(B)** mechanical characteristics of each group of rock samples.

data. As depicted in Figure 8, under the condition of a constant loading rate, the damage times of all rock samples from longest to shortest are as follows: intact rock sample, 75° rock sample, 60° rock sample, 30° rock sample, and 45° rock sample, and the appearance time of the precursor point follows the same trend. However, there is no certain pattern regarding the duration of early warning time (the early warning time is the time difference between the damage time and the precursor time). As illustrated in Figure 9, the peak stress and the stress at the precursor point are as follows (from the greatest to the smallest): intact rock samples, 75° rock samples, 60° rock samples, 30° rock samples, and 45° rock samples. This is because 45° dip angle joints are the most fracture-prone angle. In other words, rock samples close to this angle have low strength and are susceptible to damage. In all tests, the ratio of the stress at the precursor point to the peak stress exceeded 80% in most cases, which roughly corresponds to the plastic deformation stage of new fracture formation, indicating that the precursor has a clear physical meaning. In addition, the ratio of precursor point time to failure time exceeded 80%, demonstrating that the precursors have good timeliness. In a set of rock samples, differences in mechanical and CSD properties are linked to the arrangement of crystals inside the rock mass as well as the distribution of microscopic holes and fissures. That is, there is anisotropy in the rock material, which leads to variances in the mechanical characteristics and CSD characteristics of the same group of tests (Zhang et al., 2021), which may also be caused by the difference in the degree of damage caused to the rock mass during fracture formation.

In this study, after the mean statistics of mechanical and precursor characteristics of all rock samples, the damage time, time of precursor point appearance, peak stress, and precursor point stress showed a decreasing trend from intact rock samples to 45° rock samples and an increasing trend from 45° rock samples to 75° rock samples, and the trend of early warning time showed an inverse relationship to the ratio of precursor time and damage time (Figure 10).

Critical slowing down phenomenon of the sandstone damage process

Driven slowly by environmental factors, systems are pushed to evolve at a critical point where regime shifts occur and such shifts will be permanent (Dakos et al., 2015). The blue balls in Figure 11 represent the current state of the system, which varies from system to system. The red balls represent thresholds, and the slope of the basin represents resilience. Driven by external factors, the system is pushed toward the threshold (critical point), which will cause the resilience system to slow down (less slope near the threshold point), creating a CSD phenomenon and making the CSD indicators increase. In addition, small perturbations can drive the system across the boundary between two basins of attraction, leading to a large shift in the system state into another state (van de Leemput et al., 2014).

During rock damage, dissipation energy is dissipated mostly by friction between structural surfaces and by breaking the original structural surface inside the rock to form a new surface. Therefore, the dissipation energy can indicate the damage to the rock (Jin et al., 2017), and acoustic emission is a transient elastic wave formed by the quick release of local strain energy within or on the surface of the material (Vahaviolos, 1999). Thus, in this study, the dynamic evolution of dissipation energy during loading is seen as a systematic change process, and its change characteristics are employed to attempt to explain why the CSD phenomenon exists during loading.

Figure 12 the mechanism of the formation of two typical CSD phenomena in this experiment. Figure 12A depicts a relatively simple kinetic system of the sandstone, in which the system undergoes only two states during the entire process: state A and state B. Throughout the loading process, the mechanical equipment continuously injects energy into the sandstone, which acts as a driving force to alter the dissipation energy system, thereby altering the state of the sandstone. When the dissipation energy system is driven to move from state A to near the threshold, the critical slowdown phenomenon appears and

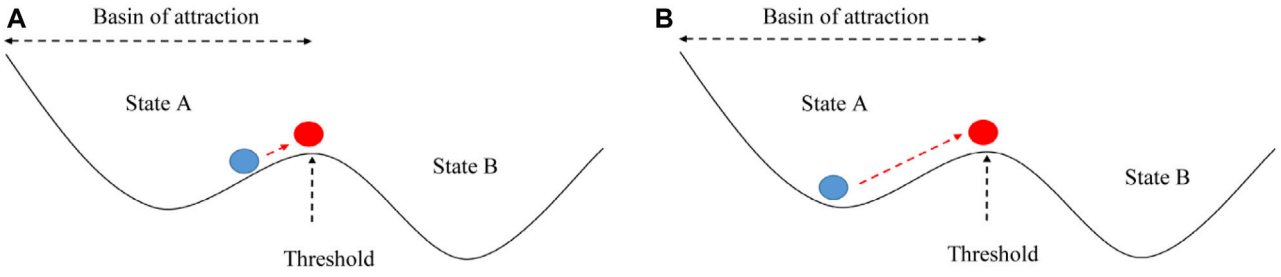

FIGURE 11
Schematic diagram of the CSD phenomenon (Dakos et al., 2015). **(A)** close to the threshold and **(B)** far from the threshold.

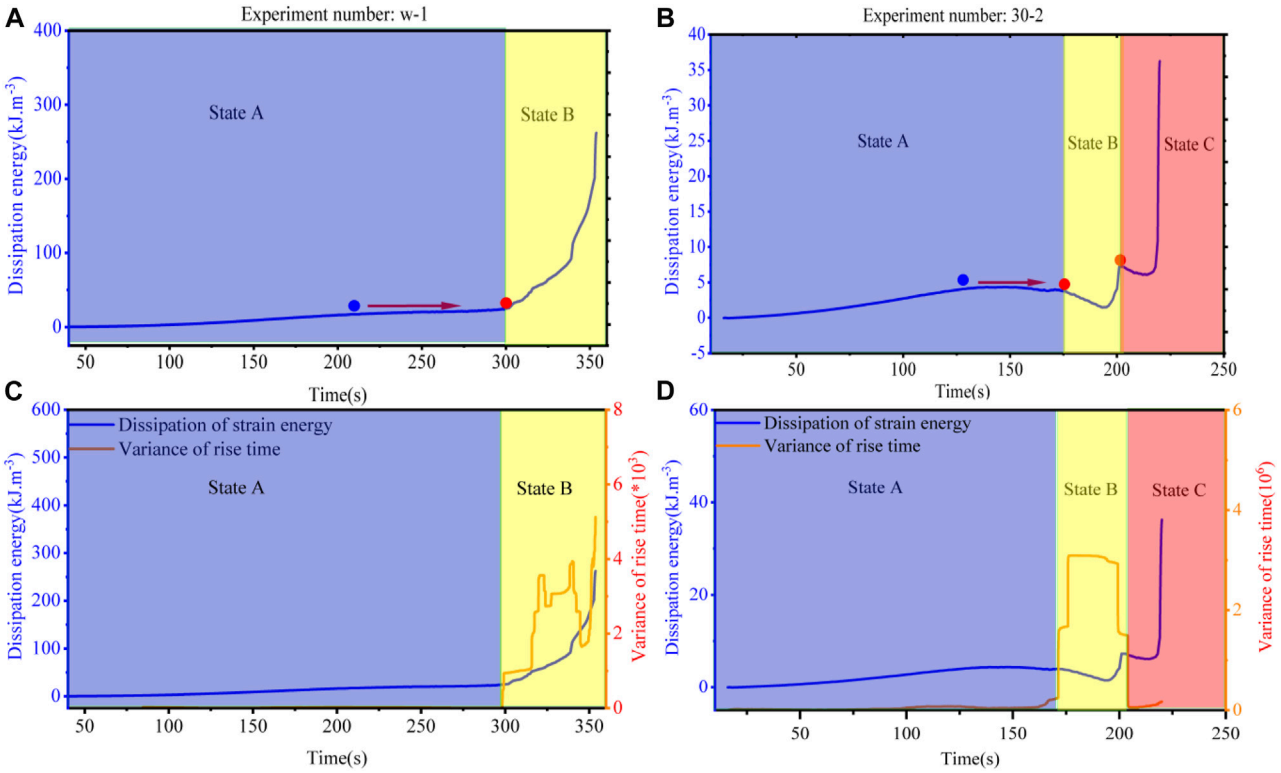

FIGURE 12
Mechanism of the CSD phenomenon in sandstone. **(A,C)** first typical kinetic system of sandstone and **(B,D)** second typical kinetic system of sandstone.

the CSD indicators rise because of a diminished ability to recover to the original state (Figure 12C). Figure 12B is a more complex dynamic system, as shown in Figure 12D, in which the system is driven to cross the boundary between two basins of attraction by an external (mechanical input of energy to the sandstone) perturbation, the system state is changed into state B, and the first CSD phenomenon (flickering) appears near the threshold, which is manifested by an increase in the CSD indicators. With the continuous increase in energy during loading, the dissipation energy system crosses the boundary of state B and state C again, the CSD phenomenon reappears close to the second threshold, and the variance appears to steadily increase. The reason for the smaller increase in variance near the second threshold rather than the first threshold is closely related to the characteristics of the CSD phenomenon, as can be seen from Figure 12D, where the slope of the first threshold point is less than the slope of the

second threshold point, i.e., the dissipation energy system recovers much more slowly near the first threshold point than the second threshold point. In the time domain, the dissipation energy system takes much more time to go from the starting point of state A (unloaded state) to the endpoint of state A than from the starting point of state B to the endpoint of state B. In a similar way, the time required from the beginning of state B to its end is longer than the time required from the beginning of state C to its end. As shown in Figure 3B, the input energy is a gradually growing process, and therefore, it will be irrecoverable after causing a change in the system state.

Discussion

Previous methods for studying the rock fracture acoustic emission precursors include singular spectrum analysis, fast Fourier transform, frequency center of mass, fractal characteristics, and wave velocity (Gong et al., 2017; Li et al., 2019; Mei et al., 2019; Zhao et al., 2020; Dong et al., 2021). However, the precursors are difficult to identify. In this study, we proposed the CSD theory and added time series indicators to the autoregressive model indicators. Through the combination of multiple CSD indicators, the probability of false alarms and missed alarms in the warning process is reduced. In addition, the formation mechanism of the CSD phenomenon of rock sample destruction is explained by energy. In actuality, the CSD phenomenon does not occur in all systems changing states; rather, it typically occurs in the following situations (Dakos et al., 2015): 1) a slow environmental change toward a tipping point, 2) slow–fast cyclic transitions, 3) a combination of random perturbations and periodic changes in the environment, and 4) strong perturbations that cause the system to cross into a new state. External drivers in practical engineering are more complex. For instance, driven by rainfall, earthquakes, and human activities, changes in temperature fields may trigger geological hazards (Roje-Bonacci et al., 2009; Ma J et al., 2018; Oswald et al., 2021; Li et al., 2022). Several studies have indicated that geological hazards such as earthquakes exhibit critical slowing phenomena (Qiao et al., 2022). However, since landslides and collapses may be caused by a combinations of multiple driving factors, this makes it challenging for detecting CSD phenomena in practical engineering. As a result, this will be our next major research emphasis.

Conclusion

In this study, uniaxial loading tests were conducted on parallel-fractured sandstone with different angles and intact sandstone, and acoustic emission was used to monitor the entire sandstone loading process in real time. On the basis of the study of the characteristics of CSD indicators of acoustic emission parameters during sandstone damage, the effect of prefabricated fracture angles on CSD phenomena, and the mechanism of CSD formation in sandstone, the following conclusion was drawn.

(1) For the autoregressive model CSD indicators, the lag step and window length have essentially no effect on the appearance time of precursor points, and the longer the window length is, the less is the fluctuation of the autoregressive model CSD indicators. Compared to the variance, the autocorrelation coefficient is more influenced by the lag step length. In addition, the autocorrelation coefficient fluctuates greatly throughout the process, making it difficult to identify the precursor points as the variance. The size of the window affects the degree of fluctuation of the CSD metric; the longer the window is, the smoother is the metric.
(2) Under the conditions of constant fracture length, width, and fracture spacing, the time of the precursor point, stress at the precursor point, peak stress, and damage time decreased from intact rock samples to 45° rock samples and had an increasing trend from 45° to 75° rock samples.
(3) In the process of sandstone failure, the total energy input to the sandstone from the loading equipment is a slowly increasing process, which, as a driving force, will drive the dissipation energy system to transfer from one state to another, and the CSD phenomenon will appear near the critical point of the two states, thus leading to the development of the state of the sandstone from a stable state to an unstable state, which is manifested by the increase in the CSD indicators. In addition, near the critical point, a small perturbation of the total energy to the dissipation energy system causes the dissipation energy to flicker across the boundary between the two states. For such a slowly developing and abruptly changing system, the change of state is permanent, which means that the rupture of the rock mass is irreparable.

Data availability statement

The raw data supporting the conclusion of this article will be made available by the authors, without undue reservation.

Author contributions

YT: conceptualization, methodology, formal analysis, investigation, data curation, and writing—original draft. XZ: conceptualization, methodology, validation, resources,

writing—review and editing, and funding acquisition. CH: methodology, investigation, and data curation. JH: validation and writing. JF: conceptualization, validation, and writing.

Funding

This work was supported by the National Natural Science Foundation of China (41877254 and 41941019), the National Key Research and Development Program (2019YFC1509602), and the Second Qinghai-Tibet Plateau Integrated Scientific Research Grant (2019QZKK0201).

Conflict of interest

The authors all declare that they have no conflict of interest.

Publisher's note

All claims expressed in this article are solely those of the authors and do not necessarily represent those of their affiliated organizations, or those of the publisher, the editors, and the reviewers. Any product that may be evaluated in this article, or claim that may be made by its manufacturer, is not guaranteed or endorsed by the publisher.

References

Ali, S. M., Hui, K. H., Hee, L. M., Leong, M. S., Abdelrhman, A. M., Al-Obaidi, M. A., et al. (2019). Observations of changes in acoustic emission parameters for varying corrosion defect in reciprocating compressor valves. *Ain Shams Eng. J.* 10, 253–265. doi:10.1016/j.asej.2019.01.003

Biggs, R., Carpenter, S. R., and Brock, W. A. (2009). Turning back from the brink: Detecting an impending regime shift in time to avert it. *Proc. Natl. Acad. Sci. U. S. A.* 106, 826–831. doi:10.1073/pnas.0811729106

Chen, A., Sanchez, A., Dai, L., and Gore, J. (2014). Dynamics of a producer-freeloader ecosystem on the brink of collapse. *Nat. Commun.* 5, 3713. doi:10.1038/ncomms4713

Dakos, V., and Bascompte, J. (2014). Critical slowing down as early warning for the onset of collapse in mutualistic communities. *Proc. Natl. Acad. Sci. U. S. A.* 111, 17546–17551. doi:10.1073/pnas.1406326111

Dakos, V., Carpenter, S. R., Brock, W. A., Ellison, A. M., Guttal, V., Ives, A. R., et al. (2012). Methods for detecting early warnings of critical transitions in time series illustrated using simulated ecological data. *PLoS ONE* 7, e41010. doi:10.1371/journal.pone.0041010

Dakos, V., Carpenter, S. R., van Nes, E. H., and Scheffer, M. (2015). Resilience indicators: Prospects and limitations for early warnings of regime shifts. *Phil. Trans. R. Soc. B* 370, 20130263. doi:10.1098/rstb.2013.0263

Diks, C., Hommes, C., and Wang, J. (2019). Critical slowing down as an early warning signal for financial crises? *Empir. Econ.* 57, 1201–1228. doi:10.1007/s00181-018-1527-3

Dong, L., Chen, Y., Sun, D., and Zhang, Y. (2021). Implications for rock instability precursors and principal stress direction from rock acoustic experiments. *Int. J. Min. Sci. Technol.* 31, 789–798. doi:10.1016/j.ijmst.2021.06.006

Du, Y., Xie, M., Jiang, Y., Chen, C., Jia, B., and Huo, L. (2021). Review on the formation mechanismand early warning of rock collapse. *Metal Mine* 535 (01), 106–119. doi:10.19614/j.cnki.jsks.202101008

Gama Dessavre, A., Southall, E., Tildesley, M. J., and Dyson, L. (2019). The problem of detrending when analysing potential indicators of disease elimination. *J. Theor. Biol.* 481, 183–193. doi:10.1016/j.jtbi.2019.04.011

Gong, Y., Song, Z., He, M., Gong, W., and Ren, F. (2017). Precursory waves and eigenfrequencies identified from acoustic emission data based on Singular Spectrum Analysis and laboratory rock-burst experiments. *Int. J. Rock Mech. Min. Sci.* 91, 155–169. doi:10.1016/j.ijrmms.2016.11.020

Guttal, V., and Jayaprakash, C. (2008). Changing skewness: an early warning signal of regime shifts in ecosystems. *Ecol. Lett.* 11, 450–460. doi:10.1111/j.1461-0248.2008.01160.x

Jin, J., Cao, P., Chen, Y., Pu, C., Mao, D., Fan, X., et al. (2017). Influence of single flaw on the failure process and energy mechanics of rock-like material. *Comput. Geotech.* 86, 150–162. doi:10.1016/j.compgeo.2017.01.011

Li, B., Zhang, G., Wang, G., and Qiao, J. (2022). Damage evolution of frozen-thawed granite based on high-resolution computed tomographic scanning. *Front. Earth Sci.* 10, 912356. doi:10.3389/feart.2022.912356

Li, D., Wang, E., Kong, X., Jia, H., Wang, D., Ali, M., et al. (2019). Damage precursor of construction rocks under uniaxial cyclic loading tests analyzed by acoustic emission. *Constr. Build. Mat.* 206, 169–178. doi:10.1016/j.conbuildmat.2019.02.074

Li, H., Shen, R., Qiao, Y., and He, M. (2021). Acoustic emission signal characteristics and its critical slowing down phenomenon during the loading process of water-bearing sandstone. *J. Appl. Geophy.* 194, 104458. doi:10.1016/j.jappgeo.2021.104458

Lin, Q., Cao, P., Wen, G., Meng, J., Cao, R., Zhao, Z., et al. (2021). Crack coalescence in rock-like specimens with two dissimilar layers and pre-existing double parallel joints under uniaxial compression. *Int. J. Rock Mech. Min. Sci.* 139, 104621. doi:10.1016/j.ijrmms.2021.104621

Ma, G., Hu, X., Yin, Y., Luo, G., and Pan, Y. (2018). Failure mechanisms and development of catastrophic rockslides triggered by precipitation and open-pit mining in Emei, Sichuan, China. *Landslides* 15, 1401–1414. doi:10.1007/s10346-018-0981-5

Ma, J., Tang, J., Yan, Z., Jiang, F., Zeng, H., and Fang, C. (2018). "Data-driven power system collapse predicting using critical slowing down indicators," in Proceeding International Conference on Power System Technology (POWERCON), Guangzhou, 06-08 November 2018 (IEEE), 1879–1884. doi:10.1109/POWERCON.2018.8602265

Maturana, M. I., Meisel, C., Dell, K., Karoly, P. J., D'Souza, W., Grayden, D. B., et al. (2020). Critical slowing down as a biomarker for seizure susceptibility. *Nat. Commun.* 11, 2172. doi:10.1038/s41467-020-15908-3

Mehrabbeik, M., Ramamoorthy, R., Rajagopal, K., Nazarimehr, F., Jafari, S., Hussain, I., et al. (2021). Critical slowing down indicators in synchronous period-doubling for salamander flicker vision. *Eur. Phys. J. Spec. Top.* 230, 3291–3298. doi:10.1140/epjs/s11734-021-00113-0

Mei, F., Hu, C., Li, P., and Zhang, J. (2019). Study on main frequency precursor characteristics of acoustic emission from deep buried dali rock explosion. *Arab. J. Geosci.* 12, 645. doi:10.1007/s12517-019-4706-4

Nannes, B., Quax, R., Ashikaga, H., Hocini, M., Dubois, R., Bernus, O., et al. (2020). "Early signs of critical slowing down in heart surface electrograms of ventricular fibrillation victims," in *Computational science – ICCS 2020 lecture notes in computer science*. Editors V. V. Krzhizhanovskaya, G. Závodszky, M. H. Lees, J. J. Dongarra, P. M. A. Sloot, S. Brissos, et al. (Cham: Springer International Publishing), 334–347. doi:10.1007/978-3-030-50423-6_25

Nazarimehr, F., Jafari, S., Perc, M., and Sprott, J. C. (2020). Critical slowing down indicators. *Europhys. Lett.* 132, 18001. doi:10.1209/0295-5075/132/18001

Ohno, K., and Ohtsu, M. (2010). Crack classification in concrete based on acoustic emission. *Constr. Build. Mat.* 24, 2339–2346. doi:10.1016/j.conbuildmat.2010.05.004

Oswald, P., Strasser, M., Hammerl, C., and Moernaut, J. (2021). Seismic control of large prehistoric rockslides in the Eastern Alps. *Nat. Commun.* 12, 1059. doi:10.1038/s41467-021-21327-9

Peng, K., Liu, Z., Zou, Q., Wu, Q., and Zhou, J. (2020). Mechanical property of granite from different buried depths under uniaxial compression and dynamic impact: An energy-based investigation. *Powder Technol.* 362, 729–744. doi:10.1016/j.powtec.2019.11.101

Qiao, Z., Wang, G., Fu, H., and Hu, X. (2022). Identification of groundwater radon precursory anomalies by critical slowing down theory: A case study in yunnan region, southwest China. *Water* 14, 541. doi:10.3390/w14040541

Roje-Bonacci, T., Miščević, P., and Števanić, D. (2009). Rock-slides on road cuttings in the dinaric karst of Croatia: Processes and factors. *Environ. Geol.* 58, 359–369. doi:10.1007/s00254-008-1602-8

Rozek, J. C., Camp, R. J., and Reed, J. M. (2017). No evidence of critical slowing down in two endangered Hawaiian honeycreepers. *PLOS ONE* 12, e0187518. doi:10.1371/journal.pone.0187518

Scheffer, M., Bascompte, J., Brock, W. A., Brovkin, V., Carpenter, S. R., Dakos, V., et al. (2009). Early-warning signals for critical transitions. *Nature* 461, 53–59. doi:10.1038/nature08227

Su, H. J., Jing, H. W., Zhao, H. H., Zhang, M. L., and ang Yin, Q. (2015207). Strength and fracture characteristic of rock mass containing parallel fissures. *Eng. Mech.* 32, 192–197. doi:10.6052/j.issn.1000-4750.2014.05.0419

Syed Musa, S. M. S., Md Noorani, M. S., Abdul Razak, F., Ismail, M., Alias, M. A., Hussain, S. I., et al. (2021). Using persistent homology as preprocessing of early warning signals for critical transition in flood. *Sci. Rep.* 11, 7234. doi:10.1038/s41598-021-86739-5

Tan, J. P. L., and Cheong, S. S. A. (2014). Critical slowing down associated with regime shifts in the US housing market. *Eur. Phys. J. B* 87, 38. doi:10.1140/epjb/e2014-41038-1

Tu, C., D'Odorico, P., and Suweis, S. (2020). Critical slowing down associated with critical transition and risk of collapse in crypto-currency. *R. Soc. Open Sci.* 7, 191450. doi:10.1098/rsos.191450

S. J. Vahaviolos (Editor) (1999). *Acoustic emission: standards and technology update*. (West Conshohocken, PA: ASTM).

van de Leemput, I. A., Wichers, M., Cramer, A. O. J., Borsboom, D., Tuerlinckx, F., Kuppens, P., et al. (2014). Critical slowing down as early warning for the onset and termination of depression. *Proc. Natl. Acad. Sci. U. S. A.* 111, 87–92. doi:10.1073/pnas.1312114110

Wei, Y., Li, Z., Kong, X., Zhang, Z., Cheng, F., Zheng, X., et al. (2018). The precursory information of acoustic emission during sandstone loading based on critical slowing down theory. *J. Geophys. Eng.* 15, 2150–2158. doi:10.1088/1742-2140/aac009

Wen, B., Wang, S., Wang, E., and Zhang, J. (2004). Characteristics of rapid giant landslides in China. *Landslides* 1, 247–261. doi:10.1007/s10346-004-0022-4

Wichers, M., and Groot, P. C.Psychosystems; ESM Group; EWS Group (2016). Critical slowing down as a personalized early warning signal for depression. *Psychother. Psychosom.* 85, 114–116. doi:10.1159/000441458

Wu, H., Hou, W., Zuo, D., Yan, P., and Zeng, Y. (2021). Early-warning signals of drought-flood state transition over the dongting lake basin based on the critical slowing down theory. *Atmosphere* 12, 1082. doi:10.3390/atmos12081082

Yang, S.-Q., and Jing, H.-W. (2011). Strength failure and crack coalescence behavior of brittle sandstone samples containing a single fissure under uniaxial compression. *Int. J. Fract.* 168, 227–250. doi:10.1007/s10704-010-9576-4

Yang, X.-X., Jing, H.-W., Tang, C.-A., and Yang, S.-Q. (2017). Effect of parallel joint interaction on mechanical behavior of jointed rock mass models. *Int. J. Rock Mech. Min. Sci.* 92, 40–53. doi:10.1016/j.ijrmms.2016.12.010

Zhang, L., Niu, F., Liu, M., Ju, X., Wang, Z., Wang, J., et al. (2022). Fracture characteristics and anisotropic strength criterion of bedded sandstone. *Front. Earth Sci.* 10, 879332. doi:10.3389/feart.2022.879332

Zhang, X., Li, Z., Niu, Y., Cheng, F., Ali, M., Bacha, S., et al. (2019). An experimental study on the precursory characteristics of EP before sandstone failure based on critical slowing down. *J. Appl. Geophy.* 170, 103818. doi:10.1016/j.jappgeo.2019.103818

Zhang, Z., Li, Y., Hu, L., Tang, C., and Zheng, H. (2021). Predicting rock failure with the critical slowing down theory. *Eng. Geol.* 280, 105960. doi:10.1016/j.enggeo.2020.105960

Zhao, K., Yang, D., Gong, C., Zhuo, Y., Wang, X., Zhong, W., et al. (2020). Evaluation of internal microcrack evolution in red sandstone based on time–frequency domain characteristics of acoustic emission signals. *Constr. Build. Mat.* 260, 120435. doi:10.1016/j.conbuildmat.2020.120435

Zhou, T., Zhu, J. B., Ju, Y., and Xie, H. P. (2019). Volumetric fracturing behavior of 3D printed artificial rocks containing single and double 3D internal flaws under static uniaxial compression. *Eng. Fract. Mech.* 205, 190–204. doi:10.1016/j.engfracmech.2018.11.030

frontiers | Frontiers in Earth Science

ORIGINAL RESEARCH
published: 29 August 2022
doi: 10.3389/feart.2022.934360

Land Lapse Phenomenon and Surface Subsidence Law of Shield Tunnel Passing Through Rock-Bearing Formation

Yu Guangming[1], *Xia Pengju*[2], *Zhang Yongyi*[1]*, *Shi Qimeng*[1], *Lei Jun*[3], *Song Pengfei*[4], *Tan Zhiwen*[4], *Liu Hao*[3] *and Chen Ze*[3]

[1]School of Civil Engineering, Qingdao University of Technology, Qingdao, China, [2]CCCC Tunnel Engineering Company Limited, Qingdao, China, [3]China Construction Fifth Bureau 5 South China Company, Guangzhou, China, [4]China Construction Tunnel Construction Co., Ltd., Chongqing, China

When constructing subway tunnels in coastal cities, boulders with high strength and large volume are often encountered. A large number of engineering practices have shown that the existence of boulders will destroy the unity and homogeneity of the stratum. If the tunnel is not properly handled during crossing construction, it will lead to the collapse of surrounding rock; in serious cases, it may induce ground collapse, damage the surrounding buildings, and endanger the safety of people's lives and property. Firstly, with the help of similar material simulation test, this paper reproduces the phenomenon of vault collapse and surface collapse when the tunnel passes through the boulder stratum, explores the law of stratum collapse and surface settlement caused by the boulder in the process of tunnel excavation, and puts forward the "weightlessness weak surface effect" of the boulder stratum disturbed. Then, taking the Liu-Bai inter-district tunnel project of Shenzhen Metro Line 13 as an example, Midas GTS NX numerical simulation software is used to compare and analyze the influence characteristics of surrounding rock deformation and surface settlement caused by the presence or absence of boulders in the tunnel through the stratum and verify the "weightlessness weak surface effect" of the boulder stratum disturbed. Finally, the engineering treatment measures for the Liu-Bai inter-district tunnel project of Shenzhen Metro Line 13 crossing the boulder stratum are given. The research results are of great significance to guide the prediction and treatment of collapse and surface settlement when crossing the boulder stratum in the tunnel construction project.

Keywords: boulder, shield construction, surrounding rock deformation, surface, tunnel

OPEN ACCESS

Edited by:
Bo Li,
Tongji University, China

Reviewed by:
Zhanping Song,
Xi'an University of Architecture and Technology, China
Minghao Liu,
Chinese Academy of Sciences (CAS), China

***Correspondence:**
Zhang Yongyi
1794700715@qq.com

Specialty section:
This article was submitted to Geohazards and Georisks, a section of the journal Frontiers in Earth Science

Received: *02 May 2022*
Accepted: *14 June 2022*
Published: *29 August 2022*

Citation:
Guangming Y, Pengju X, Yongyi Z, Qimeng S, Jun L, Pengfei S, Zhiwen T, Hao L and Ze C (2022) Land Lapse Phenomenon and Surface Subsidence Law of Shield Tunnel Passing Through Rock-Bearing Formation. Front. Earth Sci. 10:934360. doi: 10.3389/feart.2022.934360

INTRODUCTION

In the coastal granite area, due to the anisotropic arrangement of minerals and the complex distribution of fissures, uneven weathering and residual bodies retained in the residual soil and weathered rock strata are often formed in the stratum. This residual body is called the "boulder." This boulder has high strength, is very different from the surrounding rock and soil mass, and has obvious interface and deformation differences from the surrounding rock and soil mass, for example. The compressive strength of boulders encountered between the left and white areas of Shenzhen Metro

Line 13 is up to 177 MPa, 130 MPa higher than that of the surrounding weathered rock mass. This will not only cause serious wear and tear to the shield machine, or even cause damage, but also cause uneven disturbance of the stratum, overbreak of the stratum, tunnel collapse, surface settlement, and other phenomena. Therefore, studying the influence of boulders on the stability of surrounding rock and the characteristics of surface settlement during shield construction and summarizing the relevant measures for boulder treatment are conducive to taking scientific measures to control the disturbance to the stratum during the process of shield driving. Relevant scholars have carried out corresponding research on this. Zhu et al. (2021) based on the interval between Pengcuo North Station and Caicuo Station of Xiamen Metro Line 4 carried out discrete element numerical analysis for the stability of shield tunneling in the coastal isolated stone stratum. Chen et al. (2018) established the construction model of the tunnel in the stratum containing solitary stone by using the discrete element software PFC2D and studied the catastrophic mechanism and influence range of stratum collapse caused by broken solitary rock in tunnel driving. Li et al. (2021) took the construction section of Shantou Bay Tunnel as the engineering background to study the surrounding rock deformation when shield construction encounters solitary rock stratum. Hu (2019) based on the exit section of Shiniuling tunnel in the second section of Fuqing highway, through theoretical analysis, field observation test, and numerical simulation analysis, carried out a study on the characteristics of stratum movement at the entrance of fully weathered tunnel with solitary stone. Zhang (2009) studied the influence of solitary rock on the internal force distribution of the initial support of the tunnel by using the stratum structure method and the load structure method, respectively, and analyzed the failure mode of the initial supporting structure. Zhang et al. (2007) analyzed the deformation and failure process of tunnel with weak layer through similar material model test. Li et al. (2007) studied the deformation and failure mode of tunnel surrounding rock and the evolution process of deformation and fracture under different confining pressure through triaxial similar model test and digital photographic deformation measurement technology. Selby (1999) studied the formation deformation caused by shield tunnel construction by linear finite element and Lagrangian finite difference method. Zheng et al. (2019) relied on the tunnel project of Tianjin Metro Line 5, adopted the multi-stage control strategy, and studied the influence of different parameters on surface subsidence by adjusting the tunneling parameters of shield passing through bad geology. Moghaddasi and Noorian-Bidgoli (2018) combined the imperialist competition algorithm (ICA) and artificial neural network (ANN) to form a new surface subsidence prediction model (ICA-ANN); this paper also analyzes the above three prediction methods to predict the surface subsidence value caused by the shield tunnel crossing the bad geology, and the results showed the accuracy of ICA-ANN prediction results is significantly higher than that of ICA and ANN results. Sugiyama et al. (1999) used finite element software to study the changes of surface settlement caused by tunnel construction during tunnel crossing through bad geology and proposed the related measures to reduce the surface subsidence. Zhu et al. (2011) dealt with the solitary stone by drilling and blasting, so as to ensure the safety of tunnel excavation. Wang (2012) summarized the examples and related technologies of solitary stone treatment in shield engineering under different geological conditions. Liu et al. (2016) explored solitary stone strata. It was shown that the micro-motion detection method is suitable for the urban complex environmental strip. Dang (2012) adopted the geophysical method to detect the occurrence of solitary rocks along the tunnel in order to solve the influence of solitary stones on shield tunneling. Zong and Tian (2015) put forward a full set of new methods for prediction and disposal of shield solitary stones in subway tunnels, which are fretting exploration + infill geological supplementary drilling + ground drilling blasting. The principle and implementation steps of the new method are explained in detail and applied to specific engineering examples.

In summary, domestic and foreign scholars have mainly studied the stratum disturbance caused by shield tunnel passing through solitary rock and other bad geology by means of numerical simulation and similar material model test and summarized the relevant treatment measures of shield tunnel passing through the isolated boulder. Generally speaking, relevant scholars mainly focus on the treatment measures of boulders, while there are relatively few research results on the influence of boulders on the deformation of surrounding rock and surface settlement, especially the abnormal disturbance of strata caused by boulders and the occurrence of "weightlessness weak surface effect." Based on the interval between Liu Xiandong Station and Bai Mang Station of Shenzhen Metro Line 13, with the help of Midas GTS NX finite element numerical simulation software and similar material model test, this paper studies the influence of surrounding rock deformation and surface settlement under the condition of shield passing through solitary rocks, in order to provide some reference for the safe construction of the shield tunnel through the boulder formation in the later stage. The technical road map is shown in **Figure 1**.

EXPERIMENTAL STUDY ON SIMILAR MATERIAL MODEL OF TUNNEL PASSING THROUGH SOLITARY STONE STRATUM

In the actual engineering of tunnel through rock stratum construction, if the rock is not treated, through direct construction, it is likely to slide and induce the instability of the surrounding rock and soil body, resulting in large formation loss, resulting in the increase of surface subsidence or collapse. Therefore, in the process of tunnel construction, the solitary rock needs to be treated, that is, by the way of ground blasting. If the broken solitary rock is not grouted and reinforced, it is in a loose state. When the tunnel crosses, the loose rock will affect the stability of the surrounding rock and will also produce a too large surrounding rock deformation or even collapse phenomenon. This paper uses the real physical entity (physical model), which, according to the similar principle conditions, truly reflects the spatial relationship between the geological structure and the engineering structure and the accurate simulation construction

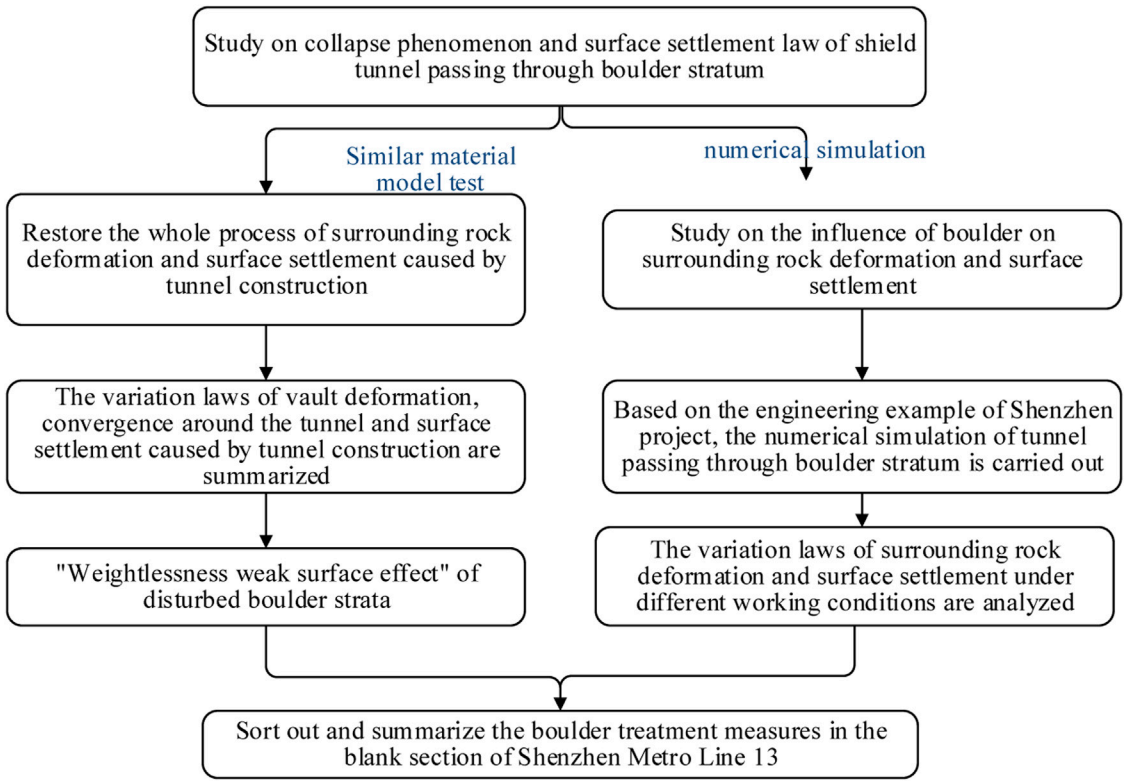

FIGURE 1 | Technology road map.

process, reproduces the tunnel construction deformation, cracking, collapse, and even transmission to the surface, and causes the surface subsidence to the whole process, stress characteristics, deformation trend, and collapse hazard characteristics.

Tunnel collapse usually refers to the phenomenon of a large amount of rock and sediment collapse due to the stress of the rock and sediment on both sides of the tunnel. There are many influencing factors leading to tunnel collapse. The main influencing factors are internal geological factors and human factors. This paper mainly considers geological factors: 1) Structural factors of rock and soil body. Rock and soil mass usually uses the fragmentation degree of the structure or the complete state of the rock and soil mass structure to express the structural state. When the rock and soil mass is in the original state, due to the long-term action of various geological structural movements, the structural surface will produce deformation, dislocation, fracture, and other damage phenomena and lose its original complete state to different degrees. Under the same lithology conditions, the greater the crushing degree of rock mass is, the more likely the tunnel becomes unstable and collapses. This is the right state of the rock broken by ground drilling and blasting, and in this case, it is the most important cause of tunnel collapse and surface collapse. 2) Engineering nature of the rock. The engineering nature of the rock usually refers to the hardness of the rock and the characteristics of the rock structure surface, in which the resistance to the surrounding rock deformation is called the hardness of the rock, which reflects the physical and mechanical properties of the block itself. When the rock mass is relatively complete, the lower the hardness of the rock mass, the worse the stability of the tunnel surrounding rock and the easier it collapses. The appearance of rock mass structure surface is usually caused by the insufficient resistance of rock resistance to shear. The appearance of structural surface not only cuts the complete rock mass but also forms many harmful geological interfaces, such as joints and weak interlayers. Therefore, the shear strength of rock mass structure surface is an important factor affecting the stability of surrounding rock. 3) In addition, the action and influence of groundwater, the initial stress state of surrounding rock, the surrounding rock level, and other geological factors will also affect the stability of surrounding rock during tunnel construction.

In this paper, barite, quartz sand, gypsum, water, and other materials are proportioned according to a certain proportion, and the physical and mechanical properties of the proportioning of the mixed materials are determined through relevant experiments. Through multiple physical and mechanical experiments on the proportioning of the mixed materials, the proportioning of the model materials corresponding to the prototype materials is prepared. Among them, the ratio of barite: quartz sand: gypsum is 13:4:1. The physical and mechanical parameters corresponding to prototype materials and model materials are shown in **Table 1**.

Using quartz sand, mica powder, and barite powder as aggregates and lime and gypsum as cementing materials, a

TABLE 1 | Physical and mechanical parameters corresponding to prototype materials and model materials.

Material	Geometric scale	Weight of soil (kN/M^3)	Poisson's ratio	E (GPa)	c (MPa)	φ (∘)
Prototype material	20	20	0.36	1.0	0.197	26.7
Model material	1	20	0.36	0.05	0.01	27
Proportion	20	1	1	20	19.7	0.99

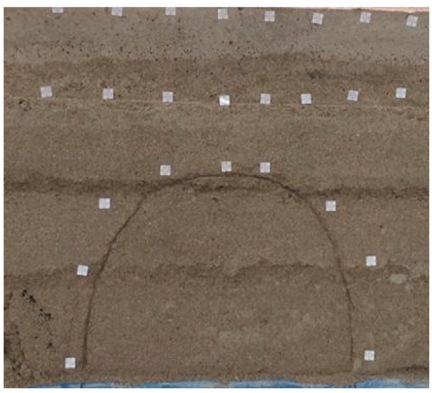

FIGURE 2 | Similar material model and measuring point layout (model front).

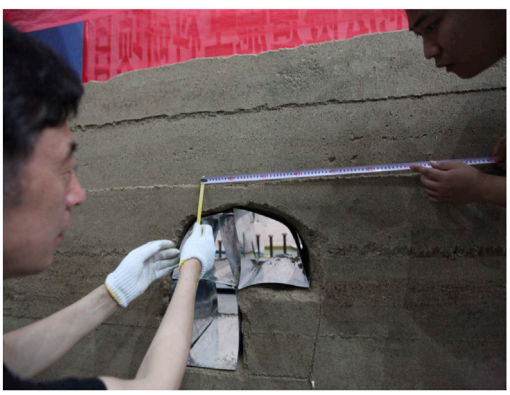

FIGURE 3 | Cracking drawing of the tunnel arch (model back).

FIGURE 4 | Real picture of tunnel collapse and even surface collapse.

FIGURE 5 | 3D laser scanner.

similar material simulation model containing the boulder stratum is constructed for tunnel construction to simulate the whole process of vault deformation, cracking, collapse, and even transmission to the surface on the tunnel cross section, resulting in excessive surface settlement and collapse, as shown in **Figures 2–4**.

This study uses quartz sand, mica powder, and barite powder as aggregates and lime and gypsum as similar materials, includes a similar material simulation model, tunnel construction, simulated tunnel cross section arch deformation, cracking, collapse, and even transfer to the surface, and causes the whole process of surface subsidence until collapse, as shown in **Figure 2~Figure 6**.

In this paper, the Faro three-dimensional laser scanner is used to monitor the surrounding rock deformation and surface settlement during the tunnel excavation in the simulation test of similar materials, as shown in **Figure 5**.

The data processing of the three-dimensional laser scanner is divided into two stages. The first stage includes noise reduction and point cloud splicing. The second stage is to compare and analyze the point clouds before and after two or more times. Before noise reduction and point cloud splicing, the scanned point cloud image format is transformed into a special format FLS, and then the point cloud is imported into scene software for noise reduction and point cloud image splicing. Finally, the noise reduced and spliced point cloud image is only kept within the range we need. On the basis of point cloud image processing in

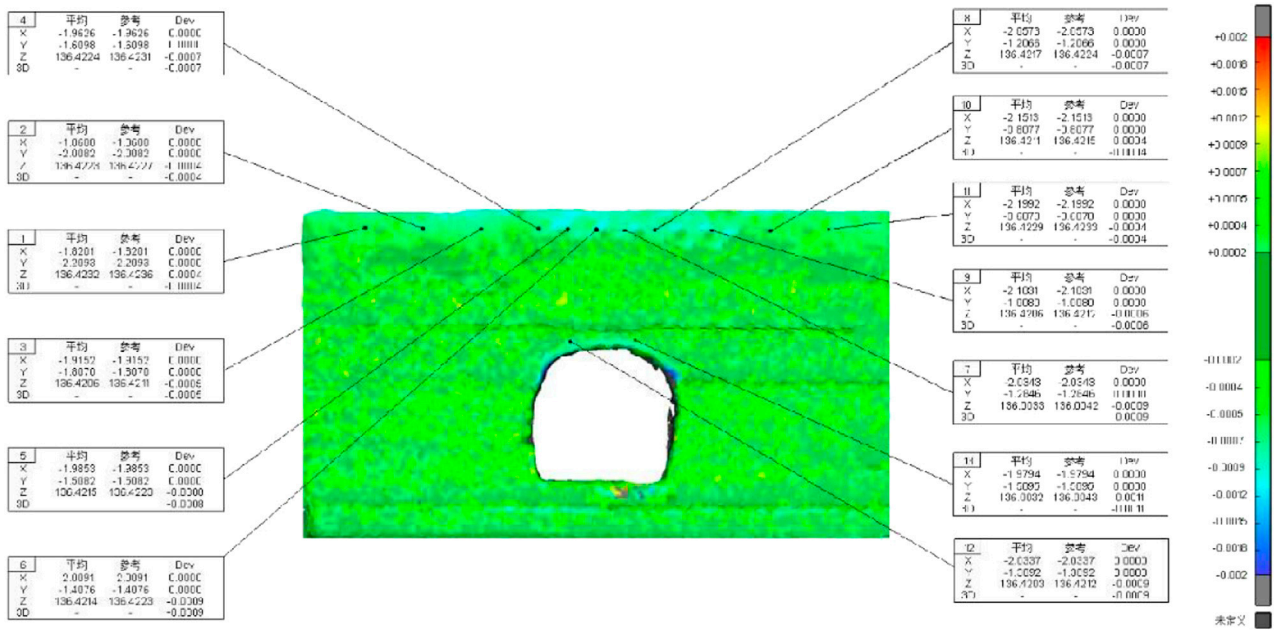

FIGURE 6 | Cloud chart of three-dimensional laser scanner monitoring convergence around the tunnel model.

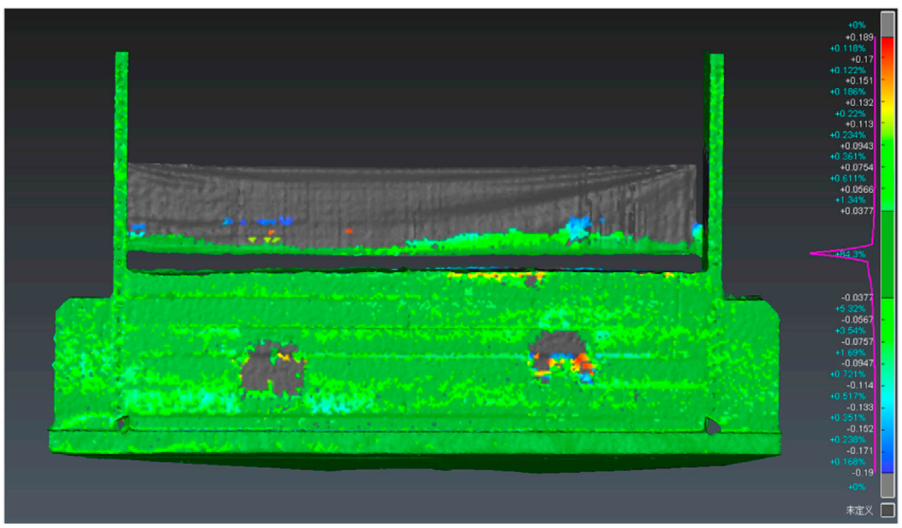

FIGURE 7 | Cloud map of surface collapse and subsidence.

the previous step, the RPS registration function under the conversion tab in 3DReshaper software is used to register the two point clouds to the same coordinate system. The former scanning point cloud is used as the fixed reference point cloud, and the latter scanning point cloud is used as the mobile registration point cloud. The registration of two point cloud maps is carried out in the same coordinate system, the two point cloud files before and after are selected, then the painted object is selected through the comparison/detection function in the measurement tab of 3DReshaper software, and finally 2D or 3D detection is performed to generate the deformation cloud map. The deformation values of the two surface layers can be compared to obtain the displacement of any point on the rock layer and the surface, as shown in **Figure 6** and **Figure 7**.

By reproducing and analyzing the deformation characteristics and collapse process of the surrounding rock and even the surface caused by tunnel construction, the following knowledge is mainly obtained: 1) In the model test, the surrounding rock has been

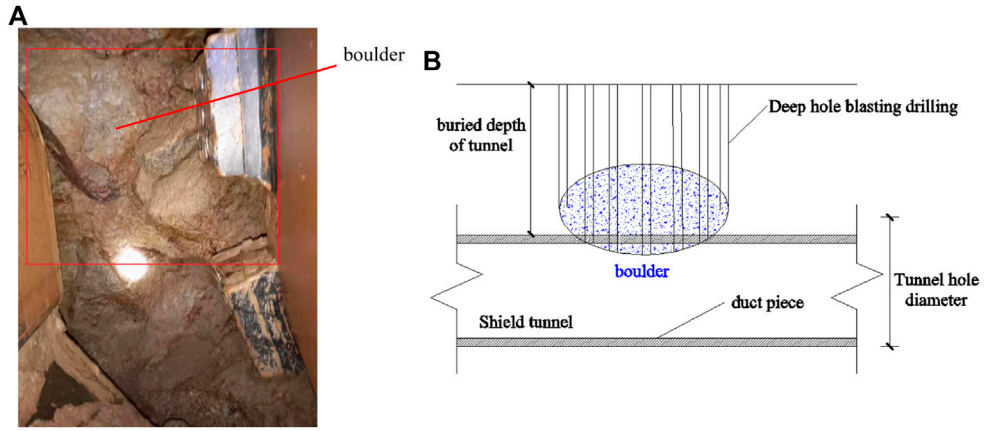

FIGURE 8 | Schematic diagram of location distribution of boulders. **(A)** Location diagram of the boulder distribution in the left ~ white interval. **(B)** Schematic diagram of position distribution of boulders in the longitudinal tunnel from left to white interval.

disturbed during the tunnel construction process. The surrounding rock above the tunnel vault cracks, which gradually develops and eventually leads to the collapse of the vault. 2) The deformation of the tunnel surrounding rock is monitored by a three-dimensional laser scanner. Some characteristics and rules of tunnel arch subsidence, hole around convergence, and even surface subsidence can be obtained, that is, under normal formation conditions, surface subsidence caused by tunnel construction is a normal and regular phenomenon. When there are special rock components such as solitary rock and joints, there will be a surface subsidence anomaly causing the landslide phenomenon.

ANALYSIS OF "WEIGHTLESSNESS WEAK SURFACE EFFECT" OF BOULDER DISTURBED WHEN TUNNEL PASSES THROUGH BOULDER STRATUM

The formation structure of the left-white section of Shenzhen Metro Line 13 is complex, with many types of rock and soil bodies, buried depth, thickness, and own properties. The tunnel crossing the stratum mainly includes strongly weathered granite, moderately weathered granite, and microweathered granite. In the process of tunnel tunneling, there are bad geological conditions such as boulders along the line. If they are not treated, the vault is prone to local damage under no support conditions, and the position relationship between boulders and the longitudinal section of the tunnel is shown in **Figure 8**.

It can be seen from **Figure 9** that when the tunnel excavation stratum does not contain boulders, the stratum area caused by the tunnel construction disturbance is mainly settlement area 1, and its stratum settlement curve is settlement curve 1. When the tunnel passes through the boulder stratum, not only the settlement deformation caused by the tunnel construction disturbance will occur near the boulder stratum, but also the stratum crossed by the tunnel is strongly weathered granite, and the stratum below the boulder lacks support, under the self-weight stress of the boulder. It is easy to form the "weightless weak surface" effect, which intensifies the vertical deformation of the stratum between the upper part of the tunnel and the boulder, promotes the continuous increase of the vertical settlement value of the tunnel vault, and finally forms a new settlement curve 2. At the same time, the weightless weak surface effect will drive the corresponding increase of the vertical deformation value of the stratum around and above the boulder, expand the influence range of the tunnel construction disturbance, and form a new settlement basin, as shown in settlement areas 1 and 2 in **Figure 9**.

STUDY ON THE LAW OF SURROUNDING ROCK DEFORMATION AND SURFACE SETTLEMENT DURING TUNNEL CROSSING ROCK STRATA

Establishment of the Numerical Model

Aiming at the stability of the surrounding rock when the tunnel crosses the solitary rock formation, the Midas GTS NX finite element simulation software is used for numerical simulation analysis. The three-dimensional numerical model size is $X \times Y \times Z = 80\ \text{m} \times 45\ \text{m} \times 60\ \text{m}$. In order to facilitate the establishment of 3D model and the determination of boundary conditions, the following three basic assumptions are set: 1) the stratum as a semi-infinite space body; 2) the surrounding rock as a homogeneous and isotropic continuum; and 3) only the self-weight stress field. Based on the above assumption, the lower surface of the model has the fixed end constraint, the X direction constraint is imposed on the left and right surfaces, and the front and back surface is the free boundary; considering the stress of the soil weight, the gravity load factor is 9.807. The 3D model map and grid division diagram of the shield tunnel through the solitary rock stratum are shown in **Figure 10**. In them, the soil and rock around the tunnel are the Mohr–Coulomb elastic plastic model, which is assumed to be round: the radius is 3 m, and the segment lining is the solid elastic model.

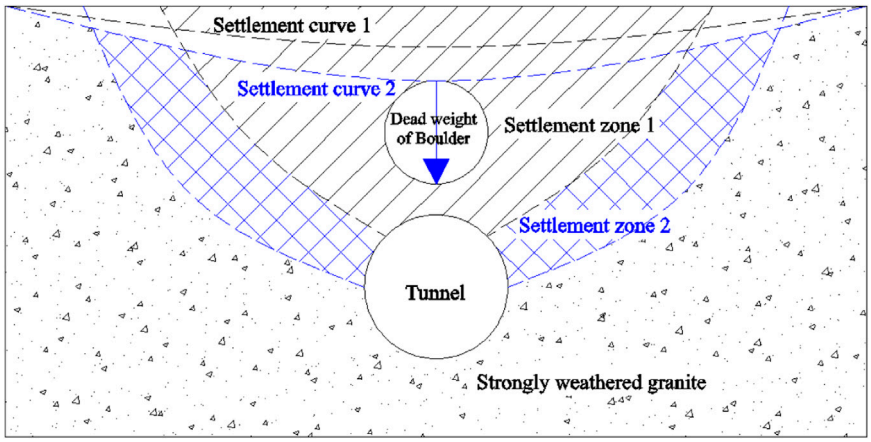

FIGURE 9 | Analysis of weak surface effect of weight loss of boulder under disturbance.

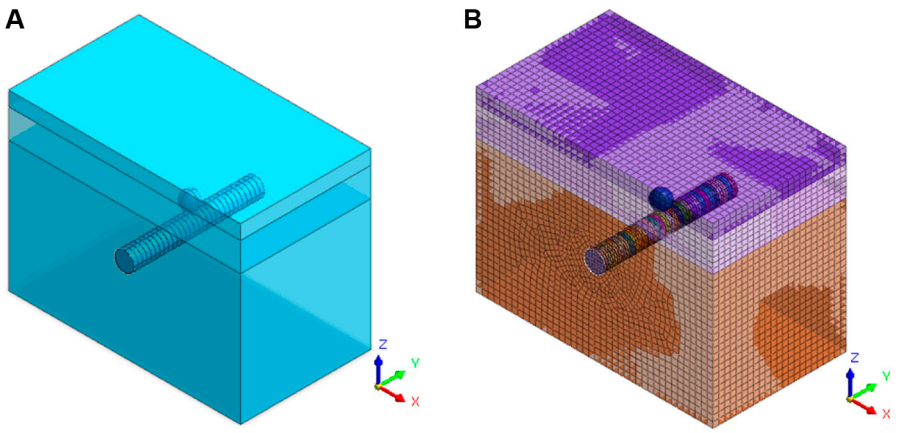

FIGURE 10 | Numerical simulation of the tunnel crossing the boulder stratum. **(A)** Geometric model of the tunnel crossing the solitary formation. **(B)** Grid model diagram of the tunnel crossing the solitary stone formation.

TABLE 2 | Physical and mechanical parameters of the lining structure.

Formation type	Weight of soil γ (kN·m^{-3})	Modulus of elasticity E (MPa)	Internal friction angle φ(°)	Cohesion c (kPa)	Poisson's ratio u
Plain fill	18	40	8	12	0.15
Hard plastic soil	18	41	20	28	0.29
Strongly weathered, mixed with granite	27	4,000	38	60	0.20
Boulder	35	20,000	—	—	0.27
Duct piece	26	34,500	—	—	0.20

Selection of Physical and Mechanical Parameters for the Simulation

The formation where the shield tunnel is located is basically strongly weathered granite, and the overlying soil layer is mixed filling soil and hard plastic soil. The physical and mechanical parameters of rock and soil layer, solitary rock, and pipe sheet are shown in **Table 2**.

Definition of the Conditions Required for the Simulation

Condition 1. Relying on Shenzhen Metro Line 13 leave ~ between the organizations of the shield tunnel engineering example, the analysis process of the model can be divided into four stages: first stage: calculation of the initial ground stress.

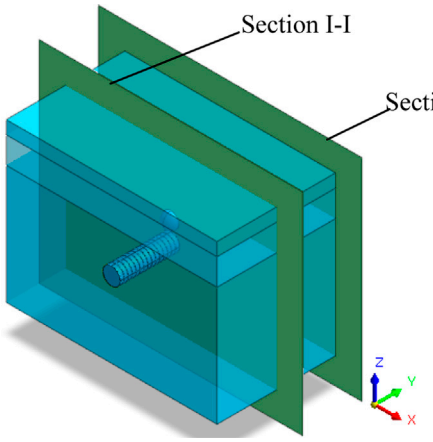

FIGURE 11 | Section I-I and section II-II distribution schematic diagram.

Activin soil filling, hard plastic soil, strongly weathered granite, solitary rock, tunnel excavation soil, and zero displacement calculated at this stage simulate the initial stress field of the formation and reduce the calculation error of the model; second stage: ring 1 ~ 11 ring tunnel excavation soil passivation and corresponding supporting structure activation; third stage: ring 12 ~ 19 ring tunnel excavation soil passivation and corresponding supporting structure activation; fourth stage: ring 20 ~ 30 ring tunnel excavation soil passivation and corresponding supporting structure activation simulate shield tunnel excavation.

Condition 2. It is basically the same as Condition 1, but the difference is that, in the first stage, the tunnel and the surrounding soil are activated at the same time and the isolated stone is activated to simulate the surrounding rock and surface deformation caused by the excavation of the shield tunnel under the condition of the existence of the lone stone.

Condition 3. Basically the same as Condition 2, but the difference is in the third stage, when the tunnel is bored near the lone rock and the grouting reinforcement area is activated, so as to simulate the grouting and reinforcement process when the shield tunnel crosses the solitary stone formation.

ANALYSIS OF THE SIMULATION RESULTS UNDER DIFFERENT CONDITIONS WHEN THE SHIELD TUNNELING PASSES THROUGH THE BOULDER FORMATION

In order to study the influence of boulders on different positions of the tunnel, sections I-I and II-II are specially set. The distance between the above sections is 22.5 and 0 m, respectively, and the specific distribution position is shown in **Figure 11**.

Analysis of the Surrounding Rock Deformation Characteristics When the Shield Tunnel Crosses the Boulder Formation

In order to study the influence of solitary stones on different sections of the tunnel, the surrounding rock deformation cloud map at section I-I and section II-II was selected for analysis, as shown in **Figure 12** and **Figure 13** (the surrounding rock deformation of case 1 at section I-I and section II-II is the same, which is only presented in **Figure 12**). As can be seen from **Figure 12**, first of all, the area of the vertical deformation concentration area at the vault is from large to small for Condition 1, Condition 2, and Condition 3; at the same time, the vertical deformation concentration area at the arch bottom is Condition 2, Condition 1, and Condition 3 in order from large to small, which can show that grouting and reinforcement of the lone stone formation can have a certain inhibitory effect on the disturbance caused by tunnel construction; secondly, the color of the vertical deformation concentration area of the surrounding rock in Condition 3 is slightly lighter than that in Conditions 1 and 2. This shows that grouting the tunnel can effectively inhibit the deformation of the surrounding rock in the grouting reinforcement area.

As can be seen from **Figure 12** and **Figure 13**, first of all, the cross section II-II cloud surrounding rock deformation under different conditions has certain differences, embodied in condition of two condition of vertical deformation, high arch area is less than one, three conditions, and the arch ascend a bulge deformation, high peak in area in the condition of 2, condition and condition of three deformation, high area, which can explain the boulder strata grouting reinforcement operation can make arch bottom deformation is relatively close to the deformation of surrounding rock in the absence of any boulder; Section in second, the condition of 2 I-I place to be significantly higher than the surrounding rock deformation of the cross section II-II surrounding rock deformation degree, suggesting that close to intensify the deformation degree, from the boulder and condition of three section I-I and cross section II-II place exactly, by contrast, surrounding rock deformation of the grouting reinforcement operation can effectively inhibit the boulder's influence on the deformation of surrounding rock; Finally, the distribution characteristics of section-Condition 1 and conditions are similar, it may indicate that after the grouting reinforcement operation, the deformation characteristics of the tunnel section far away from the boulder are gradually consistent with the strata without the boulder.

In order to further study the vertical deformation law of the surrounding rock under different conditions, the vertical deformation value of the vault under different conditions is specially selected, and the vertical deformation curve is drawn, as shown in **Figure 14**. As can be seen from **Figure 14**, when the tunnel tunneling length is within the range of 0–15 m and 30–45 m, the vertical displacement curve under different operating conditions is approximately a straight line, according to the vertical displacement value from large to small, Condition 2, Condition 3, Condition 1, when the excavation length is within the range of 15–30 m, the vertical displacement curve of Condition 1 is approximately a straight line, Condition 2 is approximate "V" Distribution, the three vertical displacement curve of condition is almost "Double

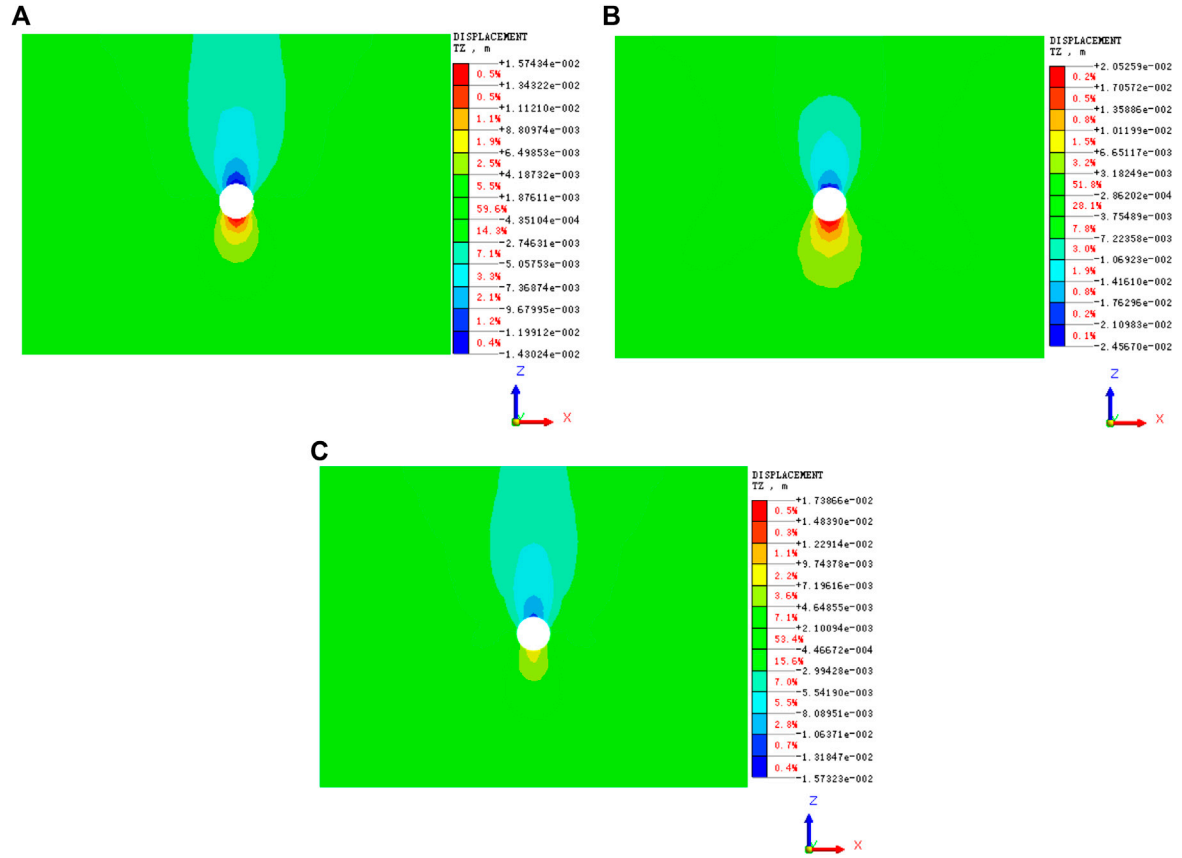

FIGURE 12 | Cloud map of section I-I under different conditions. **(A)** Cloud map of surrounding rock under Condition 1. **(B)** Cloud map of surrounding rock under Condition 2. **(C)** Cloud map of surrounding rock under Condition 3.

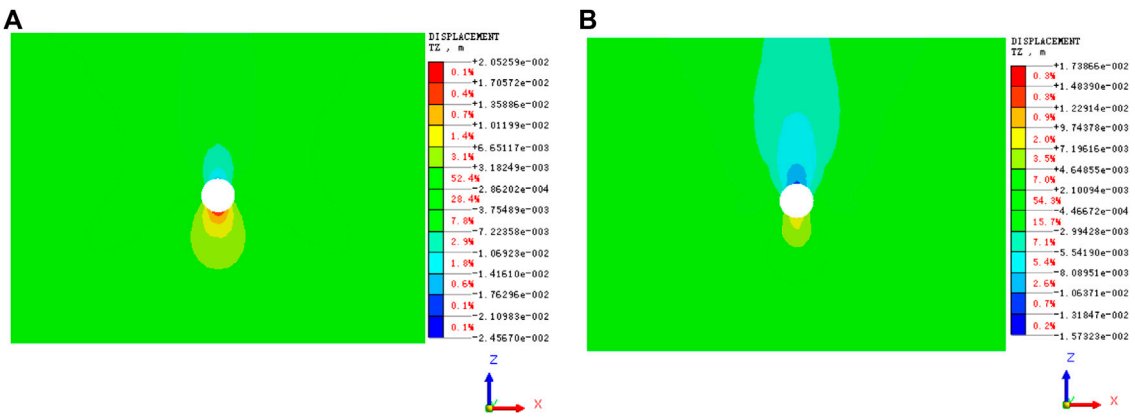

FIGURE 13 | Section II-II deformation cloud of surrounding rock under different conditions. **(A)** Cloud map of surrounding rock under Condition 1. **(B)** Cloud map of surrounding rock under Condition 2.

peak of left low right high" Distribution, and within the length of the tunnel, vertical displacement value from large to small in order for Condition 3, Condition 1, Condition 2; Secondly, Condition 2 and Condition 3 reach the maximum and minimum values of the vertical displacement of the surrounding rock at the central point of the rock, it can be shown that the boulder and grouting reinforcement have a significant impact on the surrounding rock deformation; Lastly, the vertical displacement curves of Condition 1 and Condition 2 are

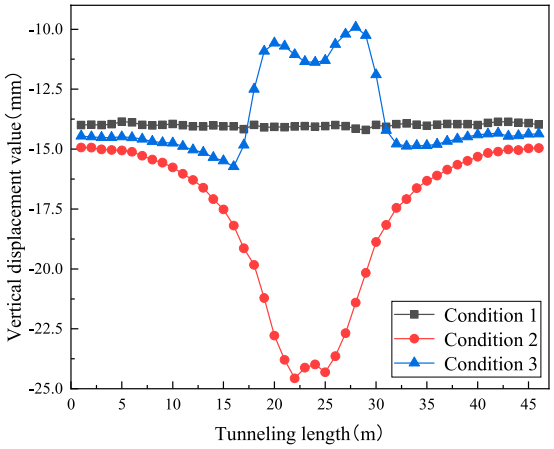

FIGURE 14 | Vertical deformation curve of the arch under different conditions.

approximately symmetrical around cross-sections i-i, while the right displacement of section i-i in the three conditions is slightly less than the left displacement value, it can be explained that the grouting reinforcement can inhibit the surrounding rock deformation caused by the subsequent tunnel construction.

Study on Surface Subsidence Law When Shield Tunnel Crossing Solitary Strata

According to **Figure 15**, the influence of boulder and grouting reinforcement measures on surrounding rock deformation is mainly concentrated near section i-i. The deformation difference between sections-conditions is relatively small. Therefore, the surface settlement curve at section i-i, supplemented by the surface settlement variation under different conditions, and the surface settlement curve at different sections of the tunnel is shown in **Figure 15**. as can be seen in **Figure 15A**, the surface settlement curve under different conditions is similar to the normal distribution, it can be shown that the solitary stone and grouting reinforcement measures will not change the distribution characteristics of the surface settlement curve; Secondly, coincident with the surface settlement curve within 0~40 m from the tunnel center line, however, the surface settlement value of the condition three within the range of-40~0 m is slightly greater than the condition one, it can be shown that the grouting reinforcement can effectively inhibit the formation deformation caused by boulders; Lastly, the surface settlement value of Condition 2 should be significantly greater than that of Condition 1 and Condition 3, it can show that it is necessary to grouting the solitary rock formation. from **Figure 15B**, the surface settlement curve of Condition 1 and Condition 3 coincide, and the surface settlement value of Condition 2 is significantly higher than Condition 1 and Condition 3, so that the grouting reinforcement measures can reduce the impact of boulder on formation deformation. Secondly, combined with **Figure 13A**, the displacement difference between Condition 2 and Condition 1 and Condition 3 is significantly greater than that in **Figure 15B**, the impact on formation deformation.

In order to study the influence of boulders on the longitudinal surface subsidence of the tunnel through the shield tunnel, the longitudinal settlement value of the surface under different conditions was selected, as shown in **Figure 16**. As can be seen from **Figure 16**, 1) With the increasing length of tunnel tunneling, The longitudinal settlement value of the surface in Condition 1 and Condition 3 gradually increases, The analysis shows that with the increasing amount of tunnel tunneling length, The influence of the tunnel construction disturbance on the unexcavated formation is gradually increased, The longer the tunneling length is, The longitudinal subsidence value of the ground surface increases accordingly; 2) The longitudinal settlement curve of Condition 1 and Condition 3 is close, It can be seen that the grouting and reinforcement operation of the boulder stratum can effectively inhibit the surrounding rock deformation and surface settlement value caused by the boulders; 3) The maximum longitudinal settlement value of the surface at condition conditions is distributed at 22.5~27.5 m tunnel length, The location of the stone, And the closer to the stone, The greater the increase in the longitudinal settlement of the ground surface is, According to the analysis, As tunnel construction gradually approaches boulders, Not only will the tunnel vault undergo settlement and deformation under its own gravity, The presence of boulders also strengthens the settlement deformation of the vault, As a result, the maximum longitudinal settlement value of the boulder stratum is mainly distributed in the boulder position; 4) The longitudinal settlement value of the surface under Condition 2 shall be significantly greater than that of Condition 1 and Condition 3, The longitudinal settlement curve of the surface in Condition 2 presents the curve distribution characteristics of "left high and right low", Condition 1 and Condition 3 are approximate to oblique straight lines, It can be seen that the surface displacement value and distribution characteristics are easily affected by boulders.

Comparison and Analysis of Simulated and Monitored Ground Settlement Values of Tunnel Crossing Boulder Stratum

According to **Figure 17**, firstly, the variation trend of the surface settlement curve of the numerical simulation value is basically consistent with the curve of the field monitoring value, but the numerical simulation value is generally smaller than the field monitoring value, and the maximum error is not more than 10%. The analysis shows that the constitutive model of rock and soil mass based on the finite element theory and the selected parameter values are different from the field actual situation, In the process of finite element numerical simulation, the construction steps and support methods of the tunnel are simplified to a certain extent. Under the joint influence of the above factors, the simulation value is smaller than the monitoring value; Secondly, the maximum values of the monitored and simulated surface settlement values appear in the center of the tunnel, and the settlement curves are approximately normal distribution; Finally, the monitoring value of ground settlement at the place about 35 m away from the center of the tunnel is about 0 mm, so the influence range on the ground surface during the tunnel construction of the project is about 70 m. To sum up, the variation laws of surface settlement and surrounding

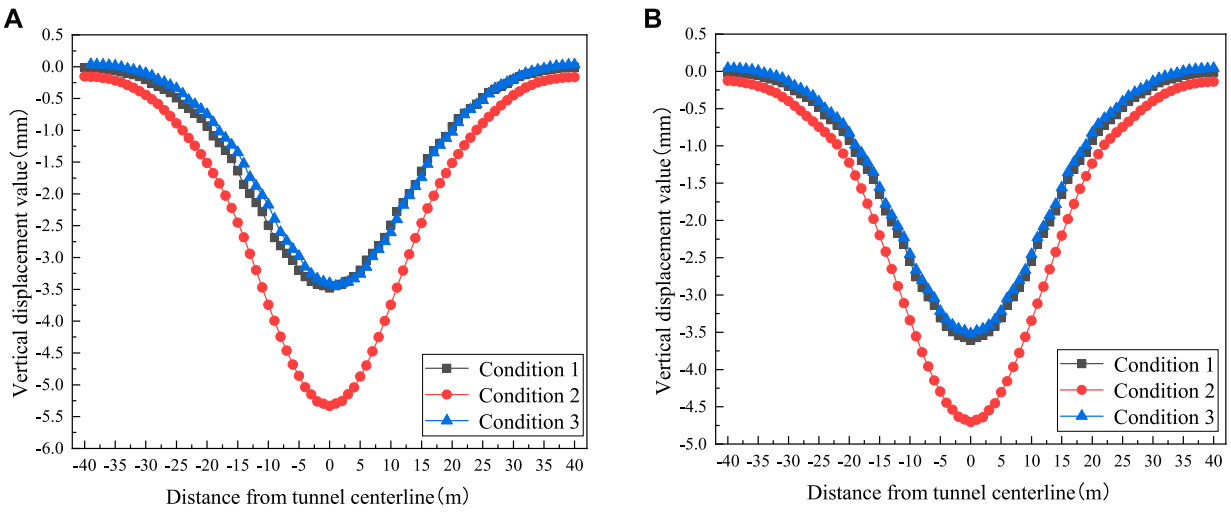

FIGURE 15 | Surface settlement curve diagram at different sections of the tunnel. **(A)** Surface subsidence curve diagram at section I-I.**(B)** Surface subsidence curve diagram at section II-II.

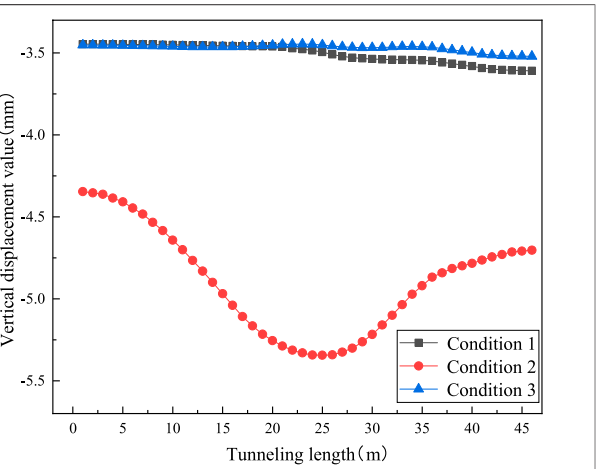

FIGURE 16 | Longitudinal surface settlement curve under different conditions.

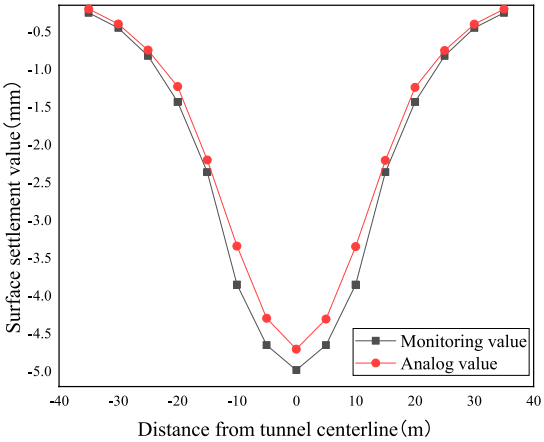

FIGURE 17 | Comparison and analysis of simulation value and monitoring value of the tunnel crossing the boulder stratum.

rock crown obtained by numerical simulation are basically consistent with the variation laws of field monitoring values, which can explain the feasibility and rationality of numerical simulation to a certain extent.

GRANITE TREATMENT MEASURES WHEN THE SHIELD TUNNEL PASSES THROUGH THE BOULDER FORMATION

When the lone rock is encountered in the shield construction and the ground construction conditions, the deep hole blasting treatment will be carried out. The specific operation steps are blasting hole layout, blasting hole taking, charging, gun hole blockage, gun hole coverage, blasting hole, blasting network, explosive single consumption, blasting effect monitoring and grouting, which is described in detail below.

1) Blasting hole layout

According to the location of the solitary rock determined by the geological exploration, the blasting hole layout is carried out, the hole spacing is arranged according to 0.6 m × 0.6 m.Geological drilling hole diameter of 108 mm.Before opening, trenches should be dug to investigate the nearby pipeline situation. When drilling, drill through the road water stabilization layer and use Luoyang shovel to hit 3 m to determine that there is no pipeline below, and then continue to drill. The schematic diagram of the gun hole layout is shown in **Figure 8**.

FIGURE 18 | Rock sample collection map.

2) Blasting hole extraction

When drilling to the design depth, remove all the gravel, sediment, mud in the hole, use PVC management and protection hole, PVC pipe connection and bottom are sealed with tape. Fill the tube with water to prevent the PVC tube from floating. Keep construction records and retain the rock samples obtained from the drilling hole, as shown in **Figure 18**.

3) Loading

Put the emulsified explosive into the PVC tube, and place 2~4 detonators, the charge length is greater than the thickness of the required blasting rock layer. After the medicine package is processed, the explosive medicine package is suspended at the blasting point with nylon wire rope, and one end is fixed at the hole mouth. The obvious markers such as small red cloth strip are tied to the rope to mark, and the length of the mark to the bottom of the PVC pipe is equal to the depth of the whole gun hole (overlay thickness + rock gun hole depth). The medicine package gradually down to the bottom of the gun hole, until the mark on the rope to the gun hole, if in ±10 cm, the approved bag is in place.

4) The blasthole is blocked

After the medicine package is in place, slowly pour sand into the blasthole, and the length of the blockage is greater than 3 m.

5) Artillery hole cover

Since the high pressure gas produced after blasting may press the muddy water in the gun hole out of the hole, in order to prevent the gushing mud water splashing and PVC pipe protrusion, it is necessary to protect the gun hole overhead and heavy pressure cover. Use the concrete precast block, put the concrete precast block on the steel bar frame, use the forklift truck to carry the whole piece, the precast block is placed on the blasting hole.

6) Blasting the network

The gun hole adopts forward loading to burst, the detonator chooses two instantaneous detonators, and respectively belong to two electric burst networks, two sets of networks in parallel.

7) Single consumption of explosives

The single consumption of boulder explosive is 1.8~5.0 kg/m^3. In order to reduce the great impact on the ground construction (structure), the blasting hole distance should be reduced, the blasting number should be increased, and each group of blasting should not exceed 10 holes.

8) Blasting effect detection

After the test blasting, the geological drilling rig is organized to drill again in the blasting area to test the blasting effect. The drilling depth is 1 m below the bottom elevation of the shield section, and the detection frequency is 30% of the number of blasting drilling holes. When drilling the core, if a rock layer of a length greater than 30 cm is found, the area near the core point should be treated again.

9) Injection pulp

Due to the solitary rock treatment blasting construction, the original road surface damage, the underground soil is loose, in order to avoid the pressure loss, the ground drilling grouting should be adopted for the blasting area, the grouting hole spacing is consistent with the blasting hole spacing, the drilling depth is 1.0 m deeper than the original blasting hole depth. After the grouting, the original ground shall be restored. For the asphalt pavement, the blasting grouting area shall be cleaned within 1~3 m according to the site situation, and the pavement structure shall be applied again.

CONCLUSION

The deformation and surface settlement of the surrounding rock when the shield tunnel is studied by similar model test and numerical simulation, and the relevant measures of isolated rock treatment in the construction site are summarized to draw the following conclusion:

1) Through similar material model test of tunnel construction caused by the surrounding rock and the deformation characteristics of the surface and collapse process, concluded that shield tunneling, tunnel construction cause surface subsidence is a normal regularity phenomenon, when the formation rock, joints and other special rock component structure, will make the surface subsidence anomaly, and even cause collapse phenomenon.
2) The presence of surrounding rock has obvious effect on the settlement deformation of surrounding rock, and its influence range is not limited to the surrounding location; the

surrounding rock deformation is significantly reduced after the grouting reinforcement, which shows that the suppression of the disturbance caused by the tunnel construction.

3) Rock and grouting reinforcement measures did not change the distribution characteristics of surface settlement curve, and grouting reinforcement can effectively inhibit formation deformation caused by rock, and the surface settlement curve overlap, and rock stratum surface settlement value is significantly higher than the above two cases, and the closer the distance, condition, three and conditions of the surface settlement deformation difference is more obvious.
4) By comparing and analyzing the surface settlement curve of the simulation value and the monitoring value when the tunnel passes through the boulder stratum, it is found that the change trend between them is relatively consistent, and the maximum error is less than 10%, which verifies the rationality and accuracy of the numerical simulation to a certain extent.
5) Summarize the construction site stone treatment measures, and the specific contents are as follow: when the shield construction and have the ground construction conditions will be deep hole blasting treatment, operation steps for blasting hole layout, blasting hole, charging, gun hole plugging, blasting network, explosive single consumption, blasting effect monitoring and grouting reinforcement.

DATA AVAILABILITY STATEMENT

The original contributions presented in the study are included in the article/Supplementary Material, further inquiries can be directed to the corresponding author.

AUTHOR CONTRIBUTIONS

All authors listed have made a substantial, direct, and intellectual contribution to the work and approved it for publication.

FUNDING

The author(s) disclosed receipt of the following financial support for the research, authorship, and/or publication of thsis article: The research of YG was funded by the National Natural Science Foundation of China (No. 52171264), NSFCRFBR (No. 5191101589), Funded by China State Construction Engineering Corporation Technology R&D Program (CSCEC-2019-Z-19). The research of M.D.K., I.V.M., and A.P.K. was funded by RFBR and NSFC according to the research project No. 20-51-53021.

REFERENCES

Chen, W., Tan, Y., and Xiang, L. (2018). Study on the Catastrophe Mechanism of Stratum Collapse Induced by Shield Tunneling Damage [J]. *Tunn. Constr. Chin. Engl.* 38 (05), 824–832.

Dang, R. (2012). A Geophysical Detection Method for the Boulders [J]. *Tunn. Constr.* 32 (S2), 56–60.

Hu, Yi (2019). *Study on Tunnel Deformation Characteristics of Fully Weathered Strata Containing Solitary Rock [D]*. Hunan University of Science and Technology.

Li, X., Zhang, W., and Chen, H. (2021). Analysis of Deformation Law of Super Large Diameter Slurry Shield Tunneling in Boulder Stratum of Sea Cofferdam -- Taking the Shield Section of Shantou Bay Tunnel as an Example [J]. *Tunn. Constr. Chin. Engl.* 41 (01), 28–36.

Li, Y., Jing, H., and Liu, G. (2007). Application of Digital PhotoMeasurement in Rock Tunnel Model [J]. *J. Rock Mech. Eng.* (08), 1684–1690.

Liu, H., Huang, J., and Sun, Z. (2016). Application of Micromotion Detection Method in the "solitary Stone" Detection of Urban Metro Shield Construction- -taking Fuzhou Metro Line 1 as an Example [J]. *Tunn. Constr.* 36 (12), 1500–1506.

Moghaddasi, M. R., and Noorian-Bidgoli, M. (2018). ICA-ANN, ANN and Multiple Regression Models for Prediction of Surface Settlement Caused by Tunneling. *Tunn. Undergr. Space Technol.* 79, 197–209. doi:10.1016/j.tust.2018.04.016

Selby, A. R. (1999). Tunnelling in Soils–Ground Movements, and Damage to Buildings in Workington, UK[J]. *Geotechnical Geol. Eng.* 17 (3), 351–371. doi:10.1023/a:1008985814841

Sugiyama, T., Hagiwara, T., Nomoto, T., Nomoto, M., Ano, Y., Mair, R. J., et al. (1999). Observations of Ground Movements during Tunnel Construction by Slurry Shield Method at the Docklands Light Railway Lewisham Extension-East London. *Soils Found.* 39 (3), 99–112. doi:10.3208/sandf.39.3_99

Wang, P. (2012). Treatment Process and Examples of Shield Engineering under Different Geological Conditions [J]. *Tunn. Constr.* 32 (04), 571–575.

Zhang, N., Wang, S., and Wang, X. (2007). Experimental Study on Tunnel Deformation and Destruction Process Containing Weak Surrounding Rock [J]. *J. Undergr. Space Eng.* (06), 1085–1088.

Zhang, W. (2009). *Study on the Mechanical Behavior of Initial Tunnel Support Construction under Complex Geological Conditions [D]*. Fuzhou University.

Zheng, G., Fan, Q., Zhang, T., Zheng, W., Sun, J., Zhou, H., et al. (2019). Multistage Regulation Strategy as a Tool to Control the Vertical Displacement of Railway Tracks Placed over the Building Site of Two Overlapped Shield Tunnels. *Tunn. Undergr. Space Technol.* 83, 282–290. doi:10.1016/j.tust.2018.09.040

Zhu, W., Huang, W., and Meng, Q. (2011). Research on the Blasting Technology of Boulder and Bedrock Intrusion in Shield Engineering [J]. *Mod. Tunn. Technol.* 48 (05), 12–17. doi:10.13807/j.cnki.mtt.2011.05.001

Zhu, X., Qian, W., and Zhu, H. (2021). Numerical Analysis of Stability of Shield Tunneling in Coastal Boulder Stratum [J]. *J. Railw. Sci. Eng.* 18 (01), 172–183.

Zong, C., and Tian, X. (2015). New Detection and Disposal of Shield Shield in Granite Formation [J]. *Sci. Technol. Eng.* 15 (26), 11–18.

Conflict of Interest: XP was employed by the company CCCC tunnel engineering company limited, LJ, LH, and CZ were employed by the company China Construction Fifth Bureau 5 South China Company, SP and TZ were employed by the company China Construction Tunnel Construction Co., Ltd.

The remaining authors declare that the research was conducted in the absence of any commercial or financial relationships that could be construed as a potential conflict of interest.

Publisher's Note: All claims expressed in this article are solely those of the authors and do not necessarily represent those of their affiliated organizations, or those of the publisher, the editors and the reviewers. Any product that may be evaluated in this article, or claim that may be made by its manufacturer, is not guaranteed or endorsed by the publisher.

Copyright © 2022 Guangming, Pengju, Yongyi, Qimeng, Jun, Pengfei, Zhiwen, Hao and Ze. This is an open-access article distributed under the terms of the Creative Commons Attribution License (CC BY). The use, distribution or reproduction in other forums is permitted, provided the original author(s) and the copyright owner(s) are credited and that the original publication in this journal is cited, in accordance with accepted academic practice. No use, distribution or reproduction is permitted which does not comply with these terms.

frontiers | Frontiers in Earth Science

TYPE Original Research
PUBLISHED 30 August 2022
DOI 10.3389/feart.2022.940438

Check for updates

OPEN ACCESS

EDITED BY
Yan Du,
University of Science and Technology Beijing, China

REVIEWED BY
Yanbin Yu,
Shandong University of Science and Technology, China
Jinge Wang,
China University of Geosciences Wuhan, China
Jia Yanchang,
North China University of Water Resources and Hydropower, China

*CORRESPONDENCE
Qisong Huang,
huangqisong123@126.com

SPECIALTY SECTION
This article was submitted to Geohazards and Georisks, a section of the journal Frontiers in Earth Science

RECEIVED 10 May 2022
ACCEPTED 26 July 2022
PUBLISHED 30 August 2022

CITATION
Xu B, Huang Q and Qian Y (2022), Stability trends of Jinpingzi landslide: A numerical study.
Front. Earth Sci. 10:940438.
doi: 10.3389/feart.2022.940438

COPYRIGHT
© 2022 Xu, Huang and Qian. This is an open-access article distributed under the terms of the Creative Commons Attribution License (CC BY). The use, distribution or reproduction in other forums is permitted, provided the original author(s) and the copyright owner(s) are credited and that the original publication in this journal is cited, in accordance with accepted academic practice. No use, distribution or reproduction is permitted which does not comply with these terms.

Stability trends of Jinpingzi landslide: A numerical study

Bo Xu[1,2], Qisong Huang[1]* and Yuandi Qian[2]

[1]Department of Civil Engineering and Architecture, Anhui University of Technology, Anhui, China, [2]China MCC17 Group Co., Ltd., Anhui, China

The occurrence and development of creeping landslides lead to a gradual destruction of the affected environment; therefore, research into creeping landslide stability trends based on the monitoring of landslide data is of considerable practical value. We investigated the Jinpingzi landslide area II using strength subtraction to analyze the relationship between stress and strain at important points and the stability of the landslide. The results confirm the relationship between the internal failure pattern, safety factor, and key point displacement of creeping landslides. Furthermore, the results confirm the change rules of displacement, in addition to changes in the safety factor. By combining the surface displacement monitoring data of Jinpingzi landslide area II, its stability trend was analyzed based on the established relationship model between deformation displacement and internal failure characteristics of creeping landslides. The results demonstrate that the Jinpingzi landslide area II is in a stable damage deformation. The sliding surface formed in the landslide and the results obtained using the model of the Jinpingzi landslide area II are consistent with the actual situation determined by analysis in the field and exploring the geology.

KEYWORDS

creep landslide, stability trend, stress and strain, displacement, safety factor

Introduction

Landslides are categorized as creeping, slow-speed, medium-speed, or high-speed landslides based on their sliding speed. Among them, creeping landslides have wide coverage, are large scale, and have an extended damage time. Generally, they undergo a long process of development and evolution and exhibit physical characteristics that can be monitored and recorded, such as surface displacement, deep displacement, internal stress, and rock and soil pressure (Ye, 2016). Therefore, it is of considerable importance to scientifically guide disaster prevention and mitigation activities by continuously monitoring a landslide, analyzing accurate data, and studying in depth the processes of landslide occurrence, development, and the resulting destruction, to master the laws of landslide development and evolution.

Many researchers have proposed landslide prediction and forecasting methods with landslide velocity and displacement as objective functions, among which landslide displacement prediction is the most common (Chen and Duan-you, 2006; Dong et al., 2007; Du et al., 2009; Li and Zhang, 2009; Ma, 2009; Liu et al., 2010; Xu et al., 2011). Miao et al.

(2016) reported a prediction model of resurrection rate and surface displacement to describe the intermittent resurrection process of old slope bank landslides. Li et al. (2016) proposed a landslide displacement prediction method called WA, along with an extreme learning machine (ELM) and an online sequential (OS)-ELM. Zhou et al. proposed a wavelet analysis-extreme learning machine (WA-ELM) landslide displacement prediction model based on chaotic time series (Zhou et al., 2015). Huang et al. (2016) proposed a variable screening method based on SVR-MIV. The variables screened by this method theoretically conform to the analysis results of the corresponding landslide deformation influence mechanism, as well as improving the actual prediction accuracy of the landslide displacement (Huang et al., 2016). Zhang et al. demonstrated that the prediction accuracy of landslide displacement based on time series and a PSO-SVR coupling model is significantly higher than that of BP neural network and support vector machine (SVM) models optimized using the network search method. This prediction method has a good theoretical basis and performance prospects for landslide displacement prediction applications (Zhang et al., 2015). Huang et al. (2014) demonstrated that smooth prior analysis is suitable for determining the slope range, which can be used as the initial search range for parameter optimization of the SVM model of landslide displacement prediction (Huang et al., 2014). Meng et al. used the H-P filtering method to decompose the trend and period terms from landslide displacement. They used the differential autoregressive moving average model (ARIMA) to smooth the trend term and calculate the displacement decomposition method for displacement prediction. In addition to the prior analysis of the landslide deformation mechanism, a more reasonable displacement decomposition result can be obtained, and the prediction accuracy of the landslide displacement can be improved (Meng et al., 2016). Huang et al. (2015) established the parameter values for SVM displacement decomposition prediction of typical reservoir landslides and recommended the trend item prediction value. They used the vector autoregressive (VAR) model to calculate the period item prediction value. The addition of the trend and period item prediction values yields the predicted value of the landslide displacement (Huang et al., 2015). Lian et al. (2016) proposed the ANNS prediction method and confirmed the effectiveness of the method via three examples of landslides in the Three Gorges region of China (Lian et al., 2016). Du et al. pointed out that the slopes of sliding beds with distributed soft and hard rock strata should be the focus of attention in risk identification for translational landslides and established a new mechanical model that evaluates the stability of creeping landslides (Du et al., 2020a; Du et al., 2020b; Du et al., 2022). Simeoni et al. proposed an operative framework based on redundancy and introduced coherence tests to validate the obtained data and results (Simeoni et al., 2020).

In summary, four types of methods enable landslide disaster prediction. The first method is the classical limit equilibrium method, which cannot consider the long-term behavior of stable rock and soil mass. Therefore, it is not always effective in dealing with large and complex rock and soil mass landslides (Crosta and Agliardi, 2003). The second method calculates the safety factor (SF), plastic strain, and deformation displacement of slope stability via the strength reduction method in numerical simulations. However, its basic idea is similar to the traditional limit equilibrium method. The third method involves studying the mechanism of slope instability via tests and mechanical analyses and uses the results to predict landslide disasters (Qin et al., 2002). However, because of the complexity of slope geometric conditions, geological conditions, and the climatic environment, it is difficult to apply the dynamic equation describing the landslide evolution process and determine its parameters (Geller et al., 1997). The fourth method is based on the observation and analysis of a large quantity of test and monitoring data, in addition to experience and a statistical model to predict the landslide time (Federico et al., 2012). For example, Saito predicted the slope failure time as per the third stage (accelerated) creep and successfully predicted a landslide on the Ooigawa railway line in Japan (Saito, 1969).

Landslide displacement prediction accurately forecasts landslide displacement trends within a certain range. However, because of the uniqueness and complexity of landslides, there is currently no established stability stage criterion method to predict displacement and deformation characteristics for a particular type of a landslide.

This study proposes a method to determine the stability stage of creeping landslides as per their displacement characteristics. For this purpose, we establish the relationship between deformation displacement and internal failure characteristics of creeping landslides, as well as examining the surface deformation characteristics and internal failure mechanism of creeping landslides. The typical displacement–time curve of the landslide was adopted as the theoretical basis, using the strength reduction method; furthermore, a typical homogeneous landslide was used as the research object to determine the theoretical model. The research process included the theoretical model research, experimental verification, and landslide case analysis. The relationship between the deformation and instability characteristics of the deformed landslide and internal failure characteristics is examined, and a corresponding model is established. A stability stage criterion method aimed for use with creeping landslides is formed based on this relationship model.

Internal damage analysis of a simple landslide

To obtain the relationship between the slope displacement and the SF, an imaginary homogeneous slope is considered as an example for analysis. After establishing the model, the bottom boundary of the slope is constrained by fixed constraints; however, the left and right boundaries are horizontally constrained. The Mohr–Coulomb model is used in the

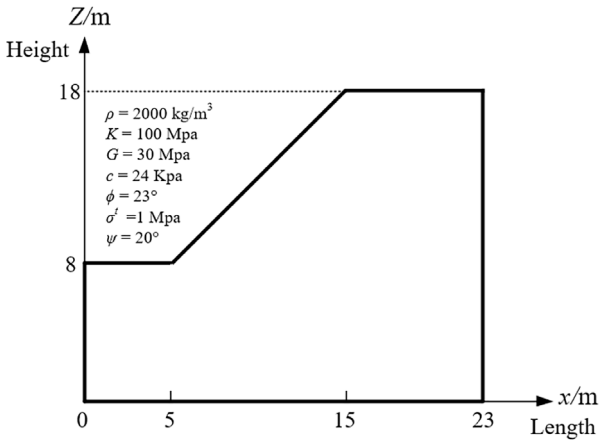

FIGURE 1
Simplified landslide size diagram.

calculation, and its geometric model is illustrated in Figure 1. In the figure, the soil density is ρ; the bulk modulus is K; the shear modulus is G; the cohesion is c, the internal friction angle is ϕ; the tensile strength is σ^t; and the dilatancy angle is Ψ.

Numerical calculation model

Fast Lagrangian Analysis of Continua (FLAC3D) can simulate the two-dimensional (2D) structural stress characteristics and plastic flow analysis of soil, rock, and other materials. By applying FLAC3D, the slope SF calculated via the reduction analysis is 1.54. Figures 2A,B show the shear strain incremental cloud and plastic zone figures, respectively.

To study the change in the displacement of simple landslides and internal stress in the strength degradation process, displacement monitoring must be set up, and a stress observation point must be established on the slope. Five displacement monitoring coefficients, ID1, ID2, ID3, ID4, and ID5, were then selected from the top to the bottom of the landslide, as shown in Figure 3A. The section to go through point (0, 5, 0) and in parallel with the XY plane was selected, and subsequently three stress monitoring coefficients, ID6, ID7, and ID8, were selected from the top to the bottom of the section, as shown in Figure 3B.

Analysis of the strength degradation process

The relationship between the displacement and development process of the plastic zone is obtained by establishing a model analysis, as shown in Figures 4, 5. The X-axis is the SF, and the Y-axis is the displacement, as shown in Figure 4. There are two points marking a changing trend in almost all displacement and safety coefficient curves. In this study, the first turning point is defined as a and the second turning point is defined as b. Consequently, the displacement is divided into three stages: 1) when the SF > 1, the displacement essentially does not change with the change in SF, and the slope is zero; 2) when the safety factor 0.95 < SF < 1, the displacement slowly increases, and the slope is no longer zero; 3) when the SF < 0.95, the displacement increases sharply, indicating large-scale sliding of the landslide, and measures to evacuate people must be considered.

The shear strain cloud and plastic zone maps of the slope during the reduction process are simultaneously recorded to assist in the analysis of apparent displacements. To highlight the changing characteristics of these maps during the occurrence and development of the slope, the initial state, occurrence, development to failure, and post-destruction maps of the slope are compared and analyzed. Changes in stress and strain can determine failure characteristics inside the slope. Figure 5 shows that with the continuous increase in the reduction factor (i.e., with the gradual decrease of the SF), the cloud map of the shear strain increment clearly shows the development trend of the sliding surface in the slope body, and the sliding surface develops from the toe of the slope and gradually extends upward to the top of the slope, thus forming an arc-shaped sliding surface. The plastic zone map shows that the first failure area is located at the toe of the slope, after which the plastic zone develops and gradually extends to the upper part of the landslide. When the SF is 1.00, the plastic zone develops to the through state. Subsequently, the sliding zone widens and increases along the sliding surface in the slope body. The plastic zone of the sliding body gradually increases, and eventually the sliding body slides down along the through slide surface and becomes unstable. When the reduction factor KS is 1.53, the SF is 1.00, which is close to a in the above displacement–reduction factor relationship diagram analysis. When the reduction factor KS is 1.59, the SF is 0.96, which is similar to b in the displacement–reduction factor relationship analysis.

We observed the changing characteristics of the internal principal stress of the slope during the strength reduction process, as shown in Figure 6. Figure 6A shows that the tensile failure primarily occurs at the top of the slope, and the compression shear failure occurs in the middle and toe of the slope. Figure 6B shows that the slope shows compression shear failure because the maximum principal stress value in the slope is larger, and the maximum principal stress value at the top of the slope is smaller. Furthermore, the minimum and maximum principal stresses do not significantly change as the SF decreases. The stress level inside the slope is primarily attributed to gravity; because the weight of the slope remains unchanged during the analysis, its stress does not significantly

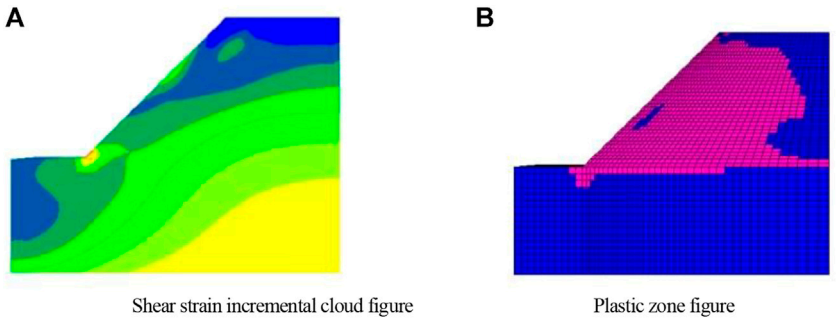

FIGURE 2
(A) Shear strain incremental cloud figure and **(B)** plastic zone figure.

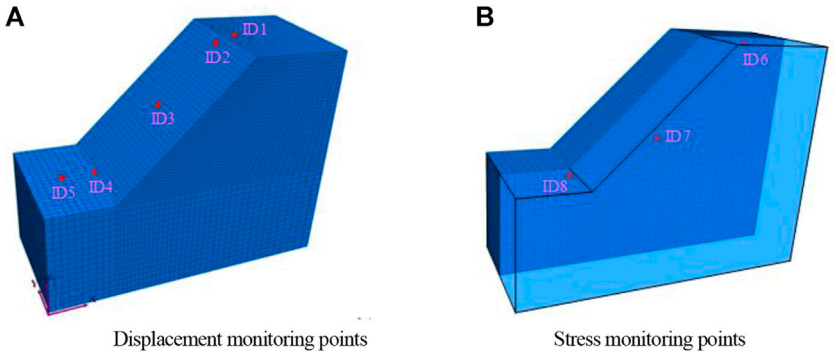

FIGURE 3
Monitoring point arrangement plan. **(A)** Displacement monitoring points **(B)** Stress monitoring points.

change. Therefore, analyzing the stability of creeping landslides by monitoring stress changes is not an appropriate solution.

Regular summary

Using the strength reduction method with the increase or decrease in the reduction of SFs, we analyzed the characteristics of the slope surface deformation and displacement, internal shear strain increment cloud map, internal plastic zone map, and internal maximum and minimum principal stress variation. Combining all these analyses, the following conclusions were obtained:

(1) There is a clear correspondence between the slope SF and slope surface displacement. The reduction factor–displacement curve undergoes a sudden change when the SF is *a* and *b*, respectively, and after each sudden change, the displacement increases at different rates.
(2) The internal failure characteristics shown by the internal shear strain increment cloud map and plastic zone map of the slope show the reasons behind the sudden change in the slope displacement–reduction coefficient curve at *a* and *b*.
(3) The minimum and maximum principal stresses on the sliding surface inside the slope fail to demonstrate evident changes with the slope failure, indicating that monitoring creeping landslides by monitoring stress changes does not yield results that are as clear as those obtained by displacement monitoring.

Based on these conclusions, this study establishes a relationship model between deformation displacement and the internal failure characteristics of creeping landslides based on the analysis of slope surface displacement characteristics, as shown in Table 1.

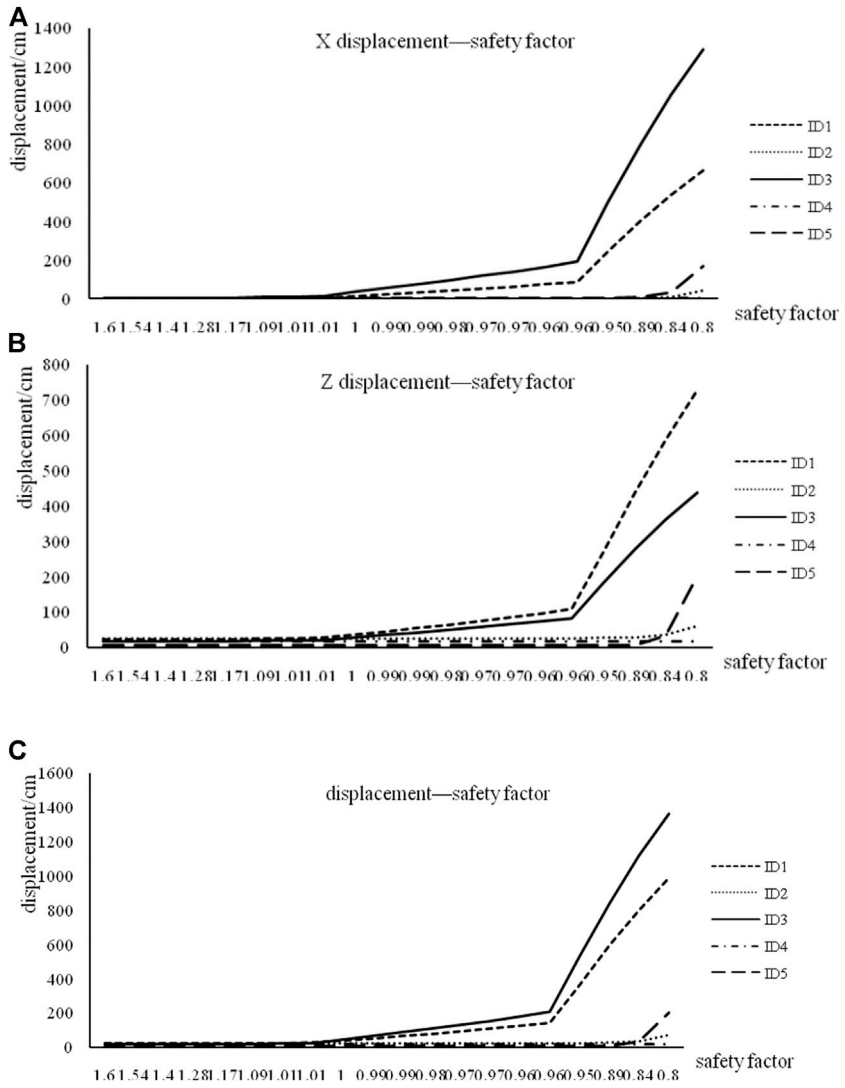

FIGURE 4
Displacement–safety factor graph. **(A)** X displacement–safety factor. **(B)** Z displacement–safety factor. **(C)** The total displacement–safety factor.

Numerical simulation of Jinpingzi landslide area II

Engineering conditions

The Jinpingzi landslide is located at the Wudongde cascade on the right bank of the Jinsha River, approximately 90 m downstream of the Wudongde dam site. Its volume, estimated by remote sensing, is approximately 620 million m^3. Its stability status, deformation trends, possible causes of instability, and scale are related to the establishment of the Wudongde hydropower cascade development and the selection of a dam site. Consequently, it received attention from various researchers (Li, 2008). The Jinpingzi landslide can be roughly divided into five areas. Because Jinpingzi landslide area II has a massive volume (approximately 27 million m^3) and its deformation is still under development, opinions on the effects on the Wudongde project vary. Thus, it is necessary to accurately predict possible causes of instability in the area and the scale of a putative landslide. In this manner, we can accurately evaluate the project's effect and consider effective measures to ensure construction safety.

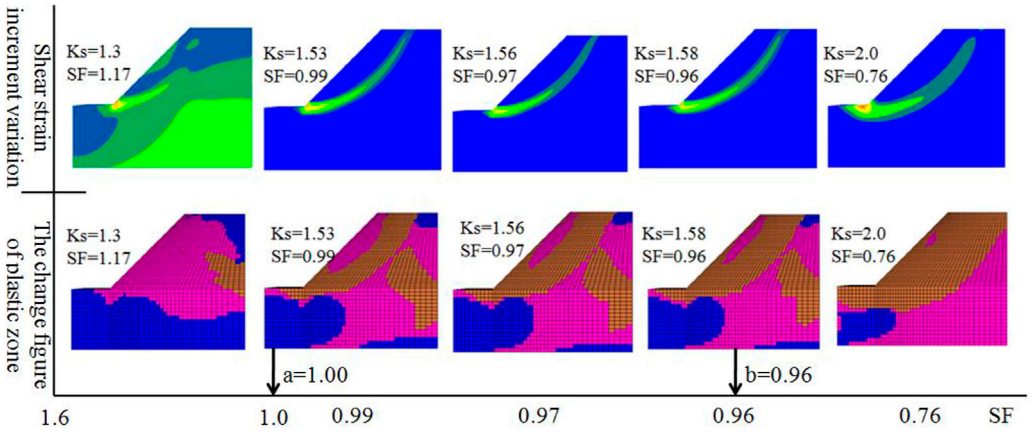

FIGURE 5
Shear strain increment variation and plastic zone development process.

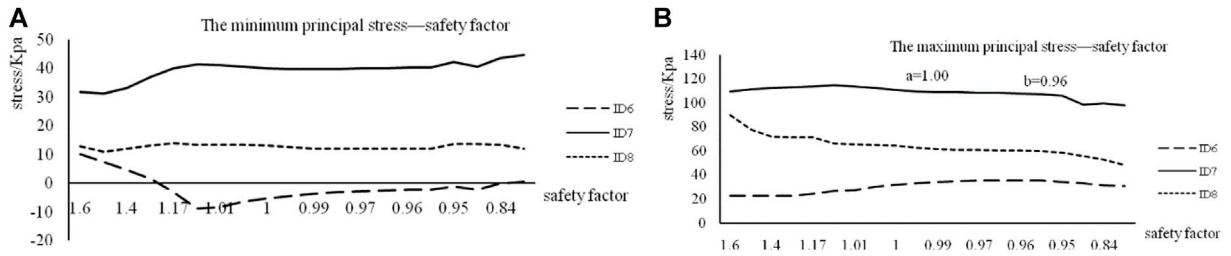

FIGURE 6
Stress–safety factor graph. **(A)** The minimum principal stress–safety factor. **(B)** The maximum principal stress–safety factor.

TABLE 1 Stability of the relational model based on the displacement characteristics of the slope surface.

Slope stability phase	Surface displacement characteristics	Safety factor SF	Characteristics of the internal plastic zone
Stabilization phase	Virtually no displacement	SF ≥ a	A penetrating plastic zone is not formed
Destruction phase	Displacement increases slowly and deforms at a uniform rate	a < SF < b	Forms a penetrating plastic zone
Instability phase	Displacement increases sharply, accelerating the deformation	SF ≤ b	Plastic zone expands rapidly

Internal damage analysis of Jinpingzi landslide area II

The geological map of the study area is shown in Figure 7. AutoCAD 3D modeling, ANSYS meshing, and FLAC3D strata division were used to establish the model of the Jinpingzi landslide area II. The final model is shown in Figure 8. The physical and mechanical parameters of rock strata are listed in Table 2.

To investigate the changes in the displacement and internal stress of the model, eight displacement monitoring points were selected based on the actual displacement monitoring point, as shown in Figure 9A. Five points (A–E) on the section with the passing point (0, 950, 0) and the normal direction (0, 1, 0) were selected, and the shear force of the Jinpingzi landslide in the process of strength reduction was calculated. The shear strain increment and plastic zone changes were then recorded.

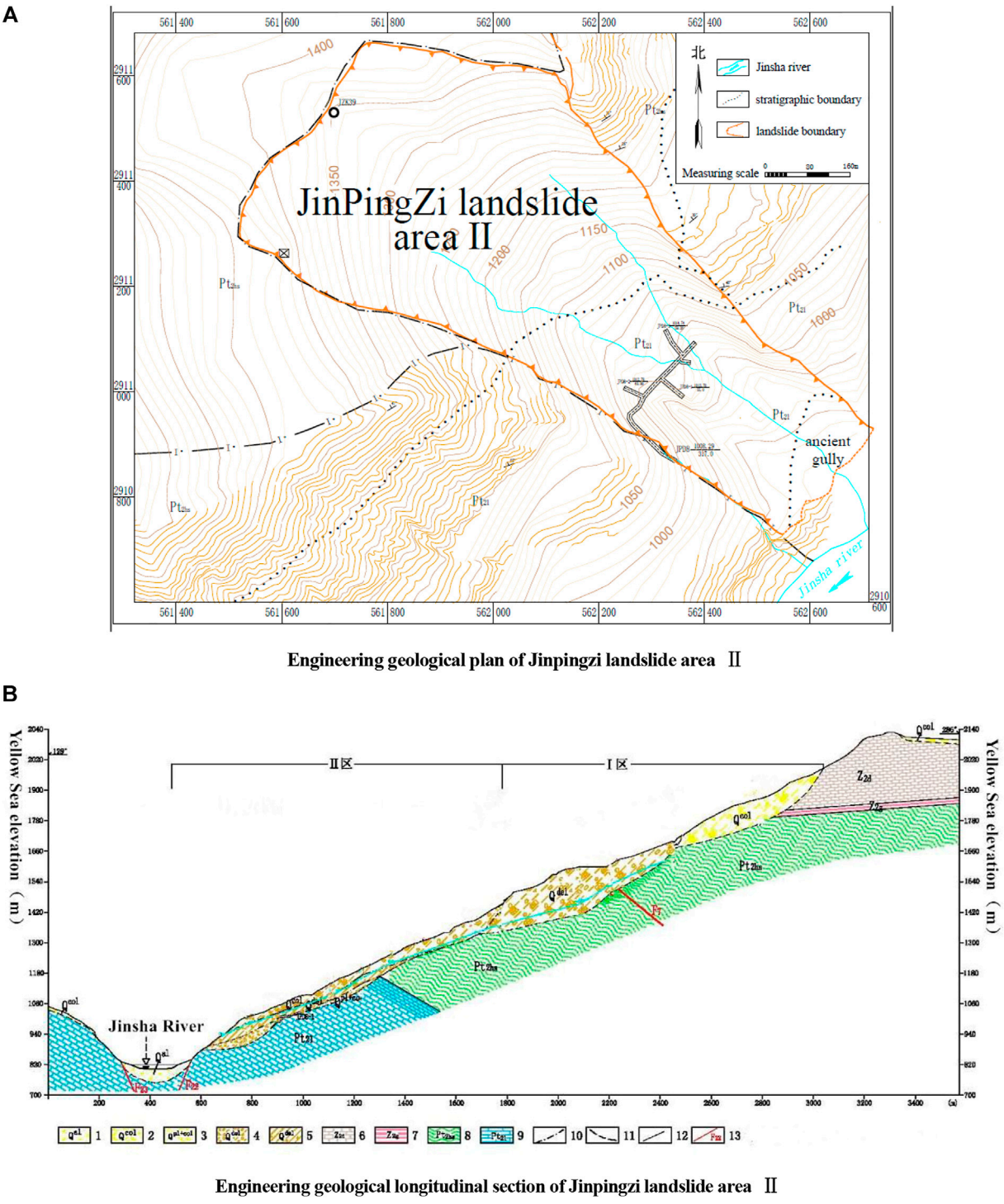

FIGURE 7
Geological map of the study area. **(A)** Engineering geological plan of Jinpingzi landslide area II. **(B)** Engineering geological longitudinal section of Jinpingzi landslide area II.

TABLE 2 Jinpingzi area II rock mechanical parameters.

Rock strata	ρ/kg·m^{-3}	c/kPa	φ/(°)	Bulk modulus (MPa)	Shear modulus (MPa)	Tensile strength (kPa)
Dolomite	21.5	50	37	33	11	200
Phyllite	22	70	28	25	50	500
Ancient gully	23	20	28	67	22	150
Pt_{21}	27.2	2,850	35	800	480	100
Pt_{2hs}	27	3,800	36	1,200	720	800

TABLE 3 Main monitoring methods and alert parameters of creeping landslide.

Monitoring content	Monitoring indicators	Alert parameters
Driving forces	Rainfall, groundwater level, etc.	Critical rainfall, water level, etc.
Surface deformation	Displacement rate, cumulative displacement, acceleration, etc.	Acceleration, etc.

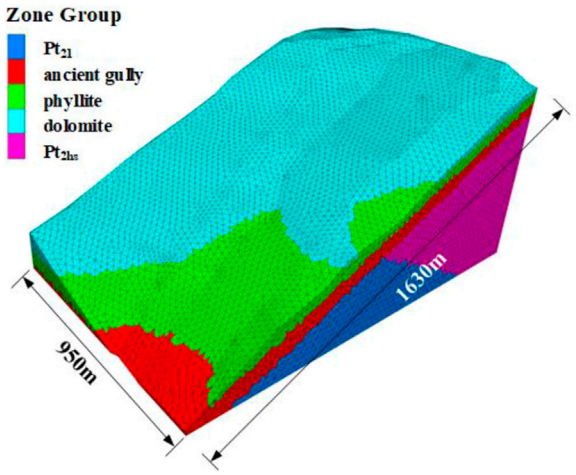

FIGURE 8
Model of Jinpingzi landslide area II diagram.

The relationship between the reduction coefficient and development of the displacement and the plastic zone are obtained via the reduction analysis of the model. The line chart of the displacement value and the SF under each reduction parameter is drawn. The X-axis is the SF, while the Y-axis is the displacement, as shown in Figure 10. There are two points marking a changing trend in almost all displacement and safety coefficient curves. The first point occurs at about SF = 1 and the second at SF = 0.83. Consequently, the displacement has three stages: 1) when the SF > 1, all displacement remains constant with the reduction of the safety factor, and the slope is zero; 2) when the safety factor 0.83 < SF < 1, the displacement increases slowly, and the gradient is no longer zero; 3) when the SF < 0.83, the displacement increases sharply, which demonstrates that the landslide experiences large-scale movements and that measures to evacuate people must be considered.

The section passing through (0, 950, 0) and the normal direction (0, 1, 0) were selected. The shear strain increment of variation and the variation of the plastic zone are shown in Figure 11.

When the reduction coefficient *Ks* is 1.65, the green band in the shear strain increment diagram is connected, indicating that the Jinpingzi landslide area II already fulfills the conditions for sliding, i.e., the plastic zone passes through from the top of the landslide to the bottom. As shown in Figure 12, c and φ continue to decrease with the increasing reduction coefficient, and the first plastic failure occurs at the trailing edge and toe of the landslide, after which it gradually extends to the upper part, when the plastic zone penetrates through. Subsequently, the plastic zone widens and increases along with the interior of the sliding body; however, the plastic zone increases and finally the Jinpingzi II zone slides down. The map depicting the changes in the plastic zone demonstrates that the rock layer with the sliding zone is composed of the phyllite overburden.

Figure 10C shows the Z-direction displacement-SF and (d) resultant displacement diagram-SF graphs: in addition to the point TP12 at the top of the landslide, the order of the remaining seven monitoring displacement sizes (absolute values) ordered from large to small is TP11 > TP10 >

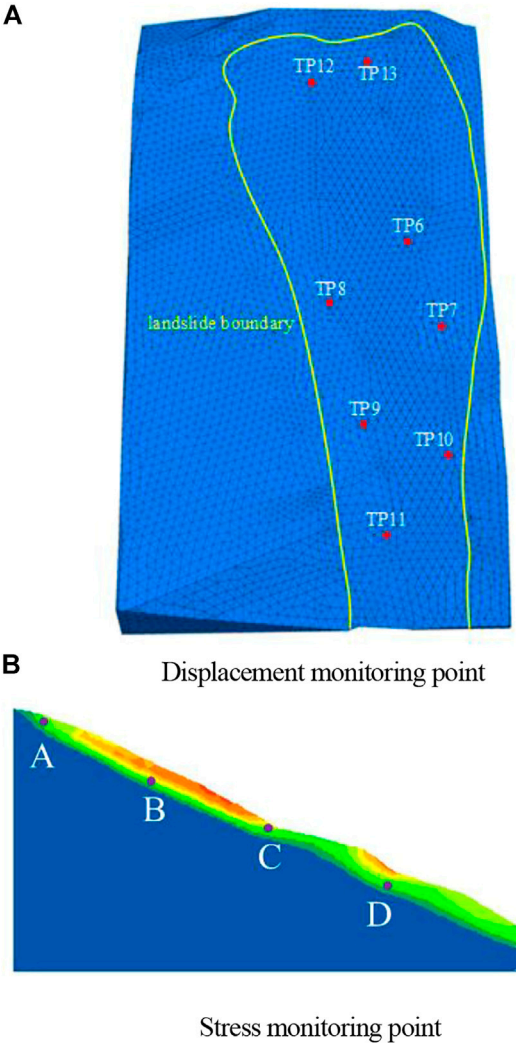

FIGURE 9
Monitoring points of Jinpingzi landslide area II. **(A)** Displacement monitoring point. **(B)** Stress monitoring point.

TP9 > TP7 > TP6 > TP13 > TP8; another position of TP11, TP10, TP9, TP7, TP6, and TP8 ranges the lower to the upper of the slope. Thus, the displacement from the lower to the upper part of Jinpingzi landslide area II decreases, i.e., the displacement at the lower parts is the largest, which conforms to the characteristics of a pull-type landslide.

The line chart of the stress and SF under each reduction parameter is drawn. The X-axis is the SF, while the Y-axis is the stress value, as shown in Figure 12. After the SF < 1, no stress variation trend is evident with the decreasing SF. This shows that the sensitivity of the displacement is larger than the stress sensitivity, such that it is more reliable to perform displacement monitoring than stress monitoring.

Comparative analysis of simulation results from a simple landslide and Jinpingzi landslide area II

From a comparative analysis of a simple landslide and the Jinpingzi landslide area II, we conclude the following:

(1) c and ϕ decrease with increasing reduction factor. The rear and toe of the landslide are damaged first, after which the plastic zone gradually develops to the upper landslide. When the SF is close to 1, the plastic zone is interconnected. Subsequently, the sliding face begins to widen along with the internal landslide, and the plastic area of the sliding body likewise gradually increases until the landslide takes place.
(2) For creep landslides, the stress does not show certain laws with the reduction of the SF, such as displacement of the landslide surface. Therefore, when the SF of a creeping landslide is < 1, the sensitivity of the displacement is larger than the stress sensitivity, indicating that displacement monitoring is more reliable than stress monitoring.
(3) There are two points that mark a changing trend in the displacement and safety coefficient curve as the SF changes. The first occurs at about SF = 1, and the second changes with the landslide change; however, its possible range is 0.8 to 0.95. Consequently, the displacement has three stages: a) when the SF > 1, the landslide is in the security state; b) when the safety factor 0.8–0.95 < SF < 1, although landslides begin to slip, there is no danger, and yellow warning signs can be initiated to adopt prevention measures or to reinforce the area; c) when the SF < 0.8–0.95, the landslide has undergone considerable sliding, and the red warning for emergency measures can be initiated.

Field monitoring of displacement in Jinpingzi landslide area II

For the creeping landslide, 17 monitoring points were installed at Jinpingzi landslide area II. As per the simulation results of a simple landslide and Jinpingzi landslide area II, as well as the measured displacement data, we selected three monitoring stations from the toe to the top of the landslide to analyze the changing trends of Jinpingzi landslide area II. These three monitoring points were TP11 (toe), TP6 (slope), and TP12 (top). The displacement data of individual monitoring stations were recorded from 3rd January 2006 to 31st July 2010. The resulting curves show the actual displacements of the three points, where the X-axis represents time, and the vertical axis represents displacement, as shown in Figure 13.

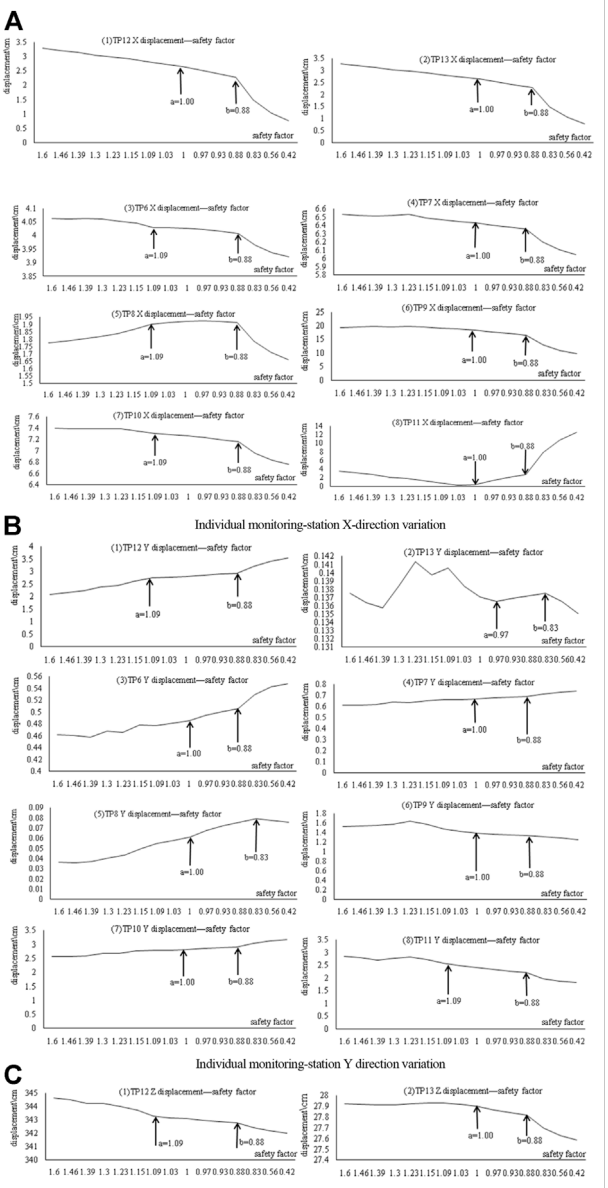

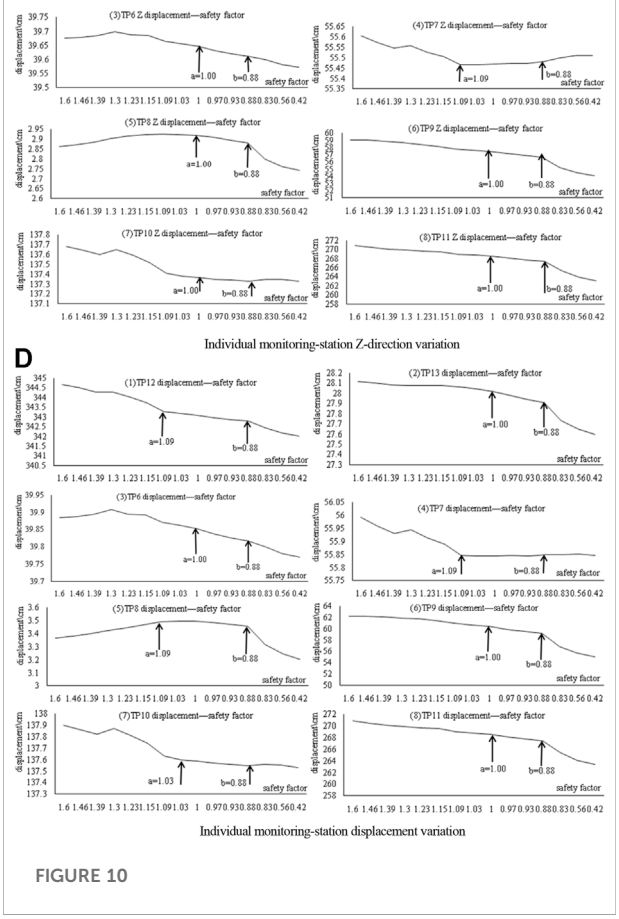

FIGURE 10
Displacement–safety factor graph of Jinpingzi landslide area II. **(A)** Individual monitoring-station X-direction variation. **(B)** Individual monitoring-station Y-direction variation. **(C)** Individual monitoring-station Z-direction variation. **(D)** Individual monitoring-station displacement variation. (continued)

The actual monitored displacement of the three points gradually increased, and there was no period of the displacement being zero. This shows that the SF of Jinpingzi landslide area II is <1. From 2006 to 2010, the displacement in the three directions x, y, and h showed no evident change in trends, which indicates that it is stable. Therefore, we can predict that it is currently in the stage of yellow warning, and it will remain there for a long period of time.

The deformation in this area is synchronous, therefore the displacement curve of any monitoring point agrees with that of other monitoring points. Considering the monitoring data from point TP10 as an example for detailed analysis, in Figures 14–16, we conclude that: a) during the monitoring period, the combined displacement of monitoring point TP10 demonstrates a linear growth trend, the displacement value increases slowly, and there is no abrupt change point; b) up to 171 days (4th November 2005), the displacement rate changes in a disorderly manner, generally exhibiting an increasing trend. After this time, the change is more regular, and the displacement rate gradually decreases and tends to stabilize, indicating that the area is in the stage of constant velocity deformation; c) up to 83 days (8th August 2005), the displacement acceleration changes significantly and exhibits an overall decreasing trend. After this time point, the change is regular, and the displacement acceleration gradually decreases and stabilizes, which is reflected in the area being in the stage of a uniform creep.

Based on the stability of the relational model, which in turn was based on the displacement characteristics of the slope surface proposed in this paper, it is suggested to continue strengthening the monitoring of landslide surface displacement. As the

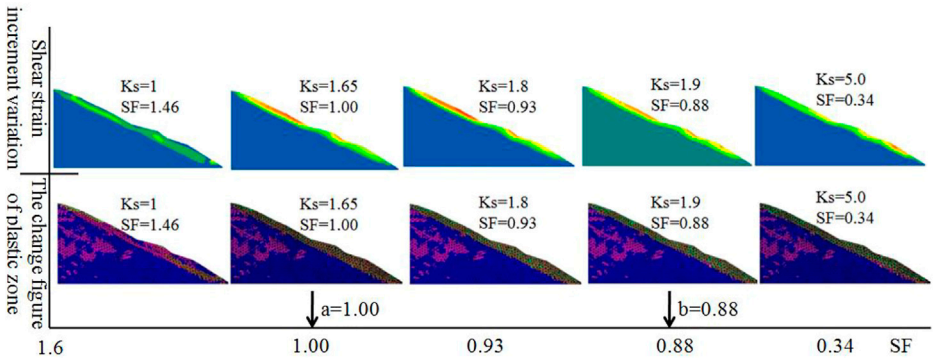

FIGURE 11
Shear strain increment variation and changes in the plastic zone.

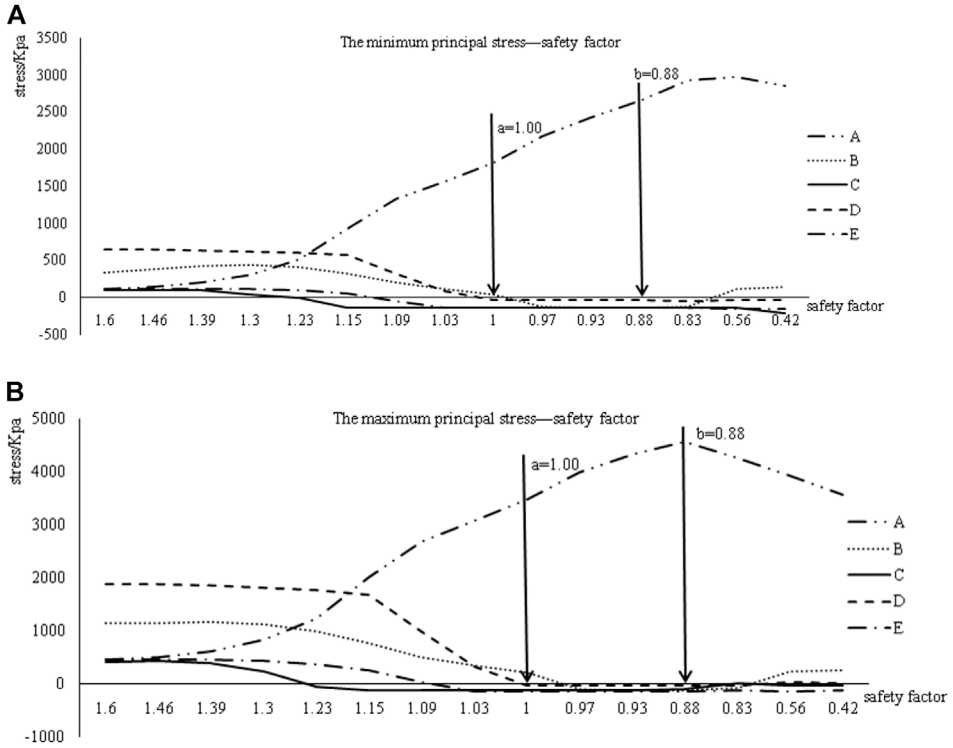

FIGURE 12
Stress–safety factor graph. **(A)** The minimum principal stress–safety factor. **(B)** The maximum principal stress–safety factor.

displacement of a landslide is related to rainfall (Wang et al., 2014), rainfall monitoring should be focused upon while monitoring landslide displacement. Landslide monitoring is only a means; the real purpose is to achieve accurate early warning of landslide disasters. Thus, attention should be paid not only to landslide monitoring but also to the early warning of a disaster; regional meteorological early warning systems should be simultaneously strengthened. The early warning of landslide disaster is mainly based on the statistical analysis of historical data, groundwater level, rainfall, and other key indicators, so this method could help to improve the accuracy and practicality of landslide early warning, as described in Table 3.

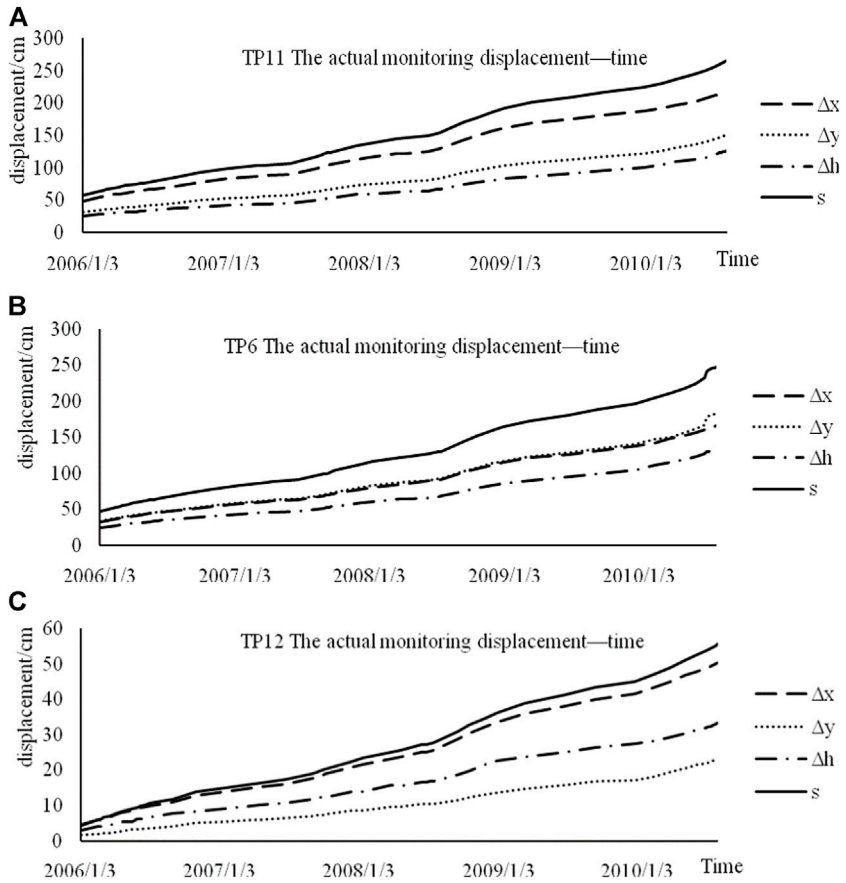

FIGURE 13
Monitored displacement–time graph. **(A)** TP11, the actual monitored displacement–time. **(B)** TP6, the actual monitored displacement–time. **(C)** TP12, the actual monitored displacement–time.

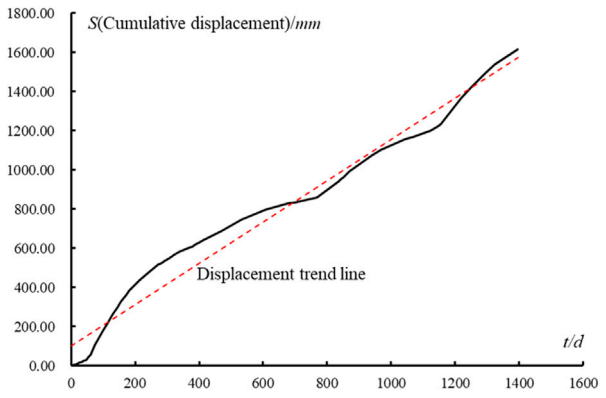

FIGURE 14
Plane resultant displacement–time curve of monitoring point TP10.

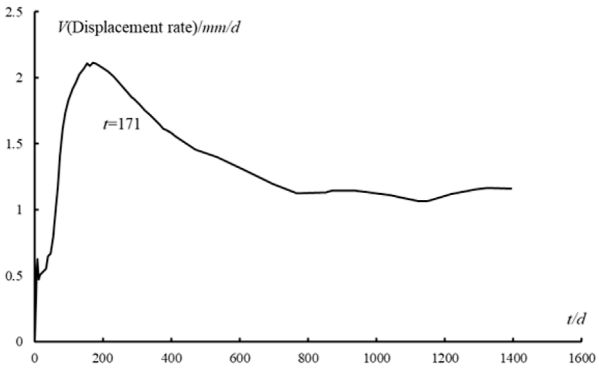

FIGURE 15
Displacement rate time curve of monitoring point TP10.

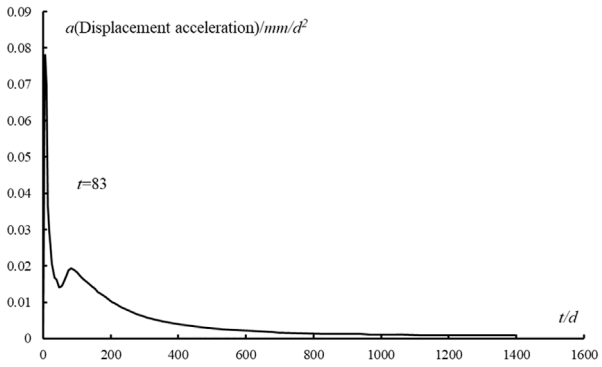

FIGURE 16
Displacement acceleration time relation curve of monitoring point TP10.

Conclusion

In this study, a homogeneous landslide was analyzed by FLAC3D, and a stability judgment model of the landslide based on displacement characteristics was established. In addition to the FLAC3D numerical simulation and using the landslide stability judgment model established in this study, a stability analysis of Jinpingzi landslide area II was performed. It was concluded that this research area is in the stability stage, which is consistent with the conclusion obtained from the actual monitoring data. The primary conclusions are as follows:

(1) With the development of a landslide, the rear and toe of the landslide are damaged first and then the plastic zone gradually develops to the upper landslide. When the SF is close to *a*, the plastic zone passes through from the top of the landslide to the bottom. Subsequently, the sliding face begins to widen along with the internal landslide, and the plastic area of the sliding body gradually increases until the landslide occurs.
(2) For a creeping landslide, when the SF of the creeping landslide is less than 1, the sensitivity of the displacement is larger than the stress sensitivity. Hence, it is more reliable to monitor the displacement than the stress.
(3) There are two points marking a change in the trend of the displacement and safety coefficient curve with respect to the SF. The first occurs at about SF = 1, whereas the second is in the range of 0.8–0.95. Consequently, the displacement comprises three stages: (1) when the SF > 1, the landslide is in the secure state; (2) when the safety factor $0.8 - 0.95 < SF < 1$, although landslides begin to slip, there is no danger, and the yellow warning is triggered to adopt prevention or reinforcement measures; (3) when the $SF < 0.8 - 0.95$, the landslide has undergone considerable sliding, and the red warning can be initiated to begin emergency measures.
(4) The Jinpingzi landslide area II is stable. Therefore, we can predict that it is currently in the yellow warning stage and will remain there for a rather long period.

Data availability statement

The original contributions presented in the study are included in the article/supplementary material, and further inquiries can be directed to the corresponding author.

Author contributions

BX and QH were responsible for the work concept and design; BX and QH were responsible for data collection; YQ was responsible for drafting the manuscript; BX was responsible for making important revisions to the manuscript; QH and YQ were responsible for approving the final version of the manuscript for publication.

Funding

This work was supported by the Natural Science Foundation granted by the Department of Education, Anhui Province (KJ2020A0235), Natural Science Foundation of Anhui Province (No. 2008085QE221), and Postdoctoral Researchers Research Activities Foundation of Anhui Province (Nos. 2021B550 and 2021B551).

Conflict of interest

Author QY was employed by the MCC17 Group Co., Ltd.

The remaining authors declare that the research was conducted in the absence of any commercial or financial relationships that could be construed as a potential conflict of interest.

Publisher's note

All claims expressed in this article are solely those of the authors and do not necessarily represent those of their affiliated organizations, or those of the publisher, the editors, and the reviewers. Any product that may be evaluated in this article, or claim that may be made by its manufacturer, is not guaranteed or endorsed by the publisher.

References

Chen, W.-b., and Duan-you, L. (2006). Prediction of Displacement in Landslide Based on Nonlinear Dynamics. ***J. Yangtze River Sci. Res. Inst.*** 23 (2), 28–30. doi:10.3969/j.issn.1001-5485.2006.02.008

Crosta, G. B., and Agliardi, F. (2003). Failure Forecast for Large Rock Slides by Surface Displacement Measurements. *Can. Geotech. J.* 40 (1), 176–191. doi:10.1139/t02-085

Dong, H., Fu, H.-L., Leng, W.-M., and Long, W.-X. (2007). Boosting Ensemble of Support Vector Regression for Landslide Prediction. *J. Hunan Univ. Nat. Sci.* 34 (9), 6–10.

Du, J., Yin, K.-l., and Chai, B. (2009). Study of Displacement Prediction Model of Landslide Based on Response Analysis of Inducing Factors. *Chin. J. Rock Mech. Eng.* 28 (9), 1783–1789. doi:10.3321/j.issn:1000-6915.2009.09.007

Du, Y., Li, H., Chicas, S. D., and Huo, L. (2022). Progress and Perspectives of Geotechnical Anchor Bolts on Slope Engineering in China. *Front. Environ. Sci.* 10, 928064. doi:10.3389/fenvs.2022.928064

Du, Y., Lu, Y.-D., Xie, M.-W., Jia, J.-L., Cong, X.-M., and Wu, Y.-Q. (2020a). Stability Evaluation of Creeping Landslide Considering Variation of Initial Conditions. *Chin. J. Rock Mech. Eng.* 39 (S01), 2828–2836. doi:10.13722/j.cnki.jrme.2019.1079

Du, Y., Xie, M.-W., and Jia, J.-L. (2020b). Stepped Settlement: A Possible Mechanism for Translational Landslides. *Catena* 187, 104365. doi:10.1016/j.catena.2019.104365

Federico, A., Popescu, M., Elia, G., Fidelibus, C., Interno, G., and Murianni, A. (2012). Prediction of Time to Slope Failure: a General Framework. ***Environ. Earth Sci.*** 66 (1), 245–256. doi:10.1007/s12665-011-1231-5

Geller, R. J., Jackson, D. D., Kagan, Y. Y., and Mulargia, F. (1997). Earthquakes Cannot Be Predicted. *Science* 275, 1616. doi:10.1126/science.275.5306.1616

Huang, H.-F., Song, K., Yi, Q.-L., Yi, W., and Zhang, G.-D. (2015). Study on Parameter Value Selection of Support Vector Machine for Displacement Prediction of Landslides. *Chin. J. Undergr. Space Eng.* 11 (4), 1053–1059.

Huang, H.-F., Yi, W., Yi, Q.-L., Lu, S.-Q., and Wang, S.-M. (2014). Smoothness Priors Approach in Displacement Decomposition and Prediction of Landslides. *Hydrogeology Eng. Geol.* 41 (5), 95–100. doi:10.16030/j.cnki.issn.1000-3665.2014.05.043

Huang, H.-F., Yi, W., Liu, Y.-L., Wang, H., and Lin, H.-Y. (2016). Study on Variables Selection Using SVR-MIV Method in Displacement Prediction of Landslides. *Chin. J. Undergr. Space Eng.* 12 (1), 213–219.

Li, H.-J., Xu, Q., He, Y.-S., and Wei, Y. (2016). Predictive Modeling of Landslide Displacement by Wavelet Analysis and Multiple Extreme Learning Machines. *J. Eng. Geol.* 24 (5), 721–731. doi:10.13544/j.cnki.jeg.2016.05.001

Li, K.-G., and Zhang, C.-Q. (2009). Neural Network Modeling and Slope Displacement Prediction Based on Time Series. *Chin. J. Undergr. Space Eng.* 5 (S1), 1418–1421. doi:10.3969/j.issn.1673-0836.2009.z1.028

Lian, C., Zeng, Z., Yao, W., Tang, H., and Philip Chen, C. L. (2016). Landslide Displacement Prediction with Uncertainty Based on Neural Networks with Random Hidden Weights. *IEEE Trans. Neural Netw. Learn. Syst.* 27 (12), 2683–2695. doi:10.1109/TNNLS.2015.2512283

Liu, X.-P., Xie, X.-B., and Luo, Y.-Z. (2010). Self-menorization Model of Dynamic System for Predicting Nonlinear Displacement of Slopes. *Chin. J. Geotechnical Eng.* 32 (10), 1535–1542. doi:10.1016/S1876-3804(11)60004-9

Ma, W.-T. (2009). Prediction of Slope Displacement Based on Wavelet Transform and Genetic Algorithm-Least Square Support Vector Machine. *Rock Soil Mech.* 30 (S2), 394–398. doi:10.16285/j.rsm.2009.s2.081

Meng, M., Chen, Z.-Q., Huang, D., Zeng, B., and Chen, C.-J. (2016). Displacement Prediction of Landslide in Three Gorges Reservoir Area Based on H-P Filter, ARIMA and VAR Models. *Rock Soil Mech.* 37 (S02), 552–560.

Miao, H.-B., Yin, K.-L., and Zhang, X.-W. (2016). Prediction of Ground Displacement of Reservoir Ancient Landslide with Intermittent Reactivation. *Geol. Sci. Technol. Inf.* 35 (5), 208–213.

Qin, S. Q., Jiao, J. J., and Wang, S. J. (2002). A Nonlinear Dynamical Model of Landslide Evolution. *Geomorphology* 43 (1), 77–85. doi:10.1016/s0169-555x(01)00122-2

Saito, M. Forecasting Time of Slope Failure by Tertiary Creep[C]. Proceedings of the 7th International Conference on Soil Mechanics and Foundation Engineering. Mexico, 1969.

Simeoni, L., Ronchetti, F., Costa, C., Joris, P., and Corsini, A. (2020). Redundancy and Coherence of Multi-Method Displacement Monitoring Data as Key Issues for the Analysis of Extremely Slow Landslides (Isarco Valley, Eastern Alps, Italy). *Eng. Geol.* 267, 105504. doi:10.1016/j.enggeo.2020.105504

Wang, L.-W., Xie, M.-W., and Chai, X.-Q. (2014). Research on Method of Displacement Speed Ratio for Spatial Evaluation of Landslide Deformation. *Rock Soil Mech.* 35 (2), 519–528. doi:10.16285/j.rsm.2014.02.019

Xu, F., Wang, Y., Du, J., and Ye, J. (2011). Study of Displacement Prediction Model of Landslide Based on Time Series Analysis. *Chin. J. Rock Mech. Eng.* 30 (4), 746–751. doi:10.1007/s12182-011-0118-0

Ye, Q. (2016). Is the "5. 8" Geological Hazard in Taining a Landslide or a Debris Flow? . *Xiamen Sci. Technol.* (4), 46–49.

Zhang, J., Yin, K.-L., Wang, J.-J., and Huang, F.-M. (2015). Displacement Prediction of Baishuihe Landslide Based on Time Series and Pso-Svr Model. *Chin. J. Rock Mech. Eng.* 34 (2), 382–391. doi:10.13722/j.cnki.jrme.2015.02.017

Zhou, C., Yin, K.-l., and Huang, F.-m. (2015). Application of the Chaotic Sequence WA-ELM Coupling Model in Landslide Displacement Prediction. *Rock Soil Mech.* 36 (9), 2674–2680. doi:10.16285/j.rsm.2015.09.030

frontiers | Frontiers in Earth Science

TYPE Original Research
PUBLISHED 31 August 2022
DOI 10.3389/feart.2022.949916

Check for updates

OPEN ACCESS

EDITED BY
Yan Du,
University of Science and Technology Beijing, China

REVIEWED BY
Yanlin Zhao,
Hunan University of Science and Technology, China
Yunliang Tan,
Shandong Univeristy of Science and Technology, China

*CORRESPONDENCE
Zhongchao Zhou,
zzc20206@qq.com

SPECIALTY SECTION
This article was submitted to Geohazards and Georisks, a section of the journal Frontiers in Earth Science

RECEIVED 21 May 2022
ACCEPTED 18 July 2022
PUBLISHED 31 August 2022

CITATION
Zhang X, Zhou Z, Yang J, Pang S, Geng J, Li W and Zhang X (2022), Creep properties of siltstone-like materials with different unloading confining pressures under seepage. *Front. Earth Sci.* 10:949916. doi: 10.3389/feart.2022.949916

COPYRIGHT
© 2022 Zhang, Zhou, Yang, Pang, Geng, Li and zhang. This is an open-access article distributed under the terms of the Creative Commons Attribution License (CC BY). The use, distribution or reproduction in other forums is permitted, provided the original author(s) and the copyright owner(s) are credited and that the original publication in this journal is cited, in accordance with accepted academic practice. No use, distribution or reproduction is permitted which does not comply with these terms.

Creep properties of siltstone-like materials with different unloading confining pressures under seepage

Xiangdong Zhang[1], Zhongchao Zhou[1]*, Jianjun Yang[2], Shuai Pang[1], Jie Geng[1], Wenliang Li[1] and Xuefeng Zhang[1]

[1]College of Civil Engineering, Liaoning Technical University, Fuxin, Liaoning, China, [2]China Northeast Architecture Design and Research Institute Co., LTD., Shenyang, Liaoning, China

Deep enclosing rocks exhibit non-homogeneous characteristics of dense joints and fissure development. Soft rocks subjected to multiple factors, such as high stress and hydrostatic pressure, are prone to damage and significant deformation, which can lead to instability of the surrounding rocks, failure of the supporting structure, and other accidents. In this study, we investigated the creep behaviour of deep soft rocks and siltstone-like materials subjected to different unloading confining pressures coupled with a high stress field and seepage. Subsequently, the laws and behaviours of parameters, such as the transient strain, creep deformation, and creep rate were derived and analysed under various conditions. The results indicate that the radial creep curve exhibits a variation pattern similar to that of the axial creep. However, the extent of radial creep exceeds that of axial creep in soft siltstone-like rocks under unloading confining pressure conditions. We derived expressions for the constitutive relation of siltstone-like specimens under various unloading confining pressure conditions in the presence of seepage using an improved viscoelasticmodel that considered the coupling effect of fissure and seepage flow. The correlation coefficients of the calculated model values with the experimental values, as obtained by the non-linear least-squares fitting, were all above 0.9178, indicating that the proposed model can accurately characterise the creep process in fissured siltstone.

KEYWORDS

seepage, siltstone-like materials, creep, constitutive model, integrity indices

Introduction

Rock masses encountered in deep underground projects are in a complex hydrogeological and tectonic stress environment. The stress distribution in the rock mass is influenced by the complex hydrological conditions within the rock mass and the gradual development of pore-water fissures. This complex rock interaction originates from subsurface pressure. However, the original equilibrium conditions of the rock mass are affected by the stress field. Challenges related to fault fracture zones and

stress-redistribution-induced rock deterioration, which can cause major engineering disasters, are common in geotechnical engineering. Therefore, the investigation of the mechanical deformation characteristics of rock masses and creep under seepage conditions is critical for geological construction.

The rheological properties of rocks have received considerable attention since the 20th century. Du et al. (2021) studied an early monitoring and early warning system for brittle failure disasters and proposed specific coping strategies and measures for the five technical bottlenecks in the early monitoring and early warning of collapse disasters. Chen et al. (2004) proposed a fracture interaction mechanism, an equivalent extension model, and a rock creep damage-elastoplastic coupling constitutive model based on the damage fissure-related mechanics theory by using the plastic damage-fracture components in conjunction with the Kelvin model. Sha et al. (2018) established a link between the macroscopic and microscopic mechanisms of sandstone fractures based on their macroscopic and microscopic characteristics. Scanning electron microscopy (SEM) investigation revealed the seepage-creep pattern and damage mechanism in coal-bearing sandstones. Long et al. (Wang and Jiang, 2018) conducted two sets of triaxial unloading creep tests on basalt under hydrodynamically coupled conditions. They observed the tensile-shear damage pattern of basalt under unloading confining pressure and hydrodynamic coupling and reported that the relationship between the confining pressure and steady-state creep rate could be described by an exponential function. Zhang et al. (2022). Studied the fracture characteristics and strength criterion of layered sandstone through triaxial compression tests of rock samples with different bedding angles under different confining pressures. It was found that the failure mode and strength of the bedding sandstone were related to the bedding dip angle, showing obvious anisotropy. Liu et al. (2022a), Liu et al. (2022b) analysed the fracture mode of single-crack limestone under different confining pressures and water pressures based on the evolution of water inflow in ultra-deep mines and a hydrogeological model considering the interaction of multiple wells using prefabricated limestone single-crack samples. They deduced the rock compression-shear fracture criterion under the action of hydraulic coupling. Wang et al. (2017) examined the effect of internal rock crack damage on the evolution of macroscopic deformation characteristics and permeability by conducting triaxial creep-seepage-acoustic emission experiments on granite from the geological disposal area of high-level radioactive waste in Beishan, Gansu Province, at different confining pressures. Liu et al. (2021) developed a three-dimensional nonlinear creep model of deformed fissured sandstone based on the study of green sandstone under the combined action of axial and hydraulic pressures. Wang et al. (2019) studied the fracture characteristics of mudstone from the No. 12 Pingdingshan coal mine and found that perturbation converts ductile-brittle coupled fracture to brittle fracture-dominated cleavage damage. Li et al. (2021), Du et al. (2017) conducted freeze–thaw tests on rocks to study the relationship between the natural vibration frequency and cohesion. It was found that frost heave of pore water caused crack initiation and development, forming intergranular and transgranular cracks. Uneven shrinkage and expansion of minerals are the main reasons for the internal degradation of dry rocks. Shan et al. (2019) studied triaxial creep and deformation damage in frozen laminated red sandstone around the shaft of the freezing project of the Shilawusu mine in the northwest region of China using a dynamically disturbed low-temperature rock triaxial test system and described its long-term mechanical properties and non-linear creep characteristics. Zhou et al. (2020) developed a coupled seepage evolution model and damage creep model for soft rocks and observed the deformation behaviour of soft rocks in three different creep stages. Zhao et al. (2021a), Zhao et al. (2021b) proposed a natural rock joint strength model and dual-media seepage model. The former more comprehensively reflects the relationship between the parameters affecting the joint surface topography and shear strength. The dual-media model includes equivalent continuous and discrete fractured media to study seepage-damage coupling effects in fractured rock masses, considering the massive water storage of the fracture network and the high conductivity of major large fractures.

However, these studies did not adequately consider the damage law of deep soft rocks and failed to elucidate the creep characteristics of the unloading confining pressure process in fissured soft rocks under the coupling effect of high stress and seepage fields. Therefore, we investigated the deformation and damage laws in fissured soft rocks and the creep properties of the unloading confining pressure process under the influence of seepage of fissured soft rocks. The findings of this study can guide the design of disaster warning systems to ensure construction safety and improve construction efficiency in water-rich ultra-deep mines with fissured enclosing rocks.

Test regime for unloading confining pressure creep in sandstone-like specimens under seepage action

For Muddy siltstone developed in the Hongqingliang coal mine was used as the research object to obtain the physical, chemical, and mechanical parameters *in situ* by indoor tests (Table 1). Subsequently, similar parameters and their ratios for siltstone-like materials were determined for the unloading confining pressure creep tests under different initial hydrostatic pressure conditions.

In the table, C_u is Poisson's ratio similarity ratio, C_l is the strain similarity ratio, C_k is the permeability coefficient similarity

TABLE 1 Relational expressions for the preparation of siltstone-like materials.

Similarity parameter	Similarity relation	Similarity parameter	Similarity relation
Geometric similarity	$C_u = C_l$	Model similarity	$C_G = C_\lambda$
Gravity similarity	$C_G = C_\gamma C_l$	Time similarity	$C_t = \sqrt{C_l}$
Stress similarity	$C_\sigma = C_\gamma C_l$	Hydrostatic coefficient similarity	$C_K = \sqrt{C_l}/C_\gamma$

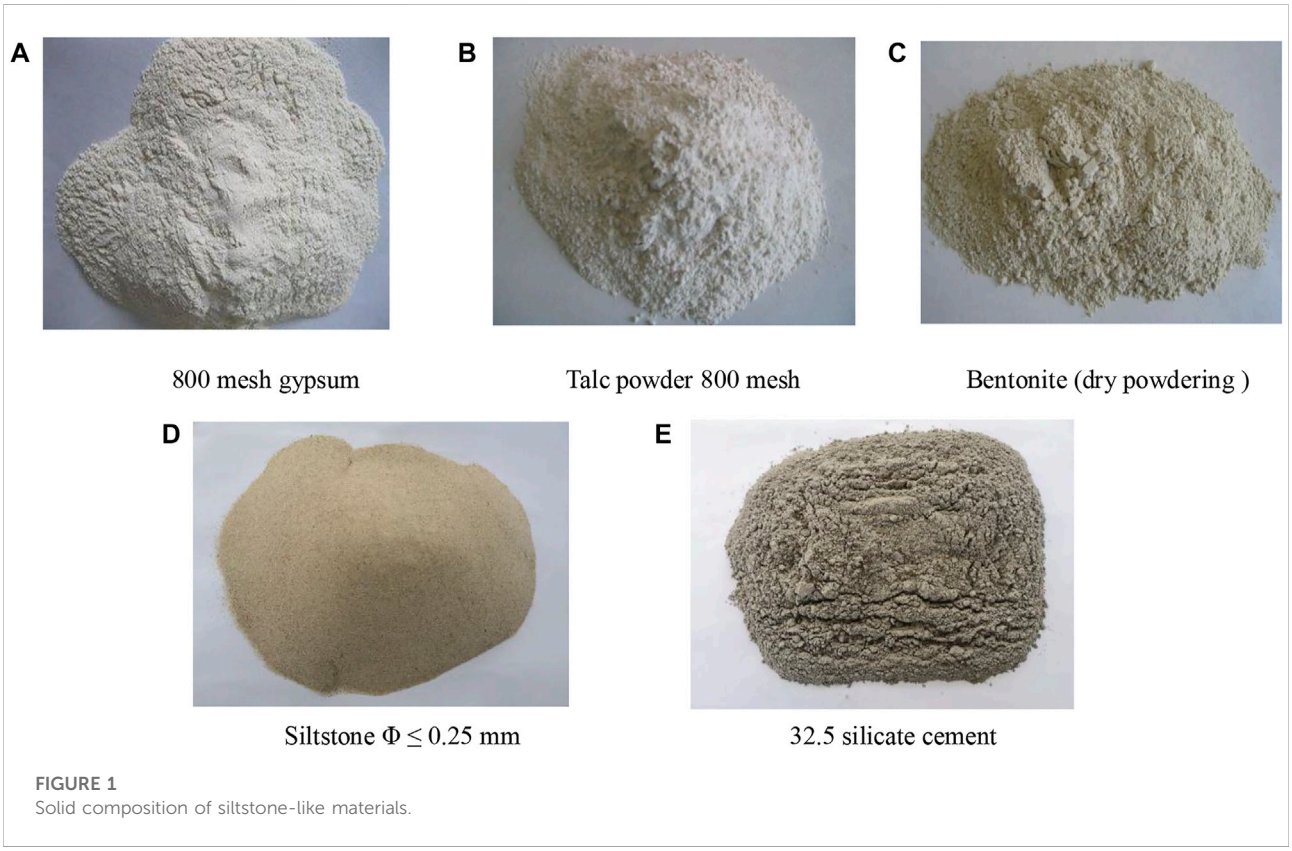

FIGURE 1
Solid composition of siltstone-like materials.

ratio, C_G is the gravity similarity ratio, C_σ is the stress similarity ratio, C_γ is the heavy similarity ratio, and C_λ is the mode force similarity ratio.

Selection of muddy siltstone-like materials

Based on long-term studies on siltstone-like materials, we determined the material specifications for this test after field sampling. Quartz sand with a grain size of less than 0.25 mm and 32.5 silicate cement was selected with saturated ammoniac thiosulfates sodium solution as the experimental water. The main factors considered were the water-binder ratio, sand-binder ratio, clay-binder ratio (the ratio of impurity components to cement mass), and mud type (talcum powder, gypsum, bentonite is dried, powdered, and passed through a 300-mesh sieve silt); the solid composition of the test materials is shown in Figures 1A-E. The specific protocol of the test was an orthogonal design with nine groups, as listed in Table 2.

Mix proportion for muddy siltstone-like specimens

Well-maintained specimens were made according to the parameters tested are shown in Table 3.

We compared the physical and mechanical parameters of muddy siltstone-like specimens in this test with those from the Hongqingliang fault fracture zone. Additionally, the permeability

TABLE 2 Preparation of fissure specimens in siltstone-like materials.

Test no.	Water-binder ratio	Sand-binder ratio	Mud-binder ratio	Type of mud
L-1	1:1.5	2.0:1	1:1.5	Talcum powder
L-2	1:1.5	2.5:1	1:1.0	Gypsum
L-3	1:1.5	3.0:1	1:0.5	Bentonite
L-4	1:2.0	2.0:1	1:1.0	Bentonite
L-5	1:2.0	2.5:1	1:0.5	Talcum powder
L-6	1:2.0	3.0:1	1:1.5	Gypsum
L-7	1:2.5	2.0:1	1:0.5	Gypsum
L-8	1:2.5	2.5:1	1:1.5	Bentonite
L-9	1:2.5	3.0:1	1:1.0	Talcum powder

TABLE 3 Physical and mechanical parameters of siltstone-like materials.

Test no.	Density ρ (g/cm^3)	Compressive strength σ_c (MPa)	Tensile Strength σ_t (MPa)	Permeability coefficient K (cm/s)	Modulus of elasticity E (GPa)
L-1	2.02	28.83	2.62	2.85 × 10−9	1.91
L-2	2.35	20.42	2.16	3.50 × 10−5	2.40
L-3	1.90	16.28	2.85	5.26 × 10−8	2.02
L-4	2.25	21.76	2.24	8.24 ×10−7	2.26
L-5	2.11	22.25	2.37	5.33 × 10−8	3.18
L-6	2.12	16.27	2.33	5.09 × 10−5	2.18
L-7	2.28	29.90	2.47	3.74 × 10−5	1.83
L-8	2.24	17.90	2.48	1.34 × 10−6	2.05
L-9	2.17	16.02	2.82	1.44 × 10−6	1.75

TABLE 4 Physical and mechanical parameters of siltstone-like specimens and protolith.

Materials	Density ρ (g/cm^3)	Modulusof elasticity E (GPa)	Poisson's ratio μ	Compressive strength σ_c (MPa)	Tensile strength σ_t (MPa)
Muddy siltstone	2.28	4.30	0.37	22.92	2.24
Similar material (L-5)	2.11	3.18	0.35	22.25	2.37
Ratio of similitude (C)	1.08	1.35	1.06	1.03	0.95

coefficient was used as the main similarity parameter for siltstone-like specimens. The mix proportion of the L-5 scheme was most similar to the comparison results. Therefore, physical and mechanical analyses were performed on the original rock and the L-5 specimens (Table 4).

The parameter similarity ratios in Table 4 indicate that $C_E \approx C_C \approx C_{\sigma c} \approx C_{\sigma t} \approx 1$ and $C_\gamma \approx C_u \approx C_\varphi \approx C_k \approx 1$, approximately achieving the required similarity criterion for the derivation. Therefore, the L-5 scheme was adopted to simulate the siltstone in the Hongqingliang fault zone. The material composition of the siltstone-like specimen was cement: sand: water: talc = 2: 2.5: 2: 2.

Test regime for unloading confining pressure creep in sandstone-like specimens

Rock mass integrity characterizes the degree of development at various geological interfaces (mainly fissures) and is the most

TABLE 5 Test scheme of graded unloading confining pressure creep tests under seepage.

Specimen no.	Integrity index Kv	Initial hydrostatic pressure SP(MPa)	Initial axial pressure σ1 (MPa)	Stage I confining pressure σ31 (MPa)	Stage II confining pressure σ32 (MPa)	Stage III confining pressure σ33 (MPa)	Stage IV confining pressure σ34 (MPa)	Stage V confining pressure σ35 (MPa)
RA-2	1	2	30	18	15	12	9	6
RA-4	1	4	30	18	15	12	9	6
RA-6	1	6	30	18	15	12	9	6
RB-4	0.716	4	30	18	15	12	9	6
RC-4	0.584	4	30	18	15	12	9	6

FIGURE 2
Specimens for unloading confining pressure creep test under seepage.

basic property affecting the stability of rock masses. The current evaluation index of rock mass integrity includes rock quality designation (RQD), rock mass block index (RBI), and rock mass integrity index K*v* (Wu et al., 2016). In this study, a rock mass integrity evaluation index (K*v*) was used to classify the enclosing rock in the engineering field, and to calculate the integrity index K*v* in the fissure and intact specimens according to the standard for engineering rock test methods (GB/T50266-2013). The calculation method is as follows.

$$K_v = \left(\frac{v_{pm}}{v_{pr}}\right)^2 \quad (1)$$

where vpm is the elastic velocity of the longitudinal wave of the fracture specimen (km/s) and vpr is the elastic velocity of the longitudinal wave of the intact specimen (km/s).

To investigate the effects of seepage and specimen integrity on the creep properties of siltstone-like specimens separately, the test was divided into two stages: a creep test of intact specimens at different initial hydrostatic pressures and a creep test at different integrity levels at the same hydrostatic pressure. According to the Raymer-Hunt-Gardner model, the longitudinal wave velocity vp of the complete sample detected by the ultrasonic tester ranges from 2.659 to 2.830 km/s, and the average value of 2.74 km/s is assumed as the longitudinal wave velocity of the complete rock

FIGURE 3
Softp-rock triaxial rheometer.

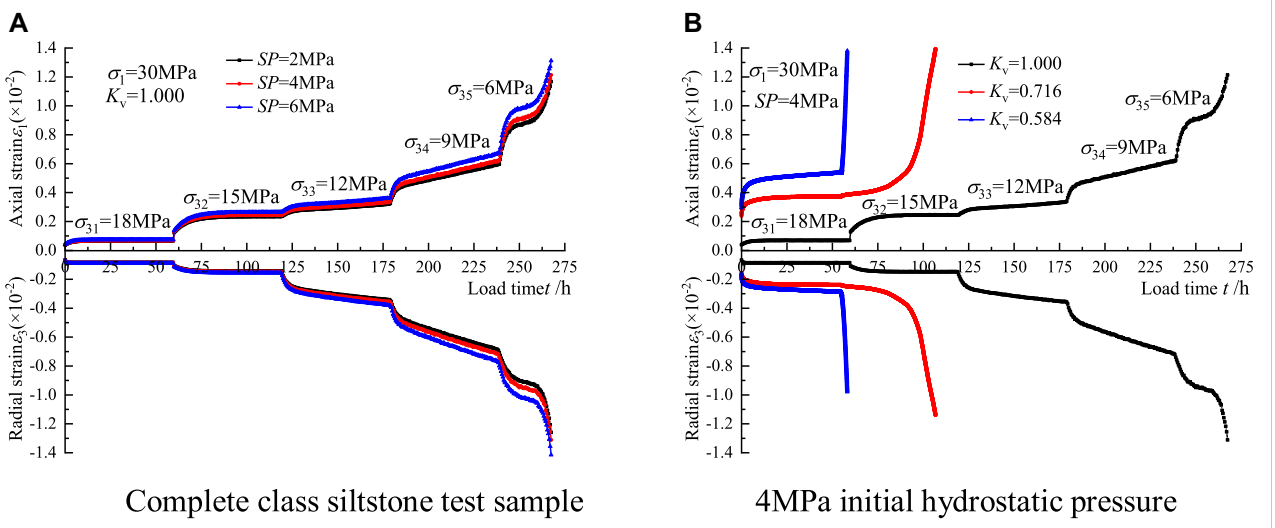

FIGURE 4
Contrcurve of creep of siltstone under the same conditions.

block. The integrity index of the sample whose measured value is greater than 2.74 km/s is recorded as 1, and the integrity index of the remaining samples is converted according to Eq. 1, then the wave velocities selected for the creep characteristics test under different hydrostatic pressures are 2.728, 2.738, and 2.734 Km/s. Initial permeability pressures of 2, 4, and 6 MPa were applied prior to the application of the axial pressure. For the latter, intact, relatively intact, and moderately intact siltstone-like specimens with wave velocities of 2.738, 2.317, and 2.093 km/s, respectively, were selected for testing. An additional initial permeability pressure of 4 MPa was applied before the application of the axial pressure. The test scheme is presented in Table 5, and the specimens are shown in Figure 2.

A soft rock triaxial rheometer was used for the tests (Figure 3). The axial pressure was maintained constant as the confining pressure was unloaded step-by-step. Based on the results of our long-term triaxial compression tests, the constant axial load for the unloading confining pressure creep test was set as 30 MPa. In addition, the unloading confining pressure process was divided into five stages, with an initial creep condition of 18 MPa for the enclosing rock, followed by 15 MPa, 12 MPa, 9 MPa, and 6 MPa. The test chamber was filled with oil using an external cell pressure controller. When the confining pressure was stabilised and the volume of silicone oil in the pump no longer fluctuated, the initial hydrostatic pressure was applied via an external back pressure controller in accordance with the test scheme. During this process, the hydrostatic pressure was maintained constant. When uniform droplets appeared at the outlet, the outlet was closed and the old back volume was selected. Subsequently, axial stress was gradually applied up to 30 MPa, while the axial pressure was maintained for 55 h. After the axial pressure stabilised, the confining pressure was unloaded to the specified confining pressure value at each stage until the specimen was damaged.

Creep properties of siltstone-like specimen unloading confining pressure under seepage

Deformation analysis

Creep tests were conducted sequentially according to the test scheme in Table 5. Full-process creep curves are shown in Figure 4.

The creep curve encompasses processes, such as transient deformation, decay creep, steady creep, and accelerated creep (Yang et al., 2017). Additionally, the following findings can be obtained from Figures 4A,B.

(1) When the confining pressure was 18 MPa, the creep process included only transient deformation and decay creep. When the loading duration exceeds 25 h, the rock enters a stable creep state.
(2) The creep curves included both decay creep and transient deformation creep when the confining pressure was unloaded to 15 MPa and 12 MPa. However, the creep rate was relatively low during the stable creep stage.
(3) Steady creep occurred in the intact specimens when the confining pressure was increased to 12 MPa.

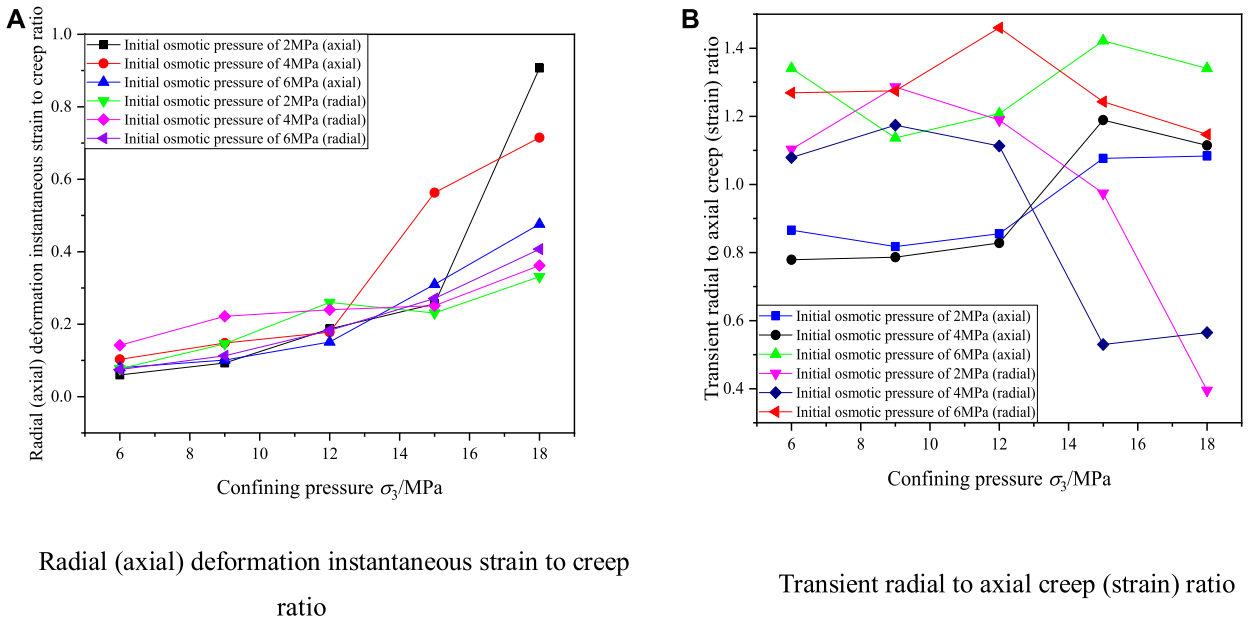

FIGURE 5
Transient to creep ratio of radial and axial directions under percolation.

(4) When the confining pressure was unloaded to 9 MPa, the creep process included decay, steady, and accelerated unsteady creep.
(5) Under the same initial hydrostatic pressure condition, as the integrity index decreased, both the relatively intact (K_v = 0.716) and moderately intact (K_v = 0.584) specimens experienced damage when the confining pressure was 15 MPa after the first unloading of the confining pressure.

Transient and creep deformation patterns under seepage

The unloading confining pressure creep curves for siltstone-like specimens under identical conditions are shown in Figure 4B. The ratio of transient deformation to creep deformation in the radial and axial directions in this unloading confining pressure test under different seepage effects is shown in Figures 5A,B. By analyzing the unloading confining pressure creep curves of the siltstone-like specimens under the same conditions and the radial to axial deformation ratio of the unloading confining pressure test under seepage, the following findings were obtained:

(1) Radial and axial creep curves have similar variation laws. However, under unloading confining pressure conditions, radial creep is greater than axial creep, which may be attributed to the weakening of the radial restraint due to the reduction of the confining pressure. Deformation is more likely to develop in the radial direction under constant axial loading.
(2) The development of radial strain is greatly affected as the specimen integrity index decreases. Radial creep remains lower than axial creep as both the relatively intact and moderately intact specimens were damaged at high confining pressure conditions (15 MPa).
(3) The transient axial deformation value of each group of specimens in the unloading confining pressure test under seepage is less than in axial tests.

Creep rate analysis under seepage

The subsurface water content of slate is not constant due to the different forms that the rock exists in within the waterlogged environment. Groundwater can have an important influence on the long-term stability of slate slope projects. Therefore, it is crucial to study the variation law of creep deformation rate of siltstone-like materials under unloading confining pressure conditions. The first-order derivation of the creep test results was performed using Origin software. Since the rate curve of specimen RA-6 is similar to that of specimens RA-2 and RA-4 and therefore not listed, the creep process rates of specimens RA-2, RA-4, RB-4, and RC-4 curve, as shown in Figures 6A-H.

The above unloading confining pressure creep strain rate curves indicated the following:

(1) The creep rates of intact siltstone-like specimens are all produced at high strain rates upon unloading the

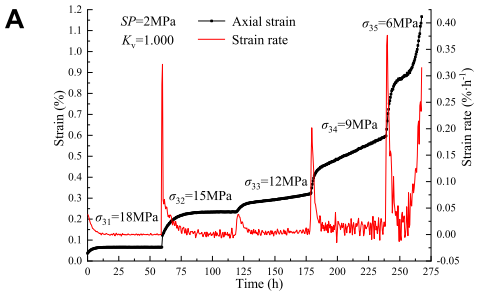

unloading confining pressure axial creep rate of specimen RA-2

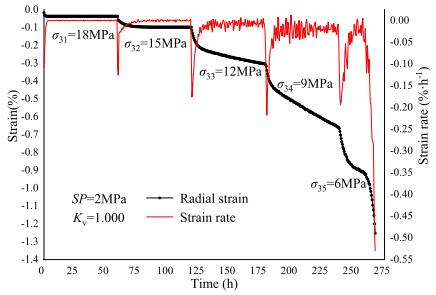

unloading confining pressure radial creep rate of specimen RA-2

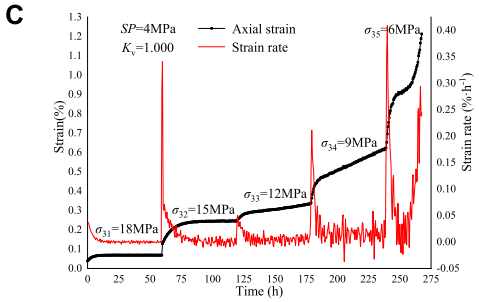

unloading confining pressure axial creep rate of specimen RA-4

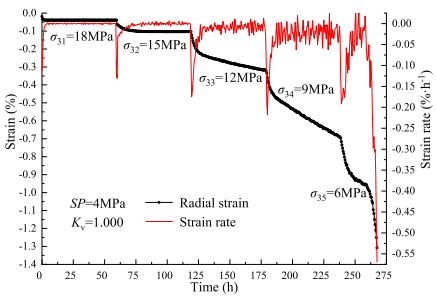

unloading confining pressure radial creep rate of specimen RA-4

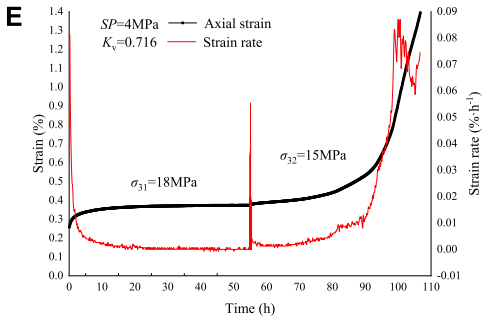

unloading confining pressure axial creep rate of specimen RB-4

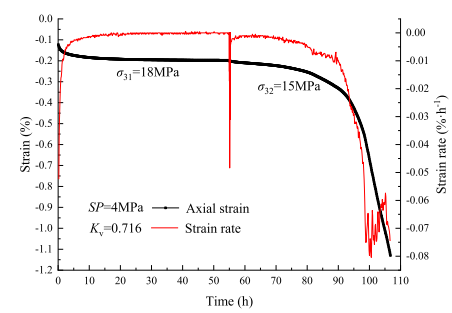

unloading confining pressure radial creep rate of specimen RB-4

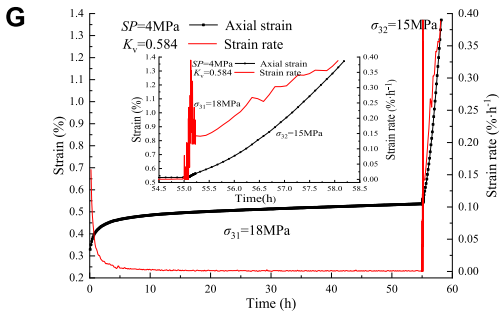

unloading confining pressure axial creep rate of specimen RC-4

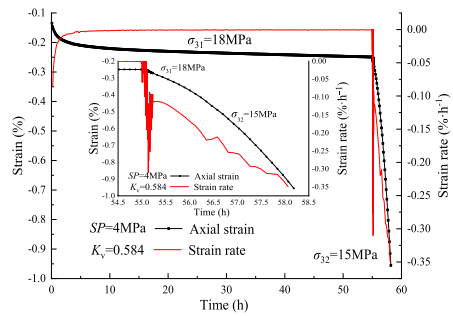

unloading confining pressure radial creep rate of specimen RC-4

FIGURE 6
Unloading confining pressure creep rate results for specimens.

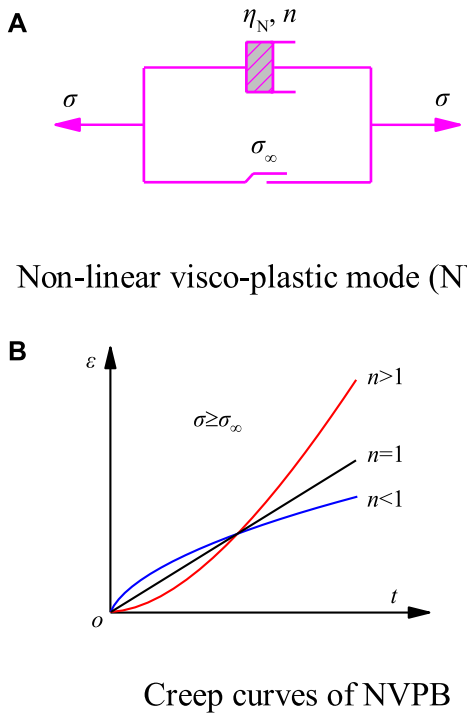

FIGURE 7
The Levenberg-Marquardt non-linear least squares method was used for the fitting analysis. The fitted curve for the theoretical creep calculation in the siltstone-like specimens at all unloading confining pressure levels was obtained for specimen RA-4, as shown in Figure 9.

confining pressure, at which point the corresponding transient deformation corresponds to several peaks in the strain-rate curve. Subsequently, the creep rate decreased in a curvilinear pattern, indicating a decay creep stage. Then, the rate undergoes fluctuations: for stable creep, the creep deformation is constant, and the creep rate is zero.

(2) If the decay rate was >0%•h^{-1} (under normal conditions, the rate was <0.05%•h^{-1}), at which time steady creep occurred, and the strain curve increased at a certain slope. For creep rate curves that partially produce accelerated creep, the creep rate increases, resulting in accelerated creep and causing damage to the specimen.

(3) The variation trends of the radial and axial creep rates are almost identical. Additionally, the creep rate of the former was greater than that of the latter in the later stages of accelerated creep, especially at higher initial hydrostatic pressures.

Creep model under seepage

Improvements to the creep model

These results demonstrate that the coupled creep test curves of the prefabricated siltstone samples under different initial hydrostatic pressures exhibit viscoelastic plasticity. Therefore, a two-component nonlinear viscoplastic model (NVPB) identified according to the creep state index n and long-time creep strength σ_∞ was tied to the original visco-elastoplastic model (Liu et al., 2020), as shown in Figure 7A. η_N is the viscoplastic viscosity coefficient, and σ is the total stress. The creep curve of NVPB is shown in Figure 7B.

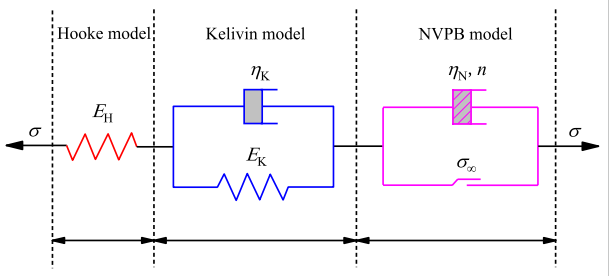

FIGURE 8
HKN-based 5-component model. (1) During $\sigma < \sigma_\infty$, the NVPB in the HKN tandem model does not participate in the creep process, and its constitutive equation is as follows.

The creep constitutive relation of nonlinear visco-plastic NVPB is as follows (2):

$$\varepsilon(t) = \frac{H(\sigma - \sigma_\infty)}{\eta_N} \frac{t^n}{t_0^{n-1}} = \frac{H(\sigma - \sigma_\infty)}{\eta_N} t^n \tag{2}$$

where n is the rheological state index; t_o is the reference time, the initial value is 1; σ_∞ is the long-term strength of rock mass. Where H can be derived by the following Eq. (3).

$$H(\sigma - \sigma_\infty) = \begin{cases} 0 & \sigma < \sigma_\infty \\ \sigma - \sigma_\infty & \sigma \geq \sigma_\infty \end{cases} \tag{3}$$

When n=1, the creep equation of NVPB is the viscoplastic model, and the strain shows a linear relationship with time.

When n>1, the creep rate exhibited a positive correlation with time, which gradually increased until the specimen was destroyed.

When n<1, the creep rate first decreases with time and then decays to a nonzero constant iso-rate steady creep state (Zhang, 2015).

The new 5-component model, obtained by combining the Hooke, Kelvin, and NVPB models, is the HKN improvement model, as shown in Figure 8. The parameter E_H in the figure is the elastic modulus, E_K is the viscoelastic modulus, η_k is the elastic viscosity coefficient, η_N is the viscoplastic viscosity coefficient, and σ is the total stress.

$$\sigma + \frac{\eta_K}{E_H + E_K}\dot{\sigma} = \frac{E_H E_K}{E_H + E_K}\varepsilon + \frac{E_H \eta_K}{E_H + E_K}\dot{\varepsilon} \tag{4}$$

where $\dot{\sigma}$ is the stress rate and $\dot{\varepsilon}$ is the strain rate.

Substituting $\sigma = \sigma_0 H(t)$ into Eq. 4, the Laplace transformation is expanded as:

$$\tilde{\varepsilon} = \frac{\sigma_0}{E_H s} + \frac{\sigma_0}{s(\eta_K s + E_K)} \tag{5}$$

where $\tilde{\varepsilon}$ is a Laplace transform of ε and S is a complex variable in Laplace transform. The above equation undergoes an inverse Laplace transformation to obtain the following creep equation for the constitutive relation of the model when $\sigma < \sigma_\infty$.

$$\varepsilon = \frac{\sigma}{E_H} + \frac{\sigma}{E_K}\left[1 - \exp\left(-\frac{E_K}{\eta_K}t\right)\right] \tag{6}$$

2) When $\sigma \geq \sigma_\infty$, the HKN-based 5-component model (Zhang, 2015) is formed, and its corresponding equation of state is as follows.

$$\begin{cases} \sigma = \sigma_H = \sigma_K = \sigma_N \\ \varepsilon = \varepsilon_H + \varepsilon_K + \varepsilon_N \\ \sigma_H = E_H \varepsilon_H \\ \sigma_K = E_K \varepsilon_K + \eta_K \dot{\varepsilon}_K \\ \sigma_N = \sigma_\infty + \eta_N \dot{\varepsilon}_N / n t^{n-1} \end{cases} \tag{7}$$

The corresponding constitutive equation is as follows.

$$p_1(\sigma - \sigma_\infty) + p_2\dot{\sigma} + \ddot{\sigma} = \frac{E_H E_K}{\eta_K}\dot{\varepsilon} + E_H\ddot{\varepsilon} \tag{8}$$

Solving Eq. 8 using $\sigma = \sigma_0 H(t)$, the Laplace transform is subsequently expanded as follows.

$$\tilde{\varepsilon} = \frac{\sigma_0}{E_H s} + \frac{\sigma_0}{s(\eta_K s + E_K)} + \frac{(\sigma_0 - \sigma_\infty)n!}{\eta_N s^{n+1}} \tag{9}$$

The inverse Laplace transformation of Eq. 9 yields the following equation for the constitutive relation when $\sigma \geq \sigma_\infty$.

$$\varepsilon = \frac{\sigma}{E_H} + \frac{\sigma}{E_K}\left[1 - \exp\left(-\frac{E_K}{\eta_K}t\right)\right] + \frac{\sigma - \sigma_\infty}{\eta_N}t^n \tag{10}$$

Combining Eqs 6,10, the following one-dimensional constitutive equation for the creep model of the fissured siltstone-like specimen is obtained.

$$\begin{cases} \varepsilon = \dfrac{\sigma}{E_H} + \dfrac{\sigma}{E_K}\left[1 - \exp\left(-\dfrac{E_K}{\eta_K}t\right)\right] \\ \varepsilon = \dfrac{\sigma}{E_H} + \dfrac{\sigma}{E_K}\left[1 - \exp\left(-\dfrac{E_K}{\eta_K}t\right)\right] + \dfrac{\sigma - \sigma_\infty}{\eta_N}t^n \end{cases} \begin{matrix} (\sigma < \sigma_\infty) \\ (\sigma \geq \sigma_\infty) \end{matrix} \tag{11}$$

Establishment of three-dimensional creep equations

According to elastodynamics, the stress and strain states at a point are decomposed into a spherical tensor and an adeviatoric tensor (Yang et al., 2017) as follows.

$$\left.\begin{aligned} \sigma_{ij} &= S_{ij} + \frac{1}{3}\sigma_{ij}\delta_{ij} \\ \varepsilon_{ij} &= e_{ij} + \frac{1}{3}\varepsilon_{ij}\delta_{ij} \end{aligned}\right\} \tag{12}$$

If volumetric and deviatoric viscous strains are only associated with the spherical and deviatoric tensors, respectively, the expression for the three-dimensional tensor transformed according to Hooke's law (Jiang et al., 2021) in elastodynamics is as follows:

$$\left.\begin{aligned} \sigma_{ii} &= 3K\varepsilon_{ii} \\ S_{ij} &= 2Ge_{ij} \end{aligned}\right\} \tag{13}$$

where, G is the elastic shear modulus and K is the elastic volume modulus. When $\sigma < \sigma_\infty$, the elastic or viscoelastic modulus appearing in Eq. 11 is expressed in three dimensions as an elastic or viscoelastic shear modulus; by contrast, when $\sigma \geq \sigma_\infty$, the correlation expression for the resulting visco-plastic deformation, the creep-related constitutive relation in three dimensions, the corresponding yield function F, and the plastic potential function Q of the siltstone when $\sigma \geq \sigma_\infty$ are as follows:

$$\dot{\varepsilon}_{ij}^{vp} = \frac{1}{\eta_2}\left\langle \Phi\left(\frac{F}{F_0}\right)\right\rangle \frac{\partial Q}{\partial \sigma_{ij}} \tag{14}$$

where,

$$\left\langle \Phi\left(\frac{F}{F_0}\right)\right\rangle = \begin{cases} 0 & (F < 0) \\ \Phi\left(\dfrac{F}{F_0}\right) & (F \geq 0) \end{cases} \tag{15}$$

where F_0 is the initial value of the rock yield function. Using the associated liquidity criterion, make $F = Q$, and use the power function representation of the opposite function to obtain:

$$\dot{\varepsilon}_{ij}^{vp} = \frac{1}{\eta_2}\left(\frac{F}{F_0}\right)^m \frac{\partial F}{\partial \sigma_{ij}} \tag{16}$$

where m is the test constant, usually m =1, and the three-dimensional visco-elastic-plastic creep constitutive equation can be obtained by combining Eqs 11–16.

$$\begin{cases} \varepsilon_{ij} = \dfrac{\sigma_m}{3K} + \dfrac{S_{ij}}{2G_H} + \dfrac{S_{ij}}{2G_K}\left[1 - \exp\left(-\dfrac{G_K}{\eta_K}t\right)\right] & (F < 0) \\ \varepsilon_{ij} = \dfrac{\sigma_m}{3K} + \dfrac{S_{ij}}{2G_H} + \dfrac{S_{ij}}{2G_K}\left[1 - \exp\left(-\dfrac{G_K}{\eta_K}t\right)\right] + \dfrac{1}{\eta_N}\dfrac{F}{F_0}\dfrac{\partial F}{\partial \sigma_{ij}} & (F \geq 0) \end{cases} \tag{17}$$

In the elastic modulus G_H and viscoelastic modulus G_K, for the plastic deformation of siltstone, according to the Mohr-Coulomb yield criterion, the subsequent yield function is:

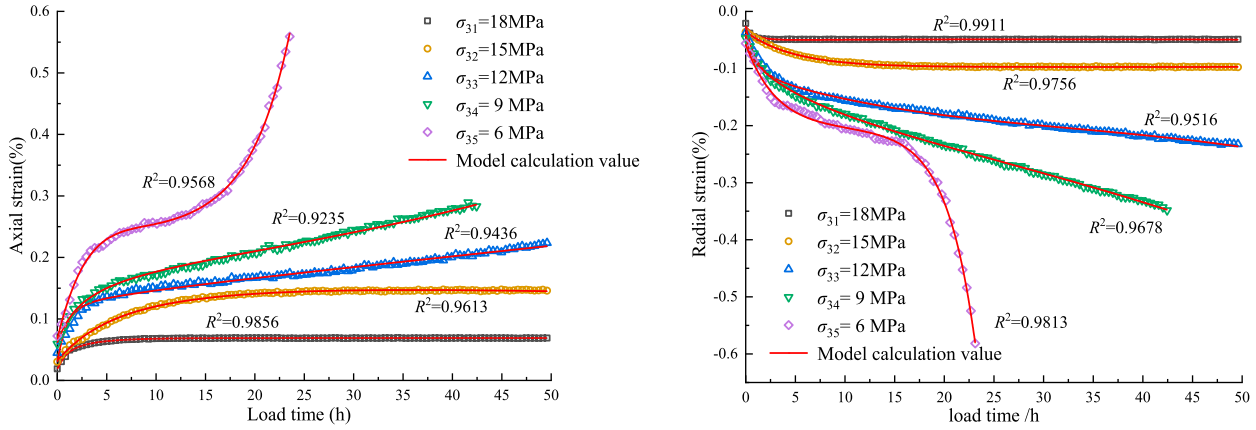

FIGURE 9
Fitted creep curves for all levels of unloading confining pressure under seepage of specimen RA-4.

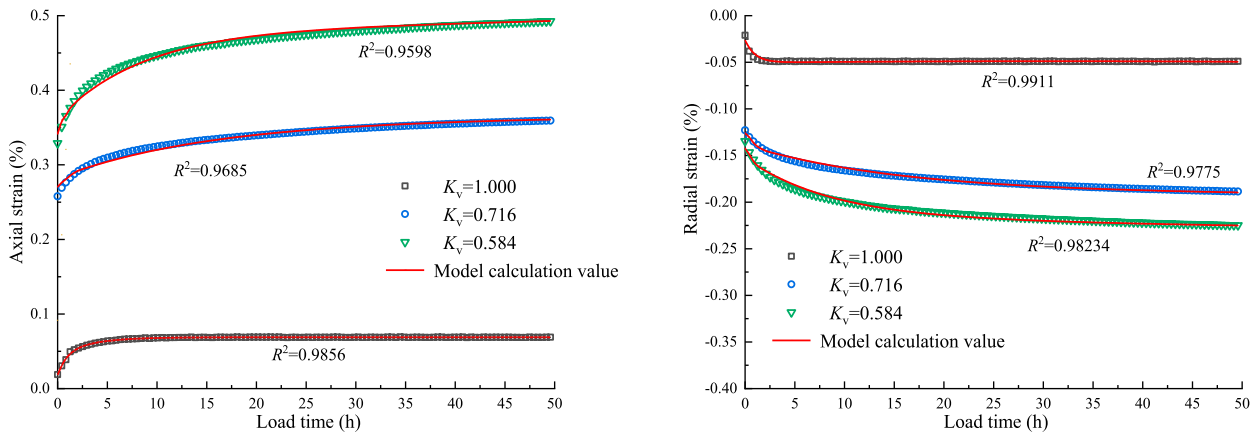

FIGURE 10
Fitted creep curves for fissured siltstone-like specimens with different integrity indices under seepage.

$$F = \sigma_1 - \sigma_3 \cdot \frac{1+\sin\bar{\phi}\left(\sigma_3, \varepsilon_{ps}\right)}{1-\sin\bar{\phi}\left(\sigma_3, \varepsilon_{ps}\right)} + 2\bar{c}\left(\sigma_3, \varepsilon_{ps}\right) \cdot \sqrt{\frac{1+\sin\bar{\phi}\left(\sigma_3, \varepsilon_{ps}\right)}{1-\sin\bar{\phi}\left(\sigma_3, \varepsilon_{ps}\right)}} \tag{18}$$

Where $\bar{c}$ represents the generalized cohesion of rock, $\bar{\phi}$ represents the generalized internal friction angle of rock, and ε_{ps} represents the equivalent plastic strain. After substituting (18) into (17), (19) can be obtained, which can be used for engineering applications.

$$\varepsilon_{ij}^{vp} = \frac{\sigma_{ij} - \sigma_{\infty}}{2\eta_N} t^n \tag{19}$$

Therefore, the three-dimensional visco-elastic-plastic creep Eq. 17 can be simplified as follows.

$$\begin{cases} \varepsilon_{ij} = \dfrac{\sigma_m}{3K} + \dfrac{S_{ij}}{2G_H} + \dfrac{S_{ij}}{2G_K}\left[1 - \exp\left(-\dfrac{G_K}{\eta_K} t\right)\right] & \left(S_{ij} < \sigma_{\infty}\right) \\ \varepsilon_{ij} = \dfrac{\sigma_m}{3K} + \dfrac{S_{ij}}{2G_H} + \dfrac{S_{ij}}{2G_K}\left[1 - \exp\left(-\dfrac{G_K}{\eta_K} t\right)\right] + \dfrac{S_{ij} - \sigma_{\infty}}{2\eta_N} \cdot t^n & \left(S_{ij} \geq \sigma_{\infty}\right) \end{cases} \tag{20}$$

In the conventional triaxial compression test, $\sigma_2 = \sigma_3$. Thus:

$$\sigma_m = \frac{\sigma_1 + \sigma_2 + \sigma_3}{3} = \frac{\sigma_1 + 2\sigma_3}{3}$$
$$S_{11} = \sigma_1 - \sigma_m = \frac{2(\sigma_1 - \sigma_3)}{3} \tag{21}$$

TABLE 6 Axial creep parameters of fractured siltstone under unloading confining pressure.

Test no.	σ_3 (MPa)	K (GPa)	α	G_H (GPa)	G_K (GPa)	η_K (GPa·h)	η_N (GPa·h)	n	R^2
RA-2	18	52.3606	0.078958	60.8093	48.3254	65.8824	—	—	0.9178
	15	16.2669	0.071877	237.0777	11.9989	37.6651	—	—	0.9948
	12	−15.6558	0.813345	50.5564	35.6184	40.6721	0.246477	0.96903	0.9312
	9	−3.395	0.838953	11.5139	11.7273	6.984	3.574547	0.873	0.9789
	6	−1.3871	0.161699	4.5396	3.9091	4.0061	3.524883	5.53773	0.9205
RA-4	18	29.4589	0.244925	115.6046	49.4603	67.415	—	—	0.9856
	15	25.317	0.557556	66.639	12.5518	39.4111	—	—	0.9613
	12	−24.3664	0.824403	67.5799	44.2029	58.8984	0.689864	0.93314	0.9436
	9	−3.4823	0.540969	9.3605	13.8419	10.9416	0.706742	0.92926	0.9235
	6	−1.5229	0.17169	5.1119	3.9576	4.0449	4.358044	5.53773	0.9568
RA-6	18	33.2904	0.015714	112.5782	51.7495	70.5384	—	—	0.9475
	15	40.7109	0.439895	50.4982	13.2502	41.5839	—	—	0.9252
	12	−36.0646	0.9603	132.9676	42.3502	50.6631	6.52131	0.93993	0.9656
	9	−15.0447	0.881439	63.6126	16.8974	10.6506	2.520545	0.74399	0.9206
	6	−2.6481	0.161699	11.6012	4.2098	4.3068	3.885141	5.5387	0.9582
RB-4	18	66.1734	0.052574	53.156	47.7143	65.0385	—	—	0.9686
	15	−0.8633	0.161699	2.4929	3.8703	3.9576	2.188223	5.53773	0.9171
RC-4	18	34.9394	0.345805	73.72	45.9004	62.565	—	—	0.9598
	15	−0.9797	0.161699	2.9585	3.6375	3.7248	3.435546	5.77353	0.9235

TABLE 7 Radial creep parameters of fractured siltstone under unloading confining pressure.

Test no.	σ_3/ MPa	α	G_H (GPa)	G_K (GPa)	η_K (GPa·h)	η_N (GPa·h)	n	R^2
RA-2	18	0.399155	138.9719	74.4766	18.2651	—	—	0.997
	15	0.194776	67.5702	12.1056	37.9949	—	—	0.9874
	12	0.893661	13.4539	15.6558	15.9371	0.690543	0.66542	0.9623
	9	0.723232	6.1789	11.349	7.5369	0.76436	0.65572	0.9651
	6	0.161699	30.9139	5.7133	9.6515	26.298058	8.29059	0.9927
RA-4	18	0.117467	123.5489	73.7879	18.0905	—	—	0.9911
	15	0.479568	136.4111	34.8909	82.0426	—	—	0.9756
	12	0.912479	48.8492	15.8498	16.1408	0.85263	0.66542	0.9516
	9	0.838662	5.141	10.6506	8.6524	2.09811	0.82353	0.9678
	6	0.161699	7.8376	5.7715	9.7291	5.325785	8.27992	0.9813
RA-6	18	0.639812	130.1546	81.4994	19.982	—	—	0.9772
	15	0.274801	148.3324	36.5981	86.0487	—	—	0.9461
	12	0.969806	15.132	16.9265	17.2369	1.408052	0.66542	0.9465
	9	0.718576	30.3125	11.2423	9.1374	1.474497	0.82353	0.9728
	6	0.161699	8.7397	6.1498	10.379	4.910431	8.28768	0.9817
RB-4	18	0.000194	144.5882	69.8885	17.1399	—	—	0.9775
	15	0.161699	6.3729	5.5193	9.2926	3.929761	8.27992	0.9577
RC-4	18	0.08051	112.4618	67.3859	16.5288	—	—	0.9823
	15	0.161699	7.5854	5.3253	8.9822	4.504971	8.28477	0.8928

Substituting Eq. 21 into Eq. 20 yields the following three-dimensional constitutive equations for conventional triaxial compression.

$$\begin{cases} \varepsilon = \dfrac{\sigma_1 + 2\sigma_3}{9K} + \dfrac{\sigma_1 - \sigma_3}{3G_H} + \dfrac{\sigma_1 - \sigma_3}{3G_K}\left[1 - \exp\left(-\dfrac{G_K}{\eta_K}t\right)\right] \\ \varepsilon_{ij} = \dfrac{\sigma_1 + 2\sigma_3}{9K} + \dfrac{\sigma_1 - \sigma_3}{3G_H} + \dfrac{\sigma_1 - \sigma_3}{3G_K}\left[1 - \exp\left(-\dfrac{G_K}{\eta_K}t\right)\right] \quad (\sigma_1 - \sigma_3 < \sigma_\infty) \\ + \dfrac{2(\sigma_1 - \sigma_3) - 3 \cdot \sigma_\infty}{6\eta_N} \cdot t^n \quad (\sigma_1 - \sigma_3 \geq \sigma_\infty) \end{cases} \tag{22}$$

Establishment of the creep model under seepage

The water in the pore medium and media skeleton plays a load-bearing role. The former is referred to as the pore water pressure SP, whereas the latter exerts a skeletal bearing role as the effective stress σ_e. These two can characterize the instability deformation properties of the rock mass and are expressed as follows (Li, 2017):

$$\sigma_e = \sigma - \alpha \cdot SP \tag{23}$$

where α is the parameter for the seepage state.

Substituting Eq. 24 into Eq. 23 yields the seepage creep-related constitutive relation as follows:

$$\begin{cases} \varepsilon = \dfrac{\sigma_1 + 2(\sigma_3 - \alpha \cdot SP)}{9K} + \dfrac{\sigma_1 - \sigma_3 + \alpha \cdot SP}{3G_H} + \dfrac{\sigma_1 - \sigma_3 + \alpha \cdot SP}{3G_K}\left[1 - \exp\left(-\dfrac{G_K}{\eta_K}t\right)\right] \quad (\sigma_1 - \sigma_3 < \sigma_\infty) \\ \varepsilon = \dfrac{\sigma_1 + 2(\sigma_3 - \alpha \cdot SP)}{9K} + \dfrac{\sigma_1 - \sigma_3 + \alpha \cdot SP}{3G_H} + \dfrac{\sigma_1 - \sigma_3 + \alpha \cdot SP}{3G_K}\left[1 - \exp\left(-\dfrac{G_K}{\eta_K}t\right)\right] \\ + \dfrac{2(\sigma_1 - \sigma_3 + \alpha \cdot SP) - 3 \cdot \sigma_\infty}{6\eta_N} \cdot t^n \quad (\sigma_1 - \sigma_3 \geq \sigma_\infty)\ (0 < n \leq 1) \\ \varepsilon = \dfrac{\sigma_1 + 2(\sigma_3 - \alpha \cdot SP)}{9K} + \dfrac{\sigma_1 - \sigma_3 + \alpha \cdot SP}{3G_H} + \dfrac{\sigma_1 - \sigma_3 + \alpha \cdot SP}{3G_K}\left[1 - \exp\left(-\dfrac{G_K}{\eta_K}t\right)\right] \\ + \dfrac{2(\sigma_1 - \sigma_3 + \alpha \cdot SP) - 3 \cdot \sigma_\infty}{6\eta_N} \cdot t^n \quad (\sigma_1 - \sigma_3 \geq \sigma_\infty)\ (n > 1) \end{cases} \tag{24}$$

The nonlinear parameters α, G_H, G_K, η_K, η_N of the constitutive model are affected by time, specimen fracture development, hydrostatic pressure conditions, and the unloading stress state (Qi et al., 2012).

Creep model validation under seepage

The Levenberg–Marquardt non-linear least squares method was used for the fitting analysis. The fitted curve for the theoretical creep calculation in the siltstone-like specimens at all unloading confining pressure levels was obtained for specimen RA-4, as shown in Figure 9. The fitted curve across the theoretical results for creep calculations at different integrity index levels of the fissured siltstone-like specimens under the same seepage effect is shown in Figure 10. The specific parameters are listed in Tables 6,7.

Based on the analysis of the creep test results in for siltstone-like specimens under seepage, the Hooke model, Kelvin model, and NVPB models were used to construct an improved visco-plastic constitutive model. This model integrated the coupling effects of fissures and seepage to derive the constitutive relation of seepage creep in siltstone-like specimens. Additionally, the model was fitted usingwith the L-M non-linear least squares method. The correlation coefficients of the calculated model relative to the experimental values all exceeded 0.9178, indicating a good fit. Overall, the model characterizes the processes of transient deformation, decay creep, steady creep, and accelerated creep in the creep process of fissured siltstone-like materials.

Conclusion

In this study, graded unloading confining pressure tests were conducted on precast siltstone-like specimens of three different integrity index types under the influence of different initial hydrostatic pressures. The NVPB was introduced to construct an improved viscoplastic constitutive model based on curve characteristics. Additionally, we obtained the constitutive relationship in seepage creep and compared the calculated values with the experimental data. The main conclusions of this study are as follows.

(1) The radial and axial creep curves exhibited a similar law of change. However, under unloading confining pressure conditions, radial creep was greater than axial creep, whereas under unloading confining pressure conditions, radial creep was greater than axial creep owing to a weakening radial constraint, as a reduction in the confining pressure weakens the weakening radial constraint. Under constant axial loading, deformation is more likely to develop in the radial direction. As the initial hydrostatic pressure increased, the radial creep of intact siltstone-like specimens also increased under pore pressure.

(2) For creep rate curves that partially produce accelerated creep, the creep rates increase and the curve rises, eventually leading to accelerated creep and damage to the specimen. The radial creep trend was similar to that of the axial creep. However, the former rate was greater than that of the latter in the later stages of accelerated creep, particularly at higher initial hydrostatic pressures.

(3) The viscoplastic constitutive model was improved using the Kelvin and NVPB models, and NVPB integrated the coupling effects of fissures and seepage. The seepage

creep-related constitutive relation was obtained for the siltstone-like specimens under unloading confining pressure conditions. The correlation coefficients between the calculated and experimental values of the model were above 0.9178, indicating that the model can well fit the creep process of siltstone.

Data availability statement

The original contributions presented in the study are included in the article/supplementary material, further inquiries can be directed to the corresponding author.

Author contributions

XZ, ZZ, JY and SP were helpful for the conception and design of this study. ZZ wrote the first draft, XZ, ZZ and WL leadership data analysis, JG and XZ interpretation results. All authors participated in the revision, reading and approval of the manuscript.

Funding

This research was supported by the National Natural Science Foundation of China (grant no: 51774166).

Conflict of interest

Author JY is employed by China Northeast Architecture Design and Research Institute Co., LTD.

The remaining authors declare that the research was conducted in the absence of any commercial or financial relationships that could be construed as a potential conflict of interest.

Publisher's note

All claims expressed in this article are solely those of the authors and do not necessarily represent those of their affiliated organizations, or those of the publisher, the editors and the reviewers. Any product that may be evaluated in this article, or claim that may be made by its manufacturer, is not guaranteed or endorsed by the publisher.

References

Chen, W. Z., Zhu, W. S., and Shao, J. F. (2004). Damage coupled time-dependent model of a jointed rock mass and application to large underground cavern excavation. *Int. J. Rock Mech. Min. Sci.* 41 (4), 669–677. doi:10.1016/j.ijrmms.2003.01.003

Du, Y., Xie, M., Jiang Y, J., Chen, C., J, B, N., and Huo, L, C. (2021). A review of research on the mechanism and early warning of rock collapse disasters. *Metal. Mines* (01), 106–119. doi:10.19614/j.cnki.jsks.202101008

Du, Y., Xie, M. W., Jiang, Y. J., Li, B., and Chicas, S. (2017). Experimental rock stability assessment using the frozen–thawing test. *Rock Mech. Rock Eng.* 50 (4), 1049–1053. doi:10.1007/s00603-016-1138-2

GB/T50266-2013 (2013). *Engineering rock mass test method standard*. China: National Standard of the People's Republic of China.

Jiang, T. J., Zhao, L. C., and Yu, J. X. (2021). Study on creep mechanical properties and rheological model of sandstone. *Hydropower Energy Sci.* (03), 124–128. cnki:sun:sdny.

Li, B., Zhang, G., Wang, G., and Qiao, J. (2021). Damage evolution of frozen-thawed granite based on high-resolution computed tomographic scanning. *Front. Earth Sci. (Lausanne).* 760. doi:10.3389/feart.2022.912356

Li, Q. W. (2017). *Study on rheological characteristics of seepage-stress coupling of fractured conglomerate under unloading confining pressure*. Fuxin: Liaoning Technical University, 111–122.

Liu, D. F., Liu, P. T., Zhang, Z. Y., Xi, Y. Y., and Chai, X. W. (2021). Creep character-istics of fractured sandstone under axial compression and water pressure coupling. *Eng. Sci. Technol.* 53 (01), 94–103. doi:10.15961/j.jsu

Liu, J. S., Jing, H. W., Meng, Bo, Wang, L. G., Zhang, X. D., and Yang, J. J. (2020). Study on creep characteristics and fractional creep model of weakly cemented softrock with water content. *Rock Soil Mech.* 41 (08), 412609261. doi:10.16285/j.rsm.2019.1739

Liu, J., Zhao, Y., Tan, T., Zhang, L., Zhu, S., and Xu, F. (2022). Evolution and modeling of mine water inflow and hazard characteristics in southern coalfields of China: A case of meitanba mine. *Int. J. Min. Sci. Technol.* 32, 513–524. doi:10.1016/j.ijmst.2022.04.001

Liu, Q., Zhao, Y., Tang, L., Liao, J., Wang, X., Tan, T., et al. (2022). Mechanical characteristics of single cracked limestone in compression-shear fracture under hydro-mechanical coupling. *Theor. Appl. Fract. Mech.* 119, 103371. doi:10.1016/j.tafmec.2022.103371

Qi, Y. J., Jiang, Q. H., Wang, Z. J., and Zhou, C. B. (2012). Improved three-dimensional creep constitutive equation of Nishihara model and its parameter identification. *Chin. J. Rock Mech. Eng.* (02), 347–355.

Sha, Z., Pu, H., Li, M., Cao, L., Liu, D., Ni, H., et al. (2018). Experimental study on the creep characteristics of coal measures sandstone under seepage action. *Processes* 6 (8), 110. doi:10.3390/pr6080110

Shan, R. L., Bai, Y., Sun, P. F., Sui, S. M., Huang, Y. L., and Chen, J. L. (2019). Study on triaxial creep characteristics and constitutive model of frozen layered red sandstone. *J. China Univ. Min. Technol.* 48 (01), 12–22. doi:10.13247/j.cnki.jcumt.000961

Wang, J. G., Yang, P. J., and Jin, B. (2019). Analysis of creep and meso-fracture mechanism of mudstone under dynamic and static loading. *J. China Univ. Min. Technol.* 48 (06), 1223–1229. doi:10.13247/j.cnkj.jcumt.001077

Wang, R., Zhuo, Z., Zhou, H. W., and Liu, J. F. (2017). A fractal derivative constitutive model for three stages in granite creep. *Results Phys.* 7, 2632–2638. doi:10.1016/j.rinp.2017.07.051

Wang, X., and Jiang, H. F. (2018). Research progress on unloading creep test of fractured rock mass. *Int. J. Civ. Eng. Mach. Manuf.* (1). doi:10.3389/feart.2021.79203

Wu, Q., Tang, H. M., Wang, L. Q., Le, G. P., and Fang, K. (2016). *Research on mechanical parameters and stability of fractured rock mass*. Wuhan: China University of Geosciences Press.

Yang, Y. J., Duan, H. Q., Liu, C. X., and Hao, J. R. (2017). Rational design of protective coal pillar in deep mining area considering long-term stability. *J. Min. Saf. Eng.* 34 (05), 921–927+932. doi:10.13545/j.cnki.jmse.2017.05.014

Zhang, J. H. (2015). *Study on rheological characteris-tics and control mechanism of surrounding rock of deep roadway considering seepage*. Xuzhou: doctoral dissertation of China University of Mining and Technology, 49–58.

Zhang, L., Niu, F., Liu, M., Ju, X., Wang, Z., Wang, J., et al. (2022). Fracture characteristics and anisotropic strength criterion of bedded sandstone. *Front. Earth Sci. (Lausanne).* 451. doi:10.3389/feart.2022.879332

Zhao, Y. L., Liu, Q., Zhang, C., Liao, J., Lin, H., and Wang, Y. (2021). Coupled seepage-damage effect in fractured rock masses: Model development and a case study. *Int. J. Rock Mech. Min. Sci.* 144, 104822. doi:10.1016/j.ijrmms.2021.104822

Zhao, Y. L., Zhang, C. S., Wang, Y. X., and Lin, H. (2021). Shear-related roughness classification and strength model of natural rock joint based on fuzzy comprehensive evaluation. *Int. J. Rock Mech. Min. Sci.* 137, 104550. doi:10.1016/j.ijrmms.2020.104550

Zhou, C., Yu, L., You, F., Liu, Z., Liang, Y., and Zhang, L. (2020). Coupled seepage and stress model and experiment verification for creep behavior of soft rock. *Int. J. Geomech.* 20 (9), 04020146. doi:10.1061/(asce)gm.1943-5622.0001774

frontiers | Frontiers in Earth Science

TYPE Methods
PUBLISHED 14 September 2022
DOI 10.3389/feart.2022.981470

Check for updates

OPEN ACCESS

EDITED BY
Bo Li,
Tongji University, China

REVIEWED BY
Danqing Song,
Tsinghua University, China
Zizheng Guo,
Hebei University of Technology, China

*CORRESPONDENCE
Qingwen Li,
qingwenli@ustb.edu.cn

SPECIALTY SECTION
This article was submitted to Geohazards and Georisks, a section of the journal Frontiers in Earth Science

RECEIVED 29 June 2022
ACCEPTED 15 August 2022
PUBLISHED 14 September 2022

CITATION
Jin Z, Li Y, Li Q, Liu Z, Wu S and Wang Z (2022), Modification of the CSIRO method in the long-term monitoring of slope-induced stress.
Front. Earth Sci. 10:981470.
doi: 10.3389/feart.2022.981470

COPYRIGHT
© 2022 Jin, Li, Li, Liu, Wu and Wang. This is an open-access article distributed under the terms of the Creative Commons Attribution License (CC BY). The use, distribution or reproduction in other forums is permitted, provided the original author(s) and the copyright owner(s) are credited and that the original publication in this journal is cited, in accordance with accepted academic practice. No use, distribution or reproduction is permitted which does not comply with these terms.

Modification of the CSIRO method in the long-term monitoring of slope-induced stress

Zhihao Jin[1], Yuan Li[1,2], Qingwen Li[1]*, Zibin Liu[1], Shibing Wu[1] and Zhuo Wang[1]

[1]Department of Civil Engineering, University of Science and Technology Beijing, Beijing, China, [2]Shunde Graduate School, University of Science and Technology Beijing, Foshan, China

The *in situ* stress measurement technique can be used in long-term monitoring of induced stress to obtain three-dimensional stress states in slope engineering. In the monitoring, the ambient temperature fluctuation, "zero" drift of the logging data, and stable power supply should be considered. A dual temperature compensation circuit and experimental calibration techniques are proposed to increase accuracy based on the principle of the CSIRO method and considering the effect of a long-term disturbance of temperature in slope engineering. In view of the characteristics of the stress field distribution of the slope rock, the strain gauge layout scheme for induced stress monitoring of slope rock is modified to achieve the acquisition of three parallel measurements at one measurement and a stress–strain relationship equation for multilayer elastic layers is derived. An *in situ* stress logging system with the function of transient logging and data-connection in power cut condition is introduced to achieve a continuous correlation of measurement data under power cut conditions. An online cloud platform is established for the slope engineering of Au Mountain Iron Mine in Maanshan City. The results show that the data deviation of logging system is ±14 με with 24 days' power off, and errors with amount of 15% were corrected by the dual temperature compensation method. The remotely transmitted data reflect the effect of temperature changes and the evolution of strain (induced stress) in real time to satisfy the demand of long-term monitoring of slope engineering.

KEYWORDS

***in situ* stress measurement, temperature compensation, long-term stress monitoring, induced stress, strain gauges**

Introduction

In recent years, as the demand for iron resources has increased and the consumption of shallow resources has grown, many iron mines are gradually entering the deep mining state (Li XB. et al., 2017; Xia et al., 2018; Cao et al., 2019; Du et al., 2020a; Liu et al., 2020). When mining open-pit iron, high and steep artificial slopes are frequently generated, of

which rock slopes are the most prominent (Han, et al., 2022). The open-pit slope of Au Mountain Iron Mine in Maanshan City, Anhui Province, for example, is as high as 392 m, with an average slope gradient of 50°. Many factors can influence slope stability, such as *in situ* stress, strong rainfall, and earthquakes (Song et al., 2018b; Du et al., 2020b). In the process of deep open-pit mining, high-stress hard rock is generally subjected to blasting operations, mechanical shock, and other dynamic disturbances, which cause changes in the stress field of the slope and degrades its stability (Guo, et al., 2017; Guo, et al., 2018; Guo, et al., 2019; Song, et al., 2021; Du and Song, 2022).

In situ stress is the fundamental force of rock damage and the measurement of *in situ* stress is a basic prerequisite for many engineering activities. Excavation activities disturb the original stress state of rock masses in a slope, and the mechanical behavior of rock masses is closely related to the induced stress. Therefore, the effect of both the original stress state and induced stress on the rock mechanics must be considered, and the disturbance caused by engineering activities is combined with the mechanical behavior of the rock mass.

In the design and construction of the excavation of rock masses, two types of *in situ* stress information are essential: the first is the absolute stress (i.e., the initial original stress state of rock), which is the natural stress existing in the stratum before the excavation of the rock (Hayashi et al., 1997; Xu et al., 2021; Li et al., 2022; Liu et al., 2022); the second is the induced stress of the rock, which is the change in the stress of the surrounding rock during and after excavation (Huang et al., 2014; Lin and Zou, 2021; Chen, 2022; Yuan et al., 2022). At present, the measurement techniques for absolute stress are relatively mature, but there is still a lack of techniques for induced stress. With the development of rock engineering, the long-term monitoring of induced stress related to time-dependent nonlinearity has become an indispensable technique in the field of slope engineering (Xie, 2017).

Long-term monitoring techniques for the induced stress of rock could be developed based on *in situ* stress measurement techniques. The purpose is to obtain the magnitude and direction of induced stress, which will enable us to master the change in stress in the earth's crust with time. Regarding the monitoring of induced stress after excavation, Wang et al. (2013) used a nonelectrical KS-type borehole stress gauge to monitor the induced stress of coal body caused by mining and obtained the characteristics of the distribution of induced stress. Zhang et al. (2016) constructed a coupled three-dimensional (3D) poroelastic finite element numerical model to examine the change in stress after a powerful M5.1 earthquake in Badong County, in China's Hubei Province. Several studies have used monitoring techniques and equipment of induced stress to obtain the stress changes before and after an earthquake (Liao et al., 2003; Cai et al., 2009; Peng et al., 2009). Clark (1982) found that, for at least the duration of several weeks or months prior to an earthquake, signs of activity on deep inception faults can be transmitted into the rock mass at depths greater than 20 m from the surface, thereby causing changes in stress. This suggests that it is possible to record the crustal activity using stress monitoring techniques. However, none of these studies have considered the effect of temperature change in long-term stress monitoring.

Among *in situ* stress measurement techniques, hydraulic fracturing and CSIRO methods are widely used quantitative methods (Ulusay, 2014; Cai, 1993; Haimson and Fa Irhurst, 1967; Zoback and Harjes, 1997; Wu et al., 2009) that are also recommended by the International Society of Rock Mechanics for measuring the *in situ* stress (Ulusay, 2014). The hydraulic fracturing method requires continuous injection of high-pressure water and splitting of the rock to determine the direction of stress. Consequently, its use in the real-time monitoring of rock stress can be difficult. The CISRO method can achieve the full 3D stress tensor and direction in a single measurement, which can be used for the long-term monitoring of induced stress of rock. However, due to the use of a resistor and Wheatstone bridge circuit, the drift of temperature mean that this measurement technique is unable to satisfy the requirements for the long-term monitoring of induced stress (Li et al., 2006; Li Y. et al., 2017).

The aim of this paper is to propose a new method for the long-term stress monitoring of slope engineering according to the CSIRO measurement techniques. An optimized layout scheme of strain gauges and the corresponding stress–strain calculation equation was proposed for slope monitoring. The calibration experiment of the temperature compensation method was improved to reduce the effect of temperature change. This paper introduces a new power system that was designed to ensure a stable supply using the temperature compensation method, an *in situ* data-logging system, and a transmission module. This technique was applied in slope engineering and an online monitoring system for induced stress was established. The application of the dual temperature compensation technique, modification of HI cell structure, and remote transmission platform improved the stability and reliability of the long-term monitoring of induced stress in slope engineering.

Theory of induced stress calculation using the CSIRO method

Circuit of a logging system for strain monitoring

Logging systems are very sensitive to temperature; thus, spurious additional strains can be generated by changes in temperature. Compensation or correction measures are essential to reduce the additional strain induced by temperature. However, the conventional compensation resistance is not bonded to the HI cell, which causes it to be unaffected by the deformation of the HI cell. Moreover, the strain gauges that are used for temperature compensation are not

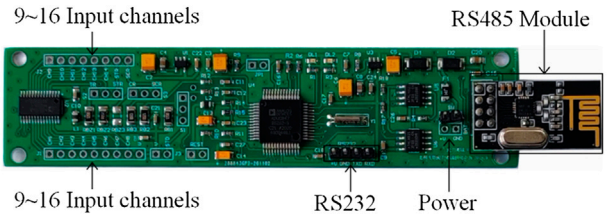

FIGURE 1
Circuit board of the logging system of the CSIRO method with dual temperature compensation.

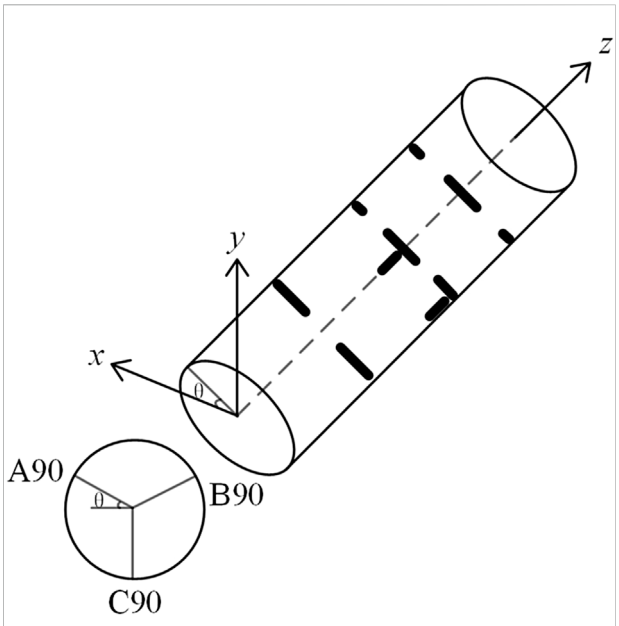

FIGURE 2
Layout scheme of strain gauges for stress monitoring in a slope rock mass.

arranged at the same location as the strain gauges of a HI cell but are placed at the end of the HI cell or in the external logging system, which cannot feel the real temperature conditions near the strain gauges. Therefore, Cai (1991) of the University of Science and Technology Beijing (USTB) proposed a complete temperature compensation method (Cai, 1993) by replacing the conventional compensation resistance by temperature measurement elements (thermosensors), placing them in the same position as the strain gauges in the HI cell, and cementing them together in the core. The temperature of the thermosensor fully reflects the temperature near the strain gauge in the HI cell. The additional strain caused by temperature changes during *in situ* stress monitoring is deducted according to the precalibrated temperature strain rate of the strain gauges in the HI cell.

During field monitoring, a HI cell is placed inside the hole and the logging system is placed in the external environment, especially in slope engineering, where the ambient temperature varies greatly. Therefore, the logging system is also affected by temperature variation. Therefore, based on the idea of complete temperature compensation, considering that the HI cell and the logging system are simultaneously affected by the temperature fluctuations in slope engineering, the dual temperature compensation method is proposed to compensate for the temperature effect of the strain gauge in a HI cell and the logging system at the same time; that is, the temperature compensation of the logging system is added on the basis of temperature compensation of the strain gauge in HI cell, which is known as the dual temperature compensation technique. In addition, according to the power supply and data-logging conditions on the site, a new CSIRO method with the function of transient logging and data-connection in power cut condition has been developed. The original circuit of the logging system was improved to ensure the consistency and stability of the thermal output–temperature correspondence of the temperature measurement channel. The improved circuit board of logging system is shown in Figure 1.

In the dual temperature compensation method, two sensors are used simultaneously: the first is arranged in the HI cell (thermosensor: for temperature measurement of the strain gauge) and the second is located in the circuit of the logging system (resistor: for temperature compensation of the circuit). The thermosensor is highly sensitive to temperature changes and its temperature sensitivity is much higher than that of a conventional resistor. The thermosensor is placed near the strain gauge in the HI cell to detect the temperature change of HI cell in the measurement hole to achieve real-time temperature monitoring. The size of the thermosensor is 2.3 mm × 2.1 mm × 0.9 mm (L × W × H), and it has a wide working temperature range (−50–300°C) and high accuracy (temperature coefficient: TCR-3850 ppm/K). A 2 ppm low temperature coefficient resistor was used in the circuit of logging system as a strain display when the temperature changes; that is, it displays the strain changes caused by temperature changes in the circuit of logging system and eliminates them in the calculation.

Induced stress calculation method

In the stress monitoring of a slope rock mass, the stress in the direction perpendicular to the excavation face was released in a certain range. Therefore, the consideration of principal stress in the other two directions can be reserved. The strain gauge layout scheme of the conventional HI cell in the *in situ* stress measurement was modified. The layout scheme for hole wall strain monitoring on the slope was designed as three groups of circumferential measurement (each group contains three strain gauges along the hoop direction, a total of nine strain gauges) and

one group of axial measurement (three strain gauges along the ring direction), as shown in Figure 2. Three groups of strain gauges were used in the circumferential strain measurement, which can be averaged to reduce the error.

According to the theory of *in situ* stress measurement, the relationship between stress and strain in each direction can be expressed as follows (Kim and Franklin, 1987; Cai, 1993):

$$\epsilon_\theta = \frac{1}{E}\{(\sigma_x + \sigma_y) + 2(1-\nu^2)[(\sigma_x - \sigma_y)\cos 2\theta - 2\tau_{xy}\sin 2\theta - \nu\sigma_z\} \tag{1}$$

$$\epsilon_z = \frac{1}{E}[\sigma_z - \nu(\sigma_x + \sigma_y)] \tag{2}$$

where ε_θ and ε_z are the circumferential strain and axial strain, respectively; and σ_x, σ_y, and σ_z are the horizontal stress, vertical stress, and axial stress, respectively.

The strains along the circumferential hole at 0°, 120°, and 240° were obtained by averaging the strain on the three measurement rings, as shown in Figure 2. According to Eq. 1, the circumferential stress–strain equation can be obtained as follows:

$$\frac{1}{3}(\epsilon_{\theta(0^\circ)} + \epsilon_{\theta(120^\circ)} + \epsilon_{\theta(240^\circ)}) = \frac{1}{E}[(\sigma_x + \sigma_y) - \nu\sigma_z] \tag{3}$$

There are three axial strain gauges along the hole at 0°, 120°, and 240°. According to Eq. 2, the axial stress–strain equation can be expressed as follows:

$$\frac{1}{3}(\epsilon_{z(0^\circ)} + \epsilon_{z(120^\circ)} + \epsilon_{z(240^\circ)}) = \frac{1}{E}[\sigma_z - \nu(\sigma_x + \sigma_y)] \tag{4}$$

The axial stress and the sum of circumferential stresses can be obtained from Eqs 3, 4.

Laboratory calibration

Stress calculation by field measured strains requires the determination of elastic parameters (modulus: *E*; Poisson's ratio: *v*) of the rock. The best way to obtain the *E* and *v* of the rock at the measurement site is to perform a biaxial pressure test on the core containing the HI cell (Amadei and Stephansson, 1997). In the measurement of absolute stress, biaxial pressure was applied to the core containing the HI cell retrieved from the site, and then *E* and *v* of the rock were derived from the measured stress–strain relationship of the core caused by the confining pressure. The elastic parameters of the core taken from the original measurement site can avoid the effect of geological conditions on the measurement results. This method can also be considered if the cores exhibit significant nonlinearity deformation.

A biaxial pressure test was conducted and a biaxial chamber that was developed by our research team was applied as the test apparatus. The maximum confining pressure that can be applied is 120 MPa and the maximum diameter of the core is 110 mm. The core is in the plane stress state. The relationship between the strain and the confining pressure can be deduced by elastic mechanics analysis as follows (Leeman, 1968):

$$E = \frac{P_0}{\epsilon_\theta}\frac{2R^2}{R^2 - r^2} \tag{5}$$

where P_0 is the confining pressure; *R* and*r* are the outer and inner radii of the hole core; and ε_θ is the average circumferential strain caused by confining pressure.

Considering the effect of behavior and thickness of glue, Cai. (1993) proposed a modification of Eq. 5, as follows:

$$E = K_1\frac{P_0}{\epsilon_\theta}\frac{2R^2}{R^2 - r^2} \tag{6}$$

In this study, the core was installed in the biaxial chamber cylindrical hole. Then, confining pressure was gradually applied, and data were recorded using the logging system. A loading–unloading path was applied, and the maximum pressure was 120 MPa.

TABLE 1 Strain drift under power cut conditions (με).

Time (Days)	35°C	40°C	45°C
0	0	0	0
3	−2	−9	−5
6	−5	−3	−12
9	12	−14	−2
12	6	−6	−14
15	−2	−1	−10
18	−2	−8	−12
21	4	−3	4
24	7	−5	−5

Calibration of the HI cell and logging system using the dual temperature compensation method

Stability test of the logging system

During long-term monitoring, a key problem is to maintain the stability of the power supply. The function of transient logging and data-connection in power cut condition was developed for the logging system, which would ensure the data recoverability if the power is cut off for a certain time. A stability test of the function was conducted. A resistor was connected to the test channel and the test was carried out under constant-temperature conditions; that is, the power was cut for a certain period of time, and the logging was started again. By comparing the data at different times for the same channel

with the same temperature, the drift of data before and after can be calculated, and then the stability of the function of logging system can be verified.

In the test, a constant-temperature chamber was used to carry out tests at different temperatures (35°C, 40°C, and 45°C, temperature error +0.5°C). The maximum time of power cut during the test is 24 days. The data collected at different times were compared and the drift was calculated under power cut conditions (see Table 1). The test results show that the maximum drift is 14 $\mu\varepsilon$ under the same temperature in the longest 24-days power cut test and the range of strain in the stress measurement in slope is generally 2000 $\mu\varepsilon$. This error is negligible in engineering applications, which verifies the stability of the function.

Calibration test for the evaluation of the temperature effect

The data-logging system is applied during the *in situ* stress measurement or long-term monitoring of induced stress, especially in the monitoring of induced stress in a slope where the measurement points are buried at a shallow depth and the ambient temperature varies greatly, which can directly affect the accuracy of the logging system and cause measurement (monitoring) errors. In the dual temperature compensation technique, temperature compensation is required for both HI cell and logging system. Therefore, the strain gauges, thermosensor, and logging system need to be calibrated in the laboratory separately.

Thermal output calibration of the strain gauges in the HI cell

The strain gauges are embedded in hollow inclusion cylinders, which are also sensitive to temperature changes; therefore, the effect of temperature on the measurement results cannot be ignored. Effective temperature compensation is required to reduce this part of the effect. The relationship between the strain and temperature (temperature strain rate) of the strain gauges is calibrated based on a temperature calibration test of the strain gauges. According to the temperature changes in the strain gauge during the stress monitoring, the additional strain caused by environmental temperature in each strain gauge can be calculated and deducted from the total strain measured during the stress monitoring to obtain the true strain of each strain gauge, thus achieving accurate measurement results.

Two thermostats are used in the calibration: the first is used to provide a constant temperature for the logging system and the second is used to provide a variable temperature for the HI cell with a strain gauge (high- and low-temperature thermostats). To ensure that the temperature near the strain gauge is the same as the thermosensor, the thermosensor is placed near the strain gauge to ensure the same temperature condition (see Figure 3).

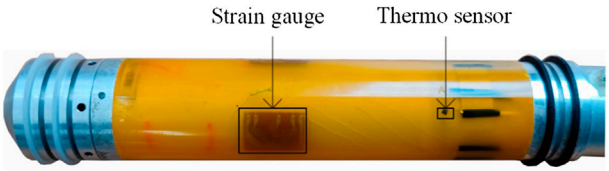

FIGURE 3
Arrangement of a thermosensor in a HI cell.

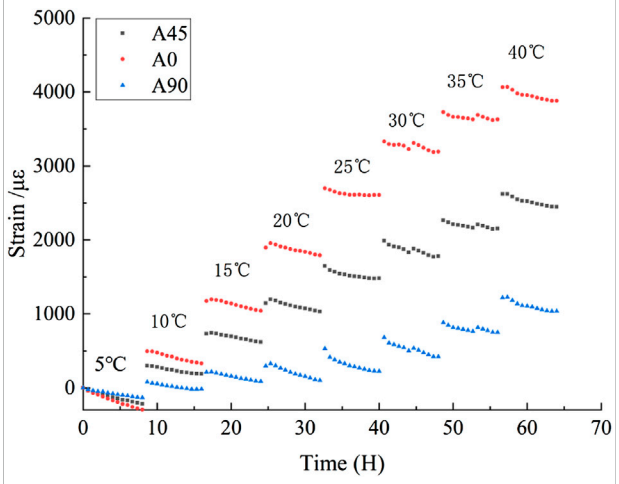

FIGURE 4
Relationship between temperature and strain of a strain gauge in a HI cell.

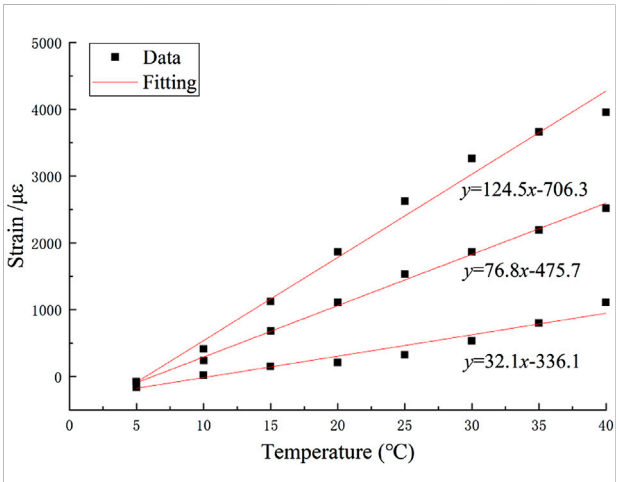

FIGURE 5
Fitting of temperature *vs.* strain of a strain gauge in a HI cell.

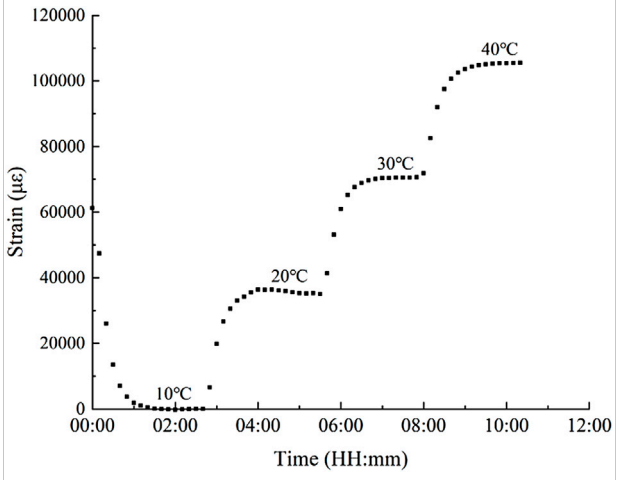

FIGURE 6
Relationship between the temperature and thermal output of a thermosensor.

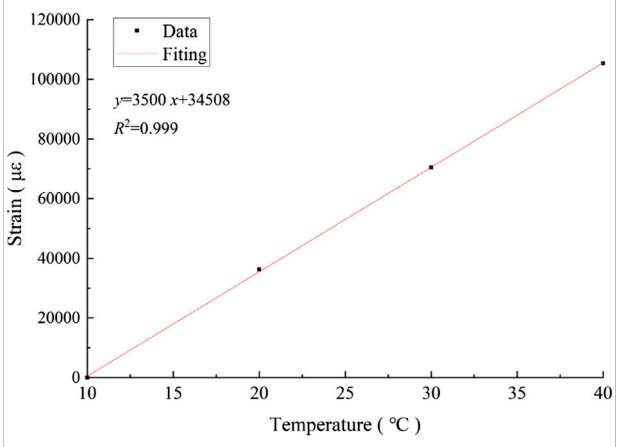

FIGURE 7
Fitting of temperature *vs.* thermal output of a thermosensor.

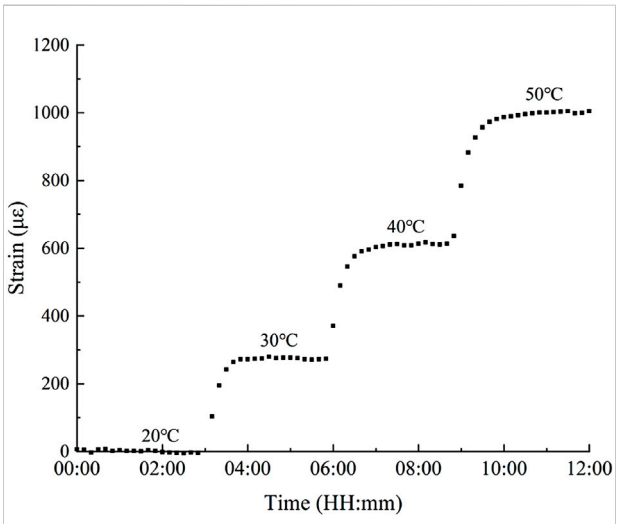

FIGURE 8
Relationship between the temperature of the logging system and the strain of resistor.

The calibration test is carried out by placing the logging system into the thermostat and maintaining the temperature at 30°C. The HI cell with strain gauge was then placed in the high- and low-temperature thermostat, and different temperatures were set for the HI cell (i.e., 5°C, 10°C, 15°C, 20°C, 25°C, 30°C, 35°C, and 40°C). The duration of each temperature gradient was 8 h. The experimental results are shown in Figure 4.

The strains of the strain gauge in HI cell at each temperature were averaged, and a trend regression analysis was performed on the temperature calibration data to obtain the relationship between the temperature and strain of the strain gauge (as shown in Figure 5). In the range of 5–40°C, the temperature and strain are linearly correlated. Therefore, the calibration equation can be obtained as follows: $y = 3500x + 34508$. The additional strain of strain gauge caused by temperature can be calculated directly from the temperature in long-term monitoring.

Calibration of the thermosensor

To obtain the actual temperature near the strain gauges, the relationship between the temperature and thermal output of the thermosensor was established by conducting a temperature calibration test on the thermosensor. The temperature near the strain gauge was calculated from the thermal output of thermosensor and used in the temperature compensation of the strain gauge.

The calibration test was carried out by placing the logging system into a thermostat and maintaining the temperature at 30°C. Then, the HI cell with thermosensor was placed in a high- and low-temperature thermostat, and different temperatures (i.e., 10°C, 20°C, 30°C, and 40°C) were set. The duration of each temperature gradient was 3 h. The experimental results are shown in Figure 6.

The thermal output of thermosensor at each temperature was averaged, and a trend regression analysis was performed on the temperature calibration data to obtain the relationship between the temperature and thermal output of the thermosensor (as shown in Figure 7). The temperature is linearly correlated with thermal output in the range of 10–40°C. Therefore, the calibration equation can be obtained as $y = 3500x + 34508$. The temperature of HI cell can be calculated directly from the thermal output of the thermosensor in long-term monitoring.

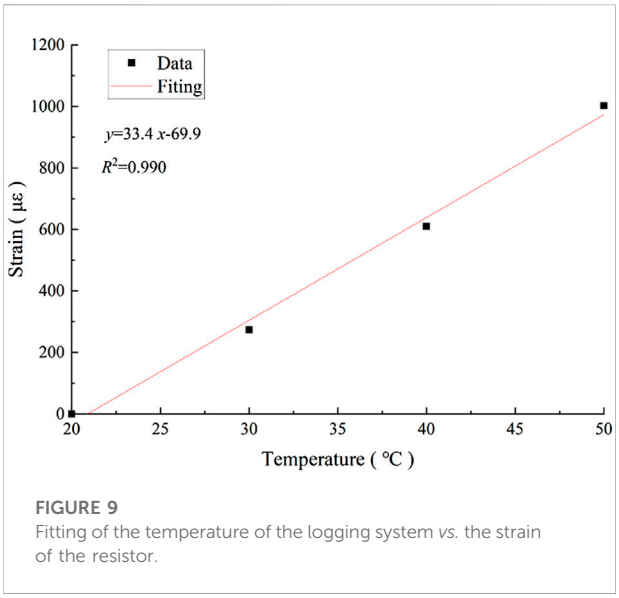

FIGURE 9
Fitting of the temperature of the logging system *vs.* the strain of the resistor.

Temperature calibration of the logging system

To calibrate the effect of temperature on the logging system, a logging system temperature calibration test was carried out to eliminate the logging error caused by the temperature changes in the logging system. In the temperature calibration test of the logging system, a 2 ppm/°C low temperature coefficient resistor obtained from Vishay, Israel was connected to the temperature compensation channel of the logging system. The logging system and resistor were placed in a high- and low-temperature thermostat, and different temperatures (i.e., 20°C, 30°C, 40°C, and 50°C) were set. The duration of each temperature gradient was 3 h. The relationship between the temperature of logging system and the strain of the resistor is shown in Figure 8. The strain variation curve reflects the error caused by the logging system due to the temperature variation.

The strains at each temperature were averaged, and a trend regression analysis was performed on the temperature calibration data to obtain the relationship between the temperature of the logging system and strain of resistor (as shown in Figure 9). In the range of 20–50°C, the temperature of the logging system is linearly correlated with the strain of the resistor. Therefore, the calibration equation can be obtained as follows: $y = 33.4x - 69.9$.

Cloud platform for online monitoring of induced stress

The data acquired during on-site monitoring need to be constantly exported, processed, and analyzed for real-time feedback. Therefore, a stable power supply system and transmission system need to be built. An induced stress online monitoring system was developed to overcome the drawbacks of long-term on-site monitoring that requires the establishment of a machine room, provision of dedicated personnel for regular power supply replacement and data logging, operation of cumbersome equipment, and high maintenance costs. The architecture of this system is shown in Figure 10. The monitoring system utilizes solar power and the power grid for equipment power supply, HI cell and logging system for strain monitoring, a network transmission module combined with fiber optic network to transmit the data to the Internet, and a remote server for data logging and storage. The monitoring cloud platform not only has the characteristics of low equipment cost of cloud platform architecture, fast system response, and high stability but it also frees the monitoring system from the limitation of transmission distance, achieves the advantage of unattended equipment in the field monitoring environment, interconnection of multiple measurement points of stress monitoring data, real-time uploading into the network to form a monitoring network, and conveniently performs a comprehensive analysis of the monitoring data through the cloud platform network. It achieves the purpose of long-term and stable monitoring of induced stress of rock masses.

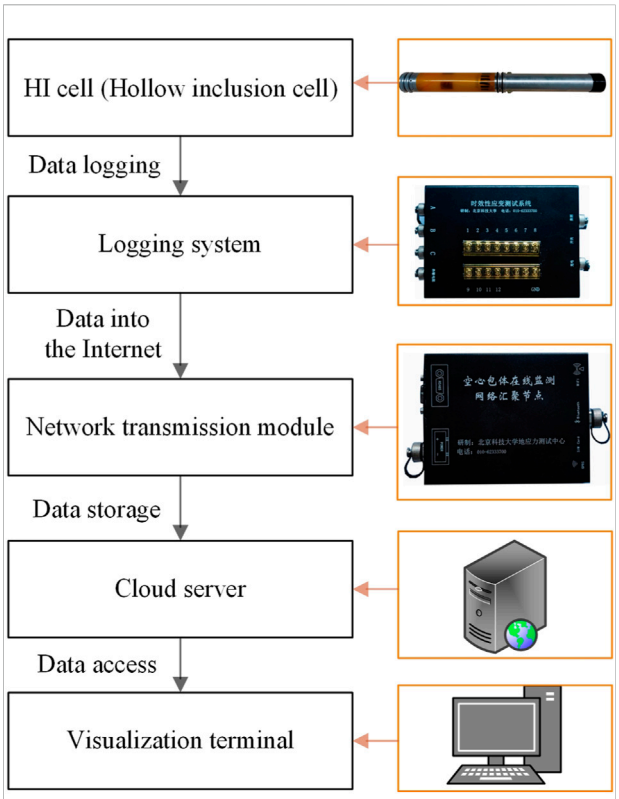

FIGURE 10
Architecture of a cloud platform monitoring system.

The system consists of the following main components:

1) Power supply system. This utilizes solar power and power grid together to provide stable power supply for the HI cell, logging system, and network transmission module.
2) HI cell. This is the core component in this system to monitor the change in a long-term induced stress of rock masses.
3) Logging system. This can record and save the monitoring data, and transfer the data to the network transmission module to access the network.
4) Network transmission module. The WIFI module (or 4G module) is an important transcoding component for transferring the data to the Internet and converting the 485 data format to TTL data format. The 4G module can be used for slope stress monitoring and the WIFI module can be used when there is a wireless network. The WIFI module can also be used for *in situ* stress monitoring in deep engineering with the downhole fiber optic network.
5) Cloud server. This is used for long-term storage, processing, and display of monitoring data.
6) Visualization terminal. The monitoring data in the cloud server are retrieved for online viewing by the end users.

Application of a monitoring system for induced stress in slope engineering

Given that the slope rock mass is affected by temperature fluctuation, blasting excavation, rain and snow, the environment is more complex than underground engineering and the range of temperature change is obviously large (the daily temperature change in the site in spring is about 20°C). Therefore, in stress monitoring, the impact of significant temperature changes on the monitoring equipment needs to be considered, in addition to long-term stable power supply and data transmission. The double temperature compensation technique developed by this research team (which was introduced earlier) can be used for temperature compensation of the equipment to reduce the effect of temperature and achieve long-term stable monitoring under strong temperature fluctuation.

Project overview

The monitoring system that is developed in this study was applied to the open-pit of Au Mountain of Maanshan Iron Mine in eastern Anhui Province, where the highest elevation of the exposed iron body is +175 m and extends down to −214 m. At present, the +45 m closed circle has formed a depression pit with an east-west length of 1,200 m, a north-south length of 980 m, and a vertical depth of 255 m. The average annual temperature is about 16°C, with an annual temperature variation range of −15 to 40°C.

Site monitoring program

A total of three boreholes were set up on the site, with two measurement points in each hole, located at 5 and 10 m depth, for a total of six measurement points. One and two holes were located at an elevation of −30 m, and three holes were located at −45 m, see Figure 11 for site layout.

Considering the problems of stable power supply, data transmission, and construction disturbance, a layout scheme of the remote monitoring system for slope rock induced stress was designed (as shown in Figure 12). HI cells are installed in the borehole, and the data-logging mode of the logging system is set for continuous logging with an interval of 30 min. The data can be transmitted to the monitoring cloud platform through the Network transmission module and downloaded at the visualization terminal.

Data logging and analysis

According to the indoor temperature calibration results, the strain data were processed by the dual temperature compensation algorithm to reduce the effect of temperature, and the strain monitoring data of 5 m hole depth in No. 2 borehole were obtained (as shown in Figure 13). Both the circumferential strain and axial strain at the monitoring point showed a linear growth trend with time. This shows that the displacement of slope rock after excavation has a linear growth trend, and it still has not reached the stable state within 30 days.

During the monitoring, there were two power cuts in the logging system due to rainy weather. However, the data showed continuity and did not show large fluctuations after the power was restored each time. This reflects the reliability of the logging system with the function of transient data-logging and data-connection in power cut condition; that is, the data can be collected after the power supply is restored and can be shut down when the power supply is insufficient. This fully reflects the superiority of the logging system in the long-term monitoring of induced stress in slope engineering.

The indoor calibration method for confining pressure described in *Laboratory Calibration Section* was used to calibrate the field retrieved cores with a HI cell in measuring the absolute stress. The variations in circumferential and axial stress were calculated using the stress–strain relationship Eqs 3, 4 as described in the *Induced Stress Calculation Method Section* (as shown in Figure 14).

Discussion

The present study concentrates on the long-term monitoring of the *in situ* stress field around the excavation surface in slope engineering with a normal ambient temperature rather than

FIGURE 11
Layout of on-site measurement points.

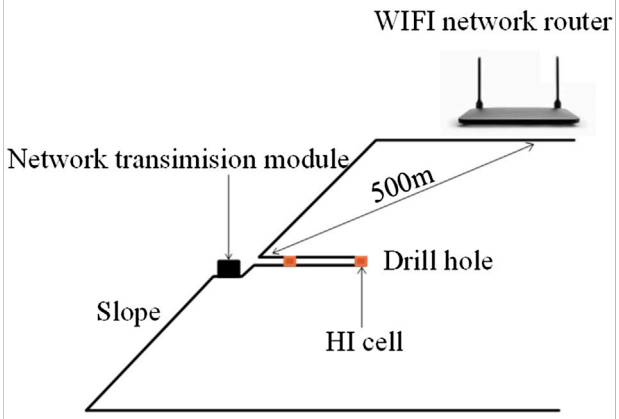

FIGURE 12
Layout scheme of a remote monitoring system.

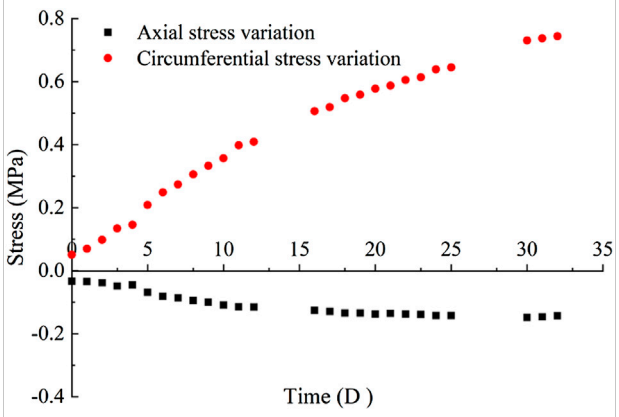

FIGURE 14
The 5 m hole depth stress variation in measurement hole No. 1.

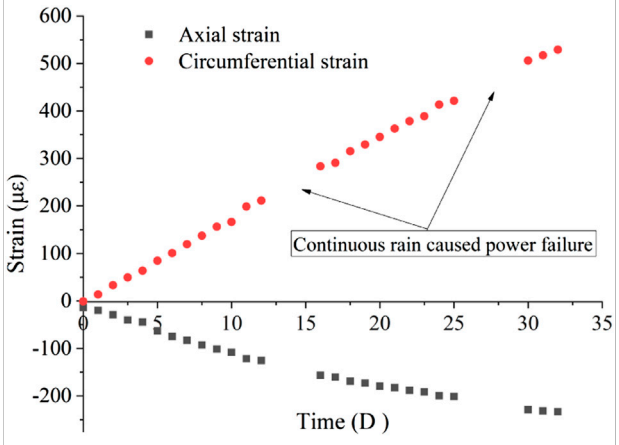

FIGURE 13
The 5 m hole depth strain monitoring data of measurement hole No. 1.

underground cavern groups with higher temperatures. However, the high-temperature resistance of the HI cell in the presence of high-temperature conditions in underground engineering needs further study. The measurement of *in situ* stress using a HI cell requires the strain to be converted into stress, which requires the participation of elastic parameters. Nevertheless, in the slope construction, it is easy to create strong disturbances to the rock of excavation surface and thus affect the rock parameters (i.e., the rock parameters are variable). However, it is difficult to adjust the calculated parameters in real time by conducting only one calibration test of biaxial pressure when acquiring rock parameters, and therefore further research on parameter acquisition methods is needed.

Conclusion

Based on the *in situ* stress measurement techniques, a new method for long-term stress monitoring of slope engineering

using HI cell was proposed by considering the characteristics of long-term stress monitoring environment of slope engineering, and improving the dual temperature compensation method and related testing techniques. The method was applied to long-term monitoring of Au Mountain Iron Mine in Maanshan City. The measurement results satisfy the engineering requirements and the remotely transmitted data reflect the effect of temperature changes:

1) The strain gauge in HI cell layout scheme was improved to achieve the logging of three parallel measurements at one measurement and the stress–strain relationship equation for multilayer elastic layers based on the HI method was derived, according to the stress characteristics in the direction perpendicular to the excavation face of the slope rock.
2) The indoor test results show that the *in situ* stress logging system with the function of transient logging and data-connection under power cut condition can maintain the data deviation of logging system at ±14 με with 24 days' power off, which satisfies the requirements of field monitoring accuracy.
3) The dual temperature compensation technique could reduce the additional strain caused by the temperature changes of the HI cell and logging system. An amount of 15% temperature compensation was corrected in the long-term stress monitoring of the slope of Au Mountain Iron Mine according to indoor temperature calibration tests for strain gauges, thermosensor, and logging system.
4) An online monitoring system for induced stress in slope engineering was established. The remotely transmitted data reflect the effect of temperature change and the evolution of strain (induced stress) in real time to satisfy the demand of long-term monitoring of slope engineering. In the 1-month monitoring, the stress changes showed a linear growth trend with small changes and the stress changes were basically stable. After the temperature compensation of each measurement channel, the axial stress remained unchanged and the circumferential stress change was 0.73 MPa.

Data availability statement

The original contributions presented in the study are included in the article/Supplementary material, and further inquiries can be directed to the corresponding author.

Author contributions

ZJ, YL, and QL mainly participated in the field work and perceived the idea of the article. ZL organized the database. SW performed the statistical analysis. ZW wrote the first draft of the manuscript. All authors contributed to manuscript revision and read and approved the submitted version.

Funding

This work is funded by the Foshan Science and Technology Innovation Special Fund Funding Project (Grant Nos. BK20BE008 and BK21BE014).

Conflict of interest

The authors declare that the research was conducted in the absence of any commercial or financial relationships that could be construed as a potential conflict of interest.

Publisher's note

All claims expressed in this article are solely those of the authors and do not necessarily represent those of their affiliated organizations, or those of the publisher, the editors and the reviewers. Any product that may be evaluated in this article, or claim that may be made by its manufacturer, is not guaranteed or endorsed by the publisher.

References

Amadei, B., and Stephansson, O. (1997). *Rock stress and its measurement*. London: Chapman & Hall.

Cai, M. F., Peng, H., Ma, X. M., and Jiang, J. (2009). Evolution of the *in situ* rock strain observed at shandan monitoring station during the M 8.0 earthquake in wenchuan, China. *Int. J. Rock Mech. Min. Sci.* 46 (5), 952–955. doi:10.1016/j.ijrmms.2008.12.004

Cai, M. F. (1993). Review of principles and methods for rock stress measurement. *Chin. J. Rock Mech. Eng.* 12 (3), 275–283.

Cai, M. F. (1991). Studies of temperature compensation techniques in rock stress measurements. *Chin. J. Rock Mech. Eng.* 10 (3), 227–235.

Cao, A. Y., Jing, G. C., Ding, Y. L., and Liu, S. (2019). Mining–induced static and dynamic loading rate effect on rock damage and acoustic emission characteristic under uniaxial compression. *Saf. Sci.* 116, 86–96. doi:10.1016/j.ssci.2019.03.003

Chen, X. Q. (2022). Influence of fault fracture zone on initial *in-situ* stress field in tongmai tunnel of the sichuan-tibet railway. *Eart. Scie.* 47, 2120. doi:10.3799/dqkx.2021.263

Clark, B. R. (1982). Monitoring changes of stress along active faults in southern California. *J. Geophys. Res.* 86 (B6), 4645–4656. doi:10.1029/JB087iB06p04645

Du, H., Song, D., Chen, Z., and Guo, Z. (2020a). Experimental study of the influence of structural planes on the mechanical properties of sandstone specimens under cyclic dynamic disturbance. *Energy Sci. Eng.* 8, 4043–4063. doi:10.1002/ese3.794

Du, H., Song, D., Chen, Z., Shu, H., and Guo, Z. (2020b). Prediction model oriented for landslide displacement with step-like curve by applying ensemble empirical mode decomposition and the PSO-elm method. *J. Clean. Prod.* 270, 122248. doi:10.1016/j.jclepro.2020.122248

Du, H., and Song, D. (2022). Investigation of failure prediction of open-pit coal mine landslides containing complex geological structures using the inverse velocity

method. *Nat. Hazards (Dordr).* 111 (3), 2819–2854. doi:10.1007/s11069-021-05159-w

Guo, Z. Z., Chen, L. X., Gui, L., Du, J., Yin, K., and Do, H. M. (2019). Landslide displacement prediction based on variational mode decomposition and WA-GWO-BP model. *Landslides* 17 (2), 567–583. doi:10.1007/s10346-019-01314-4

Guo, Z. Z., Yin, K. L., and Huang, F. M. (2018). Landslide displacement prediction based on surface monitoring data and nonlinear time series combination model. *Chin. J. Rock Mech. Eng.* 37, 1534. doi:10.13722/j.cnki.jrme.2016.1534

Guo, Z. Z., Yin, K. L., Yang, T., and Huang, F. (2017). Stability evaluation and prediction of maliulin landslide under reservoir water level decline and rainfall. *Geol. Sci. Technol. Inf.* doi:10.19509/j.cnki.dzkp.2017.0435

Haimson, B., and Fa Irhurst, C. (1967). Initiation and extension of hydraulic fractures in rocks. *Soc. Petroleum Eng.* 7 (3), 310–318. doi:10.2118/1710-PA

Han, Z., JianKang, C., Jian, K. Q., Liang, P., and Huibao, H. (2022). A fast prediction method for stability safety and reliability of reservoir bank rock slopes based on deformation monitoring data. *Front. Earth Sci.* 10, 944299. doi:10.3389/feart.2022.944299

Hayashi, K., Sato, A., and Ito, T. (1997). *In-situ* stress measurements by hydraulic fracturing for a rock mass with many planes of weakness. *Int. J. Rock Mech. Min. Sci.* 34 (1), 45–58. doi:10.1016/S1365-1609(97)80032-9

Huang, M. Q., Wu, A. X., Wang, Y. M., and Han, B. (2014). Geostress measurements near fault areas using borehole stress-relief method. *Trans. Nonferrous Metals Soc. China* 24 (11), 3660–3665. doi:10.1016/S1003-6326(14)63512-3

Kim, K., and Franklin, J. A. (1987). Suggested methods for rock stress determination. *Int. J. Rock Mech. Min. Sci. Geomechanics Abstr.* 24 (1), 55–63. doi:10.1016/0148-9062(87)91232-0

Leeman, E. R. (1968). The determination of the complete state of stress in rock in a single borehole—laboratory and underground measurements. *Int. J. Rock Mech. Min. Sci. Geomechanics Abstr.* 5 (1), 31–38. doi:10.1016/0148-9062(68)90021-1

Li, X. B., Chen, J. Z., Ma, C. D., Huang, L., Li, C., Zhang, J., et al. (2022). A novel *in-situ* stress measurement method incorporating non-oriented core ground Re-orientation and acoustic emission: A case study of a deep borehole. *Int. J. Rock Mech. Min. Sci.* 152, 105079. doi:10.1016/j.ijrmms.2022.105079

Li, X. B., Gong, F. Q., Tao, M., Dong, L., Du, K., Ma, C., et al. (2017a). Failure mechanism and coupled static–dynamic loading theory in deep hard rock mining: A review. *J. Rock Mech. Geotechnical Eng.* 9 (4), 767–782. doi:10.1016/j.jrmge.2017.04.004

Li, Y., Qiao, L., and Sun, X. S. (2006). Analyses of some factors affecting precision in *in-situ* stress measurement with method of CSIRO cells. *Chin. J. Rock Mech. Eng.* 25 (10), 2140–2144. doi:10.1016/S1872-1508(06)60035-1

Li, Y., Wang, Z., Qiao, L., Cai, M., and Li, Q. (2017b). Development of CSIRO cell with the compromised application of instantaneous data-logging, No-power data-connection and twin temperature compensation technique. *Chin. J. Geotechnical Eng.* 36 (06), 1479–1487. doi:10.13722/j.cnki.jrme.2016.1348

Liao, C. T., Zhang, C. S., Wu, M. L., Ma, Y., and Ou, M. (2003). Stress change near the kunlun fault before and after the M S 8.1 kunlun earthquake. *Geophys. Res. Lett.* 30 (20), 2003GL018106–2031. doi:10.1029/2003GL018106

Lin, C., and Zou, D. (2021). Formulation and verification of 3D *in-situ* stress estimation based on differential-direction drilling. *Int. J. Rock Mech. Min. Sci.* 145, 104833. doi:10.1016/j.ijrmms.2021.104833

Liu, G. W., Song, D. Q., Chen, Z., and Yang, J. w. (2020). Dynamic response characteristics and failure mechanism of coal slopes with weak intercalated layers under blasting loads. *Adv. Civ. Eng.* 1, 18. doi:10.1155/2020/5412795

Liu, X., Chen, J., Liu, B., Luo, Y., Zhu, Y., and Huang, X. (2022). Large deformation disaster mechanism and control technique for deep roadway in faulted zone. *Front. Earth Sci.* 10, 826661. doi:10.3389/feart.2022.826661

Peng, H., Ma, X. M., and Jiang, J. J. (2009). Process analysis of *in-situ* strain during the M S 8.0 wenchuan earthquake-data from the stress monitoring station at shandan. *Acta Geol. Sin.* 83 (4), 754–766. doi:10.1111/j.1755-6724.2009.00099.x

Song, D., Che, A., Zhu, R., and Ge, X. (2018b). Seismic stability of a rock slope with discontinuities under rapid water drawdown and earthquakes in large-scale shaking table tests. *Eng. Geol.* 245, 153–168. doi:10.1016/j.enggeo.2018.08.011

Song, D., Liu, X., Chen, J., and Cai, J. (2021). Influence of tunnel excavation on the stability of a bedded rock slope: A case study on the mountainous area in southern Anhui, China. *KSCE J. Civ. Eng.* 25, 114–123. doi:10.1007/s12205-020-0831-6

Ulusay, R. (2014). The ISRM suggested methods for rock characterization, testing and monitoring: 2007-2014. *Springer Int. Publ.* 15 (1), 47–48. doi:10.1007/978-3-319-07713-0

Wang, N. B., Zhang, N., Cui, F., Cao, J. T., and Lai, X. P. (2013). Characteristics of stope migration and roadway surrounding rock fracture for fully-mechanized top-coal caving face in steeply dipping and extra-thick coal seam. *J. China Coal Soc.* 38 (08), 1312–1318. doi:10.13225/j.cnki.jccs.2013.08.012

Wu, M. L., Zhang, Y., Liao, C., Chen, Q., Ma, Y., Wu, J., et al. (2009). Preliminary results of *in-situ* stress measurements along the longmenshan fault zone after the wenchuan ms 8.0 earthquake. *Acta Geol. Sin. - Engl. Ed.* 83, 746–753. doi:10.1111/j.1755-6724.2009.00098.x

Xia, K. Z., Chen, C. X., Deng, Y. Y., Xiao, G., Zheng, Y., Liu, X., et al. (2018). *In situ* monitoring and analysis of the mining-induced deep ground movement in a metal mine. *Int. J. Rock Mech. Min. Sci. (1997).* 109, 32–51. doi:10.1016/j.ijrmms.2018.06.014

Xie, H. P. (2017). Research framework and anticipated results of deep rock mechanics and mining theory. *Eng. Sci. Technol.* 49 (02), 1–16. doi:10.15961/j.jsuese.201700025

Xu, D. P., Huang, X., Jiang, Q., Li, S., Zheng, H., Qiu, S., et al. (2021). Estimation of the three-dimensional *in situ* stress field around a large deep underground cavern group near a valley. *J. Rock Mech. Geotechnical Eng.* doi:10.1016/j.jrmge.2020.11.007

Yuan, D., Zhang, L., Liu, X., Feng, T., Zhang, G., Xu, Z., et al. (2022). Influence of the xianshuihe fault zone on *in-situ* stress field of a deep tunnel and its engineering effect. *Front. Earth Sci.* 10, 886876. doi:10.3389/feart.2022.886876

Zhang, H., Cheng, H., Pang, Y., Shi, Y., and Yuen, D. A. (2016). Influence of the impoundment of the three gorges reservoir on the micro-seismicity and the 2013 M5.1 Badong earthquake (yangtze, China). *Phys. Earth Planet. Interiors* 261, 98–106. doi:10.1016/j.pepi.2016.06.007

Zoback, M. D., and Harjes, H. P. (1997). Injection-induced earthquakes and crustal stress at 9 km depth at the KTB deep drilling site, Germany. *J. Geophys. Res.* 102 (B8), 18477–18491. doi:10.1029/96JB02814

frontiers | Frontiers in Earth Science

TYPE Original Research
PUBLISHED 15 September 2022
DOI 10.3389/feart.2022.981503

Check for updates

OPEN ACCESS

EDITED BY
Yan Du,
University of Science and Technology Beijing, China

REVIEWED BY
Fei Guo,
China Three Gorges University, China
Zhigang Tao,
China University of Mining and Technology, China

*CORRESPONDENCE
Huajin Zhang,
huajinzhang1001@163.com

SPECIALTY SECTION
This article was submitted to Geohazards and Georisks, a section of the journal Frontiers in Earth Science

RECEIVED 29 June 2022
ACCEPTED 19 August 2022
PUBLISHED 15 September 2022

CITATION
Ai Z, Zhang H, Wu S, Jiang C, Yan Q and Ren Z (2022), Study on the slope dynamic stability considering the progressive failure of the slip surface under earthquake.
Front. Earth Sci. 10:981503.
doi: 10.3389/feart.2022.981503

COPYRIGHT
© 2022 Ai, Zhang, Wu, Jiang, Yan and Ren. This is an open-access article distributed under the terms of the Creative Commons Attribution License (CC BY). The use, distribution or reproduction in other forums is permitted, provided the original author(s) and the copyright owner(s) are credited and that the original publication in this journal is cited, in accordance with accepted academic practice. No use, distribution or reproduction is permitted which does not comply with these terms.

Study on the slope dynamic stability considering the progressive failure of the slip surface under earthquake

Zubin Ai[1], Huajin Zhang[2]*, Shunchuan Wu[2], Chuanbin Jiang[1], Qiong Yan[1] and Zijian Ren[2]

[1]Power China Road Bridge Group Co. Ltd., Beijing, China, [2]Faculty of Land Resources Engineering, Kunming University of Science and Technology, Kunming, China

The strength of a rock-soil mass shows complex and obvious weakening characteristics under seismic dynamic load. The previous stability analysis methods of a seismic slope do not fully depict the attenuation law of geotechnical materials and cannot truly reflect the stable state of a slope under earthquake action. Based on the theoretical analysis of the progressive failure mechanism and the evolution law of a seismic slope, the adverse effect of progressive failure on slope stability is clarified. According to the progressive failure process of a slope under dynamic load, the strain-softening model and vibration deterioration model are introduced to represent the attenuation law of rock strength parameters, and a calculation method of seismic slope stability coupled with vibration disturbance and progressive failure is proposed. The method considers the strength parameter characteristics of a rock-soil mass in different stages and is combined with the vector sum method to obtain the time-history curve of the slope safety factor under earthquake action, which makes the evaluation result of slope stability more accurate and reliable. The numerical examples show that this method can effectively reflect the dynamic stability of seismic slopes, and solve the problem that the traditional calculation methods are difficult to characterize the strength attenuation characteristics of rock and soil mass. If these characteristics are not considered, the calculation results will be unsafe.

KEYWORDS

slope engineering, earthquake, progressive failure, strain-softening, vibration deterioration

Introduction

Slopes exist widely in the fields of water conservancy and civil engineering, and many large-scale projects are constructed in areas where earthquakes frequently occur (Xu and Xu. 2013). At present, global seismic activity is experiencing a relatively active period. According to the statistics, there were 115 earthquakes above six magnitudes in 2021. A

serious destructive earthquake can easily trigger deadly landslides. Once a slope is damaged during an earthquake, many casualties may occur, and the economy will suffer severe losses (Valentin et al., 2016; Ma et al., 2021).

To avoid or reduce landslide disasters triggered by earthquakes, accurate evaluation of slope stability under earthquake action is the theoretical foundation of disaster prevention and anti-seismic supporting systems design (Du et al., 2022). The current seismic slope stability analysis methods mainly include theoretical analysis, numerical simulation and model test (Zhang et al., 2021; Yu et al., 2022). Numerical simulation offers the advantages of repeatability, time-saving, high efficiency, and low cost and has received widespread attention of scholars around the world. This category includes the pseudo-static method (Baker et al., 2006) and the seismic time-history analysis method (Pang et al., 2021). In the pseudo-static method, the dynamic inertia force of an earthquake is simplified as the product of the constant acceleration in the horizontal and vertical directions and the slope mass; then the static safety factor is solved generally with the limit equilibrium theory. This simple and convenient method has been widely applied in the stability analysis of seismic slopes (Karray et al., 2018; Zhao et al., 2020). However, it neglects the dynamic nonlinear behavior and evolution law of rock-soil mass and cannot reflect the mechanical response of a slope under cyclic load (Macedo and Candia 2020). After comparing the difference in calculation results of the pseudo-static method and the nonlinear dynamic approach, Bolla and Paronuzzi (2021) believed that the former was not suitable for the dynamic stability analysis of a rock slope. In the seismic time-history analysis method, the safety factor of each dynamic step is obtained through the dynamic stress field of the slope during the earthquake duration. This method can reflect the evolution of the dynamic process over the duration of the seismic event. The results of the time-history analysis method are more realistic and abundant and have gradually come to occupy a dominant position in the numerical analysis of seismic slope stability (Guo et al., 2011; Koo et al., 2016).

In the numerical simulation of the seismic slope, applying the peak or residual strength of a rock-soil mass for design and analysis will cause landslide hazards or unnecessary supporting waste. Therefore, it is of great significance to evaluate the slope stability with a reasonable and reliable constitutive model, of which the determination depends on the failure mechanism and essential features of the seismic slope. Due to the dynamic cyclic loads of earthquakes, the failure features of dynamic slopes tend to be more complex than static slopes. The failure mechanism of the slope under the earthquake can be summarized in two aspects (Eberhardt et al., 2004; Song et al., 2020; Negi et al., 2022). 1) The dynamic cyclic load reduces the strength parameters of a rock-soil mass, making the anti-sliding force of the slope smaller. For natural or man-made reasons, when the cyclic loading acts on the rock and soil, it may lead to the slow deterioration of strength and fatigue failure. Wang Y. et al. (2010) carried out uniaxial tensile tests on granite under cyclic loading, and the research showed that the dynamic strength under cyclic loading was lower than the failure strength under monotone loading. With an increase of cycling times, the rock damage and softening phenomenon occurred. 2) Under various adverse factors, slope failure is a progressive process from intact to local damage to overall penetration failure (Du et al., 2020). Many scholars believe that the dynamic failure mechanism of seismic slopes is that the cracks first appear in the structural plane or slope foot (local damage), then expand, deepen and penetrate with the continuous seismic hit, causing further damage to the surrounding rock mass. Finally, the seismic slope develops to the overall penetration failure, which shows that the entire sliding surface is penetrated (Song et al., 2020). Quinn et al. (2012) analyzed the progressive failure development of clay slope and the relationship between the failure surface and vibration time, indicating that the cyclic load caused by earthquakes makes the developing failure surface propagate freely toward overall failure.

Using the dynamic load mechanism, many scholars have examined the numerical relationship between the slope failure mechanism and strain-softening features and suggested the strain-softening model, which successfully captures the progressive slope failure features (Di et al., 2017; Wang et al., 2021). These results show that considering the strain-softening features of a rock-soil mass can provide a reasonable simulation of the slope failure process. The strain-softening model is widely used in slope stability analysis, but it only reflects the elastoplastic variation features of rock-soil mass strength, ignoring the vibration deterioration effect of the potential slip surface of a seismic slope under dynamic load. Actually, after the failure surface of the slope is generated, the residual strength of the rock mass (especially the friction force) still provides a large anti-slip force. Under the cyclic shear action of a dynamic load, wear and passivation will inevitably lead to further attenuation of the residual shear strength parameters of the failure surface (Cao et al., 2008). Some scholars have carried out dynamic cyclic shear tests on the structural planes of rock mass and analyzed the deterioration law of structural plane strength, indicating that cyclic shear load greatly reduces the shear strength of joints (Lee et al., 2001; Jafari et al., 2004). Based on the classical wear theory, Li et al. (2019) proposed a constitutive model for the shear characteristics of rock joints under cyclic loads, which is more practical than empirical models and can quantitatively evaluate the shear characteristics of rock joints with asperity degradation and debris backfilling. Ni et al. (2013) proposed a vibration deterioration model of the structural plane through a cyclic shear test, but the calculation method of this model is only applicable to the original joints, not to the secondary joints generated in the failure process. Under the cyclic shear of a dynamic load, the phenomenon of abrasion and passivation will inevitably lead to

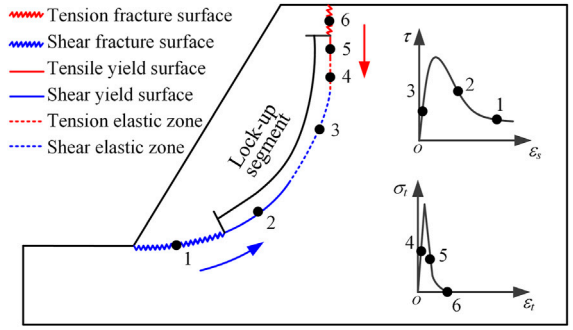

FIGURE 1
Sketch of progressive failure of the slope.

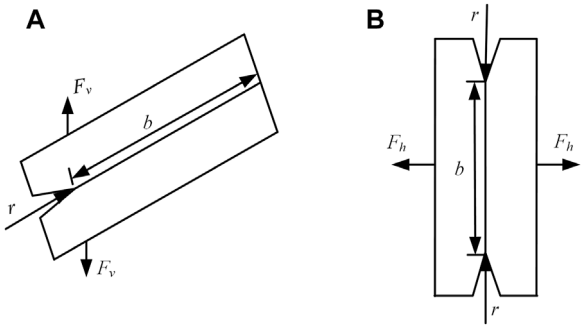

FIGURE 2
Sketch of stress concentration of slip surface. **(A,B)** Shear failure stage **(A)** and tension shear failure stage **(B)**.

the reduction of the shear strength parameters, subsequently further weakening the stability of a rock-soil mass and directly inducing landslides (Fan et al., 2017).

The failure process of the rock-soil mass in a seismic slope is of complexity that during the progressive failure process, the geotechnical materials at different positions may be in the peak, softening, or residual state, accompanied by the vibration deterioration phenomenon of the original joints and secondary cracks. The pre-existing research findings neither effectively reflect the strength weakening law of a rock-soil mass during the earthquake nor fully consider the strain-softening and vibration deterioration features of a seismic slope. Therefore, based on the failure mechanism of earthquake slope, the progressive failure process of slip surface and its influence on slope stability are discussed in this article under earthquake. A stability calculation method of the seismic slope is proposed that considers slip surface progressive failure, combined with the vector sum method of dynamic time-history analysis. This calculation integrates the dual factors of strain-softening and vibration deterioration under the earthquake in the process of dynamic slope stability analysis. In this method, the corresponding constitutive relation is endowed according to the state of the geotechnical materials and can improve the accuracy and reliability of calculation results.

Progressive failure process of seismic slope

Tension-shear progressive failure process

Wang J. et al. (2010) found that the slope instability is composed of top tension and foot shear damage through the slope survey results and numerical simulation in Wen Chuan. Shinoda et al. (2015) found that obvious tension cracks exist at the rear edge of the dynamic slope based on the shaking table model test. Zhou et al. (2019) developed a closed-form method to assess the seismic stability of slopes with zero tensile strength. The aforementioned research results show that during the process of slope instability damage under the seismic dynamic load, both shear damage and tension damage occur, as shown in Figure 1.

Suppose that points 1 to 6 of Figure 1 are on the potential slip surface, where points 1 and 6 are in the shearing and tension failure stages, respectively, forming the failure surface. Points 2 and 5 are in the shearing and tension plasticity stages, respectively, and the strength parameters of the rock-soil mass change with strain. Points 3 and 4 are in the elastic stage, and the strength parameters remain the same (Wang et al., 2018). The plastic and elastic section of the potential slip surface is defined as the lock-up segment. Under the action of the earthquake, the slope slip surface expands gradually from the foot and the top of the slope to the inside, the length of the lock-up segment decreases, and the degree of failure is large. Finally, the slip surfaces completely penetrate, causing the landslide disaster.

Mechanism of dynamic slope failure

The horizontal and vertical vibration acceleration generated by the earthquake vibration leads to damage and destruction of the slip surface. Assume the additional stress F assumed by the earthquake to the slider is:

$$\boldsymbol{F = Wa/g} \tag{1}$$

where W is the weight force of the landslide body, kN; g is gravity acceleration, $g = 9.8\ \mathrm{m/s^2}$; and a is seismic dynamic acceleration, $\mathrm{m/s^2}$.

The horizontal load F_h and vertical load F_v of the dynamical load are, respectively:

$$\begin{cases} \boldsymbol{F_h = Wa_h/g}, \\ \boldsymbol{F_v = Wa_v/g}, \end{cases} \tag{2}$$

where a_h, and a_v are the horizontal and vertical direction accelerations, m/s^2.

The following is based on the study of the dynamic failure of slopes under earthquakes. It is considered that the dynamic load of an earthquake generates the horizontal thrust and increases the sliding force of the slope and has a tensile effect on the slip surface. The vertical seismic load applies tension in the vertical direction to the slip surface (Che et al., 2016), as shown in Figure 2. When the concentrated stress at the end of the failure surface is greater than the crack initiation stress, the rock-soil mass will deform and damage, promoting the slope failure surface to expand inward. Then, the length of the lock-up segment in the potential slip surface decreases continuously, inducing the stability coefficient to steadily decline.

The concentrated stress of the free face is equal to the product of normal stress of the slip surface and stress concentration coefficient. According to the manual of stress concentration factors (STCM Science and Technology Committee of the Ministry of Aviation Industry, 1990), the stress concentration coefficient γ with deep gaps on one side is:

$$\gamma = \frac{2\left(\frac{b}{\rho}+1\right)\sqrt{\frac{b}{\rho}}}{\left(\frac{b}{\rho}+1\right)\arctan\sqrt{\frac{b}{\rho}}+\sqrt{\frac{b}{\rho}}}, \tag{3}$$

where b is the length of potential slip surface lock-up segment, m; and ρ is the curvature radius at the end of the failure surface, m.

Under the cyclic shear loadings, seismic waves result in the fragmentation of the rock-soil body and reduce the rock-soil mass integrity and strength parameters (Alfaro et al., 2012). Moreover, in the process of progressive slope damage, the failure surface still has residual strength, which can provide part of the anti-slide force. Lee et al. (2001) suggest that cyclic shear of a dynamic load will cause wear and passivation of rock mass discontinuities, and the relative velocity produced by the rock mass motion will also reduce the failure surface friction factor. As a result, the shear strength parameter of the failure surface will further attenuate under the earthquake.

Constitutive model

According to the analysis of the aforementioned seismic slope failure process, the strain-softening and failure surface vibration deterioration models are proposed to reflect the progressive failure process of slope under the earthquake action. The progressive failure of the slope is closely related to the strain-softening characteristics of geotechnical materials. The strain-softening constitutive model can effectively simulate the progressive failure process of the slope and has been the most commonly adopted model (Wang et al., 2021). The cyclic shear action of seismic loads leads to the dynamic deterioration of the mechanical properties of the rock mass structure, which will inevitably affect the stability of the seismic slope. These influence factors are considered comprehensively in the vibration deterioration model that quantitatively describes the phenomenon of wear and passivation and can accurately characterize the change of failure surface strength under cyclic shear load (Ni et al., 2013).

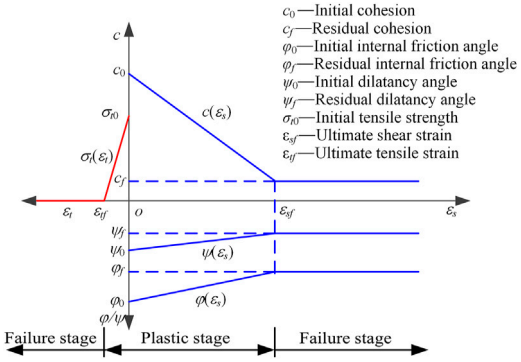

FIGURE 3
Sketch of strain-softening model strength attenuation.

Strain-softening model

Progressive failure has a great influence on the position and stability of the slip surface (Eberhardt et al., 2004). Instead of the elastoplastic model, the strain-softening model is used to simulate the characteristics of the rock-soil mass strength parameters changing with the plastic strain and to characterize the two post-failure behaviors of shear softening and tensile softening of the slope. The essence is to establish a functional relationship between strength and softening parameters in the Mohr-Coulomb yield criterion so that it can reflect the weakening of the strength parameters of geotechnical materials with the development of the yield process (Di et al., 2017).

The strain-softening model can reflect the attenuation characteristics of the rock-soil mass strength from the elastic to the failure stage, but the process is very complicated. To simplify the analysis, the simple and practical linear strain-softening Mohr-Coulomb model is adopted by most scholars (Wang et al., 2018). Based on the FLAC3D program theory in this article (Itasca 2013), we establish an attenuation function of the cumulative plastic shear strain ε_s and tensile strain ε_t as the independent variable. Cohesion c, internal friction angle φ, dilatancy angle ψ, and tensile strength σ_t are the dependent variables shown in Eq. 4.

$$\begin{cases} c = c(\varepsilon_s), \\ \varphi = \varphi(\varepsilon_s), \\ \psi = \psi(\varepsilon_s), \\ \sigma_t = \sigma_t(\varepsilon_t). \end{cases} \tag{4}$$

This function must be obtained through a reasonable laboratory test and inversion method. The common inversion method is to input the preset attenuation function into the numerical simulation software for simulation. If the simulation results are consistent with the actual laboratory test results, the attenuation functions are considered to approach the real strain-softening curve, and the next step of slope stability analysis can be carried out. The preset attenuation function curve is represented by the linear piecewise function, as shown in Figure 3. After the plastic shear strain is generated in the rock-soil mass of the slope, the rock-soil mass shear strength parameters attenuate to the residual strength parameters until shear failure. Meanwhile, if tensile yield occurs in the rock-soil mass, the tensile strength drops to zero after the ultimate tensile strain ε_{tf}.

Vibration deterioration model

The failure surface strength parameter attenuates under seismic loading, which is a complex dynamic process. According to the previous research results (Crawford and Curran 1982; Wang and Zhang 1982), the impact of dynamic load on the strength of the rock mass discontinuities is mainly derived from vibration wear and relative velocity. The cyclic shear action of seismic dynamic loads will lead to the gradual wear and passivation of a rock and soil mass structure. The strength parameters decrease with it, and the relative velocity of rock mass generated by movement will also reduce the friction coefficient of discontinuities. Ni et al. (2013) obtained the attenuation law of the shear strength parameters of the rock structure surface under the dynamic cycle load through a shaking table cyclic wear test and proposed using a vibration deterioration coefficient $D(t)$ that varies with dynamic time to quantitatively describe the attenuation characteristics of the failure surface strength parameter under earthquake. $D(t)$ mainly quantitatively describes the influence of vibration wear and relative velocity on the strength of discontinuities, which are assumed to be relatively independent during the duration of the earthquake. The relationship between $D(t)$, the cyclic shear amplitude $J(t)$, cycle-index $K(t)$, and relative speed $V(t)$ is expressed as follows:

$$D(t) = \left[R_0 + (1 - R_0)e^{bJ(t)} + (1 - R_0)\left(1 - e^{bJ(t)}\right)e^{-aK(t)}\right]\left[P_0 + (1 - P_0)e^{-m|V(t)|}\right] \tag{5}$$

where $[R_0+(1-R_0)e^{bJ(t)}+(1-R_0)\ (1-e^{bJ(t)})e^{-aK(t)}]$ is the effect of vibration wear; $[P_0+(1-P_0)e^{-m|V(t)|}]$ is the effect of relative velocity, which is a negative exponential decay law, wherein, P_0 is the convergence value of the relative motion velocity influence coefficient; R_0 is the convergence value of the cyclic shear amplitude influence coefficient; and a, b, and m are all test parameters, determined by the shaking table cyclic wear test of the structural plane. Due to limited space, the parameters are determined according to the process shown in the literature of Ni et al. (2013). In the earthquake duration process, $D(t)$ is the dynamic variation, and its value is determined by three dynamic response values of $J(t)$, $K(t)$, and $V(t)$.

The shear strength of the failure surface unit at any time may be expressed as:

$$\tau(t) = \tau_f D(t) = \sigma(t)\tan\varphi_f D(t) + c_f D(t), \tag{6}$$

where τ_f is the residual shear strength of the failure surface and $\sigma(t)$ is the normal stress acting on the failure surface at t. At any dynamic moment, the strength parameters of the failure surface can be calculated by Eq. 7.

$$\begin{cases} \varphi(t) = \arctan\left[\tan\varphi_f D(t)\right], \\ c(t) = c_f D(t). \end{cases} \tag{7}$$

Therefore, simply by obtaining the mathematical expression of the vibration deterioration coefficient $D(t)$, we can calculate the shear strength parameters in the failure surface at any time and then provide a basis for the accurate analysis of the slope stability state.

To sum, the essence of slope instability is a progressive failure process from local failure to overall instability. In the evolution process, these strain-softening and vibration deterioration phenomena will have a significant effect on the seismic slope anti-slide force, which is negative to slope stability.

Slope dynamic stability analysis

According to the aforementioned analysis results, if the attenuation characteristics of rock-soil mass strength parameters are not considered under earthquake action, the safety factor calculated by the ideal elastoplastic model may be too large, creating a very dangerous situation. The calculated safety factor meets the engineering requirements, but the slope fails in actuality. An incorrect safety factor has a serious adverse impact on the prevention of landslide disasters. Therefore, this section provides a numerical calculation method for stability analysis of a seismic slope that considers the weakening of geotechnical strength parameters, combined with the vector sum method.

Dichotomy strength reduction method

In this article, the strain-softening model, which considers that the strength parameters vary with the plastic strain, reflects the progressive failure process of the slope, but the FLAC3D

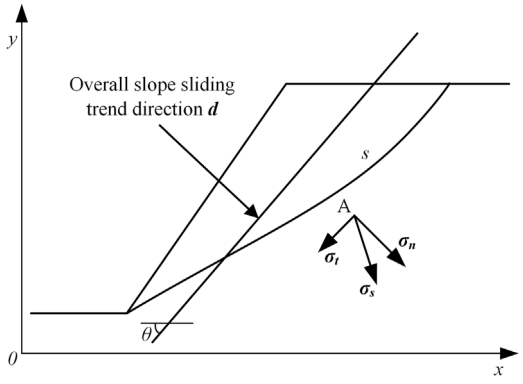

FIGURE 4
Sketch of safety factor solving by vector sum method.

built-in strength reduction method conflicts with the attenuation mode of strength parameters caused by the strain-softening model. Therefore, the dichotomy strength reduction method (Zhang et al., 2013) and maximum shear strain increment are used to search for potential slip surface of the slope to obtain the static safety factors and critical slip surface position of the slope.

The steps for calculating slope stability by the dichotomy strength reduction method are as follows: 1) preset the upper limit value K_{max}, the lower limit value K_{min} of the safety factor, and the critical value η of the difference between the K_{max} and K_{min}; 2) let $K_s = (K_{max} + K_{min})/2$ and conduct a numerical simulation calculation to judge whether the slope model converges. If convergent, $K_{min} = K_s$, $K_{max} = K_{max}$. If it does not converge, $K_{max} = K_s$, $K_{min} = K_{min}$; 3) repeat step 2 repeatedly until the value of $K_{max} - K_{min}$ is less than η and terminate the calculation of the whole strength reduction method. At this time, $(K_{max} + K_{min})/2$ is the final safety factor, and the maximum shear strain increment position of the corresponding numerical model is the critical sliding surface.

Vector sum method

As a dynamic cyclic load, an earthquake has an inertia force and cyclic shear action on the slope; therefore, the safety factor of the slope must be a dynamic variable. To reflect the time-history features of slope under earthquake action, the vector sum method proposed by professor Ge (2008) completely meets the balance conditions of the limit equilibrium methods without the reduction of strength parameters and iterative calculations. Its physical significance is clear, which can reflect the duration process of safety factors and analyze slope dynamic stability perfectly (Yang et al., 2021). The analysis procedure is as follows: given a point A in potential slip surface, $\boldsymbol{\sigma_s}$, $\boldsymbol{\sigma_t}$, and $\boldsymbol{\sigma_n}$ are the stress vector, tangential stress, and normal stress of point A, respectively, and $\boldsymbol{\sigma_t}$ and $\boldsymbol{\sigma_n}$ are the tangential and normal components of $\boldsymbol{\sigma_s}$ at point A, as shown in Figure 4.

$$\boldsymbol{\sigma_s} = \boldsymbol{\sigma n} \tag{8}$$

where $\boldsymbol{\sigma}$ is the stress tensor of point A and $\boldsymbol{n}$ is the unit normal vector of the tangent plane of point A.

Define the overall slope sliding trend direction $\boldsymbol{d}$ as the vector sum direction of the tangential stress $\boldsymbol{\sigma_t}$ of each point on the slip surface. The expression is:

$$\boldsymbol{d} = \int_s \boldsymbol{\sigma_t} \boldsymbol{ds} \tag{9}$$

where ds is the micro-segment length of the slip surface.

The anti-sliding force vector of point A is $\boldsymbol{\sigma_s}'$, its tangential component is $\boldsymbol{\sigma_t}'$, and the normal component is $\boldsymbol{\sigma_n}'$:

$$\boldsymbol{\sigma_t}' = (\boldsymbol{c} - \boldsymbol{\sigma_n} \boldsymbol{tan}\, \boldsymbol{\varphi})\boldsymbol{d_t} \tag{10}$$

$$\boldsymbol{\sigma_n}' = -\boldsymbol{\sigma_n} \tag{11}$$

$$\boldsymbol{\sigma_s}' = \boldsymbol{\sigma_t}' + \boldsymbol{\sigma_n}', \tag{12}$$

where $\boldsymbol{d_t}$ is the unit vector of tangential anti-sliding force vector direction of point A and σ_n is the normal stress of the slip surface applied by a sliding body. Since the slope is generally under pressure state, when σn > 0, it indicates that the slip surface is under tensile stress, therefore set σn = 0.

The vector sum method safety factor F_s is defined as the ratio of the algebraic sum of the total anti-sliding force vector projection and the overall sliding force vector in the direction of the overall potential sliding trend of the slope. Therefore, the safety factor F_s is:

$$\boldsymbol{F_s} = \frac{\int_s [\boldsymbol{\sigma_s}'(-\boldsymbol{d})]\boldsymbol{ds}}{\int_s (\boldsymbol{\sigma_s}\, \boldsymbol{d})\boldsymbol{ds}}, \tag{13}$$

where $\int_s[\boldsymbol{\sigma_s}'(-\boldsymbol{d})]ds$, $\int_s(\boldsymbol{\sigma_s d})ds$ are the algebraic projection sum of the anti-sliding force and the sliding force vector in the direction of the overall potential sliding of the slope, respectively.

Seismic slope stability evaluation index

The vector sum method can describe the dynamic change characteristics of seismic slope stability, but the overall slope stability cannot be evaluated directly under earthquake action. Therefore, it is necessary to calculate the equivalent safety factor of the slope with other algorithms and evaluate the slope stability.

To directly reflect the impact of the progressive failure process on slope stability, the average safety factor $\overline{F_s}$is used to evaluate the seismic slope stability. The time-history curve of the safety factors is discretized and takes the average value. The average safety factor $\overline{F_s}$is as follows:

$$\overline{\boldsymbol{F_s}} = \frac{\sum_{i=1}^{n} \boldsymbol{F_{si}}}{\boldsymbol{n}} \tag{14}$$

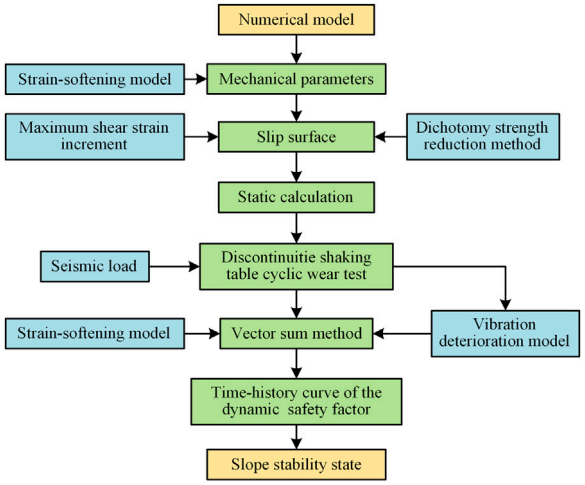

FIGURE 5
Typical workflow of seismic slope stability evaluation method.

where n is the total number of discrete points of curves and F_{si} is the ith safety factor on the curves.

The instability probability P_f is defined as the ratio of the number of safety factors less than 1 to the total number in the discretization curves, reflecting the uncertainty of slope instability during the earthquake (Falamaki et al., 2021). The expression is as follows:

$$P_f = \frac{m}{n}, \tag{15}$$

where m is the number of safety factors less than 1 in the discrete curve.

Typical workflow

A seismic slope stability analysis method considering the progressive failure of slip surface is proposed that reflects the stability state of the seismic slope, according to the characteristics that that different states of the rock-soil mass show diverse strength properties. The method combines the strain-softening model, the vibration deterioration model, and the vector sum method. The flowchart is shown in Figure 5. The specific steps are as follows:

1) Establish a numerical model according to slope geometry.
2) Determine the physical and mechanical parameters of the rock-soil mass and the expression of the strain-softening model.
3) Combine these values with the dichotomy strength reduction method, and locate the position of the critical slip surface of the slope according to the maximum shear strain increment.

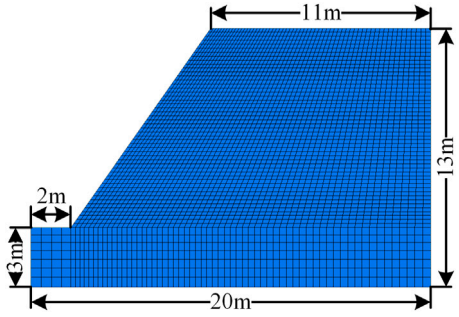

FIGURE 6
Slope numerical model.

4) Repeat the static analysis for the numerical model to obtain the initial state before the earthquake.
5) Determine the vibration deterioration model of the failure surface according to the cyclic shear test of the rock mass structural plane.
6) Input the seismic load into the numerical model and select the corresponding ideal elastoplastic, strain-softening, or vibration deterioration constitutive models according to the rock-soil mass state.
7) Based on the vector sum method, calculate the safety factor of the critical sliding body at each step. Obtain the time-history curve of the dynamic safety factor.
8) Calculate the average safety factor and instability probability of the time-history curve to determine the stability state of the seismic slope.

Numerical calculation and example verification

Numerical model and parameters

The following example will briefly explain the impact of the progressive failure of seismic slope stability. A simplified slope model is adopted in this article to explain the research process because of the large calculation workload of the actual engineering model. However, the method in this article is not limited to this simple model and is still applicable to slopes with multiple strata and structural planes. The numerical model of the slope is established by FLAC3D, as shown in Figure 6. The slope height is 10 m, and the slope angle is about 60°. The numerical slope model is divided into 10,536 units and 22,212 nodes.

The physical and mechanical parameters of the rock-soil mass are shown in Table 1 (Wang et al., 2018). The strength parameters selection process of the numerical unit is shown in Figure 7. All units in the model are searched to obtain their cumulative plastic shear and tensile strains at each step. The unit

TABLE 1 Mechanical parameters of the rock mass.

Unit weight γ/(kg·m^{-3})	Elasticity modulus E/MPa	Poisson ratio μ	Tensile strength σ_t/kPa	Cohesion c_0/kPa	Cohesion c_f/kPa
2000	15.0	0.3	4.0	26.0	6.0
Internal friction angle φ_0/(°)	Internal friction angle φ_f/(°)	Dilatancy angle ψ_0/(°)	Dilatancy angle ψ_f/(°)	Ultimate tensile strain ε_{tf}	Ultimate shear strain ε_{sf}
20.0	16.0	10.0	8.0	0.005	0.08

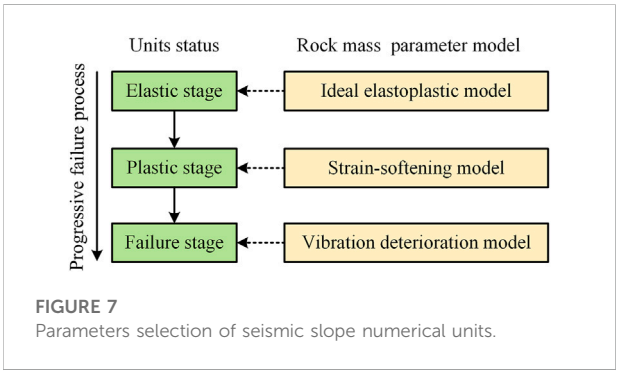

FIGURE 7
Parameters selection of seismic slope numerical units.

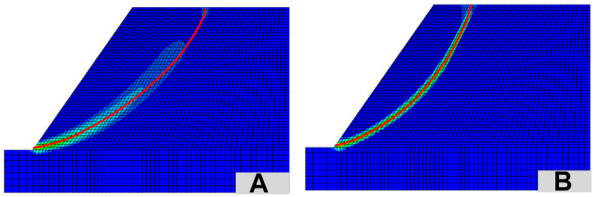

FIGURE 8
Critical slip surface obtained by dichotomy strength reduction method. **(A,B)** Elastoplastic model **(A)** and strain-softening model **(B)**.

in the elastic stage obeys the ideal elastoplastic model, and the strength parameters remain the same. When the plastic deformation occurs, the strength parameters are attenuated according to the strain-softening model shown in Figure 3. When partial units reach the ultimate plastic strain, which is the failure stage, many cracks occur in the rock-soil mass, and the bearing capacity of the slope is mainly provided by the lock-up segment and the failure surface strength parameters (Cao et al., 2008). The strength parameter of the cracks becomes the residual strength. Therefore, under the action of earthquakes, the numerical unit strength parameters of the failure stage are further attenuated according to the vibration deterioration model. From the failure of the units to the end of the seismic load, the shear strength parameters of these units at each step are the product of the residual strength and the vibration deterioration coefficient.

Critical slip surface search

Static slope stability is calculated based on the dichotomy strength reduction method, and the static safety factor of the elastoplastic model is 1.26, which coincides with the result of the built-in strength reduction method (1.27). This result shows that the dichotomy strength reduction method is reasonable and reliable. Under the critical state, the slip surface position of the elastoplastic model and strain-softening model obtained by the dichotomy strength reduction model is shown in Figure 8. It can be seen that the calculated critical slip surface of the slope with the strain-softening model is shallower and has less stability than that of the elastoplastic model because the progressive failure characteristics of geotechnical materials are considered.

Based on the aforementioned critical slip surface, the slope safety factors calculated by the three analysis methods are shown in Table 2. The safety factors calculated by the vector sum method and the two strength reduction methods are almost the same, which shows that solving the slope safety factor by the vector sum method is credible.

Dynamic stability analysis

Three models, including elastoplastic, strain-softening, and strain-softening + vibration deterioration, are taken to analyze the numerical slope model and describe the influence of rock-soil mass strength parameter attenuation on slope dynamic stability during a progressive failure. Among them, a simple harmonic vibration wave is used to simulate the seismic load, and acceleration time history is $a = \lambda\cos(2\pi ft)$, $\lambda = 1.25$ m/s^2, which is equivalent to the acceleration amplitude under seismic intensity Ⅶ. The seismic wave frequency $f = 2$ Hz, and the duration is 5 s. The vertical acceleration amplitude is 1/2 of the horizontal acceleration; the vertical peak acceleration takes 0.63 m/s^2 (Ling et al., 1997).

TABLE 2 Safety factors calculated by different methods.

Safety factor	Built-in strength reduction method	Dichotomy strength reduction method	Vector sum method
Elastoplastic model	1.27	1.26	1.24
Strain-softening model	—	1.06	1.07

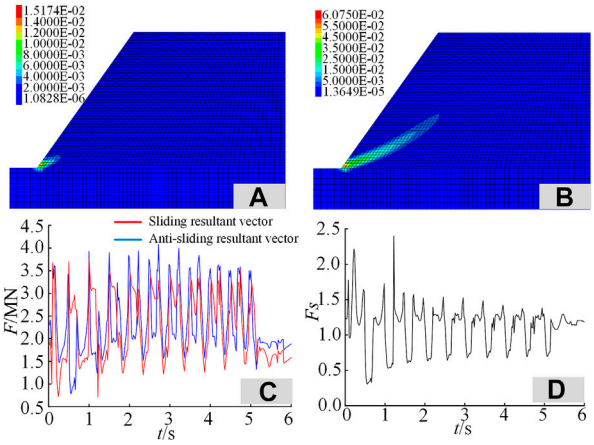

FIGURE 9
Static/dynamic slope response based on the elastoplastic model. **(A–D)** Maximum shear strain increment in the static state **(A)**, maximum shear strain increment in the dynamic state **(B)**, algebraic sum of the sliding force vector and anti-sliding force vector **(C)**, and dynamic time history safety factor **(D)**.

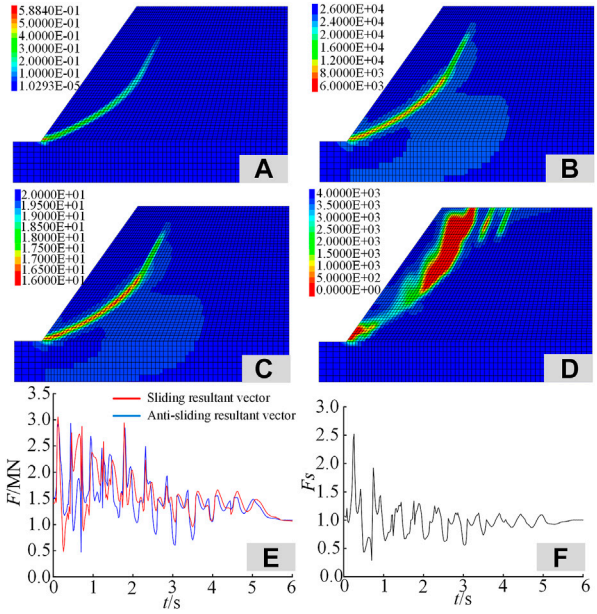

FIGURE 10
Dynamic response of slope based on the strain-softening model. **(A–F)** Maximum shear strain increment in the dynamic state **(A)**, change of cohesion **(B)**, change of internal friction angle **(C)**, change of tensile strength **(D)**, algebraic sum of the sliding force vector and anti-sliding force vector **(E)**, and dynamic time history safety factor **(F)**.

The dynamic stability analysis is based on static analysis. First, based on FLAC3D numerical analysis software, static boundary conditions and physical and mechanical parameters are set in the model, where the initial state before the earthquake is obtained by static analysis. Second, the input dynamic load, dynamic boundary conditions, and damping type are defined. In this article, viscous boundary conditions are used to absorb incident waves on the boundary, and Rayleigh damping is used to make the model converge faster, where the minimum critical damping ratio is set at 0.05, and the center frequency is set at 30 Hz (Itasca 2013). Third, all units in the model are searched to obtain their cumulative plastic shear and tensile strains at each step. The corresponding ideal elastoplastic, strain-softening, or vibration deterioration constitutive models are selected according to Figure 7, based on the rock-soil mass unit state. Then, regarding the critical sliding body obtained from the static analysis as the analysis object and the sliding direction of the unit on the critical slip surface as the direction of shear stress, the potential critical slip surface in Figure 8 is discretized into several units. Finally, the safety factor is calculated by the vector sum method to obtain the time history safety factor curve and stability evaluation results of the seismic slope.

When using the elastoplastic model for calculation under the static condition, the maximum shear strain increment is 0.015, with only local damage in the slope foot, as shown in Figure 9A. Under the action of the dynamic load, according to the critical slip surface shown in Figure 8A, the dynamic response law of the seismic slope is calculated by the vector sum method, as shown in Figures 9B–D. It can be seen that the local damage of the seismic slope extends to the inside, compared to the static conditions, and the maximum shear strain increment increases to 0.061. During the seismic dynamic process, the minimum safety factor is 0.30, and the maximum safety factor is 2.40. The corresponding times are 0.56 and 1.22 s, respectively. After the action of dynamic load, the final safety factor of a seismic slope tends to be 1.19, which is not much different from the factor before the dynamic load.

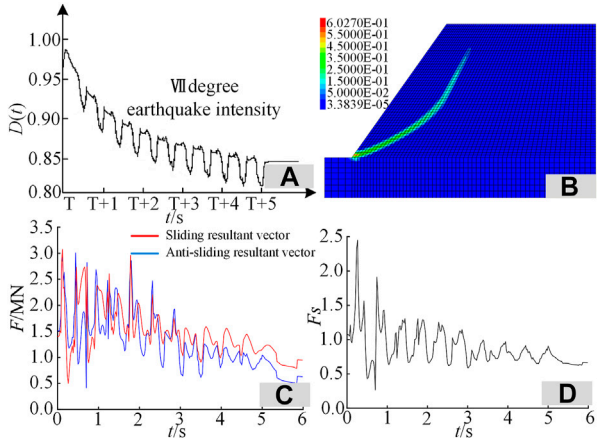

FIGURE 11
Dynamic slope response based on strain-softening + vibration deterioration model. **(A–D)** Vibration deterioration coefficient **(A)**, maximum shear strain increment in the dynamic state **(B)**, algebraic sum of the sliding force vector and anti-sliding force vector **(C)**, and dynamic time history safety factor **(D)**.

When using the strain-softening model for calculation, the response law of a seismic slope is shown in Figure 10. After the dynamic calculation, the sliding band formed by the maximum shear strain incremental cloud map is the same as the critical slip surface position of the static state search. Relative to the elastoplastic model, the slope plastic yield surface continues to expand, reaching a maximum shear strain increment of 0.588. The cohesion of some units on the slope slip surface is reduced to 6 kPa, and the internal friction angle is reduced to 16°, causing obvious shear failure of the slip surface. The tensile strength of some units in the foot and the rear edge of the slope is reduced to 0 to reach the ultimate plastic tension strain, causing tension damage. The tension crack of the rear edge of the slope top is formed, following the progressive destruction law of the seismic slope mentioned before. During the seismic dynamic load process, the minimum and maximum safety factors of the slope are 0.29 and 2.52, respectively, and the corresponding times are 0.70 and 0.26 s. After the dynamic load, the final slope safety factor tends to be 1.03, obviously less than the one calculated by the elastoplastic model. The seismic slope tends to the critical failure state.

Based on the strain-softening model, the failure state occurs when the rock-soil mass unit reaches the ultimate plastic strain. Combined with the vibration deterioration model, according to Eq. 7, the strength parameters of the units of the failure stage were reassigned by Fish language. The vibration deterioration coefficient expression is generally obtained through the shaking table cyclic wear test of the rock structure plane. To simplify the analysis process, the vibration deterioration factor $D(t)$ of the failure surface can be replaced by the result of a dynamic load test on the rock structure surface obtained by Ni et al. (2013) under a VII degree earthquake intensity (λ = 1.25 m/s^2). The vibration deterioration factor of the slope failure surface is shown in Figure 11A.

Considering the strain-softening and vibration deterioration characters of the seismic slope at the same time, the dynamic response law of a slope is shown in Figures 11B–D. It is known that the slope shear plastic yield surface is further developed, and the maximum shear strain increment reaches 0.603. During the seismic dynamic load process, vibration deterioration phenomena appear in the strength parameters of the failure surface. According to Eqs 10–12, the attenuation of the shear strength parameter results in the anti-sliding vector $\boldsymbol{\sigma_s}'$ declining. Compared to the sliding force vector $\int_s(\boldsymbol{\sigma_s d})ds$, the slope anti-slide force vector $\int_s[\boldsymbol{\sigma_s}'(-\boldsymbol{d})]ds$ falls, resulting in the overall slope safety factor dropping. The minimum and the maximum safety factors are 0.27 and 2.45, respectively, and the corresponding times are 0.70 and 0.26 s; the time is consistent with the strain-softening model. The final safety factor tends to be 0.67, indicating that the slope is in a destructive state.

Under the aforementioned three models, the calculated seismic slope stability evaluation indicators are shown in Table 3 according to Eqs 14, 15. Without considering the progressive slope damage, the elastoplastic model is used for numerical calculation, and the average safety factor and the instability probability of the seismic slope are 1.11% and 28.57%, respectively. When considering the progressive failure under the earthquake, the average safety factor of the seismic slope calculated in this method drops significantly to 0.88, the instability probability increases significantly to 73.42%, and the slope becomes unstable. For seismic slope engineering with strict safety grades, a shaking table cyclic wear test should be carried out to determine the model parameters of the failure surface vibration deterioration. Meanwhile, considering the strain-softening and failure surface vibration deterioration characteristics of a rock-soil mass is crucial to truly characterize the stability state of a seismic slope.

Discussion

In the numerical simulation of slope engineering, a proper constitutive model is crucial for the accurate evaluation of slope stability. However, under different stress-strain states, the mechanical properties of geotechnical materials show significant differences, leading to a unified constitutive model that cannot be adopted to express their mechanical response features under external forces (Cheng and Lau, 2008). The stability of the seismic slope is the result of the joint action of internal and external factors. Under the cyclic shear action of a seismic load, there is both a strain-softening effect in the geotechnical materials in the slope and a wear and passivation

TABLE 3 Stability evaluation index under different models.

Model types	Average safety factor $\overline{F_s}$	Instability probability P_f
Elastoplastic model	1.11	28.57%
Strain-softening model	0.99	56.48%
Strain-softening + vibration deterioration model	0.88	73.42%

phenomenon in the rock mass structure (Ni et al., 2013). Previous studies have ignored the interrelation between rock-soil materials and dynamic load in a seismic slope and have not fully considered the influence of dynamic loading on the strength deterioration of a rock-soil mass in a seismic slope.

According to the failure mechanism of a slope subject to an earthquake, the strain-softening and vibration deterioration models are integrated into the numerical simulation. The corresponding constitutive relation is given based on the state of geotechnical materials, then the stability analysis method of a seismic slope that considers the progressive failure of slip surface is proposed. This method has the following advantages. 1) The strain-softening model and vibration deterioration model are introduced to quantitatively characterize the strength of a rock-soil mass, and a bridge between numerical simulation and material parameter assignment is constructed. These two models describe the features of geotechnical materials at different stages under the action of seismic dynamic loading, which can accurately describe the rock-soil strength variation of a seismic slope. 2) The strain-softening model, vibration deterioration model, and vector sum method are reasonably integrated to obtain the dynamic time-history safety factor of the slope under the action of the earthquake, which can represent the stability state of seismic slopes more comprehensively and reliably. 3) As shown in Figures 10B–D, the proposed method can obtain the contour figure of rock-soil mass strength parameter variation, which can reflect the failure features inside the slope. This result shows the formation process of a slip surface on a slope and is of great value to the research of slope failure mechanism and progressive development process. 4) The effectiveness of the proposed method is further illustrated through an example. If the traditional elastoplastic model is used to calculate the stability of the seismic slope, the strength weakening and progressive failure features in the slope failure process will be ignored, and the calculation results are a little unsafe. Based on the aforementioned analysis, the method in this article can reasonably calculate the safety factor of the seismic slope by considering the internal and external factors of the earthquake and has a good application prospect in accurately evaluating the seismic slope stability.

Although the stability results of the seismic slope calculated by the proposed method are more reasonable and reliable than those of existing studies, there are still some limitations and deficiencies. 1) There are some simplifying assumptions in the calculation. For example, the strain-softening model is simplified into a linear piecewise function, which will lead to certain calculation errors between the calculation results and the actual stability. This is a defect in all slope stability calculation methods. 2) The vibration deterioration model is related to the properties of rock mass structure and dynamic load conditions, and the expression is relatively complex. The vibration deterioration model needs to be further explored by more shaking table cyclic shear tests for a more general mathematical expression. 3) Construction of the strain-softening and vibration deterioration model requires various rock mechanics tests, especially cyclic shear tests. The richer the experiment, the more accurate the constructed model, but the lower the efficiency. Therefore, seeking the balance between accuracy and efficiency of the constructed model will be the focus of the next research stage.

Conclusion

The progressive failure mechanism of a seismic slope can be described according to the characteristics of the action of seismic loads on geotechnical materials. Strain-softening and vibration deterioration models are introduced to characterize the progressive failure process of the plasticity failure stage, which can accurately describe the attenuation of the rock-soil strength of a seismic slope.

The strain-softening and vibration deterioration models are embedded in the seismic slope stability calculation and allow for selecting an appropriate rock-soil mass constitutive model according to the stress-strain state of the slope. A seismic slope stability analysis method that considers progressive failure and is combined with the vector sum method is formed using the dichotomy strength reduction method to locate the position of the critical slip surface of the slope and then calculate the dynamic time history safety factor. The proposed method can represent the stability

state of seismic slopes more comprehensively and reliably than existing methods.

This method is used to analyze the dynamic stability of the calculation examples. The seismic slope produces shear and tension failure, which verifies the progressive failure evolution of the slip surface of the seismic slope. The comparative analysis of the safety factor in the three models shows that the calculation results using the traditional elastoplastic model are unsafe, which verifies the necessity and rationality of considering strain-softening and vibration deterioration when analyzing the dynamic stability of a seismic slope.

Data availability statement

The original contributions presented in the study are included in the article/Supplementary Material. Further inquiries can be directed to the corresponding author.

Author contributions

Conceptualization, ZA; investigation, HZ; writing—original draft preparation, HZ and QY; writing—review and editing, ZA, CJ, and ZR; supervision, SW; and funding, SW. All authors listed have made a substantial, direct, and intellectual contribution to the work and approved it for publication.

Funding

Funding for this work was supported by the National Key Research and Development Funding Projects of China (Grant No. 2017YFC0805303) and the Yunnan Innovation Team (Grant No. 202105AE160023).

Conflict of interest

ZA, CJ, and QY were employed by Power China Road Bridge Group Co. Ltd.

The remaining authors declare that the research was conducted in the absence of any commercial or financial relationships that could be construed as a potential conflict of interest.

Publisher's note

All claims expressed in this article are solely those of the authors and do not necessarily represent those of their affiliated organizations, or those of the publisher, the editors, and the reviewers. Any product that may be evaluated in this article, or claim that may be made by its manufacturer, is not guaranteed or endorsed by the publisher.

References

Alfaro, P., Delgado, J., García-Tortosa, F., Giner, J., Lenti, L., López-Casado, C., et al. (2012). The role of near-field interaction between seismic waves and slope on the triggering of a rockslide at Lorca. *Nat. Hazard Earth Sys.* 12, 3631–3643. doi:10.5194/nhess-12-3631–2012

Baker, R., Shukha, R., Operstein, V., and Frydman, S. (2006). Stability charts for pseudo-static slope stability analysis. *Soil Dyn. Earthq. Eng.* 26, 813–823. doi:10.1016/j.soildyn.2006.01.023

Bolla, A., and Paronuzzi, P. (2021). Seismic analysis of a limestone rock slope through numerical modelling: Pseudo-static vs. non-linear dynamic approach. In IOP Conference Series: Earth and Environmental Science 906, 012093.

Cao, W. G., Zhao, H., Zhang, L., and Zhang, Y. J. (2008). Dynamic stability softening constitutive model for rock considering effect of damage threshold and its parameters determination method. *Chin. J. Rock Mech. Eng.* 6, 1148.

Che, A., Yang, H., Wang, B., and Ge, X. (2016). Wave propagations through jointed rock masses and their effects on the stability of slopes. *Eng. Geol.* 201, 45–56. doi:10.1016/j.enggeo.2015.12.018

Cheng, Y. M., and Lau, C. K. (2008). *Slope stability analysis and stabilization: New methods and insight*. London: CRC Press.

Crawford, A. W., and Curran, J. H. (1982). The influence of rate and displacement dependent shear resistance on the response of rock slopes to seismic loads. *Int. J. Rock Mech. Min. Sci. Geomechanics Abstr.* 19, 1–8. doi:10.1016/0148-9062(82)90704-5

Di, B., Stamatopoulos, C. A., Dandoulaki, M., Stavrogiannopoulou, E., Zhang, M., and Bampina, P. (2017). A method predicting the earthquake-induced landslide risk by back analyses of past landslides and its application in the region of the Wenchuan 12/5/2008 earthquake. *Nat. hazards* 85, 903–927. doi:10.1007/s11069-016-2611-7

Du, Y., Li, H., Chicas, S. D., and Huo, L. (2022). Progress and perspectives of geotechnical anchor bolts on slope engineering in China. *Front. Environ. Sci.* 10, 928064. doi:10.3389/fenvs.2022.928064

Du, Y., Xie, M., and Jia, J. (2020). Stepped settlement: A possible mechanism for translational landslides. *Catena* 187, 104365. doi:10.1016/j.catena.2019.104365

Eberhardt, E., Stead, D., and Coggan, J. S. (2004). Numerical analysis of initiation and progressive failure in natural rock slopes—The 1991 randa rockslide. *Int. J. Rock Mech. Min. Sci. (1997).* 41, 69–87. doi:10.1016/S1365-1609(03)00076-5

Falamaki, A., Shafiee, A., and Shafiee, A. H. (2021). Under and post-construction probabilistic static and seismic slope stability analysis of Barmshour Landfill, Shiraz City, Iran. *Bull. Eng. Geol. Environ.* 80, 5451–5465. doi:10.1007/s10064-021-02277-4

Fan, X., Qiang, X., Scaringi, G., Dai, L., Li, W., Dong, X., et al. (2017). Failure mechanism and kinematics of the deadly june 24th 2017 Xinmo landslide, maoxian, Sichuan, China. *Landslides* 14, 2129–2146. doi:10.1007/s10346-017-0907-7

Ge, X. R. (2008). Deformation control law of rock fatigue failure, real-time X-ray CT scan of geotechnical testing, and new method of stability analysis of slopes and dam foundations. *Chin. J. Geotech. Eng.* 1, 1.

Guo, M., Ge, X., and Wang, S. (2011). Slope stability analysis under seismic load by vector sum analysis method. *J. Rock Mech. Geotechnical Eng.* 3, 282–288. doi:10.3724/SP.J.1235.2011.00282

Itasca (2013). *Fast Lagrangian analysis of continua in 3 dimensions*. Online Man.

Jafari, M. K., Pellet, F., Boulon, M., and Hosseini, K. A. (2004). Experimental study of mechanical behaviour of rock joints under cyclic loading. *Rock Mech. Rock Eng.* 37, 3–23. doi:10.1007/s00603-003-0001-4

Karray, M., Hussien, M. N., Delisle, M. C., and Ledoux, C. (2018). Framework to assess pseudo-static approach for seismic stability of clayey slopes. *Can. Geotech. J.* 55, 1860–1876. doi:10.1139/cgj-2017-0383

Koo, R. C., Kwan, J. S., and Sze, E. H. (2016). Stability assessment of soil slopes subject to blasting vibrations based on time history analyses. *HKIE Trans.* 23, 130–137. doi:10.1080/1023697X.2016.1201438

Lee, H. S., Park, Y. J., Cho, T. F., and You, K. H. (2001). Influence of asperity degradation on the mechanical behavior of rough rock joints under cyclic shear loading. *Int. J. Rock Mech. Min. Sci. (1997).* 38, 967–980. doi:10.1016/S1365-1609(01)00060-0

Li, Y., Wu, W., and Liu, B. (2019). Predicting the shear characteristics of rock joints with asperity degradation and debris backfilling under cyclic loading conditions. *Int. J. Rock Mech. Min. Sci. (1997).* 120, 108–118. doi:10.1016/j.ijrmms.2019.06.001

Ling, H. I., Leshchinsky, D., and Mohri, Y. (1997). Soil slopes under combined horizontal and vertical seismic accelerations. *Earthq. Eng. Struct. Dyn.* 26, 1231–1241. doi:10.1002/(sici)1096-9845(199712)26:12<1231::aid-eqe707>3.0.co;2-z

Ma, Z. Y., Liao, H. J., Dang, F. N., and Cheng, Y. X. (2021). Seismic slope stability and failure process analysis using explicit finite element method. *Bull. Eng. Geol. Environ.* 80, 1287–1301. doi:10.1007/s10064-020-01989-3

Macedo, J., and Candia, G. (2020). Performance-based assessment of the seismic pseudo-static coefficient used in slope stability analysis. *Soil Dyn. Earthq. Eng.* 133, 106109. doi:10.1016/j.soildyn.2020.106109

Negi, P., Chakraborty, T., and Bhalla, S. (2022). Viability of electro-mechanical impedance technique for monitoring damage in rocks under cyclic loading. *Acta Geotech.* 17, 483–495. doi:10.1007/s11440-021-01181-1

Ni, W. D., Tang, H. M., Liu, X., and Wu, Y. P. (2013). Dynamic stability analysis of rock slope considering vibration deterioration of structural planes under seismic loading. *Chin. J. Rock Mech. Eng.* 32, 492.

Pang, R., Xu, B., Zhou, Y., and Song, L. (2021). Seismic time-history response and system reliability analysis of slopes considering uncertainty of multi-parameters and earthquake excitations. *Comput. Geotech.* 136, 104245. doi:10.1016/j.compgeo.2021.104245

Quinn, P. E., Diederichs, M. S., Rowe, R. K., and Hutchinson, D. J. (2012). Development of progressive failure in sensitive clay slopes. *Can. Geotech. J.* 49, 782–795. doi:10.1139/t2012-034

Shinoda, M., Watanabe, K., Sanagawa, T., Abe, K., Nakamura, H., Kawai, T., et al. (2015). Dynamic behavior of slope models with various slope inclinations. *Soils Found.* 55, 127–142. doi:10.1016/j.sandf.2014.12.010

Song, D., Chen, Z., Ke, Y., and Nie, W. (2020). Seismic response analysis of a bedding rock slope based on the time-frequency joint analysis method: A case study from the middle reach of the jinsha river, China. *Eng. Geol.* 274, 105731. doi:10.1016/j.enggeo.2020.105731

STCM Science and Technology Committee of the Ministry of Aviation Industry (1990). *Manual of stress concentration factors*. Beijing: Higher Education Press.

Valentin, G., Giona, P., and Erik, E. (2016). Numerical investigation of seismically induced rock mass fatigue as a mechanism contributing to the progressive failure of deep-seated landslides. *Rock Mech. Rock Eng.* 49, 2457–2478. doi:10.1007/s00603-015-0821-z

Wang, J., Yao, L., and Hussain, A. (2010). Analysis of earthquake-triggered failure mechanisms of slopes and sliding surfaces. *J. Mt. Sci.* 7, 282–290. doi:10.1007/s11629-010-2020-4

Wang, L., Zhang, X., and Tinti, S. (2021). Large deformation dynamic analysis of progressive failure in layered clayey slopes under seismic loading using the particle finite element method. *Acta Geotech.* 16, 2435–2448. doi:10.1007/s11440-021-01142-8

Wang, S. J., and Zhang, J. M. (1982). Dynamic analysis of sliding stability of slope rock mass. *Sci. Geol. Sin.* 2, 162.

Wang, W., Chen, G. Q., Zhu, J., and Huang, R. Q. (2018). Slope stability calculated with strength reduction method considering tensile and shear progressive failure. *Chin. J. Rock Mech. Eng.* 37, 2064.

Wang, Y., Wu, S. X., Zhou, J. K., and Shen, D. J. (2010). Experimental study of dynamic axial tensile mechanical properties of granite. *Chin. J. Rock Mech. Eng.* 29, 2328.

Xu, C., and Xu, X. (2013). Controlling parameter analyses and hazard mapping for earthquake-triggered landslides: An example from a square region in beichuan county, sichuan province, China. *Arab. J. Geosci.* 6, 3827–3839. doi:10.1007/s12517-012-0646-y

Yang, Y., Wu, W., and Zheng, H. (2021). Stability analysis of slopes using the vector sum numerical manifold method. *Bull. Eng. Geol. Environ.* 80, 345–352. doi:10.1007/s10064-020-01903-x

Yu, G., Bu, L., Wang, C., and Farooq, A. (2022). Composition analysis and distributed assumption GIS model of normal stress on the slope sliding surface. *Front. Earth Sci.* 10, 923620. doi:10.3389/feart.2022.923620

Zhang, B., Jiang, Y., Cheng, H., and Liu, Z. (2021). Upper bound analysis of the stability of 3D slopes in the saturated soft clay subjected to seismic effect. *Front. Earth Sci.* 9, 785854. doi:10.3389/feart.2021.795854

Zhang, K., Cao, P., and Bao, R. (2013). Progressive failure analysis of slope with strain-softening behaviour based on strength reduction method. *J. Zhejiang Univ. Sci. A* 14, 101–109. doi:10.1631/jzus.A1200121

Zhao, L., Jiao, K., Zuo, S., Yu, C., and Tang, G. (2020). Pseudo-static stability analysis of wedges based on the nonlinear Barton-Bandis failure criterion. *Geomech. Eng.* 20, 287–297. doi:10.12989/gae.2020.20.4.287

Zhou, Y., Zhang, F., Wang, J., Gao, Y., and Dai, G. (2019). Seismic stability of Earth slopes with tension crack. *Front. Struct. Civ. Eng.* 13, 950–964. doi:10.1007/s11709-019-0529-3

frontiers | Frontiers in Environmental Science

TYPE Original Research
PUBLISHED 23 September 2022
DOI 10.3389/fenvs.2022.1012057

Check for updates

OPEN ACCESS

EDITED BY
Yan Du,
University of Science and Technology Beijing, China

REVIEWED BY
Wang Liwei,
Yanshan University, China
Qiaorui Si,
Jiangsu University, China

*CORRESPONDENCE
Chen Yang,
yangchen@ncwu.edu.cn

SPECIALTY SECTION
This article was submitted to Environmental Informatics and Remote Sensing, a section of the journal Frontiers in Environmental Science

RECEIVED 05 August 2022
ACCEPTED 05 September 2022
PUBLISHED 23 September 2022

CITATION
Yang X, Jia Y, Yang C, He X, Jia Y and Xu L (2022), Research on formulation optimization and hydration mechanism of phosphogypsum-based filling cementitious materials.
Front. Environ. Sci. 10:1012057.
doi: 10.3389/fenvs.2022.1012057

COPYRIGHT
© 2022 Yang, Jia, Yang, He, Jia and Xu. This is an open-access article distributed under the terms of the Creative Commons Attribution License (CC BY). The use, distribution or reproduction in other forums is permitted, provided the original author(s) and the copyright owner(s) are credited and that the original publication in this journal is cited, in accordance with accepted academic practice. No use, distribution or reproduction is permitted which does not comply with these terms.

Research on formulation optimization and hydration mechanism of phosphogypsum-based filling cementitious materials

Xiao Yang, Yongxiang Jia, Chen Yang*, Xiaoke He, Yanchang Jia and Leige Xu

North China University of Water Resources and Electric Power, Zhengzhou, China

Phosphogypsum is a solid waste produced in the production of wet-process phosphoric acid. The main component is calcium sulfate dihydrate, and its constant calcium activity is very low. It is a very difficult waste to handle. The slag produced in the ironmaking processes of the Jiuquan Iron and Steel Company has high activity and can be mixed with phosphogypsum to prepare backfilling cementitious materials for the backfilling of goaf (see Introduction below) to prevent its subsidence and cracking and subsequent subsidence of the land surface above the goaf. In this paper, an orthogonal test of material strength under different ratios and finenesses was carried out, and the optimal formula of phosphogypsum-based cementitious material was obtained. On this basis, SEM (Scanning Electron Microscope) and XRD (X-ray Diffraction) were used to observe the internal structure of phosphogypsum-based cementitious materials. The results show that: when the content of quicklime is 5.5%–6.0%, the content of phosphogypsum is 30%–33%, the content of NaOH is 1.5%–2.0%, the content of Glauber's salt is 2.5%–3%, the average particle size is 15.88 μm, and grinding aids and an early strengthening agent were added, and in the case of the strengthening agent, the 3-days and 7-days strengths of the filling reached the highest values of 1.58 MPa (mean flexural strength) and 4.1 MPa, respectively. The formation of calcium silicate hydrates gel (C-S-H) and ettringite (AFt) gradually increased with age, and the structure became denser. The ettringite plays the role of interspersed support in the filling body, thereby improving the overall strength. This research provides a theoretical basis and practical reference for the treatment of goaf.

KEYWORDS

goaf, phosphogypsum, solid waste, hydration mechanism, compressive strength

1 Introduction

Goaf is any underground void created by human excavation or natural geological movement under the surface of the planet (Du et al., 2017). The existence of a goaf causes the safe production of a mine to encounter great safety problems (Du et al., 2021). Personnel and mechanical equipment may fall into the goaf and be injured or damaged (Sun et al., 2022). At present, the underground goaf has become an important problem restricting the development of mines and the urbanization of the upper part of the goaf (Zhang et al., 2022). With the deep mining of mines, collapse accidents are prone to occur, and buildings cannot be built affected by goafs, which brings inconvenience to people's life and production (Li et al., 2022). A large number of stopes, chambers, and roadways left in underground mining have not been treated in time, which has brought serious hidden dangers to open-pit mining and posed a serious threat to mine staff and equipment (Du et al., 2020).The latest research shows that the stepped subsidence of the ground caused by a goaf is one of the main reasons for the instability and damage of landslides (Zhou et al., 2022). Therefore, an effective way to reduce the geological risks of any mining area is to carry out backfilling of the goaf and reduce the subsidence of the ground surface (Du et al., 2022).

Solid waste refers to solid and semi-solid waste materials produced by human beings in production, consumption, life, and other activities (Li et al., 2019). It mainly includes solid particles, garbage, slag, sludge, abandoned products, damaged utensils, defective products, animal carcasses, spoiled food, human and animal manure, etc (Huang and Lin, 2010). These solid wastes will cause great damage to the ecological environment. In the guiding opinions on the comprehensive utilization of bulk solid waste in the "14th Five-Year Plan," it is pointed out that bulk solid waste is the core area of comprehensive utilization of resources due to its large volume and wide range, prominent environmental impact, and broad utilization prospects (Xiao et al., 2019). Promoting the comprehensive utilization of bulk solid waste is of great significance to improving resource utilization efficiency and environmental quality, and promoting a comprehensive green transformation of economic and social development (Sun et al., 2020). At present, the cumulative stockpiles of bulk solid waste total about 60 billion tons, and annual new stockpiles are nearly 3 billion tons. Among them, the utilization rates of solid wastes such as red mud, phosphogypsum, and steel slag is still low, occupying a large amount of land resources, and present large environmental safety hazards (Luo et al., 2020). It is necessary to thoroughly implement the Law of the People's Republic of China on the Prevention and Control of Environmental Pollution by Solid Waste and other laws and regulations, to vigorously promote the reduction, resource utilization and safe disposal of bulk solid wastes at their source, strengthen the whole-chain governance, focus on solving prominent contradictions and problems, and promote the comprehensive utilization of resources to allow industry to realize new development (Szajerski et al., 2019).

Phosphogypsum is one such type of solid waste (Mohammed et al., 2018). Phosphogypsum mainly comprises two kinds, gray-black and gray-white, and has a particle diameter generally of 5–50 μm and a crystal water content of 20%–25% (Liu et al., 2019; Pinto et al., 2020; Wang et al., 2020). Phosphogypsum is a solid waste produced in the production of wet-process phosphoric acid, and its component is mainly calcium sulfate dihydrate (He et al., 2012; Chen et al., 2016; Cao, 2018; Sun, 2020). The composition of phosphogypsum is relatively complex. In addition to calcium sulfate, there are incompletely decomposed phosphate rock, residual phosphoric acid, fluoride, acid-insoluble matter, organic matter, etc. Among them, the existence of fluorine and organic matter has the greatest impact on the resource utilization of phosphogypsum (He et al., 2014; Cui et al., 2021). The random discharge and accumulation of phosphogypsum has seriously damaged the ecological environment, not only polluting groundwater resources, but also causing a waste of land resources (Luo et al., 2013; Bouchhima et al., 2017).

Slag is a by-product of the blast furnace ironmaking process. In the ironmaking process, iron oxide is reduced to metallic iron at high temperatures, and impurities such as silica and alumina in iron ore react with lime to form a melt with silicate and aluminosilicate as the main components. After quenching, it becomes a loose and porous granular material, which is known as blast furnace slag, often referred to as simply slag (Hua et al., 2016). Slag is also a type of solid waste (Rosales et al., 2020). The phosphogypsum-based cementitious material prepared based on JISCO slag fully utilizes phosphogypsum and JISCO slag.

The phosphogypsum-based cementitious material prepared based on JISCO slag not only makes full use of phosphogypsum, but also saves the filling cost of Jinchuan mine filling-method mining. The filling method is to backfill these wastes into the goaf, which not only treats the waste, which reduces pollution, but also reduces the probability of surface subsidence caused by mining (Min et al., 2019; Yin et al., 2019; Zhou et al., 2020). Since mining is going on all the time, it cannot be suspended due to the need for backfilling, so the backfilled body needs to have a certain strength at an early stage to avoid taking up time. Using cement as aggregate will cost the purchase of cement and transportation, while the JISCO slag and phosphogypsum used in this paper are sourced near the Jinchuan Mine, so there are basically no transportation costs and a low total cost. It not only saves money, but also saves the cost of slag treatment and reduces the pollution to the environment. In this paper, an orthogonal test of material strength under different ratios and finenesses was carried out. According to its 3ays and 7 days early strength, the optimal formulation of phosphogypsum-based filling cementitious material was found. The hydration process of gypsum-based cementitious materials was analyzed.

Figure 1 is a schematic diagram of goaf filling.

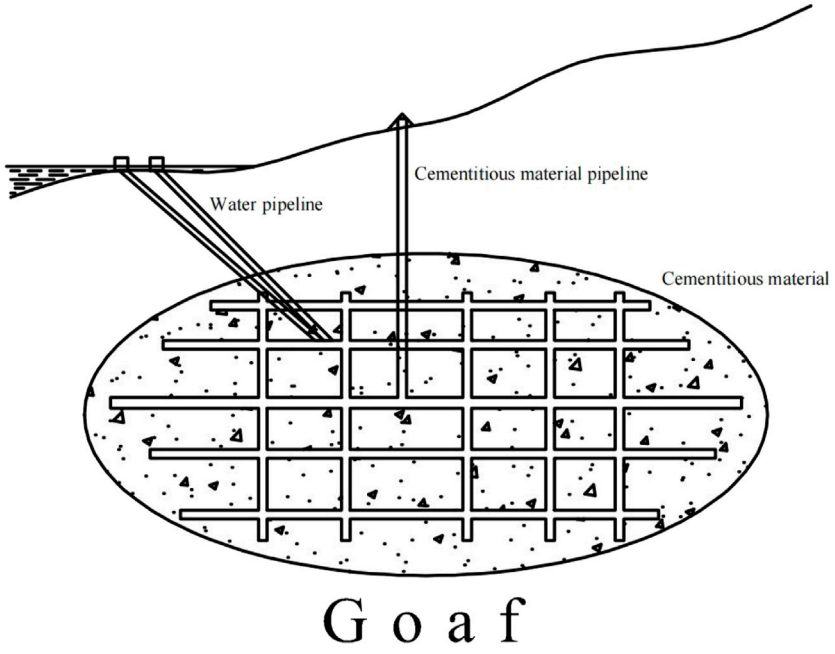

FIGURE 1
Schematic diagram of goaf filling.

2 Research on the formulation of phosphogypsum-based cementitious materials

2.1 Strength test of cemented fillings with different fineness of cementitious materials

The research results show that for the development of new cementitious materials based on slag micropowder, the strength of the cemented backfill is not only related to the properties of the backfill aggregate, mortar ratio, and slurry concentration, but also to the quality, activity, micropowder fineness, gradation, and excitation of the slag. Formulations are closely related. Therefore, tests are carried out on the strength of cemented fillings with different finenesses of cementitious materials.

In the laboratory, an ND6-4L small ball mill was used to grind the original slag micropowder of Jiugang Company for 30 min, 60 min, and 90 min, respectively, and three kinds of slag micropowder with different finenesses were obtained. After grinding for 30 , 60 , and 90 min, the average particle size was 20.00 microns, 15.88 microns, and 12.26 microns, respectively, which were 17.5%, 38.6%, and 52.8% lower than the original slag powder particle size of 24.31 microns, respectively. The content of slag with a particle size larger than 45 microns was 10.2%, 8.0%, and 3.9%, respectively.

The original slag powder, the medium-fine slag powder (ground for 60 min), and the ultra-fine slag powder (ground for 90 min) of Jiuzhou Iron and Steel Co., Ltd., Were selected to carry out the strength test of the cemented filling body of phosphogypsum-based filling cementitious materials. The test aggregate is the coarse aggregate of crushed waste rock in Longshou Mine, the test mortar ratio is 1:4, and the slurry mass concentration is 80%.

2.1.1 Analysis of test results of original fineness phosphogypsum-based cementitious materials

It can be seen from Table 1 that the maximum strength of the cemented backfill at 3 days is 0.70 MPa, which is 63% of the cement cementitious material. The maximum strength of the cemented backfill at 7 days is 3.80 MPa, which is 1.9 times that of the cement cementitious material. It can be seen from Table 2 that the main factor affecting the strength of the cemented backfill at 3 and 7 days is quicklime. The quicklime, NaOH, and Glauber's salt in the optimal formula for 3 and 7 days are the same, 5.5%, 2.0%, and 3.0% respectively, but the phosphogypsum is different, being 30% for 3 days and 33% for 7 days.

2.1.2 Analysis of test results of medium fineness phosphogypsum-based cementitious materials

It can be seen from Table 1 that the maximum strength of the cemented backfill at 3 days is 1.09 MPa, which is equivalent to 87% of the cement strength, and which is 56% higher than the

TABLE 1 Orthogonal test results of filling body strength.

Numbering	Quicklime/%	Phosphogypsum/%	NaOH/%	Glauber's salt/%	Undisturbed slag powder/%	Original fineness compressive strength/MPa		Medium fineness compressive strength/MPa		Superfineness compressive strength/MPa	
						3d	7d	3d	7d	3d	7d
A1	5.5	30	1.5	2.0	61	0.70	3.32	0.42	4.72	0.24	6.32
A2	5.5	33	2.0	2.5	57	0.54	3.62	0.79	5.84	0.69	6.40
A3	5.5	36	2.5	3.0	53	0.46	3.80	0.80	5.26	1.26	5.84
A4	6	30	2.0	3.0	59	0.57	3.65	0.54	6.23	0.70	4.56
A5	6	33	2.5	2.0	56.5	0.20	3.67	1.06	5.02	0.68	6.17
A6	6	36	1.5	2.5	54	0.26	2.67	0.92	1.46	0.48	6.38
A7	6.5	30	2.5	2.5	58.5	0.26	2.53	0.92	4.67	0.53	5.86
A8	6.5	33	1.5	3.0	56	0.35	2.97	0.61	4.15	0.50	6.65
A9	6.5	36	2.0	2.0	53.5	0.33	2.93	1.09	4.72	0.58	5.74
Mean value	6	33	2	2.5	56.5	0.41	3.24	0.81	4.67	0.61	5.99
Jinchuan Mine Cement Cementitious Material	1.11	2.01	1.25	2.32	1.41	2.85					

10.3389/fenvs.2022.1012057

TABLE 2 Orthogonal test range analysis results.

Fineness	Age (d)	Convergence rate	Quicklime	Phosphogypsum	NaOH	Glauber's salt	Factor	Quicklime	Phosphogypsum	NaOH	Glauber's salt
Original fineness	3d	Extremely poor Rj	0.253	0.16	0.173	0.107	Optimal	5.5	30	2	3
		Relative weights	2.4	1.5	1.6	1	formula				
	7d	Extremely poor Rj	0.77	0.287	0.413	0.533	Optimal	5.5	33	2	3
		Relative weights	2.7	1	1.4	1.9	formula				
Medium fineness	3d	Extremely poor Rj	0.203	0.31	0.277	0.227	Optimal formula	6.5	36	2.5	2.5
		Relative weights	1	1.5	1.4	1.1					
	7d	Extremely poor Rj	1.037	1.393	2.153	1.223	Optimal formula	5.5	30	2	3
		Relative weights	1	1.3	2.4	1.2					
Superfineness	3d	Extremely poor Rj	0.193	0.283	0.417	0.32	Optimal formula	5.5	36	2.5	3
		Relative weights	1	1.5	2.2	1.7					
	7d	Extremely poor Rj	0.483	0.827	0.883	0.53	Optimal formula	5.5	33	1.5	2.5
		Relative weights	1	1.7	1.8	1.1					

10.3389/fenvs.2022.1012057

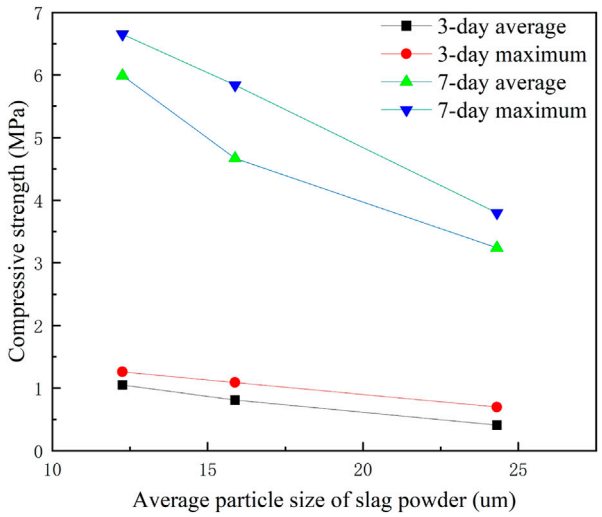

FIGURE 2
The relationship between the strength of the filling body and the average particle size of the powder.

original slag powder strength. At 7 days, the maximum strength of the cemented backfill is 5.84 MPa, which is equivalent to 2.5 times the strength of cement, and is 54% higher than the strength of the original slag powder.

It can be seen from Table 2 that the strength activator of the medium-fine phosphogypsum-based cementitious material changed from the quicklime of the original phosphogypsum-based cementitious material to phosphogypsum at 3 days, and the quicklime in the optimal formula changed from the original 5.5%–6.5%, phosphogypsum changed from 30% to 36%, NaOH changed from 2.0% to 2.5%, and thenardite changed from 3.0% to 2.5%. At 7 days, the strength activator of the medium-fine phosphogypsum-based cementitious material changed from the quicklime of the original phosphogypsum-based cementitious material to NaOH, and the quicklime phosphogypsum in the optimal formula changed from the original 33%–30%, while the others remained unchanged.

2.1.3 Analysis of test results of ultrafine phosphogypsum-based cementitious materials

It can be seen from Table 1 that the maximum strength of the cemented backfill at 3 days is 1.26 MPa, which is equivalent to 89% of the cement strength, 80% higher than the original slag powder strength, and 15% higher than the medium and fine slag powder strength. At 7 days, the maximum strength of the cemented backfill is 6.65 MPa, which is 2.1 times that of cement, 58% higher than that of undisturbed slag powder, and 2% higher than that of medium and fine slag powder.

It can be seen from Table 2 that the strength activator of the ultra-fine phosphogypsum-based cementitious material changed from the phosphogypsum of the medium-fine phosphogypsum-based cementitious material to NaOH at 3 days, and the optimal formula was from the quicklime of the medium-fineness, which changed from 6.5% to 5.5%, and thenardite 2.5% became 3.0%. At 7 days, the strength activator of ultra-fine phosphogypsum-based cementitious material is the same as that of medium-fine phosphogypsum-based cementitious material. The optimal formula changes from 30% of phosphogypsum in medium-fineness to 33%, 2.0% of NaOH changes to 1.5%, and 3.0% of Glauber's salt changes to 2.5%.

2.1.4 Comprehensive analysis of phosphogypsum-based cementitious materials with different fineness

Comprehensive analysis was carried out on the 3-days and 7-days data obtained from the above three different fineness phosphogypsum-based cementitious materials cemented backfill strength tests. From this the following conclusions are drawn:

(1) It can be seen from Figure 2 that the strength of the cemented filling body of phosphogypsum-based cementitious material decreases linearly with the increase of the average particle size of the powder at 3 days.

(2) It can be seen that the average particle size of the filling body is 12.26 μm when the strength is the highest, that is, the ultra-fine slag powder. However, when the average particle size is 15.88 μm, that is, the medium-fine slag powder, the strength of the backfill at 3 days is only 13.5% lower than that of the ultra-fine slag powder. Therefore, increasing the grinding time of the slag powder will not only increase the cost, but also have little effect on the increase of strength. Therefore, the average particle size of the slag powder is 15.88 μm, that is, the medium and fine slag powder, is best. Therefore, the average particle size of slag micropowder is less than 16 μm, and the content of slag micropowder +45 μm is less than 8%, corresponding to a 3-days average strength of 0.81 MPa and 7-days average strength of 4.67 MPa.

2.2 Experiment on the effect of external agents on phosphogypsum filling cementitious materials

It can be seen from the above test that the strength at 3 days still cannot meet the requirements of Jinchuan Mine for cementitious materials, and adding appropriate additives will be a good choice. To this end, orthogonal experiments

TABLE 3 Orthogonal test results of filling body strength.

Numbering	Grinding aid		Stimulating agent/%		Phosphogypsum-based materials (100%)/%			Compressive strength/MPa	
	Product	Addition amount/%	Glauber's salt	NaOH	Quicklime	Phosphogypsum	JISCO Slag Powder	3d	7d
A1	SA115	0.05	1	0.0	6	34	60	0.46	3.46
A2	SA115	0.10	2	0.5	6	34	60	0.85	2.68
A3	SA115	0.15	3	1.0	6	34	60	0.71	3.17
A4	SA117	0.05	2	1.0	6	34	60	1.21	2.86
A5	SA117	0.10	3	0.0	6	34	60	0.75	3.57
A6	SA117	0.15	1	0.5	6	34	60	0.50	2.06
A7	SA119	0.05	3	0.5	6	34	60	0.83	2.76
A8	SA119	0.10	1	1.0	6	34	60	0.60	2.82
A9	SA119	0.15	2	0.0	6	34	60	0.68	3.45
average value	0.10	2	0.5	6	34	60	0.73	2.98	

Note: The added amount of grinding aid and stimulant is the percentage of phosphogypsum-based material.

10.3389/fenvs.2022.1012057

TABLE 4 Orthogonal test results of filling body strength.

Numbering	Grinding aid SA117/%		Compound early strength stimulant*/%		Phosphogypsum-based materials (100%)/%			Compressive strength/MPa	
	Glauber's salt		NaOH	NaCl	quicklime	Phosphogypsum	JISCO Slag Powder	3d	7d
B1	0.05	1	0.5	1.0	6	34	60	0.98	4.12
B2	0.05	1	1.0	1.5	6	34	60	1.67	5.25
B3	0.05	1	1.5	2.0	6	34	60	1.82	4.61
B4	0.05	2	0.5	1.5	6	34	60	1.69	5.59
B5	0.05	2	1.0	2.0	6	34	60	1.73	5.15
B6	0.05	2	1.5	1.0	6	34	60	1.53	2.63
B7	0.05	3	0.5	2.0	6	34	60	1.51	3.66
B8	0.05	3	1.0	1.0	6	34	60	1.46	3.06
B9	0.05	3	1.5	1.5	6	34	60	1.82	2.82
Mean value	0.05	2	1.0	1.5	6	34	60	1.58	4.10

Note: The added amount of grinding aids and early strength stimulators are the percentages of phosphogypsum-based materials.

10.3389/fenvs.2022.1012057

will be carried out for different admixtures, and appropriate admixtures will be selected to improve the strength of phosphogypsum-based cementitious materials.

2.2.1 Influence of grinding aids on phosphogypsum-based cementitious materials

A grinding aid is used to make the grinding fineness finer when the ball mill is grinding, thereby improving the mechanical properties of the cementitious material. In order to choose the grinding aid more suitable for JISCO slag, three grinding aids, SA115, SA117, and SA119, provided by Beijing Yuanxin Tongxin Technology Co., Ltd., were used to carry out the orthogonal test of the strength of phosphogypsum-based cementitious materials.

According to the filling system and process parameters of Longshou Mine in the Jinchuan Mine, the aggregate is a coarse aggregate of waste rock, a cement-sand ratio of 1:4, and a slurry concentration of 80%. According to the strength test of cemented backfill with different fineness cementitious materials, the fineness of phosphogypsum cementitious material is determined as medium fineness, with 6% quicklime, 34% phosphogypsum, and 60% slag powder. Since mirabilite excitation and NaOH alkali excitation may have compound effects with grinding aids, orthogonal tests of four factors and three levels of grinding aid product, grinding aid addition, and thenardite and NaOH were carried out.

It can be seen from Table 3 that the maximum compressive strength at 3 days is 1.21 MPa, while the maximum strength of the medium-fine phosphogypsum-based cementitious material is 1.26 MPa. It can be seen that only adding grinding aids has little effect on the strength of the filling. Among them, the SA117 grinding aid had the best effect on strength at 3 days.

2.2.2 Experiment on the effects of early strength agents on phosphogypsum-based cementitious materials

Since the addition of grinding aids has little effect on phosphogypsum-based cementitious materials, an experiment on the effects of early strength agents on phosphogypsum-based cementitious materials was carried out. The aggregate, mortar ratio, and slurry concentration tested were the same as in the above test. According to the test results of the above 3 days, SA117 was used as the grinding aid, and the dosage was 0.05%. The compound early-strength activator was designed by a three-level orthogonal design of Glauber's salt, NaOH, and NaCl.

It can be seen from Table 4 that the maximum strength of the filling body is 1.82 MPa at 3 days, and the maximum strength of the filling body is 5.59 MPa at 7 days. The composite early strength agent can significantly improve the strength of the filling body. The average strength of the filling body was 1.58 MPa at 3 days, and the average strength of the filling body at 7 days was 4.1 MPa.

3 Study on hydration mechanism of phosphogypsum-based cementitious materials

3.1 Chemical reactions in the hydration process of cementitious materials

The strength formation process of the new early-strength cementitious material is the hydration process of the new cementitious material, which is a very complex physical and chemical change process. In recent years, a lot of research has been done on the hydration mechanism of slag cementitious materials. It is generally believed that water-quenched slag is a potentially active vitreous structure. This vitreous body contains a high crystallinity energy, but the hydration speed in pure water is very high. Add water slowly, because the water-quenched slag will form a dense and indeterminate acidic film on the particle surface after contact with water. The main purpose of the hydration of water-quenched slag is to destroy the acidity of the glassy surface of the water-quenched slag under the excitation of the activator, causing the protective film to disperse, dissolve, and hydrate the water-quenched slag glass body. This is the reason why the water-quenched slag has no activity at normal temperature of pure water, but can have higher gelling performance under the excitation of alkaline solution, so it is necessary to add an activator for excitation, which is indispensable.

3.1.1 Chemical composition of raw materials for cementitious materials

It can be seen from the above experiments that the optimal formula for preparing phosphogypsum-based cementitious materials based on JISCO slag is: quicklime 5.5%–6.0%, phosphogypsum 30%–33%, NaOH 1.5%–2.0%, and Glauber's salt 2.5%–3%. Water-quenched slag, also known as slag or iron slag, is the solid waste discharged during the ironmaking process, and its main chemical composition is CaO accounts for 37.78%, SiO_2 accounts for 37.55%, Al_2O_3 accounts for 11.06%, and MgO accounts for 7.65%. Jiugang slag is the main component of our phosphogypsum-based filling cementitious material, and also the main material of the hydration reaction.

Phosphogypsum is an industrial by-product of the wet process production of phosphoric acid in phosphorus chemical enterprises. The main component of phosphogypsum is calcium sulfate dihydrate ($CaSO_4{\cdot}2H_2O$). Phosphogypsum also contains many other impurities. The chemical composition of phosphogypsum discharged from Jinchang Wengfu Chemical Plant is: 49% $CaSO_4$, 29% CaO, 2% MgO, and 2% P_2O_5. Phosphogypsum participates in the hydration reaction of the new cementitious material and acts as an activator.

The main component of quicklime is calcium oxide (CaO). Quicklime participates in the hydration reaction of the new cementitious material and acts as an activator. Glauber's salt,

also known as sodium sulfate, mirabilite, horse's tooth salt, sodium nitrate, or pot salt, has the chemical composition of sodium sulfate decahydrate ($Na_2SO_4{\cdot}10H_2O$). Glauber's salt participates in the hydration reaction of the new cementitious material and acts as an early-strength agent. NaOH, sodium hydroxide, commonly known as caustic soda, is easily soluble in water and forms an alkaline solution. NaOH participates in the hydration reaction of the new gelling material and acts as an early-strength agent.

3.1.2 Chemical reaction of alkali excitation

First of all, the alkaline solution formed by calcium oxide (CaO) in the slurry when it meets water creates favorable conditions for the dispersion and dissolution of the water-quenched slag glassy body. Calcium oxide (CaO) reacts with water to form calcium hydroxide $Ca(OH)_2$, which produces a large amount of Ca^{2+} ions and OH^- ions in the slurry. The reaction method is as follows:

$$CaO + H_2O \rightarrow Ca(OH)_2$$

The Ca^{2+} ions and OH^- ions in the slurry enter the protective film on the surface of the water-quenched slag, and the surface of the slag will form a layer of alkaline film solution containing Ca^{2+} ions and OH^- ions. The concentration of OH^- ions in the slurry is very large, and it is easier than water molecules to enter the internal cavities of the slag glassy network structure, thereby promoting the dispersion, dissolution, and hydration of the water-quenched slag. The hydration process of the water-quenched slag is firstly the pozzolanic reaction of active SiO_2, Al_2O_3, and $Ca(OH)_2$ in the water-quenched slag, resulting in the formation of calcium silicate hydrates gel (C-S-H) and calcium aluminate hydrates gel (C-A-H), respectively, which reacts as follows:

$$\text{Active } SiO_2 + m_1Ca(OH)_2 + nH_2O \rightarrow m_1CaO \cdot SiO_2 \cdot nH_2O$$
$$\text{Active } Al_2O_3 + m_2Ca(OH)_2 + nH_2O \rightarrow m_2CaO \cdot Al_2O_3 \cdot nH_2O$$

With the continuous supply of water in the slurry, the pozzolanic reaction continues until the slag is fully hydrated.

3.1.3 Chemical reaction of salt excitation

Since the filling material contains a large amount of phosphogypsum ($CaSO_4{\cdot}2H_2O$), the phosphogypsum can act as a sulfate activator, and calcium sulfate reacts with the formed calcium aluminate hydrates gel (C-A-H) to generate calcium sulfoaluminate hydrates ($3CaO{\cdot}Al_2O_3{\cdot}3CaSO_4{\cdot}32H_2O$), namely ettringite (AFt, or alumina, ferric oxide, tri-sulfate), and has the following chemical reaction formula:

$$3CaO \cdot Al_2O_3 \cdot 6H_2O + 3CaSO_4 + 26H_2O \rightarrow 3CaO \cdot Al_2O_3 \cdot 3CaSO_4 \cdot 32H_2O$$

Due to the formation of ettringite, the calcium aluminate hydrate, the main hydration product of slag hydration, is consumed, the moisture in the slurry is absorbed, and the hydration and hardening process of the slag is accelerated. In conclusion, the main products of the hydration reaction are calcium silicate hydrates gel (C-S-H) and ettringite (AFt).

3.1.4 Analysis on formation mechanism of backfill strength

During the hydration process in the early alkaline environment, the active silicon dioxide (SiO_2) and aluminum oxide (Al_2O_3) in the water-quenched slag were continuously dissolved from the glassy body and participated in the hydration reaction, resulting in the formation of calcium silicate hydrates condensate gel (C-S-H) and calcium aluminate hydrates gel (C-A-H). These reactions, as well as the reaction between calcium oxide and water, absorbed a large amount of free water, and the resulting gel components, the micropowder, and aggregate bonded together, which provided the early strength, but the whole system was weak during this period. There are also a large number of voids, and the large number of voids and the fragile substances on the surface reduce the strength of the filling body, so the strength is not high. With the gradual increase of reaction products and the action of sulfates such as phosphogypsum, as the calcium aluminate hydrates gel (C-A-H) continuously reacts with $CaSO_4{\cdot}2H_2O$ to form hydraulic ettringite ($CaO{\cdot}Al_2O_3{\cdot}3CaSO_4{\cdot}32H_2O$, AFt), the hydration products gradually increase, the quantity of free water gradually decreases, the ettringite and calcium silicate hydrates gel are intertwined to fill the voids, and the slurry hardens, the structure of the filling body is gradually more dense, and the strength of the filling body increases. In later stages, with the passage of time, the strength will increase steadily and slowly, and the structure will become denser and denser, which will further improve the compactness and mechanical strength of the filling body, so that it can reach a higher strength and form a filling with higher strength and a hardened body.

3.1.5 Mechanism analysis of early strength of NaOH and Glauber's salt

Because the solubility of the alkali $Ca(OH)_2$ is small, the OH^- concentration in the solution is low, so the hydration rate of the slag is very slow. After adding NaOH, the concentration of OH^- in the solution is greatly increased, which not only accelerates the dissolution of slag and the depolymerization of ion groups, but also accelerates the hydration of slag, so a large amount of ettringite (AFt) and calcium aluminate hydrates gel (C-A-H) improves the early strength of the new gelling material and shortens the setting time. Because the phosphogypsum ($CaSO_4{\cdot}2H_2O$) in the filling material dissolves slowly in water, it affects the hydration of the $CaSO_4$ and C-A-H gel in the early stage of hydration, and the formation of ettringite is minor at first, which makes the early strength of the filling body low. After adding Glauber's salt ($Na_2SO_4{\cdot}10H_2O$), the Glauber's salt will

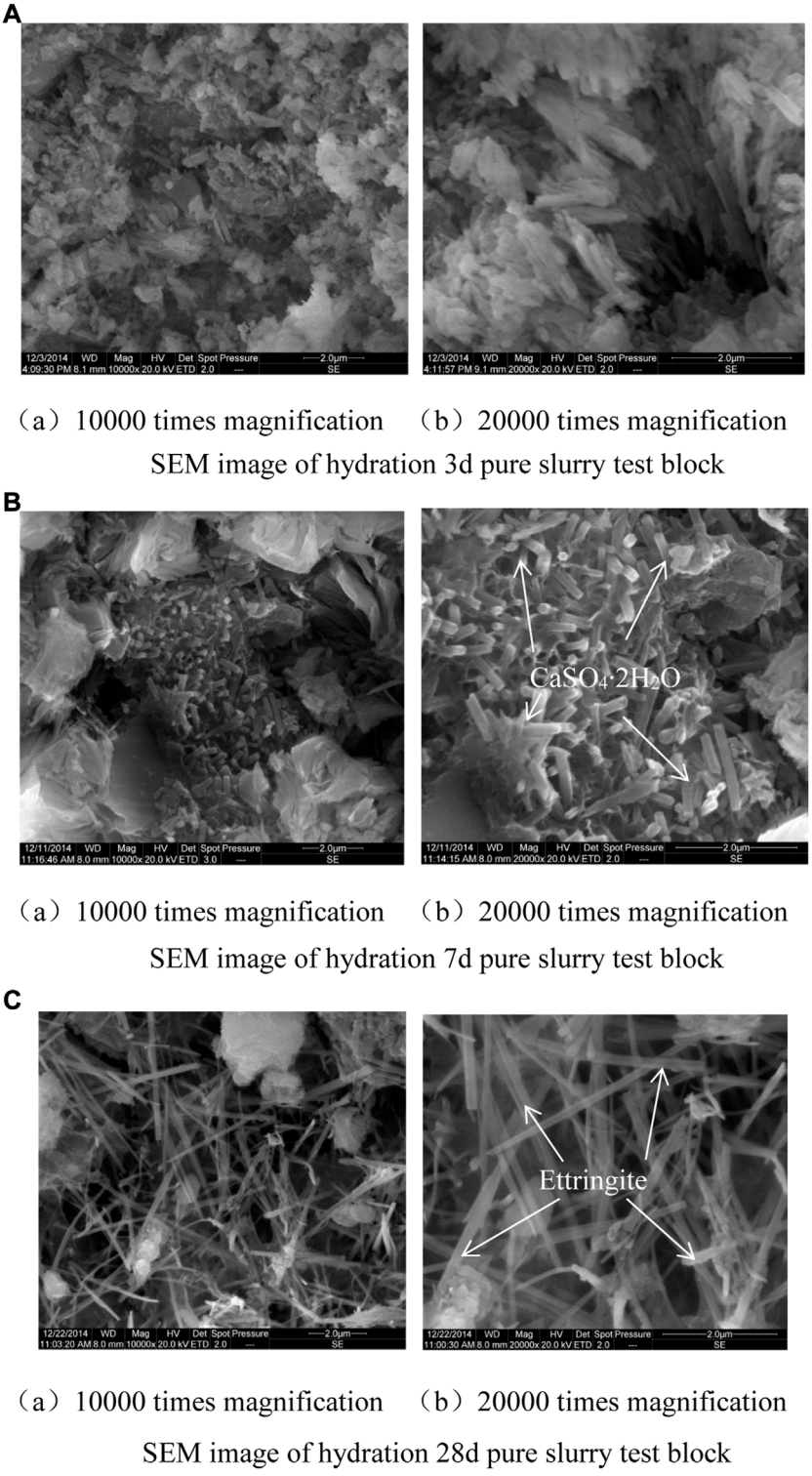

FIGURE 3
SEM image of new cementitious material. **(A)** SEM image of hydration 3d pure slurry test block. **(B)** SEM image of hydration 7d pure slurry test block. **(C)** SEM image of hydration 28d pure slurry test block.

quickly dissolve in water and react with calcium hydroxide as follows:

$$Na_2SO_4 + Ca(OH)_2 + 2H_2O \rightarrow CaSO_4 \cdot 2H_2O + 2NaOH$$

The addition of Glauber's salt increases the concentration of $CaSO_4$ and OH^- in the slurry, which provides conditions for the formation of ettringite, accelerates the hydration of slag, and increases the quantity of ettringite in the early stages. Therefore, with the new type of cementitious material, the early strength is improved and the setting time is shortened.

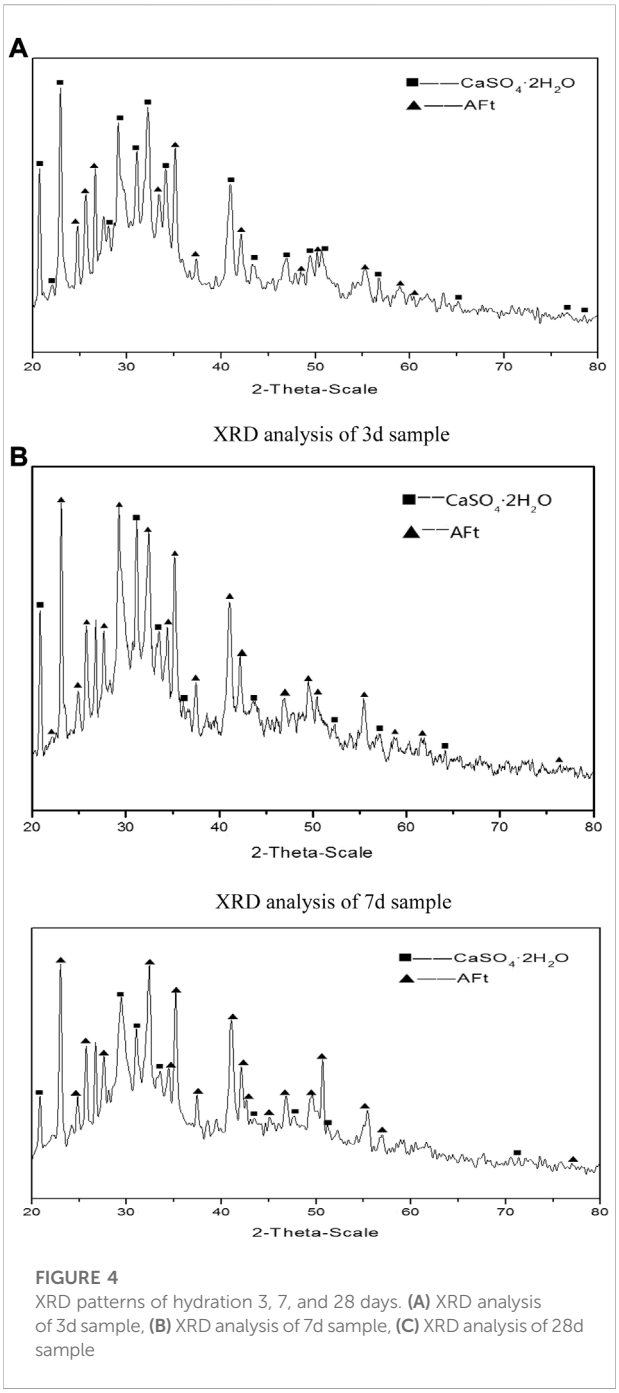

FIGURE 4
XRD patterns of hydration 3, 7, and 28 days. **(A)** XRD analysis of 3d sample, **(B)** XRD analysis of 7d sample, **(C)** XRD analysis of 28d sample

3.2 Scanning electron microscope test of cementitious materials

3.2.1 Scanning electron microscope

(1) Technical parameters of the instrument. The scanning electron microscope used was a scanning electron microscope produced by Beijing Zhongke Instrument Technology Development Co., Ltd., model KYKY-2800B; the resolution is 4.5 nm (tungsten wire cathode); the magnification is 15×-250000×; the electron gun is a forked tungsten wire Cathode; accelerating voltage range 0–30 kV; lens system is a three-stage electromagnetic lens. The purpose is to observe the microstructure and appearance of samples at different ages, and to make semi-quantitative energy spectrum analysis of characteristic substances by electron probes.

(2) The working principle of the instrument. The focused electron beam (5 nm) strikes the surface of the sample, and the surface of the sample is scanned point by point under the action of the deflection coil to excite different secondary signals. The detector collects these signals and converts them into optical signals, and then passes them through the amplifier. The processing is enlarged to a picture tube to form a three-dimensional dynamic image.

(3) Preparation of test pieces. In order to prevent unnecessary interference to the SEM image caused by the addition of aggregates, a pure slurry without aggregates was selected in this test to analyze the test blocks. We prepared a certain concentration of slurry, poured the slurry into a 7.07 × 7.07× 7.07 cm triple test mold, and put it into a constant temperature and humidity curing box (20 ± 1°C, humidity not lower than 90%) for curing. With a hammer, we knocked open the test block of the filling that has been cured to the specified age, retained a small piece from the middle, and immerse it in anhydrous ethanol to stop the hydration reaction, then took it out for surface carbon spray treatment, and then sent it to professionals for SEM test analysis.

3.2.2 Analysis of Scanning electron microscope test results of cementitious materials

First, the new type of cementitious material is made into a pure slurry with a concentration of 78%, then poured into the test block mold, and put into a curing box with constant temperature and humidity for curing. SEM observation. Figure 3 shows the SEM pictures of the pure pulp test block after curing for 3, 7, and 28 days, respectively.

In the SEM image of the new cementitious material, the crystals of calcium sulfate dihydrate ($CaSO_4 \cdot 2H_2O$) are thin and short columns with uniform crystal size, and the ettringite

crystals are needle-shaped. It can be seen from Figure 3 that there are unreacted slag particles, dihydrate phosphogypsum crystals, and ettringite, C-S-H gel generated by the hydration reaction in the filling body, and C-S-H gel covers the slag particles, dihydrate phosphogypsum crystals, and the surface of the ettringite, the filling body takes the ettringite crystals and wollenite as a skeleton to form a strong structure, and the strength of the filling body mainly comes from this formed structure.

After 3 days of hydration, the filling of the cementitious material has produced a large amount of hydration products, and some acicular (needle-like) substances have grown radially, so that the filling cementitious material has a relatively good early strength. However, its shape is still relatively coarse, the amount of ettringite generated is relatively small, and it is not separated from other generated substances and original substances, that is, the development of ettringite is not very good at this time, and the crystal size is small, which offers less support. At the same time, a small amount of amorphous C-S-H gel can be seen on the surface of the slag.

After 7 days of hydration, the hydration has been very deep, resulting in a large quantity of dense amorphous C-S-H gel; the number and size of acicular ettringite crystals has further increased, and cross-filled in larger pores to form a relatively tight network At the same time, it can be seen that the needle-like crystals of ettringite are relatively short, that is, the formation process of ettringite is still in progress; the co-growth and combination of ettringite, the amorphous C-S-H gel that makes up the gelling material, and the hydration products have gradually intertwined, and the structure is much denser than that of at 3 days, so that the strength is also greatly improved compared to that of 3 days.

After 28 days of hydration, the filling cementitious material undergoes a large degree of hydration reaction. At this time, the ettringite is more fully developed, and the crystals are more slender. They grow and overlap each other in the filling sample, and grow alternately with the amorphous C-S-H gel. The final formed C-S-H gel and the slender and coarse ettringite crystals are intertwined and have filled in the pores of the filling body, intertwined into a dense internal structure, and no obvious gap can be seen. The compressive strength of the filling body test block at this time is already high.

3.3 XRD test of cementitious material

3.3.1 X-ray diffractometer

(1) Technical parameters of the instrument. The X-ray diffractometer used is a D8 ADVANCE, the maximum output power is ≥ 2.2 kW; the Cu target is used as the radiation source; the scanning angle range is $2\theta = --110–168^{\circ}$; the maximum positioning speed is ≥ 1,500°/min; the light pipe power is 2.2 kW; Long fine focal spot 0.4 × 12 mm; Maximum tube pressure 60 kV; Maximum tube flow 80 mA.

(2) The working principle of the instrument. Using the X-ray diffraction wave, when it is projected onto the sample, a discontinuous diffraction pattern will be generated due to the relative position of the single atom and its scattering ability. The diffraction pattern of a substance can be characterized by its angular position, symmetry relationship, and Bragg reflection intensity, and the phase and structure of the crystal can be analyzed by using the diffraction data.

(3) Preparation of test pieces. In order to prevent the unnecessary interference of the addition of aggregates to the XRD spectrum analysis process, a pure slurry without aggregates was used in this experiment, and test blocks were made for analysis. The filling cementitious material was made into pure slurry of a certain ratio and concentration, and a test block was made. The test block was cured in a standard curing box. After curing to a specified age, the test block was taken out, and the carbonized layer on the surface of the test block was removed. It was immediately soaked in pure ethanol for 24 h to stop the hydration reaction of the test block. The test block was taken out and dried, and then subjected to XRD diffraction analysis.

3.3.2 Analysis of XRD test results of cementitious materials

According to the optimal ratio of phosphogypsum-based new cementitious materials (5.5%–6.0% quicklime, 30%–33% phosphogypsum, 1.5%–2.0% NaOH, and 2.5%–3% mirabilite), the production concentration is a 78% slurry, poured into a module, and then put into a curing box for curing. After curing to the corresponding age, we stopped the hydration and made samples, and then conducted XRD diffraction analysis.

The XRD diffractometer model used in this experiment was a D8 ADVANCE. Test conditions: 2-Theta angle range (scanning range) is 20°–80°; scanning speed is 1°/min; scanning mode is continuous scanning. The XRD patterns of hydration at 3, 7, and 28 days are shown in Figure 4.

(1) It can be seen from the XRD analysis diagram of hydration 3 days in Figure 4 that the three strong peaks of the XRD pattern are expressed as $CaSO_4{\cdot}2H_2O$, the main component of phosphogypsum, indicating that after the hydration reaction has been carried out for 3 days, the amount of phosphogypsum involved in the hydration reaction was a bit less. From the intensity of the diffraction peaks, it can be seen that $CaSO_4{\cdot}2H_2O$ is the main component of the cementitious material, and while ettringite is also formed after the hydration reaction, the intensity of its diffraction peaks is low, and the proportion of components in the filling is relatively small. The formation of ettringite still provides support for the early strength.

(2) It can be seen from the XRD analysis diagram of hydration 7 days in Figure 4 that the intensity of the diffraction peak of

ettringite has greatly increased compared with that of 3 days, while the intensity of the corresponding diffraction peak of $CaSO_4·2H_2O$ has weakened. The progress of the hydration reaction is as has been described above. The ettringite occupies a large amount in the filling body, which greatly improves the strength of the filling body at 7 days.

(3) It can be seen from the XRD analysis diagram of 28 days hydration in Figure 4 that when the hydration reaction is carried out for 28 days, the state of the diffraction peak is basically opposite to that of the diffraction peak at 3 days. At this time, the three strong peaks of the XRD pattern are ettringite, that is, that now ettringite accounts for most of the filling body.

(4) It can be seen from the comparison in Figure 4 that as the hydration time continues to increase, the diffraction peak of phosphogypsum ($CaSO_4·2H_2O$) in the filling body is constantly weakening, which indicates that the content of phosphogypsum in the cementitious material is constantly decreasing, which provides a strong proof for the participation of phosphogypsum in the hydration reaction.

(5) After the hsydration reaction for 3 days, $Ca_6Al_2(SO_4)_3(OH)_{12}·26H_2O$ (ettringite AFt) is formed, and the formation of ettringite is the main reason for the high early strength of the filling cementitious material. From the XRD patterns of 3, 7, and 28 days, it can be seen that the diffraction peak intensity of hydration product ettringite is continuously increasing, and the increasing hydration product ettringite provides a strong support for the later higher strength of the filling cementitious material.

(6) According to the dispersion peak in Figure 4, it can be seen that with the increase of hydration reaction time, the dispersion peak gradually weakens, but it increases at 28 days. It shows that with the increase of hydration reaction time, the hydration process of the slag is accelerating, and the content of slag is decreasing. The enhancement of the 28 days dispersion peak indicates that a large quantity of amorphous C-S-H gel appeared in the hydration product at this time, which led to the appearance of dispersion peaks in the XRD pattern.

(7) The main hydration products of the filling cementitious material are ettringite and amorphous C-S-H gel, which provide the main support for the strength of the cementitious material.

4 Conclusion

In order to eliminate the serious risks posed by the goaf, the orthogonal test of the backfill strength of three different slag fine powders and two different admixtures for the preparation of phosphogypsum-based cementitious materials from Jiugang slag was carried out. The optimal formulation of the new cementitious material, and then based on this, the hydration reaction mechanism was studied by SEM and XRD. We have concluded as follows:

(1) A new type of backfilling cementitious material prepared from phosphogysum and JISCO slag was developed, and its formula is 5.5%–6.0% quicklime, 30%–33% phosphogypsum, 1.5%–2.0% NaOH and 2.5%–3% mirabilite, and the average particle size is 15.88 um. Compared with the traditional use of cement as filling material, not only the cost is greatly reduced, but also the accumulation and discharge of wastes such as phosphogypsum and slag are solved.

(2) The strength of this new type of cementitious material is 1.58 MPa at 3 days and 4.1 MPa at 7 days, when adding proper amount of grinding aid and early strength agent. It can play a supporting role in the goaf timely, prevent collapse of the goaf, and significantly reduce the risk of geological disasters such as subsidence and landslide in the goaf.

(3) Through the observation and analysis of hydration mechanism of phosphogypsum based filling cementitious materials, it is found that with the increase of age, the amount of hydrated calcium silicate gel (C-S-H) and Ettringite (AFT) is increasing, and the structure is gradually dense. The hydrated calcium silicate gel plays a role of filling adhesion in the filling body, and Ettringite plays a role of interspersed support in the filling body. It provides reference value for the development and deepening of follow-up scientific research.

Data availability statement

The original contributions presented in the study are included in the article/Supplementary Material, further inquiries can be directed to the corresponding author.

Author contributions

XY (Associate Professor) and YJ (Postgraduate) designed the research plan, accomplished its processes, and wrote the manuscript. CY (Professor), XH (Associate Professor), YJ (Associate Professor), and LX (Associate Professor) reviewed the manuscript.

Funding

Key scientific research project of colleges and universities in Henan Province in 2022: Research on remote monitoring and early warning technology of filling pipeline transportation system in nonferrous metal mines (22A130005). The 61st batch of high-level talents

scientific research start-up project of North China University of Water Resources and Electric Power (201803002).

Conflict of interest

The authors declare that the research was conducted in the absence of any commercial or financial relationships that could be construed as a potential conflict of interest.

Publisher's note

All claims expressed in this article are solely those of the authors and do not necessarily represent those of their affiliated organizations, or those of the publisher, the editors and the reviewers. Any product that may be evaluated in this article, or claim that may be made by its manufacturer, is not guaranteed or endorsed by the publisher.

References

Bouchhima, L., Rouis, M. J., and Choura, M. (2017). A study of compaction pressure influence on properties of phosphogypsum-based bricks. *Rev. Romana Mater. Rom. J. Mater.* 47 (4), 476–483.

Cao, B. (2018). Study on factors affecting the strength of phosphogypsum-based composite cementitious materials. *New Build. Mater.* 45 (03), 23–26. doi:10.3969/j.issn.1001-702X

Chen, W., Tang, Y., Tian, J., Li, B., and Fan, J. (2016). Preparation and properties of polyaluminum modified phosphogypsum-based supersulfur slag cementitious materials. *J. Wuhan Univ. Technol.* 38 (02), 1–6.

Cui, X. W., Di, Y. Q., Wang, C. L., Wang, Y. B., Zhang, S. H., Zhai, Y. X., et al. (2021). Preparation and performance of vanadium tailings-reservoir sedimentphosphogypsum-based foamed concretevol. *Math. PROBLEMS Eng.*, 1–11. doi:10.1155/2021/8468063

Du, Y., Xie, M., Jiang, Y., Li, B., and Chicas, S. (2017). Experimental rock stability assessment using the frozen–thawing test. *Rock Mech. Rock Eng.* 50, 1049–1053. doi:10.1007/s00603-016-1138-2

Du, Y., Xie, M., and Jia, J. (2020). Stepped settlement: A possible mechanism for translational landslides. *Catena* 187, 104365. doi:10.1016/j.catena.2019.104365

Du, Y., Xie, M., Jiang, U., Chen, C., Jia, B., Huo, L., et al. (2021). Review on the formation mechanism and early warning of rock collapse. *Metal. Mine* 535 (01), 106–119. doi:10.5040/9781782259206.ch-016

Du, Y., Li, H., Chicas, S. D., and Huo, L. (2022). Progress and perspectives of geotechnical anchor bolts on slope engineering in China. *Front. Environ. Sci.* 10, 928064. doi:10.3389/fenvs.2022.928064

He, Y., Hua, S., Yao, X., Zhu, H., and Zhang, L. (2012). Preparation and properties of phosphogypsum-slag-based cementitious materials. *Inorg. Salt Ind.* 44 (10), 21–23. doi:10.3969/j.issn.1006-4990.2012.10.006

He, H., Dong, F. Q., He, P., and Xu, L. (2014). Effect of glycerol on the preparation of phosphogypsum-based CaSO4·0.5H2O whiskers. *J. Mat. Sci.* 49, 1957–1963. doi:10.1007/s10853-013-7825-4

Hua, S. D., Wang, K. J., and Yao, X. (2016). Developing high performance phosphogypsum-based cementitious materials for oil-well cementing through a step-by-step optimization method. *Cem. Concr. Compos.* 72, 299–308. doi:10.1016/j.cemconcomp.2016.05.017

Huang, Y., and Lin, Z. (2010). Effect of sodium hydroxide on the properties of phosphogypsum based cement. *J. Wuhan Univ. Technol. Mater. Sci. Ed* 25 (2), 342–345. doi:10.1007/s11595-010-3342-7

Li, X., Zhou, S., Zhou, Y., Min, C., Cao, Z., Du, J., et al. (2019). Durability evaluation of phosphogypsum-based cemented backfill through drying-wetting cycles. *MINERALS* 9, 321. doi:10.3390/min9050321

Li, B., Zhang, G., Wang, G., and Qiao, J. (2022). Damage evolution of frozen-thawed granite based on high-resolution computed tomographic scanning. *Front. Earth Sci. (Lausanne).* 10, 912356. doi:10.3389/feart.2022.912356

Liu, S. H., Wang, L., and Yu, B. Y. (2019). Effect of modified phosphogypsum on the hydration properties of the phosphogypsum-based supersulfated cement. *Constr. Build. Mater.* 214, 9–16. doi:10.1016/j.conbuildmat.2019.04.052

Luo, H., Zhu, H. P., Zi, J. M., and Lu, Y. F. (2013). Application research on anti-cracking agent for semi-rigid base. *J. Test. Eval.* 41, 103905. doi:10.1520/JTE103905

Luo, S., Fu, R., Sun, D., Xie, L., Zhou, Y., and Zhao, Y. (2020). Review on the effect of admixtures on water resistance and strength of phosphogypsum-based composite cementitious materials. *Inorg. Salt Ind.* 52 (11), 6–11. doi:10.11962/1006-4990.2020-0029

Min, C. D., Li, X. B., He, S. Y., Zhou, S. T., Zhou, S., Yang, S., et al. (2019). Effect of mixing time on the properties of phosphogypsum-based cemented backfill. *Constr. Build. Mater.* 210, 564–573. doi:10.1016/j.conbuildmat.2019.03.187

Mohammed, F., Biswas, W. K., Yao, H. M., and Tade, M. (2018). Sustainability assessment of symbiotic processes for the reuse of phosphogypsum. *J. Clean. Prod.* 188, 497–507. doi:10.1016/j.jclepro.2018.03.309

Pinto, S., Angulski da Luz, C., Munhoz, G., and Medeiros-Junior, R. (2020). Durability of phosphogypsum-based supersulfated cement mortar against external attack by sodium and magnesium sulfate. *Cem. concerte Res.* 136, 106172. doi:10.1016/j.cemconres.2020.106172

Rosales, J., Perez, S. M., Cabrera, M., Gázquezd, M. J., Bolivar, J. P., Brito, J., et al. (2020). Treated phosphogypsum as an alternative set regulator and mineral addition in cement production. *J. Clean. Prod.* 244, 118752. doi:10.1016/j.jclepro.2019.118752

Sun, T., Hu, T., Wang, G. M., Shui, Z., Ge, K., Dai, Q., et al. (2020). Influence of clinker and SCMs on soluble chemicals and expansion of phosphogypsum-based cementitious materials. *J. Test. Eval.* 48, 20190127. doi:10.1520/JTE20190127

Sun, M., Liang, H., Zhu, Y., Gao, X., Liu, H., and Zhu, Z. (2022). Deformation and failure mode analysis of the tunnel structure based on the tunnel-related landslides cases. *Front. Earth Sci. (Lausanne).* 10, 906884. doi:10.3389/feart.2022.906884

Sun, X. (2020). *Properties of calcined phosphogypsum-slag-alkaline activator cementitious materials [D]*. Zhengzhou, China: Zhengzhou University. doi:10.27466/d.cnki.gzzdu.2020.002056

Szajerski, P., Bogobowicz, A., Bem, H., and Gasiorowski, A. (2019). Quantitative evaluation and leaching behavior of cobalt immobilized in sulfur polymer concrete composites based on lignite fly ash, slag and phosphogypsum. *J. Clean. Prod.* 222, 90–102. doi:10.1016/j.jclepro.2019.03.010

Wang, Q., Cui, Y., and Xue, J. F. (2020). Study on the improvement of the waterproof and mechanical properties of hemihydrate phosphogypsum-based foam insulation materials. *Constr. Build. Mater.* 230, 117014. doi:10.1016/j.conbuildmat.2019.117014

Xiao, W., Yao, X., and Zhang, F. Y. (2019). Recycling of oily sludge as a roadbed material utilizing phosphogypsum-based cementitious materials. *Adv. Civ. Eng.* 2019, 1–10. doi:10.1155/2019/6280715

Yin, T. B., Yang, R. S., Du, J., and Shi, Y. (2019). Effects of acid and phosphate on arsenic solidification in a phosphogypsum-based cement backfill process. *RSC Adv.* 9, 28095–28101. doi:10.1039/c9ra04624k

Zhang, L., Niu, F., Liu, M., Ju, X., Wang, Z., Wang, J., et al. (2022). Fracture characteristics and anisotropic strength criterion of bedded sandstone. *Front. Earth Sci. (Lausanne).* 10, 879332. doi:10.3389/feart.2022.879332

Zhou, S. T., Li, X. B., Zhou, Y. N., Min, C. D., and Shi, Y. (2020). Effect of phosphorus on the properties of phosphogypsum-based cemented backfill. *J. Hazard. Mater.* 399, 122993. doi:10.1016/j.jhazmat.2020.122993

Zhou, J., Li, F., Wang, J., Gao, A., and He, C. (2022). Stability Control of slopes in open-pit mines and resilience methods for disaster prevention in urban areas: A case study of fushun west open pit mine. *Front. Earth Sci. (Lausanne).* 10, 879387. doi:10.3389/feart.2022.879387

frontiers | Frontiers in Environmental Science

TYPE Original Research
PUBLISHED 28 September 2022
DOI 10.3389/fenvs.2022.982069

Check for updates

OPEN ACCESS

EDITED BY
Yan Du,
University of Science and Technology Beijing, China

REVIEWED BY
Qiang Guo,
China Jiliang University, China
Baiyu Chen,
University of California, Berkeley, United States

*CORRESPONDENCE
Hongsheng Liu,
1769303449@qq.com

SPECIALTY SECTION
This article was submitted to Environmental Informatics and Remote Sensing, a section of the journal Frontiers in Environmental Science

RECEIVED 30 June 2022
ACCEPTED 24 August 2022
PUBLISHED 28 September 2022

CITATION
Jiang S, Liu H, Lian M, Lu C, Zhang S, Li J and Li P (2022), Rock slope displacement prediction based on multi-source information fusion and SSA-DELM model.
Front. Environ. Sci. 10:982069.
doi: 10.3389/fenvs.2022.982069

COPYRIGHT
© 2022 Jiang, Liu, Lian, Lu, Zhang, Li and Li. This is an open-access article distributed under the terms of the Creative Commons Attribution License (CC BY). The use, distribution or reproduction in other forums is permitted, provided the original author(s) and the copyright owner(s) are credited and that the original publication in this journal is cited, in accordance with accepted academic practice. No use, distribution or reproduction is permitted which does not comply with these terms.

Rock slope displacement prediction based on multi-source information fusion and SSA-DELM model

Song Jiang[1,2,3], Hongsheng Liu[1,2]*, Minjie Lian[1,4], Caiwu Lu[1,2], Sai Zhang[1,2], Jinyuan Li[1,2] and PengCheng Li[5]

[1]Xi'an University of Architecture and Technology, School of Resources Engineering, Xi'an, China, [2]Xi'an Key Laboratory of Smart Industry Perception Computing and Decision Making, Xi'an, China, [3]Xi'an U-MINE Intelligent Mining Research Institute Co Ltd, Xi'an, China, [4]Sinosteel Mining Development Co Ltd, Beijing, China, [5]Jidong Cement Tongchuan Ltd., Tongchuan, China

In order to solve the inefficient use of multi-source heterogeneous data information cross fusion and the low accuracy of prediction of landslide displacement, the current research proposed a new prediction model combining variable selection, sparrow search algorithm, and deep extreme learning machine. A cement mine in Fengxiang, Shaanxi Province, was studied as a case. The study first identified the variables related to landslide displacement of rock slope, and removed redundant variables by using Pearson correlation and gray correlation analysis. To avoid the impacts of random input weights and random thresholds in the DELM model, the SSA algorithm is used to optimize the model's parameters, which can generate the optimal parameter combinations. The results showed an enhanced generalization ability of the model by removal of redundant variables by Pearson correlation and gray correlation analysis, and higher accuracy in the prediction of landside displacement of rock slope by SSA-DELM compared to other traditional machine learning algorithms. The current study is significant in the literature on rock slope disaster analysis.

KEYWORDS

multi-source data fusion, displacement prediction, SSA algorithm, deep extreme learning machine, variable selection

Introduction

In the construction of mountain housing, transportation, mining, water conservancy and hydropower projects, rock slope stability problems are inevitably encountered (Li et al., 2019; Du et al., 2022; Yi et al., 2022; Zhao et al., 2022). Rock slope stability problems can cause geological disasters such as rock loosening, relaxation cracking, creeping, landslides and rock fall (Liu et al., 2020; Meng et al., 2021; Xu et al., 2022). Therefore, monitoring and early warning are pivotal in preventing rock slope disasters. In rock slope disaster monitoring and early warning, the research is often conducted on static indicators (such as deformation, stress, etc.)or environmental indicators (such as groundwater,

rainfall, etc.) (Du et al., 2019), among which displacement is an intuitive and reliable monitoring quantity under the influence of internal and external environment. The scientific analysis of displacement data and the establishment of real-time prediction models are essential research contents in large-scale engineering safety monitoring.

In order to obtain accurate, comprehensive, and real-time information on landslide deformation, it is necessary to monitor both surface and subsurface deformation, as well as triggering factors and related environmental factors, so multiple means of landslide monitoring must be used simultaneously to achieve effective monitoring results (Zhang et al., 2020). Nowadays, the techniques applied in mainstream rock slope monitoring include synthetic aperture radar (Pieraccini et al., 2006; Atzeni et al., 2015; Qin et al., 2020), microseismic monitoring (Salvoni and Dight., 2016; Xu et al., 2016; Ma et al., 2017; Chen et al., 2022), GNSS displacement monitoring (Lian et al., 2020; Šegina et al., 2020; Yan et al., 2022), etc. These monitoring techniques mainly focus on the surface and deep deformation of rock slopes, and some scholars also combine environmental quantity indicators for monitoring and research, such as Pang (Pang, 2019) proposed an automated monitoring system, which contains GPS monitoring station, rain gauge, crack gauge, rain gauge, groundwater level gauge and other sensors to monitor the slope in real-time, which can respond to the slope deformation parts in time with a broader perspective to ensure the safety of high-risk slopes and their surroundings; Liu et al. (Liu et al., 2022) combined slope deformation monitoring data, displacement monitoring data, inclination monitoring data, groundwater level monitoring data, rainfall monitoring data and other multi-source data, based on machine learning method to monitor abnormal events of monitoring data to provide support for disaster early warning; Peng et al. (Peng et al., 2014) combined multiple sensor monitoring data and multiple mechanical parameters to update soil or rock model parameters, slope safety coefficients and damage efficiency using Markov chain Monte Carlo simulation, which made the assessment more reliable; Li et al. (Li et al., 2021) combined field experiments and blasting vibration monitoring to systematically study the three-dimensional dynamic stability of adjacent high slopes after blasting vibration, providing technical support and theoretical guidance for mine blasting and improving mine stability.

The use of multiple sensors to monitor slopes can obtain a large amount of multi-source heterogeneous data, which have specific correlation, randomness, and ambiguity (Wang et al., 2020). How to fully use these multi-source heterogeneous data is the focus of scholars' attention and the problems that have been needed. Over the past few years, the multi-source data fusion method has been increasingly favored by some experts and scholars in the field of slope research, and it has begun to be gradually applied in engineering. Some scholars have used multi-source data fusion technology for the prediction and stability analysis of slope safety factor (Sakellariou and Ferentinou., 2005; Liu et al., 2014.; Jiang et al., 2022), and some scholars at home and abroad have used multi-source heterogeneous data fusion technology for risk warning and analysis of landslides to study the characteristic mechanism and dynamics evolution law of the deformation and damage process of landslides (Du et al., 2020; Zhang et al., 2020; Li et al., 2021). In recent years, multi-source data fusion techniques have been more successfully applied to landslide displacement prediction. Liu et al. (Liu et al., 2020) introduced two concepts, trend sequence and sensitivity, to quantitatively characterize landslide displacement caused by external factors and internal landslide state, respectively, and proposed a nonlinear model for landslide displacement prediction by fusing trend sequence and sensitivity state; Wang et al. (Wang et al., 2021) used Pearson correlation coefficient, and mutual information were used to screen environmental factors and deep learning was used to predict landslide displacements; Duan et al. (Duan et al., 2017) used comprehensive landslide monitoring data to extract the most relevant factors affecting landslide deformation and used an autoregressive integrated movement model for prediction. Wang and Zhang (Wang et al., 2022; Zhang et al., 2022) considered the hydrodynamic effects affecting landslides, used a variational modal decomposition method to decompose the cumulative displacement into the trend, periodic and stochastic terms, and used different deep learning methods to make predictions for three Different deep learning methods are used to predict the three different displacement subterms.

Scholars have rarely considered the relationship between the dependent variables in the prediction of landslide displacement using multi-source heterogeneous data of slopes, which can lead to overfitting and low prediction accuracy in the prediction. Nowadays, the mainstream methods of variable selection mainly include correlation analysis (Guo et al., 2022), mutual information (Li, 2021), and lasso (Jin et al., 2021). However, these methods are relatively single, and it is difficult to select the appropriate number of variables when screening the variables, and too few input variables will lead to lower prediction accuracy. On the other hand, too many input variables will result in redundant variables and increase the model running time.

In the past, scholars did not consider the redundancy among the dependent variables when using multi-source heterogeneous data of slopes for landslide displacement prediction, leading to overfitting and low prediction accuracy. To this end, this paper proposes a method of variable selection by combining Pearson correlation and gray correlation analysis. The Pearson correlation analysis is used to calculate the correlation coefficients of each variable factor, judging whether there are uncorrelated or redundant relationships among them. Then the model combines the correlation coefficients between variables and displacement to eliminate redundant variables. Finally, the sparrow search algorithm optimized by the depth limit learning machine is utilized to predict displacement, which provides a

TABLE 1 The value range of |r|and its meaning.

The value range of |r|	The meaning of |r|
[0.0.2]	Extremely low correlation
[0.2.0.4]	Low correlation
[0.4.0.6]	Moderate correlation
[0.6.0.8]	High correlation
[0.8.1]	Extremely high correlation

reference for the subsequent displacement change and reduces the occurrence of slope disaster.

Principles of algorithms

Pearson correlation analysis

Karl Pearson introduced the Pearson correlation coefficient (PCC) in the 1880s. The correlation coefficient determines whether each input variable is closely correlated with each other, and if two variables are highly correlated with each other, they belong to duplicate features and can be removed to achieve de-duplication or dimensionality reduction (Lin et al., 2019). The Pearson correlation coefficient is then expressed as follows:

$$r = \frac{\sum_{i=1}^{N}(x_i - \bar{x})(y_i - \bar{y})}{\sum_{i=1}^{N}(x_i - \bar{x})^2 \sum_{i=1}^{N}(y_i - \bar{y})^2} \quad (1)$$

Where r is the Pearson correlation coefficient; x_i is the different value corresponding to the variable x; is the average of the variables x;y_i is the different value corresponding to the variable y; is the average of the variables y; $N$is the number of variables. The value range of the correlation coefficient is [-1.1]. When $|r|>0$, it is a positive correlation; conversely, it is a negative one. The magnitude of the absolute value of the corresponding Pearson correlation coefficient between two variables determines the strength of the relationship between the two variables, and the specific range of values and their representative meanings are shown in Table 1.

Gray relational analysis

Gray relational analysis theory, an essential part of gray system theory, is a multifactor statistical analysis theory that describes the strength, magnitude, and order among factors in terms of gray correlation degree based on sample data of each factor. Gray correlation is essentially a comparison of how close the geometric shapes of the data curves are. The closer the geometry, the closer the trend of change and the greater the correlation (Liu et al., 2012). The analysis steps are as follows:

Step1. Identify the mother series and characteristic series. Generally, the dependent variable is determined as the mother series, and the independent variable is determined as the characteristic series. In this paper, the landslide displacement is determined as the mother series, and the landslide impact factor is determined as the characteristic series.

Step2. Undimensionalize the data. The dimensionless processing is typically done by initialization, homogenization, and normalization, and this paper uses normalization for the dimensionless processing of data. The calculation formula of normalization is then expressed as follows:

$$X_{\text{norm}} = \frac{X - X_{min}}{X_{max} - X_{min}} \quad (2)$$

Where $X$is the raw data; $X_{\max}$, $X_{\min}$ are respectively the maximum and minimum values of the data.

Step3. Solve for the gray relational coefficient value between the parent sequence and the feature sequence. The relational coefficient represents the degree of correlation between the feature series and the mother series in the corresponding dimension, and the larger the number, the stronger the correlation. The calculation formula of the correlation coefficient is then expressed as follows:

$$\xi_e(k) = \frac{\min\limits_{e}\min\limits_{k}|x_0(k) - x_e(k)| + \rho \max\limits_{e}\max\limits_{k}|x_0(k) - x_e(k)|}{|x_0(k) - x_e(k)| + \rho \max\limits_{e}\max\limits_{k}|x_0(k) - x_e(k)|} \quad (3)$$

Where $\xi_e(k)$ is the value of correlation coefficients of feature sequence x_e to feature sequence x_0 on the kth indicator.

Step4. Calculate the correlation between the mother sequence and the feature sequence. Larger correlation degree proves that the corresponding feature sequence has more influence on the mother sequence. The calculation formula of correlation degree is then expressed as follows:

Where n is the sample size; r_ε is the correlation degree of feature sequence, and the indicator weight.

$$r_e = \frac{1}{n}\sum_{k=1}^{n}\omega_k \xi_e(k) \quad (4)$$

Sparrow search algorithm

The Sparrow Search Algorithm (SSA) is a relatively novel algorithm inspired by the foraging and anti-predatory behaviors of sparrows (Xue and Shen., 2020), which has the advantages of

merit-seeking solid ability, fast convergence, and robustness. The bionic principle is as follows:

When sparrows search for food, they need to divide the whole sparrow population into three categories according to their different divisions of labor: producers searching for food, joiners grabbing food of their kind, and vigilantes finding enemies. Producers are generally the highest energy sparrows in the whole population because they need to search for food and guide the direction of the population. In continuous iteration, producers and joiners can transform each other, but the proportion of the two species in the whole population will not change in the transformation process. In the bionic experiment, the sparrow population and fitness values need to be initialized first, and the sparrow population and fitness value initialization expressions are then expressed as follows:

$$X = \begin{pmatrix} x_{1,1} & x_{1,2} & \cdots & x_{1,d} \\ x_{2,1} & x_{2,2} & \cdots & x_{2,d} \\ \vdots & \vdots & & \vdots \\ x_{n,1} & x_{n,2} & \cdots & x_{n,d} \end{pmatrix} \tag{5}$$

$$F_x = \begin{bmatrix} f([x1,1\ x1,2 \cdots x1,d]) \\ f([x2,1\ x2,2 \cdots x2,d]) \\ \cdots \\ \cdots \\ f([xn,1\ xn,2 \cdots xn,d]) \end{bmatrix} \tag{6}$$

Where n is the number of sparrows; d is the dimension of the variable to be optimized, which is the number of independent parameters; $x_{n,d}$is the value of the nth sparrow in the dth dimension.

After determining the location and fitness value of each sparrow, the initial fitness value of each sparrow needs to be sorted, the sparrows with the better fitness value will be identified as the producer. The producer can be given priority to obtain food when food is found and guide the whole group to the direction of food. The producer will continue to search for food in different places elsewhere, the location will keep changing, and the movement rules will also change when the enemy is encountered, at the moment, the producer location update rules are then expressed as follows:

$$x_{i,j}^{t+1} = \begin{cases} x_{i,j}^{t} \, exp\left(-\dfrac{i}{\alpha itermax}\right), & if\ R_2 < ST \\ x_{i,j}^{t} + QL, & if\ R_2 \geq ST \end{cases} \tag{7}$$

Where t is the current number of iterations; $j \in \{1, 2, 3, \cdots, d\}$;$x_{i,j}^{t}$is the value of the ith dimension of the jth sparrow at the tth iteration; $\alpha \in (0, 1]$, is a random number; $iter_{\max}$ is the maximum number of iterations; $R_2 \in [0, 1]$, is the alarm value; $ST \in [0, 1]$, is the safety threshold; Q is a random number that follows a normal distribution; L is a matrix of order $1 \times d$(all elements are 1). When $R_2 < ST$, it means that there are no natural predators in the area, which means that the area is safe and the producer will continue to expand its foraging range; when $R_2 > ST$, it means that the producer has found a predator and warned other sparrows that all sparrows need to leave the area for a safe area.

For the joiners, the producers are monitored at all times, and if the producers find food, the joiners will immediately be aware of it and quickly fly to the food source to grab the food with the producer. At this time, the joiners' position update rule is then expressed as follows:

$$x_{i,j}^{t+1} = \begin{cases} Q\,exp\left(\dfrac{x_{worst}^{t} - x_{i,j}^{t}}{t^2}\right), & i > \dfrac{n}{2} \\ x_{p}^{t+1} + \left|x_{i,j}^{t} - x_{p}^{t+1}\right| A^{+} L, & \text{else other} \end{cases} \tag{8}$$

Where x_p is the best position occupied by the producer; x_{worst} is the global worst position; A is the matrix of order $1 \times d$, each element is randomly 1 or -1;$A^{+} = A^{T}(AA^{T})^{-1}$; When $i > \frac{n}{2}$, it means that the less adaptive first joiner fails to grab food and needs to change its position to get food in other areas.

Alerters are randomly generated in the entire population, usually 10–20% of the entire population. The initial position is then randomly generated, with the rule is then expressed as follows:

$$x_{i,j}^{t+1} = \begin{cases} x_{best}^{t} + \beta\left|x_{i,j}^{t} - x_{best}^{t}\right|, & if\ fi > fg \\ x_{i,j}^{t} + K\left(\dfrac{\left|x_{i,j}^{t} - x_{worst}^{t}\right|}{(fi - fw) + \varepsilon}\right), & if\ fi = fg \end{cases} \tag{9}$$

Where f_i is the current sparrow adaptation value; f_g is the global best adaptation value; f_w is the global worst adaptation value; β is the step control function, which is a normally distributed random number with mean 0 and variance 1; K is the direction of sparrow movement; ε is the minimum constant, avoiding zero denominator; x_{best} is the global best position; x_{worst} is the global worst position. When $f_i > f_g$, it means that the vigilantes are located at the edge of the whole population and will fly to the safe area when scouting for enemies; When $f_i = f_g$, it means that the vigilantes in the centre of the population are aware of the danger and will fly to the other sparrows to avoid the danger.

Deep Extreme Learning Machine

An extreme learning machine is a single hidden layer feedforward neural network (Sulandri et al., 2021). Unlike the traditional gradient-based feedforward neural network algorithm, the input weights and thresholds of the hidden layer of the extreme learning machine network are randomly generated in the training process. Therefore, only the generalized inverse matrix theory can be used to calculate the output weights to complete the learning. Therefore, ELM network has the advantages of fast learning speed and strong generalization ability. However, because ELM is a single hidden layer

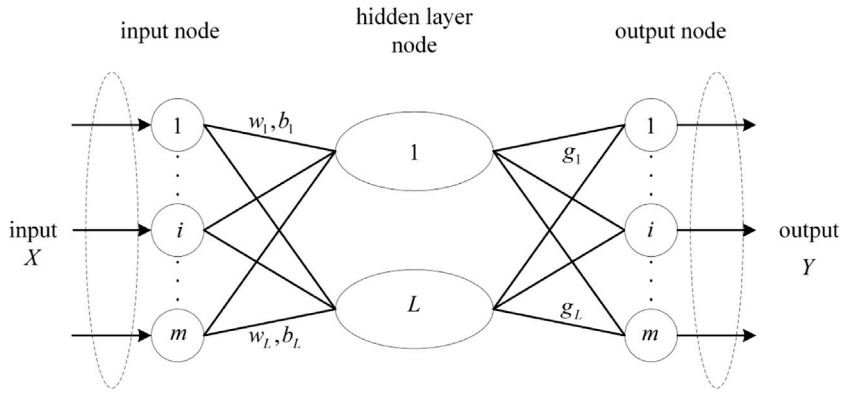

FIGURE 1
ELM-AE network structure diagram.

structure, it cannot capture the effective features of the data in the case of high data, and high dimensionality of data. So more scholars use DELM (Tuerxun et al., 2021), which is a derivative algorithm of ELM.

Deep Extreme Learning Machine (DELM) is an ELM derivative algorithm that improves the network's representational capability by superimposing an Extreme Learning Machine-Autoencoder (ELM-AE) to construct a multilayer network structure. When the ELM is confronted with input and output variables with an excessive amount of input data and high dimensionality, it solves the problem that an extreme learning machine with only one hidden layer cannot capture the effective features of the data (Sulandri et al., 2021). DELM is a combination of an extreme learning machine and an autoencoder, which constitutes an extreme learning machine-autoencoder, and the ELM-AE structure is shown in Figure 1.

ELM-AE is a general approximator characterized by enabling the output of the network to be the same as the input and the input parameters of the hidden layer to be orthogonal after random generation. The output of ELM-AE can be then as follows:

$$xj = \sum_{i=1}^{L} \beta i G(ai, bi, xj), ai \in R^m, \beta i \in R^m, j = 1, 2, \cdots, N, a^T a = I, b^T b = 1 \tag{10}$$

Where a is the matrix composed of a_i , and b is the vector composed of b_i. The output weights of the hidden layer are then expressed as follows:

$$\beta = \left(\frac{I}{C} + H^T H\right)^{-1} HTX \tag{11}$$

Where $X = [X_1, X_2, X_3, \cdots X_N]$ is the input data.

Because of its feature representation capability, ELM-AE is used as the basic unit of the deep extreme learning machine DELM. Like traditional deep learning algorithms, DELM also uses a layer-by-layer greedy training method to train the network, and the input weights of each hidden layer of DELM are initialized using ELM-AE to perform hierarchical unsupervised training, but unlike traditional deep learning algorithms, DELM does not need reverse fine-tuning process. The structure of DELM is shown in Figure 2.

Assuming that the model has N hidden layers, the first output weight matrix β_1 is obtained from the input data X according to ELM-AE theory and then the feature vector of the hidden layer H^1. The output weight matrix β_N of N layers and the feature vectors H^N of the hidden layers can be obtained. As shown in Figure 3, the DELM first uses multiple ELM-AEs for unsupervised pre-training and then uses the output weights of each ELM-AE to initialize the whole DELM. During the ELM-AE training process, the input layer weights and thresholds are randomly generated orthogonal random matrices; meanwhile, the ELM-AE unsupervised training process uses the least squares method to update the parameters. However, in this process, only the output layer weight parameters are updated, while the input layer weights and thresholds are fixed, which will result in the prediction accuracy of the DELM being affected by the random input weights and random thresholds of each ELM-AE. Therefore, it is necessary to optimize these two parameters.

Establishment of SSA-DELM predict model

Multiple ELM-AEs stack DELM, and the input weights and random thresholds in ELM-AEs are randomly generated, leading to random variables in the DELM model and unstable results. So these two parameters are iteratively optimized by the SSA algorithm, giving the whole model high prediction accuracy

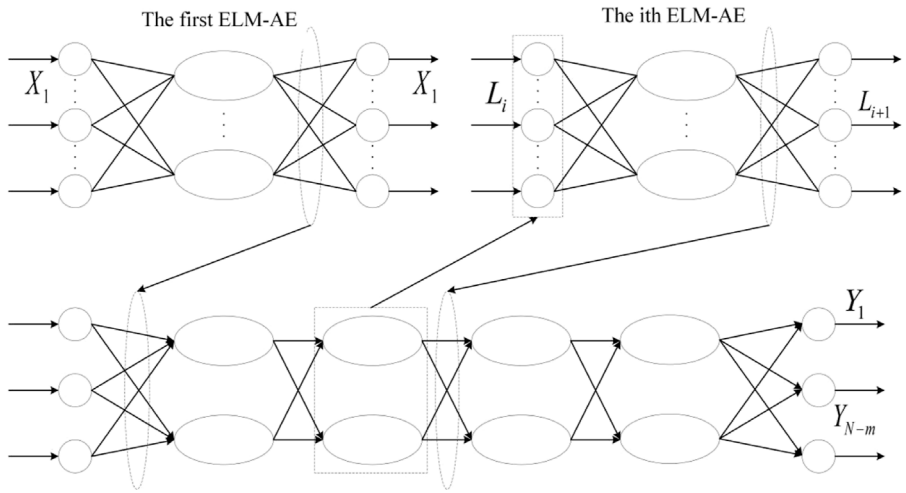

FIGURE 2
DELM structure diagram.

and fast convergence, which can well ensure the stability of the results. The optimization process and flow chart (Zeng et al., 2021) are then as follows.

1) Initialize the SSA algorithm parameters. Set the maximum number of training iterations, the number of sparrow populations, the alert threshold, the proportion of discoverers, and the proportion of alerters.
2) Calculate the initial fitness value of the sparrow population. Then, the sparrows with the current best and worst fitness values are selected along with their locations.
3) The positions of predators, joiners, and vigilantes are continuously updated according to Eqs 7–9.
4) After updating the positions, calculate the optimal and worst fitness values of the whole population and their positions, determine whether the maximum number of iterations is satisfied or the stopping condition is met, and if the condition is fulfilled, output the optimal value, otherwise, return to step 2).
5) The obtained results are input into the DELM model to calculate the input values and thresholds of the optimal hidden layer.

Landslide displacement modeling based on PCC-GRA-SSA-DELM

There are various manifestations of rock slope deformation, and landslide displacement is one of them. In this paper, we will combine actual engineering cases and literature, collect multiple sensor data and multiple environmental factors affecting rock slope displacement as the input parameters of SSA-DELM prediction model, and take displacement as the output parameters of the model. Since the redundancy among the factors will reduce the accuracy of the prediction model, this paper uses Person correlation analysis to calculate the correlation coefficients of the influencing factors. It then uses gray correlation analysis to calculate the correlation between the influencing factors and the landslide displacements to eliminate redundant and uncorrelated variables between them. The screened out in the prediction model, the rock slope displacement prediction model based on the PCC-GRA-SSA-DELM model is established based on four steps: data collection, data processing, variable selection, and result prediction. In this case, the obtained results are more accurate. The calculation process (as shown in Figure 4) is as follows:

1) Data collection. Multiple data sources are collected from the slope monitoring system, including displacement data, meteorological data, mechanics-related data, etc.
2) Normalizing the experimental data. Normalization limits the preprocessed data to a certain range eliminates the undesirable effects caused by odd sample data and performs inverse normalization after the model output results.
3) Variable selection. The correlation coefficients of the influencing factors were firstly calculated by using Person correlation analysis to judge the redundancy degree among the factors, and then the correlation degree between the influencing factors and landslide displacement was calculated by using gray correlation analysis, and the redundant variables and unrelated variables among them were eliminated by comprehensive comparison.

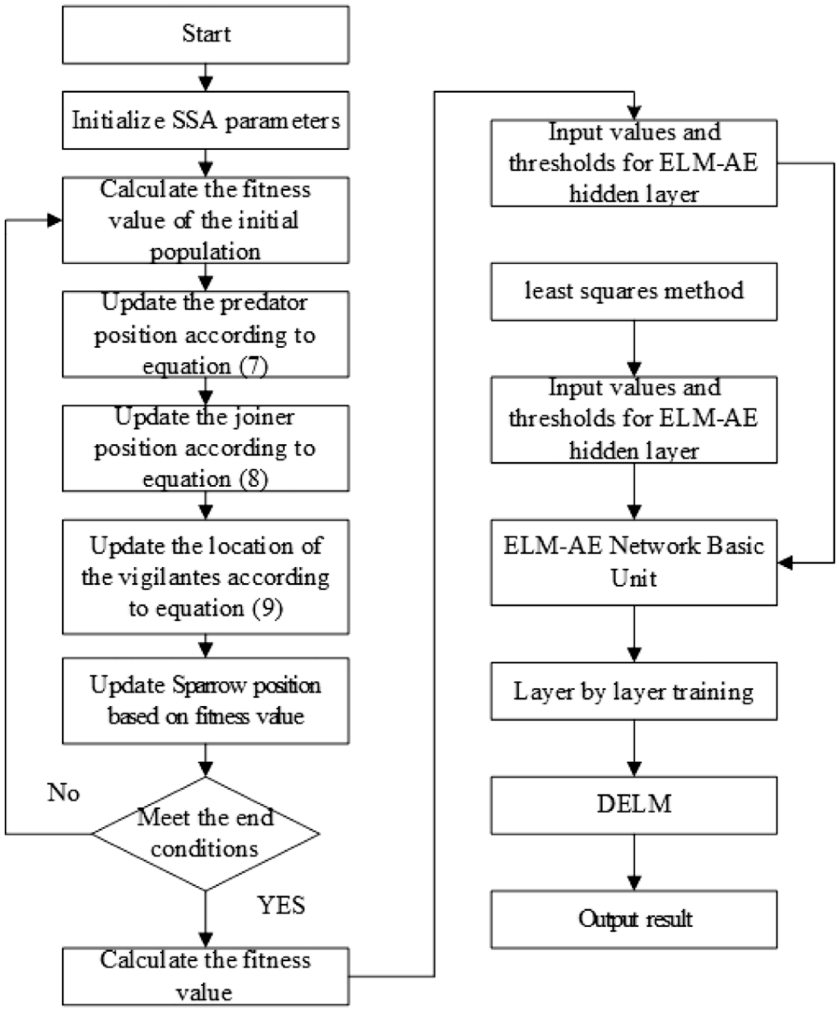

FIGURE 3
SSA-DELM flow chart.

4) Result prediction. The samples are applied in the trained SSA-DELM model, the predicted values are output, and the feasibility and accuracy of the results are analyzed and verified.
5) Evaluation metrics. In this paper, the mean absolute error (MAE), and the mean square error (RMSE) are taken as the evaluation indexes of the model and calculated as follows:

$$X_{MAE} = \frac{1}{N}\sum_{i=1}^{N}|\hat{y}_i - y_i| \tag{12}$$

$$X_{RMSE} = \sqrt{\frac{1}{N}\sum_{i=1}^{N}|\hat{y}_i - y_i|^2} \tag{13}$$

Where N is the number of samples predicted; y_i is the actual value of displacement; $\hat{y}_i$ is the predicted value of displacement.

Numerical calculation and analysis

Introduction of case projects

A cement mine in Fengxiang District is located in Fengxiang District, Baoji City, Shaanxi Province, China, at latitude 34°32′43″-34°32′54″N and longitude 107°30′26″-107°30′57″E. The quarry slope is mainly composed of the Devonian medium-thick laminated hard tuff rock group, with tangential slope and reverse slope, which is more favorable to the stability of the slope, with good stability of the slope in general, and not easy to produce large-scale landslide, collapse and other geological disasters. On the other hand, the structure of the upper residual slope and weathered, broken layer is loose, with poor stability, which is prone to small-scale collapse and landslide geological disasters under rainfall and vibration.

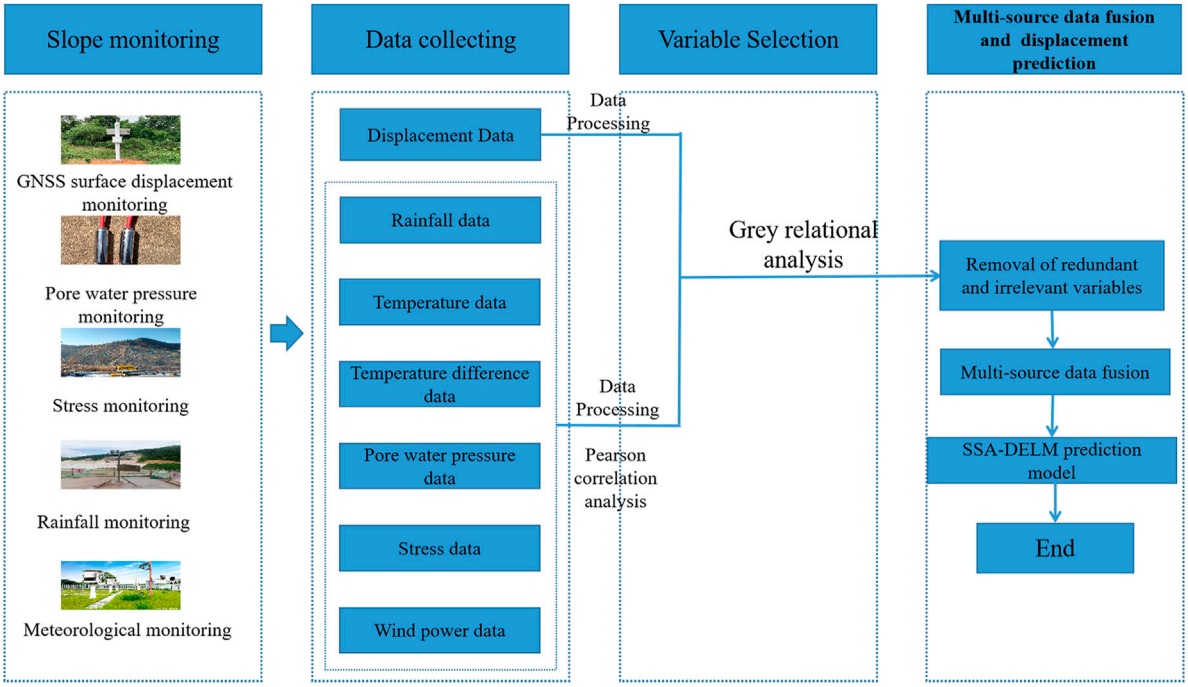

FIGURE 4
PCC-GRA-SSA-DELM model prediction flow chart.

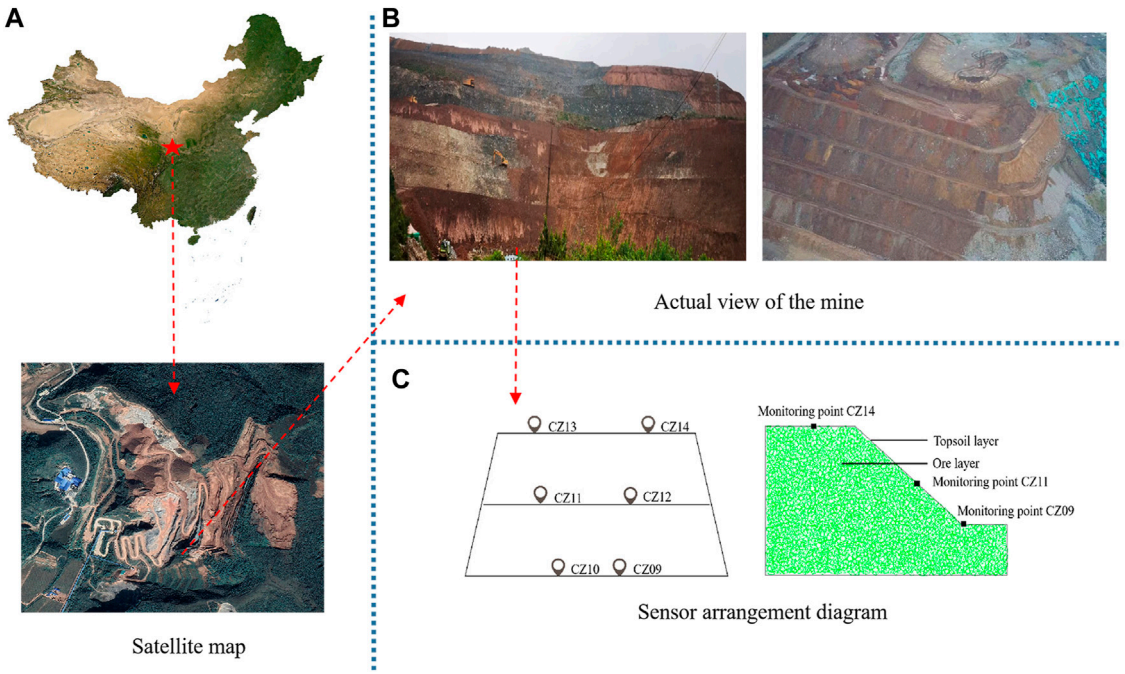

FIGURE 5
Mine location diagram and monitoring point layout chart.

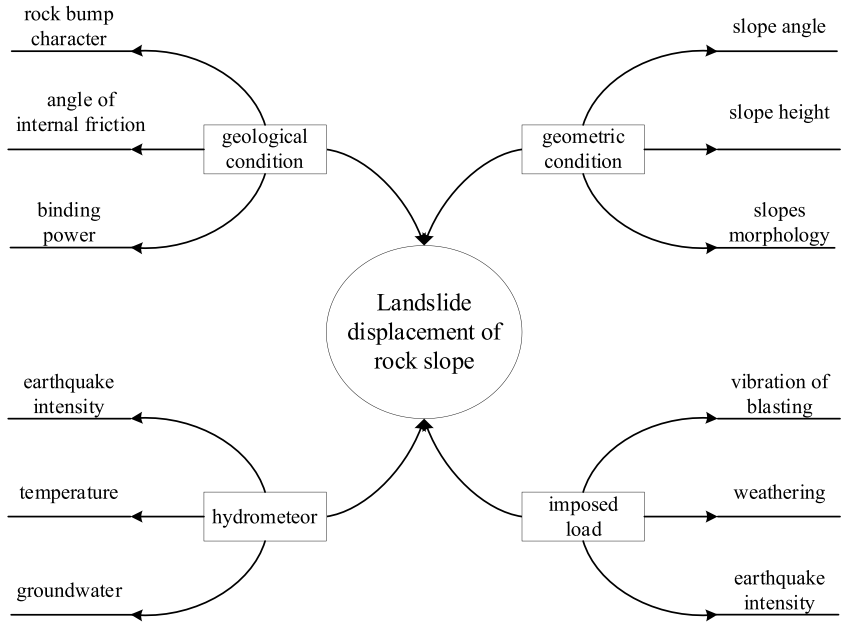

FIGURE 6
Diagram of influence factors of slope and landslide displacement.

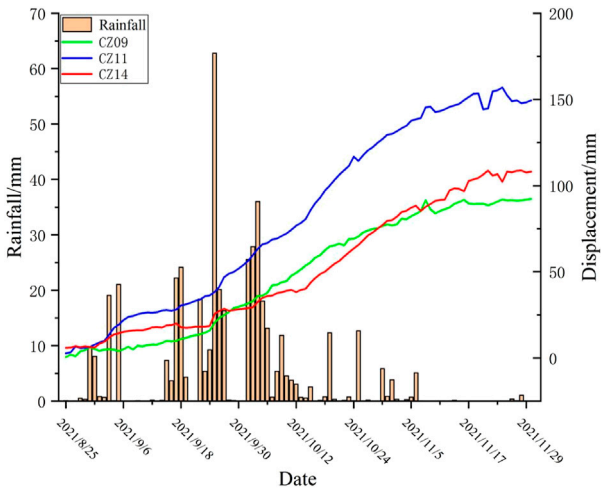

FIGURE 7
The changes of accumulated displacement of landslide and single-day precipitation during the monitoring period.

When the mine started to be mined, the relevant management department continuously monitored the slope deformation, mainly including GNSS surface displacement, stress meter, pore water pressure meter, etc. The location map of GNSS surface displacement monitoring points is shown in Figure 5, which includes two base stations (JZ01 and JZ02) and 14 observation stations. This paper selects three monitoring points CZ14, CZ11 and CZ09 in base station JZ02 located in the west section of the mine. These three monitoring points are located at the slope's top, middle and foot in the west section of the mine, representing the deformation characteristics and trends of the front, middle and back of the slope.

The stability of rock slope is influenced by a variety of factors, which are mainly divided into four categories: engineering geology, geometric conditions, hydro-meteorology, and applied loads (as shown in Figure 6). Among them, rainfall is one of the critical factors affecting landslide deformation, and the changes in accumulated displacement of landslides and single-day precipitation during the monitoring period are shown in Figure 7. Temperature is one of the main factors affecting the mechanical properties of rocks (Li et al., 2022), and Weathering is the effect of changing the physical properties and chemical composition of rocks under atmospheric conditions. When other factors work together to a certain extent, it is very easy to cause slope instability, such as landslides, cave-ins, and other geological disasters, and rainfall, atmospheric radiation, temperature, and temperature difference are the main reasons affecting the weathering of rock slope. By geological survey of the mine site as well as its surrounding geology and literature query, the mine is divided into two segments, the left side of the western

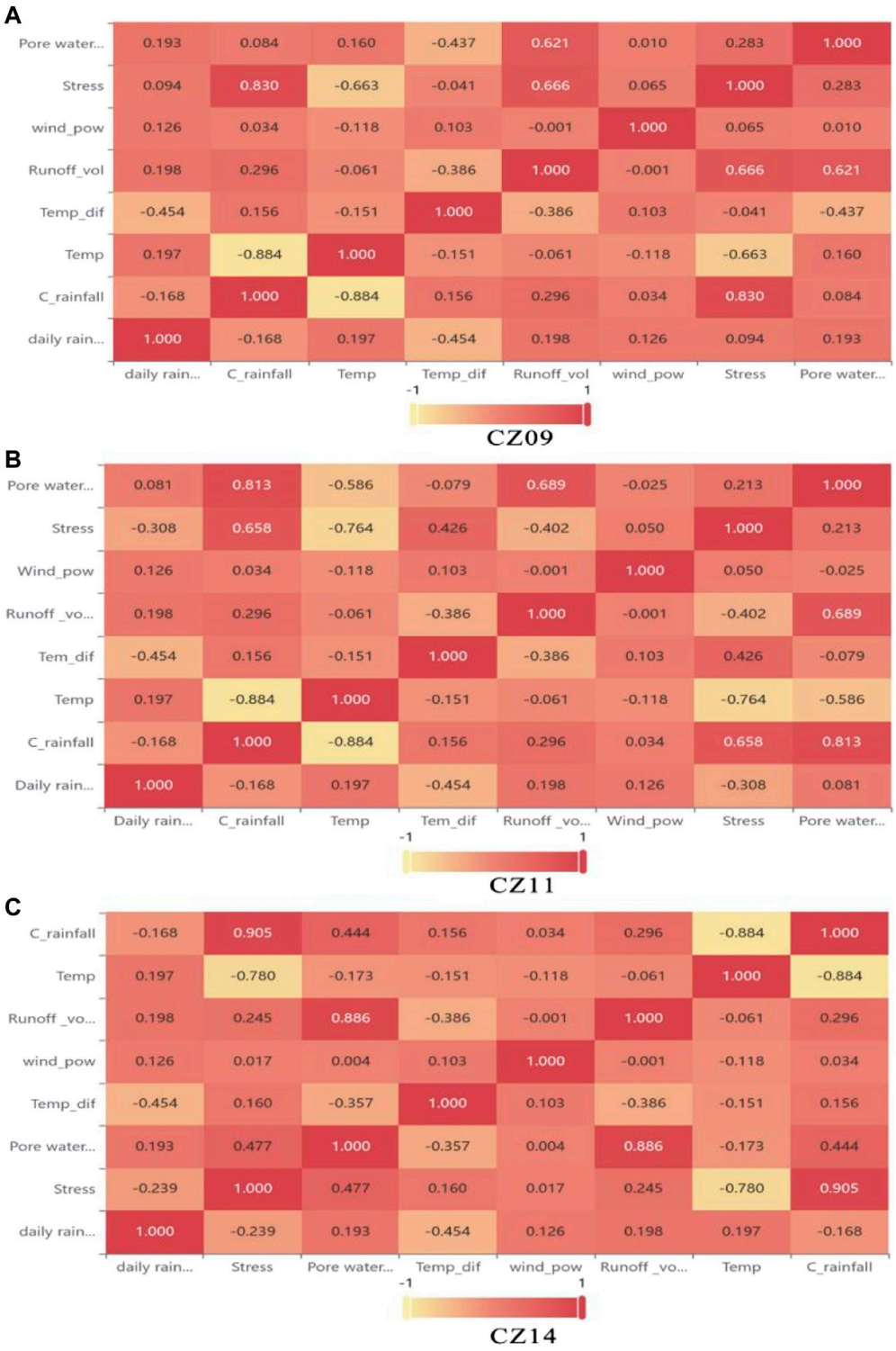

FIGURE 8
Correlation coefficient of three monitoring points influence factor **(A)** CZ09, **(B)** CZ11, **(C)** CZ14.

section is close to the Heng Shui River, and there is a tributary inflow, the size of the runoff from the Heng Shui River also affects the height of the groundwater level in the mine area, the rise and fall of the groundwater level cause the slope geotechnical body to produce deformation, slippage, collapse instability and other adverse geological

TABLE 2 The correlation between the influence factors of the three monitoring points and the displacement.

Monitoring points	Cumulative rainfall	Runoff volume	Porewater pressure	Stress	Temperature	Wind power	Temperature difference	Daily rainfall
CZ09	0.971	0.889	0.911	0.917	0.856	0.907	0.918	0.831
CZ11	0.973	0.894	0.926	0.957	0.864	0.914	0.923	0.832
CZ14	0.958	0.886	0.912	0.922	0.861	0.909	0.921	0.829

TABLE 3 Error analysis table of 3 monitoring points.

Predictive model	CZ09		CZ11		CZ14	
	MAE	RMSE	MAE	RMSE	MAE	RMSE
PCC-GRA-SSA-DELM	1.3	1.75	1.06	1.44	1.19	1.68

phenomena, the groundwater level monitoring is mainly by means of pore water pressure sensors and stress gauges. Considering the above and the lag of some environmental impact factors on rock slope, the factors selected in this paper are daily rainfall (mm), accumulated rainfall (mm), daily average temperature (°C), daily temperature difference (°C), stress (Kpa), pore water pressure (Kpa), runoff (km), wind speed (m/s), among which the data of six factors such as rainfall, temperature, runoff and wind speed come from the meteorological monitoring station in Fengxiang District, Baoji City, Shaanxi Province. The stress and pore water pressure data comes from the measurement data of mine monitoring points.

Influencing factors selection

Pearson correlation analysis was performed on the eight influencing factors, and their correlation coefficients were calculated (Figure 8). Taking the correlation analysis of impact factors of the monitoring point CZ11 as an example, The correlation coefficients between cumulative rainfall and pore water pressure, temperature and stress were 0.815, -884 and 0.658, respectively, while the correlation coefficients between runoff and pore water pressure were, 0.680 and between temperature and stress were -0.764, respectively. It shows a very high degree of correlation with a close relationship. In summarizing, all eight influence factors have a certain correlation with each other, which proves that there is redundancy among the data, and if the prediction is directly fused, the prediction performance of the prediction model will be affected to some extent. Therefore, this section calculated the correlation between each influence factor and landslide displacement using gray correlation analysis combined with the actual data from the experiment. The main influence factors were derived as the input variables of the prediction model (as shown in Table 2).

Taking monitoring point CZ11 as an example for analysis, combining Pearson correlation analysis and gray relational analysis for variable selection. Among the eight influencing factors, the top three correlations with landslide cumulative displacement are cumulative rainfall, stress, and pore water pressure, which are 0.973, 0.957, and 0.926, respectively. However, the correlation coefficients of cumulative rainfall and pore water pressure and stress are relatively large and strongly correlated. The two indicators of pore water pressure and stress are excluded, and the remaining six influencing factors are selected as input variables. Similarly, In monitoring points CZ09 and CZ14, the gray correlation between cumulative displacement and influence factors is greater for cumulative rainfall, stress, and temperature difference. However, since the correlation coefficients between cumulative rainfall and stress and temperature are higher, the two variables of stress and temperature are excluded, and the remaining six variables are retained as input variables.

Landslide displacement prediction

In the present study, the actual monitoring data of the Fengxiang cement mine from 25 August 2021, to 30 November 2021, are used as the experimental data, and there are 98 sets of valid data in total. As the slope has different responses to external influences at different locations, three sensors at different locations of the same slope will be selected for this experiment. The surface displacement data from

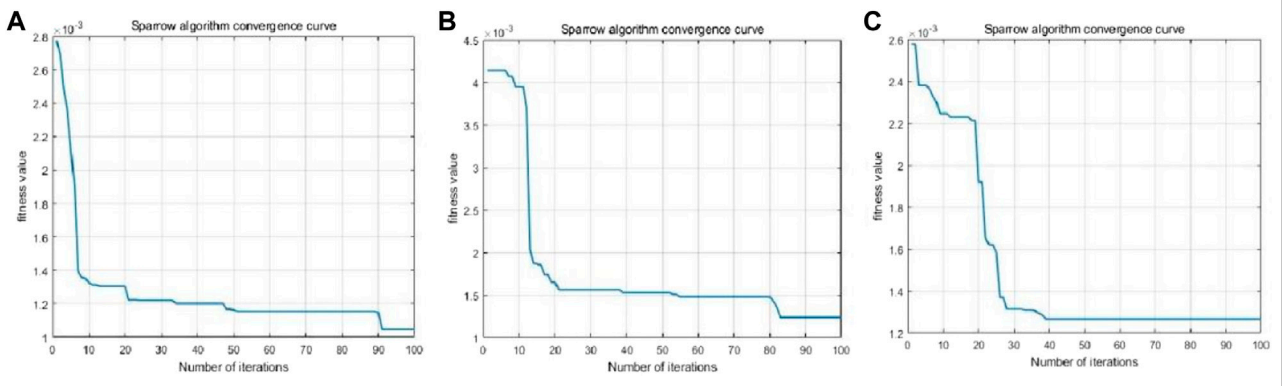

FIGURE 9
Data convergence speed graph for different measurement points, **(A)** CZ09, **(B)** CZ11, **(C)** CZ14.

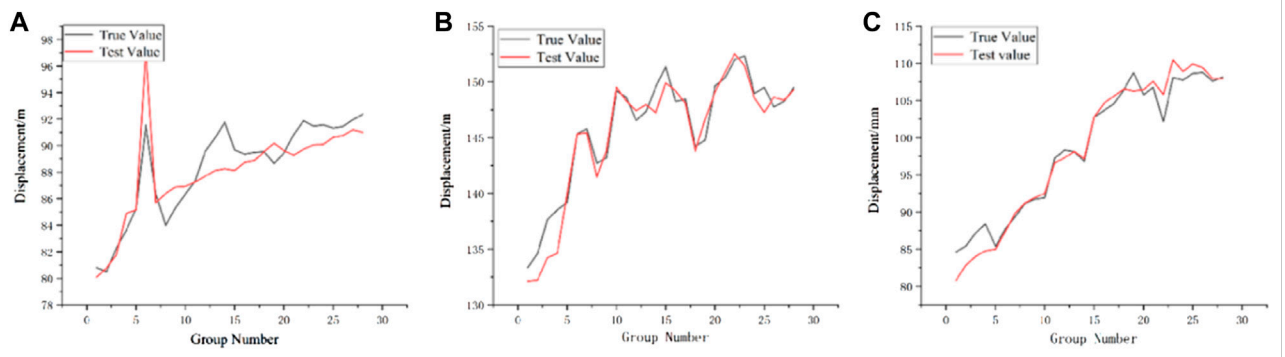

FIGURE 10
Comparison of predicted and actual values of three monitoring points, **(A)** CZ09, **(B)** CZ11, **(C)** CZ14.

each sensor will be predicted, the first 70 sets of data from each sensor will be selected as the training sample set, and the last 28 monitoring data will be used as the prediction sample set.

The parameters of the SSA-DELM method were set as follows: the population size of sparrows was 100; the proportion of discoverers was 0.7, and the proportion of vigilantes was 0.2; the hidden layer of the DELM model was set to 4 layers, the number of nodes in each implicit layer was set to 10, and the maximum number of iterations was 100; the excitation function was selected as sigmoid, and the excitation function was able to achieve nonlinear transformation in the feature space, and the SSA algorithm to optimize the implied layers and input thresholds of DELM. The convergence speed is shown in Figure 9, and it can be seen that the SSA-DELM model converges within 100 iterations, and the fitness values can all be maintained at about 1.2×10^{-3}, indicating that the model converges quickly and has high prediction accuracy. The influence factors screened in the above section are used as input parameters and the accumulated displacement as output parameters.

As shown in Table 3, the displacement prediction errors at three different locations are relatively small by using the PCC-GRA-SSA-DELM prediction model, among which, the smallest RMSE and MAE is monitoring point CZ11 with RMSE of 1.44. From the plots (b) and (c) in Figure 10, it can be seen that the predicted displacement trends of monitoring point CZ11 and monitoring point CZ14 are the same as the actual displacement trends. Basically, the larger errors are in the first five groups of the test set. Besides, their actual values of them are lager than the predicted values. Accidental loads or human activities during the mining can cause this phenomenon. Monitoring point CZ09 has the largest RMSE and MAE, and the points with larger errors are basically located in the second half of the test set, which is attributed to the fact that monitoring point CZ09 is located at the foot of the slope, and the accidental displacements

TABLE 4 Comparison of errors of different prediction models.

Predictive model	CZ09		CZ11		CZ14	
	MAE	RMSE	MAE	RMSE	MAE	RMSE
PGSD	1.3	1.75	1.06	1.44	1.19	1.68
SSA-DELM	1.57	1.80	3.26	3.68	2.95	3.47
ELM	7.25	11.33	7.21	8.65	6.94	9.28
SVM	12.25	15.3	8.46	9.55	2.98	4.19
DELM	7.26	7.86	5.98	6.43	5.47	6.24

generated by mining activities and vehicle transportation will affect the accuracy of displacement prediction. In conclusion, the overall effect of the PCC-GRA-SSA-DELM prediction model is excellent and can be applied to the actual landslide displacement prediction.

Comparison verification

In order to verify the supremacy of the proposed model in this paper, a support vector machine (SVM), extreme learning machine (ELM), deep extreme learning machine (DELM), and SSA-DElM were built in Matlab to conduct comparison experiments with this paper's model PCC-GRA-SSA-DELM (referred to as PGSD in the table) respectively. The prediction results of three different location sensors are shown in Table 4, among which the robustness of the ELM model is lowest.

The comparison experiments use MAE and RMSE as evaluation indicators, where the smaller the two values are, the better their prediction. Among them, ELM has the lowest prediction accuracy compared with the other two derived algorithms, DELM and SSA-DELM. DELM has more ELM-AEs than ELM, which increases the stability and merit-seeking ability of the model. However, during the ELM-AE training process, the input layer weights and thresholds are randomly generated orthogonal random matrices in the DELM model. The ELM-AE unsupervised training process uses least squares to update the parameters. Only the output layer weights parameters are updated, while the input layer weights and thresholds are fixed. That means the prediction accuracy of DELM is affected by the random input weights and random thresholds of each ELM-AE. But the SSA can solve this problem. Therefore, SSA-DELM has the highest prediction accuracy. The PGSD model proposed in this paper reduces the dimensionality of input variables, removes strongly correlated variables, enhances of the relationship between input and output variables, avoids overfitting, and improves the overall model prediction accuracy. Compared to SSA-DELM, the results showed the accuracy by the PGSD model increased by 2.86, 60.8, and 51.59% at three different measurement points, respectively.

Conclusion

The present work combined variable selection and sparrow search algorithm-deep extreme learning machine algorithm to predict landslide displacement. The results were validated using monitoring data for a cement mine in Baoji City. The main findings of the study are summarized as follows:

1) The advantage of the variable selection is that it can remove redundancy between multi-variables and eliminate multicollinearity problems. The Pearson correlation analysis method identified the correlation coefficients between each variable. The magnitude of the correlation coefficients can be used to identify the redundancy between the variables. By combining with gray correlation analysis, the correlation between each input variable and the displacement can be calculated to eliminate the redundant variables and improve the accuracy of the prediction model.
2) The paper selected the locations of monitoring points at different locations of the same mine slope for the study. As a result, the correlation coefficients between landslide displacements and impact factors are different for different monitoring points, and the redundant and redundant variables to be eliminated are also different.
3) The PCC-GRA-SSA-DELM prediction model has a high predictive effect, and the overall effectiveness of fitting on three different monitoring points is strong, which can meet the demands of practical mine monitoring and early warning.
4) Compared with ELM, DELM and SVM traditional prediction algorithms, the PCC-GRA-SSA-DELM prediction model proposed in the research has higher prediction accuracy and prediction efficiency in rock slope landslide displacement prediction. Therefore, it is more suitable for the prediction of rock slope displacement.

In sum, the PCC-GRA-SSA-DELM fusion model proposed in this paper enriches the literature on the reliability of rock slope landslide monitoring and warning. The current research also has limits because the errors in original data caused by arbitrary factors, such as mining work, and human activities, are not considered. Therefore, future works can further focus on predicting periodic and trend term displacement by using the signal decomposition method to further enhance accuracy and reliability.

Data availability statement

The original contributions presented in the study are included in the article/Supplementary Material, further inquiries can be directed to the corresponding author.

Author contributions

SJ provided the ideas and framework for this study, including the methods and theories in the paper; HL, conducted the experiments and wrote this paper; ML, CL, and SZ, performed the preliminary reading of the first draft and gave critical comments; JL, assisted in the data processing and data analysis of this paper; PL, provided the test site and raw data, including the geographic location map of the mine, sensor data, etc. for this paper.

Funding

This work was supported by the research project of National Natural Science Foundation of China: Disaster identification and early warning of complex slope in open pit mine based on data knowledge hybrid drive (52104146); And the research project of Shaanxi Natural Science Foundation: Research on driverless vehicle road collaborative intelligent control system in open pit mine integrating 5G Technology (2021JQ-509); And Shaanxi Social Science Foundation: Research on intelligent comprehensive perception and disaster emergency decision-making of National Central Cities Based on big data (2020R005).

Conflict of interest

Author SJ was employed by the company Xi'an U-MINE Intelligent Mining Research Institute Co Ltd, Author ML was employed by the company Sinosteel Mining Development Co Ltd, and Author PL was employed by the company Jidong Cement Tongchuan Ltd.

The remaining authors declare that the research was conducted in the absence of any commercial or financial relationships that could be construed as a potential conflict of interest.

Publisher's note

All claims expressed in this article are solely those of the authors and do not necessarily represent those of their affiliated organizations, or those of the publisher, the editors and the reviewers. Any product that may be evaluated in this article, or claim that may be made by its manufacturer, is not guaranteed or endorsed by the publisher.

Supplementary material

The Supplementary Material for this article can be found online at: https://www.frontiersin.org/articles/10.3389/fenvs.2022.982069/full#supplementary-material

References

Atzeni, C., Barla, M., Pieraccini, M., and Antolini, F (2015). Early warning monitoring of natural and engineered slopes with ground-based synthetic-aperture radar. *Rock Mech. Rock Eng.* 48, 235–246. doi:10.1007/s00603-014-0554-4

Chen, J., Zhu, C., Du, J. S., Pu, Y. Y., Pan, P. Z., Bai, J. B., et al. (2022). A quantitative pre-warning for coal burst hazard in a deep coal mine based on the spatio-temporal forecast of microseismic events. *Process Saf. Environ. Prot.* 159, 110. doi:10.1016/j.psep.2022.01.082

Du, Y., Li, H., Chicas, S. D., and Huo, L. C. (2022). Progress and perspectives of geotechnical anchor bolts on slope engineering in China. *Front. Environ. Sci.* 10. doi:10.3389/fenvs.2022.928064

Du, Y., Xie, M., and Jia, J. (2020). Stepped settlement: A possible mechanism for translational landslides. *Catena* 187, 104365. doi:10.1016/j.catena.2019.104365

Du, Y., Xie, M. W., Jiang, Y. J., Liu, W. N., Liu, R. C., and Liu, Q. Q. (2019). Research progress on dynamic monitoring index for early warning of rock collapse [J]. *Chin. J. Eng.* 41 (04), 427–435. doi:10.13374/j.issn2095-9389.2019.04.002

Duan, G. H., Niu, R. Q., Peng, L., and Fu, Jie. (2017). A landslide displacement prediction research based on optimizationparameter ARIMA model under the inducing factors[J]. *Geomatics Inf. Sci. Wuhan Univ.* 42 (04), 531–536. doi:10.13203/j.whugis20140913

Guo, Y. K., Zhang, S. A., Wang, J. J., Zhang, Q., and Xie, X. F. (2022). Feature variable selection combined with SVM for hyperspectral inversion of cultivated soil Hg content[J]. *Eng. Surv. Mapp.* 31 (01), 17–23. doi:10.19349/j.cnki.issn1006-7949.2022.01.003

Jiang, S., Li, J. Y., Zhang, S., Gu, Q. H., Lu, C. W., and Liu, H. S. (2022). Landslide risk prediction by using GBRT algorithm: Application of artificial intelligence in disaster prevention of energy mining. *Process Saf. Environ. Prot.* 166, 386. doi:10.1016/j.psep.2022.08.043

Jin, X. Z., Liu, Y., Yu, J., Wang, J. F., and Qie, Y. J. (2021). Prediction of outlet SO2 concentration based on variable selection and EMD-LSTM network[J]. *Proc. CSEE* 41 (24), 8475–8484. doi:10.13334/j.0258-8013.pcsee.202589

Li, B., Zhou, K., Ye, J., and Sha, P. (2019). Application of a probabilistic method based on neutrosophic number in rock slope stability assessment. *Appl. Sci. (Basel).* 9, 2309. doi:10.3390/app9112309

Li, H. W., Zhao, S. B., and Li, Z. (2021). Design and implementation of landslide early warning system based on multi-source monitoring data[J]. *Sci-Tech Dev. Enterp.* 2021 (12), 38–40. doi:10.3969/j.issn.1674-0688.2021.12.014

Li, P. X. (2021). Application of mutual information in feature selection algorithm [J]. *Int. Core J. Eng.* 7 (12), 0082. doi:10.6919/ICJE.202112_7(12).0082

Li, X. S., Li, Q. H., Hu, Y. J., Chen, Q. S., Peng, J., Xie, Y. L., et al. (2021). Study on three-dimensional dynamic stability of open-pit high slope under blasting vibration [J]. *Lithosphere* 2021, 6426550. doi:10.2113/2022/6426550

Li, X. S., Peng, J., Xie, Y. L., Li, Q. H., Zhou, T., Wang, J. W., et al. (2022). Influence of high-temperature treatment on strength and failure behaviors of a quartz-rich sandstone under true triaxial condition [J]. *Lithosphere* 2022, 3086647. doi:10.2113/2022/3086647

Lian, X. G., Li, Z. J., Yuan, H. Y., Hu, H. F., Cai, Y. H., and Liu, X. Y. (2020). Determination of the stability of high-steep slopes by global navigation satellite system (GNSS) real-time monitoring in long wall mining. *Appl. Sci.* 10 (6), 1952. doi:10.3390/app10061952

Lin, X., Liu, Z. S., Gao, Y., and Wu, B. Y. (2019). Analysis of main controlling factors of oil production based on machine learning[J]. *China CIO News* 2019(12), 94–97+99. doi:10.3969/j.issn.1001-2362.2019.12.044

Liu, G., Ye, L. X., Chen, Q. Y., Chen, G. S., and Fan, M. Y. (2022). Abnormal event detection of city slope monitoring data based on multi-sensor information fusion [J]. *Bull. Geol. Sci. Technol.* 41 (02), 13–25. doi:10.19509/j.cnki.dzkq.2022.0060

Liu, W. Y., Men, D. Y., Liang, J. F., and Wang, W. Z. (2012). Monthly load forecasting based on gray relational degree and least squares support vector machine[J]. *Power Syst. Technol.* 36 (08), 228–232. doi:10.13335/j.1000-3673.pst.2012.08.036

Liu, Y., Xu, C., Huang, B., Ren, X. W., Liu, C. Q., Hu, B. D., et al. (2020). Landslide displacement prediction based on multi-source data fusion and sensitivity states. *Eng. Geol.* 271, 105608. doi:10.1016/j.enggeo.2020.105608

Liu, Z. B., Shao, J. F., Xu, W. Y., Chen, H. J., and Zhang, Y. (2014). An extreme learning machine approach for slope stability evaluation and prediction. *Nat. Hazards (Dordr).* 73 (2), 787–804. doi:10.1007/s11069-014-1106-7

Liu, Z. X., Han, K. W., Yang, S., and Liu, Y. X. (2020). Fractal evolution mechanism of rock fracture in undersea metal mining. *J. Cent. South Univ.* 27, 1320–1333. doi:10.1007/s11771-020-4369-z

Ma, K., Tang, C. A., Liang, Z. Z., Zhuang, D. Y., and Zhang, Q. B. (2017). Stability analysis and reinforcement evaluation of high-steep rock slope by microseismic monitoring. *Eng. Geol.* 218, 22–38. doi:10.1016/j.enggeo.2016.12.020

Meng, Q. X., Wang, J., Tao, Z. G., Ren, D. Z., Zhang, G. C., Li, X. S., et al. (2021) 3D nonlinear analysis of stilling basin in complex fractured dam foundation, *Lithosphere* 2021. 2738130. doi:10.2113/2022/2738130

Pang, J. (2019). Application of automatic monitoring system in high-risk slope monitoring project[J]. *Surv. World* 2019, 70–73. doi:10.3969/j.issn.1673-7563.2019.02.019

Peng, M., Li, X. Y., Li, D. Q., Jiang, S. H., and Zhang, L. M. (2014). Slope safety evaluation by integrating multi-source monitoring information. *Struct. Saf.* 49, 65–74. doi:10.1016/j.strusafe.2013.08.007

Pieraccini, M., Luzi, G., Mecatti, D., Noferini, L., and Atzeni, C. (2006). Ground-based SAR for short and long term monitoring of unstable slopes. *IEEE* 2006, 92–95. doi:10.1109/EURAD.2006.280281

Qin, H. N., Ma, H., N., and Yu, Z. X. (2020). Analysis method of landslide early warning and prediction supported by ground-based SAR technology[J]. *Geomatics Inf. Sci. Wuhan Univer-sity* 45 (11), 1697–1706. doi:10.13203/j.whugis20200268

Sakellariou, M. G., and Ferentinou, M. D. (2005). A study of slope stability prediction using neural networks. *Geotech. Geol. Eng. (Dordr).* 23, 419–445. doi:10.1007/s10706-004-8680-5

Salvoni, M., and Dight, P. M. (2016). Rock damage assessment in a large unstable slope from microseismic monitoring - MMG Century mine (Queensland, Australia) case study. *Eng. Geol.* 210, 45–56. doi:10.1016/j.enggeo.2016.06.002

Šegina, E., Peterne, l. T., Urbančič, T., Realini, E., Zupan, M., Jez, J., et al. (2020). Monitoring surface displacement of a deep-seated landslide by a low-cost and near real-time GNSS system. *Remote Sens.* 12 (20), 3375. doi:10.3390/rs12203375

Sulandri, S., Basuki, A., and Bachtiar, F. A. (2021). Metode deteksi intrusi menggunakan algoritme extreme learning machine dengan correlation-based feature selection. *J. Teknol. Inf. Dan. Ilmu Kompute* 8 (1), 103–110. doi:10.25126/jtiik.0813358

Tuerxun, M., Zhao, M. J., Ning, C. B., and Kong, Q. H. (2021). Prediction of diesel engine exhuast emissions based on deep extreme learning machine[J]. *Sci. Technol. Eng.* 21 (36), 15646–15654. doi:10.3969/j.issn.1671-1815.2021.36.046

Wang, L., Xu, H., Shu, B., and Tian, Y. Q. (2021). A multi-source heterogeneous data fusion method for landslide monitoring with mutual information and IPSO-lstm neural network[J]. *Geomatics Inf. Sci. Wuhan Univ.* 46 (10), 1478–1488. doi:10.13203/j.whugis20210131

Wang, R. B., Zhang, K., Qi, J., Xu, W. Y., Long, Y., and Huang, H. F. (2022). A prediction model of hydrodynamic landslide evolution process based on deep learning supported by monitoring big data. *Front. Earth Sci. (Lausanne).* 10, 15. doi:10.3389/feart.2022.829221

Wang, Z. W., Wang, L., Huang, G. W., Han, Q. Q., Xu, F., and Yue, C. (2020). Research on multi-source heterogeneous data fusion algorithm of landslide monitoring based on BP neural network [J]. *J. Geomechanics* 26, 575–582. doi:10.12090/j.issn.1006-6616.2020.26.04.050

Xu, B., Huang, Q. S., and Qian, Y. D. (2022). Stability trends of Jinpingzi landslide: Numerical study. *Front. Earth Sci.* 1465, 940438. doi:10.3389/feart.2022.940438

Xu, N. W., Li, B., Dai, F., Fang, Y. L., and Xu, J. (2016). Stability analysis of bedding rock slopes during excavation based on microseismic monitoring[J]. *Chin. J. Rock Mech. Eng.* 35 (10), 2089–2097. doi:10.13722/j.cnki.jrme.2015.0747

Xue, J., and Shen, B. (2020). A novel swarm intelligence optimization approach: Sparrow search algorithm. *Syst. Sci. Control Eng.* 8 (1), 22–34. doi:10.1080/21642583.2019.1708830

Yan, Y., Xiong, G. L., Zhou, J. J., Wang, R. H., Huang, R. H., Yang, M. W., et al. (2022). A whole process risk management system for the monitoring and early warning of slope hazards affecting gas and oil pipelines. *Front. Earth Sci. (Lausanne).* 9, 1336. doi:10.3389/feart.2021.812527

Yi, T., Han, X., Weitao, Y., Wenbing, G., Erhu, B., Tingye, Q., et al. (2022). Study on the overburden failure law of high-intensity mining in gully areas with exposed bedrock. *Front. Earth Sci.* 10, 833384. doi:10.3389/feart.2022.833384

Zeng, L., Lei, S. M., Wang, S. S., and Chang, Y. F. (2021). Ultra-short-term wind power prediction based on OVMD-SSA-DELM-GM model[J]. *Power Syst. Technol.* 45 (12), 4701–4712. doi:10.13335/j.1000-3673.pst.2021.0552

Zhang, L. F., Chen, Z. H., Zhou, T. B., Nian, G., Q., Wang, J., M., and Zhou, Z., H. (2020). Multi-source information fusion and stablity prediction of slope based on gradient boosting decision tree[J]. *J. China Coal Soc.* 45 (S1), 173–180. doi:10.13225/j.cnki.jccs.2020.0137

Zhang, Y. G., Tang, J., Cheng, Y. M., Huang, L., Guo, F., Yin, X. J., et al. (2022). Prediction of landslide displacement with dynamic features using intelligent approaches. *Int. J. Min. Sci. Technol.* 32, 539–549. doi:10.1016/j.ijmst.2022.02.004

Zhang, Y. H., Wang, Li., Shu, B., Haibo, H., and Long, L. (2020). "Application of an adaptive weighted estimation fusion algorithm in landslide deformation monitoring data processing," in IOP Conference Series:Earth and Environmental Science, Changchun, China, 21-23 August 2020.

Zhao, M. H., Liu, J. Y., Zhao, H., and Hou, J. C. (2022). Stability analysis of rock slopes based on MSDP criterion[J]. *Chin. J. Rock Mech. Eng.* 41 (01), 10–18. doi:10.13722/j.cnki.jrme.2021.0362

frontiers | Frontiers in Earth Science

TYPE Original Research
PUBLISHED 06 January 2023
DOI 10.3389/feart.2022.990454

Check for updates

OPEN ACCESS

EDITED BY
Yan Du,
University of Science and Technology Beijing, China

REVIEWED BY
Yanlin Zhao,
Hunan University of Science and Technology, China
Lei Xue,
Institute of Geology and Geophysics (CAS), China
Linwei Li,
Guizhou University, China
Jia Yanchang,
College of Geosciences and Engineering North China University of water resources and hydropower, China
Zhanping Song,
Xi'an University of Architecture and Technology, China
Yunliang Tan,
Shandong Univeristy of Science and Technology, China

*CORRESPONDENCE
Yifan Zhao,
zyf_neu@126.com

SPECIALTY SECTION
This article was submitted to Geohazards and Georisks, a section of the journal Frontiers in Earth Science

RECEIVED 10 July 2022
ACCEPTED 07 September 2022
PUBLISHED 06 January 2023

CITATION
Zhao X, Zhao Y and Yu W (2023), The safety factor of a heterogeneous slope in an open-pit metal mine: A case study from the Tanjianshan gold mine. *Front. Earth Sci.* 10:990454. doi: 10.3389/feart.2022.990454

COPYRIGHT
© 2023 Zhao, Zhao and Yu. This is an open-access article distributed under the terms of the Creative Commons Attribution License (CC BY). The use, distribution or reproduction in other forums is permitted, provided the original author(s) and the copyright owner(s) are credited and that the original publication in this journal is cited, in accordance with accepted academic practice. No use, distribution or reproduction is permitted which does not comply with these terms.

The safety factor of a heterogeneous slope in an open-pit metal mine: A case study from the Tanjianshan gold mine

Xingdong Zhao, Yifan Zhao* and Wenlong Yu

School of Resources and Civil Engineering, Northeastern University, Shenyang, Liaoning, China

A landslide of the north open-pit (323N) and the stability and design optimization of the south open-pit (323S) slope in the 323 belts of the Tanjianshan Gold Mine were studied. On 14 September 2020, a large landslide occurred on the east side of 323N, which posed a severe threat to the safety production of the mine. To avoid a similar slide on the south open-pit in the 323S, the limit equilibrium method was used to estimate the stability of the final slope of the designed initially open-pit in the 323N. The results show that the location and scale of the landslide are in good agreement with the three-dimensional laser scanning data. The effectiveness of the limit equilibrium method in slope stability analysis of the Tanjianshan Gold Mine was validated. The stability of the final slope of the initial design of 323S was analyzed. The sensitivity of the safety factor of homogeneous slope and heterogeneous rock slope to the bench face angle (BFA) and the difference of landslide type were compared and studied. When the spatial geometric relationship of rock masses with different lithology is complex, the engineering analogy method is inapplicable to calculation of parameters such as the BFA of heterogeneous rock slope and overall slope angle of the open-pit. The slope safety factor should be checked, and the slope step parameters are warranted to be optimized. The safety and economic benefits of the slope can be improved.

KEYWORDS

open-pit mine, slope, heterogeneous, metal mine, safety factor

1 Introduction

Herein, the term "slope" is used to refer to stacked rock and soil with an inclined or vertical angle. Many projects involve slopes in geotechnical engineering, geological engineering, and other fields. In terms of the causes of slope formation, it is generally divided into artificial slopes and natural slopes (Wu, 2019). In mining engineering, the design of slopes is increasing day by day, and there are two contradictory requirements: steepening the slope to reduce the amount of excavation can save money; the stability of

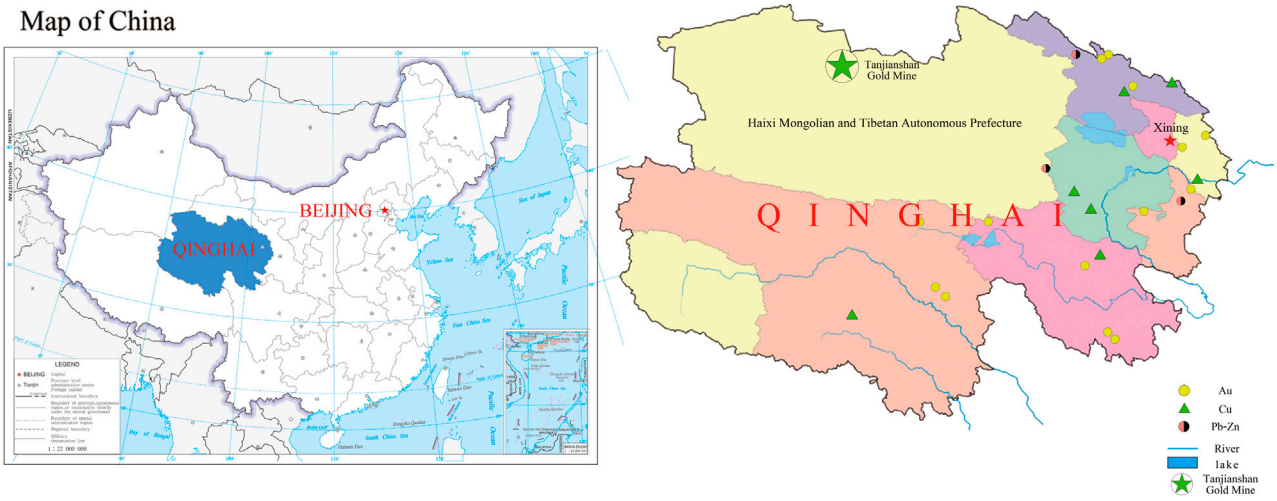

FIGURE 1
Location of the study area.

excessively steep slopes becomes worse, which may threaten the safety of life and property (Hoek and Bray, 1977). The design and stability of the open-pit slope need to be explored to achieve the goal of economic optimization on the premise of safety (Cai et al., 2004). There are mainly two kinds of slope stability analysis methods; one is the limit equilibrium method based on the rigid body limit equilibrium theory (Chen, 2003; Duncan, 1996), and the other is the numerical calculation method represented by the finite element method (Duncan, 1996; Griffiths and Lane, 2001; Zhang, 2002; Zheng et al., 2002). The Fellenius method proposed by Petersson in 1916 is the earliest limit equilibrium method (Wu, 2019). Currently, there are more than 10 limit equilibrium slice methods (Zhu et al., 2003), the difference between them lies in the assumption of interslice force and the equilibrium conditions to be satisfied (Zhu et al., 2005). For the general shape sliding surface, both theoretical and engineering analysts believe that the strict slice method must be adopted, that is, the slice meets all the equilibrium conditions (Duncan, 1996), to obtain a more reasonable safety factor. Morgenstern–Price method (Price and Morgenstern, 1967), Spencer's method (Spencer, 1968), and strict Janbu's method (Janbu, 1973) are widely used strict slice methods. The solution using the Morgenstern–Price method to calculate the safety factor is quite complex. Although some scholars have proposed various iterative methods for its solution (Chen and Morgenstern, 1983; Zhu et al., 2001), it is still difficult to master. Sarma's method (Sarma, 1973) is recognized as the most suitable method for rock slopes with steep discontinuities.

There are significant differences between rock mass and rock in metal mine slope engineering. Rock mass refers to the general term of *in-situ* media containing layers, faults, joints, folds, and other structural characteristics. The rock mass is discontinuous and has heterogeneous engineering properties (Brady and Brown, 2006). The geotechnical types and properties of heterogeneous slopes rock mass may vary greatly over even a short distance (Keefer and Larsen, 2007).

The limit equilibrium method can calculate the slope safety factor with clear physical meaning and the possible failure surface (Duncan, 1996), The slope safety factors calculated by the limit equilibrium method and the finite element method are similar, so it has become the most widely used method in slope stability analysis and is especially welcomed by the engineering community (Zeng and Tian, 2005).

Du Yan and Xie Mowen *et al.* proposed a possible mechanism for translational landslides, stepwise subsidence, which shows that geological conditions are the fundamental factors underlying translational land-slides (Du et al., 2020). Divya Shaunik and Mahendra Singh proposed a method of calculation for the bearing capacity of foundations on rock slopes intersected by a non-persistent discontinuity (Shaunik and Singh, 2020). A set of building reinforcement and community resilience enhancement methods that can resist slope deformation were proposed to improve the ability of urban areas to cope with slope geological hazards and emergency response (Jiaxing et al., 2022). A new method combining variable selection, the sparrow search algorithm, and a deep extreme-learning machine was proposed to investigate complex rock slope collapse, landslide, and other engineering disasters (Jiang et al., 2022).

Through communication with open-pit slope designers, it is found that the initial design of open-pit slopes in China is still based on an empirical analogy method, and the final slope angle given is an interval, which is not accurate enough. The empirical

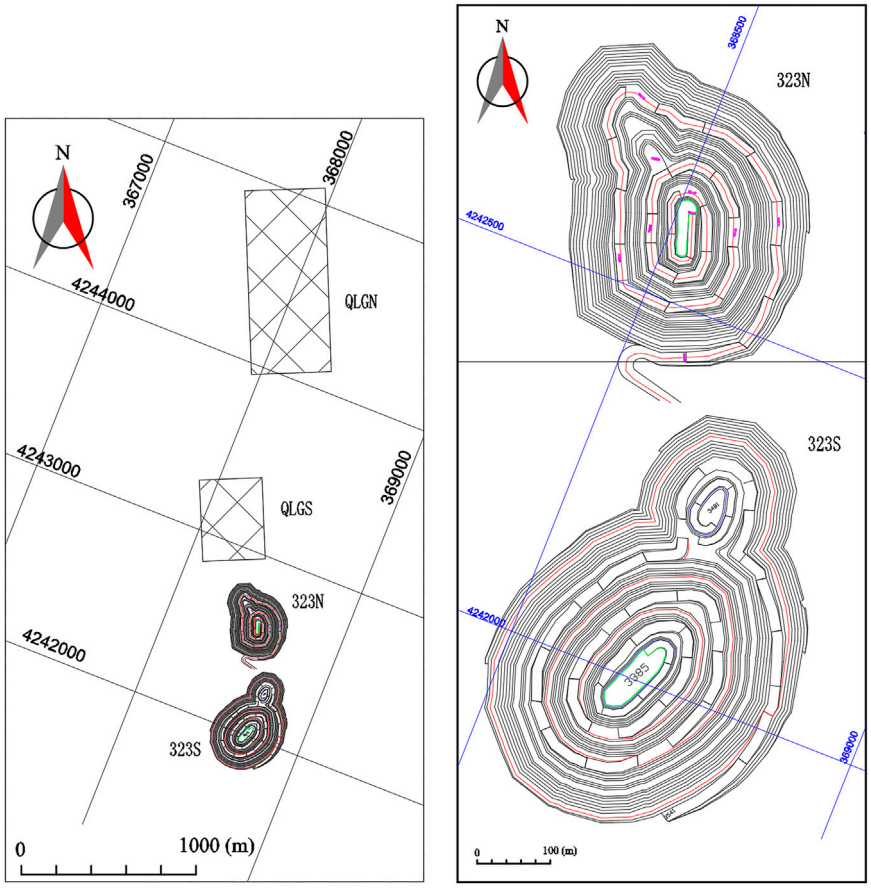

FIGURE 2
Location of the ore block.

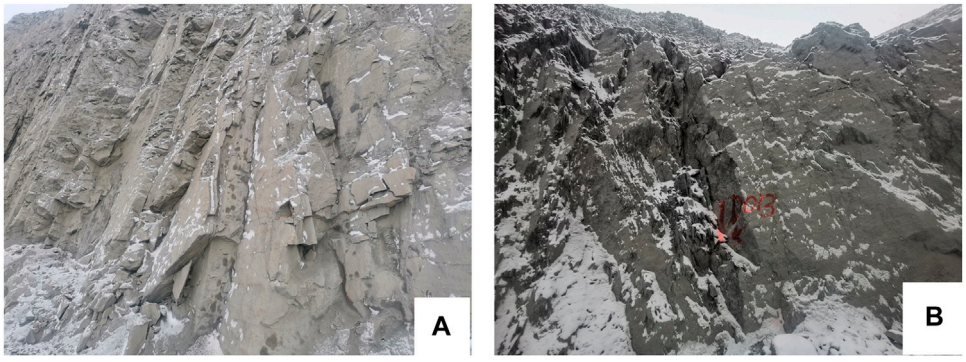

FIGURE 3
On-site photographs showing rock strata at the open slope site. **(A)** joints are not well developed. **(B)** only rocks and ores near the fold axis and the fault zone are broken.

analogy method is usually accurate for homogeneous slope. In the design of heterogeneous slope, there will be a variety of staggered distribution of rock layers. It is impossible to draw an analogy according to the strength of a certain rock. In the present work, the limit equilibrium method software Rocscience Slide was used to analyze the stability of the final slope of the open-pit

TABLE 1 The physico-mechanical parameters of the rock mass.

Lithology code	Lithology	Density	Young's modulus	Poisson's ratio	Tensile strength (MPa)	Cohesion (MPa)	Friction angle (/°)
		(kg/m^3)	(GPa)				
TDP	Marble	2,750	9.63	0.19	0.14	0.31	31.49
MGG	Gabbro	2,750	14.14	0.31	0.16	0.61	27.8
TPO	phyllite	2,750	2.4	0.1	0.03	0.06	23.96
Gravels	Gravels	2000	0.5	0.45	0	0.015	30
Faults/shears	Faults/ shears	2,750	2.5	0.4	0.004	0.025	15.3
Average value	—	2,727	3.2	0.17	0.038	0.083	23.6

initially designed in 323N. The results show that the location and scale of the landslide can well match three-dimensional laser scanning data. The effectiveness of the limit equilibrium method in slope stability analysis of the Tanjianshan Gold Mine was verified. The stability of the final slope of the initial design of 323S was estimated.

2 Motivation and the objective of the study

A landslide event occurred in 323N during the production process. 323S is about 70 m away from the straight-line distance of 323N. The open-pit slope of 323S is designed by using the engineering analogy method. To avoid similar landslide events, the safety factor calculation and parameter optimization of the initial design of 323S were conducted. The present work covers the slope design process using the observational method or engineering analogy method to determine the final slope angles to study the possible problems, observational method, and engineering analogy method relies on determining parameters such as the coefficient of a rock mass slope angle can determine the final stability and angle of repose, it is generally believed rock strength is higher, the greater the final slope angles can be, that is to say, the when final slope angle is smaller so the safety factor is larger. The landslide of 323N shows that the empirical method to determine the final slope angle has some shortcomings. When the spatial geometric relationship of rock masses with different lithology is complex, the engineering analogy method does not apply to calculating parameters such as the bench face angle (BFA) of heterogeneous rock slope and overall slope angle of an open-pit. The slope safety factor should be checked, and the slope step parameters should be optimized. The safety and economic benefits of the slope can be improved.

3 Engineering background

3.1 Engineering situation

The Tanjianshan Gold Mine is located in Dachaidan Town, Haixi Mongolian and Tibetan Autonomous Prefecture, Qinghai Province (Figure 1). Geographical coordinates: 94°23′22″–94°34′2″ east longitude; 38°13′00″~38°22′ 51″ north latitude; transportation in the mining area is relatively convenient.

As shown in Figure 2, there are currently four ore blocks in the Tanjianshan Gold Mine: the Qinglonggou North ore block, Qinglonggou South ore block (QLGS), 323N and 323S from north to south. The four ore blocks will form independent mining units. In this paper, 323N and 323S open-pits with a minimum straight-line distance of 70 m are taken as research objects. Geological conditions of them are basically the same. The engineering analogy method is applied to the mining design of 323. The mining design of 323S refers to the slope instability problem that occurs in the mining process of 323N, and the slope parameters are optimized.

3.2 Geological setting

The main faults in the mining area strike NW-SE, incline to SW, and dip at 60°. It has little influence on slope stability.

The rocks exposed in the mining area mainly include dolomite marble, phyllite, meta sandstone, schist, *etc.* Except for the relatively low hardness of phyllite, others are relatively hard. Generally, complete rock masses demonstrate good stability.

Figure 3A indicates that fissures and joints are not well developed, and the degree of fragmentation is low. As can be seen from Figure 3B, only rocks and ores near the fold axis and the fault zone are broken, and fissures, cleavages and schistosity are developed. The rock mass shows good stability, and the rock mass in the compressed schistosity zone formed by local tectonism has poor stability.

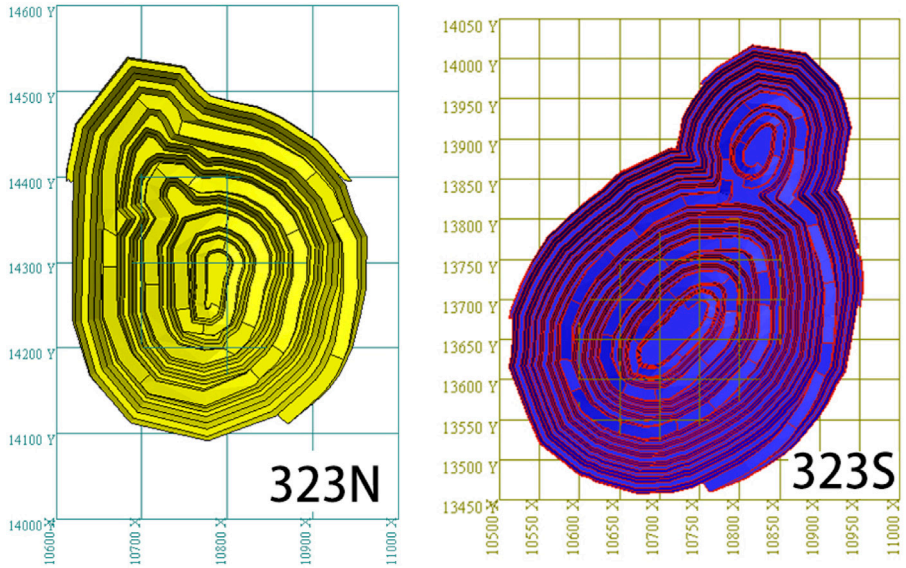

FIGURE 4
Design of 323N and 323S open-pits.

TABLE 2 Parameters of the open-pit.

	322N	323S
Surface size (m)	470 × 370	600 × 450
Pit bottom size (m)	80 × 30	110 × 35, 55 × 30
Bench height (m)	10	6
Bench face angle (°)	60–70 (Quaternary55)	60–75 (Quaternary50-55)
Width of safety platform (m)	3–5	3–5
Width of cleaning platform (m)	5–8	6–8
Width of transportation platform (m)	11.5 (Single lane), 16.5 (double lane)	10 (Single lane), 14.5 (double lane)
Highest elevation (m)	3,580	3,560
Bottom elevation (m)	3,430	3,385
Final slope angle (°)	30–41	37–44

The geomorphic type of the mining area shows that the borehole reveals that the mining area is not a high-pressure area. *In-situ* stress arises mainly from self-weight vertical stress. Modern tectonic stress has little effect on the stability of the slope.

The mining area has a typical continental plateau climate and belongs to the inland arid climate area. This area has an average annual precipitation of less than 100 mm and small water volume in the open-pit, which mainly stems from atmospheric precipitation. Groundwater has little effect on slope stability.

3.3 Physical and mechanical properties of rock mass

In 2015, relevant staff of University of Science and Technology Beijing conducted on-site rock samples (core diameters were all 61 mm). A total of 66 specimens were tested. Except for two specimens that were damaged in the process of core cutting and grinding, the remaining 64 specimens were all involved in the test. The test items included uniaxial compressive strength test of rock, uniaxial compressive deformation test of rock, tensile strength test of

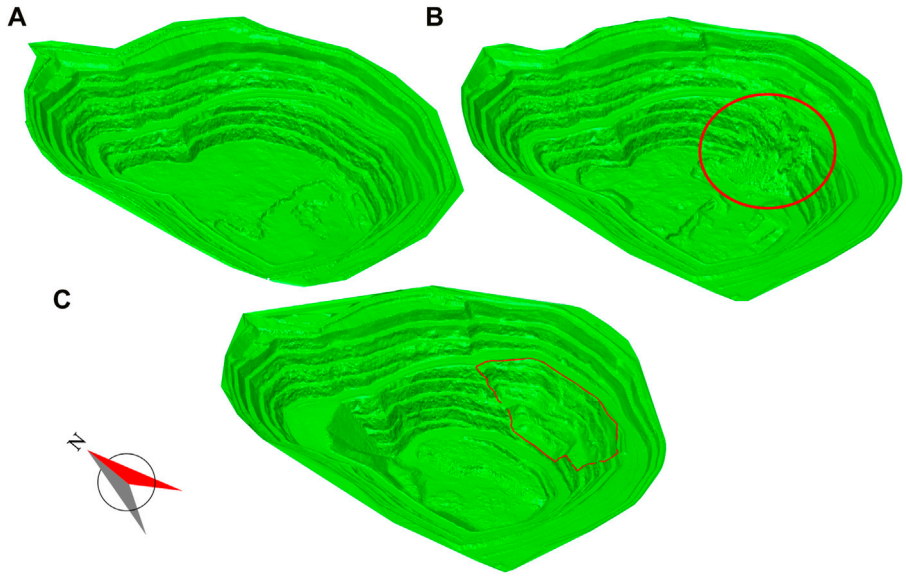

FIGURE 5
Three-dimensional laser scanning model. **(A)** Before the landslide, **(B)** After the landslide, **(C)** After the landslide rock is cleared.

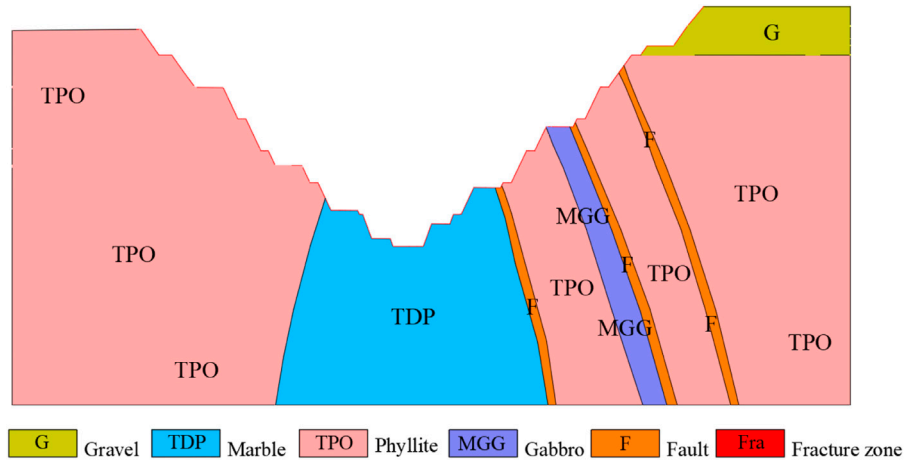

FIGURE 6
Schematic diagram of the lithology of the corresponding section in the landslide area.

rock, and shear test of structural plane of rock. The physico-mechanical parameters of the rock were obtained.

Hoek mentioned in the technical description of RocNews in 2012 that the blasting disturbance coefficient *D* reflects the impact of blasting and slope movement on rock mass strength (Hoek, 2012). When determining the value of disturbance coefficient *D*, factors such as blasting scale and bench height of open-pit mine should be considered. When mining the open-pit slope, the conventional blasting coefficient is taken as 1.0, for mechanical excavation it is set to 0.7, and in controlled blasting it is set to between 0.8 and 0.9 (herein we use $D = 1.0$). Based on the rock mechanics experiment, this paper obtains the rock mechanics parameters according to the rock strength calculation method proposed by Hoek (Table 1).

According to the proportion of different lithology in the 2# section, the strength of different lithology is taken from the basis of the weighted average. The average value is obtained as the rock mass strength of the whole slope. At this time, it is

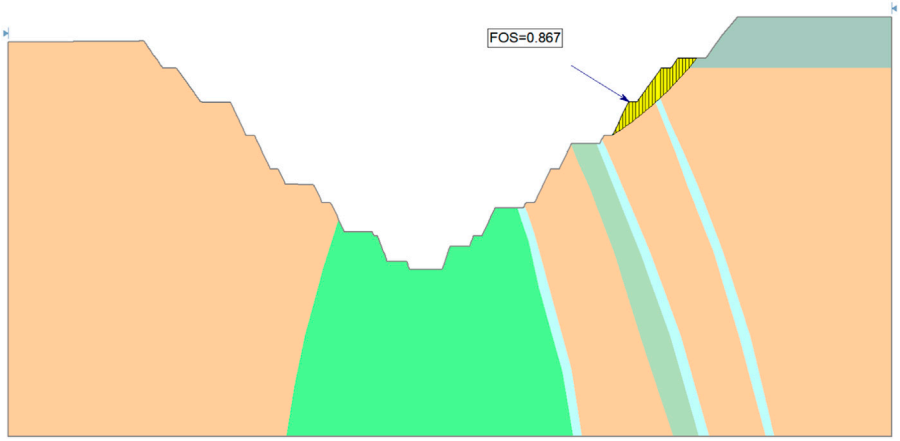

FIGURE 7
Schematic diagram of the safety factor calculation.

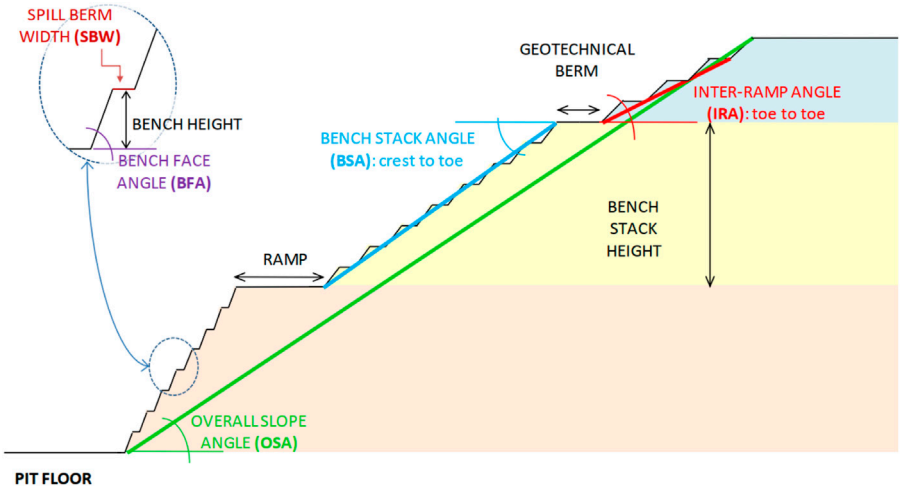

FIGURE 8
Schematic diagram of slope elements.

considered that the slope is homogeneous rock mass, and the safety factor is calculated and compared with that of an equivalent heterogeneous slope.

4 Stability analysis of the open-pit slope

4.1 Stability analysis of the open-pit slope in 323N

323N comprises 45 ore bodies, and the mining objects are the M6 to M44 ore bodies. It is distributed in the NNW trending mineralized zone, which is about 650 m long and 135 m wide. The control elevation is 3,314–3,555 m, the depth is generally 30–151 m, and the burial depth of individual ore bodies is more than 187 m. The ore body trend is NNW-SSE, inclining to NE and nearly vertical. The average thickness of the ore body is 1 m to several meters, and the maximum thickness is 13.68 m. The gold grade in the ore body is generally 1.00–6.00 g/t.

4.1.1 Initial design of the final slope

According to the engineering geological and hydrogeological conditions, combined with the factors such as slope height and service life, the final slope of the open-pit

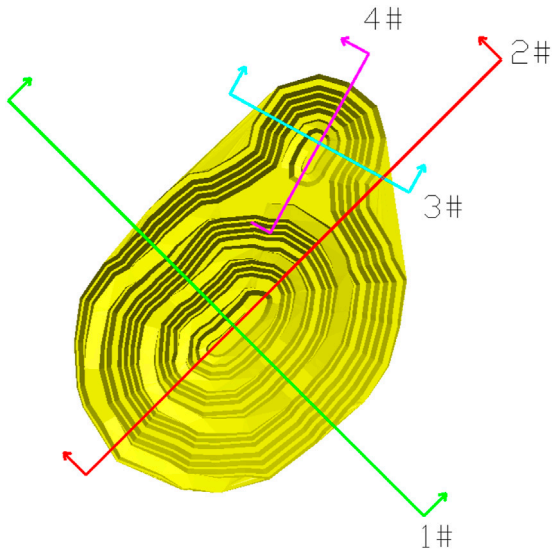

FIGURE 9
Schematic representation of profile position.

was designed using the engineering analogy method with reference to the relevant slope data of the Jinlonggou open-pit boundary of the adjacent mining area of the mine. The open-pit mining is shown in Figure 4, and the parameters of the open-pit are listed in Table 2.

4.1.2 Stability analysis of an open-pit slope

A landslide event occurred in 323N During the production process, on 14 September 2020, a landslide mass some 215.48 m long, 65.32 m wide, 49 m high (elevation 3,489–3,538 m) and 63,650 m^3 in volume slipped. The mine regularly uses three-dimensional laser scanning to measure and record the open-pit slope. The slope shapes before and after the landslide are shown in Figure 5. Figure 5A shows the slope before the landslide, Figure 5B displays the slope after the landslide, and Figure 5C exhibits the slope shape after the landslide mass is cleared and the slope is expanded. The landslide classification proposed by Varnes is more detailed and comprehensive. The system of landslide classification devised by the late D.J. Varnes has become the most widely used system (Varnes, 1958; Varnes, 1978; Cruden and Varnes, 1996). Hungr et al. (2014) proposed an update to this in 2014, The primary recommendation is to modify the definition of landslide-forming materials, to provide compatibility with accepted geotechnical and geological terminology of rocks and soils. According to the shape of the landslide and rock type, the slide is of the rock rotational slide-type, with an arc sliding surface. Due to the strength of the rock mass being lower than the design expectation, as the mining depth and slope height increase, the strength of rock mass is insufficient to maintain the stability of slopes.

The profile analysis of the landslide area is shown in Figures 6, 7.

The safety factor of the slope calculated by using Janbu's method is 0.867, and the landslide mass is shown in Figure 7, which is similar to the actual location of the landslide mass. The safety factor of the open-pit slope in the initial design of 323N is too low, leading to a landslide. The results show that the location and scale of the landslide are in good agreement with the three-dimensional laser scanning data. The effectiveness of the limit equilibrium method in slope stability analysis of the Tanjianshan Gold Mine was verified. When analyzing the final slope stability of 323N, the safety factor, landslide location and landslide scale of the slope can be assessed by using a limit equilibrium slice method.

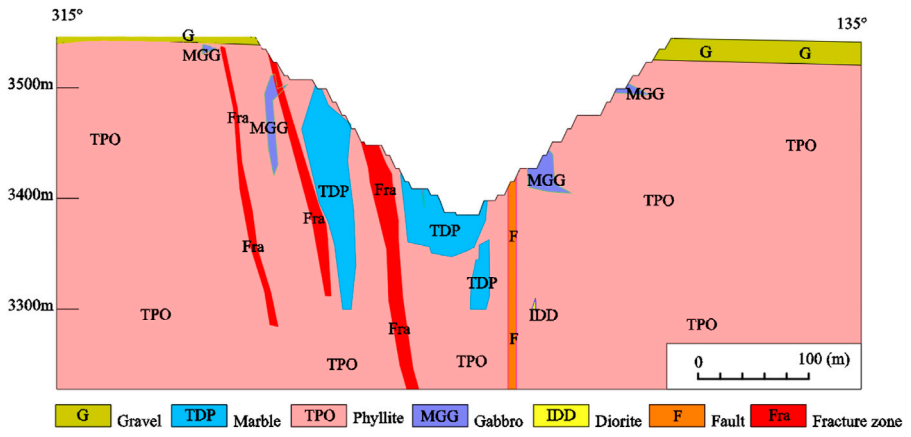

FIGURE 10
Schematic representation of 1#Profile lithology.

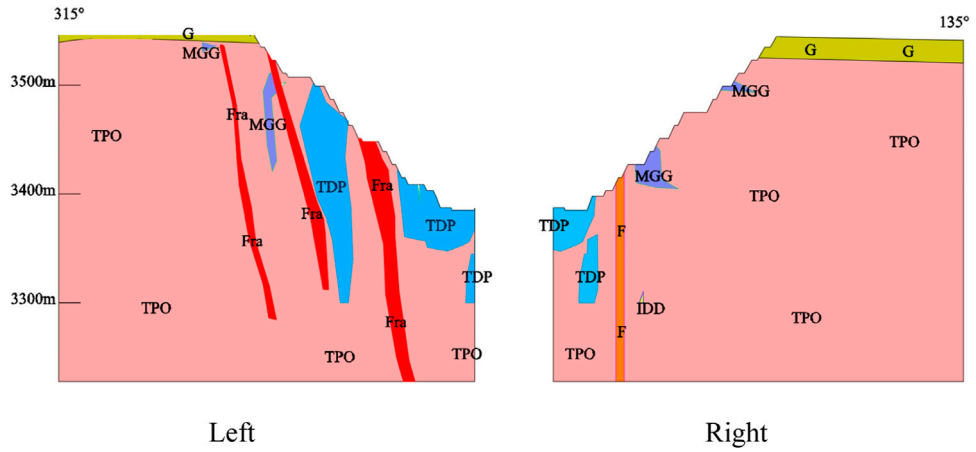

FIGURE 11
The 1#Profile.

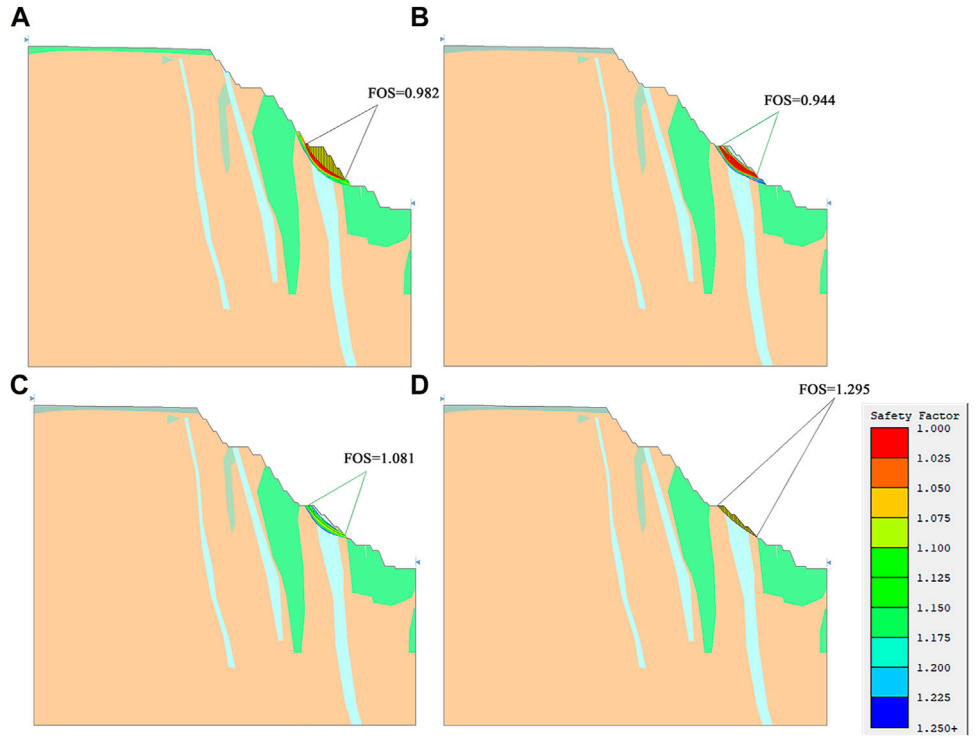

FIGURE 12
Calculation process of the slope FOS of 1# profile-left. **(A)** Initial design slope, **(B)** The BFA is modified from 65° to 55°, **(C)** The BFA is modified from 55° to 50°, **(D)** The BFA is modified from 50° to 49°.

4.2 Stability analysis of the open-pit slope in 323S

323S comprises 16 ore bodies, which are II-M1–II-M12 and III-M1–III-M4, respectively. The main ore body is II-M1, which occurs at an elevation of 3,300–3,513 m. The quaternary covers the surface, and the burial depth exceeds 35 m. The strike of the ore body is 169°–206°, the overall dip is northeast, and the dip angle is 55°–90°. The average thickness of the ore body is 7.00 m, and the average grade is 7.21 g/t.

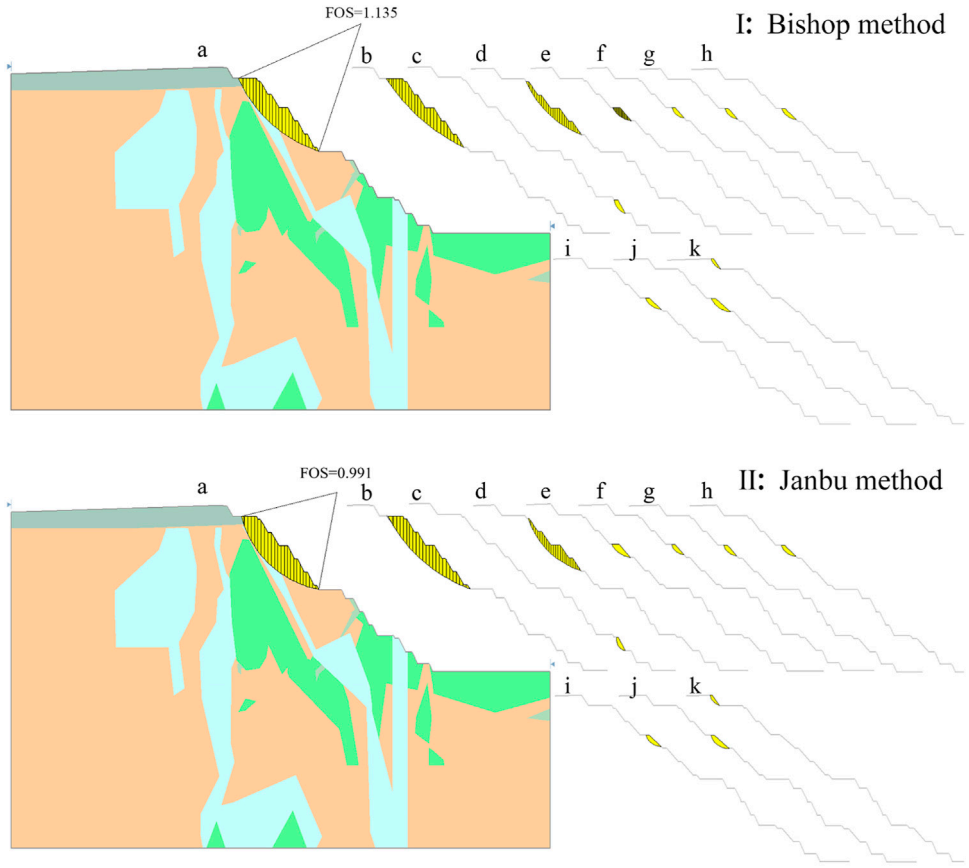

FIGURE 13
Calculation process of the slope FOS of 1# profile-left by Bishop and Janbu method. **(A)** Initial design slope, **(B–K)** The BFA was gradually reduced to optimize the slope parameters.

4.2.1 Initial design of final slope

According to the engineering geological and hydrogeological conditions, combined with the factors such as slope height and service life, the final slope of the open-pit was designed by using the engineering analogy method with reference to the relevant slope data of the 323N open-pit (a straight-line distance of about 70 m). The open-pit mining is shown in Figure 4, and the parameters of the open-pit are listed in Table 2.

4.2.2 Calculation of the slope safety factor and parameter optimization

According to Chinese National Standard GB51016-2014 Technical code for non-coal open-pit mines slope engineering, the slope of 323S is more than 160 m high, and the landslide may cause casualties and direct economic losses of more than 1 million yuan and potential economic losses of more than 10 million yuan. The hazard level of the slope is level I, the corresponding safety level is level I, and the load combination includes self-weight, blasting vibration force and groundwater. The load combination in the non-production period is self-weight and groundwater. By checking the relevant table, the design safety factor is determined to be 1.2–1.25. For conservatism, the design safety factor is not less than 1.25. The initial design slope is taken as the initial state, and its factor of safety (FOS) is calculated. If FOS is below 1.25, the BFA is reduced to obtain a larger safety factor, and the road width, sweeping platform width and safety platform width remain unchanged. The elements of the open-pit slope are shown in Figure 8. After the initial design is determined, the slope stability is optimized by reducing and changing the BFA to improve the slope safety factor.

The profile of the open-pit is shown in Figure 9. According to the three-dimensional geological model of lithologic data provided by the mine, the profile shown in Figure 10 is obtained.

The slope can be divided into two parts during the calculation, as shown in Figure 11. This research calculated the safety factors of the left and right slopes, constantly modified the slope parameters (BFA and final slope angle)

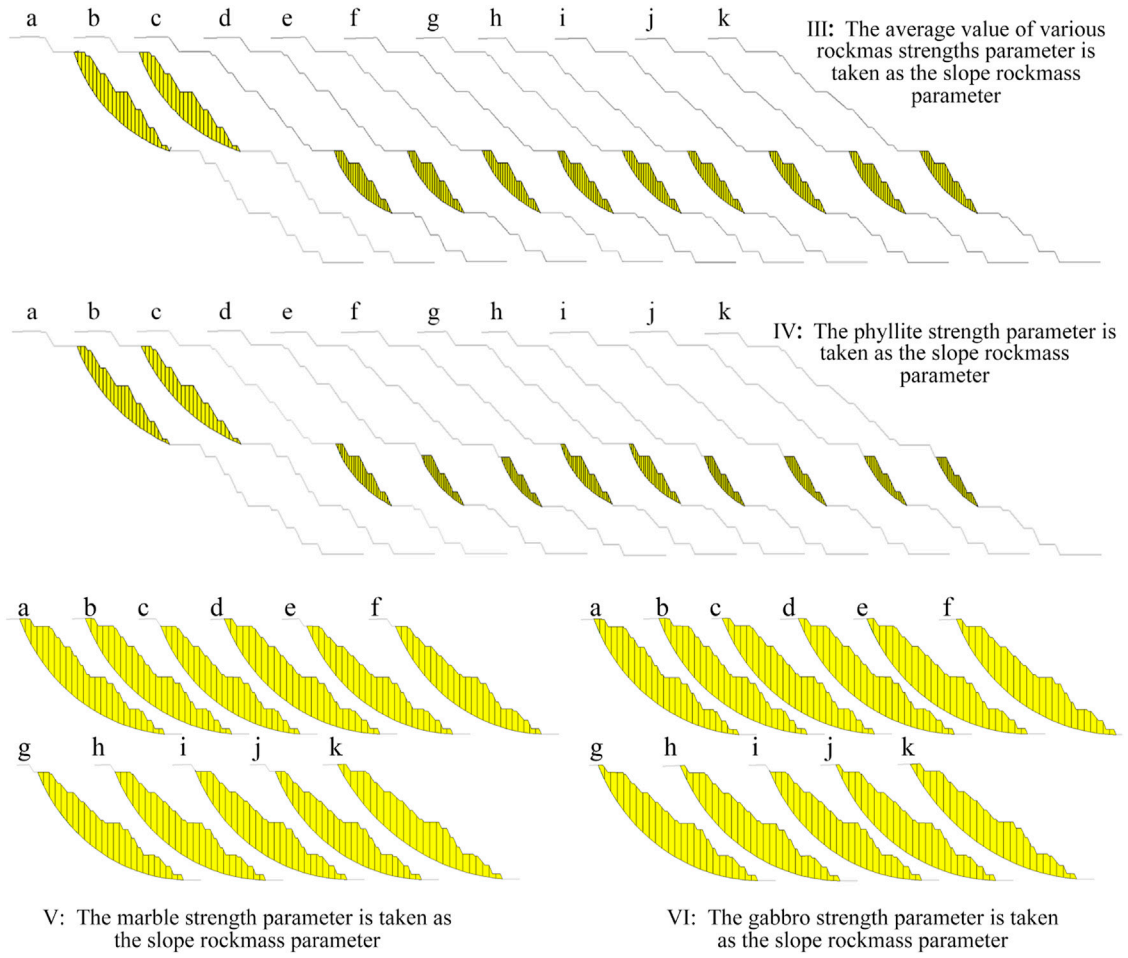

FIGURE 14
Changes in the safety factor and landslide location.

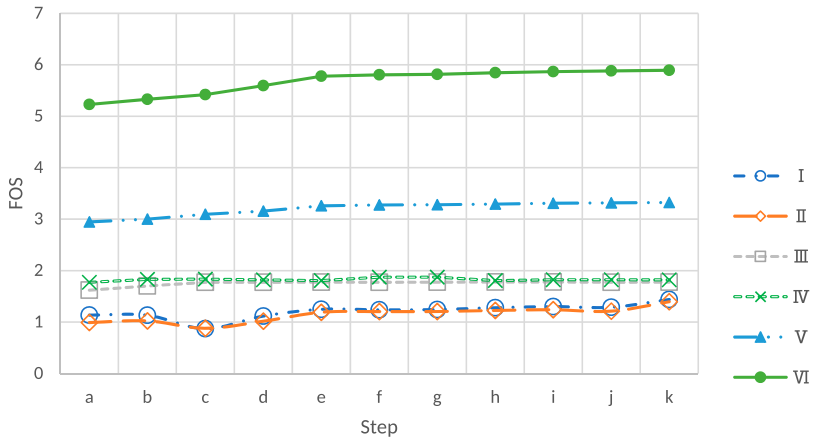

FIGURE 15
Variation of the slope FOS.

TABLE 3 Details of the data plotted Figure 15.

Calculation steps	I	II	III	IV	V	VI
a	1.135	0.991	1.619	1.773	2.946	5.229
b	1.132	1.023	1.702	1.829	3.002	5.328
c	0.871	0.88	1.773	1.834	3.094	5.419
d	1.116	1.017	1.773	1.821	3.156	5.594
e	1.247	1.19	1.775	1.805	3.26	5.779
f	1.237	1.203	1.772	1.872	3.275	5.805
g	1.243	1.205	1.775	1.873	3.28	5.815
h	1.278	1.225	1.777	1.806	3.293	5.845
i	1.3	1.239	1.778	1.823	3.309	5.867
j	1.288	1.212	1.772	1.823	3.317	5.881
k	1.437	1.394	1.775	1.821	3.324	5.893

and calculated the safety factor. Simplified Bishop method, GLE/Morgenstern-Price method, Janbu's method, modified Janbu's method, ordinary slice method/Fellenius method, Spencer's method, Lowe-Karafiath method, etc., were used for calculations. Due to the different calculation principles of different methods, the calculated FOS is slightly different. To ensure safety, the minimum value of FOS in different calculation methods was selected as the result.

As illustrated in Figure 12A, the safety factor of the slope is 0.982, and the arc line in the figure is the landslide line with a safety factor of less than 1.25. (a) Initial design slope; (b) The BFA at the landslide (the part with FOS less than 1.25) is modified from 65° to 55°, and the safety factor is 0.944, mainly because the fracture zone has been exposed after modification; (c) The BFA at the landslide (the part with FOS less than 1.25) BFA is adjusted from 55° to 50°; (d) The BFA at the landslide (the part with FOS less than 1.25) is changed from 50° to 49°. The safety factor is 1.295, which meets the requirements. The BFA of benches at the fracture zone and fault is 49°, the BFA of benches above and below the fracture zone is 55°, and the BFA of other benches is 60°. The BFA of Quaternary steps is 55°. The final slope angle is 38°.

As shown in Figure 13A, the safety factor of the slope is 1.135 and 0.982. (a) Initial design slope; (b) Modifying the BFA at the landslide (the part with FOS less than 1.25) from 65° to 60°; (c) Adjusting the BFA at the landslide (the part with FOS less than 1.25) from 60° to 55°, the landslide is located at the faults; (d) The BFA of benches at the faults is modified to 49°. The landslide is located at the fracture zone and four adjacent benches at the lower part; (e) The BFA of benches at the fracture zone is modified to 49°. The BFA of four adjacent benches at the lower part of the fracture zone is changed to be 50°; (f)The BFA of four adjacent benches at the lower part of the fracture zone is modified to be 49°; (g) The BFA of benches at the fracture zone is modified to 48°; (h) The BFA of benches at the fracture zone is modified to 45°; (i) The BFA of benches at the fracture zone is modified to 43°; (j) The BFA of benches at the fracture zone is modified to 42°; (k) The BFA of benches at the fracture zone is modified to 41°, the safety factor is 1.394, which meets the requirements. The BFA of benches at the fracture zone and fault is 41°, the BFA of four adjacent benches at the lower part of the fracture zone is 49°, and the BFA of other benches is 60–65°. The BFA of Quaternary steps is 55°. The final slope angle is 35°.

Curves I–VI shown in Figure 15 correspond to Figures 13, 14 respectively. Figure 15 and Table 3 indicate that the I–VI curve corresponds to the change of the slope FOS in Figures 13, 14, respectively. As shown in Figure 14, the strength of rock mass is shown to affect the shape of slope landslides. When the strength of the homogeneous slope is low, it is generally only a local landslide, ranging from a few meters to tens of meters, covering several steps. When a homogeneous slope is subjected to a high strength, the landslide is the landslide of the whole slope. Comparing Figure 13 and Figure14, heterogeneous slopes generally show landslides in weak rock mass or faults, that is, local landslides.

As shown in Figure 15, for heterogeneous slopes, the FOS did not increase monotonically with the decrease of BFA during the optimization process. Targeted reduction of step slope angle in areas with small safety factors can improve the FOS of the slope. From the curve of the homogeneous slope, the optimization after step C does not affect the FOS of the homogeneous slope; because the metal open-pit mine does not comprise a homogeneous single lithology, it is not appropriate to use the homogeneous slope to calculate the FOS and design the final slope. When compared with other mines, the lithology and rock mass strength are often compared, and the occurrence form of rock and slope form and the relationship between them are more ignored. The slope safety factor obtained in this way is often inappropriate. For example, the initial design of 323S refers to the design of 323N exposed slope, which is only 70 m away and has been adjusted according to the landslide event. The safety factor of the 323S initial design is still less than 1.

5 Conclusion

The two open-pit slopes of the Tanjianshan Gold Mine as the research object of this paper, are heterogeneous, and the following conclusions are drawn:

1) The engineering analogy method is adopted to design the final slope of the open-pit in the 323N and 323S. There are three types of the safety factors of the slope: ① If the safety factor is greater than the requirements of the relevant specifications, the final slope angle will be smaller, the stripped rock engineering work will be increased, and the mining efficiency and enterprise economic benefits will be reduced; ② Meeting the requirements of the safety factor of relevant specifications; ③ If the safety factor is less than the

requirements of the safety factor of relevant specifications, which needs to be avoided, the risk of a landslide on the slope will occur, which is not conducive to the safety and stability of the mine;

2) When the same rock mass exists in the open-pit slope with the same slope parameters in different forms, its safety factor is different. The fault/fracture zone herein has different forms, and whether it is exposed or not will greatly affect the safety factor of the slope;
3) Generally, reducing the BFA of the slope will increase the safety factor of the slope when reducing the final slope angle, however, the study found that the safety factor does not increase linearly with the decrease of step slope angle, and sometimes the safety factor will decrease as the step slope angle decreases;
4) Generally speaking, when using the traditional engineering analogy method to design the final slope of the open-pit, the limit equilibrium method or numerical simulation method should be used to evaluate the stability of the slope, check the safety factor, and optimize the slope parameters after the initial design is completed.

Data availability statement

The raw data supporting the conclusion of this article will be made available by the authors, without undue reservation.

Author contributions

Investigation, XZ and YZ; methodology, XZ and YZ. Writing—original draft preparation, YZ and WY; Writing—review and editing, YZ and WY; data curation, XZ and WY. All authors have read, and agreed upon the published version of the manuscript.

Funding

This work was supported by a project of the NSFC Shandong United Fund (U1806208) and the Key Projects of National Natural Science Foundation of China (52130403), the Fundamental Research Funds for the Central Universities (N2001033 and N2101022) and the Opening Project of State Key Laboratory of Nickel and Cobalt Re-sources Comprehensive Utilization.

Conflict of interest

The authors declare that the research was conducted in the absence of any commercial or financial relationships that could be construed as a potential conflict of interest.

Publisher's note

All claims expressed in this article are solely those of the authors and do not necessarily represent those of their affiliated organizations, or those of the publisher, the editors and the reviewers. Any product that may be evaluated in this article, or claim that may be made by its manufacturer, is not guaranteed or endorsed by the publisher.

References

Brady, B. H., and Brown, E. T. (2006). *Rock mechanics: For underground mining*. Berlin: Springer science & business media.

Cai, M., Qiao, L., Li, C., and Wng, J. (2004). Stability analysis and design optimization of High and Steep Slope in deep concave open-pit Mine. *Journal of University of Science and Technology Beijing* 26(05), 6. doi:10.13374/j.issn1001-053x.2004.05.004

Chen, Z., and Morgenstern, N. R. (1983). Extensions to the generalized method of slices for stability analysis. *Can. Geotech. J.* 20 (1), 104–119. doi:10.1139/t83-010

Chen, Z. (2003). *Soil slope stability analysis: Theory, methods and program*. Beijing: China Water Power Press.

Cruden, D. M., and Varnes, D. J. (1996). "Landslide types and processes," in *Landslides-investigation and mitigation. National research council transportation research board special report 247*. Editors K. A. Turner and R. L. Schuster (Washington, DC: National Academy Press).

Du, Y., Xie, M., and Jia, J. (2020). Stepped settlement: A possible mechanism for translational landslides. *Catena* 187, 104365. doi:10.1016/j.catena.2019.104365

Duncan, J. M. (1996). State of the art: Limit equilibrium and finite-element analysis of slopes. *J. Geotech. Engrg.* 123 (7), 577–596. doi:10.1061/(asce)0733-9410(1996)122:7(577)

Griffiths, D. V., and Lane, P. A. (2001). Slope stability analysis by finite elements. *Géotechnique* 51 (7), 653–654. doi:10.1680/geot.1999.49.3.387

Hoek, E. (2012). "Blast damage factor D," in *Technical note for RocNews*, 1–7. February 2, 2012, Winter 2012 Issue, RocScience (2012). Available at: http://www.rocscience.com/assets/files/uploads/8584.pdf

Hoek, E., and Bray, J. (1977). *Rock slope engineering*. Revised Second Edition. London: Institute of Mining & Metallurgy.

Hungr, O., Leroueil, S., and Picarelli, L. (2014). The Varnes classification of landslide types, an update. *Landslides* 11 (2), 167–194. doi:10.1007/s10346-013-0436-y

Janbu, N. (1973). *Slope stability computations*. New Jersey, United States: John Wiley and Sons. Incorporated.

Jiang, S., Liu, H., Lian, M., Lu, C., Zhang, S., Li, J., et al. (2022). Multi-source information fusion and displacement prediction of rock slope based on variable selection and SSA-DELM model. *Front. Environ. Sci.* 982069.

Jiaxing, Z., Fei, L., Jin-an, W., Anqi, G., and Chengyuan, H. (2022). Stability control of slopes in open-pit mines and resilience methods for disaster prevention in urban areas: A case study of fushun west open pit mine. *Front. Earth Sci. (Lausanne).* 10879387. doi:10.3389/feart.2022.879387

Keefer, D. K., and Larsen, M. C. (2007). Assessing landslide hazards. *Science* 316 (5828), 1136–1138. doi:10.1126/science.1143308

Price, V. E., and Morgenstern, N. R. (1967). The analysis of stability of general slip surface. *Geotechnique* 15 (3), 393–394.

Sarma, S. K. (1973). Stability analysis of embankments and slopes. *Géotechnique* 23 (3), 423–433. doi:10.1680/geot.1973.23.3.423

Shaunik, D., and Singh, M. (2020). Bearing capacity of foundations on rock slopes intersected by non-persistent discontinuity. *Int. J. Min. Sci. Technol.* 30 (5), 669–674. doi:10.1016/j.ijmst.2020.03.018

Spencer &, E. (1968). A method of analysis of the stability of embankments assuming parallel inter-slice forces. *Géotechnique* 18 (3), 384–386. doi:10.1680/geot.1968.18.3.384

Varnes, D. J. (1958). "Landslide types and processes," in *Landslides and engineering practice*, 24: 20–47. State of California: National Research Council (U.S.). Highway Research Board Reprinted.

Varnes, D. J. (1978). Slope movement types and processes. In: in Editor Schuster RL. and RJ. Krizek. *(eds) Landslides, analysis and control, special report 176: Transportation research board*National Academy of SciencesWashington, DC, 11–33.

Wu, S. (2019). *Slope engineering*. Beijing: Metallurgical Industry Press.

Zeng, Y., and Tian, W. (2005). Slope stability analysis by combining FEM with equilibrium method. *Journal of Rock Mechanics and Engineering* 24 (S2), 5355–5359.

Zhang, J. (2002). Finite element simulation and stability evaluation of slope excavation. *Journal of Rock Mechanics and Engineering* 21 (06), 843–847. doi:10.3321/j.issn:1000-6915.2002.06.016

Zheng, H., Li, C., Li, Z., and Ge, X. (2002). Finite element method for solving safety factor. *Journal of Geotechnical Engineering*. (05), 626–628. doi:10.3321/j.issn:1000-6915.2002.06.016

Zhu, D., Li, Z., Huang, M., and Qian, Q. (2005). Modification to three well-known methods if slope stability analysis. *Journal of Rock Mechanics and Engineering*. 24 (02), 183–194. doi:10.3321/j.issn:1000-6915.2005.02.001

Zhu, D. Y., Lee, C. F., and Jiang, H. D. (2003). Generalised framework of limit equilibrium methods for slope stability analysis. *Géotechnique* 53 (4), 377–395. doi:10.1680/geot.53.4.377.37322

Zhu, D. Y., Lee, C. F., Qian, Q. H., Zou, Z. S., and Sun, F. (2001). A new procedure for computing the factor of safety using the Morgenstern-Price method. *Can. Geotech. J.* 38 (4), 882–888. doi:10.1139/t01-002

frontiers | Frontiers in Earth Science

TYPE Original Research
PUBLISHED 10 January 2023
DOI 10.3389/feart.2022.982939

Check for updates

OPEN ACCESS

EDITED BY
Bo Li,
Tongji University, China

REVIEWED BY
Danqing Song,
Tsinghua University, China
Fei Guo,
China Three Gorges University, China

*CORRESPONDENCE
Changshuo Wang,
wcshuo@126.com
Zhanyou Luo,
lzy0395@163.com

SPECIALTY SECTION
This article was submitted to Geohazards and Georisks, a section of the journal Frontiers in Earth Science

RECEIVED 30 June 2022
ACCEPTED 20 September 2022
PUBLISHED 10 January 2023

CITATION
Luo Z, Zheng W, Du S, Huang M and Wang C (2023), Experimental study on normal deformation characteristics of filled rock joints with typical fluctuation morphology.
Front. Earth Sci. 10:982939.
doi: 10.3389/feart.2022.982939

COPYRIGHT
© 2023 Luo, Zheng, Du, Huang and Wang. This is an open-access article distributed under the terms of the Creative Commons Attribution License (CC BY). The use, distribution or reproduction in other forums is permitted, provided the original author(s) and the copyright owner(s) are credited and that the original publication in this journal is cited, in accordance with accepted academic practice. No use, distribution or reproduction is permitted which does not comply with these terms.

Experimental study on normal deformation characteristics of filled rock joints with typical fluctuation morphology

Zhanyou Luo[1,2,3]*, Wei Zheng[1], Shigui Du[2], Man Huang[3] and Changshuo Wang[2]*

[1]Tunnel and Underground Space Academy, Zhejiang University of Science and Technology, Hangzhou, Zhejiang, China, [2]Institute of Rock Mechanics, Ningbo University, Ningbo, Zhejiang, China, [3]Department of Civil Engineering, Shaoxing University, Shaoxing, Zhejiang, China

The uneven deformation of filled rock joints subjected to ground stress can easily cause instability in engineering rock masses. Fluctuations in morphology and filling are the main factors affecting the normal deformation of filled rock joints. To study the effect of the degree of filling and the degree of morphology fluctuation on the normal deformation of filled rock joints, we conducted a systematic experimental study. First, rock joints with joint roughness coefficients of 1,5, 9, 13, and 17 were selected based on Barton's typical curves. Then, filled rock joint samples were made using a self-developed filled rock joint sample mold and three-dimensional engraving technology. Lastly, compression tests were carried out to analyze the effect of the degree of filling and the degree of morphology fluctuation on the normal deformation characteristics of filled rock joints. The results show that the degree of filling significantly affects the normal deformation of filled rock joint samples. The normal deformation of filled rock joints has a nonlinear relationship with normal stress. The power function equation can well represent the normal closure deformation behavior of filled rock joints. Additionally, a relationship between the maximum closure deformation of filled rock joints and the degree of filling was established based on Bandis's empirical formula. The proposed equation takes into account the effect of the degree of filling by replacing the rock joint opening with filling thickness, and the predicted values are in good agreement with the experimental results.

KEYWORDS

rock joint, normal deformation, compression test, filling degree, fluctuation morphology

1 Introduction

The normal deformation of rock joints is an important mechanical behavior of rock masses, which can have a major effect on the safe construction and production operation of many engineering projects, such as oil or gas exploitation, enhanced geothermal systems, and the underground disposal of nuclear waste (Muller, 1977). The uneven

deformation of rock joints can easily cause instability in engineering rock masses, resulting in engineering accidents. Therefore, it is of great importance to engineering to conduct experimental studies on the normal deformation characteristics of filled rock joints. Scholars have carried out extensive experimental and theoretical studies into the normal closure deformation of jointed rock masses and have obtained some important results.

In laboratory investigations into the normal deformation characteristics of rock joints, Makurat et al. (1995) conducted normal cyclic loading and unloading tests on natural rock joints using a CSFT device and obtained a normal stress-closure deformation curve of rock joints. Qiao and Li. (2016) suggested that the relationship between the normal stress and rock joint closure deformation is typically nonlinear, based on compression test results. Zhao (2017) conducted an experimental study on the loading rate effect of the normal deformation of rock joints and obtained the relationship between normal deformation and loading rate. Yuan (2017) revealed the variation law of maximum normal deformation, initial normal stiffness, and rock joint opening degree with joint roughness coefficient (JRC), by conducting normal compression tests of rock joints with different morphologies. Luo and Jiang (2021) studied the effect of stress on the mechanical properties of rock joints. Huang et al. (2022) analyzed the interaction mechanism between stress and liquid-filled rock joints.

In establishing a constitutive model, Shehata (1971) and Sun (1983) suggested that a power function model and a semi-pair function model could fit well the normal stress-rock joint closure deformation curve, but the power function model was not able to predict the maximum rock joint closure deformation. Then, a hyperbolic equation was proposed by Bandis et al. (1983) and later modified by Bandis and Barton (1985) to improve the prediction performance. Two free parameters, the maximum rock joint closure and initial normal stiffness, were used to shape the hyperbola. Saeb and Amadei (1992) proposed an analytical equation to predict the maximum rock joint closure of an opened rock joint. Additionally, Malama and Kulatilake (2003) established a unified index model based on the deviation between the predicted results of a modified hyperbolic model and test data. Furthermore, Guo and Su (2010) used five different models to fit the normal stress-closure deformation curve. Their results showed that the modified hyperbolic model could well represent the normal deformation behavior of rock joints. Wu and Gao (2015) used a hyperbolic model to fit the normal stress-closure deformation curves obtained from the normal cyclic loading-unloading test and realized for the first time the numerical simulation analysis of cyclic loading-unloading. Zhang and Ding (2017) considered that the power function model can be used to represent the relationship between normal stress and rock joint closure deformation in different load stages under low stress conditions. Li and Cui (2021) analyzed the variation rule of parameters in the power function equation by performing a numerical simulation.

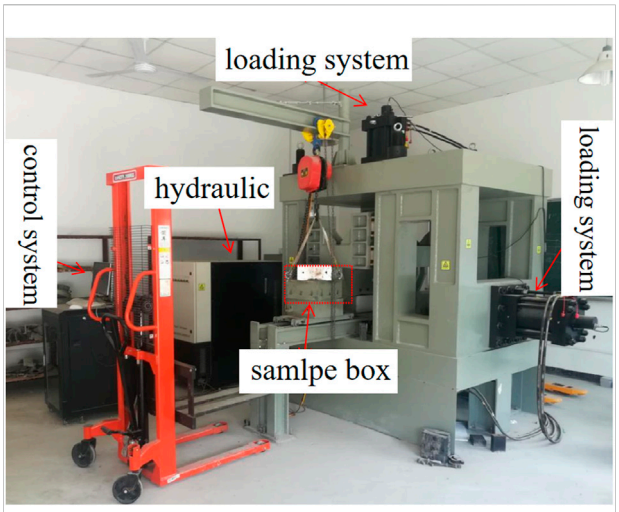

FIGURE 1
Multifunctional rock-soil contact damage test system.

In summary, although scholars have carried out extensive studies into the normal deformation characteristics of rock joints, there have been few studies of filled rock joints. This paper presents the results of a systematic study of the normal deformation characteristics of filled rock joints with different fluctuation morphologies. We propose a new formula that can better represent the relationship between maximum closure deformation of filled rock joints and the degree of filling, based on Bandis's empirical formula, and its performance was verified using test results.

2 Methodology

2.1 Multifunctional rock-soil contact damage test system

All of the compression tests of rock joints with differing degrees of morphology fluctuation and filling were conducted using a multifunctional rock-soil contact damage test system. The test system was composed of a loading system, sample box system, control system, and hydraulic system, as shown in Figure 1. Loading stress was provided by a MOOG D633 1000 kN hydraulic actuator, and the maximum pressure was 1000 kN. A force sensor and a displacement sensor were fixed on the axial steel columns to monitor the pressure and axial deformation of the samples. The technical parameters of the multifunctional rock-soil contact damage test system are shown in Table 1.

TABLE 1 Technical parameters of the multifunctional rock-soil contact damage test system.

Number	Name	Technical parameter
1	Dimension (length × width × height)	2735 mm × 2850 mm × 3000 mm
2	Maximum normal loading test force	1000 kN
3	Load precision	±1%
4	Displacement precision	0.01 mm
5	Normal deformation measurement range	0–100 mm

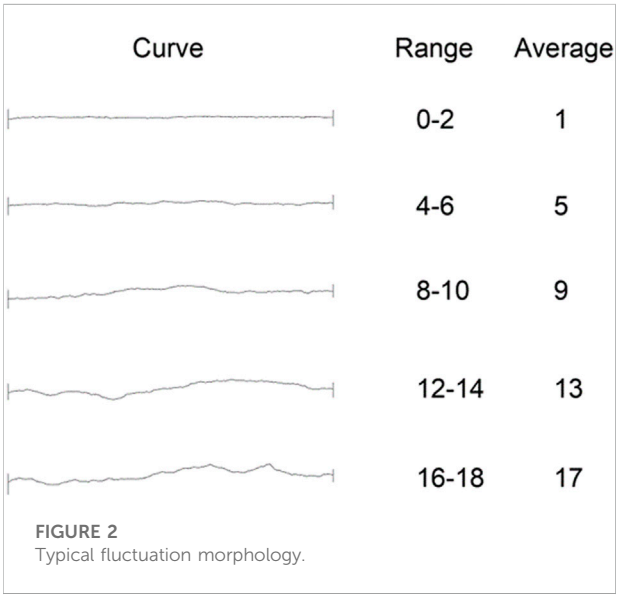

FIGURE 2
Typical fluctuation morphology.

2.2 Test material

2.2.1 Rock samples

For tests, the upper and lower specimens of rock joints usually comprise a similar material or natural rock. To make the mechanical properties of the rock samples the same as the field rock mass, diabase was used in this study.

A uniaxial test of the diabase was carried out using rock triaxial apparatus (MATEST C089-19CR), and the compressive strength was found to be 113.6 MPa.

2.2.2 Typical fluctuation morphology of rock joints

Fluctuation morphology is a major factor that affects the normal deformation of rock joints. To study the effect of the degree of morphology fluctuation on the normal closure deformation of filled rock joint, rock joints with JRCs of 1, 5, 9, 13, and 17 were selected based on a typical Barton curve, as shown in Figure 2.

According to the method for the quantitative description of rock joints recommended by the International Society of Rock Mechanics, the average degree of fluctuation of a rock joint profile is used as a quantitative parameter to describe the degree of fluctuation of rock joint morphology. The average degree of fluctuation of rock joints is defined as:

$$\boldsymbol{a} = \frac{\mathbf{1}}{\mathbf{2}}(\boldsymbol{a_1} + \boldsymbol{a_2}) \tag{1}$$

Where a_1 is the left morphology degree of fluctuation, mm; a_2 is the right morphology degree of fluctuation, mm.

The average degree of fluctuation of a selected Barton curve is shown in Table 2.

2.2.3 Filling

Rock joints generate interlayer fracture zones under the action of weathering, ground stress, and other factors, and rock is broken, forming fillings. Diabase fragments were used as the filling material in this study, and the filling acquisition process is shown in Figure 3. Diabase fragments were produced using a three-dimensional (3D) numerical control engraving machine. Then, fragments with particle size less than 1 mm were collected after screening. Lastly, a filling with a moisture content of 5% was prepared after adding an appropriate quantity of water to the fragments.

The composition and content of the filling are shown in the Table 3:

2.3 Sample preparation

2.3.1 Engraving of rock joint fluctuation morphology

It is difficult to obtain natural rock joints in the field, and some rock joint conditions can barely meet the test design requirements. Therefore, in this study 3D engraving technology was used to sample rock joints with different fluctuation morphologies. First, a model of rock joint morphology was established using modeling software. Next, a path file was generated using path processing software, which was then imported into the engraving control software. Lastly, rock joints were engraved using the numerical engraving machine, as shown in Figure 4.

TABLE 2 Average degree of fluctuation of the Barton curve.

JRC	Degree of left morphology fluctuation/mm	Degree of right morphology fluctuation/mm	Average degree of fluctuation/mm
1	1.5	0.84	1.17
5	2.24	3.88	3.06
9	2.62	9.64	6.13
13	8.86	8.68	8.77
17	13.54	7.88	10.71

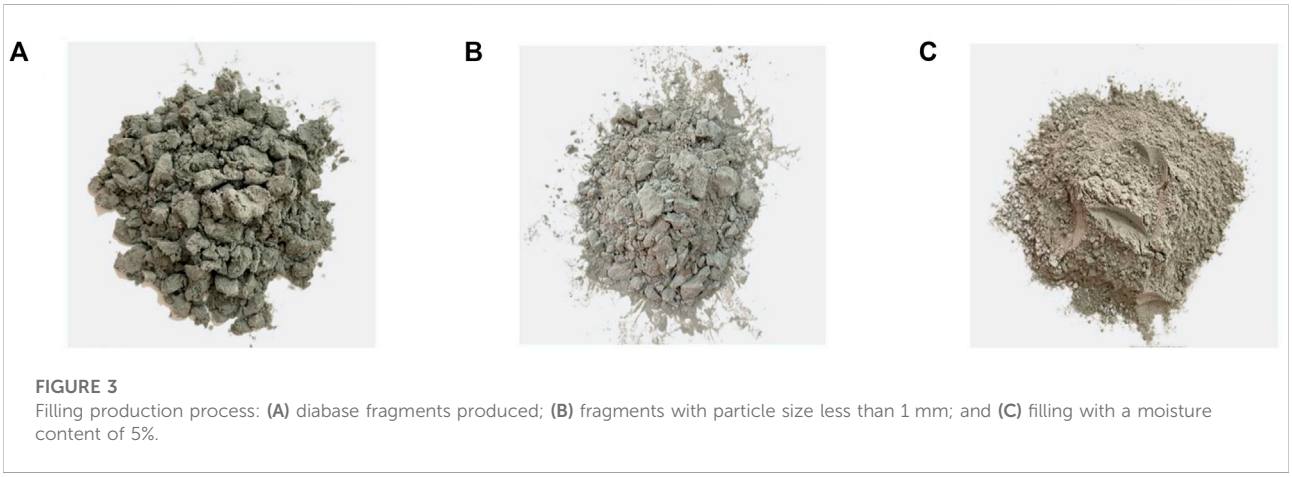

FIGURE 3
Filling production process: **(A)** diabase fragments produced; **(B)** fragments with particle size less than 1 mm; and **(C)** filling with a moisture content of 5%.

TABLE 3 Composition and content of filling.

Number	Composition	Content (%)
1	Silicon dioxide (SiO_2)	70.87
2	Aluminum oxide (Al_2O_3)	12.57
3	Calcium oxide (CaO)	2.18
4	Magnesium oxide (MgO)	1.56
5	Potassium oxide (K_2O)	2.55
6	Sodium oxide (Na_2O)	3.34
7	Titanium dioxide (TiO_2)	0.7

2.3.2 Preparation of filled rock joint samples

The pre-experiment showed that the following relationship between filling mass and thickness exists:

$$m_{soil} = \alpha \cdot t \tag{2}$$

Where m_{soil} is the filling mass, g; α is the empirical coefficient, g·mm^{-1}; and t is the filling thickness, mm.

Compression test results showed that the filling thickness was 5.1 mm after preloading on a filled rock joint sample with a filling mass of 200 g. Thus, the coefficient α was calculated to be 39.2 g mm^{-1} according to Eq. 2.

The preparation of filled rock joint samples is a key process in compression tests. The production process is as follows. First, the lower rock joint specimen is placed in the sample box, and then the prepared filling is added to the lower rock joint specimen in three layers. Finally, the upper rock joint specimen is placed on the filling. The specific process is shown in Figure 5.

2.4 Test plan

The compression tests were carried out under a lateral limit to prevent filling extrusion. A normal stress of 12.5 MPa was determined, to avoid the occurrence of fractures in the rock joint sample during the loading stage. This experiment was divided into five groups, with each group containing five rock joint samples with filling degrees k of 0, 0.5, 1, 1.5, and 2. The specific test scheme is shown in Table 4.

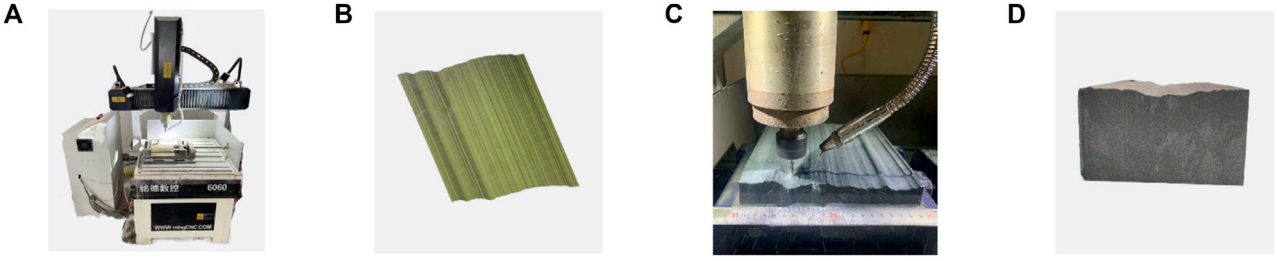

FIGURE 4
(A) Engraving machine; **(B)** the path file generated; **(C)** the engraving process; and **(D)** an engraved rock joint sample.

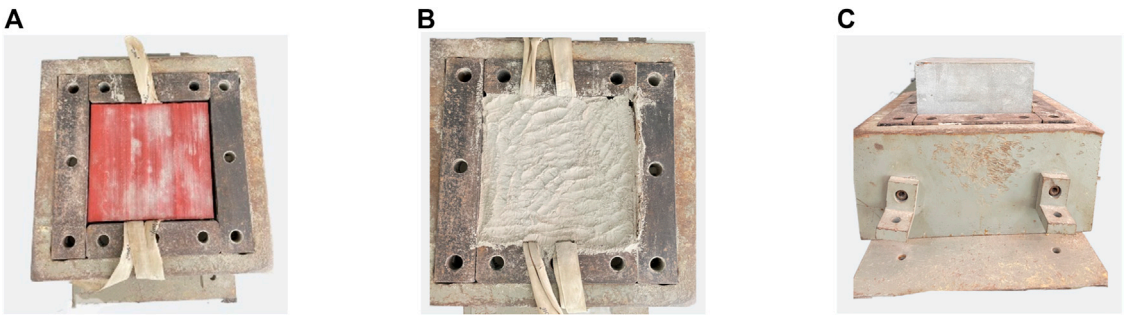

FIGURE 5
Sample preparation process: **(A)** rock joint lower specimen; **(B)** filling is added; and **(C)** rock joint upper specimen.

TABLE 4 The thickness of the filling.

Degree of filling	JRC1 (mm)	JRC5 (mm)	JRC9 (mm)	JRC13 (mm)	JRC17 (mm)
0	0	0	0	0	0
0.5	0.58	1.53	3.07	4.39	5.36
1	1.17	3.06	6.13	8.77	10.71
1.5	1.76	4.59	9.20	13.16	16.07
2	2.34	6.13	12.26	17.54	21.42

3 Analysis of test results

3.1 The normal stress-closure deformation curve of unfilled rock joints

Figure 6 shows the normal stress-closure deformation curve of an intact sample and that of a rock jointed sample. The closure deformation of rock joints was calculated by the normal deformation of the rock jointed sample minus that of the intact sample.

Figure 7 shows the curves of normal stress-closure deformation of unfilled rock joints and initial normal stiffness-JRC of unfilled rock joints. It can be seen from Figure 7A that the closure deformation of rock joints has a nonlinear relationship with normal stress. Closure deformation shows an increasing trend with the increase of normal stress. Additionally, there is a critical value of normal stress in a normal stress-closure deformation curve. Closure deformation of the rock joint increases rapidly with the increase of normal stress, when the normal stress is lower than the critical value. The

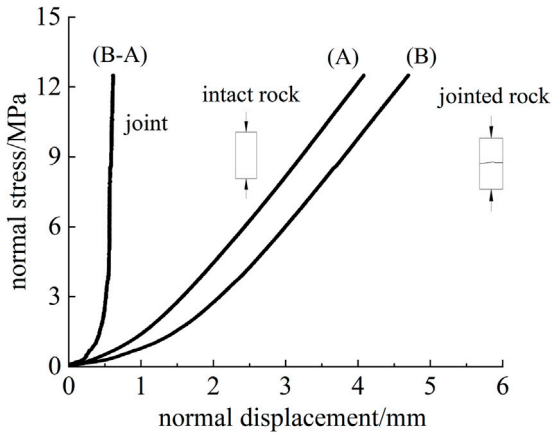

FIGURE 6
Normal deformation of a rock joint with a JRC of 13.

increasing rate of closure deformation slows down as the normal stress exceeds the critical value. The test results (Figure 7B) indicate that closure deformation of unfilled rock joints decreases and initial normal stiffness increases with the increasing degree of morphology fluctuation.

3.2 The normal stress-closure deformation curve of filled rock joints

Figure 8 shows the curves of normal stress-closure deformation of filled rock joints under different degrees of filling. It can be seen from Figure 8 that closure deformation of filled rock joints increases with the increase of normal stress and that the curve possesses a high degree of nonlinearity. The primary reason is that filling is the main factor affecting the normal closure deformation of filled rock joints, and the deformation of filled rock joints is significantly greater than that of unfilled rock joints.

Figure 9 shows the curve of normal stress-closure deformation of filled rock joints under same filling thickness. The test results indicate that under same filling thickness, rock joint closure deformation decreases with the increasing degree of morphology fluctuation.

3.3 The normal stress-closure deformation curve of filled rock joints in the loading-unloading stage

Figure 10 shows the curve of normal stress-closure deformation of a filled rock joint sample in the loading-unloading stage. It can be seen from Figure 10 that the filled rock joint sample exhibits a hysteresis loop between the loading and unloading paths. An irreversible deformation is observed after unloading. The irreversible deformation of a high degree of filling (k=2) rock jointed sample is significantly greater than the low degree of filling (k=0.5) rock jointed sample. The main reason is that the degree of filling contributes more to hysteresis and irrecoverable deformation than the degree of morphology fluctuation does.

4 Normal closure characteristics of filled rock joints

4.1 Normal stress-closure deformation relationship of filled rock joints

The power function is a commonly used normal constitutive model of rock joints. A test curve of filled rock joints with a JRC of 17 was fitted using a power function model. The results are shown in Figure 11, and the fitting parameters are shown in Table 5. The test results show that the power function equation

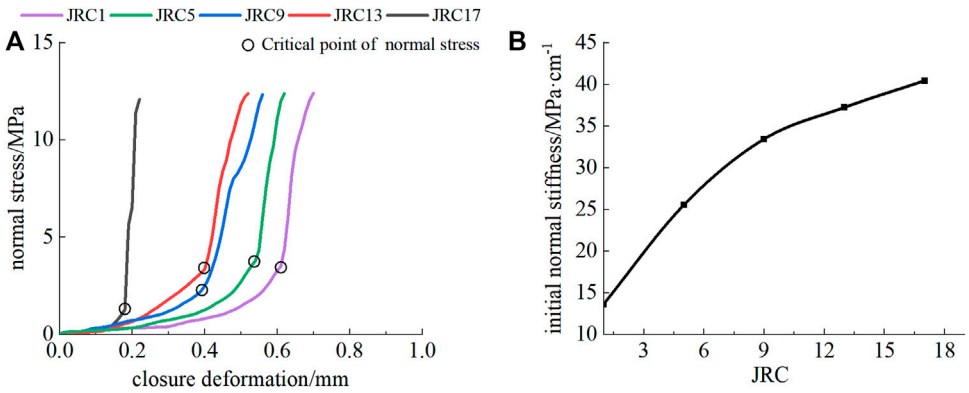

FIGURE 7
(A) Normal stress-closure deformation curve of an unfilled rock joint and **(B)** initial normal stiffness-JRC curve of an unfilled rock joint.

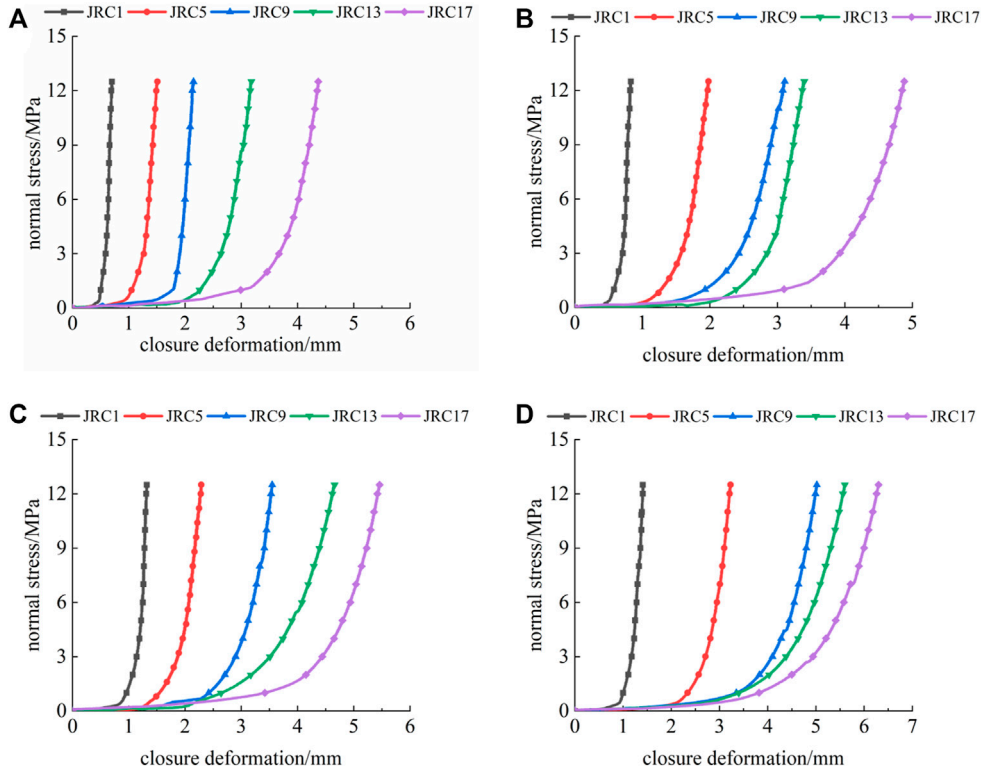

FIGURE 8
Normal stress-closure deformation curve of a filled rock joint under different degrees of filling: **(A)** k=0.5; **(B)** k=1.0; **(C)** k=1.5; and **(D)** k=2.

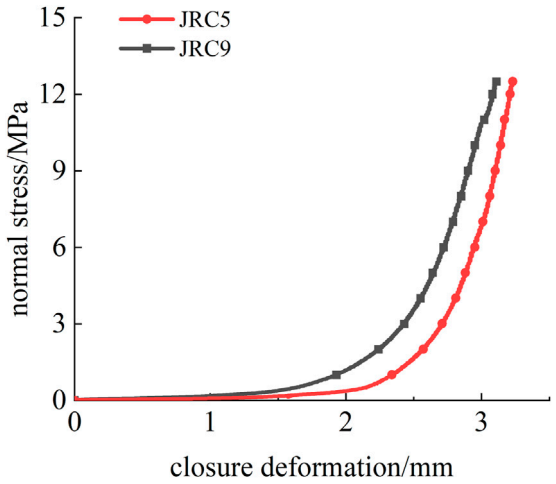

FIGURE 9
Normal stress-closure deformation curve of a filled rock joint under the same filling thickness.

can well represent the normal deformation behavior of filled rock joints. The fitting correlation coefficients between the power function model and a test curve under different filling degrees are greater than 0.99. Nevertheless, the values predicted by the power function model show deviation from the test results in the early stage of loading, but the degree of agreement between test results and predicted values is high in the later stages of loading. Additionally, the fitting of parameters *a* and *b* of the model shows an increasing trend with the increase in the degree of filling. The fitting curve can stably represent the normal deformation behavior of filled rock joints.

4.2 Influence of the degree of morphology fluctuation on the normal closure characteristics of filled rock joints

Existing experimental studies show that the deformation of rock jointed rock changes from rock joint closure to elastic deformation of rock as the normal stress is $1/3\sigma_c$ (Liu and Tang, 1999). Therefore, when the normal stress reaches $1/3\sigma_c$, the deformation of a rock joint reaches the maximum closure deformation V_m. Figure 12A shows the curve of normal stress-closure deformation of filled rock joints with different degrees of morphology fluctuation. It can be seen from Figure 12A that the normal stress-closure deformation curve of filled rock joints possesses a high degree of nonlinearity. The

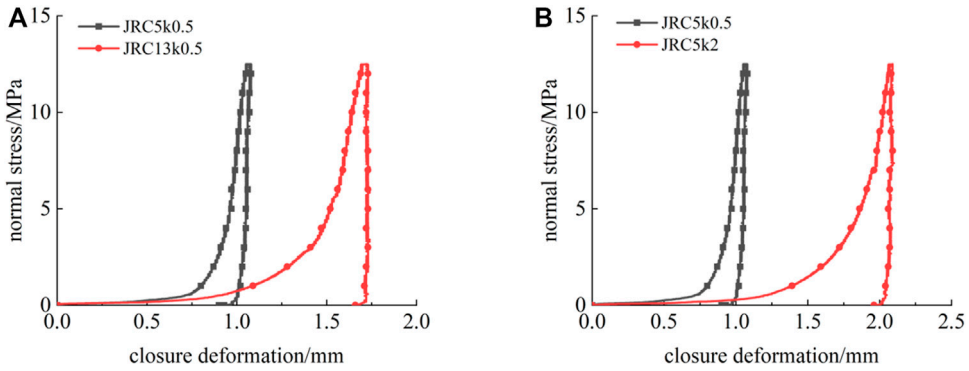

FIGURE 10
Normal stress-closure deformation curve of a filled rock joint sample in the loading-unloading stage: **(A)** k=0.5 and **(B)** JRC=5.

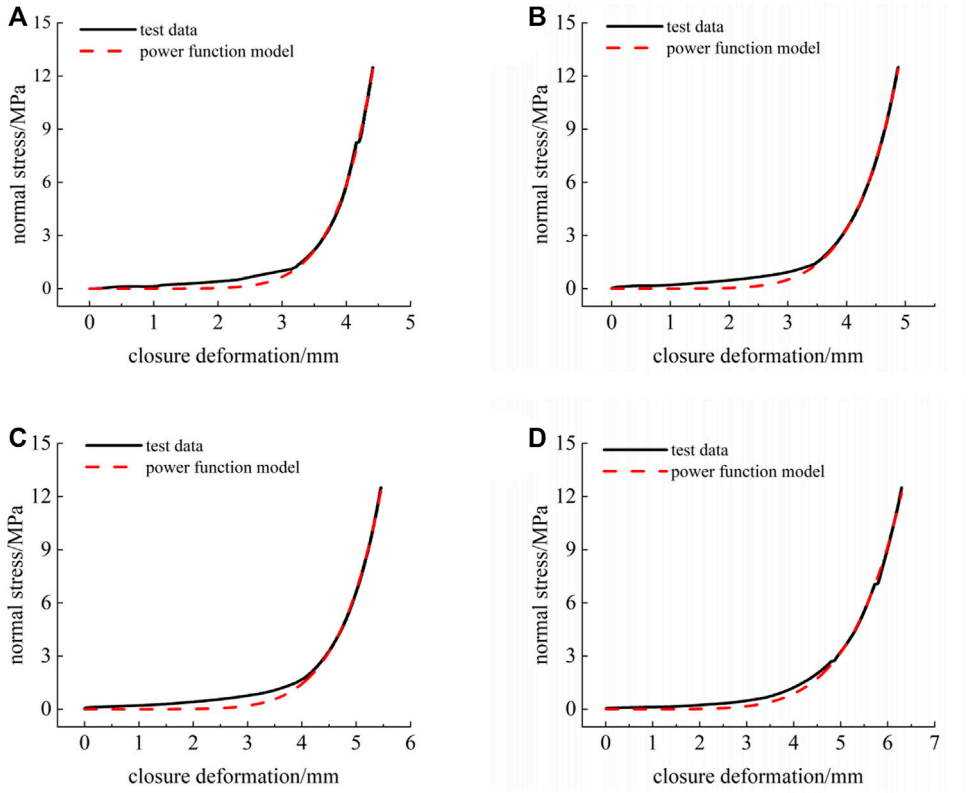

FIGURE 11
Power function fitting curve: **(A)** k=0.5; **(B)** k=1.0; **(C)** k=1.5; and **(D)** k=2.

stiffness of rock joints increases with the increase in closure deformation.

Figure 12B shows the curve of the maximum closure deformation-JRC. It can be seen from Figure 12B that under the same degree of morphology fluctuation, the maximum closure deformation of filled rock joints increases as the degree of filling increases. The primary reason is that the closure deformation of filled rock joints is mainly caused by the deformation due to filling. Additionally, under the same degree of filling, the maximum closure deformation of filled rock joints increases with the increase in the degree of morphology fluctuation.

TABLE 5 Fitting parameters of the power function model.

Degree of filling	Functional equation	Fitting parameter *a*	Fitting parameter *b*	Fitting correlation coefficient R^2
0.5	$\sigma_n = (\Delta V_j/b)^{\frac{1}{a}}$	0.1319	3.1675	0.9975
1		0.1518	3.3296	0.9985
1.5		0.1539	3.8021	0.9974
2		0.1722	4.0949	0.9971

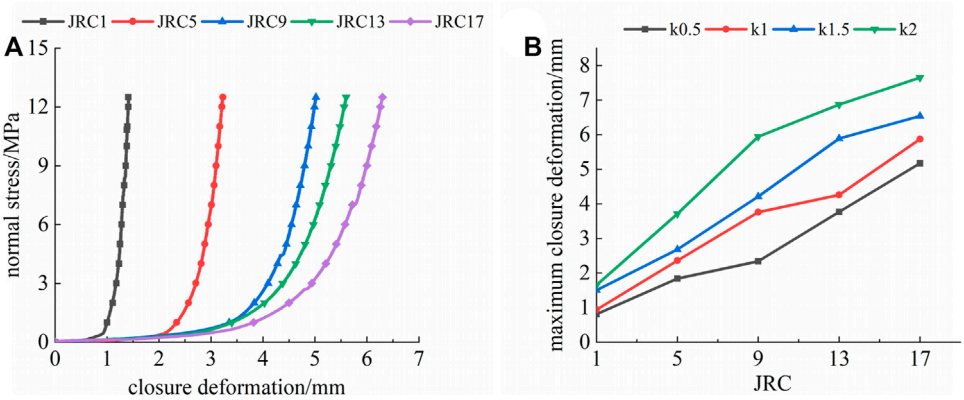

FIGURE 12
Effect of the degree of morphology fluctuation on the normal closure deformation characteristics of filled rock joints: **(A)** normal stress-closure deformation curve of a filled rock joint (k=2) and **(B)** maximum closure deformation-JRC curve of a filled rock joint.

Bandis proposed a formula that can represent the relationship between maximum closure deformation of unfilled rock joints and morphology fluctuation degree, based on a large number of experiments, as shown in Eq. 3.

$$V_m = A + B(JRC) + C\left(\frac{JCS}{e}\right)^D \tag{3}$$

Where V_m is the rock joint maximum closure deformation, mm; *JRC* is the rock joint roughness coefficient; *JCS* is the rock joint compression strength, MPa; *e* is the rock joint degree of opening, mm; and *A*, *B*, *C*, and *D* are fitting parameters.

As shown in Figure 13, a high degree of linearity can be possessed by average fluctuation degree-JRC curve. To consider the effect of the degree of filling on the maximum closure deformation of rock joints, the rock joint opening *e* in Eq. 3 is replaced with filling thickness. The specific equation is shown in Eq. 4.

$$t = [M(JRC) + N] \cdot k \tag{4}$$

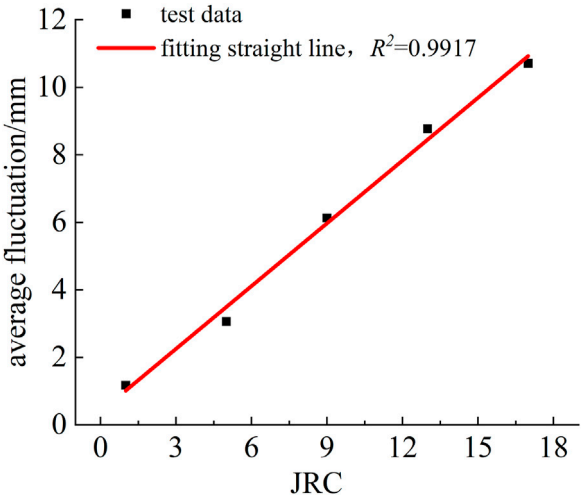

FIGURE 13
Average fluctuation-JRC fitting curve.

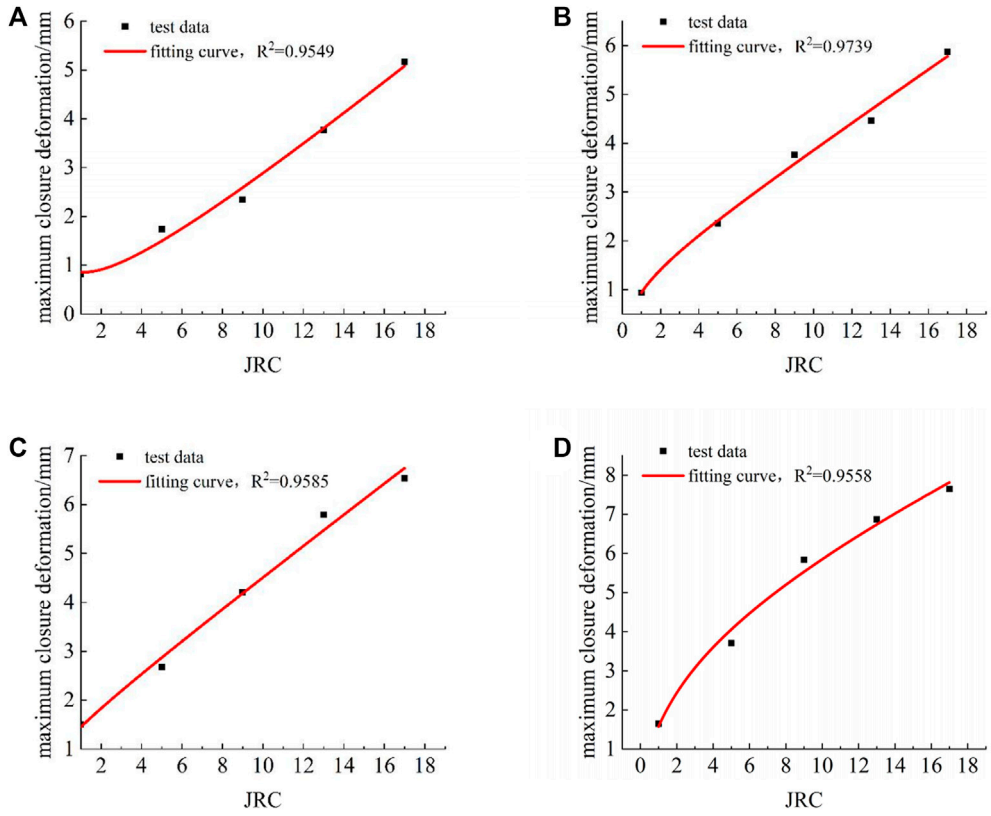

FIGURE 14
Maximum closure deformation-JRC curve under different degrees of filling: **(A)** k=0.5; **(B)** k=1.0; **(C)** k=1.5; and **(D)** k=2.

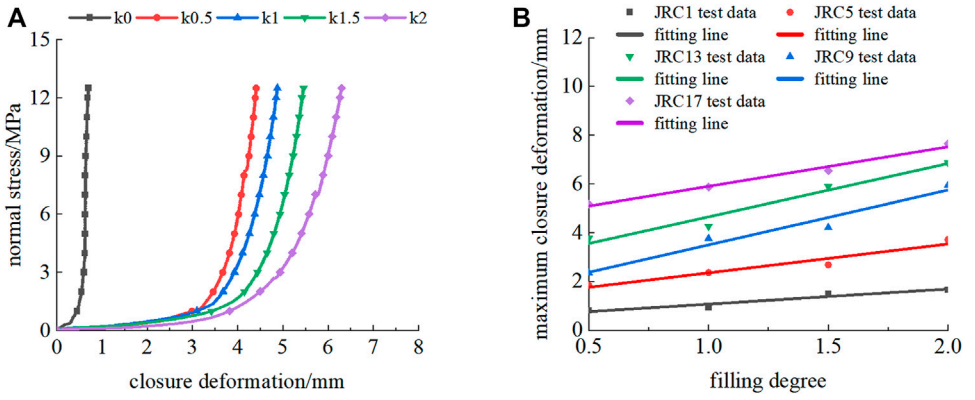

FIGURE 15
Effect of the degree of filling on the normal closure deformation characteristics of a rock joint: **(A)** normal stress-closure deformation curve of a filled rock joint (JRC=17) and **(B)** maximum closure deformation-filling degree curve.

TABLE 6 Fitting parameters of the linear function.

JRC	Fitting parameter P	Fitting parameter Q	Fitting correlation coefficient R^2
1	0.616	0.455	0.9301
5	1.186	1.165	0.9429
9	2.25	1.25	0.9581
13	2.186	2.465	0.9644
17	1.622	4.28	0.9841

Where t is the filling thickness, mm; k is the degree of filling; and M and N are fitting parameters.

The parameters M and N obtained by fitting the test curve are 0.6197 and 0.3902, respectively. The relationship between maximum closure deformation of filled rock joints and the degree of filling is as follows:

$$V_m = A + B(JRC) + C\left(\frac{JCS}{k \cdot [0.6197(JRC) + 0.3902]}\right)^D \quad (5)$$

Eq. 5 is used to fit the maximum closure deformation-JRC curve under different degrees of filling, and the results are shown in Figure 14. It can be seen from Figure 14 that the modified empirical formula of Bandis can well fit the maximum closure deformation of the filled rock joint-JRC curve, with a fitting correlation coefficient that is higher than 0.95. The degree of agreement between test results and predicted values from the modified formula is high.

4.3 Influence of the degree of filling on the normal closure characteristics of rock joints

Figure 15A shows the normal stress-closure deformation curve of rock joints with different degrees of filling. The test results (Figure 15A) indicate that the variation law of closure deformation of filled rock joints is approximately consistent under different degrees of filling. The closure deformation of filled rock joints increases with the increase in the degree of filling, and the closure deformation of unfilled rock joints is the smallest.

The maximum closure deformation-filling degree curve of filled rock joints is fitted by a linear function of $\Delta V_m = P \cdot k + Q$, where ΔV_m is the maximum closure deformation of rock joints, mm; k is the degree of filling; and P and Q are the fitting parameters. The fitting results are shown in Figure 15B, and the fitting parameters are shown in Table 6. The fitting results show that the maximum closure deformation-filling degree curve of filled rock joints possesses a high degree of linearity, without considering the degree of morphological fluctuation. The maximum closure deformation increases with the increase in the degree of filling. Moreover, the linear function can well fit the maximum closure deformation-filling degree curve of filled rock joints. The fitting correlation coefficient is higher than 0.93.

5 Conclusion

Fluctuations in morphology and filling are the main factors affecting the normal deformation of filled rock joints. We conducted a systematic experimental study to investigate the effect of the degree of filling and the degree of morphology fluctuation on the normal deformation of filled rock joints. The main conclusions are as follows:

1) The degree of filling significantly affects the normal deformation of filled rock joint samples. The normal closure deformation of filled rock joints increases with the increase in the degree of filling.
2) Under the same filling thickness, the normal closure deformation of filled rock joints decreases and initial normal stiffness increases with the increase in the degree of morphology fluctuation.
3) A filled rock joint sample exhibits a hysteresis loop between the loading and unloading paths. Irreversible deformation is observed after unloading, and the deformation of a large degree of filling (k=2) of a rock jointed sample is significantly greater than a small degree of filling (k=0.5) rock jointed sample.
4) Under normal stress, the normal deformation behavior of filled rock joints is nonlinear, and the stiffness of rock joints increases with increasing closure deformation. The power function equation can well represent the normal deformation behavior of filled rock joints.
5) A formula that describes the relationship between the maximum closure deformation of filled rock joints and the degree of filling was established based on Bandis's empirical formula. The formulation takes into account the effect of the degree of filling by replacing the rock joint opening with filling thickness. The degree of agreement between test results and the predicted values from the modified formula is high.

Data availability statement

The raw data supporting the conclusions of this article will be made available by the authors, without undue reservation.

Author contributions

ZL and WZ were responsible for the acquisition and analysis of experimental data and general writing of the manuscript; SD put forward the idea and designed the study; MH was consulted on some issues; CW completed the revision of some figures and improvements in the language.

Funding

This work was supported by the National Natural Science Foundation of China (No. 42277147) and the Special Support Plan for High Level Talents of Zhejiang Province (2020R52028).

Conflict of interest

The authors declare that the research was conducted in the absence of any commercial or financial relationships that could be construed as a potential conflict of interest.

Publisher's note

All claims expressed in this article are solely those of the authors and do not necessarily represent those of their affiliated organizations, or those of the publisher, the editors and the reviewers. Any product that may be evaluated in this article, or claim that may be made by its manufacturer, is not guaranteed or endorsed by the publisher.

References

Bandis, S. C., Barton, N. R., and Bakhtar, K. (1985). Strength, deformation and conductivity coupling of rock joints. *Int. J. Rock Mech. Min. Sci. Geomechanics Abstr.* 22 (3), 121–140. doi:10.1016/0148-9062(85)93227-9

Bandis, S. C., Lumsden, A. C., and Barton, N. R. (1983). Fundamentals of rock joint deformation. *Int. J. rock Mech. Min. Sci. geomechanics Abstr.* 20 (6), 249–268. doi:10.1016/0148-9062(83)90595-8

Guo, B., and Su, C. (2010). Fitting analysis of normal closure curve of coarse-grained marble fractures[C]. *Chin. J. Rock Mech. Eng.* 20, 105.

Huang, J., Liu, X., Song, D., Zhao, J., Wang, E., and Zhang, J. (2022). Laboratory-scale investigation of response characteristics of liquid-filled rock joints with different joint inclinations under dynamic loading. *J. Rock Mech. Geotechnical Eng.* 14 (2), 396–406. doi:10.1016/j.jrmge.2021.08.014

Li, B., and Cui, X. (2021). Study on deformation behavior of dislocation fracture in sandstone under normal stress[J]. *Rock Soil Mech.* 42 (07), 1850–1860. doi:10.16285/j.rsm.2020.1802

Liu, Y., and Tang, H. (1999). *Rock Mechanics[M]*. Wu Han, China: China University of Geosciences Press, 75–80.

Luo, Z., Jiang, M., Mo, L., Zou, B., and Huang, M. (2021). Stress effect & scale effect on shear properties of double saw-tooth rock joint surface. *Appl. Rheol.* 31 (1), 39–49. doi:10.1515/arh-2020-0117

Makurat, A., Ahola, M., Khair, K., Noorishad, J., Rosengren, L., and Rutqvist, J. (1995). The DECOVALEX test—case one. *Int. J. Rock Mech. Min. Sci. Geomechanics Abstr.* 32 (5), 399–408. doi:10.1016/0148-9062(95)00032-C

Malama, B., and Kulatilake, P. H. S. W. (2003). Models for normal fracture deformation under compressive loading. *Int. J. Rock Mech. Min. Sci.* 40 (6), 893–901. doi:10.1016/S1365-1609(03)00071-6

Muller, L. (1977). The use of deformation measurements in dimensioning the lining of subway tunnels[C]. International symposium on field measurements in rock Mechanics. *Zurich* 2, 451–471. doi:10.1016/0148-9062(79)90590-4

Qiao, L., and Li, Q. (2016). Normal deformation characteristics of structural plane under rock wall deformation conditions[J]. *J. Northeast. Univ. Nat. Sci.* 37 (10), 1479–1484. doi:10.3969/j.issn.1005-3026.2016.10.024

Saeb, S., and Amadei, B. (1992). Modelling rock joints under shear and normal loading. *Int. J. rock Mech. Min. Sci. geomechanics Abstr.* 29 (3), 267–278. doi:10.1016/0148-9062(92)93660-C

Shehata, W. M. (1971). Geohydrology of mount vernon canyon area [D]. Jefferson County, Colorado: Colorado School of Mines. PhD Thesis.

Sun, Z. (1983). Fracture Mechanics and tribology of rocks androck joint. *Lulea Univ. Technol.* 20 (4), 102. doi:10.1016/0148-9062(83)90977-4

Wu, S., and Gao, Y. (2015). Study on mechanical characteristics of rock joint under normal cyclic loading and unloading[J]. *Chin. J. Rock Mech. Eng.* 34 (S2), 3683–3693. doi:10.13722/j.cnki.jrme.2015.0610

Yuan, B. (2017). *Study on influence of coincidence degree on rock joint normal deformation characteristics[D]*. Nan Jing, China: Nan Jing University. doi:10.27235/d.cnki.gnjiu.2017.000383

Zhang, Y., and Ding, X. (2017). Study on normal cyclic loading deformation characteristics of natural structural plane with thickness. *[J]. Rock Soil Mech.* 38 (10), 2865–2872. doi:10.16285/j.rsm.2017.10.012

Zhao, S. (2017). *Study on loading rate effect of rock joint normal deformation [D]*. Nan Jing, China: Nan Jing University. doi:10.27235/d.cnki.gnjiu.2017.000402

frontiers | Frontiers in Earth Science

TYPE Original Research
PUBLISHED 16 January 2023
DOI 10.3389/feart.2022.982937

Check for updates

OPEN ACCESS

EDITED BY
Bo Li,
Tongji University, China

REVIEWED BY
Danqing Song,
Tsinghua University, China
Luqi Wang,
Chongqing University, China

*CORRESPONDENCE
Zhanyou Luo,
lzy0395@163.com
Yuanjun Lyu,
lvyuanjun222@163.com

SPECIALTY SECTION
This article was submitted to Geohazards and Georisks, a section of the journal Frontiers in Earth Science

RECEIVED 30 June 2022
ACCEPTED 01 August 2022
PUBLISHED 16 January 2023

CITATION
Luo Z, Zhang Y, Du S, Huang M and Lyu Y (2023), Experimental study on shear performance of saw-tooth rock joint with weak interlayer under different moisture contents and filling degrees. *Front. Earth Sci.* 10:982937. doi: 10.3389/feart.2022.982937

COPYRIGHT
© 2023 Luo, Zhang, Du, Huang and Lyu. This is an open-access article distributed under the terms of the Creative Commons Attribution License (CC BY). The use, distribution or reproduction in other forums is permitted, provided the original author(s) and the copyright owner(s) are credited and that the original publication in this journal is cited, in accordance with accepted academic practice. No use, distribution or reproduction is permitted which does not comply with these terms.

Experimental study on shear performance of saw-tooth rock joint with weak interlayer under different moisture contents and filling degrees

Zhanyou Luo[1,2,3]*, Yufan Zhang[1], Shigui Du[2], Man Huang[3] and Yuanjun Lyu[2]*

[1]Tunnel and Underground Space Academy, Zhejiang University of Science and Technology, Hangzhou, Zhejiang, China, [2]Institute of Rock Mechanics, Ningbo University, Ningbo, Zhejiang, China, [3]Department of Civil Engineering, Shaoxing University, Shaoxing, Zhejiang, China

Rock joints are important factors affecting natural disasters such as landslides, and weak interlayer is the decisive factor for rock joint stability. Therefore, it is necessary to carry out shear test research on rock joints with weak interlayer. In this paper, the red sandstone was used as rock joint material, and consistent saw-tooth rock joints were produced by the 3D carving technology. According to the on-site composition analysis, the weak interlayer used in the test was obtained through remodeling. Weak interlayer with different moisture contents and filling degrees were produced by the Constant Dry Mass Method (CDMM). Shear strength test of rock joint with weak interlayer of different filling degree and moisture content under multi-level normal stress was carried out by the self-developed direct shear apparatus. The test results show that peak shear strength of rock joint with weak interlayer increases firstly and then decreases with the raise of moisture content. Peak shear strength of rock joint with weak interlayer decreases firstly and then tends to a stable value with the raise of filling degree. As the filling degree of weak interlayer changes from small (less than 1.0) to large (more than 1.0), dilatancy mode of saw-tooth rock joint changes from dilatation to contraction during shearing. Peak shear strength of rock joint with weak interlayer increases with the raise of normal stress.

KEYWORDS

saw-tooth rock joint, weak interlayer, moisture content, filling degree, shear performance

Introduction

Rock joint such as fault, bedding and weak interlayer is a common geological phenomenon in rock mass, and the existence of this joint is a significant source of disasters. A large number of research and achievements on rock joint are carried out by scholars (Du, et al., 2020; Luo et al., 2021). However, the study on coupling effect of moisture content and filling degree of weak interlayer is not enough. Therefore, it is of great significance to study the shear performance of rock joint with weak interlayer.

In terms of moisture content, Sun, 1981 considered moisture content was significant factors in mechanical effect of rock joint by shearing tests. Li et al. (2008) believed that shear strength of sandstone joint with weak interlayer decreased with the increase of moisture content by the shear creep test. Liu et al. (2017) considered that the cohesion and friction angle increased firstly and then decreased with the raise of moisture content by direct shear test for strongly weathered mudstone, and the optimum moisture content was 12.7%.

In terms of filling degree, Goodman, (1976) found that shear strength of rock joint was affected by the coupling effect of rock joint morphology and weak interlayer as the filling degree was smaller than 1.0. However, shear strength was controlled by weak interlayer itself as the filling degree was larger than 2.0. Ladanyi and Archambault (1977) defined the ratio of the thickness of weak interlayer ***(t)*** to the fluctuation degree of rock joint surface morphology ***(a)*** as a new variable, which is generally called filling degree. Many scholars supposed that shear strength parameters of rock joint decreased with the increase of clay content of weak interlayer (Skempton 1985; Mesri and Cepeda-Diaz, 1986; Gibo et al., 1987; Xiang, 1989). Indraratna considered that there was a critical thickness of the weak interlayer through experiments and theoretical studies (Indraratna et al., 1999; Indraratna et al., 2008; Indraratna et al., 2010; Indraratna et al., 2013; Indraratna et al., 2014). Papaliangas et al., 1993 gained that the critical filling degree of rock joint with fly ash interlayer is about 1.5 by direct shear test. Yang, 2002 used the interlayer method and the continuum method to deal with thin and thick interlayer problems respectively.

In summary, scholars have done a lot of research on the influence of moisture content and thickness on shear performance of rock joint, and have also made corresponding research results. However, there are few studies on saw-tooth rock joint with weak interlayer under coupling effect of different moisture contents, filling degrees and normal stresses. In this paper, the red sandstone is used as the upper and lower specimens, and consistent saw-tooth rock joints are produced by the 3D carving technology. Samples (38 items in total) of saw-tooth rock joint with different interlayer moisture contents and filling degrees are produced by CDMM and confining device. Shear test of saw-tooth rock joint is carried out by developed direct shear apparatus, and variation laws of shear performance (shear stress-displacement curve, peak shear strength, normal displacement, *etc.*) with interlayer moisture contents, filling degrees and normal stressed are analyzed.

Test preparation

Test equipment

Conventional direct shear apparatus can only carry out test of the rock joint without filling. According to the experimental characteristics of rock joint with weak interlayer, a direct shear apparatus is developed in this paper. The apparatus was mainly composed of loading platform, loading system, measuring system, controller, shear box and supporting computer software (Figure 1). The sensor measured normal and tangential load were applied by mechanical lever and stepping motor. Normal and tangential displacement were obtained by measurement

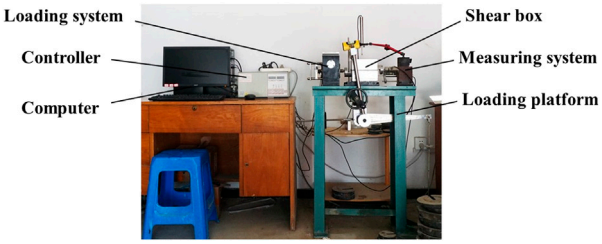

FIGURE 1
Direct shear apparatus for rock joint with weak interlayer.

TABLE 1 Technical indicators of the apparatus.

Technical indicators	Parameter
Sample specification (length × width × height)	100mm × 100mm × 100mm
Normal loading leverage ratio	1:20
Normal loading force range	0 ~ 9.6kN
Tangential loading force range	0 ~ 10kN
Loading rate range	0.02 ~ 2.4mm/min
Normal displacement range	0 ~ 30mm
Shear displacement range	0 ~ 30mm

TABLE 2 Mix proportion of weak interlayer.

Mineral nutrient species	Quartzite	Quartzite	Calcite	Calcite	Calcite	Montmorillonite	Illite
mesh number	300	800	120	325	600	325	325
Proportion(%)	7.5	15	1.25	2.50	3.75	35	35

sensor. Specific technical indicators of the apparatus are shown in Table 1.

Rock joint and weak interlayer

The sample of rock joint was mainly composed by upper specimen, lower specimen and weak interlayer. The red sandstone used in the specimens had the same uniaxial compressive strength as the rock in the field. The weak interlayer was a mixture of montmorillonite, illite and other minerals. Moreover, the weak interlayer used in the test was obtained through remodeling according to the on-site composition analysis. The specific mix proportion is shown in Table 2.

Sample preparation

Morphology of rock joint

Morphology of rock joint is one of the main factors affecting shear strength of weak interlayer (Du et al., 2022). In order to study the influence of moisture content and filling degree on shear strength, the regular saw-tooth rock joint is adopted with specific tooth height of 3 mm and width of 12 mm. Red sandstones were carved by MD-6060 numerical engraving machine. The specific steps were as follows. Firstly, the corresponding saw-tooth morphology model was established in modeling software, and the generated path file was imported into control software of the numerical engraving machine. Secondly, red sandstone was put into the engraving machine and fixed by bolts. Thirdly, the engraving program was started by the control software, and cutter head was controlled to carve the red sandstone according to specified path. Finally, the morphology of the saw-tooth was carved completely (Figure 2).

Weak interlayer

The mineral mixture was prepared by the mix proportion shown in Table 2 and placed in oven at 105°C for 12 h. The mineral mixture after drying was shown in Figure 3A. The large grains were removed through the geotechnical sieve with a diameter of 1.0 mm after static cooling in room. Appropriate amount of water was added to mineral mixture after screening, and the weak interlayer with moisture contents of 10%, 15%, 20% and 25% was prepared respectively (Figures 3B–E). The mass of weak interlayer with different thickness was determined by CDMM, as shown in formula 1. Under different filling degrees, the mass of weak interlayer corresponding to moisture contents is shown in Table 3:

$$m_n = a(n+1)t \quad (1)$$

Where n is the moisture content of weak interlayers; m_n is the quality of weak interlayers with n moisture content, g; a is the test coefficient, g/mm, with a value of 15.22; t is the thickness of weak interlayer, mm.

Sample making

The lower specimen was fixed by self-developed confining device, and weak interlayer that corresponds to the thickness was weighed according to formula 1. Before the upper specimen was placed, weak interlayer was evenly spread on the joint of lower specimen and layered compaction. Finally, two-halves of the specimens were tied and placed on shaking table for compaction (Figure 4). Repeated these steps and prepared saw-tooth rock joint with weak interlayer samples with filling degrees of 0, 0.5, 1.0 and 2.0 respectively (Figure 5).

Test plan

The main influencing factors of the shear performance of saw-tooth rock joint with weak interlayer are moisture

FIGURE 2
Engraving of saw-tooth morphology.

FIGURE 3
Weak interlayer with different moisture content: **(A)** 0; **(B)** 10%; **(C)** 15%; **(D)** 20%; **(E)** 25%.

TABLE 3 The mass of weak interlayer corresponding to moisture content.

Filling degree	0	0.5	1.0	2.0
Mass/g				
m_{10}	0	25.13	50.25	100.5
m_{15}	0	26.27	52.53	105.06
m_{20}	0	27.41	54.81	109.62
m_{25}	0	28.55	57.09	114.18

contents, filling degrees and normal stresses. The moisture contents of the weak interlayer are 10%, 15%, 20%, 25%. The filling degrees are 0, 0.5, 1.0, 2.0, and the normal stresses are 200 kPa, 400 kPa, 600 kPa. The specific test scheme is shown in Table 4.

Effect of moisture content on shear performance

Relationship between shear stress-displacement curve and moisture content

Shear stress-displacement curve of saw-tooth rock joint under the same filling degree and different moisture contents is shown in Figure 6. The test results (Figure 6) indicate that variation law of shear stress-displacement of saw-tooth rock joint with weak interlayer is approximately consistent under the same filling degree, normal stress and different moisture contents. When filling degree is 0.5, shear stress of the saw-tooth rock joint with weak interlayer firstly reaches maximum and decreases sharply with the increase of shear displacement.

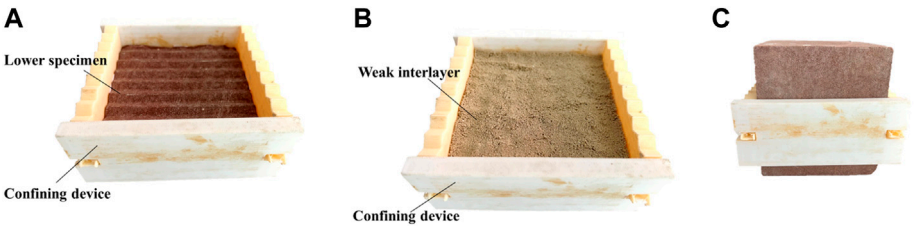

FIGURE 4
Process of sample preparation: **(A)** Installation of confining device; **(B)** Add weak interlayer; **(C)** Sample preparation.

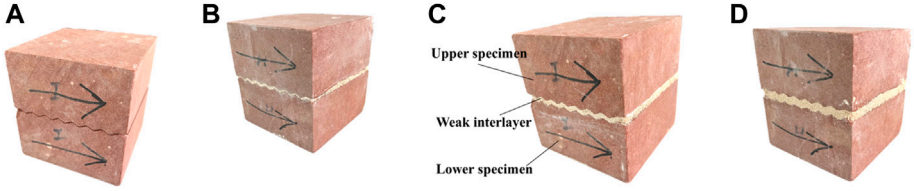

FIGURE 5
Sample of rock joint with different filling degrees: **(A)** k = 0; **(B)** k = 0.5; **(C)** k = 1.0; **(D)** k = 2.0.

TABLE 4 Test Scheme for saw-tooth rock joint with weak interlayer.

Numbering	Moisture content/%	Filling degree	Normal stress/kPa	Numbering	Moisture content/%	Filling degree	Normal stress/kPa
C0-1	-	0	200	C2-9	15	2.0	600
C0-2	-	0	400	C3-1	20	0.5	200
C1-1	10	0.5	200	C3-2	20	0.5	400
C1-2	10	0.5	400	C3-3	20	0.5	600
C1-3	10	0.5	600	C3-4	20	1.0	200
C1-4	10	1.0	200	C3-5	20	1.0	400
C1-5	10	1.0	400	C3-6	20	1.0	600
C1-6	10	1.0	600	C3-7	20	2.0	200
C1-7	10	2.0	200	C3-8	20	2.0	400
C1-8	10	2.0	400	C3-9	20	2.0	600
C1-9	10	2.0	600	C4-1	25	0.5	200
C2-1	15	0.5	200	C4-2	25	0.5	400
C2-2	15	0.5	400	C4-3	25	0.5	600
C2-3	15	0.5	600	C4-4	25	1.0	200
C2-4	15	1.0	200	C4-5	25	1.0	400
C2-5	15	1.0	400	C4-6	25	1.0	600
C2-6	15	1.0	600	C4-7	25	2.0	200
C2-7	15	2.0	200	C4-8	25	2.0	400
C2-8	15	2.0	400	C4-9	25	2.0	600

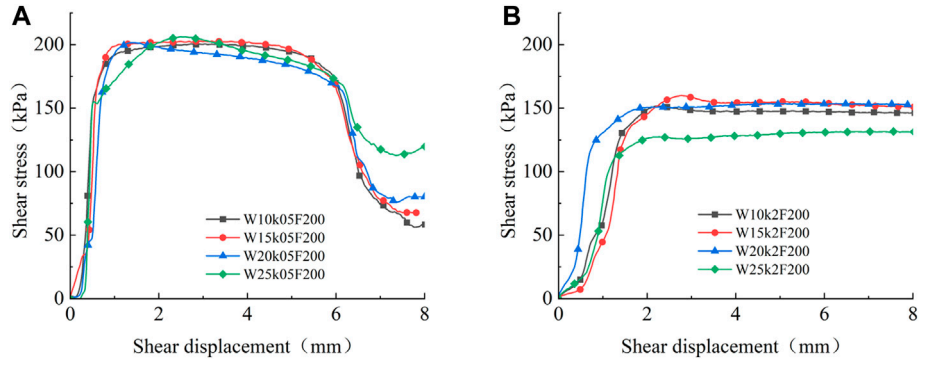

FIGURE 6
Shear stress–displacement curve under different moisture contents: **(A)** k = 0.5, F = 200 kPa; **(B)** k = 2.0, F = 200 kPa.

The main reason is that the upper specimen drops sharply after it climbs to the highest point of saw-tooth during the shear process. Moreover, shear stress of saw-tooth rock joint with weak interlayer increases firstly and then tends to a stable value with the growth of shear displacement when filling degree is larger than 2.0.

Relationship between peak shear strength and moisture content

Figure 7 displays the relationship between peak shear strength of saw-tooth rock joint with weak interlayer and moisture content under the same filling degree. The test results (Figure 7) reveal that peak shear strength of saw-tooth rock joint with weak interlayer

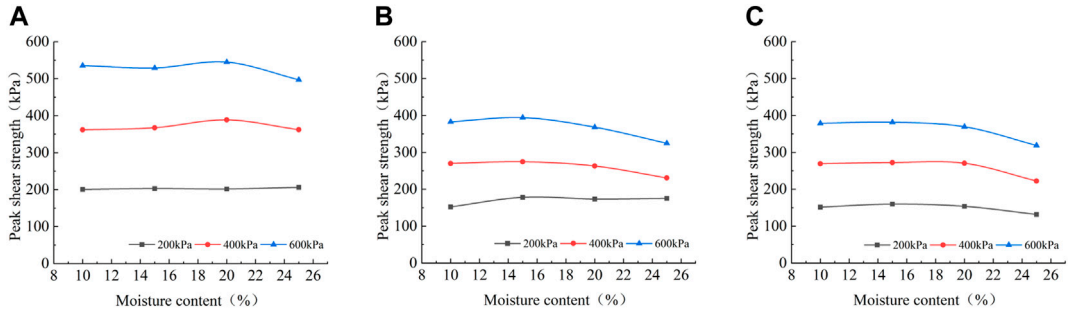

FIGURE 7
Peak shear strength under different moisture contents: **(A)** k = 0.5; **(B)** k = 1.0; **(C)** k = 2.0.

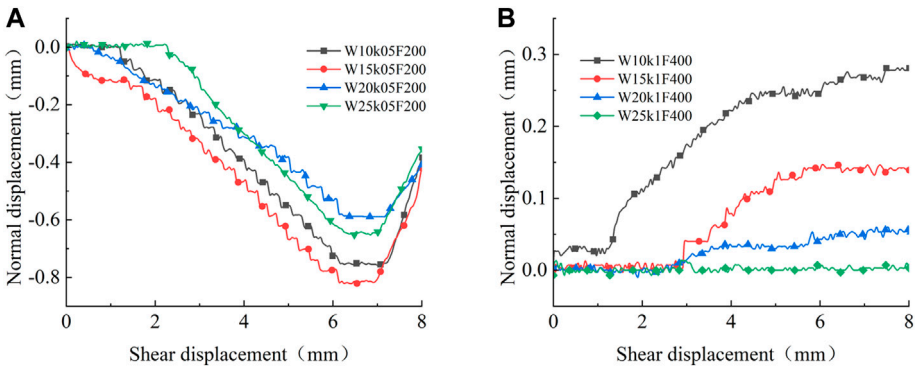

FIGURE 8
Normal–shear displacement curve under different moisture contents: **(A)** k = 0.5, F = 200kPa; **(B)** k=1.0, F=400kPa.

increases firstly and then declines with the increase of moisture content under the same filling degree and normal stress. Moreover, peak shear strength reaches the maximum as moisture content between 15% and 20% because the cohesion and friction angle increase with the raise of moisture content which is lower than 15% during the shear process of soil-rock interface. However, the cohesion and friction angle decrease with the raise of moisture content which is higher than 20% during the shear process.

Relationship between normal displacement and moisture content

Normal-shear displacement curve of saw-tooth rock joint with weak interlayer under the same filling degree and different moisture contents is shown in Figure 8. Where, shear contraction corresponds to the positive value on the graph which is located on the upper side of the X coordinate axis. Conversely, shear dilatation corresponds negative value which is located below the X axis. It can be recognized from Figure 8 that variation of the normal-shear displacement curve of the saw-tooth rock joint with weak interlayer under different moisture content is approximately the same when filling degree is 0.5, and the upper specimen with different moisture contents reach the maximum displacement of shear dilatancy as shear displacement is 6 mm. This is due to the joint climbs to the highest point of saw-tooth after the shear displacement reaches half tooth width, which also indicates that the normal displacement is less affected by moisture content. Moreover, the normal displacement decreases with the increase of moisture content when filling degree is larger than 1.0. As moisture content increases further, the normal displacement almost does not change.

Effect of filling degree on shear performance

Relationship between shear stress-displacement curve and filling degree

Shear stress-displacement curve of saw-tooth rock joint with weak interlayer under the same moisture content and different filling degrees is shown in Figure 9. The test results (Figure 9) reveal that the

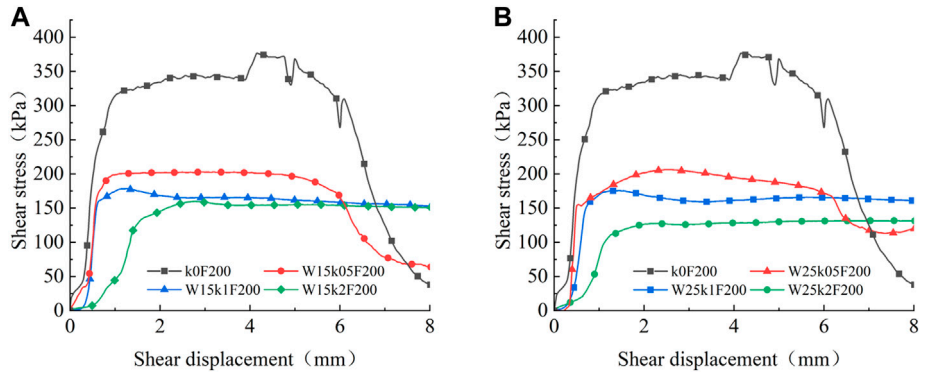

FIGURE 9
Shear stress–displacement curve under different filling degrees: **(A)** W = 15%; **(B)** W = 25%.

shear stress increases firstly and tends to a stable value, and finally decreases with the increase of shear displacement when there is no filling. This is due to a decline section appearing after the upper specimen climbing to the highest point of saw-tooth. Besides, shear stress boosts or drops sharply during the process of direct shear because the failure of upper and lower specimen joint surface during shearing. Shear strength of saw-tooth rock joint with weak interlayer decreases with increase of filling degree under the same moisture content, and the decreasing range also declines gradually. Peak shear strength tends to a stable value when filling degree is larger than 2.0 because failure location of the sample changes from the mutual failure inside rock masses to the location between rock masses and interlayers, and finally to the location inside interlayers with increase of filling degree. Moreover, peak shear strength does not change significantly after the filling degree reaching the critical value. When filling degree is smaller than 0.5, the shear stress of saw-tooth rock joint with weak interlayer decreases sharply after shear displacement reaches about 6 mm. While it does not appear as filling degree is larger than 1.0 because shear strength of the sample is mainly affected by rock joint as filling degree is small. It also shows that climbing process of the specimens appears under these conditions. In addition, shear strength of the specimen is affected by rock joint and weak interlayer as filling degree is large, and there will be no climbing process and sudden decrease of shear stress.

Relationship between peak shear strength and filling degree

Figure 10 displays the relationship curve between peak shear strength and filling degree of saw-tooth rock joint with weak interlayer under the same moisture content. The test results (Figure 10) indicate that under the same moisture content, peak shear strength of saw-tooth rock joint with weak interlayer decreases firstly and then tends to a stable value with increase of filling degree, and peak shear strength does not change significantly after the filling degree exceeds 1.0. This is because shear strength of saw-tooth rock joint under small filling degrees is mostly borne by the rock-rock interface, which causes the shear strength be higher. Shear strength is gradually borne by soil-rock interface and soil-soil interface with the increase of filling degree which causes great reduction of the shear strength. Finally, the shear strength is completely borne by weak interlayer as the filling degree increase to critical value.

Relationship between normal displacement and filling degree

Figure 11 shows the normal-shear displacement curve of saw-tooth rock joint with weak interlayer under the same moisture content and different filling degrees. Where, shear contraction corresponds to the positive value on the graph which is located on the upper side of the X coordinate axis. Conversely, shear dilatation corresponds negative which is located below the X axis. The results (Figure 11) show that rock joint without interlayer has upward displacement (shear dilatation) under different normal stresses, and the normal displacement reaches maximum as the shear displacement reaches 6 mm. This is because the rock joint climbs to the highest point of the saw-tooth as there is no filling, and the value of 6 mm is shear displacement corresponding to the highest point of saw-tooth. It is also corresponding to stress mutation of shear stress-displacement curve in Figure 9A, which reflects that the sudden increase or decrease of shear stress is due to failure of two-halves of the specimens during shearing. Moreover, most upper specimens appear downward displacement during shear process with the increase of filling degree. The main reason is that weak interlayer is compressed through shearing, and the decrease of volume expands normal displacement.

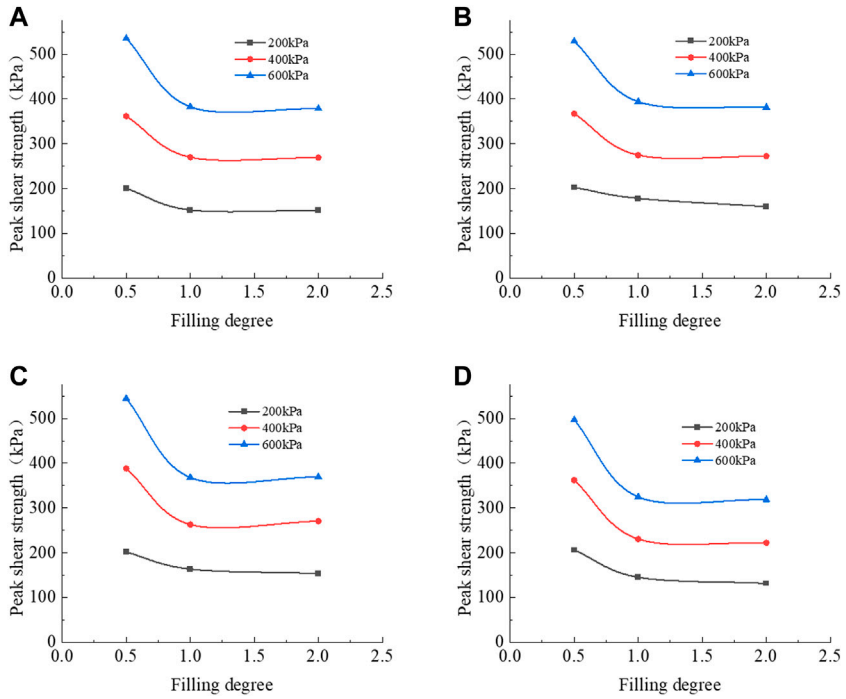

FIGURE 10
Peak Shear Strength under different filling degrees: **(A)** W = 10%; **(B)** W = 15%; **(C)** W = 20%; **(D)** W = 25%.

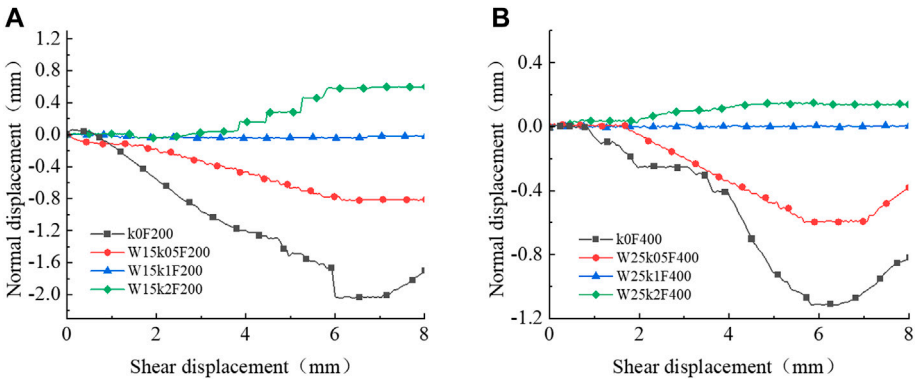

FIGURE 11
Normal–shear displacement curve under different filling degrees: **(A)** W = 15%, F = 200kPa; **(B)** W = 25%, F = 400kPa.

Effect of normal stress on shear performance

Figure 12 shows the relationship between peak shear strength and normal stress. The test results (Figure 12) indicate that peak shear strength of rock joint with weak interlayer under different moisture contents increases nonlinearly with the increase of normal stress, showing the characteristics of stress effect. Moreover, peak shear strength of weak interlayer with 15% moisture content is the highest under different normal stresses. It also shows that moisture content of 15% is closer to the optimal value.

Figure 13 shows the normal-shear displacement curve of saw-tooth rock joint with weak interlayer under different normal stresses. The test results (Figure 13) indicate that upward displacement of upper specimen rock joint occurs as normal stress is low, and slope rate of shear dilatation curve

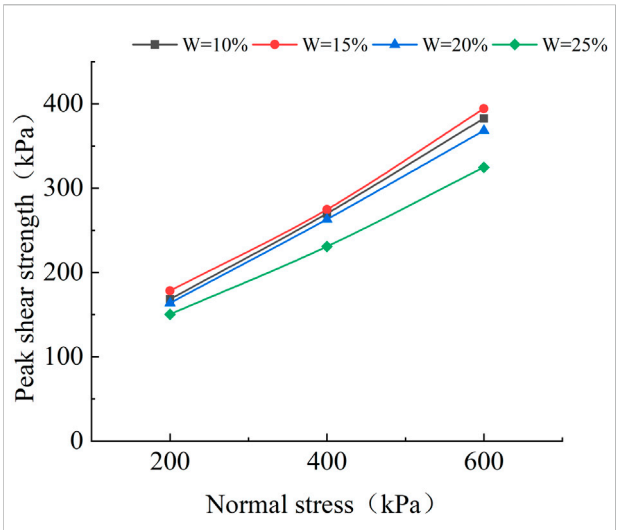

FIGURE 12
Peak shear strength under different normal stresses.

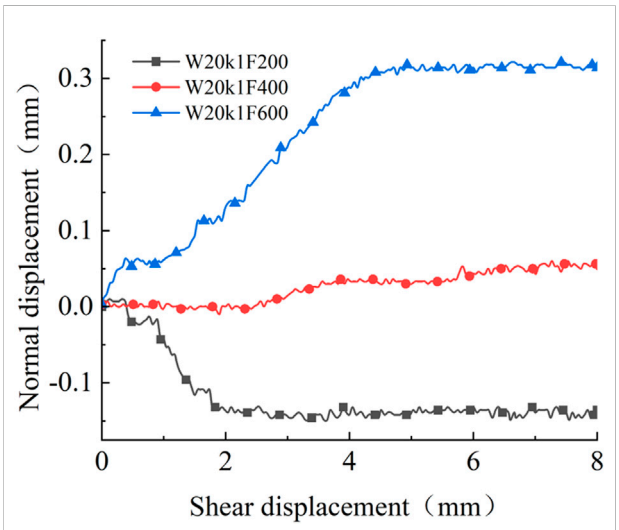

FIGURE 13
The normal–shear displacement curve under different normal stresses.

slows down rapidly as rock joint reaches peak shear strength. The main reason is that weak interlayer shows dilatancy characteristics under low normal stress which causes the soil grains to move and slip. Shear dilatation characteristics of rock joint disappears with the increase of normal stress. In addition, shear dilatation turns to contraction with the further increase of normal stress, and the downward displacement of upper specimen leads to the contact wear of two-halves of specimens.

Conclusion

Weak interlayer is a common weak surface in rock mass, which is a key factor to control the stability of rock joint and affects safety of rock engineering. In this paper, shear strength of rock joint is studied by direct shear apparatus for joint with weak interlayer under different moisture contents, filling degrees and normal stresses. The main conclusions of shear performance of saw-tooth rock joint with weak interlayer are as follows:

(1) Peak shear strength of rock joint with weak interlayer increases firstly and then decreases with the increase of moisture content. Peak shear strength reaches the maximum as weak interlayer achieves the optimal moisture content.
(2) Peak shear strength of rock joint with weak interlayer decreases firstly and then tends to a constant value with the increase of filling degree. Peak shear strength reaches a stable value as weak interlayer exceeds the critical filling degree.
(3) Normal stress also has a significant influence on peak shear strength of saw-tooth rock joint with weak interlayer, and peak shear strength increases with the raise of normal stress.
(4) Saw-tooth rock joint with weak interlayer appears climbing phenomenon in the direct shear process under the condition of small filling degrees, and failure location is mainly between the joint surface of upper and lower specimen. However, shear contraction phenomenon appears in the direct shear process, and failure location turn to internal failure of weak interlayer under the condition of large filling degrees.

Data availability statement

The raw data supporting the conclusions of this article will be made available by the authors, without undue reservation.

Author contributions

The first author, ZL, and the second author, YZ, are responsible for the general writing of the manuscript and completing main experimental; and the third author, SD, put forward the idea and designed the study; the fourth author, MH, provided data processing assistance; and the fifth author, YL, is responsible for consulting on some test instruments.

Funding

This paper was supported by the National Natural Science Foundation of China (No. 42277147) and Special Support Plan for

High Level Talents of Zhejiang Province (2020R52028). Their supports are gratefully acknowledged.

Conflict of interest

The authors declare that the research was conducted in the absence of any commercial or financial relationships that could be construed as a potential conflict of interest.

Publisher's note

All claims expressed in this article are solely those of the authors and do not necessarily represent those of their affiliated organizations, or those of the publisher, the editors and the reviewers. Any product that may be evaluated in this article, or claim that may be made by its manufacturer, is not guaranteed or endorsed by the publisher.

References

Du, H., Song, D., Chen, Z., and Guo, Z. (2020). Experimental study of the influence of structural planes on the mechanical properties of sandstone specimens under cyclic dynamic disturbance. *Energy Sci. Eng.* 8 (11), 4043–4063. doi:10.1002/ese3.794

Du, S., Lin, H., Yong, R., and Liu, G. J. (2022). Characterization of joint roughness heterogeneity and its application in representative sample investigations. *Rock Mech. Rock Eng.* 55, 3253–3277. doi:10.1007/s00603-022-02837-4

Gibo, S., Egashira, K., and Ohtsubo, M. (1987). Residual strength of smectite-dominated soils from the Kamenose landslide in Japan[J]. *Can. Geotech. J.* 24 (3), 456–462. doi:10.1139/t87-057

Goodman, R. (1976). Methods of geological engineering in discontinuous rocks [J]. *Int. J. Rock Mech. Min. Sci. Geomechanics Abstr.* 13 (10), 115. doi:10.1016/0148-9062(76)90566-0

Indraratna, B., Haque, A., and Aziz, N. (1999). Shear behaviour of idealized infilled joints under constant normal stiffness. *Geotechnique* 49 (3), 331–355. doi:10.1680/geot.1999.49.3.331

Indraratna, B., Jayanathan, M., and Brown, E. T. (2008). Shear strength model for overconsolidated clay-infilled idealised rock joints. *Geotechnique* 58 (1), 55–65. doi:10.1680/geot.2008.58.1.55

Indraratna, B., Oliveira, D. A. F., and Brown, E. T. (2010). A shear-displacement criterion for soil-infilled rock discontinuities. *Geotechnique* 60 (8), 623–633. doi:10.1680/geot.8.p.094

Indraratna, B., Premadasa, W., Brown, E. T., Gens, A., and Heitor, A. (2014). Shear strength of rock joints influenced by compacted infill. *Int. J. Rock Mech. Min. Sci.* 70, 296–307. doi:10.1016/j.ijrmms.2014.04.019

Indraratna, B., Premadasa, W., and Brown, E. T. (2013). Shear behaviour of rock joints with unsaturated infill. *Geotechnique* 63 (15), 1356–1360. doi:10.1680/geot.12.P.065

Ladanyi, B., and Archambault, G. (1977). "Shear strength and deformability of filled indented joints[C]," in Proceedings of International Symposium on Geotechnics of Structurally Complex Formations, Capri, Italy, 13 January, 1977, 317–326.

Li, P., Liu, J., Zhu, J., and He, H. (2008). Study on relationship between shear creep characteristics and moisture content of weak joint [J]. *Geotechnics* 44 (07), 1865–1871. doi:10.3969/j.issn.1000-3665.2009.06.011

Liu, H., Li, K., Yuan, Q., Liao, J., and Qin, L. (2017). Direct shear test on soil-rock interface of High fill bedding slope under different moisture contents[J]. *Quick Rep. Water Conservancy Hydropower* 38 (09), 46–48. doi:10.15974/j.cnki.slsdkb.2017.09.018

Luo, Z., Jiang, M., Mo, L., Zou, B., and Huang, M. (2021). Stress effect & scale effect on shear properties of double saw-tooth rock joint surface. *Appl. Rheol.* 31 (1), 39–49. doi:10.1515/ARH-2020-0117

Mesri, G., and Cepeda-Diaz, A. F. (1986). Residual shear strength of clays and shales. *Geotechnique* 36 (2), 269–274. doi:10.1680/geot.1986.36.2.269

Papaliangas, T., Hencher, S. R., Lumsden, A. C., and Manolopoulou, S. (1993). The effect of frictional fill thickness on the shear strength of rock discontinuities. *Int. J. Rock Mech. Min. Sci. Geomechanics Abstr.* 30 (2), 81–91. doi:10.1016/0148-9062(93)90702-f

Skempton, A. W. (1985). Residual strength of clays in landslides, folded strata and the laboratory. *Geotechnique* 35 (1), 3–18. doi:10.1680/geot.1985.35.1.3

Sun, W. (1981). *Mechanical effect of weak interlayer thickness[J]*. China: Engineering Geology Department of Wuhan University of Water Resources and Electric Power, 33–39.

Xiang, W. (1989). Empirical formula between clay content of weak interlayer and shear strength parameters[J]. *Hydrogeology Eng. Geol.* 48 (05), 45–46. doi:10.16030/j.cnki.issn.1989.05.011

Yang, L. (2002). Discussion on contact and strength of weak interlayer[J]. *Tech. Conservancy Hydropower* 23 (06), 17–19. doi:10.3969/j.issn.1000-0860.2002.06.005

frontiers | Frontiers in Earth Science

TYPE Original Research
PUBLISHED 05 May 2023
DOI 10.3389/feart.2022.982658

Check for updates

OPEN ACCESS

EDITED BY
Bo Li,
Tongji University, China

REVIEWED BY
Zhanping Song,
Xi'an University of Architecture and Technology, China
Linwei Li,
Guizhou University, China
Jia Yanchang,
College of Geosciences and Engineering North China University of water resources and hydropower, China
Yanbin Yu,
Shandong University of Science and Technology, China
Yanlin Zhao,
Hunan University of Science and Technology, China

*CORRESPONDENCE
Xiaoqiang Zhang,
zhangxiaoqiang@kust.edu.cn

SPECIALTY SECTION
This article was submitted to Geohazards and Georisks, a section of the journal Frontiers in Earth Science

RECEIVED 30 June 2022
ACCEPTED 31 October 2022
PUBLISHED 05 May 2023

CITATION
Zhang X, Song X and Wu S (2023), Simulation of collapse failure process of rock slope based on the smoothed particle hydrodynamics method. *Front. Earth Sci.* 10:982658. doi: 10.3389/feart.2022.982658

COPYRIGHT
© 2023 Zhang, Song and Wu. This is an open-access article distributed under the terms of the Creative Commons Attribution License (CC BY). The use, distribution or reproduction in other forums is permitted, provided the original author(s) and the copyright owner(s) are credited and that the original publication in this journal is cited, in accordance with accepted academic practice. No use, distribution or reproduction is permitted which does not comply with these terms.

Simulation of collapse failure process of rock slope based on the smoothed particle hydrodynamics method

Xiaoqiang Zhang[1,2]*, Xiong Song[2] and Shunchuan Wu[1,2]

[1]Key Laboratory of Ministry of Education of China for Efficient Mining and Safety of Metal Mines, University of Science and Technology Beijing, Beijing, China, [2]Faculty of Land Resources Engineering, Kunming University of Science and Technology, Kunming, China

The limit equilibrium method (LEM) or finite element method (FEM) for slope problems most frequently focusses on the stability analysis. There are, however, still some problems with the LEM or FEM when considering damage and failure evolution of a rock slope because of the distortion of mesh. In this work, a mesh-free particle approach, named the smoothed particle hydrodynamics (SPH) method, is presented and is improved to analyze the damage and failure process of a rock slope. In order to better describe the cause and mechanism of brittle failure for a rock slope, the plastic factor was suggested and introduced into the SPH algorithm, and the conservation equations of SPH for brittleness characteristics were obtained. Based on the variation of displacement and time, an effective criterion was proposed to define the factor of safety in SPH simulation. The Drucker-Prager Mohr-Coulomb strength criterion was implemented into the SPH algorithm to describe the elastic-plastic behavior. Then, three rock-slope models with different precast cracks were analyzed to illustrate the performance of the proposed method. It is shown that the proposed SPH algorithm can be effectively applied in the prediction of the deformation and failure process of rock slope.

KEYWORDS

rock slope, smoothed particle hydrodynamics, slope collapse, instability process, slope failure

1 Introduction

Collapse is a widespread phenomenon in both natural and excavated rock slopes. It is a mass movement of rock characterized by downslope sliding, which can involve damage extension, penetration, and collapse. Therefore, the collapse of a rock slope has the obvious characteristics of a large deformation. The large deformation and failure process of rock slopes are so complex that obtaining an analytical solution is very difficult. In this sense, how to correctly describe the large deformation characteristics of rock slopes has been a hot but difficult problem in recent years. Compared with the complexities of experimental research and the limitations of theoretical research (Li et al., 2012), numerical simulation can give accurate solutions and predictions as long as

reasonable constitutive relations and calculation parameters are given. Hence, the simulation of the deformation and failure of rock structures has been more and more popular among scholars all over the world.

In recent years, some numerical methods have become increasingly popular to analyze large deformation and post-failure of slope, such as the Discrete Element Method (DEM) (Cundall and Strack, 1979; Wong et al., 1996), the Discontinuous Deformation Analysis (DDA) (Shi, 1991), the Remeshing and Interpolation Technique with Small Strain (RITSS) method (Hu and Randolph, 1998; Sitar et al., 2005; Tian et al., 2014) and Eulerian finite element methods (Wang et al., 2013). The most common software implementation of DEM is PFC2D and PFC3D, which was developed by Itasca. Although the DEM has the advantages of capturing the micromechanics of rock materials and handling large deformation of rock mechanics engineering (Zhang, 2012; Cao et al., 2016; Lin et al., 2019; Wang et al., 2020; Zhang et al., 2021), it is limited to small-scale problems because of the computational cost and large amounts of micro parameters. The DDA is mainly used to study the failure of rock engineering; the entire rock failure process of the slope has not yet been considered and there are difficulties in realistically modelling (Ning et al., 2012; Liu et al., 2019). The other two methods have significant drawbacks are, respectively, computational cost of remeshing in RITSS, and difficulty in handling free surfaces, multiple materials, and history variables in Eularian methods. On the other hand, several mesh-free methods have been developed and applied to solving rock fracture mechanics with large deformation and high non-linearity. Zhang et al. (2005) and Kwok et al. (2015) studied the stability and large deformation failure of the soil slope using the reproducing kernel particle method (RKPM). Wang et al. (2011) presented an efficient Galerkin meshfree formulation for the large deformation failure simulation of soil slope. Guo and Nairn (2006) applied the material point method (MPM) to simulate the large deformation of solids. Although meshless methods are suitable for solving the large deformation failure problem, they have difficulties in imposing an essential boundary condition and still have some limitations (Li and Liu, 2002). For example, the MPM method needs to match the material points through background grids (Zhang et al., 2009). Therefore, a suitable numerical simulation method is urgently needed for better modeling of the evolution process and interpretation of the mechanism of collapse.

A pure Lagrange mesh-less recently numerical method, namely, the smoothed particle hydrodynamics (SPH), was originally used in astrophysical problems (Gingold and Monaghan, 1977; Lucy, 1977). Subsequently, it has been widely applied in solving complex geotechnical problems. For example, Chen et al. (2012) applied the SPH method to the simulation of granular materials under large deformation. Bui and Fukagawa (2013) used the SPH to simulate large deformation and post-failure of the soil slope. Due to its Lagrangian properties, it has a unique advantage in dealing with problems of large deformations and discontinuities. Hence, it also seems promising for a complete rock failure analysis.

The object of this paper is to use the SPH method to model the large deformation and failure process of rock slopes. For large deformation and failure process of slope problems, its essence is the elastic-plastic deformation (Gao et al., 2006; Kong et al., 2014; Drucker and Prager, 2013). In this paper, the Drucker-Prager (D-P) constitutive model with a non-associated plastic flow rule is implemented in the SPH code to simulate the large deformation and failure of a slope. In the following sections, numerical examples involving the collapse of a slope are carried out to demonstrate the effectiveness of the proposed method, which show that SPH is much more efficient than FEM in simulating slope problems, especially where large deformation and failure process are involved. The research results can provide some references for the applications of the SPH method to understand the mechanisms of crack propagation and early warning of rock slope instability.

2 Fundamental theory of SPH

2.1 Basic formulation of SPH algorithms

In the SPH method, an object is expressed as an assembly of particles with associated variables, such as mass, energy, and stress tensors. The basic idea behind this method is to provide stable and accurate numerical solutions for partial differential equations (PDEs) using a group of particles. The SPH method is based on interpolation theory. The governing equations, in the form of PDEs, can be transformed into SPH form through two main steps. The first step is to represent a function in continuous form as an integral representation using an interpolation function:

$$\langle f(x)\rangle = \int_{\Omega} f(x')w(x-x',h)dx' \tag{1}$$

where the angle brackets < > denote a kernel approximation, x represents the location vector of the particle, Ω is the volume of the integral that contain x, and x' is a neighboring particle in the support area. The parameter h defines the size of the kernel support, known as the smoothing length. $W(x-x_j,h)$ is the smoothing or kernel function. The second step is named the particle approximation, and is expressed as follows:

$$\langle f(x)\rangle = \sum_{j=1}^{N} m_j \frac{f(x_j)}{\rho_j} W(x-x_j,h) \tag{2}$$

where N is the total number of neighboring particles, m is the mass, ρ is the density, and j is the j-th particle. This step makes the SPH method simple without requiring a background mesh for

numerical integration. W is the smoothing or kernel function, which can be expressed as:

$$W(q,h) = \alpha_d \times \begin{cases} \frac{2}{3} - q^2 + \frac{1}{2}q^3, & 0 \le q < 1 \\ \frac{1}{6}(2-q)^3, & 1 \le q < 2 \\ 0, & q \ge 2 \end{cases} \tag{3}$$

where $\alpha_d = \frac{10}{(7\pi h^2)}$ for two dimensional conditions, q is the normalized distance between particles i and j, defined as $q = \frac{r}{h} = \frac{|x-x'|}{h}$, and h is the smoothing length.

2.2 Governing equations and discretization

In this study, the governing equations are mainly based on the solid mechanics. So, the equations of continuity and motion can be expressed as follows:

Equation of continuity:

$$\frac{D\rho}{Dt} = -\frac{1}{\rho}\frac{\partial v^\alpha}{\partial x^\alpha} \tag{4}$$

Equation of motion:

$$\frac{Dv^\alpha}{Dt} = \frac{1}{\rho}\frac{\partial \sigma^{\alpha\beta}}{\partial x^\beta} + g^\alpha \tag{5}$$

where x^α, v^α, and $\sigma^{\alpha\beta}$ are, respectively, elements of the spatial coordinate, velocity vector, and Cauchy stress tensor (σ), which is given by:

$$\sigma^{\alpha\beta} = \tau^{\alpha\beta} - p\delta^{\alpha\beta} \tag{6}$$

$\frac{d}{dt}$ is the time derivation taken in the moving Lagrange framework, and the superscripts α, β = 1, 2 are integer indices for the two spatial directions. g is the component of acceleration caused by external force, which is the gravity force in this study.

The differential form of the conservation equations can be converted to a discretized weak form as:

$$\frac{d\rho_i}{dt} = \sum_j m_j v_{ij}^\beta W_{ij,\beta} \tag{7}$$

$$\frac{dv_i^\alpha}{dt} = -\sum_j m_j \left(\frac{\sigma_i^{\alpha\beta}}{\rho_i^2} + \frac{\sigma_j^{\alpha\beta}}{\rho_j^2}\right) W_{ij,\beta} \tag{8}$$

where $v_{ij}^\alpha = v_i^\alpha - v_j^\alpha$, and $W_{ij,\beta} = \frac{\partial W(x_j - x_i, h)}{\partial x_i^\beta}$ is the kernel gradient with smoothing length h.

2.3 Elastic-plastic constitutive model

Here, the elastic-plastic constitutive model of soil material implemented in the SPH code is described in detail. The component of the total strain rate tensor is given by:

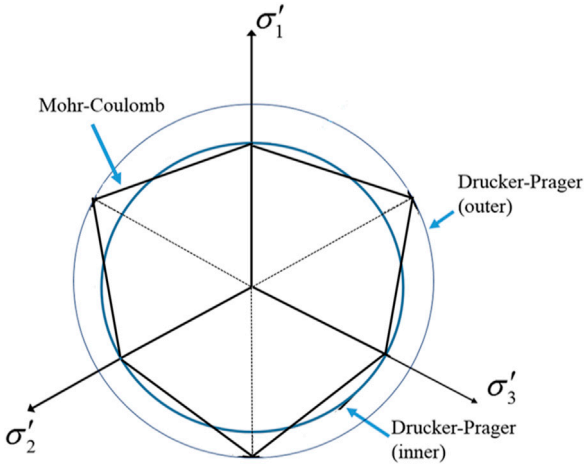

FIGURE 1
π-plane section of the Drucker-Prager yield surface.

$$\dot{\varepsilon}^{\alpha\beta} = \frac{1}{2}\left(\frac{\partial v^\alpha}{\partial x^\beta} + \frac{\partial v^\beta}{\partial x^\alpha}\right) \tag{9}$$

For the elastoplastic material, the total strain rate tensor $\dot{\varepsilon}^{\alpha\beta}$ is obtained by the following formula:

$$\dot{\varepsilon}^{\alpha\beta} = \dot{\varepsilon}_e^{\alpha\beta} + \dot{\varepsilon}_p^{\alpha\beta} \tag{10}$$

where the elastic strain rate tensor $\dot{\varepsilon}_e^{\alpha\beta}$ can be expressed as

$$\dot{\varepsilon}_e^{\alpha\beta} = \frac{\dot{s}^{\alpha\beta}}{2G} + \frac{1-2\nu}{3E}\dot{\sigma}^{\gamma\gamma}\delta^{\alpha\beta} \tag{11}$$

where G is shear modulus, $\dot{s}^{\alpha\beta}$ is the deviatoric stress rate tensor, E is the elasticity modulus, and ν is Poisson's ratio. $\delta^{\alpha\beta}$ is named Kronecker's delta, where $\delta^{\alpha\beta}$ = 1.0 when $\alpha = \beta$, and $\delta^{\alpha\beta}$ = 0.0 when $\alpha \neq \beta$. The plastic strain rate tensor, $\dot{\varepsilon}_p^{\alpha\beta}$, of any particle can be given by the plastic flow rules:

$$\dot{\varepsilon}_p^{\alpha\beta} = \dot{\lambda}\frac{\partial g}{\partial \sigma^{\alpha\beta}} \tag{12}$$

where $\dot{\lambda}$ is the rate of change of the plastic multiplier λ. The value of plastic multiplier λ can be calculated by using the consistency condition.

2.4 Drucker-Prager (D-P) model

Rock material is a kind of brittle material. When the load reaches the yield strength, it will be damaged and weakened, at which point it is an elastic-plastic body. In this paper, the D-P criterion is selected as the yield criterion of elastoplastic materials. The expression is as follows:

$$f(\sigma, c) = \sqrt{J_2(s)} + \alpha_\varphi I_1(\sigma) - k_c \tag{13}$$

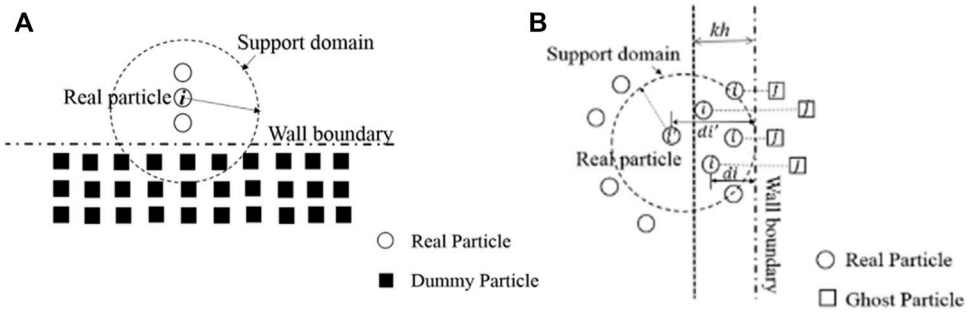

FIGURE 2
The sketch of two types of boundary condition: **(A)** dummy particles for fixed boundary; **(B)** ghost particles for free-rolling boundary.

where

$$\alpha_\varphi = \frac{\tan\varphi}{\sqrt{9 + 12\tan^2\varphi}} \tag{14a}$$

for 2D plane strain conditions and

$$k_c = \frac{3c}{\sqrt{9 + 12\tan^2\varphi}} \tag{14b}$$

where c and φ are the cohesion internal and friction angle of geomaterials. In the principal stress space, the yield surface of the D-P criterion is a cone, and the yield curves corresponding to different material parameters are circles of different sizes on the off plane (see Figure 1).

In the present study, the non-associated flow rule is considered to determine the stress-strain relationship. The plastic potential function, g, is calculated by:

$$g(\sigma, c) = \sqrt{J_2(s)} + \alpha_\psi I_1(\sigma) - \sin\psi \tag{15}$$

where ψ is the dilatancy angle, α_ψ is a dilatancy factor which is related to the dilatancy angle, and I_1 and J_2 respectively denote the first and second stress invariant.

Here, the D-P yield criterion is employed to determine the plastic region of soils. Plastic strain is initiated from a particle when stresses in the particle satisfy the D-P yield criterion. Once plastic state is reached in one particle, the plastic deformation is initiated from this particle. Therefore, the discrete conservation equations of SPH for plastic characteristics can be expressed as:

$$\frac{dv_i^\alpha}{dt} = -\sum_{j\in U}^{N} m_j\left(\frac{\sigma_i^{\alpha\beta}}{\rho_i^2} + \frac{\sigma_j^{\alpha\beta}}{\rho_j^2}\right)W_{ij,\beta} - f_{\text{Plastic}}\cdot\sum_{j\in P}^{N} m_j\left(\frac{\sigma_i^{\alpha\beta}}{\rho_i^2} + \frac{\sigma_j^{\alpha\beta}}{\rho_j^2}\right)W_{ij,\beta} + \mathrm{g}^\alpha \tag{16}$$

$$\frac{d\rho_i}{dt} = \sum_{j\in U}^{N} m_j v_{ij}^\beta W_{ij,\beta} + f_{Plastic}\cdot\sum_{j\in P}^{N} m_j v_{ij}^\beta W_{ij,\beta} \tag{17}$$

where v_i^α denotes the velocity vector of the i-th particle, $v_{ij}^\beta = v_i^\beta - v_j^\beta$; m_j is the mass of the j-th particle; ρ_i is the mass density of the i-th particle; and f_{Plastic} is the plastic factor, which defines the plastic level between the i-th and j-th particles. For the elastic state particles, $f_{\text{Plastic}} = 1.0$, and for the plastic state particles, $f_{\text{Plastic}} = 0.0$.

3 Boundary treatment and verification

3.1 Boundary treatment

Particle deficiency might be encountered near or on a boundary by using the SPH method. Therefore, the boundary condition is a significant input in achieving accurate simulation results. Several methods were put forward to resolve this problem, but the most effective way is to use ghost particles and dummy particles. For the slope problem, this is divided into two kinds of boundary conditions: fixed boundary conditions and free-rolling boundary conditions.

To simulate the fixed boundary, three layers of dummy particles are generated on boundaries. If the support domain of particle i intersects with the wall boundary, the dummy particles in the intersecting region assist to the SPH calculation like real particles, as shown in Figure 2A. The velocity of boundary particles is set to zero, which means the fixed condition. The stress value of boundary particles is given the stress value of the real particle i. As for free-rolling boundary condition, it is modeled by adopting ghost particles. As shown in Figure 2B, if the horizontal distance di (particle i) is less than a certain distance kh, a ghost particle is placed symmetrically on the outside of the boundary and if di' (particle i') is greater than kh, the ghost particle is not added. The velocity and stress tensor of ghost particles can be assigned *via*

$$v_G^{xx} = v_i^{xx} \text{ and } v_G^{yy} = v_i^{yy} \tag{18a}$$

$$\sigma_G^{\alpha\beta} = \begin{cases} \sigma_i^{\alpha\beta}, & if\ \alpha = \beta \\ -\sigma_i^{\alpha\beta}, & if\ \alpha \neq \beta \end{cases} \tag{18b}$$

where v_G^{xx} denotes normal velocity of ghost particles, v_G^{yy} denotes normal velocity of ghost particles, and v_i^{xx} and v_i^{yy} are the velocity of real particles. $\sigma_G^{\alpha\beta}$ is the stress tensor of ghost particles, and $\sigma_i^{\alpha\beta}$ is the stress tensor of real particles.

3.2 Treatment effect verification

The developed FORTRAN program is validated with a 2D rectangle model. In the SPH simulation, a total number of 5000 real particles and 3000 boundary particles are used to form a rectangular area 4.0 m in length and 2.0 m in height, as shown in Figure 3. The material properties of the simulated rock are: Young's modulus, $E = 1.8$MPa; Poisson's ratio, $\mu = 0.3$; density, $\rho = 1850$ g/cm^3; cohesion, $c = 5.0$ kPa; and internal friction angle, $\varphi = 30^\circ$. The SPH particles are arranged in a square lattice with an initial lattice constant of 0.04 cm and an initial smoothing length of 0.048 cm.The time step is 0.0001s.

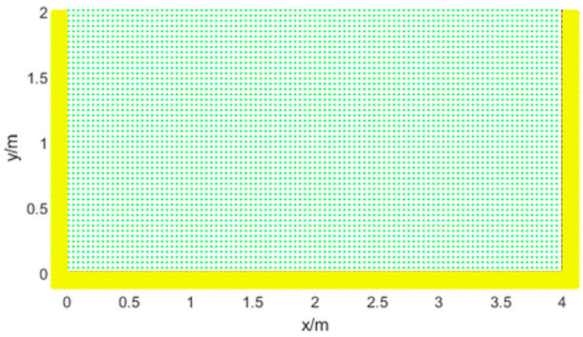

FIGURE 3
Initial setting conditions in SPH model.

Under the action of self weight, the vertical stress distribution of the model is shown in Figure 4. In the model, a fixed boundary is adopted at the bottom and a free-slip boundary is adopted at both sides. It can be seen that the vertical stress distribution is uniform and increases gradually with the depth, which conforms to the general law. Figure 4B shows the boundary without kernel interpolation treatment. Since the dummy particles at the bottom do not generate confining pressure, the constraint on the real particles at the bottom only depends on the repulsion force of the fixed dummy particles, and the selection of the repulsion force is subjective, resulting in obvious layered oscillation of the particle stress at the bottom. By comparison, in Figure 4A the stress distribution of particles at the bottom of the boundary treated by kernel interpolation is uniform, indicating that the boundary treated by kernel interpolation can effectively ensure the stress transfer. Therefore, the stress stratification can be effectively removed by treating the boundary with dummy particles and ghost particles in the SPH method, and the stability of stress transfer can be maintained, which shows that this method is feasible.

4 Application of the SPH numerical method

In this section, rock slopes with one and three pre-cracks are simulated using the proposed method. Meanwhile, a determining method for SPH safety factor based on a strength reduction method is proposed. The result is then compared with those of the finite element numerical simulation method (FEM) to verify the correctness of the proposed method. In all examples, the linear cohesive law is adopted, and the smoothing length (h) is chosen to be $h = 1.2dx$ with dx being the initial spacing between

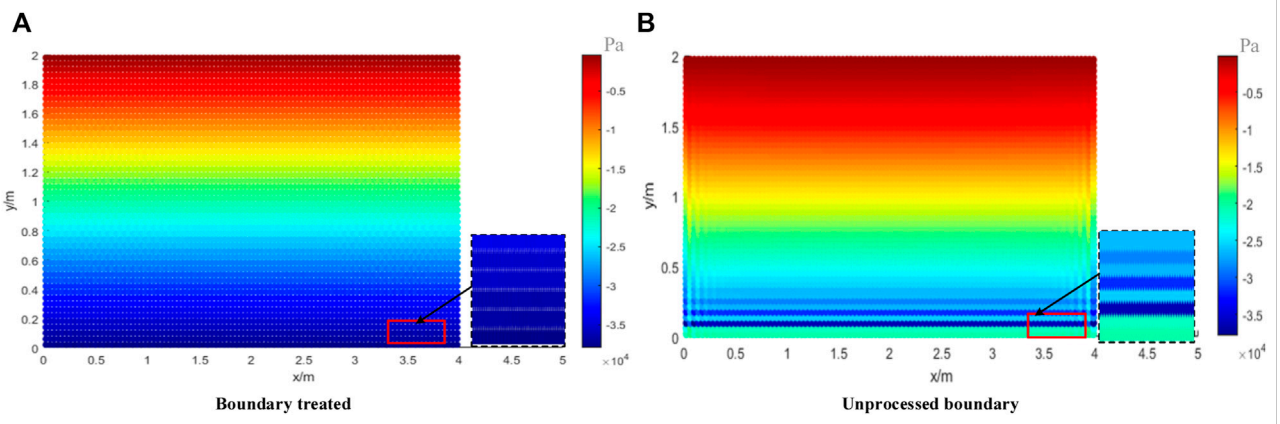

FIGURE 4
Comparison of boundary treatment results: **(A)** Vertical stress distribution of soil after boundary treatment; **(B)** Vertical stress distribution of soil without boundary treatment.

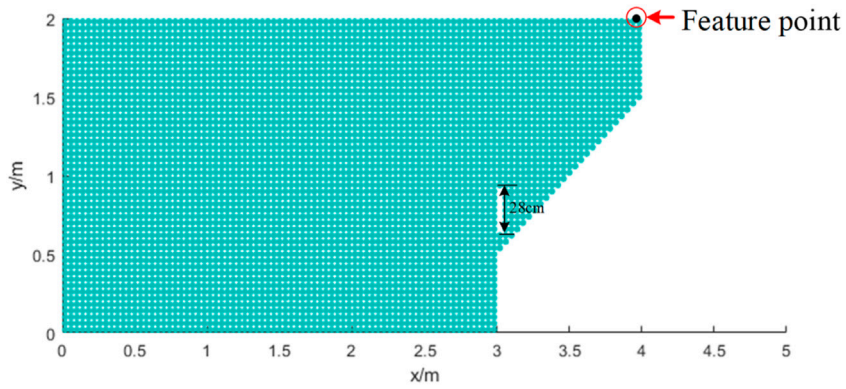

FIGURE 5
Schematic of SPH model, flaw length is 28 cm.

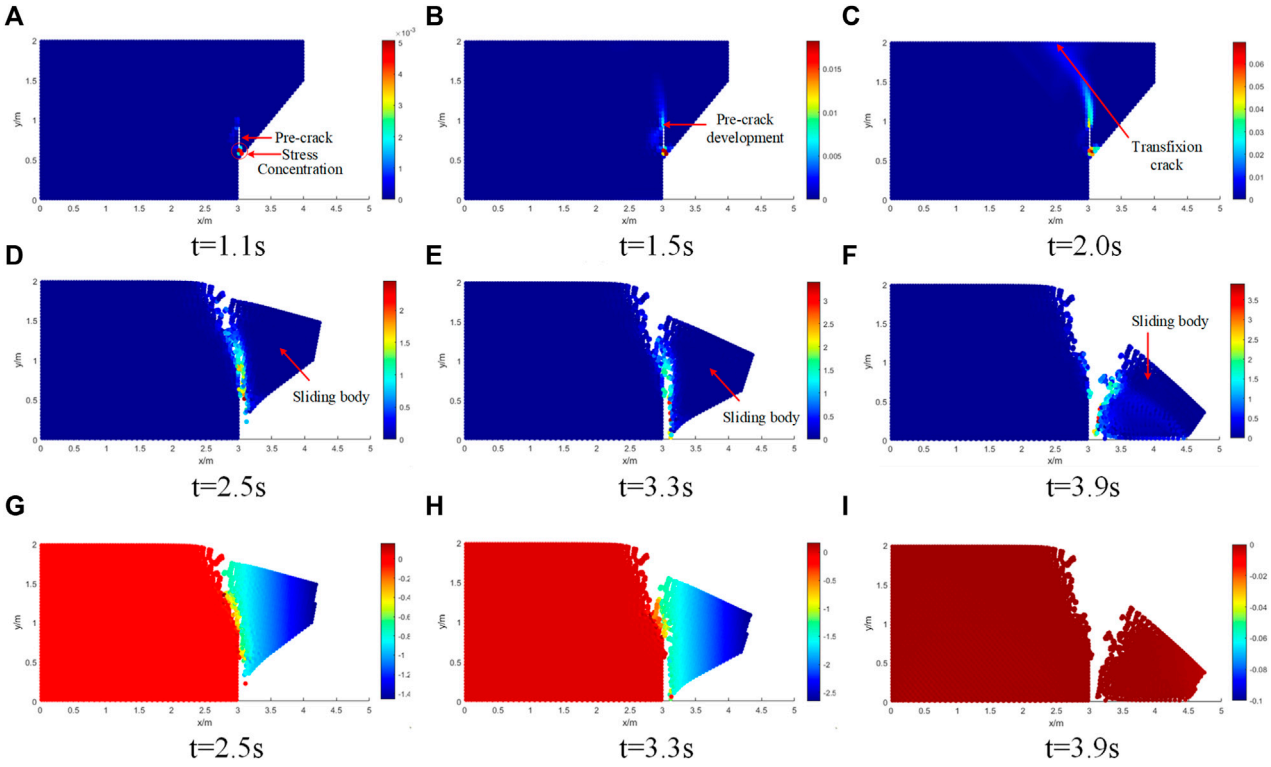

FIGURE 6
Development of collapse and sliding velocity at different times: Cumulative equivalent plastic strain **(A-F)**; Slip velocity **(G-I)**.

TABLE 1 Physical parameters of SPH model.

Young's modulus, *E*/MPa	Poisson's ratio, *v*	Density, ρ/(g/cm^3)	Cohesion, *c*/kPa	Internal friction angleφ/°
50	0.3	1850	20	25

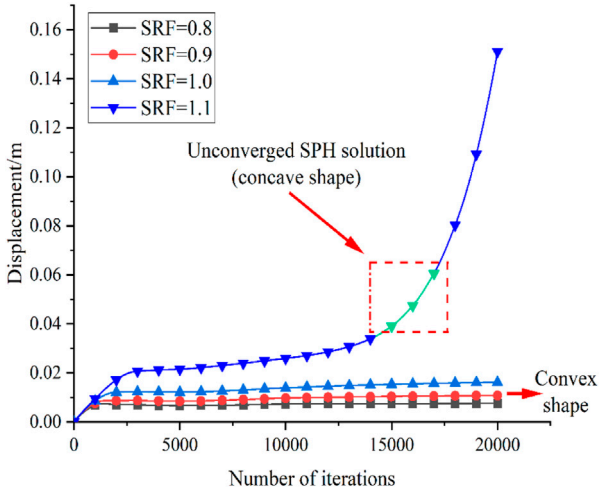

FIGURE 7
Relationship between displacement and strength reduction coefficient (SRF).

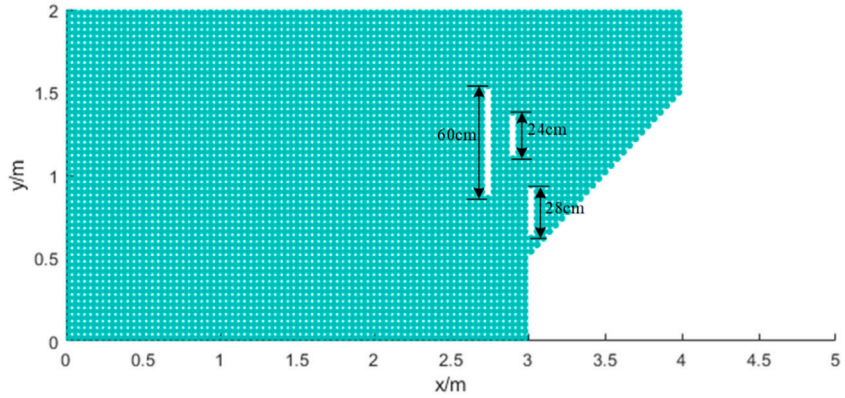

FIGURE 8
Schematic of SPH model, flaws length are 60, 28, and 24 cm, respectively.

two consecutive SPH particles. All numerical tests are carried out in the plane stress condition.

4.1 Simulation of a rock slope collapse process with one pre-crack

A rock slope model produced by the SPH method is carried out in this section. The purpose of this test is to verify the performance of the proposed numerical framework in simulating slope collapse. The geometry and boundary conditions of this test are shown in Figure 5. The model is 400 cm long and 200 cm height. The initial pre-crack has a width of 4 cm and a length of 28 cm. A total of 4368 particles have been used and the initial distance between particles is $\Delta x = 0.04m$ in the SPH model. The boundary conditions are described in Section 3.1. The material parameters are given in Table 1.

The development process of failure and collapse plotted by accumulated equivalent plastic strain for the rock slope at different times is shown in Figure 6. The development of the velocity of rock failure at different times is shown in Figure 6G–I.

Figure 6A shows the stress concentration at the tip of the pre-crack under the action of gravity. Figure 6B shows that the pre-crack development and the slope is in a state of stability but does

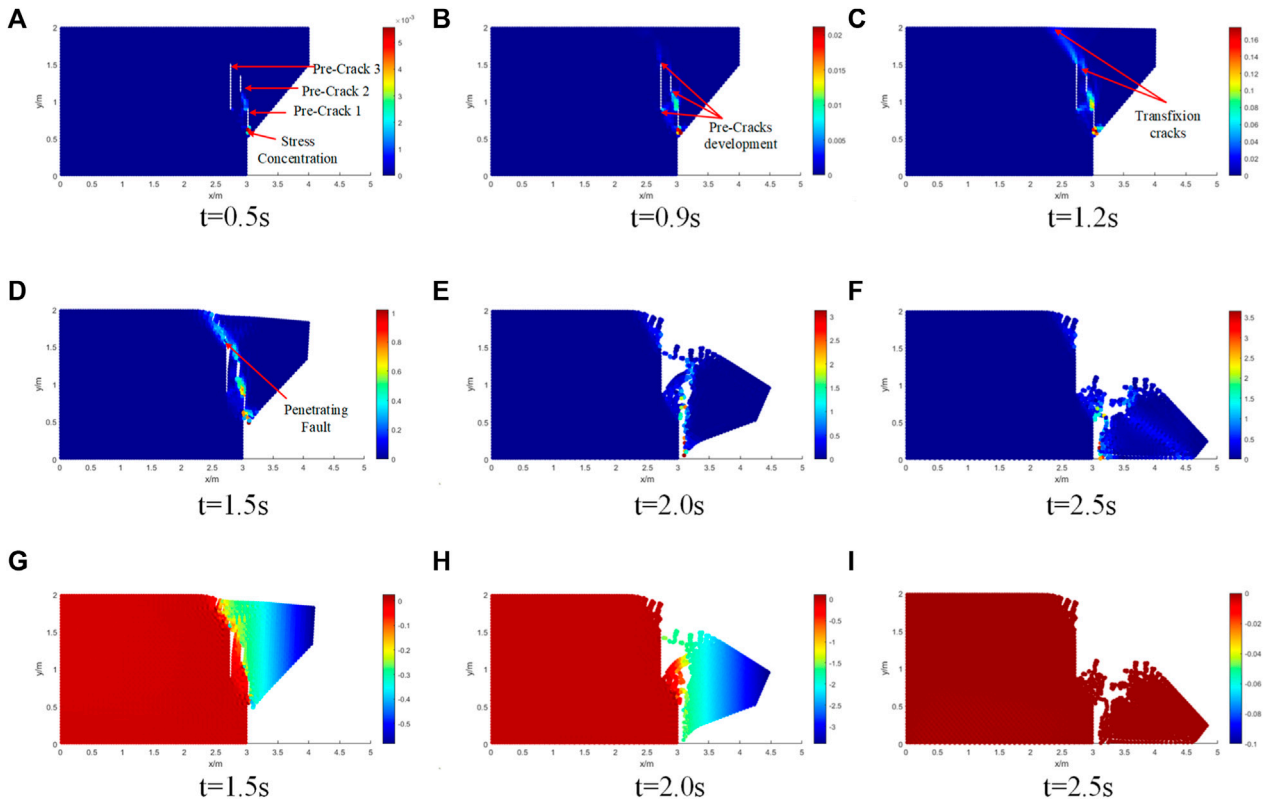

FIGURE 9
Development of collapse and sliding velocity at different times: Cumulative equivalent plastic strain **(A-F)**; Slip velocity **(G-I)**.

not completely fail at T=1.5 s, because the accumulated equivalent plastic strain zone is propagating from the toe to the crest at this moment. Then, the plastic shear strains band spreads forwards and upwards, and eventually the plastic shear strains are connected from the crest to the toe of the slope in Figure 6C, forming a slip surface. Figure 6D clearly shows that the slope begins to fail as a block along the surface, and the sliding body is not completely separated from the slope body. As time progresses, the sliding body displacement experiences a significant horizontal direction downwards as completely seen in the discrete block in Figures 6E,F. It can be corroborated by the velocity nephogram, as shown in Figure 6I, that the sliding velocity of slope collapse is zero, which means that the movement and collapse of the slope has stopped.

4.2 Determination of safety factor

The failure criterion for slope stability analysis in the finite element method with shear strength reduction (SRF) technique, proposed by Griffiths and Lane (1999), is based on consideration of the relation between node displacements and SRF values. If a sudden change is observed in the node displacement within a user-specified maximum number of interactions, the computation is considered to be non-convergent, and the critical value of SRF yielding a non-convergent solution is considered to be the safety factor of the slope. However, the failure criterion for slope stability analysis in SPH is not applicable to the FEM, because SPH simulation cannot cause a non-convergent solution with any reduction factor. Rather, a simple approach is proposed to define the factor of safety in an SPH simulation.

The approach is based on the maximum displacement at the feature point (see Figure 5) during a specified time duration for each value of SRF. If the maximum displacement at the feature point remains unchanged or the value of this maximum displacement is relatively small at a reduction factor, the slope is defined as stable. On the other hand, if the maximum displacement cannot converge to a small and stable value, the failure develops, and the corresponding SRF is considered as the safety factor of the slope.

In this paper, the process of the reduction is described as follows: The reduction factor of the SRF is initially set as 1.0 and then is increased by a step size of 0.1 during the next calculation.

Note that if SRF is less than 1.0, this factor would be reduced, and the criterion determining the safety factor of the slope should be adjusted. When a sudden increase in feature point displacement appears, the failure of the slope occurs. Thus, the corresponding SRF at current computation is considered to be the safety factor. Thus, Figure 7 shows the calculation result as a safety factor is 1.1.

4.3 Simulation of a rock slope collapse process with three precast-cracks

Similarly, in order to further verify the effectiveness of the proposed method in the instability prediction and failure process of a rock slope, a model produced by the SPH method is carried out with three precast cracks. The initial pre-cracks have a width of 4 cm and lengths of 60cm, 28 and 24 cm, respectively (see Figure 8). The material parameters, initial distance between particles and boundary conditions are consistent with those described above (Table 1).

The development process of the failure surface plotted by accumulated equivalent plastic strain for rock slope at different times is shown in Figure 9 and also documents the nature of the slope failure mechanism.

As shown in Figure 9A, under the action of self weight, pre-crack one shows stress concentration and expands to crack 2. When the time is equal to 0.9s, cracks one and 2 run through. At the same time, stress concentration occurs at the bottom of crack 3, as shown in Figure 9B. As can be seen from Figure 9C, with the increase of calculation time, the top of crack three runs through the top of the slope, and the stress concentration appears at the top of crack 2 and extends to the top of crack 3.

With the further increase of time, the cracks completely penetrated the whole slope body, the slope body became unstable, and local collapse occurred, as shown in Figure 9D. The collapse is further aggravated, as shown in Figure 9E, but the sliding body is not completely separated from the slope body at this time. Compared with Figure 9H, it is found that the sliding body still has a certain speed at this time, indicating that the slope collapse has not stopped. When the time is equal to 2.5 s, the sliding body completely separates from the slope body. According to the comparison of Figure 9I, the speed of the sliding body is zero at this time, which demonstrates the complete collapse of the slope and reflects the movement characteristics after instability.

5 Conclusion

The SPH code with D-P constitutive model is applied to investigate the collapse of rock slopes for the first time in this paper. For slope stability, the development of the shear band or failure process is well predicted through the accumulated plastic strain. The numerical results show that the SPH method is a reliable and robust method to simulate failure and collapse processes of geomaterials. Meanwhile, the successful application in rock slope collapse modeling indicates that the SPH method should be allowed further developments for other applications in geotechnical engineering.

Data availability statement

The raw data supporting the conclusions of this article will be made available by the authors, without undue reservation.

Author contributions

XZ and ZS were responsible for the work concept or design; XS was responsible for drafting the manuscript; SW were responsible for making important revisions to the manuscript; XZ and SW were responsible for approving the final version of the manuscript for publication.

Funding

The work was supported by the National Natural Science Foundation of China (Nos. 51934003), the Key Laboratory of Ministry of Education of China for Efficient Mining and Safety of Metal Mines (No. ustbmslab201906), the Research Start-up Fund for Introduced Talent of Kunming University of Science and Technology (KKSY201921029), The Yunnan Fundamental Research (NO. 202001AU070027).

Conflict of interest

The authors declare that the research was conducted in the absence of any commercial or financial relationships that could be construed as a potential conflict of interest.

Publisher's note

All claims expressed in this article are solely those of the authors and do not necessarily represent those of their affiliated organizations, or those of the publisher, the editors and the reviewers. Any product that may be evaluated in this article, or claim that may be made by its manufacturer, is not guaranteed or endorsed by the publisher.

References

Bui, H. H., and Fukagawa, R. (2013). An improved sph method for saturated soils and its application to investigate the mechanisms of embankment failure: Case of hydrostatic pore-water pressure. *Int. J. Numer. Anal. Methods Geomech.* 37 (1), 31–50. doi:10.1002/nag.1084

Cao, R. H., Cao, P., Fan, X., Xiong, X., and Lin, H. (2016). An experimental and numerical study on mechanical behavior of ubiquitous-joint brittle rock-like specimens under uniaxial compression. *Rock Mech. Rock Eng.* 49 (11), 4319–4338. doi:10.1007/s00603-016-1029-6

Chen, W., Qiu, Tong., and Asce, M. (2012). Numerical simulations of granular materials using smoothed particle hydrodynamics method. *Int. J. Geomechanics* 12 (2), 127–135. doi:10.1061/47628(407)20

Cundall, P. A., and Strack, O. D. L. (1979). A discrete numerical model for granular assemblies. *Geotechnique* 29 (1), 47–65. doi:10.1680/geot.1979.29.1.47

Drucker, D. C., and Prager, W. (2013). Soil mechanics and plastic analysis or limit design. *Q. Appl. Math.* 10 (2), 157–165. doi:10.1090/qam/48291

Gao, Y. F., Bower, A. F., Kim, K. S., Lev, L., and Cheng, Y. T. (2006). The behavior of an elastic–perfectly plastic sinusoidal surface under contact loading. *Wear* 261 (2), 145–154. doi:10.1016/j.wear.2005.09.016

Gingold, R. A., and Monaghan, J. J. (1977). Smoothed particle hydrodynamics: Theory and application to non-spherical stars. *Mon. notices R. astronomical Soc.* 181, 375–389. doi:10.1093/mnras/181.3.375

Griffiths, D. V., and Lane, P. A. (1999). Slope stability analysis by finite elements. *Geotechnique* 49 (3), 387–403. doi:10.1680/geot.1999.49.3.387

Guo, Y. J., and Nairn, J. A. (2006). Three-dimensional dynamic fracture analysis using the material point method. *Comput. Model. Eng. Sci.* 16 (1), 141–155. doi:10.1139/T07-900

Hu, Y., and Randolph, M. F. (1998). H-adaptive FE analysis of elasto-plastic non-homogeneous soil with large deformation. *Comput. Geotech.* 23 (2), 61–83. doi:10.1016/S0266-352X(98)00012-3

Kong, G., Zhou, H., Cao, Z., and Liu, H. (2014). Analytical solution for pressure-controlled elliptical cavity expansion in elastic–perfectly plastic soil. *Geotech. Lett.* 4 (2), 72–78. doi:10.1680/geolett.14.00004

Kwok, O. L. A., Guan, P. C., Cheng, W. P., and Sun, C. T. (2015). Semi-Lagrangian reproducing kernel particle method for slope stability analysis and post-failure simulation. *KSCE J. Civ. Eng.* 19 (1), 107–115. doi:10.1007/s12205-013-0550-3

Li, S., and Liu, W. K. (2002). Meshfree and particle methods and their applications. *Appl. Mech. Rev.* 55 (1), 1–34. doi:10.1115/1.1431547

Li, W. C., Li, H. J., Dai, F. C., and Lee, L. M. (2012). Discrete element modeling of a rainfall-induced flowslide. *Eng. Geol.* 149-150, 22–34. doi:10.1016/j.enggeo.2012.08.006

Lin, H., Yang, H., Wang, Y., Zhao, Y., and Cao, R. (2019). Determination of the stress field and crack initiation angle of an open flaw tip under uniaxial compression. *Theor. Appl. Fract. Mech.* 104, 102358. doi:10.1016/j.tafmec.2019.102358

Liu, G., Li, J., and Kang, F. (2019). Failure mechanisms of toppling rock slopes using a three-dimensional discontinuous deformation analysis method. *Rock Mech. Rock Eng.* 52, 3825–3848. doi:10.1007/s00603-019-01797-6

Lucy, L. B. (1977). A numerical approach to the testing of the fission hypothesis. *Astron. J.* 8 (12), 1013–1024. doi:10.1086/112164

Ning, Y. J., An, X. M., Lü, Q., and Ma, G. W. (2012). Modeling rock failure using the numerical manifold method followed by the discontinuous deformation analysis. *Acta Mech. Sin.* 28 (3), 760–773. doi:10.1007/s10409-012-0055-1

Shi, G. H. (1991). *Manifold method of material analysis. Transactions of the 9 army conference on applied mathematics and computing*. Durham, United States: U. S. Army Research Office.

Sitar, N., Maclaughlin, M. M., and Doolin, D. M. (2005). Influence of kinematics on landslide mobility and failure mode. *J. Geotech. Geoenviron. Eng.* 131 (6), 716–728. doi:10.1061/(asce)1090-0241(2005)131:6(716)

Tian, Y., Cassidy, M. J., Randolph, M. F., Dong, W., and Gaudin, C. (2014). A simple implementation of ritss and its application in large deformation analysis. *Comput. Geotech.* 56 (3), 160–167. doi:10.1016/j.compgeo.2013.12.001

Wang, D. D., Li, Z. Y., Li, L., and Wu, Y. C. (2011). Three dimensional efficient meshfree simulation of large deformation failure evolution in soil medium. *Sci. China Technol. Sci.* 54, 573–580. doi:10.1007/s11431-010-4287-7

Wang, D., Randolph, M. F., and White, D. J. (2013). A dynamic large deformation finite element method based on mesh regeneration. *Comput. Geotechnics* 54 (10), 192–201. doi:10.1016/j.compgeo.2013.07.005

Wang, J., Wei, W., Zhang, J., and Mishra, B. (2020). Numerical investigation on the caving mechanism with different standard deviations of top coal block size in LTCC. *Int. J. Min. Sci. Technol.* 30 (5), 583–591. doi:10.1016/j.ijmst.2020.06.001

Wong, R., Chau, K. T., and Wang, P. (1996). Microcracking and grain size effect in yuen long marbles. *Int. J. Rock Mech. Min. Sci. Geomechanics Abstr.* 33 (5), 479–485. doi:10.1016/0148-9062(96)00007-1

Zhang, B., He, Q., Lin, Z., and Li, Z. (2021). Experimental study on the flow behaviour of water-sand mixtures in fractured rock specimens. *Int. J. Min. Sci. Technol.* 31 (3), 377–385. doi:10.1016/j.ijmst.2020.09.001

Zhang, H. W., Wang, K. P., and Chen, Z. (2009). Material point method for dynamic analysis of saturated porous media (ii): Dynamic contact analysis between saturated porous media and solid bodies. *Chin. J. Geotechnical Eng.* 31 (11), 1672–1679. doi:10.1115/1.1431547

Zhang, J. F., Zhang, W. P., and Yao, Z. (2005). A meshfree method and its applications to elasto-plastic problems. *J. Zhejiang Univ. Sci.* 6 (2), 148–154. doi:10.1631/jzus.2005.a0148

Zhang, L., Jin, H., Huang, J., Lu, H., Guan, Y., Chen, X., et al. (2012). Local delivery of pravastatin inhibits intimal formation in a mouse vein graft model. *Can. J. Cardiol.* 28 (6), 750–757. doi:10.1016/j.cjca.2012.01.018

Frontiers in Earth Science

Investigates the processes operating within the major spheres of our planet

Advances our understanding across the earth sciences, providing a theoretical background for better use of our planet's resources and equipping us to face major environmental challenges.

Discover the latest Research Topics

See more →

Frontiers

Avenue du Tribunal-Fédéral 34
1005 Lausanne, Switzerland
frontiersin.org

Contact us

+41 (0)21 510 17 00
frontiersin.org/about/contact